# Mechanochemical Reactions and Strengthening in Epoxy-Cast Aluminum Iron-Oxide Mixtures

A Dissertation
Presented to
The Academic Faculty

by

Louis Ferranti, Jr.

In Partial Fulfillment
of the Requirements for the Degree
Doctor of Philosophy

in the

School of Materials Science and Engineering

Georgia Institute of Technology
December 2007

# Mechanochemical Reactions and Strengthening in Epoxy-Cast Aluminum Iron-Oxide Mixtures

Approved by:


Dr. Naresh N. Thadhani, Chairperson
School of Materials Science & Engineering
and School of Mechanical Engineering
*Georgia Institute of Technology*

Dr. Kenneth A. Gall
School of Materials Science & Engineering
*Georgia Institute of Technology*

Dr. Min Zhou
School of Mechanical Engineering and
School of Materials Science & Engineering
*Georgia Institute of Technology*

Dr. Ronald W. Armstrong, Emeritus
School of Mechanical Engineering
*University of Maryland*

Dr. David L. McDowell
School of Mechanical Engineering and
School of Materials Science & Engineering
*Georgia Institute of Technology*

Dr. Yasuyuki Horie
Energetic Materials Division of
Munitions Directorate (MNME)
*Air Force Research Laboratory*



Date Approved: 25 October 2007

*In loving memory of*
*Grace and Mario*

# ACKNOWLEDGEMENTS

Many people have been instrumental in the completion of this work. I would like to express my sincere gratitude to my advisor Dr. Naresh Thadhani for his guidance and advice throughout the course of this work. I would also like to thank the members of the thesis reading committee, Dr. Min Zhou, Dr. Dave McDowell, Dr. Ken Gall, Dr. Ron Armstrong, and Dr. Yuki Horie for their insightful thoughts, suggestions, and guidance. I especially thank Dr. Ron Armstrong for his mentoring, particularly while serving as senior scientist for the Energetic Materials Branch of the Air Force Research Laboratory and for being instrumental in establishing collaboration for the first graduate student internship of its kind. I have been inspired by his dedication, work ethics, and principles that I will continue to value as I embark upon my career, and will aspire to such always.

My respectful gratitude also goes to my colleagues and previous research group members Jennifer Jordan, Greg Kennedy, Rodney Russell, Kevin Vandersall, and Xiao Xu (Chris), as well as current members Anthony Fredenberg, Kit Neel, Morgana Martin, Dan Eakins, Chris Wehrenberg, and Brad White. I am thankful to our former post doc Dr. Zhiqiang Jin for all of his assistance and to our current post doc Dr. Chengda Dai. I would also like to thank Ryan Austin, Nitin Patel, Vikas Tomar, Phillip Grahm, Mike Middlemas, and Melony Kirkham for their helpful collaboration and assistance.

Our research group had an outstanding undergraduate crew that supported the daily work performed in the laboratory and assisted with miscellaneous tasks that were instrumental in completing this research. I would like to thank Jim Painter, Philip Draa, Charles Ballowe, Arsalan Siddiqi, Daniel Miller, Ryan Crawford, and Jim Amato for all of their assistance. I would also like to thank the staff in the Materials Science and Engineering Department for their daily support, especially Susan Bowman, Vicki Speights, and Marlene White. I additionally thank John Graham, from the Mechanical Engineering Machine Shop, for his help with specimen preparation and expertise in shop equipment operation.

Funding for this work was provided in part by the Air Force Office of Scientific Research (AFOSR) Multi-University Research Initiative (MURI) under grant F49620-02-1-0382 (Dr. Craig Hartley, program manager) and by a graduate research internship through Air Force Research Laboratory, Eglin AFB, Energetic Materials Division of Munitions Directorate (AFRL/MNME) under contract F08630-03-C-001 (David Wayne Richards, program manager). I would like to thank the members of AFRL High Explosives Research and Development Facility (HERD) for their assistance both during my term before and throughout the course of this work. I would especially like to thank Wayne Richards, John Corley, Bill Wilson, Mike Kramer, Robin Hunt-Kramer, Russ Maines, Chad Rumchik, Greg Glenn, Mark Grimmonpre, Tom Sprague, Jennifer Jordan, and Richard Dick for assistance both in conducting experiments vital to this work and their wonderful hospitality during my many visits. Critical experiments were also conducted at the Advanced Warheads Experimental Facility (AFRL/AWEF). My gratitude goes to Joel House and all of the technicians from the B-Range for taking the

time to help me conduct Taylor impact testing. I was also fortunate to receive instrumental training at Sandia National Laboratories in the preparation and execution of instrumented impact experiments critical to this study. My thanks go to Mark Anderson, Robert Setchell, and David Cox for their detailed instruction and countless discussions.

Finally, I would like to express my sincere thanks and gratitude to my mother, sister, family, and friends for their love and support. I would also like to thank my wife, Sultana, for her inspiration and encouragement. I could not have achieved my goals without her love and support.

TABLE OF CONTENTS

LIST OF TABLES

LIST OF FIGURES

# SUMMARY

Epoxy-cast Al+$Fe_2O_3$ thermite composites are an example of a structural energetic material that can simultaneously release chemical energy while providing structural strength. The structural/mechanical response and chemical reaction behavior are closely interlinked through characteristics of deformation and intermixing of reactants. In this work, the structural and energetic response of composites made from stoichiometric mixtures of nano- and micro-scale aluminum and hematite ($Fe_2O_3$) powders dispersed in 47 to 78 *vol.%* epoxy was investigated by characterizing the mechanical behavior under high-strain rate and shock loading conditions.

The main focus of the work was to understand the influence of microstructure on mechanical behavior in epoxy-cast Al+$Fe_2O_3$ materials when exposed to high stress, large strain, and high rate loading conditions. The material's Hugoniot at pressures up to approximately 20 GPa for an Al+$Fe_2O_3$+78 *vol.%* epoxy composite and up to approximately 8 GPa for Al+$Fe_2O_3$+60 *vol.%* epoxy composite has been determined. The results reveal an inert pressure-relative volume (*P*-*V*) and shock-particle velocity ($U_S$ - $U_P$) response in the range of the shock-conditions explored, with the Al+$Fe_2O_3$+60 *vol.%* epoxy composite showing a greater shock stiffness. The addition of solid particle inclusions alters the Hugoniot response as compared to pure epoxy behavior. This is attributed to possible induced bulk damage that changes the

composite's response as impact stress increases. While the 78 *vol.%* epoxy composition shows a transition from "undamaged" to "damaged" behavior that approaches pure epoxy response, the 60 *vol.%* epoxy composition exhibits a gradual toughening behavior. Impact experiments have also been conducted for characterizing the high-strain rate deformation and fracture response obtained from instrumented reverse Taylor tests using high-speed camera and velocity interferometry. The results show that these composite materials exhibit viscoelastic-viscoplastic deformation and brittle fracture behaviors. Significant elastic and plastic deformation during both loading and unloading stages is observed, with approximately 50% elastic recovery of total axial strain occurring rapidly (tens of microseconds) after impact. Coupling high-speed camera images and velocity interferometry measurements shows that the elastic recovery coincides with peak axial strain and the elastic and plastic wave interaction. The incorporation of nano-scale aluminum particles enhances the dynamic stress-strain response and significantly improves the composites' resilience to impact as compared to pure epoxy, and with the use of micron-scale aluminum particles.

Post-mortem analysis of recovered Taylor impacted specimens indicates evidence of early stages of strain-induced reactions occurring at select stress, strain, and strain rates. The observed reaction products correlate with results of thermal analysis, which include DTA and *in situ* high temperature x-ray diffraction (HTXRD).

Central to this study was the interaction of metal-oxide powder mixtures with the epoxy matrix and how their chemical and mechanical properties balance to form a structural energetic material system. The study focuses on describing the underlying principles governing the deformation and fracture behavior, processing characteristics of

epoxy-cast Al+$Fe_2O_3$ powder mixtures, mechanochemical sensitivity, and reaction response. In order to accomplish this, the effects of size, morphology, and distribution of particles were evaluated based on mechanical and chemical response to high pressures and combined stress-strain states using time-resolved measurements.

# CHAPTER I

# INTRODUCTION

Materials that integrate both relatively high-strength and enhanced chemical reactivity attributes are investigated in this work. The candidate material system studied is based on a classic oxidation-reduction reaction with a metal and metal-oxide [1]. Specifically, aluminum constituting the fuel (or reduction agent) and hematite ($Fe_2O_3$) forming the oxidizer, are cast with epoxy to develop a material that has a combination of structural strength and chemical reactivity when subjected to a range of elevated pressures (or stresses), large strains, and high-strain rates. The study examines the pressure-volume compressibility and the high-strain rate dynamic response of epoxy-cast mixtures subjected to extreme mechanical loading achieved from high-velocity impacts. The measured compressibility and dynamic mechanical properties are correlated with microstructural characterization of the constituent's morphology. High-pressure states ranging from approximately 2 GPa to slightly over 20 GPa, generating a range of conditions from uniaxial stress to uniaxial strain and, in some cases, a combination of both states, are examined. This study is specifically aimed at verifying the supposition that a complex stress state coinciding with highly strained material is necessary for reaction initiation to occur in this material system.

## 1.1 Research Motivation

Conventional warhead designs typically constitute a high explosive encompassed in a steel casing. Under the pressure of the rapidly expanding gases generated from the explosive detonation, the casing expands and breaks into fragments, with approximately 30 % of the explosive energy released [2] being dissipated in fragmenting the case. A structural energetic material has the potential to allow improved efficiency with the coupling of chemical and kinetic energies.

An epoxy-cast Al+$Fe_2O_3$ mixture is a potential candidate material that has been considered for modeling the application of structural energetic materials. The fundamental understanding of the mechanical properties, energy states, probable reaction pathways, and criteria for initiation and propagation of the chemical species need to be addressed before such materials and concepts can be fully considered. It is also essential to develop an understanding of the effect epoxy has on chemical reactivity and structural strength, in order to develop a composition that has improved mechanical strength while maintaining chemical reactivity.

Early studies performed in the mid 1930's by Bridgman [3-6] showed that it was possible to initiate reactions for a wide variety of materials, including thermite mixtures and explosives, under the combined conditions of very high static and shear pressures. Bridgman made qualitative observations for thermite mixtures such as Mg+$SiO_2$, Al+$K_2C_2O_4$, and Si+MgO detonating under the static pressure application of approximately 5 GPa. Similarly, a thermite mixture composed of Al+$Fe_2O_3$ experienced a detonation, though more violent, under a lower static pressure ranging from 2 to 3 GPa.

However, shock recovery experiments performed later by Graham [7] on the Al+$Fe_2O_3$ mixture revealed evidence for a chemical reaction threshold above 15 GPa. It should be noted that this threshold was revealed under uniaxial strain loading conditions suggesting the chemical reactivity difference between these studies is highly influenced by experimental loading conditions. It is possible that initiation of chemical reactions subjected to these extreme loading conditions may be caused by a mechanism that is more easily facilitated by a combined stress-strain state and is also significantly influenced by microstructural morphology. To confirm this notion, a detailed investigation of the reaction behavior correlated with microstructural characterization of the affects of morphology under a variety of controlled loading conditions, is necessary. The role of strain rate accompanying the different loading conditions and its influence on chemical reactivity and mechanical properties also needs to be established.

Qualitative results obtained at the Air Force Research Laboratory (AFRL/MNME) have demonstrated epoxy-cast powder mixtures react violently when subjected to high velocity impacts [8]. However, questions remain about the reaction mechanisms involved, influence and nature of complex stress states and strain rates occurring during these experiments, and the effect epoxy has on both reactivity and structural strength when subjected to these extreme conditions.

## 1.2 Overview of Thesis

The present investigation concentrates on understanding the equation of state, high-strain rate mechanical properties, and mechanochemical reactivity, based both on

micron-scale and nano-scale morphologies of reactants in the epoxy-cast Al+$Fe_2O_3$ mixture. Nanoenergetic materials have been shown to reveal additional benefits of increased performance (*e.g.* energy density, rate of energy release, *etc.*), long-term storage stability, and sensitivity to unintended initiation when compared to micron-scale materials of the same composition. The reactive properties of energetic materials are strongly affected by their microscopic and mesoscopic morphologies whereby the alteration, for example, of the reactants' particle size or other microstructural attributes may enhance or inhibit specific energetic and structural characteristics. The challenge is to understand the synergistic behavior of structural and energetic properties and the effect their manipulation may have on overall material behavior. Materials at the nanometric-scale also pose an additional strengthening benefit by altering the mesoscale (grain or particle scale) behavior and, consequently, the deformation and fracture mechanisms due to increased grain boundary area. Developing nanostructured materials can enhance many desired properties, however, these relationships are currently not completely understood and require systematic study to ascertain the influence of microstructure or morphology on mechanical properties and chemical reactivity.

The investigation in the general area of the dynamic response of epoxy-cast metal-oxide-type material has been motivated by the need to understand the fundamental behavior of such materials subjected to rapidly applied loads. Applied stress, strain, and strain rates likely to be experienced particularly during high-speed impacts and penetrations need to be systematically studied in conjunction with chemical reactivity attributed to a mechanical stimulus in the form of a transient deformation wave. In addition, the fundamental understanding of dynamic material response allows the

development of material models used to predict behavior when subjected to dynamic loading conditions.

The overall objective of this work is to develop an understanding of the influence of reactants microstructure on mechanical behavior and chemical reactivity of an epoxy-cast aluminum and iron-oxide powder mixture composite. Additionally, it is also desirable to establish the required stress and strain state or combination essential for initiating a chemical reaction in this material system. Prior work describing dynamic deformation, fracture response, and microstructural influence for materials subjected to high-strain rate experiments will be reviewed first in relevance to the present work. Next, the selection of materials, and methods used for specimen fabrication will be discussed. Following that, the methodology for the experimental investigation will be outlined, and results from quasistatic and dynamic impact experiments will be presented and discussed. Finally, an analysis of the key issues will be presented followed by concluding remarks including a summary of results and suggestions for future work.

# CHAPTER II

# LITERATURE REVIEW

The interaction of a projectile impacting a target introduces extreme loading conditions that produce complex stress states comprised of uniaxial stress and strain or a combination of both. Depending on the impact velocity, geometry, and materials involved, elastic-plastic waves or shock waves propagate through the material causing dynamic deformation and/or fracture. The use of epoxy-cast metal-oxide material systems requires knowledge of their deformation behavior up to and beyond failure when subjected to high-strain rates as a result of high velocity impacts.

Exposing material systems to the combination of high pressure, shear, and assorted strain rates can lead to mechanochemical reactions over a wide time interval ranging from the duration of the peak pressure state to the time scale of thermal equilibrium. To evaluate their performance, typically, materials are forced into a state of extreme stress and strain by subjecting them to high pressure mechanical waves resulting from a high velocity impact or an explosive detonation. In extreme cases, the time to achieve peak pressure may be less than one nanosecond. However, more often, less intense pressure or stress waves are encountered and times to achieve peak pressure may be on the order of hundreds of nanoseconds or more. The rapid application of a high pressure and high stress state is controlled by the inertial response of the materials

themselves as they are plastically deformed introducing a high concentration of defects. Assessment of the material response to these loading conditions contains detailed information describing the mechanical and chemical properties and processes encountered over this short interval.

The identification of shock-induced reactivity in powder mixtures has been traditionally studied using post-mortem material analysis from confined sample recovery experiments [7,9]. However, more recent developments using time-resolved measurement techniques has resulted in greater confidence and higher sensitivity in stress [10-12] and velocity [11,13] measurements as a way to infer the occurrence of chemical activity. Furthermore, these measurements are performed over time intervals relative to the shock front propagation, thereby providing information on reaction kinetics in addition to providing a means for obtaining shock Hugoniot material property data.

The following section will give a brief description of structural energetic materials, followed by a discussion of dynamic material response as relevant to plastic deformation and shock wave loading conditions. The physics and mechanics of shock waves will first be examined to establish the mathematical treatment for describing the material state behind and ahead of the shock front. Next, mechanochemically initiated reactions will be discussed followed by the dynamic behavior of reactive metal–oxides. Additionally, the effect of an organic binder on reactivity will be presented. The constitutive response of polymeric materials will next be presented and the use of nanometric energetic materials will be discussed as they pertain to enhancing chemical reactivity by the alteration of reactant particle sizes. Finally, recent experimental studies pertaining to the strengthening of epoxy-cast composites will be reviewed.

## 2.1 Structural Energetic Materials

Structural energetic materials are comprised of components with dual-functionality: an energetic component and a structural load-bearing capability. They are a class of multifunctional materials that incorporate characteristics of high energy density and rapid energy release along with enhanced mechanical strength. Reactive foils used for micro-welding [14] and structural propellants [15] are a few examples of such materials. The challenge is to preserve the energetic characteristics of these materials when introducing reinforcement and coupling strength and reactivity features within the material system.

To realize advancements in energetics that can reduce weight and enhance performance, there is a need to design novel energetic materials and structures that are capable of multifunctional performance. Thermite powder mixtures undergoing oxidation-reduction type reactions provide an opportunity of multi-functionality if these can also be processed as structural materials. The design of such materials requires characterization of energetic and mechanical properties under dynamic loading conditions.

## 2.2 Material Behavior Under Shock-Compression and Loading

Determination of Hugoniot states over a range of shock conditions is a fundamental method for characterizing material response to high-strain rate loading. Hugoniot curves identify thermodynamic states that can be achieved in a material through

adiabatic compression with the application of a steady shock wave. Mass, momentum, and energy conservation across the shock front relate thermodynamic variables to the shock and particle velocities associated with the wave motion. If the material response to loading causes an unsteady shock motion, methods that utilize transmitted-wave measurements are not suitable for determining Hugoniot states. However, a relatively accurate technique for determining arbitrary material behavior at high-strain rates is achieved through parallel-plate impact experiments. For these experiments, the material of interest is subjected to high velocity impact whereby a flyer plate is accelerated to impact the target material in a planar, normal, parallel orientation. Planar shock waves are generated in both the target material and flyer plate, where the axial stress and/or the particle velocity are identical across the impact boundary of the two materials as shown in Figure 2.1(*a-c*). Measurement of either the axial stress or particle velocity of the interface provide a stress-velocity Hugoniot state of the test material and permits other

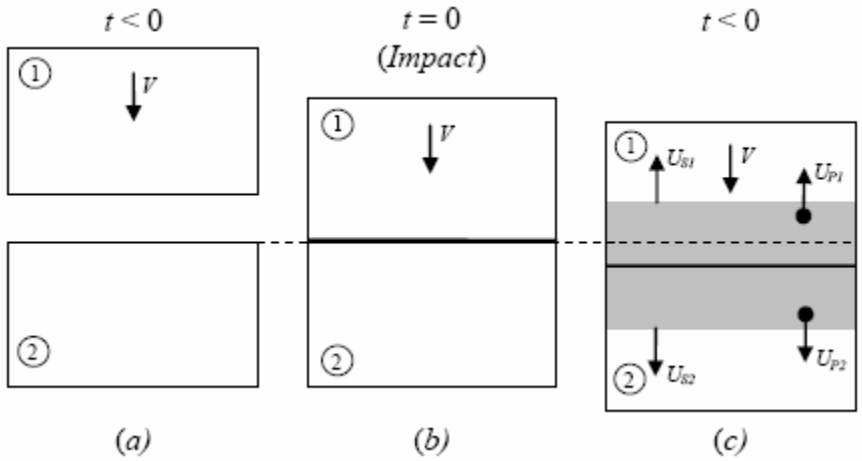


**Figure 2.1** Schematic illustration obtained from Meyers [16] from a planar, normal, parallel, impact of a projectile (material '1') moving at a velocity, *V*, at a time *a*) prior to and *b*) at the moment of impact with material '2'. *c*) Shows the position after impact, while the disturbance wave is propagating within the materials.

thermodynamic variables to be also determined. The following sections will give insight into the behavior of materials subjected to shock-compression through high velocity impact experiments as described above or by some other means, such as explosive loading, forming a steady shock wave within the target specimen. A general overview of shock wave analysis in terms of the Rankine-Hugoniot conservation equations will be discussed first and the mathematical foundation necessary to evaluate material behavior when subjected to high-strain rates will be established. This is followed by a discussion regarding stress initiated reaction behavior and illustrated with examples of material systems which exhibit this behavior. The section concludes with a discussion about reactive behavior of metal-oxide powders or thermite mixtures subjected to dynamic loading, highlighting experimental studies concentrating mainly on the $Al+Fe_2O_3$ system.

### 2.2.1 Analysis of Shock Waves

In the hydrodynamic or shock regime, where pressures are orders of magnitude beyond the material yield strength, the localized material behavior dominates the strength response and the dynamic material behavior is generally described by hydrodynamic shock wave theory. A shock wave is a mechanical disturbance that produces a discontinuity in the state variables (temperature, pressure, and density or volume) behind and ahead of the shock front. The shock loaded material is characterized as a region of uniaxial strain incapable of lateral material flow, due to the increasing hydrostatic stress component exceeds the dynamic flow strength of the material. The well known Rankine-Hugoniot conservation equations [17] of mass, momentum, and energy have

therefore, been established as jump conditions defining the material state on either side of this disturbance or discontinuity.

$$\rho_0 U_S = \rho(U_S - U_P) \tag{2.1}$$

$$P - P_0 = \rho_0 U_S U_P \tag{2.2}$$

$$E - E_0 = \frac{1}{2}(P - P_0)(V_0 - V) \tag{2.3}$$

In the above equations, $P$, indicates the pressure, $\rho$, the density, $U_S$, the shock velocity, $U_P$, the particle velocity, $E$, the energy, and $V$, the volume, where the zero subscript represents the initial state. A fourth equation necessary to fully define the system, known as the equation of state (EOS) for the material, is based on an empirical relationship between shock and particle velocities. Assuming no phase transformations take place, the EOS for many materials is expressed as:

$$U_S = C_b + SU_P, \tag{2.4}$$

where $C_b$ is the bulk sound velocity in the material at atmospheric pressure and $S$ is a constant, which is a characteristic of the material. Consequently, by the application of these equations it is possible to determine all the shock wave parameters once any two variables are known. Typically, dynamic experiments are designed to measure the shock velocity, particle velocity, and pressure. Often the shock parameters are plotted in the form of pressure and particle velocity ($P - U_P$), pressure and specific volume ($P - V/V_0$), in addition to shock speed and particle velocity ($U_S - U_P$), as well as other relationships.

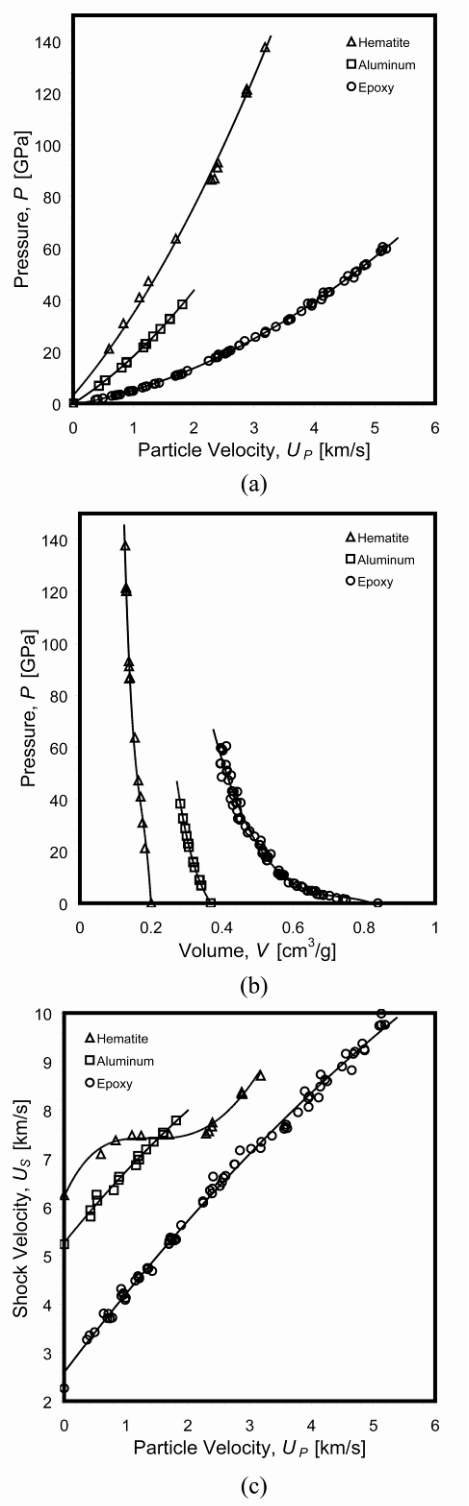


**Figure 2.2** Shock Hugoniot plots for aluminum and hematite showing *a*) $P$-$U_P$, *b*) $P$-$V$, and *c*) $U_S$-$U_P$ parameter relationships, respectively [18].

Examples of these plots, also known as Hugoniot plots, are shown in Figure 2.2(*a*-*c*) separately for each of the constitutive materials used in this present study; aluminum, hematite, and epoxy [18]. These shock parameters are useful for determining shock response of materials and connecting shock-induced chemical, mechanical, or physical changes that manifest as discontinuities or kinks in the Hugoniot plots.

### 2.2.2 Stress Initiated Reaction Behavior

Mechanical material response and reaction behavior are closely interlinked through deformation characteristics of reactive constituents. Fundamental mechanisms controlling chemical reactions in powder mixtures occur during the stress-pulse rise time and microsecond duration of peak pressure. Critical processes that occur involve plastic deformation causing particle configuration changes that promote mixing of the reactant powders, particularly within and around voids by plastic flow. All of these processes enhance solid-state reactivity of powder materials and are accompanied by moderate temperature increases under high-pressure shock loading.

These reactions take place as a result of a shock wave moving through the material and manifest as “shock-assisted” or “shock-induced” chemical reactions. Chemical processes which occur following the unloading of the material to ambient pressure are known as shock-assisted reactions. These reactions occur during the time interval of thermal equilibrium (several microseconds to milliseconds) once the shock wave has passed through the material. In contrast, shock-induced chemical reactions occur within the pressure equilibrium time of microsecond duration.

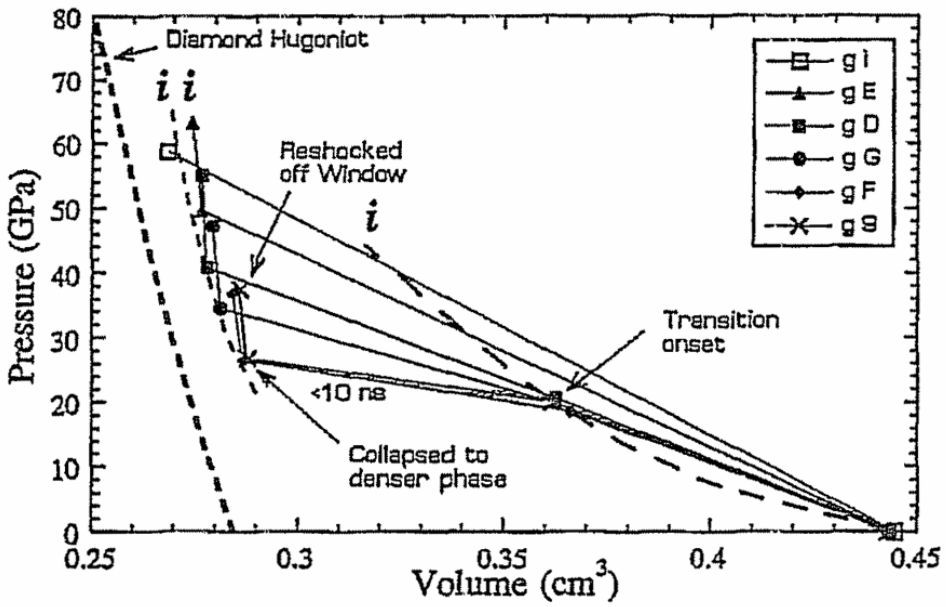


**Figure 2.3** Example of a shock-induced structural phase transformation for graphite-to-diamond [19]. The transition takes place at approximately 20 GPa.

Examples of shock-induced structural phase transformations such as martensitic transformations in iron [20,21] and graphite-to-diamond transitions [19,22,23] can manifest as shifts or discontinuities in shock adiabats and disclose evidence of microstructural changes in recovered materials. This transition is illustrated in Figure 2.3 for graphite-to-diamond occurring at approximately 20 GPa. However, microstructural observations in recovered shock compressed materials do not typically provide information on whether the observed structural or chemical changes are shock-induced or shock-assisted.

The most revealing evidence of shock-induced mechanochemical reactions has been based on time-resolved Hugoniot measurements showing deviation in the shock adiabats. Pressure-volume plots shown in Figure 2.4(*a,b*) demonstrate compressibility changes and increases in shock-wave velocity, which are both associated with

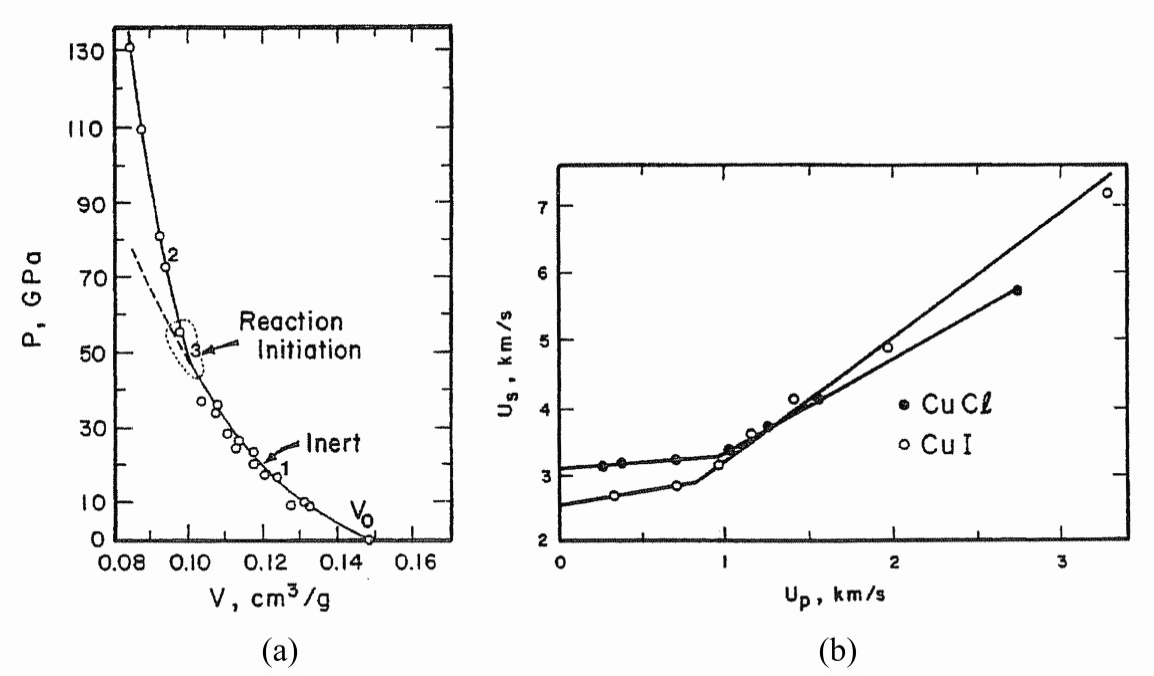


**Figure 2.4** Time-resolved Hugoniot measurements showing *a*) pressure-volume plot displaying compressibility change for Sn+Te [24] and *b*) increased shock wave velocity for CuI and CuCl [25,26].

reaction initiation and the formation of intermetallic compounds. Furthermore, Batsanov, *et al.* [24,27,28] have used manganin stress gauges to detect chemical reactions in Sn+S, Sn+Te, and Al+S powder mixtures and phase transformations in CuI [25] and CuCl [26].

The effect of particle size on shock-induced reactions has been experimentally studied [29] for powder mixtures of Ti and Si. From microstructural observations and time-resolved experiments, the shock initiation of chemical reactions was attributed to a solid-state mechanochemical process with particle size and morphology directly influencing the occurrence of reaction. Mixtures of medium size Si and Ti powders (10-40 μm) were observed to react under shock compression at pressures of 1.5 to 3.0 GPa, while no reaction was observed in the fine (Ti = 1-3 μm, Si < 10 μm) and coarse

(Ti = 105-149 μm, Si = 45-149 μm) powder mixtures under identical loading conditions.

Shock-induced reaction behavior is closely linked with the material's mechanical response when subjected to high-pressure loading. The tendency for a material to deform by plastic flow or localized shear banding can influence the strength and ability for reactants to undergo shock-initiated reactions. Thus, it is important to identify the conditions necessary to promote these reactions and extend the understanding of mechanical property influence on reaction initiation.

### 2.2.3 Dynamic Behavior of Reactive Metal-Oxide Mixtures

The assistance of shock waves to activate self-sustaining chemical reactions in thermite powder mixtures has been explored in many studies for the purpose of synthesizing a number of materials with unique microstructures [30-33]. The mechanical and reaction behavior of energetic materials is strongly associated through deformation characteristics occurring from plastic deformation of constituent materials or by localized shear banding [34]. Additionally, the reactive properties of energetic materials are strongly affected by their microscopic and mesoscopic morphologies [35,36].

Mechanisms controlling "stress-initiated" chemical reactions in metal–oxide powder mixtures are dominated by processes occurring during the microsecond duration of the peak pressure state [9]. The initial configuration of the constituent powders, a function of their initial packing density and particle morphology, strongly influences the overall process by setting up the conditions necessary for enhanced mass mixing and fluid-like flow of particles at the shock front. As the shock wave propagates through

porous or distended solids, energy is dissipated in the form of plastic deformation due to crushing the solid and filling the voids. Additionally, the shock wave introduces a large concentration of defects.

Reaction initiation mechanism(s) during shock loading of epoxy-cast thermite materials may exhibit characteristics unique to both shock densification behavior of powders and solids. Epoxy-cast metal-oxide materials exhibit morphologies which may "passivate" their reactive nature by surrounding reactive agglomerates with epoxy, forming intimately mixed local regions of reactants as a result of mixing during processing. The metal-oxide constituent particles are in intimate contact within these local regions, but may be separated by an epoxy "barrier" that can discourage reaction initiation. The presence of epoxy may also limit the propagation of deformation into the metallic and oxide constituents. The propagation of a shock wave through this material may have local effects throughout the agglomerated regions that are characteristic of powder densification, however, the overall response may more resemble that of typical low impedance solid.

Several studies have explored shock compression of aluminum and hematite (thermite) powder mixtures. These studies have addressed the influence of starting material characterization on their response to shock loading, with highly exothermic reactions in some cases. Important material properties investigated in these studies are effects of powder particle size, morphology, and initial packing density [37], effect of shock pressure [7,37-39], volumetric powder mixture distributions [37,39], and the intrinsic differences in constituent material properties of various thermite systems.

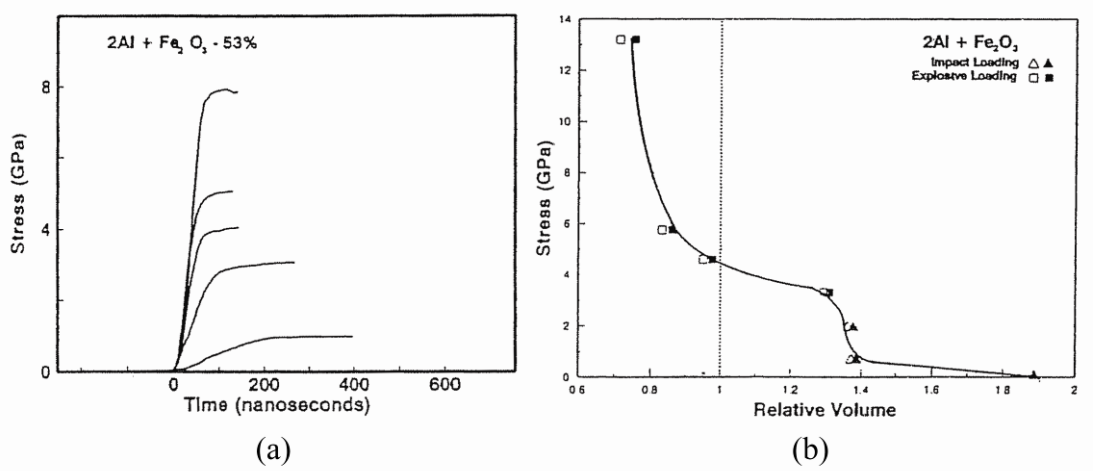


**Figure 2.5** Dispersive wave behavior for stoichiometric powder mixtures of Al+$Fe_2O_3$ subjected to shock loading showing *a*) extended rise times, rounding to the peak pressure state, and *b*) from a pressure-volume plot, two different crush-up slopes [38,39].

The application of a shock wave through a stoichiometric powder mixture of aluminum and iron-oxide has shown unique dispersive wave behavior as illustrated in Figure 2.5(*a,b*). Pressure-volume plots display two different crush-up slopes with a steeper slope occurring at higher pressures (0.67 to 3.2 GPa) and consequently a smaller compression toward solid density. The dissimilarity in slopes may be attributed to the differences in the individual crush-up strengths of aluminum and iron-oxide, or due to the voids in the powder being filled as a result of particle size differences between the two constituent powders. Experiments performed to examine the shock compression response of Al and $Fe_2O_3$ powders [39] mixed in different volumetric ratios equivalent to 50:50, 40:50, and 25:75 (Al:$Fe_2O_3$) have shown propagated wave dispersion varying with the volumetric ratio at peak input pressures of 2 GPa. The equivolumetric mixture also revealed crush-up of the powders to solid density (or crush strength) occurring at significantly lower pressures, indicating that a more dominant crush-up effect may be attributed to the lower strength aluminum than iron-oxide. The observed differences in

crush strength may be expected to influence the shock-induced reaction initiation behavior, requiring a greater pressure for reaction initiation for materials showing increasing crush strength.

Shock recovery studies [7] also examining this metal-oxide system have exhibited a reaction initiation threshold above 15 GPa. Experiments showed evidence that strong exothermic reactions are acutely dependent on shock loading conditions. For example, identical experimental conditions where a peak loading pressure of 17 GPa was attained using two different explosives for shock loading caused the mixtures to exhibit different reaction behaviors. The first explosive produced a lower pressure early in the detonation and gave no evidence of reaction in the specimen. However, an explosive having a higher pressure early in the detonation showed evidence of a fully reacted specimen. This indicates first that the material's intrinsic properties, such as heat of reaction, may not play a significant role in the reaction initiation. Furthermore, examination of the recovered specimen, which underwent a chemical reaction, showed evidence that it occurred during the shock event along the outer edge of the specimen and this reaction caused a subsequent thermally activated reaction to occur in the bulk of the specimen. Thermal analysis (DTA) of the shock-modified powder which did not undergo reaction showed a preignition exotherm indicating the presence of shock-produced Hercynite (spinel phase $FeAl_2O_4$), giving direct evidence for the influence of mechanical activation and shock-induced mixing as processing influences the solid-state reaction chemistry. Additional experimental studies have indicated similar results showing that both highly exothermic reactions such as $Al+Fe_2O_3$ (285 kJ/mol of reactants) and weakly exothermic reactions such as solid organic acids and their esters reacting with solid alkalis

(40-60 kJ/mole) are not associated with thermal activation resulting from bulk or local heating of the system [40].

Shock-initiated reactions are also influenced by initial powder packing density. Subramanian and Thadhani [37] examined the reaction behavior by shock compression of equivolumetric powder mixtures of Al+$Fe_2O_3$ and Al+$Fe_3O_4$ consisting of both fine and coarse particle morphologies. In this study, variations in initial packing densities (53 % and 70 % TMD) and several shock peak pressure conditions (5, 16, and 22 GPa) were explored. The recovered specimens showed evidence of chemical reaction as a function of initial packing density and shock loading conditions. Specimens with an initial packing density of 53 % TMD demonstrated that the reaction took place above 16 GPa whereas an initial packing density of 70 % TMD required a higher shock pressure (22 GPa) for reaction to occur. No reactions occurred at the 5 GPa pressure level for both packing densities examined and particle morphology did not appear to have a significant detectable role on the chemical reactivity under these conditions.

Boslough [41] performed planar impact experiments on porous stoichiometric mixtures of aluminum and hematite hot pressed with approximately 50 % porosity. In this study, shock temperatures were measured using time-resolved radiation pyrometry. Experimentally measured temperatures were compared to calculated values obtained from a simple thermochemical model indicating shock temperatures should be approximately 1000 and 4000 °K for the reactants and product Hugoniots, respectively. He observed an initial temperature spike upon impact and attributed it to the collapsing of pores in the mixture. This work demonstrated that the metal-oxide specimen undergoes a partial reaction immediately behind the shock front when shocked to pressures above

4 GPa. The measured temperature range from 2700 to 3400 °K fell below the theoretically calculated temperature for full reaction, but did indicate occurrence of a partial reaction. Furthermore, this illustrates dynamic mixing occurring within the shock front controls the rate of chemical reaction. The observation of reaction not going to completion after the passage of the shock wave suggests that reaction propagation kinetics were inhibited, which was attributed by Boslough to inadequate levels of local reactant mixing.

The dynamic mechanical behavior of thermite mixtures has also been studied by Walley, *et al*. [42], initially using drop-weight impact experiments to evaluate the reaction sensitivity of five different thermite materials, and then performing subsequent gas gun shock loading experiments on the material to be determined most reactive. The drop-weight impact experiments were performed on loose powders, cylindrically pressed disks, and pre-sheared pressed disk-shaped specimens evaluating impact sensitivity under both uniaxial compression and shear strain states introduced by an inclined anvil (angle of 30°). In general, they found that the pressed disks of thermite powders were more sensitive to impact than the loose powders. A comparison of pressed disk specimens also showed that the pre-sheared disk qualitatively reacted (deflagrated) more violently. The authors suggested that the mechanism of reaction during drop-weight experiments was due to "hot-spot" formation being more likely in higher strength pressed disks where more energy is consumed during the deformation event than in loose powders. High-speed camera records gave evidence of this showing very rapid thermite reactions taking place at initiation sites along the outer edges of the specimen. Additionally, "jetting" of the material was also observed on these outer edges giving

some direct evidence that the stress state of the thermite material induces the chemical reaction in regions where the specimen is highly deformed and plastically flowing. Having been established as the most reactive thermite composition from the drop-weight impact studies, several equation of state experiments were conducted for a thermite powder mixture comprised of 40 % aluminum and 60 % potassium perchlorate. These experiments provided the material Hugoniot up to approximately 17 GPa, which however showed no chemical reaction initiation in these uniaxial strain shock-loading experiments.

Clearly, these studies indicate there are several key parameters that must collaborate to induce mechanochemical reaction initiation in reactive metal-oxide powder mixtures. Material parameters such as particle size and morphology are important for the efficient mixing of reactants. Likewise, the complex stress states, strain rates, and their duration are also important aspects that must be considered.

## 2.3 Mechanical and Chemical Response of Shock-Compressed Polymer-Matrix Composites

Studies discussed in the previous section have mostly examined the reactivity of thermite powder systems with no addition of a binder. One effect important to this current study, which lacks comprehension, is the threshold conditions necessary for initiating chemical reaction for polymer matrix composites (epoxy-cast thermite materials) when an epoxy binder is used to provide mechanical integrity and improved strength. For reaction initiation to occur, it is first necessary to have intimate contact between the metal and metal-oxide constituents which comprise the thermite mixture.

This has been established through prior work clarifying reaction mechanisms of aluminum iron-oxide thermite powder mixtures at normal ambient conditions [43]. Comparing specimens made from consolidated thermite powders (without binder) and epoxy-cast thermite powders, it is conceivable that chemical reactions would be easier to induce and become self-sustaining in the consolidated material because of intimacy between mixed reactants. Epoxy, therefore, may inhibit the reaction initiation. However, once initiated, epoxy may have the added benefit of contributing to the overall reaction in the form of a gas generator. Therefore, it is necessary to identify the mechanical stimulus necessary to initiate reactions in these epoxy-thermite systems.

### 2.3.1 Effect of Organic Binder

It is thought that the conditions necessary for mechanochemical initiation of reactions in epoxy-cast metal-oxide materials requires a state of high shear deformation. Indeed, this has been the observation for many studies examining thermite-type mixtures and explosives. Ames [44] has studied energetic materials manufactured with metal powders dispersed within a fluoropolymer binder. A mixture consisting of aluminum (26.5 *wt.%*) and polytetrafluoroethylene (PTFE) was used to investigate impact-initiation through Taylor [45] impact experiments. This study provided insight into the importance of shear stress as a component necessary for the ignition process and related the reaction to impact properties such as impact speed or impact stress. The study was conducted by gradually increasing the impact velocity until reaction is observed visually using high-speed photography. Lee, *et al.* [46] conducted high velocity impact ignition studies

of solid spheres and rods also comprised of PTFE, however, with a slightly lower concentration of aluminum (24 *wt.%*). In this work, the authors used time-resolved light spectroscopy techniques to identify reaction species from high velocity impacts of this energetic material in conjunction with observing the impact event with high-speed photography. Their experiments applied three different impact conditions consisting of *i*) direct impact where a spherically shaped specimen was accelerated into a hardened steel anvil, *ii*) indirect impact where a rod shaped specimen was sandwiched between two steel anvils in both compression and compression-shear arrangements, and *iii*) two-step impact configuration where a spherical projectile was launched at two parallel-spaced steel plates 1.5 and 25.4 mm thick, respectively. Direct and indirect configurations showed similar behaviors whereby heating and some reaction occurred at the moment of first impact with the anvil. However, majority of the reaction occurred following the material breaking up and its subsequent impact onto a secondary surface. In contrast, for the two-step impact configuration, reaction initiation was not observed at the moment of first impact with the thin plate (1.5 mm), but rather from subsequently formed fragments impacting the thicker (25.4 mm) stationary anvil plate.

Under quasistatic or static loads, these materials have an inert behavior and are safe to handle. However, early work performed by Bridgman showed it was possible to initiate reactions for a wide variety of materials, including explosives and thermite mixtures, under static conditions, whereby the combination of very high static and shearing pressures induce a powerful detonation [4-6]. The introduction of the material to high pressure and temperature states combined with shear stress is essential to stimulate reaction initiation.

Davis and coworkers [47] have looked at the possibility of metals and metal-oxides mixed with a fluorinated polymer detonating when subjected to shock impacts. A series of experiments were performed on Ti+20 % Teflon and Al+$Fe_2O_3$+10 % Teflon (by weight) mixtures using a gas gun flyer impact configuration. The Ti+20 % Teflon mixture (92.5 % TMD) showed chemical reactions being initiated between shock pressures of 1.95 and 3.48 GPa, however a higher pressure ranging from 4.93 to 13.35 GPa gave no evidence of reaction initiation. Similarly, the $Fe_2O_3$+Al+10 % Teflon mixture (80 % TMD) was subjected to shock pressures ranging from 1.71 to 10.29 GPa and reaction initiation was limited to a pressure of 1.71 GPa. In both material systems thermal decomposition of the Teflon liberates the very reactive fluorine compound. The authors suggest the decomposition of Teflon is likely a precursor to the reaction initiation, but the metals are believed to react with the Teflon products within the shock front. Additionally, the materials prepared for this study had initial porosity (Ti-Teflon 92.5 % and Al+$Fe_2O_3$+Teflon 80 % TMD) which was necessary to facilitate shear stresses in the material and initiate the reactions.

The analysis of shock-induced chemical reactions for a powder mixture of aluminum and hematite with Teflon was also conducted [48]. Two main chemical reactions are thought to take place in this powder mixture consisting of the Al and $Fe_2O_3$ reaction in addition to the Teflon decomposing and reacting with aluminum to produce a gaseous product. The study also suggested that the gas produced may differ depending upon the loading condition. Several different chemical reaction models were evaluated to describe Hugoniots using hypothesized shock-induced reactions. Results based on the reaction models were compared with the experimental data obtained from polyvinylidene

di-fluoride (PVDF) stress gauges used to monitor shock pressure profiles in the powder mixture. Based on the hypothesized reaction models, shock wave profiles were calculated by VRR+DYNA hydrodynamic code and compared to experimental data. The Teflon+Al reaction produces aluminum fluoride according to $AlF_j$, where the number $j$ is thought to be influenced by the shock pressure. The greater the shock pressure, the more hematite reacts with aluminum, and the lower value of $j$ results. Other studies have observed similar results. Lee, *et al.* [49] have conducted thermal reaction studies for many metal/polymer compounds, specifically Al/PTFE and Ti/PTFE. Their results indicate that the reactions became more exothermic as the bond strength between Al-F becomes stronger.

The addition of certain polymers to explosives can also affect their sensitivity for reaction initiation when subjected to impacts. Swallowe and Field [50] studied the impact behavior of polymers and explosives during deformation using a modified drop-weight test with a transparent glass anvil combined with high-speed photography. Polymers such as polycarbonate (PC) and polysulphone (PS) were observed to sensitize pentaerythritoltetranitrate (PETN) explosive while polypropylene (PP) does not, and in fact has the opposite effect of de-sensitizing the explosive. Their conclusion was that the sensitizing effect is due to the mechanical behavior of the polymer particles. Ignition of the explosive occurs after or during the catastrophic failure, cracking, and fast flow of the polymer, and the initiation site was in close proximity to the polymer region. This sensitizing effect was observed for only the polymers that undergo catastrophic failure during impact.

A comparison between traditional explosives and thermite mixtures illustrates the involvement of different reaction mechanisms. Explosives undergo reaction initiation by the decomposition of a single molecule comprised of the fuel and oxidant. This differs from thermite powder mixtures where one particle is the fuel and another particle is the oxidant, and the interaction between the two constituents is required for reaction to occur. This suggests that the particle-particle interaction between the metal and metal-oxide is required for the reaction to take place, unlike explosives where the fuel and oxidant decompose and are contained in the same molecule. However, it has been shown that pyrotechnic or thermite materials also have the ability to detonate as violently as an explosive [47].

### 2.3.2 Polymeric Binder Materials

The previous discussion has alluded to the importance of a polymeric binder for structural reinforcement for many energetic material systems including traditional explosives and new generation reactive thermite mixtures. The polymer binder or matrix material holds the reinforcement phase in an arranged pattern and helps transfer the load among the reinforcement particles or fibers that makeup the composite. Composite materials composed of a polymeric binder phase result in a lightweight material with relatively high structural strength. The development of many composite materials has used a variety of polymers for the matrix phase. Two polymers in particular have been discussed in previous sections for use in energetic materials such as polytetrafluoroethylene (PTFE) or Teflon and epoxy. PTFE is a completely fluorinated

polymer formed by the free-radical chain polymerization of tetrafluoroethylene gas to produce liner chains of – $CF_2$ – units. PTFE has a combination of chemical, electrical, and thermal performance unmatched by any other commercially available material. It is a very inert material that has an extremely low coefficient of friction and high melting point (327 °C). It is a crystalline polymer that also has outstanding electrical insulating properties. Its mechanical properties are low compared to other engineering polymers, but its properties remain at useful levels over a great temperature range (-240 to 260 °C). Its impact strength is high, but its tensile strength, wear, and creep resistance is low when compared with other polymers. The small size of the fluorinated carbon chain polymer results in a highly dense crystalline polymeric material. The density of PTFE is high for polymeric materials ranging from 2.13 to 2.19 $g/cm^3$. Large amounts of thermal energy are required to break down the material since it is composed of strong carbon-carbon and carbon-fluorine bonds. However, decomposition of PTFE can lead to its constituents undergoing chemical reactions with other components. PTFE in powder form is used in pyrotechnic compositions as an oxidizer together with powdered metals such as aluminum (Al), magnesium (Mg), titanium (Ti), and hafnium (Hf). Upon ignition these mixtures form metal fluoride and release large amounts of heat. They are used as infrared decoy flares and igniters for solid fuel rocket propellants [51]. The chemical structure of Teflon is shown in Figure 2.6.

Epoxy resins are regarded as thermosetting polymers and have found various commercial applications after crosslinking with adequate curing agents. These resins are polymer-forming systems containing two principal components that interact to produce highly crosslinked products with exceptional toughness. The curing reaction or

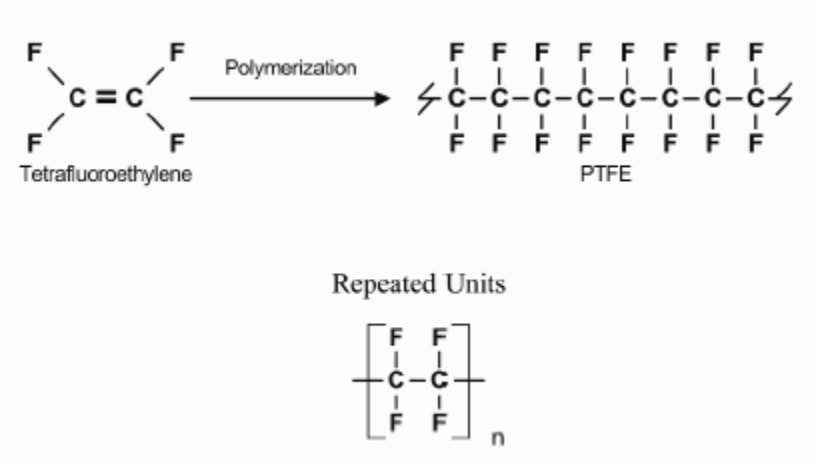


**Figure 2.6** Chemical structure of polytetrafluoroethylene (PTFE) formed from the reaction with tetrafluoroethylene.

crosslinking occurs without the formation of any by-product, and consequently the polymer has low cure shrinkage. They also have good adhesion to other materials, good chemical and environmental resistance, good mechanical properties, and good electrical insulating properties.

Epoxy resins are characterized by having two or more epoxy groups per molecule. The key participant in the polymerization is epoxy functionality; a strained, three-membered ring consisting of one oxygen and two carbon atoms. The chemical structure of an epoxide group is shown in Figure 2.7(*a*). The most widely used epoxy resin is a low molecular weight polymer with epoxy groups at its ends; the diglycidyl ether of bisphenol-A (DGEBA) also shown in Figure 2.7(*b*). The DGEBA is composed of linear molecules with different molecular weights according to the variation of the repeated number (n) in the structural formula. To form a solid thermosetting material, epoxy resins must be cured by using crosslinking agents and/or catalysts to develop desired properties. The epoxy and hydroxyl groups (– OH) are the reaction sites for crosslinking.

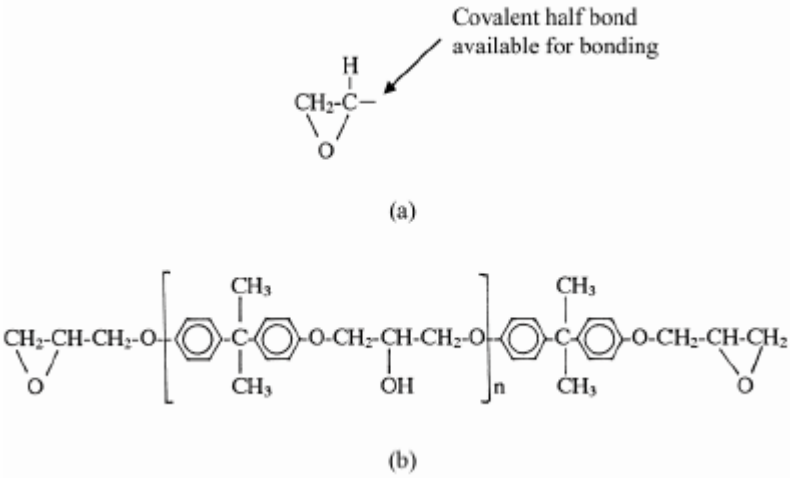


**Figure 2.7** Chemical structure for epoxy showing *a*) the epoxide group and *b*) the low molecular weight resin polymer diglycidyl ether of bisphenol-A (DGEBA) with epoxy groups at its ends.

The low molecular weight of uncured epoxide resins in the liquid state gives them high molecular mobility during processing. This property allows the liquid resin to quickly and thoroughly wet surfaces. This wetting action is important for epoxy utilized for reinforced materials and adhesives. Also, the ability to be poured into a final form is important for electrical potting, encapsulating, and for the processing of particle-reinforced matrix materials. The high reactivity of the epoxide group with curing agents such as amines provides a high degree of crosslinking and produces good hardness, strength, and chemical resistance.

### 2.3.3 Strength of Epoxy-Cast Composites

Particle-reinforced polymer composites have many favorable properties including increased strength and toughness. Toughness is an indication of the energy that a material can absorb before breaking and therefore is related to impact strength.

Typically, strengthening and improved toughness for particle-reinforced polymers are provided by plastic deformation and/or pull-out of particles dispersed within the polymer matrix. Additionally, toughening may also be provided by dispersed particles causing cracks to deflect around the reinforcement throughout the matrix phase when a sufficient stress is applied.

There are many reasons for using composite materials rather than less complicated homogeneous polymers. Some of these reasons include increased stiffness, strength, dimensional stability, and as mentioned previously, toughness or impact strength. However, not all of these desirable features are found in any single composite. The advantages that a particular composite may offer for a specific application must be balanced against their undesirable properties, which may include difficult fabrication techniques as well as a reduction in some physical and mechanical properties.

The properties of composite materials are dictated by the shape of the filler particles, the morphology of the system's microstructure, or the nature of the interfaces between the different phases. The adhesion between reinforcement particles and the polymer matrix tend to have a profound effect on the overall strength of the composite. Most studies on the modification of polymers with the addition of rigid particles report a significant loss of toughness compared to the neat polymer. Generally, the addition of particles will have an embrittling effect and decrease the impact energy significantly particularly when poor adhesion between reinforcement particles and the polymer matrix are present [52]. However, some studies have demonstrated an increase in toughness with the addition of rigid particles in certain polymer systems such as filled polypropylene [53] and filled polyethylene [54-56]. Most studies have shown that the

toughness is determined mainly by morphological factors, including particle size, particle volume fraction, particle size distribution and spatial distribution. All of these morphological factors have been described by a single parameter, namely the matrix ligament thickness (surface-to-surface interparticle distance) [57]. A material that exhibits relatively high toughness will have an interparticle matrix ligament thickness that is smaller than a certain critical value which is essentially unique for a given matrix polymer. In general, a composite with the addition of rigid particles that are dispersed without agglomeration is tougher. Studies have focused on the addition of many different types of reinforcement particles including rubbers [58], glass spheres [52], ceramics such as calcium carbonate [53-55], calcium silicate [59], and alumina [59], in addition to metallic particles [60,61] all with various particle sizes, shapes, and volume fraction additions with the main focus to increase overall strength of the composite material.

The addition of metal particles to polymer matrices produces composites of greater density, while improving mechanical strength and increased stiffness. The dynamic moduli of metal-filled polymers depend on the stress-strain fields developed around the individual particles during the application of dynamic loads. Particularly, the size, shape, and distribution of particles in the matrix highly influence the developing stress-strain fields and alter the mechanical response of the material. The nature of the interfacial bond between the matrix and filler particles is of equal importance, however, imperfect adhesion in addition to cracks, voids, and flaws are often present which can extensively distort the stress-strain fields arising in the composite [61,62].

The behavior of thermoplastic polymers and polymeric composites subjected to large deformations is in general viscoelastic, where the stress (or strain) varies over time.

Simply stated, viscoelastic materials exhibit both elastic and viscous flow characteristics. One interesting feature is that a given polymer can display all the intermediate range of properties between an elastic solid and a viscous liquid depending on temperature and timescale for dynamic mechanical measurements. The effects of temperature on viscoelastic properties typically show very large changes [62]. As the temperature is raised, the frequency of molecular rearrangements increases, thus a glassy polymer will become rubber-like at a sufficiently high temperature. Similarly, this same effect is observed when the time-scale is increased for an experiment that subjects the specimen to an alternating strain while simultaneously measuring stress. The inverse effect is also true in both cases, that is for earlier times or temperatures below the glass transition $T_g$, polymers behave like glassy solids. Thus, the effect of temperature and applied loading histories from dynamic mechanical analysis (DMA) studies are useful for obtaining a molecular interpretation of viscoelastic material behavior. They permit studying of glass transitions and yield information about the morphology of polymers.

The influence of molecular entanglements such as the addition of rigid foreign additives with very large surface areas or the incorporation of crystallites, as in semicrystalline polymers, may enhance mechanical properties and alter the glass transition temperature relative to the same polymer absent of these modifications. Aharoni [63] suggests the glass transition temperature of a polymer increases when a combination of conditions are encountered with regard to the introduction of nanometric-scale inclusions. In particular, the nanometric inclusions should provide very large contact surface areas additionally having a strong interaction between the surfaces of the additive inclusion and the polymer comprising the composite. When the attractive

interactions between the polymer and inclusions are negligible, the overall modulus of the system may still be altered by their addition, however, leaving the $T_g$ either marginally elevated or with no effect at all.

Van Melick, *et al.* [64] have found that strain hardening in polymers is proportional to network density for an amorphous polymer that is altered by blending with polyphenylene oxide and by crosslinking. The authors conclude strain hardening is proportional to network density irrespective of the nature of the entangled polymer network through physical entanglements or chemical crosslinks. Wetzel, *et al.* [59], showed the addition of alumina nanoparticles into epoxy with concentrations of 1–2 *vol.%* improved stiffness, impact energy, and failure strain by impeding chain mobility thus hindering molecular motion.

Recent studies of structural energetic materials at Georgia Institute of Technology have involved work on polymer-based composites with nickel and aluminum powder mixtures. Rod-shaped specimens, prepared by a cast-cure method using cylindrical shaped molds, were evaluated using quasistatic compression test and dynamic impact experiments [65,66]. Micron-scale Ni powder and nano- and micron-scale Al powders were premixed and dispersed in 20 and 30 *wt.%* (47 and 60 *vol.%*) epoxy. Stress-strain histories obtained from static compression tests showed samples containing the nano-scale aluminum powder exhibited strain hardening in addition to increased elastic modulus. Observed failure in these epoxy-cast materials is typically by means of nanometric aluminum particles pulling-out of the epoxy matrix. Additionally, both Ni and Al particles did not appear to experience any plastic deformation, however, increased toughness was also attributed to cracks deflecting around the Ni particles.

Quasistatic compression tests presented only slight improvements in mechanical properties with the addition of Ni+micron-Al powders to epoxy. In contrast, the addition of nano-Al showed a significant increase in yield strength with Ni+nano-Al+20 *wt.%* epoxy exhibiting the highest yield strength (≈ 157 % increase), followed by Ni+nano-Al+30 *wt.%* epoxy composition (≈ 130 % increase). Additionally, the Ni+nano-Al+20 *wt.%* epoxy composition also had the highest elastic modulus. Specimens containing nano-Al particles also showed significant strain hardening when compared to micron-scale Al particle additions. This illustrates the improvement to mechanical properties that nano-scale particles have on the strengthening of epoxies.

Reverse Taylor anvil impact experiments were also conducted on the various particle-filled composites (with impact velocities of 61 to 100 m/s), in addition to pure epoxy specimens (85 and 152 m/s). However, experiments conducted at the lowest impact velocities (61 and 85 m/s) were insufficient to cause permanent deformation in the specimens. Following impact, sample fragments were recovered and high-speed digital photography was taken to capture transient deformation profiles of the specimens which were used to compare the dynamic response of the various compositions. Since the specimens fractured during these experiments, dynamic yield strength determined by length or area change could not be applied. However, captured images showing the transient deformation profiles of each specimen were used to analyze dynamic behavior by calculating incremental strains (both axial and areal) before fracturing occurred. Incremental strains were normalized by $\rho U^2$ to eliminate any variability caused by specimen density, $\rho$ and impact velocity, $U$. Plotting normalized strain as a function of time after impact (see Figure 2.8(*a,b*)) shows the Ni+nano-Al+epoxy composites

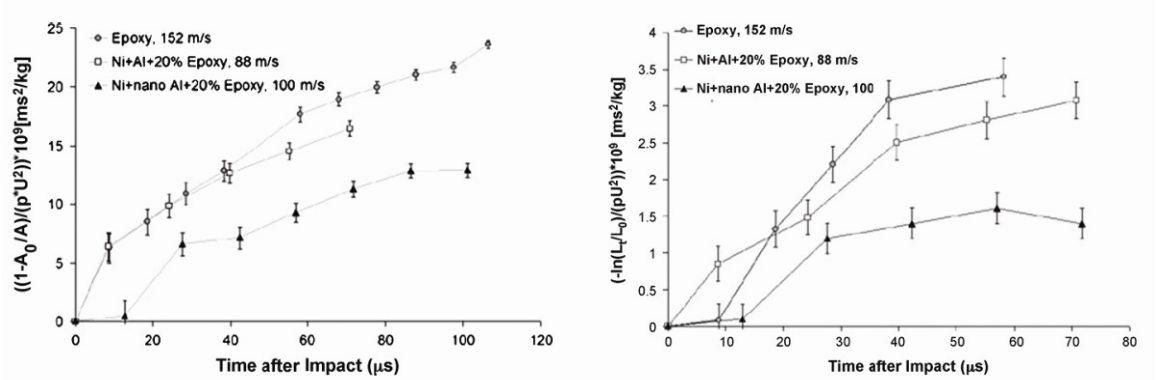


(a) (b)

**Figure 2.8** Normalized *a*) areal strain and *b*) axial strain histories from reverse Taylor impact experiments conducted on pure epoxy and Ni+Al+20 *wt.%* epoxy composites using both micron- and nano-scale Al powders. Incremental strain measurements are taken from high-speed digital camera images and error bars correspond to a three-pixel uncertainty for detecting the edge of the specimen [66].

experience less strain than both pure epoxy and composites containing micron-scale Al particles. These results are used to infer the strength of these materials with the Ni+nano-Al+20 *wt.%* epoxy again showing the best mechanical properties compared to all the specimens tested.

The addition of Ni+Al powders to epoxy showed a slight improvement of mechanical properties for both static and dynamic experiments and even more pronounced improvements for compositions with nano-Al additions. The enhanced strengthening for nano-scale aluminum compositions is attributed to the nano-particles altering the molecular structure of the epoxy causing physical entanglements and loss in polymer chain mobility. Additionally, nano-particles have very large surface areas which can improve the cohesive strength between the epoxy and particulate reinforcements. Dynamic mechanical analysis (DMA) was used to further investigate this effect and validate the mechanism altering of mechanical response of these composites.

Data from DMA measurements verified that the crosslink density for nano-scale Al particle additions to epoxy increase substantially (by a factor of two) thus explaining the increase strengthening observed for these materials. Calculations show an increase in crosslink density resulting from the reduction in aluminum particle size from micron- to nano-scale for Ni and micron- or nano-scale Al powder reinforced composites. Figure 2.9 shows the storage modulus measured as a function of temperature for Ni+Al composites contrasting the behavior for nano-scale and micron-scale additions of aluminum particles. In addition to the increased strength from nano-scale particles (approximately double as compared to the micron-scale particle strengthened composite), there is a noticeable effect on glass transition temperature $T_g$, increasing for the nano- scale Al dispersed composite. The increase of $T_g$ suggests there is an attractive interaction between the polymer altering the chemistry of the epoxy and chain mobility,

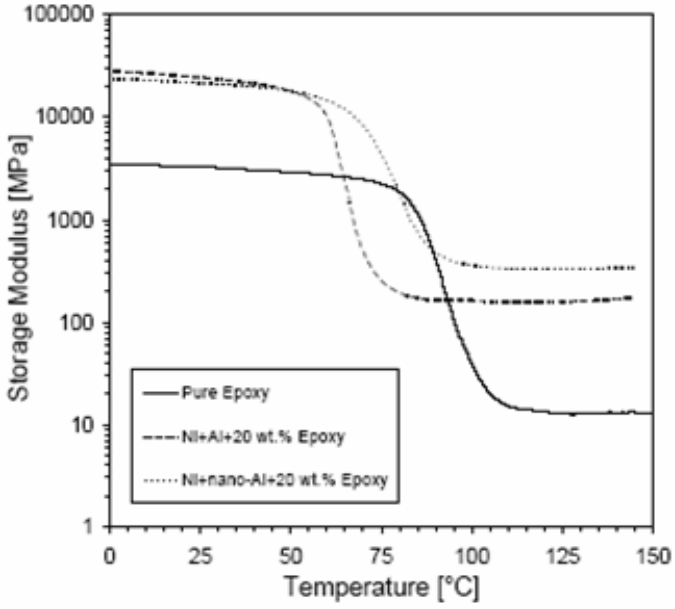


**Figure 2.9** Results from dynamic mechanical analysis (DMA) experiments for selected epoxy-cast Ni+Al composites contrasting nano- and micron-scale Al particle effects [66].

possibly attributed mostly to the very high surface area provided by the addition of nanometric particles. An unexpected reduction in $T_g$ is observed when comparing these compositions with pure epoxy. Misra, *et al.* [67] demonstrated that the distribution of crosslink density can also have an effect particularly lowering $T_g$ for polymers with narrow crosslink distributions. The interactions of nano- and micron-scale particles with epoxy altering the composites' chemistry is apparent, however, the exact mechanism of this complex interaction resulting from their addition is not obvious from this limited study. Possibly the principal information ascertained from these types of experiments are the extent to which the nanometric aluminum particles are distributed throughout the epoxy.

In a separate study conducted by Patel [68], the dynamic compressive behavior of $Al+Fe_2O_3$ thermite mixtures dispersed in an epoxy matrix has been investigated at intermediate strain-rates on the order of $10^3$ 1/s. Dynamic compression experiments using a split-Hopkinson pressure bar (SHPB) were conducted on cylindrical specimens 6.35 mm in length and diameter. Test specimens were prepared from mixtures of micron-scale aluminum and sub-micron scale hematite powders dispersed in epoxy with concentrations ranging from approximately 20 to 50 *wt.%* (47 to 78 *vol.%*). Experiments were also conducted for pure epoxy specimens manufactured from a 12:1 ratio of Epon® 826 resin and diethanolamine (DEA) as the curing agent.

The experimental study showed evidence that the deformation behavior was mostly dominated by the epoxy phase of these composites. The stress-strain response typically showed an initial linear elastic response which transitioned into a nonlinear stress-strain region, followed by an apparent yield point that resulted in a slight work

softening in the material. This was followed by either continued work softening or work hardening regions depending on the specimen composition.

The addition of Al and $Fe_2O_3$ particles to the epoxy slightly improved mechanical properties observable from the stress-strain behavior exhibiting a work hardening response as the volume fraction of particles increased. In contrast, pure epoxy as well as a composition that contained Al+$Fe_2O_3$ particles dispersed in 50 *wt.%* epoxy showed a strain softening behavior. Moreover, the addition of dispersed particles caused the linear elastic response of the material to increase as volume fraction of the epoxy matrix decreased. The ability for these materials to absorb energy generated from dynamic impacts was also examined in this study. Evaluation was carried out by the integration of stress-strain curves and calculating the stress work at select levels of strain. As expected, the stress work increases with decreasing epoxy binder content.

The experimental results discussed previously were used to develop constitutive equations that described the material behavior when subjected to dynamic impacts. Once more, the response of the composite materials was predominantly determined by the behavior of the binder phase. The Hasan-Boyce [69] constitutive equation gave good correlation with experimental results despite being developed specifically for unfilled glassy polymers.

Furthermore, high-strain rate experiments for particle-reinforced composites have a very complex behavior when subjected to shock loading conditions and have been performed on alumina-filled (identified as ALOX for recent studies by Sandia National Laboratories) and unfilled epoxies to observe transmitted waveforms under corresponding shock loading conditions. The alumina-filled epoxy specimens showed

typical dispersive material characteristics, whereby extended rise times and rounding to the peak pressure state are typically observed. In contrast, unfilled epoxy specimens showed unaltered shock waveforms propagating through the material. High-strain rate studies focused on various neat polymers, including epoxy and filled epoxies such as Sandia's ALOX material, will be discussed next in more detail.

### 2.3.4 Shock-Compression Behavior of Filled and Unfilled Polymers

The high-strain rate behavior of various polymers has been studied comprehensively for over 30 years. Some polymers have been studied more extensively than others because of their use throughout the shock physics community. For example, a great deal of information is available spanning relatively high pressure ranges and large strain rates for epoxy because of its importance for use in target assemblies. Studies have examined the dynamic impact behavior spanning the lower pressure range from 1 to 2 GPa up to pressures in excess of 30 GPa, and under strain rates typically achieved for split Hopkinson pressure bar ($10^3$ to $10^4$ 1/s) as well as parallel-plate impact experiments ($10^5$ to $10^6$ 1/s). Considerable shock-wave data has also been collected for polymers such as polyethylene (PE) [70] and polymethylmethacrylate (PMMA) [71], and this subject continues to be the focus of many experimental studies.

The most comprehensive dynamic analysis for polymers, including both thermosetting and thermoplastic types, has been conducted by Carter and Marsh [72] through shock waves generated from high explosives. Traces obtained from streak cameras were used to record wave arrival times and obtain a measure of shock velocity

through the specimen. Impedance-matching (see Meyers [16] pp. 188-200 for details) was then used to determine the associated particle velocity to construct $U_S$-$U_P$ Hugoniot curves for each polymer. Table 2.1 list all the polymers examined by Carter and Marsh [72] and shows their idealized monomer structures. Two particularly interesting features common to all of the polymers examined have been detailed through this study. The first such feature shows that the $U_S$-$U_P$ behavior of all the polymers exhibits considerable curvature in the lower pressure regime and extrapolation from higher pressure data to the ambient pressure axis demonstrates higher bulk sound velocities than ultrasonically measured values. For example, bulk sound velocity measured ultrasonically for epoxy has a value of 2.26 mm/μs as compared to extrapolated $U_S$-$U_P$ experimental data intercept with a value of 2.69 mm/μs for the lower pressure region (1.4 to 22.5 GPa) and 2.88 mm/μs for the higher pressure region (32.6 to 60.5 GPa) above a transformation pressure beginning at 23.1 GPa. Actually each intercept has a value very close to the ultrasonically measured longitudinal wave speed, falling either slightly above or below the experimental intercept. The authors suggest this behavior may be attributed to the "two-dimensional" nature of polymer compression, which rules out the possibility of a low-pressure phase change examined through static compression experiments. Similarly, early dynamic experiments conducted on PMMA have also exhibited considerable curvature at the low-pressure end of the $U_S$-$U_P$ curve [73]. This effect is common to other polymers as well and considerable theoretical work has been conducted by Pastine [74,75] for understanding this two-dimensional response for polyethylene. Dominant covalently bonded carbon atoms along the backbone of a polymer chain have bonds that are an order of magnitude greater than adjacent chains

**Table 2.1** Representative idealized monomer structures examined in high-strain rate impact experiments conducted by Carter and Marsh [72].

| | | | |
|---|---|---|---|
| polyethylene | 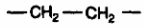 | cellulose acetate | 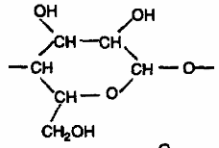 |
| polyvinyl chloride | 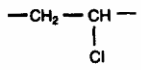 | epoxy | 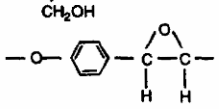 |
| polyvinylidene fluoride |  | phenolic | 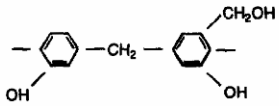 |
| polychlorotrifluoroethylene | 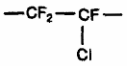 | phenoxy | 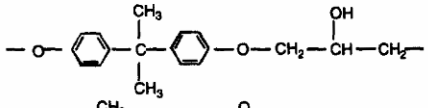 |
| polytetrafluoroethylene | 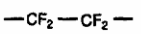 | polycarbonate | 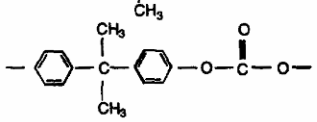 |
| polypropylene | 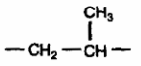 | polyester | 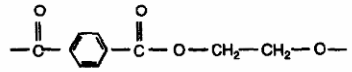 |
| 4-methyl-1-pentene-4 | 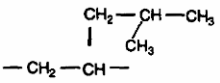 | polyimide | 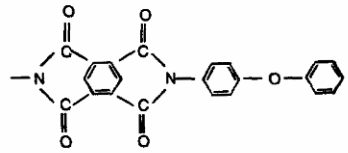 |
| polyamide | 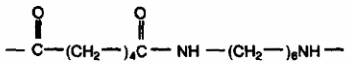 | polyphenylquinoxyline | 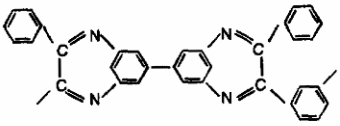 |
| polymethylmethacrylate | 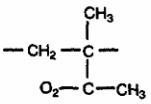 | polysulfone | 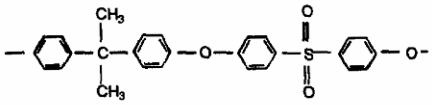 |
| polystyrene | 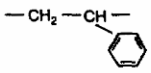 | polyurethane | 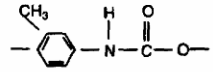 |

held together by van der Waals type bonds. Hence, the hydrostatic compression causes a length decrease in weak adjacent chains while the backbone remains relatively unaffected. The initial microscopic response to compression will be of a "two-dimensional" nature involving the weakly bonded adjacent chains rather than a "three-dimensional" nature involving both the adjacent chains and the backbone of the polymer. This idea has been experimentally verified for polyethylene and is presented in the low-pressure Hugoniot shown in Figure 2.10. Two densities of polyethylene ($\rho_0$ = 0.999 g/cm$^3$ and $\rho_0$ = 0.886 g/cm$^3$) used to represent degrees of crystallinity of approximately 90 % and 55 % have been studied and are shown in the figure along with theoretical Hugoniots derived based on the calculations by Pastine [74,75]. Additionally, static data obtained from Warfield [76] for highly crystalline material and Bridgeman's [77] data are also shown. The agreements between experimental and theoretical results are excellent.

The second feature observed for polymers studied in this work is a relatively high pressure phase transformation occurring in the range of 20-30 GPa identified by a change of slope in the $U_S$-$U_P$ Hugoniot space. As mentioned earlier, epoxy has a phase transformation that begins at 23.1 GPa and continues up to 32.6 GPa. These transformations are believed to be associated with pressure-induced cross bonding and are explained by the extension of the ideas already encountered at low pressures. Unlike polymorphic transformations in the traditional sense where the material exists in more than one crystal structure and thereby different physical and chemical properties, these transformations occur in completely amorphous materials such as polystyrene. Additionally, these transformations are not associated with melting or vaporization

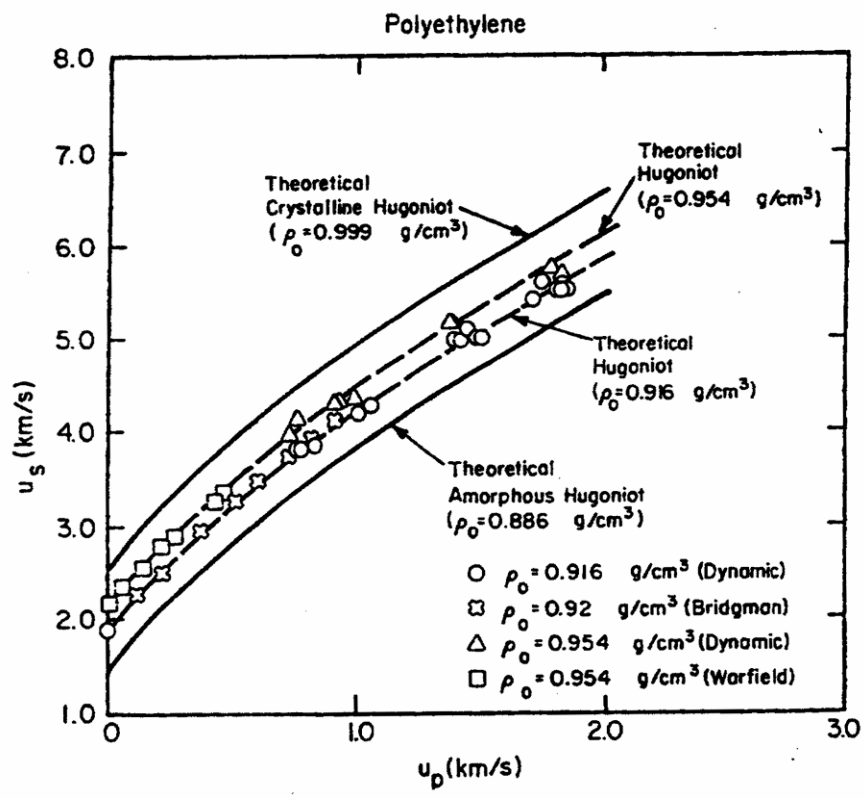


**Figure 2.10** Low pressure Hugoniot data for polyethylene. Solid and dashed lines are theoretical calculations based on the work of Pastine [74,75], while the symbols are either dynamic data or static data transformed to the $U_S$-$U_P$ plane through conservation relations [72].

because they occur in both thermosetting and thermoplastic polymers. The most likely explanation for the high-pressure transformations is due to a three-dimensional type compressive behavior of the polymer chains dominated by the backbone chain response. At the transformation a major molecular reordering is evident from the large volume change observed experimentally. Carter and Marsh [72] suggested this reordering would be such that the distance between chains has been reduced by pressure to a point where interchain interaction is possible. They have shown that the transformation behavior is more pronounced in polymers that exhibit an "open" structure containing covalent-bonded carbon atoms in benzene rings. This effect is shown in Figure 2.11 where

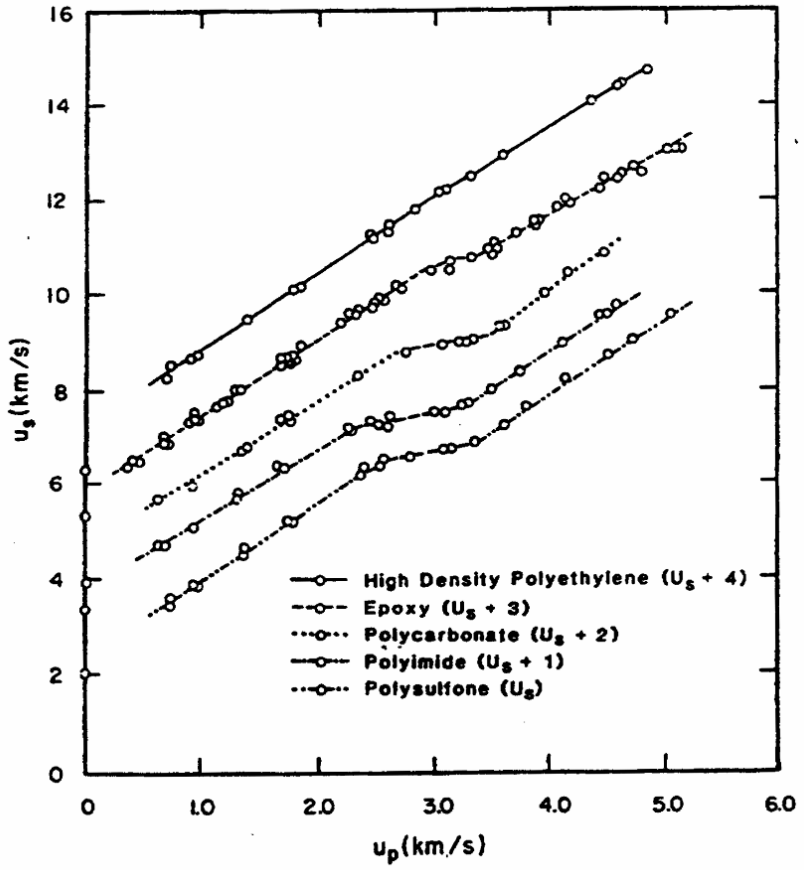


**Figure 2.11** Hugoniot $U_S$-$U_P$ data for several polymers studied by Carter and Marsh [72]. It is seen from Table 2.1 that, in general, those materials having more open units such as benzene rings in their monomer structure also display a more pronounced transition.

polymers such as polysulfone and polymide that have extremely open structures are characterized by large volume changes. Reference is also made to Table 2.1 which shows the idealized monomer structure for many polymers. The effect is minimized for linear hydrocarbons such as high density polyethylene which shows a slight change in slope and exhibits a small volume change at the transition pressure range. The compression of polymers is two-dimensional in nature until the pressure reaches a critical value where the interaction of the chains becomes appreciable and the material

compresses in a manner more typical of a three-dimension solid.

Epoxy based materials are of significant interest both because of their use as adhesives during the assembly of targets for shock loading experiments and as binder phases in composite materials. In addition to the work performed by Carter and Marsh [72], other studies have examined the response of epoxy to shock loading. Munson and May [78] investigated epoxies made from three different curing agents and showed that, within experimental error, the Hugoniot of all three materials were identical. They used different hardeners to produce variations in polymer crosslinking that were measured by variations in glass transition temperature. However, changes in crosslinking and structural variations did not appear to impose significant shock response deviations. Ultrasonic measurements show a noticeable decrease in wave speed with decreasing glass transition temperature and, thus, differences in the initial slope of compressibility curves as a function of polymer structure. This caused a slight stress offset which became uniform at relatively high stresses.

The response of epoxy subjected to planar shock waves generated from plate impact experiments has also been conducted by Millett, *et al.* [79]. Hugoniot measurements were made by embedded manganin stress gauges located 10 mm apart in a longitudinal orientation for two plate-shaped specimens. Lateral stress was also measured by sectioning a single epoxy plate in half and placing another manganin stress gauge 4 mm from the impact face. Very close agreements were shown for the Hugoniotdata in this study and in that of Carter and Marsh [72] discussed previously. Table 2.2 lists Hugoniot data obtained from various studies for epoxy materials. Lateral stress measurements in conjunction with longitudinal stress measurements indicate a

**Table 2.2** Equation of state properties determined from shock-compression studies for several cured epoxies. Select epoxies use Epon® 828-Shell resin unless otherwise indicated by superscript character.

| $C_b$ [mm/μs] | $S$ | $U_P$ range [mm/μs] | $\rho_0$ [g/cm$^3$] | Author [Reference] |
|---|---|---|---|---|
| 2.69 | 1.52 | 0.4 - 2.8 | 1.192 | Carter & Marsh [72] |
| 3.05 | 1.31 | 3.4 – 5.2 | 1.192 | *Carter & Marsh [72] |
| 2.58 | 1.47 | 0.2 - 0.74 | 1.14 ± 0.01 | +Millet, Bourne & Barnes [79] |
| 2.64 | 1.66 | 0.07 - 2.3 | 1.194 | Munson & May [78] |
| 2.55 | 1.68 | 0.05 - 2.4 | 1.202 | Munson & May [78] |
| 2.68 | 1.52 | 0.4 – 5.1 | 1.198 | McQueen, *et al.*, [80] |

*Particle velocity range after phase transformation.
+Study used an epoxy resin mixture; see reference [79] for more details.

decrease in lateral stress behind the shock front as impact stress increases. This implies an increase in shear strength as the shock wave is passing through the material. Similar results have been obtained for other polymers such as PMMA [71,81], where it has been suggested that this effect is due to the viscoelastic/viscoplastic nature of polymers. The authors also suggest that even though a Hugoniot elastic limit (HEL) for epoxy was not directly observed in the manganin gauge records, it is estimated to be approximately 0.6 GPa from the deviation of shear strength obtained from calculated elastic material behavior.

In addition to the shock response of neat polymers, particle-reinforced polymer composites exhibiting relatively significant volume fractions of epoxy have also been investigated. The discussion will be focused mainly on the extensive work carried out by Sandia National Laboratories on an aluminum oxide (ALOX) filled epoxy. ALOX is used as a dielectric encapsulant for ferroelectric ceramic pulsed power devices. In this

case, the encapsulant behavior during shock wave loading and release strongly influences the stress experienced by the ferroelectric element of the device. Alumina-filled epoxies have been the focus of study for over 30 years, beginning with the work by Munson and Schuler [82]. However, the most comprehensive experimental study conducted on this material was carried out by Munson, *et al.* [83] in 1978.

Plate impact experiments were performed on three different compositions of $Al_2O_3$ powders dispersed in epoxy prepared from Shell Epon® 828 resin and *Z* curing agent. Specimens used for this study had volume fractions with 20, 34, and 42 % of alumina. Particle sizes for $Al_2O_3$ filler material ranged between 2 and 30 μm with the average particle size of 8 μm. Three types of transmitted stress experiments were performed to produce either sustained shocks followed by release or recompression waves, or "thin-pulse" conditions where a release wave has overtaken a leading compression wave. Particle velocity time histories were obtained using laser interferometry from gas-gun impact experiments. The shock profiles showed characteristic features of a dispersed wave with a highly rounded leading wave front as it approaches peak velocity. Intercepts of Hugoniots with zero particle velocity axis agree well with longitudinal ultrasonic velocity values similar to neat polymers response to dynamic loading discussed earlier. However, the particulate-filled material does not appear to exhibit the same $U_S$-$U_P$ Hugoniot curvature as showcased by the neat polymers. This difference may be attributed to a slightly lower particle velocity range examined in this study. The geometry of these experiments also permitted the identification of the release wave arrival, which allowed calculating release velocity within the specimen. Interestingly, the release velocity was significantly greater than the measured shock

velocities, which were a slowly varying function of particle velocity. In contrast, the release wave velocity was a strong function of particle velocity. The authors remark that this phenomenon typically has only been found in porous materials. Additionally, this effect becomes more pronounced as the volume fraction of $Al_2O_3$ increases suggesting that there are large micromechanical differences between the compression and release processes due to the constituents having highly dissimilar mechanical properties.

Following the initial experimental work by Munson and Schuler [82] and Munson, *et al.* [83], Anderson, *et al.* [84-87] have continued to study the shock and release behavior for alumina-filled epoxies using planar impact gas gun experiments. Setchell and Anderson [88] give an excellent review of previous work and details on their current study of alumina-filled epoxy composite materials. In this series of work, several material features have been analyzed including morphological effects by altering $Al_2O_3$ particle size and volume fraction additions, direct comparison of filled and unfilled epoxy materials, and temperature effects with variation from -50 to +70 °C. These studies have mainly used velocity interferometry, Velocity Interferometer System for Any Reflector (VISAR) diagnostics for measuring transmitted compressive wave and the subsequent release wave profiles. Imbedded PVDF gauges have also had limited use in conjunction with VISAR diagnostics permitting the direct comparison of the two methods, which indicates the piezoelectric gauge may have a rate-dependent response to shock loading [84].

Similar to previous studies, transmitted waveforms showed extended rise times and characteristic dispersive material behavior such as a pronounced rounding of the leading wave profile to peak velocity. For studying compositional effects [87], ALOX

specimens were prepared with several different morphologies while keeping sample dimensions and impact velocity constant. This permits the evaluation of each composition at identical shock-compression states with common peak particle velocities. Table 2.3 gives a summary of ALOX compositions studied and the corresponding densities measured for each specimen. The first material was identical to that prepared in previous studies conducted by Munson, *et al.* [83] and contained 43 % T64 tabular aluminum, however, in this study the powder consisted of particles varying in size from 5 to 50 μm. Samples used different spherical alumina powders with nominal diameters of 18 and 5 μm and still contain the same 43 % volume fraction of powders. The next sample used 43 % T64 tabular aluminum in a different epoxy consisting of Epon® 826 resin and a non-commercial curing agent. The remaining materials had volume fractions

**Table 2.3** Summary of Sandia's aluminum oxide-epoxy (ALOX) compositions used for shock compression studies comprised of T64 tabular alumina and spherical alumina AA5 and AA18 with nominal diameters of 5 and 18 micron respectively [87].

| Epoxy | Alumina | Volume [%] | Density [g/cm$^3$] |
|---|---|---|---|
| 828/Z | T64 | 43 | 2.377 |
| 828/Z | AA18 | 43 | 2.389 |
| 828/Z | AA5 | 43 | 2.391 |
| 828/custom | T64 | 43 | 2.339 |
| 828/Z | T64 | 38 | 2.233 |
| 828/Z | T64 | 34 | 2.121 |
| 828/Z | T64 | 20 | 1.750 |
| 828/Z | T64 | 0 | 1.200 |

of T64 tabular aluminum ranging from 38 % to 0 %. All of the materials tested in this study used Epon® 828 resin and *Z* hardener except where noted for one case.

Transmitted wave profiles measured by VISAR show only minor observable differences as the alumina particle morphology was changed from tabular T64 to smaller spherical powders. Peak stress, shock velocity, and release velocity are all generally similar for each composition, while wave rise times were also generally similar with one exception. The specimen containing 5 μm spherical alumina particles exhibited a short rise time measured at the half peak particle velocity as compared to the two other compositions. Similarly, results from varying the epoxy matrix composition showed only slightly smaller peak stress and shock velocity values for the second epoxy (Epon® 826 resin and non-commercial hardener). These differences are attributed by the authors to the second epoxy having a lower density (1.14 g/cm$^3$) as compared to the 828/Z epoxy (1.20 g/cm$^3$).

More noticeable differences are seen for varying the fraction of alumina particles added to the 828/Z epoxy matrix. As the volume fraction decreases, the peak axial stress, average shock wave velocity, shock rise-time, and release-wave velocity all decrease. This is not an unexpected trend and some significant aspects of the alumina loading fraction can be identified by examining these wave propagation results in more detail. The addition of alumina particles to an epoxy matrix changes its dynamic loading response from an initial elastic shock for the pure epoxy specimen to a more viscoelastic behavior with no signature of an elastic precursor for filled material. However, more significant effects were observed for "thin-pulse" experiments where the sample dimensions permit the release wave to overtake and attenuate the shock wave. In this

case, the impact stress decreased significantly as the alumina content decreased and the peak particle velocity gradually increased. This effect is a consequence of the decreasing ratio of release velocity to shock velocity as the alumina volume fraction decreases, thus permitting the transmitted wave to experience less attenuation.

Next, the shock and release behavior of alumina-filled and unfilled epoxies were examined [84]. The direct comparison of filled and unfilled epoxy materials showed expected differences based on previous studies in the observed waveforms. Figure 2.12 shows the normalized relaxation behavior of filled (1.68 GPa peak) and unfilled epoxies (1.52 GPa peak) from a reverse-impact experiment configuration where the epoxy sample impacts a stationary fused silica target. Similarly, observable differences in the loading and release behavior for transmitted wave experiments are shown in Figure 2.13 where the filled-epoxy specimen has an extended rise time and a more pronounced dispersive rounding when compared to unfilled-epoxy specimens. These two figures show how wave propagation characteristics change with the addition of alumina particle filler.

The shock and release behaviors of both filled and unfilled epoxies have also been examined over an initial temperature range of -50 to +70 °C [85]. Transmitted wave experiments were first conducted on unfilled epoxy samples for -30, 20, and 70 °C and a nominal impact velocity of 547 m/s. The epoxy used in these experiments consisted of Epon® 828 resin mixed with diethanolamine (DEA) hardener in a 100:12 weight ratio, and cured at 90 °C for 16 hours. The effect of initial temperature showed a significant reduction in release wave speed with decreasing temperature. The transition of the initial shock front to an equilibrium velocity also decreased with decreasing temperature. The waveforms also exhibit a more pronounced rounding effect as temperature decreases.

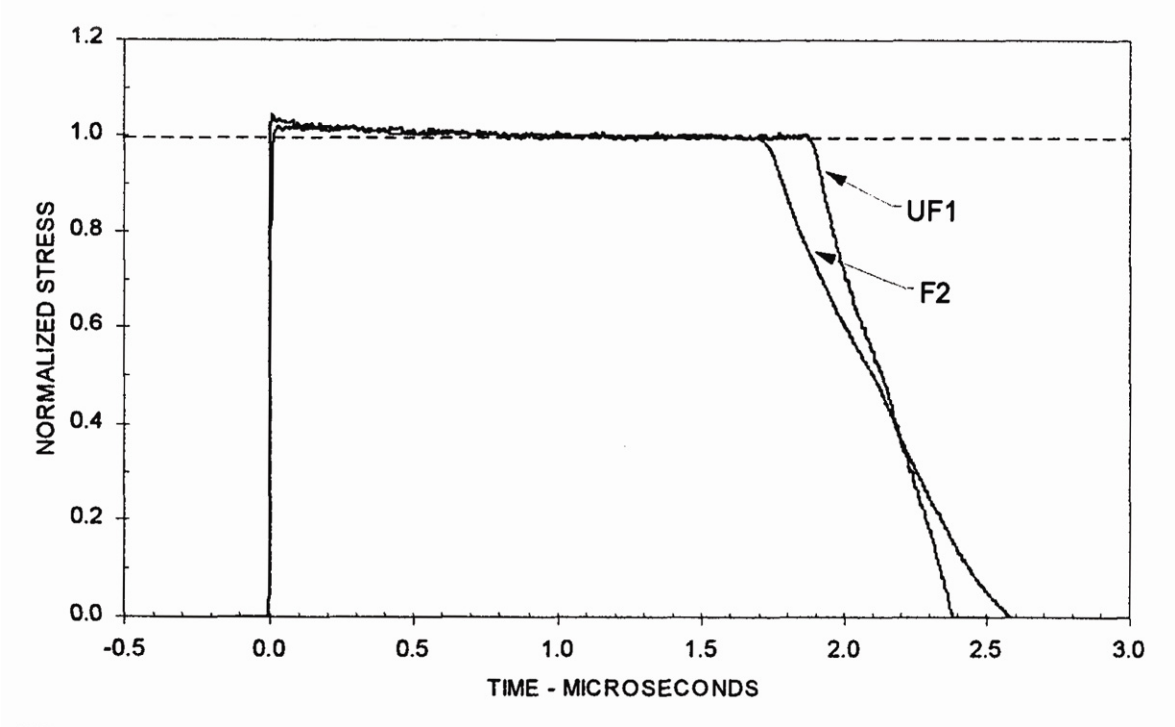


**Figure 2.12** Comparison of normalized stress profiles for alumina-filled epoxy (ALOX) and unfilled-epoxy specimens subjected to high-strain rates from a reverse impact experimental configuration [84].

Additionally, transmitted wave experiments were conducted for alumina-filled epoxy specimens with 42 % volume fraction of $Al_2O_3$ particles. In this case, the epoxy matrix was made from Epon® 826 resin and an amine hardener mixture. The nominal impact velocity for this series of experiments was 357 m/s and initial temperatures examined were -50, 20, and 70 °C. As in the case for unfilled epoxy specimens, release wave speeds were observed to decrease with decreasing temperature. However, a more dispersive behavior was apparent for the filled specimens as the temperature decreases. These results show that the shock response of both filled and unfilled epoxies has increasingly inelastic behavior as temperature is reduced.

Further studies performed by Mock and Holt [89] determined the shock wave

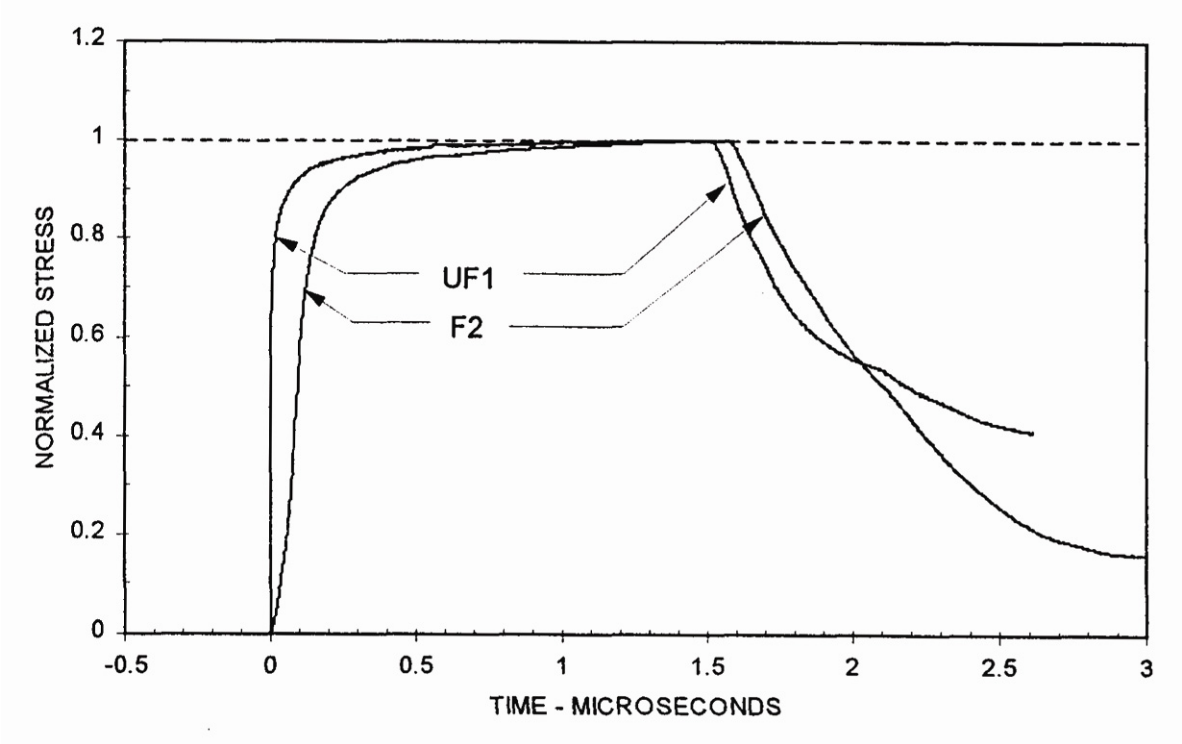


**Figure 2.13** Comparison of transmitted wave experiments for alumina-filled epoxy (ALOX) and unfilled-epoxy specimens. Wave profiles show the charasteristic properties of a dispersive wave [84].

equation of state for a commercially available alumina-filled epoxy composite and compared these results to a higher density composite over a stress range of 0.4 to 3.7 GPa. The alumina-filled composite for this study consisted of 37 % volume fraction of $Al_2O_3$ particles and was compared to a higher density and volume fraction $Al_2O_3$-epoxy composition. Equation of state results indicates that the $U_S$-$U_P$ Hugoniot curve falls between the higher density composite and that of pure epoxy. Close examination of these curves suggests the addition of $Al_2O_3$ particles to epoxy shifts the $U_S$-$U_P$ curve upward with a negligible slope change. This behavior indicates the large concentration of epoxy in these specimens controls the $U_S$-$U_P$ dependence for the overall composite material.

Similar results have also been obtained by Millet, *et al.* [90] where the equations of state for two different volume fractions of alumina dispersed in epoxy have been evaluated in terms of shock velocity and particle velocity. For this particular study, manganin stress gauges were embedded between 10 mm thick plates made from the alumina-epoxy composite. The composite examined in this work showed close agreement with other studies, and both the shock velocity and the shock stress increased with increasing alumina loading.

## 2.4 Plastic Waves and Uniaxial Stress Waves in Solids

The response of material to dynamic loading and stress propagation is determined from equilibrium equations of motion and the material's constitutive relations. The propagation of a disturbance wave within a cylindrical bar takes on a two wave structure (elastic and plastic) when the velocity of impact is above a certain critical value (material's elastic limit). For a propagating disturbance, in which the magnitude falls below the material's elastic limit, the equation of motion for an elastic wave is derived from Newton's second law, $\Sigma F = ma$. A rod segment of original length $dx$ is considered with initial cross sectional area, $A_0$, and initial density, $\rho_0$, as shown in Figure 2.14. Summing the forces across the material element results in [16]:

$$F = ma = m\frac{\partial^2 u}{\partial t^2}, \tag{2.5}$$

$$-A_0\sigma + A_0\left(\sigma + \frac{\partial \sigma}{\partial x}dx\right) = A_0\rho_0\frac{\partial^2 u}{\partial t^2}dx, \tag{2.6}$$

$$\frac{\partial \sigma}{\partial x} = \rho_0 \frac{\partial^2 u}{\partial t^2}. \tag{2.7}$$

Hooke's law, ($\sigma = E\varepsilon$) is invoked since the deformation is purely elastic and substitution into equation (2.7) gives:

$$\frac{\partial}{\partial x}\left( E \frac{\partial u}{\partial x} \right) = \rho_0 \frac{\partial^2 u}{\partial t^2}, \tag{2.8}$$

where $\varepsilon$ is the strain defined as $\partial u / \partial x$ and the displacement equation of motion is given by [16]:

$$\frac{\partial^2 u}{\partial t^2} = \frac{E}{\rho_0} \frac{\partial^2 u}{\partial x^2}. \tag{2.9}$$

The analysis of plastic wave propagation requires a mathematical description of the material behavior as a function of strain. Inelastic or plastic wave propagation theory was developed independently by von Karman and Duwez (1942) in the United States, Taylor (1942) in England, and Rakhmatulin (1945) in Russia [91]. The analysis conducted by von Karman and Duwez's [92] will be presented here.

The presumed material behavior may be described by a single-value relationship between the stress and strain, ($\sigma = \sigma(\varepsilon)$). The theory is completely uniaxial in nature and neglects any three-dimensional effects. Again, the equation of motion is derived from Newton's second law, as described previously, for an elastic wave in a

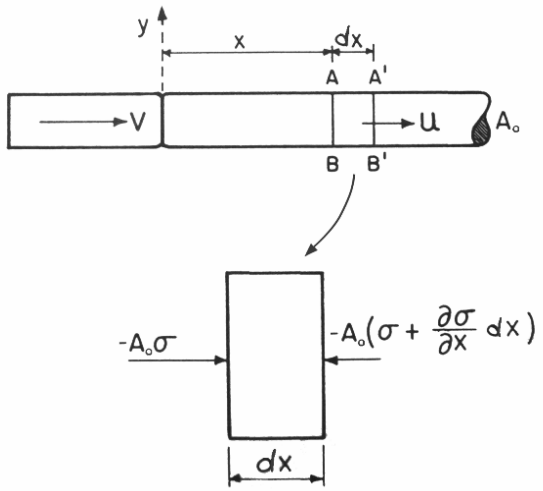


**Figure 2.14** Schematic diagram illustrating material response to dynamic loading determined from a compressive elastic stress wave propagating in a cylindrical rod produced by an impact at velocity *V*.

cylindrical bar. However, since there is a state of plastic deformation and the relationship between stress is a direct function of strain, ($\sigma = \sigma(\varepsilon)$), the material behavior is rate-independent; thus, equation (2.7) can be written as:

$$\rho_0 \frac{\partial^2 u}{\partial t^2} = T \frac{\partial^2 u}{\partial x^2}, \tag{2.10}$$

where $T = d\sigma/d\varepsilon$ is the elastic (below the yield strength) or plastic (above the yield strength) modulus of deformation or the stress-strain slope at a given stress. The application of boundary conditions (shown in equation 2.11) for an impact at the end of a semi-infinite bar allows the determination of the wave profile within the material.

$$u = \begin{cases} v_1 & at\ x = 0 \\ 0 & at\ x = -\infty \end{cases}, \tag{2.11}$$

where $v_1$ is the particle velocity for a bar originally occupying the region -∞ to 0. Three solutions to equation 2.10 are found valid in different regions (see reference [92] for a rigorous proof of these solutions):

$$u = v_1\left(t + \frac{x}{C_1}\right) \quad or \quad \varepsilon = \frac{\partial u}{\partial x} = \frac{v_1}{C_1} = constant\,, \tag{2.12}$$

$$\frac{E}{\rho} = \frac{x^2}{t^2}\,, \tag{2.13}$$

$$\varepsilon = 0\,. \tag{2.14}$$

The three solutions are pieced together to give the complete solution as follows:

*a)* For $|x| < C_1 t$, $C_1$ is the velocity of the plastic wave front and the strain is constant and equal to $\varepsilon_1$;

*b)* For $C_1 t < |x| < C_0 t$, $C_0$ is the velocity of the elastic wave front, where $\frac{x}{t} = \left(\frac{T(\varepsilon)}{\rho_0}\right)^{1/2}$;

*c)* For $|x| > C_0 t$, $\varepsilon_1 = 0$.

Figure 2.15 graphically shows the variation of strain as a function of $\xi = x/t$, where both elastic and plastic wave fronts are traveling at different velocities. The plastic wave velocity, $C_1$ and the maximum strain, $\varepsilon_1$ as a function of impact velocity, $v_1$ must be

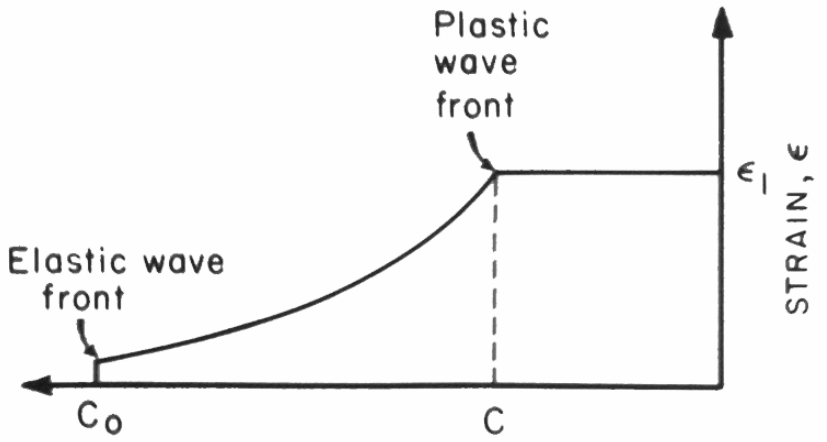


**Figure 2.15** Schematic representation of elastic and plastic wave profiles showing how strain varies as a function of $\xi = x/t$ [92].

determined to completely solve the problem. Assuming $\varepsilon = f(\xi)$; the displacement, $u$ has the form [92]:

$$u = \int_{-\infty}^{x} \frac{\partial u}{\partial x} dx = \int_{-\infty}^{x} f(\xi) dx = t \int_{-\infty}^{0} f(\xi) d\xi . \tag{2.15}$$

The displacement at the end of the rod as a function of time is given by:

$$v_1 = \frac{u(0,t)}{t} = \int_{-\infty}^{0} f(\xi) d\xi , \tag{2.16}$$

and by changing variables,

$$v_1 = \int_{0}^{\varepsilon_1} \xi \, d\varepsilon . \tag{2.17}$$

Next, substituting for $\xi$ from

$$\xi = \frac{x}{t} = \left( \frac{T(\varepsilon)}{\rho_0} \right)^{1/2} \tag{2.18}$$

results in:

$$v_1 = \int_0^{\varepsilon_1} \left( \frac{T(\varepsilon)}{\rho_0} \right)^{1/2} d\varepsilon \,. \tag{2.19}$$

Equation (2.19) determines $\varepsilon_1$ as a function of $v_1$. If the deformation remains in the elastic limit, $T(\varepsilon) = E = constant$ and $v_1 = \varepsilon_1 c_0$. Therefore [92],

$$v_1 = \varepsilon_1 \left( \frac{E}{\rho_0} \right)^{1/2} . \tag{2.20}$$

From equation 2.19, the stress is given by [92]:

$$\sigma_1 = E\varepsilon_1 = \rho_0 v_1 C_0 \,. \tag{2.21}$$

Notice that equation 2.20 is used for calculating the stress produced by an elastic body subjected to an impact velocity $v_1$. However, equation 2.19 replaces equation 2.20 when the impact velocity is sufficient to cause deformation beyond the elastic limit of the material.

The next section begins with a review of the Taylor anvil impact experiment developed to determine the dynamic yield strength of materials. Over the years, hundreds of papers have been published on this topic, including many variations from the original test configuration [93]. Taylor impact experiments have commonly been performed on metallic systems, although some work has been carried out on brittle materials and polymers and is highlighted in the next section. This is followed by a general discussion about constitutive response of polymeric materials in both quasistatic and higher strain rate experiments.

### 2.4.1 Taylor Anvil Impact Experiment

The Taylor test [45] was developed to determine material properties at high-strain rates. It was focused on estimating the average dynamic yield strength of materials based on the overall deformation imparted to the test specimen from a high velocity impact. The experiment is conducted by striking a cylindrical shaped specimen against a rigid anvil and making post-impact measurements of the deformed shape. The theory assumes an ideally rigid-plastic material model exhibiting rate-independent behavior and simple one-dimensional wave propagation concepts that neglect radial inertia. According to Taylor's simplified approach, a cylindrical projectile of length, $L$ impacts a target at a velocity, $U$. The sequence of deformed specimen geometry is schematically depicted in Figure 2.16. Upon impact, an elastic compression wave propagates through the rod followed by a much slower plastic wave. The deformed region propagates away from the anvil face and the stress in this region is assumed to be constant and equal to the yield

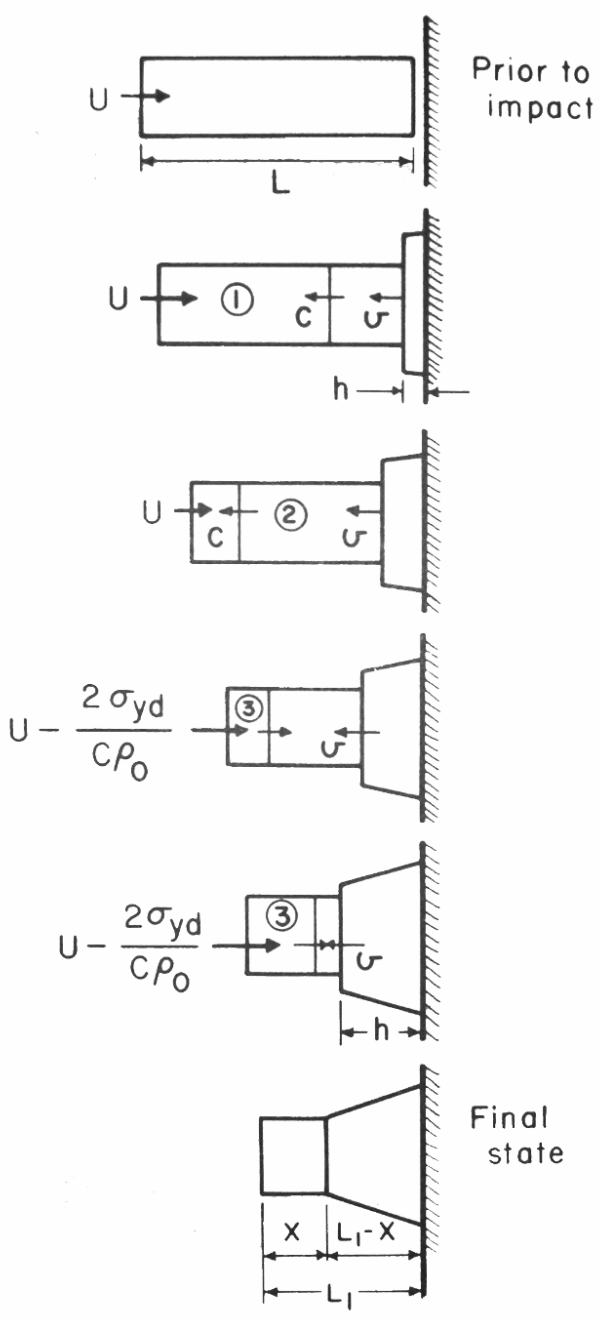


**Figure 2.16** Schematic illustration obtained from Meyers [16] for the deformation sequence that occurs from a Taylor anvil impact experiment [45] where a cylindrical projectile impacts a rigid surface.

stress of the material (dynamic yield stress, $\sigma_{yd}$) at a unique (constant) strain rate. The elastic wave continues to propagate the length of the specimen until it is reflected from the back surface and returns towards the propagating plastic wave as a release wave. Upon reflection, the elastic wave interacts with the plastic wave and reduces the stress within the region to zero, thus bringing the deformation process to a conclusion.

Based on computer simulations for the Taylor test, Wilkins and Guinan [94] obtained a correlation between final cylinder length and yield strength parameters for several metallic projectiles with the application of elastic-plastic theory. They first verified that the ratio of the cylinder final length to original length ($L_f/L_0$) was constant for a given impact velocity, and thus considered the dynamic response of the material to be independent of this ratio. For their analysis, it was assumed that the projectile decelerates as a rigid body and plastic deformation occurs at the impact face. This suggests that the change in specimen length over time is equal to the instantaneous velocity $U$ and is given by [94]:

$$\frac{dL}{dt} = -U \,. \tag{2.22}$$

Deceleration of the specimen exerts a force which is equal to the product of dynamic yield stress $\sigma_{yd}$ and the cross-sectional area. Applying Newton's second law yields:

$$\sigma_{yd} A = -\rho_0 L A \frac{dU}{dt}, \tag{2.23}$$

given by the mass of the specimen $\rho_0 LA$ and its deceleration $dU/dt$. Combining equations (2.22) and (2.23) results in:

$$\frac{dL}{L} = \frac{\rho_0 U}{\sigma_{yd}} dU \,. \tag{2.24}$$

Integration of equation (2.24) and rearranging terms gives [94]:

$$\sigma_{yd} = -\frac{\rho_0 U^2}{2\,ln\left(L_f / L_0\right)}. \tag{2.25}$$

The dynamic yield stress can thus be estimated through measurements of density, impact velocity, and the initial and final lengths of the specimen.

Modified versions of Taylor impact experiments have been conducted in conjunction with velocity interferometry (VISAR) to measure material response during dynamic loading [95]. For these experiments, a reverse Taylor impact configuration is utilized where the specimen of interest is held stationary and a rigid anvil, accelerated using a gas gun, impacts the target specimen. This configuration permits a velocity-time signal to be obtained from the back surface of the specimen. With this type of diagnostics, the detection of the elastic wave arrival at the back surface of the specimen is possible. Furthermore, combining this analysis with post impact sample geometry makes it possible to validate numerical simulations and the constitutive response of the material at high-strain rates.

For these particular experiments, the modified Taylor impact tests with VISAR, have been used to investigate the dynamic behavior of high strength steel (35NiCrMoV109) cylindrical specimens at impact velocities between 256 and 361 m/s. Dynamic yield stress, strain, and strain rate data are then used in numerical simulations to reproduce the experimentally obtained VISAR traces. Figure 2.17 shows a schematic representation of elastic and plastic wave propagation and interaction in a thin rod after impact. Upon impact, an elastic wave travels through the specimen and reflects off of the back free surface causing a velocity increase detected by VISAR. The elastic wave is totally reflected because of the large impedance difference between steel and air. The back end of the specimen is accelerated from elastic wave reflections and causes a stepwise increase in free surface velocity as shown schematically in Figure 2.17. This is

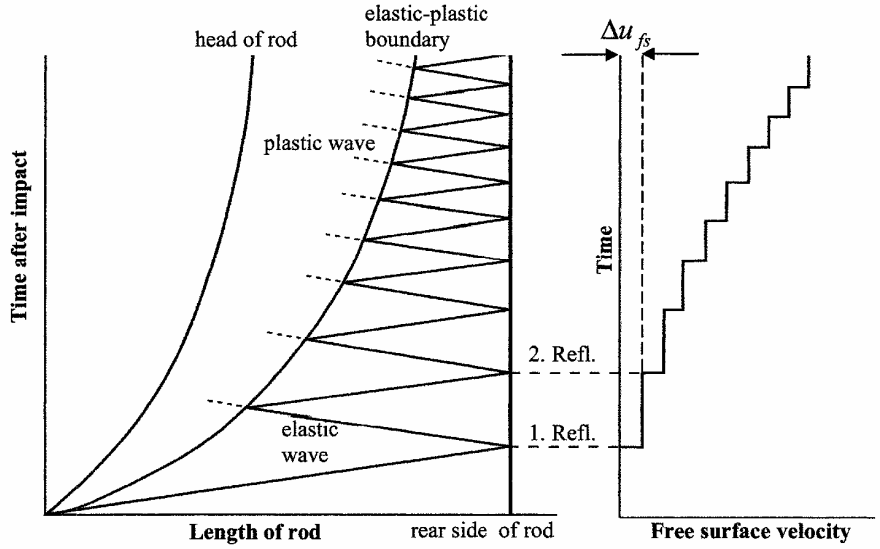


**Figure 2.17** Schematic representation of elastic and plastic wave propagation and interaction in a thin rod after impact. Wave propagation within the rod is shown to the left while the stepwise free surface velocity history is shown to the right after multiple reflections of the elastic wave at the back surface of the specimen [95].

followed by a nonlinear plastic wave which deforms the material and interacts with the reflected elastic wave traveling back towards the impact end of the specimen. Successive reflections occur within the material bounded by the free surface and the propagating plastic wave until the elastic wave motion is completely dissipated. The dynamic material data is determined directly from measuring the free surface velocity and applying it to the equilibrium equation determined by the conservation of momentum given below:

$$\sigma_Y = \frac{1}{2} C_0 \rho \Delta u_{fs}, \tag{2.26}$$

where $\Delta u_{fs} = u_{fs1} - u_{fs2}$ (Figure 2.17) is the free surface velocity at the back surface of the specimen measured with VISAR. Strain at the yield point is then given by:

$$\varepsilon = \frac{u_{fs}}{2C_0} = \frac{u_p}{C_0}, \tag{2.27}$$

and the strain rate at yield point is given by:

$$\frac{d\varepsilon}{dt} = \frac{\varepsilon}{\Delta t}. \tag{2.28}$$

The post impact distortion of the specimen from both the experiment and simulations are compared to verify the accuracy of the material model and experimentally determined input parameters. Figure 2.18 illustrates a comparison of the VISAR free

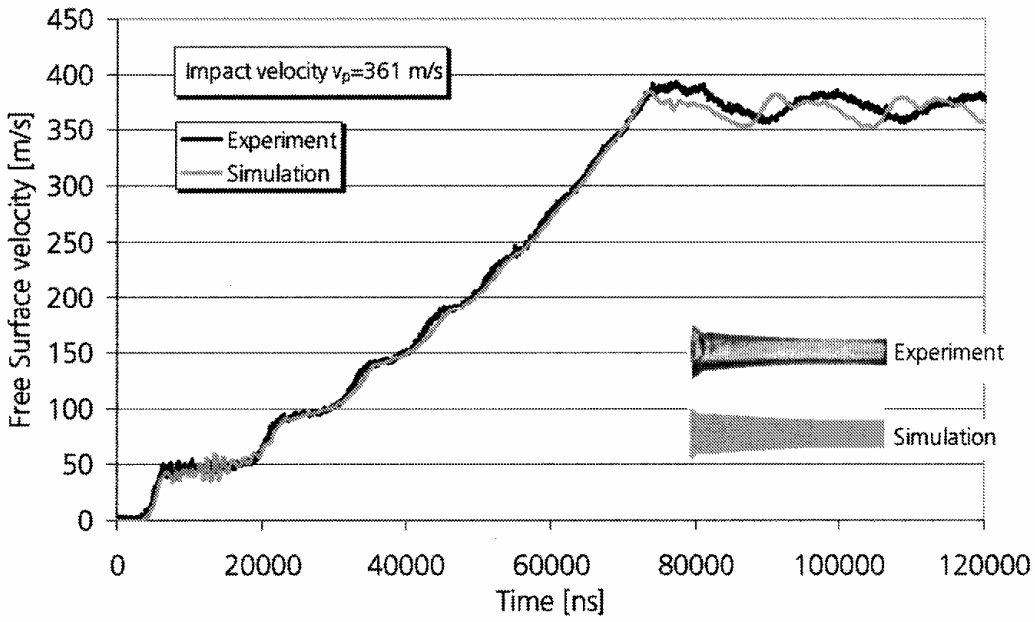


**Figure 2.18** Comparison of experiment and simulation results for reverse Taylor impact tests conducted on high strength steel (35 NiCrMoV109) [95].

surface velocity signal with numerical calculations, showing excellent agreement. The modified Taylor test in combination with numerical simulations is a useful tool for determining dynamic material properties.

Illustrating another variation for the test, House, *et al.* [96] developed a method for capturing the transient deformation during Taylor impact experiments using high-speed photography measurements. The deformation profile, photographed at different times during the experiment, was used to estimate the strain rate and the stress-strain response of a rod-shaped OFE copper specimen. The specimen radius was measured incrementally along its axial length for specific times during the impact, as shown in Figure 2.19(*a*). This provided a measure of the specimen's length for specific time instances; enabling the calculation of back end speed given by:

$$u = \frac{l_1 - l_2}{t_2 - t_1}, \tag{2.29}$$

where $l_1$ and $l_2$ are the specimen lengths at corresponding times $t_1$ and $t_2$. Areal strains were calculated using Taylor's definition [45]:

$$e = 1 - \frac{A_0}{A}, \tag{2.30}$$

where $A_0$ is the cross-sectional area prior to impact and $A$ is the incremental area for a specific location along the axial length of the specimen. The measured axial length profiles are transformed into areal strain profiles as shown in Figure 2.19(*b*). A series of plastic wave speeds are next calculated by selecting two axial positions $h_1$ and $h_2$ for obtaining corresponding strains, $e_1$ and $e_2$ from Figure 2.19(*b*). The average Eulerian wave speed, $v$, for a strain level, $e_1$, is given over the time interval, $t_1$ to $t_2$, by:

$$v = \frac{h_2 - h_1}{t_2 - t_1}. \tag{2.31}$$

The approximated strain rate is also obtained from Figure 2.19(*b*) by observing the change of strain over the time interval $t_1$ to $t_2$.

Taylor's [45] original approach was used to determine the stress over the time interval examined. The stress, $\sigma_1$, associated with strain, $e_1$, is given by:

$$\sigma_1 = \rho(u + v)v, \tag{2.32}$$

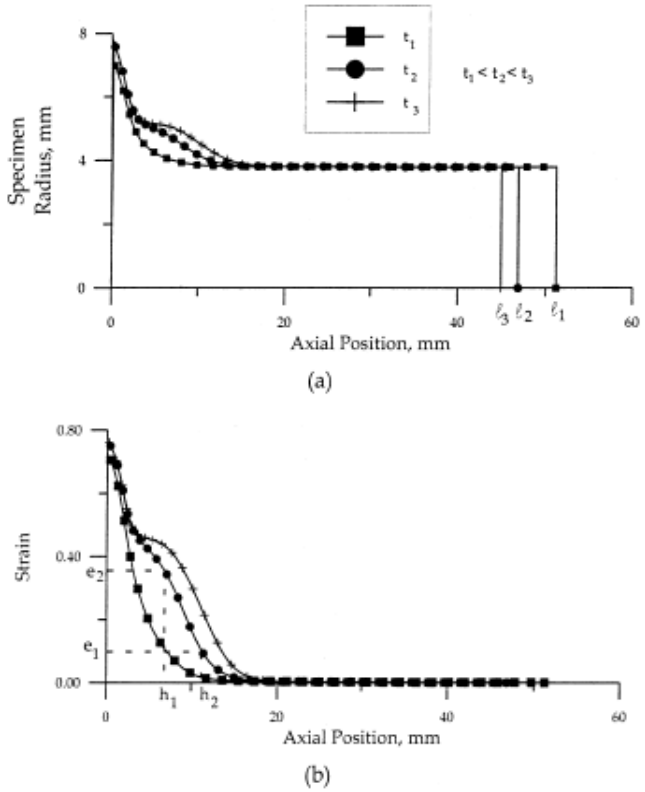


**Figure 2.19** Plot of measured *a*) specimen radius and *b*) calculated areal strains along the specimen's axial length obtained from high-speed camera images [96].

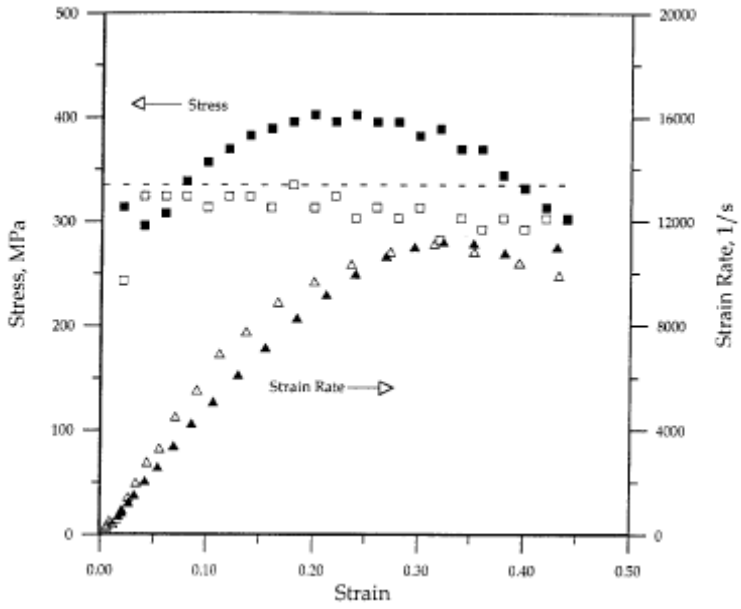


**Figure 2.20** Stress and strain-rate data obtained from OFE copper Taylor tests as a function of strain [96]. The solid points are from strain profiles taken at times 33.3 and 63.3 μs, while the open points are from strain profiles taken at times 63.3 and 79.9 μs.

where $\rho$ is the mass density. Stress-strain pairs are then constructed by selecting multiple strain locations along the specimen's axial length and calculating the corresponding stress. The results are demonstrated by the stress and strain rate versus strain plots obtained for OFE copper as shown in Figure 2.20. The figure shows the strain rate approaches $10^4$ 1/s for the deformed region of the rod shaped specimen selected for this analysis and corresponding to strain profiles measured at times of 33.3 and 63.3 μs after impact.

### 2.4.2 Dynamic Properties of Polymers Determined from the Taylor Test

For the case of impacts with polymeric materials, elastic strains in general are not negligible compared to plastic strains; and the rigid-plastic material behavior assumed by Taylor for metallic materials, which inherently neglects elastic strains, cannot be applied. Briscoe and Hutchings [97] studied the impact yielding of high density polyethylene using Taylor's analysis and found uncharacteristically high values of flow stress. Large elastic strains are not accounted for in the theory, which results in an over estimate of the flow stress.

Hutchings [98] later used a one-dimensional elastic-plastic wave propagation analysis to determine the dynamic yield strength of polycarbonate. For this analysis, the mechanical properties of polycarbonate subjected to dynamic impacts are assumed to be represented by an ideal elastic perfectly-plastic material model, which is strain rate independent. Additionally, the material is assumed to behave in the same manner during both elastic loading and unloading, consequently having the same modulus.

For this analysis, the classic Taylor anvil impact experiments were conducted on polycarbonate cylindrical specimens, 16 mm in diameter and 38 mm long, using a compressed-gas gun. Specimen initial length, $L_0$ and final length, $L$ were measured before and after high velocity impacts, respectively. The undeformed section of the specimen, $X$ was additionally measured after impact.

Theories for metallic materials that assume a rigid-plastic behavior and neglect elastic strains would predict some plastic deformation in the specimen at any finite, non-zero impact velocity. Nevertheless, this is not the case for polymeric materials. Polycarbonate specimens did not show any change in length for impact velocities below approximately 100 m/s. However, above this critical velocity, the change in specimen length increased linearly as a function of impact velocity. Figure 2.21 shows the fractional change in overall specimen length as a function of impact velocity, which intercepts the velocity axis at 104 m/s [98]. The figure also shows the fraction of initial length which remains undeformed after impact and decreases without variation with increasing impact velocity.

Hutchings [98] recognized that any theory considered for predicting the behavior of polymeric materials using the Taylor test would have to consider substantial elastic strains which polymers can experience before yielding plastically. Consequently, Hutchings modified the rigid-perfectly plastic theory to allow for elastic strains which polymers undergo before yielding. With knowledge of the polycarbonate projectile length after impact and critical velocity below which no plastic deformation occurs, the dynamic yield strength was determined. Figure 2.22 makes comparison of calculated dynamic yield stress values using Taylor's original analysis and the modified elastic-

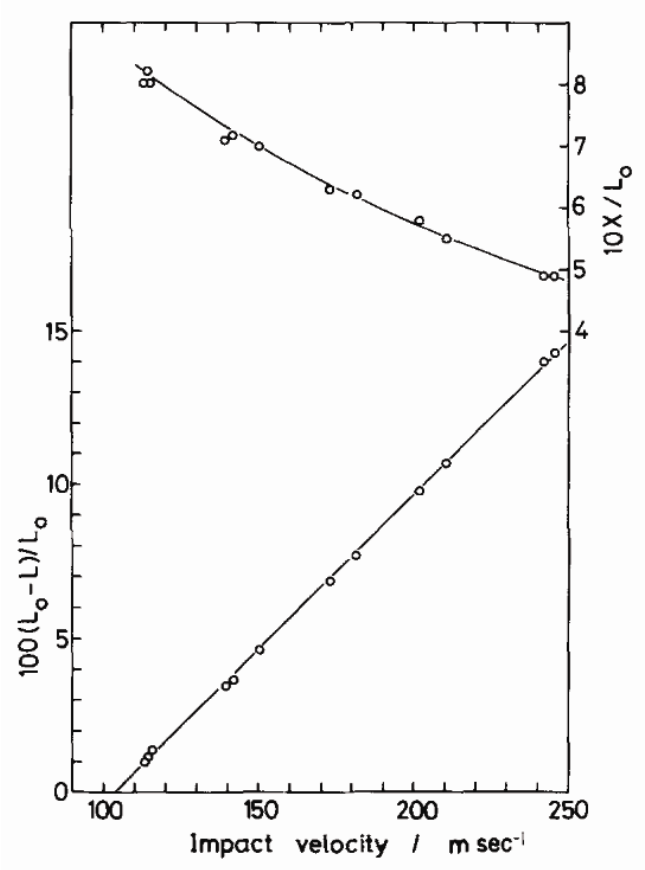


**Figure 2.21** Experimental data obtained for polycarbonate from Taylor impact tests. Upper points show the fraction of initial length which remains undeformed while the lower points show the fractional change in overall length and the critical impact velocity above which plastic deformation begins [98].

plastic wave method developed by Hutchings for polycarbonate [98]. The yield stress calculated by Taylor's analysis varies rapidly with impact velocity and is not applicable to estimate yield stress for polymeric materials. The elastic-plastic wave propagation method, however, gives results which are almost independent of velocity and are in good agreement with values estimated from Taylor's analysis at high velocities.

Taylor anvil impact experiments have also been conducted on thermoplastic polyether ether ketone (PEEK) cylinders with impact velocities from 152 to 408 m/s [99]. High-speed photography was used to observe the transient deformation during impact

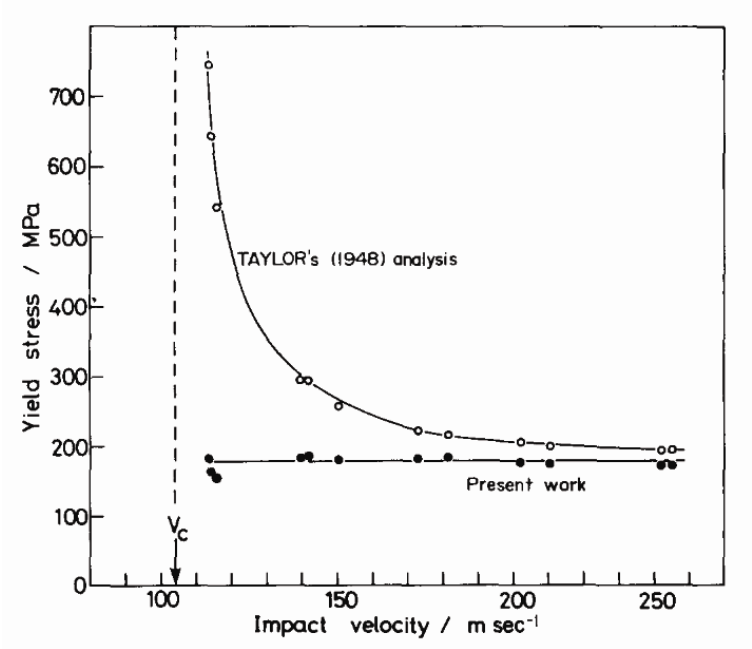


**Figure 2.22** Comparison of calculated yield stress values obtained from experimental data using Taylor's analysis (open circles) and the elastic-plastic wave method from Hutchings [98].

and samples were recovered for post impact analysis. Several interesting features were observed for this material system and became more evident as impact velocity was increased. The deformation of the specimens showed a characteristic "mushroom" shape up to impact velocities of 303 m/s, before fracturing was observed at the impact face. Fracturing appears to be ductile in nature and no evidence of brittle failure was observed. Examination of axially sectioned cylinders after impact shows a discolored region immediately behind the impact face of the specimen. The authors suggest that these darker regions may be associated with heating in the area and attribute these to either shock and strain-heating, or an oxidation process from air being trapped between the anvil and sample, and its adiabatic heating during impact. However, heating was not extensive enough to show any melting or alteration of the material's chemistry [99].

The impact end of each recovered specimen had a concave shape and it experienced considerable relaxation after the load was removed. This corresponds to features observed from high-speed photography. Similar concave shaped impact faces have been observed for high density polyethylene [97]. Stresses were calculated at the moment of impact, assuming one-dimensional strain conditions and based on impedance matching techniques with the assumption that the steel anvil behaved purely elastic. Maximum radial strain measurements obtained from high-speed images were approximately 13 % greater than those measured from recovered specimens.

This work was extended by Rae and Brown on commercially available extruded PEEK (grade 450G) [100]. Taylor anvil impact experiments were conducted at impact velocities between 150 and 360 m/s and at temperatures of 23 and 100 °C. No evident differences in the material response were observed for the two temperatures besides the typical decrease of yield strength at elevated temperatures. Normal deformation patterns were observed for specimens subjected to low impact velocity (150 - 250 m/s) conditions. More extensive deformation was observed at medium impact velocities (250 - 315 m/s) in addition to the formation of small radial cracks. The specimen formed a concave shape, similar to that observed by Millett, *et al.* [99], on the face of the impact end of the specimen for this velocity range. At the highest velocity range, (315 - 360 m/s), tearing within the "pullback" zone was evident and radial cracking was no longer observed. As previously observed by Millett, *et al.* [99], darkening of the rod was observed in highly deformed regions. Examination of photographed virgin material and three cross-sections of PEEK that experienced large strain deformation gave evidence that the color change is associated with the large strain state experienced by the material.

Other interesting features for polymeric materials have also been observed through Taylor anvil impact experiments. PTFE is typically a ductile polymer, but it undergoes an abrupt ductile-brittle transition at moderate impact velocities. It is a complex material that exhibits at least four known phase changes depending on temperature and pressure [101]. This pressure-induced phase transformation has also been observed in Taylor impact experiments conducted to examine PTFE material response to dynamic loading [102,103]. A critical fracture threshold exists, whereby the specimens fracture above impact velocities of 134 ± 1 m/s at room temperature. Results of these experiments are shown in Figure 2.23. The mechanical response of PTFE is highly affected by temperature such that yield strength increases as temperature is lowered yet fracture toughness decreases. The Taylor experiments present evidence for a

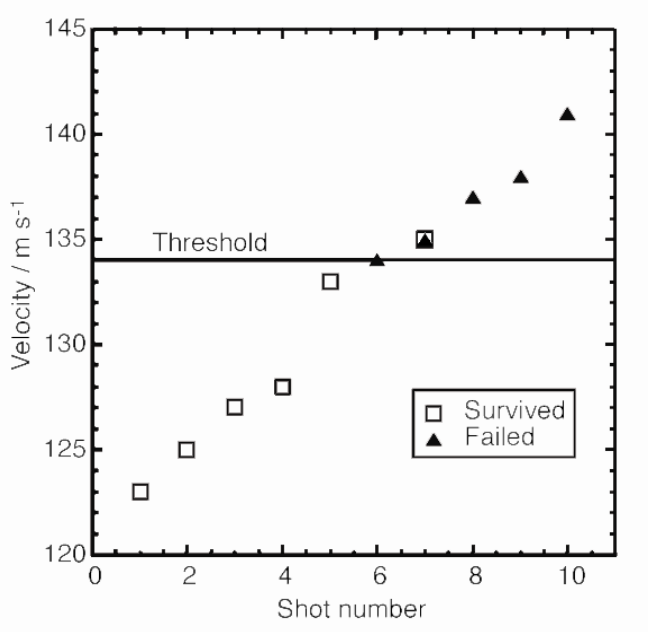


**Figure 2.23** Fracture velocity threshold map for PTFE determined from Taylor impact experiments at room temperature. Material has a critical impact velocity of 134 ± 1 m/s where a ductile-brittle transition behavior is observed [102,103].

pressure-induced phase transformation being responsible for the ductile-brittle transition found in PTFE because the critical velocity increases for decreasing temperature, even though the material fracture toughness decreases. Evidence of this is given by Taylor impact experiments conducted for specimens at temperatures of 1 and 40 °C which have transition velocities of 139 ± 2 and 131 ± 1 m/s, respectively. The phase transition occurs at approximately 0.65 GPa at 21 °C. Finite element calculations modeling Taylor impact experiment of PTFE at 135 m/s indicate that the stress magnitude coincides with the phase transition stress.

### 2.4.3 Constitutive Response of Polymer Materials

The response of viscoelastic materials to applied loads consists of a creep phase followed by a relaxation phase. As illustrated in Figure 2.24, initially the material is loaded at a constant rate, resulting in constant strain rate deformation. At point '1', the loading is held constant, however, the material continues to strain in response to this loading until the load is removed at point '2'. Upon unloading, the material relaxes at a specific decay rate and deformation is completely recovered only after a long time. The schematic in Figure 2.25 contrasts the stress-strain response of a perfectly elastic solid with that of viscoelastic solid. As illustrated, a perfectly elastic material retraces the same stress-strain path upon unloading as it followed during loading, regardless of strain rate. Furthermore, upon reloading, the stress-strain relationship is not altered. In contrast, a viscoelastic material relaxes along a different path from which it was loaded. Upon reloading, a viscoelastic material will exhibit a different stress-strain response

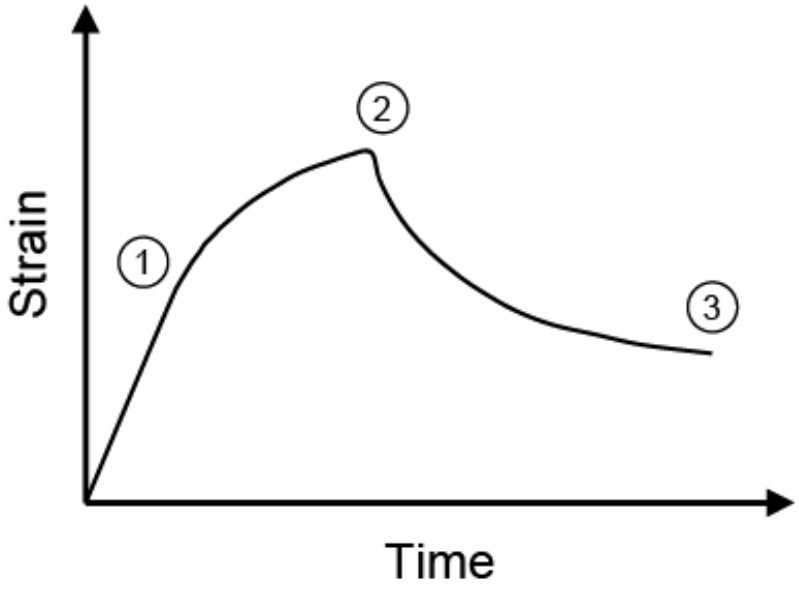


**Figure 2.24** Schematic plot showing strain versus time for a viscoelastic material loaded at a constant rate, followed by a constant load and then removed.

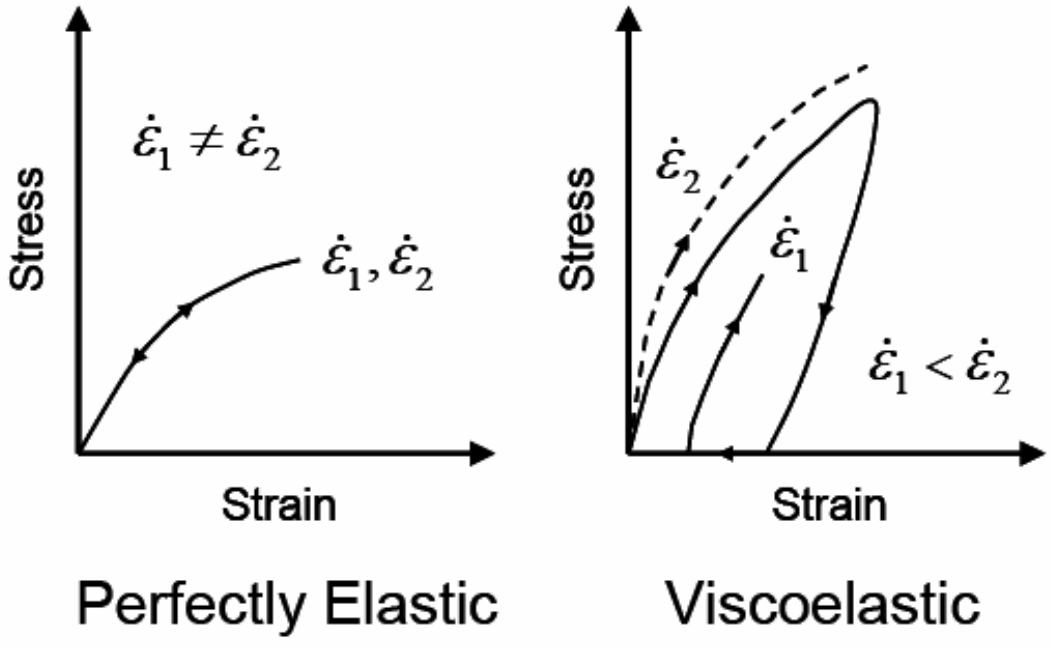


**Figure 2.25** Idealized material behaviors contrasting a perfectly elastic solid with that of a viscoelastic solid.

throughout its entire loading history. Additionally, the stress-strain response of a viscoelastic material may be a function of strain rate. Approaches to modeling this behavior often involve simulating the material response with networks of massless Hookean springs to represent the elastic strain components and Newtonian dashpots to represent viscous, time dependent flow [62]. The number of elements included in the viscoelastic model depends on the complexity of the mechanical material behavior.

The classical linear theory of viscoelasticity quantitatively describes the characteristic behavior of polymers such as creep and relaxation, however, it is generally limited to very narrow loading-rates and temperature regimes. The linear spring constitutive equation is of the form:

$$\sigma_S = E\varepsilon_S , \tag{2.33}$$

where $\sigma_S$ and $\varepsilon_S$ are the stress and strain of the spring, respectively. Similarly, the linear dashpot constitutive equation is of the form:

$$\sigma_D = \eta\dot{\varepsilon}_d , \tag{2.34}$$

where $\sigma_D$ and $\dot{\varepsilon}_d$ are the stress and strain rate of the dashpot, respectively and $\eta$ is the constant viscosity and implies a Newtonian viscosity effect. However, most polymers do not exhibit constant viscosity and show that it decreases with increasing strain rate. The stress-strain response in the spring is instantaneous while the dashpot response is time-dependent. Additionally, polymers are known to exhibit totally different responses

under various temperature conditions. At low temperatures they behave in a brittle elastic manner and at high temperatures, above the glass transition temperature, the behavior is more "rubbery" in nature. Moreover, existence of imperfections and discontinuities in the material can enhance the nonlinear viscoelastic behavior. Linear theory of viscoelasticity is unable to closely model these observed responses and thus there is a need for a non-linear theory of viscoelasticity.

Most nonlinear theories of viscoelasticity follow a similar pattern and are based on the notion that the stress in a viscoelastic material depends on the entire deformation history; or alternatively, the strain in a viscoelastic material depends on the entire stress history. Modeling approaches that have been applied with some success have used linear viscoelasticity equations comprised of linear spring and dashpot models and adapted them to nonlinear conditions [62]. Zerilli and Armstrong [104,105] describe a constitutive model for polymers where the total strain is divided into viscoplastic and viscoelastic parts. The viscoplastic component is described by a non-linear thermal activation dashpot which modifies the standard linear solid so that the movement of the dashpot is governed by an activation process using an Eyring type model [62]. In this model, the deformation of a polymer is a thermally activated rate process involving the motion of segment of chain molecules over potential barriers. In this way, the model parameters now include activation energy and activation volume that may give an indication of the underlying molecular mechanisms of the polymer. The viscoelastic component is described in terms of a Maxwell-Weichert linear viscoelastic model [62], which is a parallel arrangement of multiple elements comprised of a spring and dashpot placed in series. Zerilli and Armstrong's model [104,105] describes the response of

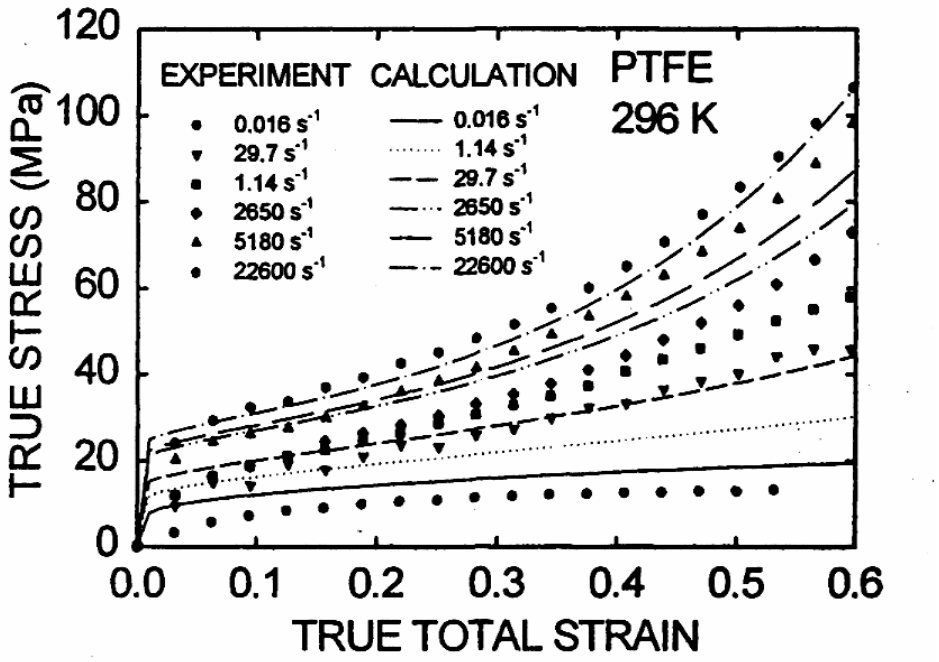


**Figure 2.26** Comparison of viscoelastic/viscoplastic model with stress-strain histories for PTFE loaded at various strain rates reported by Walley and Field [106].

polytetrafluoroethylene (PTFE) reasonably well for split Hopkinson pressure bar data reported by several investigators for a number of strain, strain rates, and temperatures, and by using tensile stress-strain data for various hydrostatic pressures. Figure 2.26 illustrates this from split Hopkinson data reported by Walley and Field [106].

Quasistatic and dynamic uniaxial compressive experiments carried out by Chen and Zhou [107] show that the stress strain response of epoxy (Epon® 828/T-403) is characterized by (*i*) linear elasticity, followed by (*ii*) nonlinear elasticity, (*iii*) yield-like behavior, (*iv*) strain softening, and (*v*) nearly perfect plastic flow. They also found that an increase in strain rate caused the measured peak strength to increase. Modeling of the stress-strain behavior using a modified empirical model based on Johnson-Cook showed good agreement only at small strain levels. Lu, *et al*., [108] later use a model developed

by Hasan and Boyce [69] to better describe the viscoelastic and viscoplastic behavior of Epon® 828/T-403 over several strain rates and describe the large deformation behavior reasonably well up to true strains of approximately 35 %.

The model proposed by Hasan and Boyce [69] was developed for predicting the large strain, time-dependent, and temperature-dependent response of glassy polymers. In the Hasan-Boyce framework, the total deformation gradient is decomposed into elastic and plastic components. Deformation of glassy polymers is dominated by local rearrangements of molecules which are thermally activated and formulated in terms of activation free energy, thermal energy, and attempt frequency within the model. The model uses a distribution of activation energies to characterize energy barriers to localized shear transformations. The activation energy is modified by applied external and internal stresses. In a glassy polymer, there is a greater possibility that a local shear transformation event will occur at relatively lower activation barrier sites. The sites with low activation barrier energy during the initial stage of deformation can transform and the stress-strain behavior begins to deviate from linearity. As the stress is increased, regions of relatively higher activation energy become available for shear transformation and the mechanical behavior becomes increasingly nonlinear. As the number of transformed sites increases, the surrounding material is no longer capable of storing the corresponding transformation energy and a defect is created thus resulting in the lowering of local activation energy, and strain softening of the material is observed. As the material is significantly deformed further, work hardening begins by the reorientation of the polymeric chains. The development of constitutive models that describe the behavior of thermoplastic polymers and polymeric composites require detailed quantitative

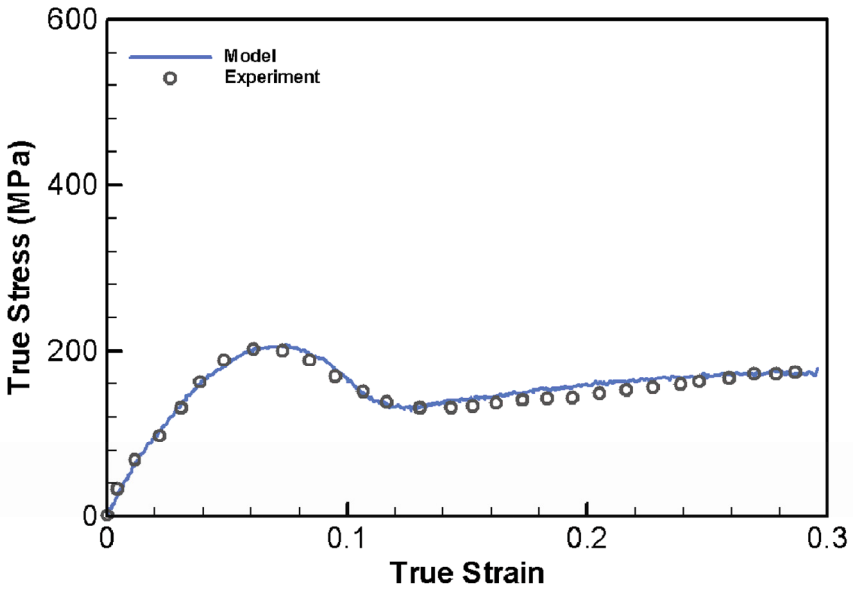


**Figure 2.27** Stress-strain history calculated using Hasan-Boyce model for Al+$Fe_2O_3$+50 *wt.%* epoxy composite obtained from split Hopkinson pressure bar experiments [68].

knowledge of the effects that temperature and strain rate have on their mechanical response.

Recent experimental work has been conducted on Al+$Fe_2O_3$+epoxy composites with epoxy concentrations ranging from 20 to 50 *wt.%* (47 to 78 *vol.%*) and compared to the Hasan-Boyce model with data obtained from split Hopkinson bar experiments [68]. Figure 2.27 compares the measured room-temperature response of an epoxy-cast mixture containing 50 *wt.%* epoxy. Good agreement between the model and experimental data are shown, for the case where the strain rate was essentially constant (on the order of $10^3$ 1/s). However, as the epoxy concentration decrease to 20 *wt.%*, the ability of the Hasan-Boyce model to fit the experimental data was observed to diminish. Hence, the correlation seems to be best under conditions where the dynamic deformation response of the composite is completely dominated by the epoxy.

## 2.5 Chemical Reactivity of Thermite Mixtures

The behavior and reaction mechanisms of thermite materials have been studied extensively. Once initiated, these materials are self-propagating and attain temperatures up to 4000 °C at heating rates up to a million degrees centigrade per second. However, combustion waves generated from thermite mixtures typically propagate relatively slow in comparison to an explosive detonation. Traditional explosives exhibit entirely different reaction mechanisms since the interaction of the fuel and oxidizer is contained within the explosive molecule itself. The understanding of chemical reaction mechanisms in thermite mixtures sets importance on the influence of particle morphology or essentially how interaction between the fuel and oxidizer influences the kinetics of the reaction. These types of reactions are diffusion controlled and can be altered mainly by changing the particle size or intimacy of the reactants. This has been a very active area of research and many authors have looked at thermite mixtures that utilize nanoscale aluminum as the fuel or reduction agent. There are several elements that can be utilized to very rapidly release high chemical energy if the morphology is correct. In addition, these thermite mixtures can be highly tailored for specific applications. Table 2.4 provides details about many energetic material systems and lists theoretical heats of reaction for several thermite mixtures, intermetallic compounds, and explosives.

Small particle, high-surface area metals are a potential new class of energetic materials that can be tailored for specific energetic requirements. The overall approach has been directed to the development of a fundamental understanding of nanometric

**Table 2.4** Comparison of energetic material systems including thermite mixtures [109], intermetallic compounds [109], and explosives [110] based on theoretical heats of reaction.

| Oxidizer + Fuel Reaction | $\Delta H_R$ [kJ/mol] | $\Delta H_R$ [kJ/g] |
|---|---|---|
| $Fe_2O_3 + 2\,Al \rightarrow 2\,Fe + Al_2O_3$ | -285 | -4.01 |
| $3\,MnO_2 + 4\,Al \rightarrow 3\,Mn + 2\,Al_2O_3$ | -256 | -6.35 |
| $5\,Fe_2O_3 + 6\,Ta \rightarrow 10\,Fe + 3\,Ta_2O_5$ | -185 | -1.08 |
| $5\,MnO_2 + 4\,Ta \rightarrow 5\,Mn + 2\,Ta_2O_5$ | -165 | -1.28 |
| (TNT) $C_7H_5N_3O_6 \rightarrow 3.5\,CO + 2.5\,H_2O + 1.5\,N_2 + 3.5\,C$ | -942 | -4.15 |
| (RDX) $C_3H_6N_6O_6 \rightarrow 3\,CO + 3\,H_2O + 3\,N_2$ | -1119 | -5.04 |
| (HMX) $C_4H_8N_8O_8 \rightarrow 4\,CO + 4\,H_2O + 4\,N_2$ | -1457 | -4.92 |
| $Ti + 2B \rightarrow TiB_2$ | -107 | -1.54 |
| $Ti + Si \rightarrow TiSi$ | -65 | -0.86 |
| $Ni + Al \rightarrow NiAl$ | -59 | -0.69 |

energetic compounds and the associated benefits of their use in weapons as well as rocket motors and other systems. The optimization and tailorability of energy release rates of these materials is an important feature and have been the focus through extensive experimental and theoretical studies. The following sections give information regarding the thermite reaction of Al+$Fe_2O_3$ and thermites in general. This is followed by a section that highlights the advantages of nanoenergetic materials and altering the particle morphology of energetic mixtures to the nanometric scale.

### 2.5.1 Aluminum-Hematite Thermite System

Thermite reactions are usually described as a class of reactions which involve a metal reacting with a metallic or non-metallic oxide forming a more stable oxide and the corresponding metal or non-metal of the reduced oxide. For example, the $Al+Fe_2O_3$ thermite mixture forms stable aluminum oxide and molten iron products. Traditionally thermite reactions of this type have been used to fabricate refractory ceramics and composite materials [111]. The term combustion-synthesis or self-propagating high-temperature synthesis (SHS) refers to an exothermic chemical reaction process that utilizes the heat generated by the reaction to ignite and sustain the propagating combustion wave through the reactants to produce desired products [112]. Frequently these reactions, also known as gasless combustion are identified as SHS reactions when applied to the synthesis of refractory compounds. SHS thermite-type reactions are self-sustaining and require a relatively small heating source to initiate. Once initiated, the reaction front propagates rapidly through the precursor powders until they are consumed. The potential advantages of this reaction are that the process requires little energy and very fast compositional formation is achieved in seconds. The reaction can reach temperatures ranging from 1500 to 4000 °C at heating rates up to a million degrees centigrade per second [113]. Additionally, formation of metastable phases is also possible because the reactions are very quick causing the molecules to solidify as structures that would be unstable under normal processing conditions.

The classic thermite mixture for aluminum and iron-oxide shown in equation 2.35 can attain temperatures higher than 3000 °C, which is above the melting points for both

iron and aluminum oxide [111].

$$2Al + Fe_2O_3 \rightarrow Al_2O_3 + 2Fe \Rightarrow \Delta H_R = -285\ kJ/mol \qquad (2.35)$$

Thermite reactions have been utilized to synthesize refractory ceramics and composite materials. For example, highly reactive metal particles ignite in contact with boron, carbon, nitrogen, and silica to form ceramics such as borides, carbides, nitrides, and silicides, for a wide variety of engineering applications. A comprehensive list of these materials and their energetic properties are given by Fischer and Grubelich [114]. Wang, *et al.* [111] provide a thorough review of thermite reactions and discuss additional applications for thermite synthesized materials.

The understanding of what happens along the combustion front of the reaction wave is a subject of significant research [112,113]. The combustion front is a region of small thickness (0.05 to 0.5 mm thick) where the final material forms. Varma, *et al.* [115] have used high-speed video recording to conduct *in situ* observations of processes occurring at the microscopic level during reaction of several binary systems. SHS reaction waves are classified into two general types: quasi-homogeneous and scintillating. A quasi-homogeneous wave moves at a steady rate with little temperature variation along the combustion front. This is the ideal situation for making material with uniform structure and sustaining the combustion wave. The scintillating wave, in contrast, has extreme temperature variations. This wave pattern occurs when one material melts during the reaction. The particles start to melt just ahead of the combustion front causing hot spots to form resulting in synthesis of a non-uniform material. Periodic cracking just ahead of the reaction front has also been observed which

induces oscillations in the propagation velocity thus promoting the scintillating wave behavior. Despite extensive studies, the mechanism(s) of reaction wave propagation are still not well understood.

The reaction mechanism between the aluminum and iron-oxide thermite system has been studied by Mei, *et al.* [116]. This study concentrated on the reaction process between $Fe_2O_3$ (average particle size of 5 μm) and liquid aluminum by intentionally slowing down the reaction by either reducing the contact area between aluminum and iron-oxide or by controlling the heat treatment of the mixture. Thermal analysis (DTA) was used to study the reaction sequence occurring during the thermite processes while electron microscopy and x-ray diffraction techniques were used to identify phases and composition of reaction products. Mei, *et al.* [116] deduced that there are two transition stages for reaction initiation, the first occurring at 960 °C producing $Fe_3O_4$ and $Al_2O_3$ while the next reaction occurs at 1060 °C forming Fe, $FeAl_2O_4$ and $Al_2O_3$. The reaction sequence first forming the product $Fe_3O_4$ and $Al_2O_3$ is shown below followed by the subsequent reaction forming $Al_2O_3$ and Fe.

$$9Fe_2O_3 + 2Al \rightarrow 6Fe_3O_4 + Al_2O_3 \qquad (2.36)$$

$$Fe_2O_3 + 2Al \rightarrow Al_2O_3 + 2Fe \qquad (2.37)$$

Another study by Korchagin and Podergin [117] also detected traces of $Fe_3O_4$ and proposed that the decomposition of $Fe_2O_3$ (according to equation 2.38) precedes the interaction between iron-oxide and aluminum:

$$Fe_2O_3 \rightarrow Fe_3O_4 \rightarrow FeO\,. \tag{2.38}$$

The presence of FeO leads to the formation of $FeAl_2O_4$ according to:

$$3Fe_2O_3 \rightarrow 2Fe_3O_4 + \frac{1}{2}O_2\,, \tag{2.39}$$

$$Fe_3O_4 + \frac{2}{3}Al \rightarrow 3FeO + \frac{1}{3}Al_2O_3\,, \tag{2.40}$$

$$FeO + Al_2O_3 \rightarrow FeAl_2O_4\,. \tag{2.41}$$

No complete phase diagram has been reported for the Al-Fe-O system, however certain reactions of mainly industrial importance have been investigated, especially the sub-solidus reaction in the partial systems $FeO\text{-}Al_2O_3\text{-}Fe_2O_3$ and $Al\text{-}Al_2O_3\text{-}Fe_2O_3\text{-}Fe$. The binary phase diagrams Al-O [118] (Figure 2.28(*a*)), Al-Fe [119] (Figure 2.28(*b*)), and Fe-O [119] (Figure 2.28(*c*)) have been used, as well as the pseudobinary system $FeO\text{-}Al_2O_3$ [120] (Figure 2.29) to infer features of the Al-Fe-O system.

Reaction in mixtures of reactive powders depend on diffusion and thermal conduction as the primary processes responsible for reactant mixing and chemical activation in the solid phase. Recent studies have focused on improving the reaction kinetics for thermite mixtures by improving the interparticle contact between reactants by means of *i)* foils composed of alternating layers of fuel and oxidizer [14,121]; *ii)* composites of nanoparticles prepared by ultrasonic mixing, metastable intermolecular composites (MICs) [122-124]; and *iii)* composites prepared using sol-gel processing [125-127]. Although each technique offers advantages and does improve

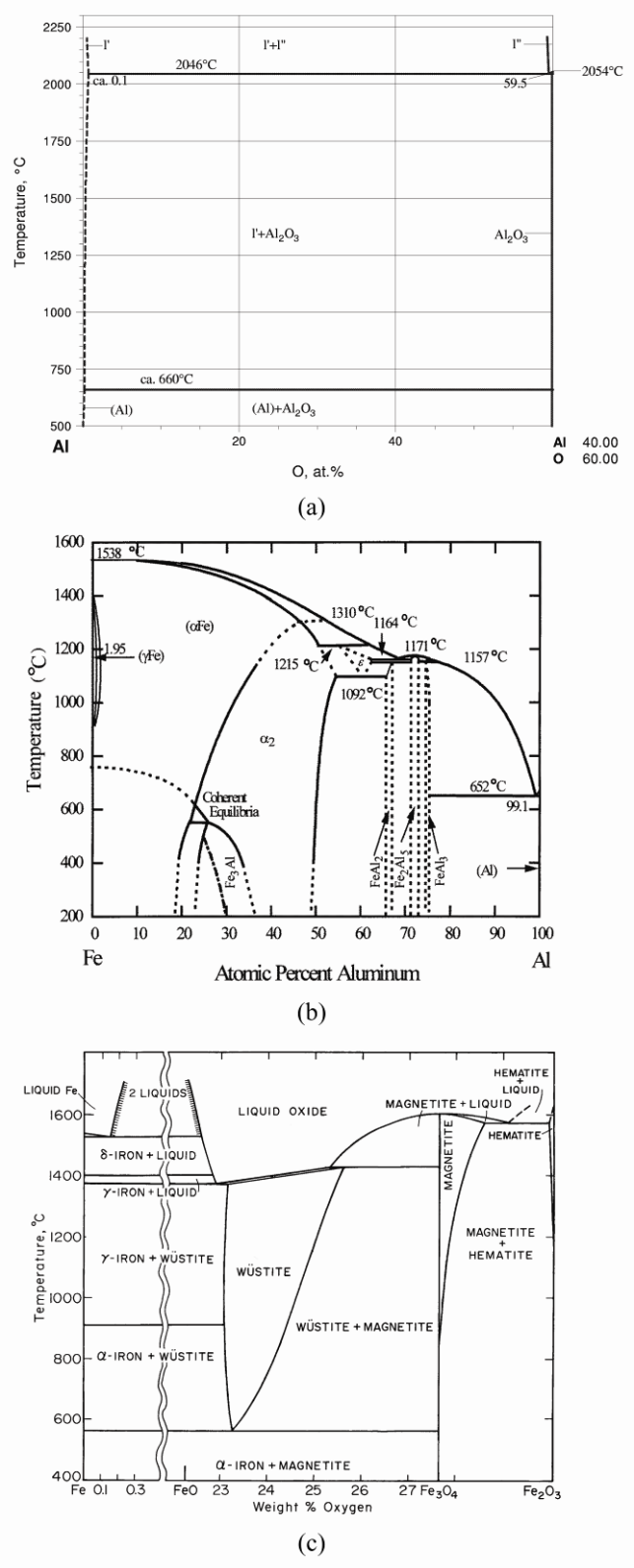


**Figure 2.28** Binary phase diagrams for *a*) Al-O [118], *b*) Al-Fe [119], and *c*) Fe-O [119].

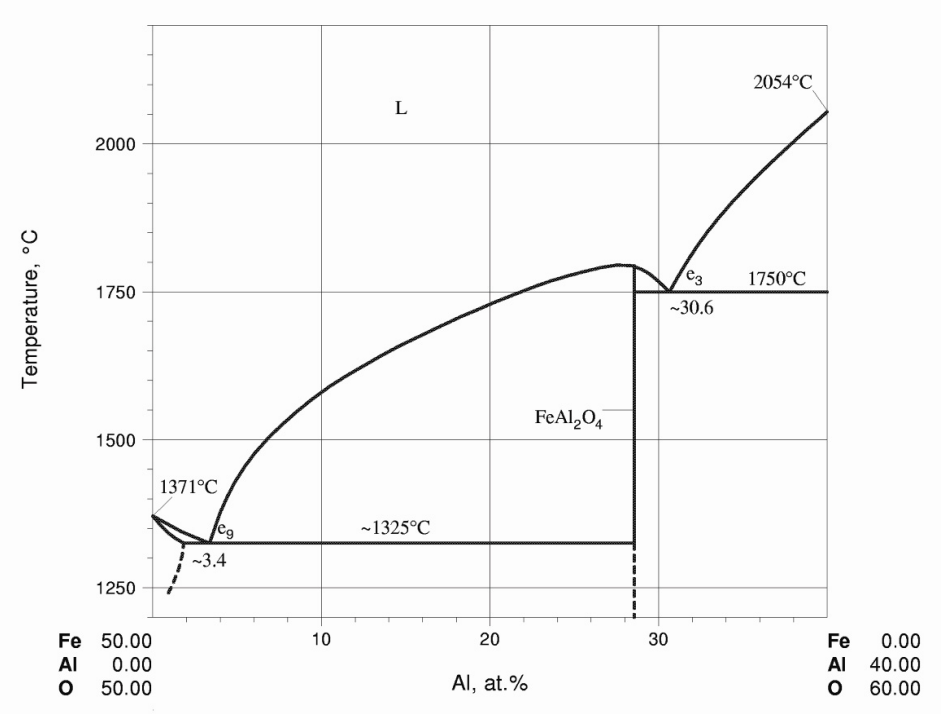


**Figure 2.29** Pseudobinary phase diagram for the $FeO$-$Al_2O_3$ system [120].

interparticle contact between the reactants, they also suffer from some disadvantages. For example, foil layering offers very good processing control so that the amount and diffusion distance between reactants can be tailored, however, the procedure is very time consuming and expensive. Mechanical or ultrasonic mixing of reactant particles is relatively inexpensive and large batches of material can be made quickly, however this process does not offer the exceptional structure control as exemplified by the foil layering technique. The final approach combines the fuel and oxidizer using sol-gel chemistry and provides a means of controlling microstructural properties such as particle size and morphology, and chemical composition of the composite. This method uniformly disperses solid fuel within a nanoscale oxidizer matrix. The reactivity of each of these systems have been evaluated on the bases of flame propagation studies.

Platier, *et al.* [128] has conducted flame propagation studies for assessing combustion wave speeds of nanoscale aluminum powders mixed with sol-gel synthesized iron-oxide (xerogel and aerogel) thus effectively altering diffusing distances for the $Al+Fe_2O_3$ thermite system for evaluation. The study found that combustion wave speeds are highly affected by the oxidizer synthesis technique (xerogel versus aerogel) and showed that the aerogel had the greatest combustion wave speed, over 900 m/s compared to 300 m/s for the xerogel. Combustion wave speed differences were attributed to morphological dissimilarities between the two compositions with the aerogel benefiting from having a more open structure that permits open channel burning and an increased surface area for the reaction to take place, therefore, enhancing convection mechanisms important to flame propagation. The authors indicate that the intimate mixing between the nanoscale reactants was an important factor for obtaining steady combustion wave fronts.

### 2.5.2 Nanometric Scale Energetic Materials

Nanoscale energetic materials are capable of storing greater amounts of energy than conventional C, H, N, and O based organic chemistries of explosives, while also showing increased performance in areas such as sensitivity, stability, energy release, and mechanical properties, in addition to having the ability to tailor energy release in efficient ways [129]. These attributes have directed the way for extensive studies aimed at exploiting the unique properties of nanomaterials that have the potential to be used in energetic formulations. Two requirements for energetic materials such as propellants and

thermites or explosives are to have the ability to store large amounts of energy and to efficiently release this energy when desired. For explosives, this class of energetic material is exemplified by trinitrotoluene (TNT) which has both the fuel (carbon) and the oxidizer ($O_2$) contained in the same molecule. TNT is normally metastable at ambient conditions and upon fragmentation produces highly stable products and releases large amounts of energy. However, TNT is not the most efficient when releasing chemical energy, thus resulting in incomplete oxidation of the carbon fuel. In contrast, energetic materials such as propellants and thermite mixtures are capable of yielding large amounts of energy through an exothermic reaction produced from mixtures containing individual oxidizer and fuel particles. Reactants and reaction products are stable when held separately, or no extra energy is provided for the reaction to proceed. In this class of materials, the reaction products are more stable than the reactants, and energy is released mostly in the form of heat.

The novel chemistry brought about by nanoscale materials, which possess a large surface-to-volume ratio, permits the design and synthesis of materials that optimize the two requirements for energetic materials, namely capability of storage and efficient release of energy. For example, nanoscale aluminum is very reactive and can interact with $CO_2$ and water, releasing energy in the form of heat. Reactions with CO and $H_2$ with bulk aluminum yield -821 kJ/mol and -946 kJ/mol of energy respectively. However, the drawbacks for use of nanoscale aluminum are the concerns derived from safe handling and storage because of its high reactivity. Many nanoscale metals have not been extensively developed because of their high reactivity making them dangerous to produce and handle [130]. Additionally, nanoscale aluminum particles interact with an

oxidizer forming a dense aluminum oxide layer that blocks diffusion of oxygen, preventing further oxidation of the inner aluminum core and resulting in incomplete combustion. Manufacturers are producing nano-aluminum particles with various aluminum oxide thicknesses ranging from 1 to 5 nm thick [130]. Controlling variations in particle size and oxide thickness determines the aluminum content of the particles. For example, a 20 nm particle with a 5 nm aluminum oxide coating contains approximately 10 *wt.%* of pure aluminum. In contrast, that same 20 nm particle with a 1 nm aluminum oxide coating contains approximately 60 *wt.%* aluminum. However, energetic metastable thermite mixtures are possible because aluminum particles form an aluminum oxide shell encapsulating a core of aluminum, and remain isolated from the oxidizer until external energy applied to the composite causes the oxide shell to fail resulting in initiation of a self-propagating reaction.

Fairly recently, the use of energetic materials to replace traditional organic explosives such as HMX and RDX has been a main topic of study. Thermite mixtures comprised of fuel and oxidizer particles such as Al+$Fe_2O_3$ and Ni+Al are particularly of interest. The energy release rate in microscopic systems is limited by the mass transfer process which requires the reactants to be physically mixed thus promoting self-sustaining chemical processes. Recent work has focused on minimizing the mass transfer effect by utilizing nanometric scale fuel and oxidizers [125,131]. This also permits the possibility of tailoring energy release rates by varying the size of the components and effectively altering the reaction pathway. With this in mind, increased performance may be realized by enhanced mixing of energetic ingredients produced at the nanometric scale.

It is well known that the size distribution and the degree of intermixing between the metal-oxide reactants increase the propensity of reaction initiation and significantly affect burn rate. For instance, powder mixtures of nanometric size Al and $MoO_3$ have burn rates approximately 1000 times higher than conventional micron-scale constituents [132,133]. Nanoscale particles enhance chemical reactivity by significantly altering the surface area to volume ratio of particles as their size is reduced, promoting more fuel to be in contact with the oxidizer. Armstrong, *et al.* [134] suggest that there is a burn rate behavior dependence on the inverse square of particle diameter attributed to the energy release rate being determined by increasing available particle surface area per unit volume as the particle size decreases.

Nanostructured energetic materials represent a new paradigm for improved energetic material research and development utilizing many elements from the periodic table. Nanoscale energetic materials have increased performance including better sensitivity, stability, energy release, and mechanical properties. Early studies have found that nanoenergetic materials can store more energy than conventional energetic materials and can be tailored to release energy with the maximum benefits [42,131], namely more efficient coupling with targets and increased lethality. Reactant particle size, morphology, and the distribution of these affect chemical reactivity, enhance energy content and the rate of energy release, as well as reduce sensitivity to unintentional reaction. Furthermore, improved dynamic mechanical properties are also realized by the particle size reduction of reactants in these material systems.

Interest in nanostructures is driven by the potential for finding novel properties and technologically useful characteristics of material structures that have small physical

dimensions. Nanoscale aluminum has found its way into applications such as additives for propellants, munitions, and other energetic applications because of its ability to enhance their chemical reactivity. Ignition behaviors of several thermite mixtures containing nanoscale aluminum show a dramatic decrease in ignition temperatures [123,124]. Nanoscale aluminum particles are becoming more readily available and provide an opportunity to enhance the reactivity of thermite mixtures by increasing the combustion velocity.

## 2.6 High-Strain Rate Simulations for Energetic Materials

The unique environments that reactive materials experience during shock compression, which can promote chemical reactivity, are influenced by particle-level behavior. Time-resolved experimental methods characterize the bulk material response to dynamic loading. However, numerical methods are needed to give full spatial resolution of the materials response. Numerical simulations of shock waves propagating through aluminum iron-oxide thermite powder mixtures dispersed in a polymer binder have been examined to provide insight into thermomechanical and chemical response at the particle level and develop Hugoniot data [135,136]. For the simulation, the stress-strain response of the constituent phases has been modeled explicitly at high-strain rates for thermite mixtures containing 20 and 50 *wt.%* (47 and 78 *vol.%*) epoxy.

Microstructures were reconstructed by algorithms that synthetically generate particle locations based on prescribed mixture parameters to resemble physically acquired microstructures for this material system. Figure 2.30 shows an example of a

reconstructed microstructure for Al+$Fe_2O_3$+20 *wt.%* epoxy composition. Finite element simulations for this study were performed using a 2D multi-material Eulerian hydrocode called Raven, developed by Benson [137]. Thermal and mechanical responses of the material system were studied through particle level material deformation, and spatial distributions of temperature and pressure were probed. However, chemical reactivity of the thermite mixture was not considered in this study.

The same microstructure for an Al+$Fe_2O_3$+20 *wt.%* epoxy mixture was considered for two different loading conditions. Figure 2.31 shows post-shock microstructure morphologies for two simulations that are subjected to a high-velocity ($U_P$ = 1.0 km/s) and low-velocity ($U_P$ = 0.5 km/s) loading conditions. The first observation is that the higher velocity case exhibits substantially higher plastic deformation than that at the lower velocity. Plastic deformation of the aluminum phase is particularly severe with the iron-oxide phase showing a relatively stiffer response.

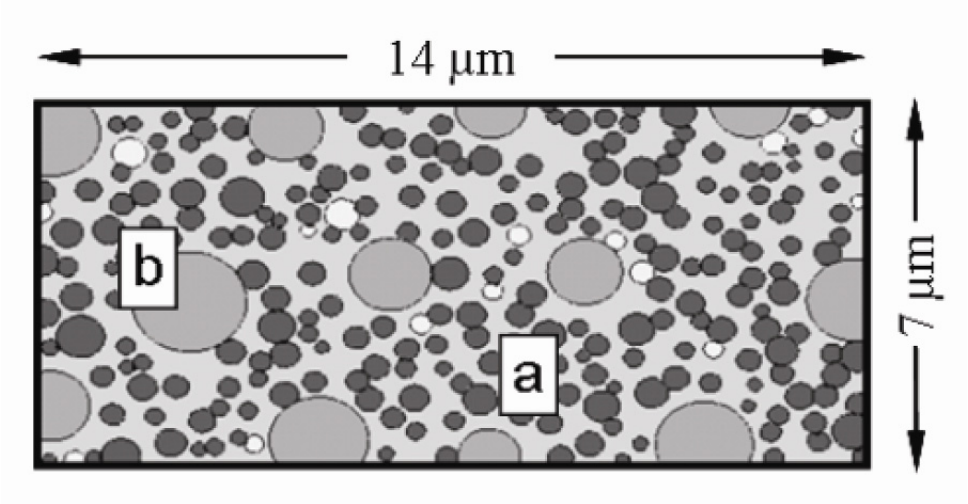


**Figure 2.30** Example of a reconstruction microstructure with 20 *wt.%* epoxy compostion. Markers indicate *a*) iron-oxide agglomerates and *b*) aluminum particles with voids as the remaining white areas [135,136].

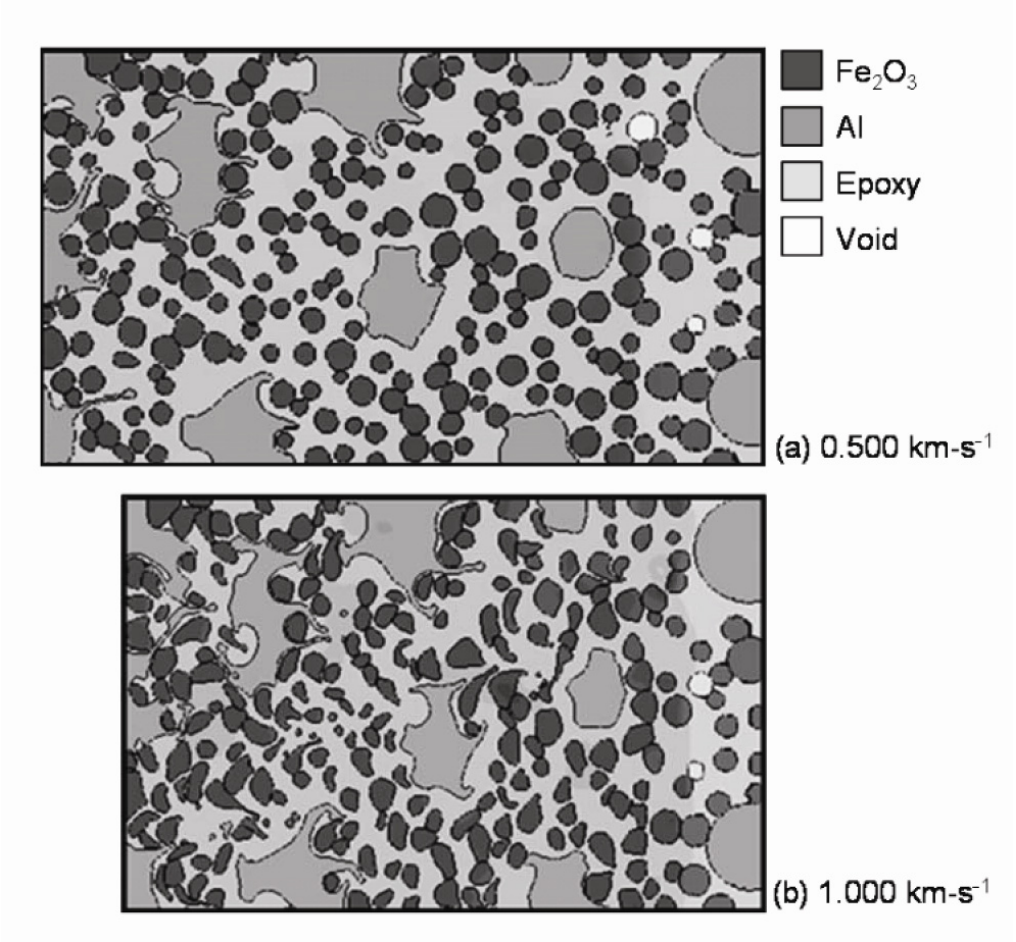


**Figure 2.31** Post-shock microstructure morphologies for *a*) $U_P$ = 500 m/s, and *b*) $U_P$ = 1000 m/s [135,136].

For the high velocity case, aluminum particles appear to flow around and between iron-oxide particles.

This is a significant result since microstructures can be designed to optimize this behavior for enhanced material strength or promote shock-induced chemical reactions. In addition, the temperature and pressure profiles along specific locations within the microstructure were also obtained through simulations. The profiles showed that the decomposition of the epoxy phase closely follows the shock front as it propagates across

the material. Iron-oxide particles experience limited amount of melting at the particle surfaces and the aluminum particles experience no melting at all. An insignificant amount of melting for the iron-oxide phase is expected due to its high melting temperature. However, the fact that aluminum particles do not melt suggests that the time scales involved are too short for the effects of heat conduction to take place. The Hugoniot for the 50 *wt.%* epoxy composition was also characterized by the $P$-$U_P$ and $U_S$-$U_P$ relations calculated in the finite element models, and correlated with experimental data.

Tomar [138,139], has performed classic molecular-dynamic (MD) simulations for analyzing the mechanical deformation in nanocrystalline materials (Al and $Fe_2O_3$), and nanocrystalline Al+$Fe_2O_3$ composites. The research focused on the development of interatomic potentials for describing the behavior of *fcc*-Al, $\alpha$-$Fe_2O_3$, and Al+$Fe_2O_3$ nanocomposites. The MD framework was applied to analyze the nanoscale mechanical behavior for both quasistatic and dynamic loading conditions, in addition to accounting for chemical reactivity resulting in reaction product formation from the deformation of Al and $Fe_2O_3$ mixtures.

Structures generated for the mechanical deformation analysis included nanocrystalline Al and $Fe_2O_3$, and Al+$Fe_2O_3$ nanocomposites with three different average grain sizes (7.2, 4.7, and 3.9 nm for each type). The Al+$Fe_2O_3$ nanocomposites were composed of two different volume fractions; 60 % *fcc*-Al+40 % $\alpha$-$Fe_2O_3$ and 40 % *fcc*-Al+60 % $\alpha$-$Fe_2O_3$. Grain morphology and orientation in nanocrystalline structures have a significant effect in determining strength.

The quasistatic deformation mechanisms for nanocrystalline Al observed in the MD simulations were comprised of three main categories: *i*) uncorrelated atom shuffling resulting in grain boundary sliding (intergranular), *ii*) partial dislocations and twinning (intragranular), and *iii*) microshear banding. A softening trend in strength was observed as the average grain size decreased, as illustrated for nanocrystalline Al in Figure 2.32(*a*). It was observed that after significant deformation, the flow was mainly governed by grain boundary sliding, and the 3.9 nm structure had lower flow strength at the later deformation stages. The so-called "reverse" Hall-Petch relationship was observed (as illustrated in Figure 2.32(*b*)) for the dependence of flow strength with square root of the average grain size, showing a deviation from linearity. In structures where the $Fe_2O_3$ phase is present, the deformation mechanism was also affected by electrostatic forces, enhancing grain boundary sliding. Consequently, the volume fraction of $Fe_2O_3$ phase strongly influenced the strength-grain size relations as depicted in Figure 2.33(*a,b*),

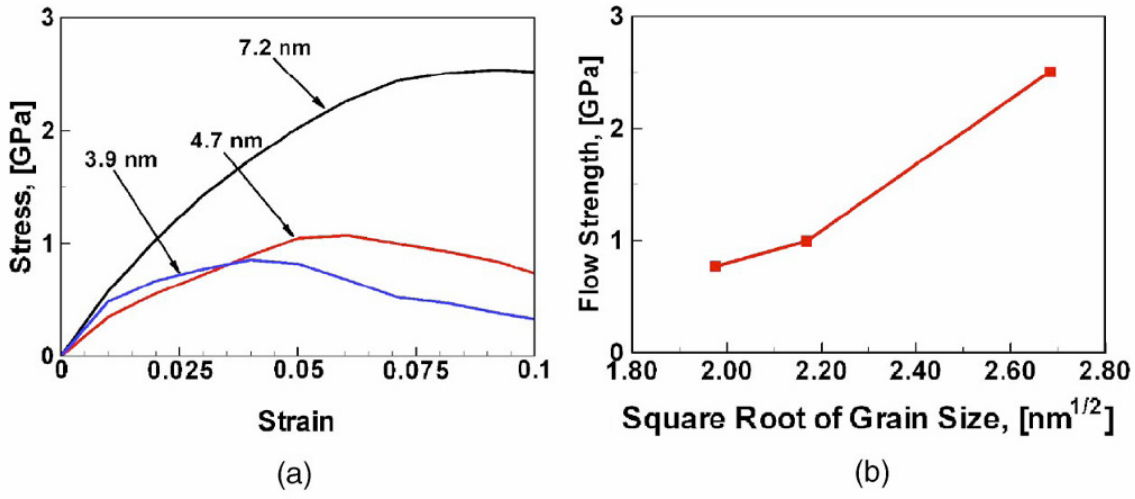


**Figure 2.32** Molecular-dynamics calculations obtained for nanocrystalline aluminum *a*) comparing tensile stress-strain curves with different grain sizes and *b*) the dependence of flow strength on average grain size [138,139].

which shows that structures with higher volume fractions of $Fe_2O_3$ have steeper slopes. The reverse Hall-Petch relationship for the composite structure ranged between those for Al and $Fe_2O_3$ as is evident in Figure 2.33(*a,b*).

Shock wave analysis for different crystallographic orientations of Al and $Fe_2O_3$ was also performed to determine the dynamic mechanical behavior for particle velocities ranging from 0.5 to 4.0 km/s. The study presented MD analysis of shock wave propagation in <100>, <110>, and <111> oriented single crystal Al, in <0001> oriented single crystalline $Fe_2O_3$, and through an interface between {100} surfaces of Al and {0001} surfaces of $Fe_2O_3$. Results showed that the $U_S$-$U_P$ relationship for single crystal material was dependent upon crystallographic orientation. However, the $U_S$-$U_P$ relationship did not deviate severely from experimentally determined polycrystalline behavior. Similar results were obtained for $Fe_2O_3$ and the $U_S$-$U_P$ relationship showed good agreement with experimental values. Analysis of shock wave propagation through

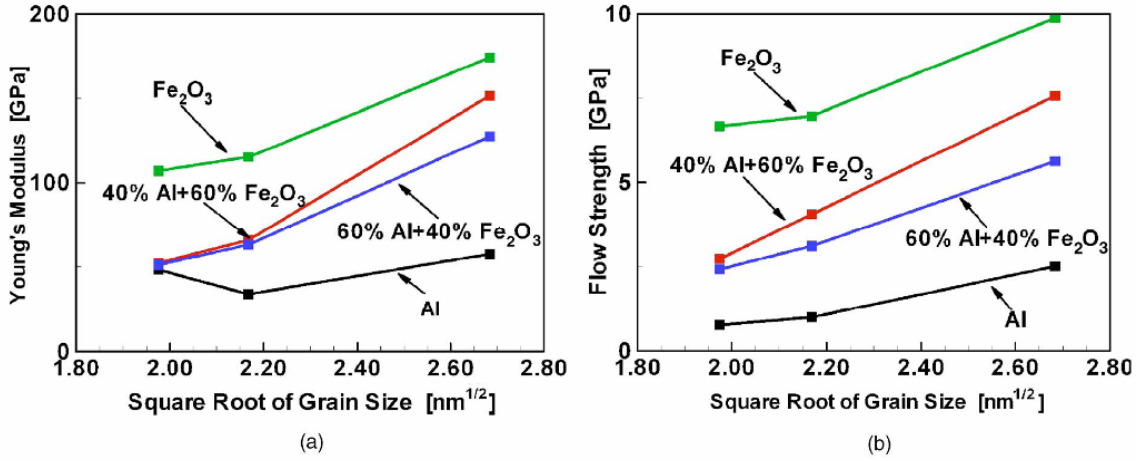


**Figure 2.33** The reverse Hall-Petch dependence of *a*) elastic moduli and *b*) flow strength on grain size in nanocrystalline Al and $Fe_2O_3$ structures and nanocomposites calculated from molecular-dynamics simulations [138,139].

Al and $Fe_2O_3$ interfaces showed that the crystalline structure for the two phases was not maintained during the passage of the wave, and the crystalline material underwent an amorphous phase transformation. The transformation occurs partly due to increased atomic mixing in the interfacial area and a reduction in mass transport. The extent of mixing is dependent on impact velocity and it increases with increasing impact velocity.

Calculations for an impact velocity of 2.0 km/s showed that the transformation was accompanied with a temperature rise of approximately 900 K which was close to the melting temperature of Al and suggests the possibility of shock-induced chemical reactions or simple phase mixing occurring within the mixture. The investigation of nanocrystalline material systems establishes an important computational approach for understanding the complex mechanical behavior of nanostructured materials at atomic length and time scales.

# CHAPTER III

# EXPERIMENTAL APPROACH

The objective of this study was to describe the underlying principles governing the deformation and fracture behavior, mechanochemical sensitivity and reaction response, and processing characteristics of epoxy-cast Al+$Fe_2O_3$ powder mixtures. The approach involved processing a class of materials that was composed of an energetic thermite-based powder mixture (Al+$Fe_2O_3$) dispersed within an epoxy matrix of varying concentrations. Specimens were subjected to mechanical testing ranging from quasistatic compression to high-strain rate dynamic impacts. Material characteristics such as chemical reactivity and microstructure morphology were also examined in this study.

In this chapter, the experimental approach for processing epoxy-cast specimens is detailed along with the techniques used for characterizing the microstructure, mechanical properties, and chemical reactivity. This chapter will also present details for the preparation and techniques utilized to conduct shock-compression and dynamic high-strain rate impact experiments. Shock-compression testing included instrumented equation of state (EOS) experiments using a parallel-plate impact configuration and the high-strain rate constitutive response experiments were performed using both “direct” and “reverse” Taylor anvil impact configurations.

### 3.1 Processing of Aluminum-Hematite Epoxy-Cast Composites

The synthesis of epoxy-cast Al+$Fe_2O_3$ powder mixtures was divided into several processing steps that included the mixing of stoichiometric quantities of nano- and micron-scale aluminum with submicron hematite ($Fe_2O_3$) powders and their dispersion in epoxy. The candidate material system for this study was based on a classic oxidation-reduction reaction with a metal and metal-oxide. Specifically, aluminum constituting the fuel (or reduction agent) and hematite ($Fe_2O_3$) forming the oxidizer, were cast with epoxy to develop a material that has combined structural strength and enhanced chemical reactivity.

Composite materials were manufactured by combining stoichiometric quantities of aluminum and hematite powders (25.26 *wt.%* Al and 74.74 *wt.%* $Fe_2O_3$) with Epon® 826 resin (Miller-Stephenson; Danbury, CT) and diethanolamine (DEA) anionic catalytic curing agent (Sigma-Aldrich; St. Louis, MO). Table 3.1 gives details about the as-received powders used to produce epoxy-cast composite materials in this study. Individual 250 $cm^3$ batches were prepared, consisting of compositions with Al+$Fe_2O_3$ powder mixtures combined with epoxy volume fractions ranging from 47 to 78 % according to Table 3.2. Not all the compositions listed in Table 3.2 were possible since the addition of nanoscale particles caused the viscosity of the mixture to increase significantly and introduced processing difficulties that could not be overcome using a cast-cure process. Furthermore, density measurements of cured specimens suggested that composite materials made from Al+$Fe_2O_3$+47 *vol.%* epoxy exhibited significant porosity (in the range of 4 to 5 %). Therefore, compositions comprised of Al+$Fe_2O_3$+60 *vol.%*

**Table 3.1** Characteristics of metal and metal-oxide powders used for processing epoxy-cast composites.

| Material | Particle Size | Purity | Manufacturer |
|---|---|---|---|
| Aluminum | 3.2 μm (avg.) | 99.7 *wt.%* Al | Valimet, Inc; Stockton, CA |
| Nano-Aluminum | 56.3 nm (avg.) 2.1 nm oxide layer | 72.7 *wt.%* Al | Technanogy; Irvine, CA |
| Hematite | 0.1 - 0.3 μm | 99.9 *wt.%* $Fe_2O_3$ | Fisher Scientific; Fairlawn, NJ |

**Table 3.2** Epoxy-cast Al+$Fe_2O_3$ mixture ratios based on weight and volume fractions. Theoretical densities were also calculated for each based on the individual constituents properties.

| **Weight Fraction** | | | **Volume Fraction** | | | Theoretical Density [g/cm$^3$] |
|---|---|---|---|---|---|---|
| Epoxy [*wt.%*] | Aluminum [*wt.%*] | Hematite [*wt.%*] | Epoxy [*vol.%*] | Aluminum [*vol.%*] | Hematite [*vol.%*] | |
| 100 | 0 | 0 | 100 | 0 | 0 | 1.1967 |
| 50 | 12.63 | 37.37 | 77.97 | 8.71 | 13.32 | 1.8661 |
| 40 | 15.16 | 44.84 | 70.23 | 11.77 | 17.99 | 2.1012 |
| 30 | 17.68 | 52.32 | 60.27 | 15.71 | 24.02 | 2.4040 |
| 20 | 20.21 | 59.79 | 46.94 | 20.98 | 32.07 | 2.8089 |
| 0 | 25.26 | 74.74 | 0 | 39.55 | 60.45 | 4.2353 |

epoxy using micron-scale aluminum were found to have the best mechanical properties. These were also the composites that contained the least amount of epoxy possible while typically exhibiting 1 % or less porosity; hence, were used mainly for experimental characterization. For similar reasons, Al+$Fe_2O_3$ composite compositions that used nanoscale aluminum powder contained 70 *vol.%* epoxy and exhibited less than 1 % porosity.

The epoxy resin used in this study was very similar to the Epon® 828 resin used in many other shock studies available in the literature. Differences between the two epoxies arise through their viscosities, where a slight increase in temperature will result in a marked decrease in viscosity as shown in Figure 3.1. Epon® 826 resin has a lower

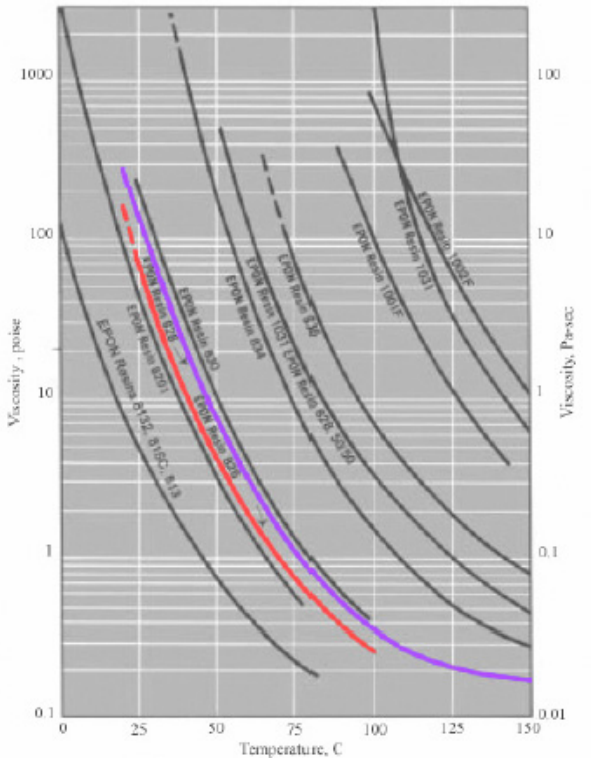


**Figure 3.1** Viscosity and temperature profiles for EPON® resins, including lower viscosity Epon 826 (*red trace*) compared to Epon 828 (*blue trace*) resin [140].

viscosity (0.8 poise at 75 °C) and was more suited for accepting particulate fillers capable of impregnating small, confined areas [140]. Epon® 828 (> 1.0 poise at 75 °C) is a general-purpose epoxy resin that is widely used in high-strain rate experiments [140]. The resin and hardener were prepared with a 12:1 mixing ratio, respectively. The resin was preheated to approximately 80 °C, which reduced its viscosity and improved wetting properties for solid particle additions. Adolf, *et al.* [141], specifically examined the temperature dependent viscosities of Epon® 828 resin, as well as its combination with several curing agents, including diethanolamine (DEA). Such characterization was applied to optimize the mixing procedure used for processing epoxy-cast Al+$Fe_2O_3$ composites in this current study.

Two different mixing procedures have been utilized to manufacture epoxy-cast specimens. In most cases, specimens were prepared using premixed stoichiometric quantities of aluminum and hematite powders obtained from the turning action of a tumble mixer, specifically a twin shell dry v-blender (The Patterson Kelly Company, Inc.; East Stroudsburg, PA) and mixed for 48 hours in a Nalgene container. Earlier sample preparation consisted of adding small individual quantities of aluminum and hematite powder directly to the warm resin and mixing after each addition. However, premixing of the powders was thought to improve the contact between fuel and oxidizer components of the thermite mixture and enhance the chances of chemical reactivity. Regardless of the powder state before addition to the resin (premixed in the v-blender or the individual additions of aluminum and hematite to the resin), the following processing steps were identical in both cases.

Small fractions of the powders were added to the preheated resin in several steps. Between each addition, the powder-resin was carefully combined using a mixing blade attached to a drill and then placed into an oven set at 120 °C. This process was repeated until all of the powder additions were combined with the resin. To ensure low viscosity of the mixture, aluminum and hematite powders were also preheated to 80 °C before being added to the epoxy resin in an effort to prevent cooling, thus keeping the viscosity of the mixture low. Mixing also causes the Al+$Fe_2O_3$+epoxy mixture to cool and therefore, it was placed in the oven to reheat after each addition of the powder to the resin. Once all of the powder was added to the mixture and the viscosity was low enough to pour, the DEA curing agent was combined thoroughly and the mixture was again placed in the oven for approximately fifteen minutes. After the mixture was at temperature, a vacuum degassing step in a desiccator for approximately five minutes was used to remove trapped air bubbles introduced during mixing. The degassed mixture was then placed in the oven again for another fifteen minutes to reduce viscosity and permit easy pouring of the mixture into molds.

Aluminum two-piece molds were manufactured into several simple cylindrical geometries capable of casting specimens with nominal diameters of ⅝", ⅞", and 2", as shown in Figure 3.2. Molds were first prepared by coating the inside surfaces with vacuum grease (Dow Corning Corporation; Midland, MI) and sealing the seams with aluminum foil adhesive tape. Molds were placed in the oven and preheated to 120 °C. Specimens were prepared by slowly pouring the mixture into the heated molds, being careful to avoid the formation of additional air bubbles. It was found unnecessary to repeat the degassing step after the mixture was poured into the molds. The molds were

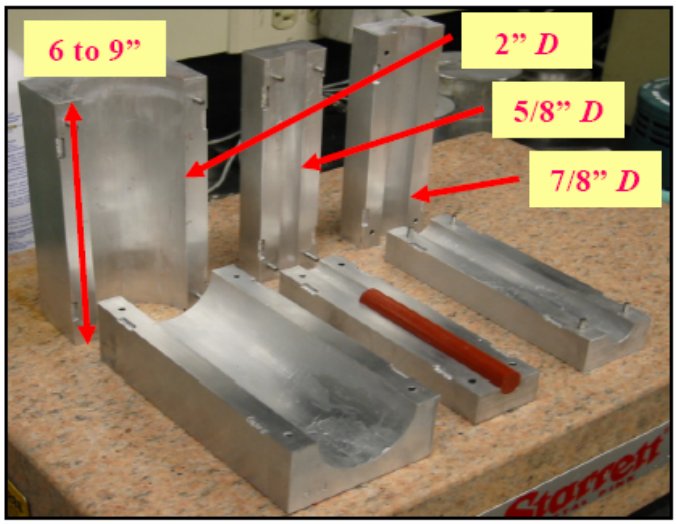


**Figure 3.2** Aluminum split-molds used for manufacturing epoxy-cast specimens with different cylindrical geometries used throughout this study are shown.

placed back in the oven and the temperature was reduced after 30 minutes to 80 °C. The mixture was allowed to cure in the oven for 48 hours. After the mixture cured, castings were removed from the molds and kept in a ventilated hood for at least a week. The curing schedule for specimens used in this study was not thoroughly examined, however no measurable physical changes such as dimensional shrinkage or density variation was observed from measurements taken several weeks or several months after curing. Physical properties of epoxy resins cured with DEA hardener have been studied previously by Lundberg [142] and suggest that a full cure is obtained in eight days at 24 °C, three days at 40 °C, and eighteen hours at 75 °C. These results give a good indication that the specimens prepared in the current study were processed using sufficient conditions to achieve full polymerization.

Final preparation of specimens for quasistatic and dynamic experiments began by first turning the cast rods on the lathe to desired diameters and then sectioning to form

desired geometries (cylinders, disks, *etc.*). Figure 3.3 shows examples of the geometries used for quasistatic compression tests, continuous spherical ball indentations, Taylor anvil impact experiments, and parallel plate impacts. Once sectioned, the flat surfaces of the specimens were lapped in two stages first using 45 μm diamond slurry and then 15 μm as a finishing step. Specimens were checked for flatness and planarity, typically

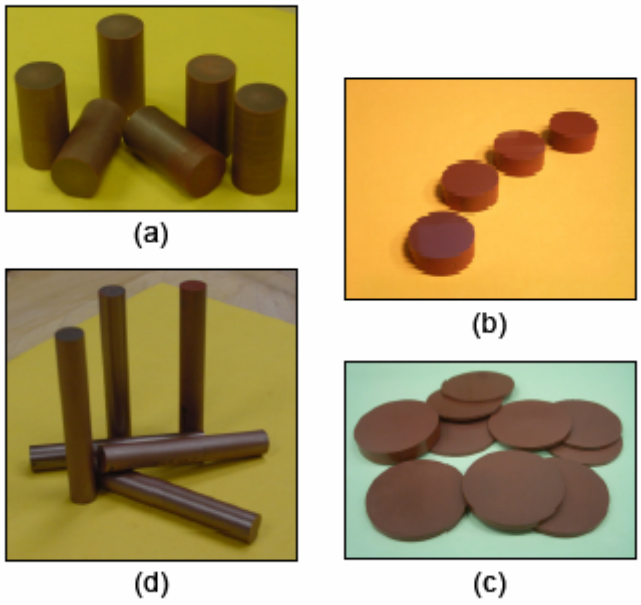


**Figure 3.3** Finished specimen used for *a*) quasistatic compression, *b*) continuous indentation, *c*) parallel-plate impacts, and *d*) Taylor impact experiments.

parallel to within 0.0051 mm or better. Lapping polymeric material was more challenging than metallic materials which tend to have better dimension stability. The addition of aluminum and hematite particles helps with this aspect, however the high volume fraction of epoxy tends to dominate the material's dimensional instability particularly as the specimen aspect ratio between length and diameter becomes very large

**Table 3.3** Specimen dimensions and tolerances used for quasistatic and dynamic mechanical property experiments performed on epoxy-cast Al+$Fe_2O_3$ composites and pure epoxy.

| Testing Method | Measured Property | Specimen Dimensions [in.] | Nominal Strain Rate [1/s] | ASTM Standard and/or [Ref] |
|---|---|---|---|---|
| Continuous Spherical Ball Indentation | Compressive Strength, Compressive Modulus, Stress-Strain Response $E$, $\sigma$, $\varepsilon$, $\sigma_y$, $\varepsilon_y$ | $D = 0.85 \pm 0.05$<br>$t = 0.35 \pm 0.05$ | $10^{-4}$ | Ferranti, *et al.* [143] |
| Three-Point Bend | Flexural Strength, Flexural Modulus, Flexural Stress-Strain Response $E$, $\sigma$, $\varepsilon$, $MOR$ | $l = 5.00 \pm 0.01$<br>$w = 0.50 \pm 0.01$<br>$t = 0.125 \pm 0.001$ | $10^{-4}$ | D 790-03 [144] |
| Dynamic Mechanical Analysis (*tensile loading*) | Storage Modulus, Loss Modulus, Phase Angle, Glass Transition Temperature $E'$, $E''$, $\tan\delta$, $T_g$ | $l = 0.750 \pm 0.001$<br>$w = 0.150 \pm 0.001$<br>$t = 0.015 \pm 0.001$ | n/a | D 5026-06 [145]<br>D 4092-01 [146] |
| Compression | Compressive Strength, Compressive Modulus, Stress-Strain Response $E$, $\sigma$, $\varepsilon$, $\sigma_y$, $\varepsilon_y$ | $D = 0.50 \pm 0.01$<br>$l = 1.00 \pm 0.05$ | $10^{-2}$ | D 695-02a [147] |
| Charpy Impact* | Breaking energy, impact resistance $E_S$, $I_S$ | $A = 0.400 \pm 0.002$<br>$B = \begin{matrix}2.50\ max.\\2.40\ min.\end{matrix}$<br>$C = \begin{matrix}5.00\ max.\\4.90\ min.\end{matrix}$<br>$D = 0.010R \pm 0.002$<br>$E = 0.500 \pm 0.006$<br>$F = 0.500 \pm 0.006$ | $10^3$ | D 6110-02 [148] |
| Taylor Impact☺ | Dynamic Strength, Dynamic Modulus, Stress-Strain Response $Y$, $E$, $\sigma$, $\varepsilon$,$\sigma_y$, $\varepsilon_y$ | $D = 0.300 \pm 0.002$<br>$l = 50.80 \pm 0.05$ | $10^3$ to $10^4$ | Taylor [45]<br>Hutchings [98] |
| Parallel-Plate Impact | Compressive Stress, Shock Velocity, Particle Velocity $P$, $U_S$, $U_P$, | $D = 50.50 \pm 0.05$<br>$t = 0.125 \pm 0.005$ | $10^5$ to $10^6$ | Meyers [16] |

*Refer to Figure 3.5 for dimension descriptions.

☺Taylor impact experiments experience a range of strain-rates (up to $10^6$ 1/s at the first moment of impact) along the axial length of the specimen depending on impact velocity.

as in the Taylor test specimens ($L/D \approx 6.5$). Table 3.3 lists typical specimen dimensions and tolerances used for machining the various specimen geometries utilized in quasistatic and dynamic experiments. Specimen tolerances are typically specified by ASTM testing standards when available and also identified in Table 3.3.

## 3.2 Specimen Characterization

Physical features of cast-cure specimens were characterized by density measurements and examined using optical and scanning electron microscopy (SEM) after processing. Density evaluation was an important indicator of structural/mechanical property performance since introduction of a small percentage of porosity was detrimental to mechanical properties. Observations of microstructures using optical microscopy and SEM techniques were performed to obtain qualitative and quantitative information about particle size and distributions within each composition.

Density was measured using Archimedes' method for each specimen cut from epoxy-cast rod geometries. Pieces were submerged in distilled water with 3 drops of a dispersing agent. Dry mass, $m_d$ and wet mass or buoyancy, $B$ of the sample was measured using a digital scale capable of 0.1 mg accuracy. Temperature of the distilled water at the time of each measurement was also recorded. Density was calculated for each specimen according to equation (3.1).

$$\rho = \frac{m_d}{-B}\rho_0(T), \tag{3.1}$$

where $\rho_0(T)$ is the specific density of distilled water at temperature, $T$ °C. Typically, $\rho_0$ has a value of 0.9980 g/cm$^3$, which correspond to the density at a temperature of 21.0 °C.

Microstructural features were observed on individual cut sections after lapping and polishing. Samples were polished using diamond suspension (Buehler; Lake Bluff, IL) starting with a 15 μm step to make the polished face and back face of the specimen coplanar. Polishing continued with the 9 and 3 μm steps until surfaces had a high quality finish that permitted examination of microstructures using an optical microscope. All polishing steps were carried out using a Texmet® 1000 pad (Buehler; Lake Bluff, IL).

Characterization of microstructures was performed on a Leica DM IRM optical microscope (Leica; Bannockburn, IL). Digital images were obtained using a CoolSnap CCD video camera (Media Cybernetics; Silver Springs, MD), capable of capturing high-resolution digital images (1390 x 1040 pixels, 4.65 micron pixels). Images were imported into Image-Pro Plus analytical imaging software (Media Cybernetics; Silver Springs, MD) where a number of features such as phase volume fraction, average phase size, *etc.* was measured.

Scanning electron microscopy was performed using a LEO 1530 and LEO 1550 (JOEL USA, Inc.; Peabody, MA) scanning electron microscopes (SEM). SEM analysis was mainly utilized for qualitative estimates of particle size and phase distribution in each composition formulated, in addition to observing as-received powders from manufacturers. Recovered specimens and fragments were also examined after dynamic impact experiments and included EDS chemical analysis.

### 3.3 Reaction Energetics Characterization

Differential Thermal Analysis (DTA) was used to examine physical properties of cast specimens, while being subjected to a controlled rate heating/cooling cycle. DTA involves the heating or cooling of a test specimen and an inert reference (usually alumina) under identical conditions. Temperature differences between the sample and reference material were plotted against time or temperature (furnace temperature following heating or cooling program). Changes in the specimen which lead to the absorption (endothermic reaction or melting) or evolution (exothermic reaction) of heat were detected relative to the inert reference material.

The DTA study was performed using a Perkin Elmer DTA 7 (Perkin Elmer; Boston, MA) on representative samples of each epoxy-cast composition and pure epoxy material. All of the starting constituent materials were additionally analyzed including nano- and micron-scale aluminum, and nano- and micron-scale Al+$Fe_2O_3$ stoichiometric powder mixtures. Care was necessary in preparing these specimens since the packing state of the powder sample becomes important and can lead to large variations between apparently identical samples. Hence, pressed pellets were used to have a "consistent" packing arrangement for each powder and powder composition.

Specimens used for DTA measurements weighed approximately 10 mg and were typically comprised of a single uniform piece of material. Specimens were placed in an alumina crucible on approximately 2 mg of an alumina powder bed, which was then covered with approximately 30 mg of alumina powder. The reference crucible contained alumina powder with an approximately identical quantity used in the crucible containing

the specimen. Prior to the experiment, the furnace temperature was set to 50 °C under the flow of argon gas. The system was allowed to come to thermal equilibrium before the heating program was initiated, typically taking approximately 30 minutes. The experiments were typically conducted up to a temperature of 1200 °C at a heating rate of 10 °C/min. Temperature data obtained from these measurements was analyzed using a Pyris software package (Perkin Elmer; Boston, MA). The software permitted the determination of onset temperatures for endothermic and exothermic reaction events and the calculation of enthalpy changes measured from the area under the exothermic or endothermic peaks. The DTA was calibrated by measuring the melting temperature and latent heat of transformation of aluminum and gold reference standards (Perkin Elmer; Boston, MA), thus, giving two points of reference that were obtained for temperatures of 660 and 1063 °C for aluminum and gold, respectively. The peak area values and onset temperatures determined by the calibration test run were input into the Pyris software and automatically corrected all future data collected by the instrument.

High-temperature *in situ* x-ray diffraction (HTXRD) experiments were also conducted for identifying chemical species evolving during controlled heating. Experiments were used to complement the DTA study of these materials and correlate the exothermic and endothermic peak events with the presence of specific chemical species. These experiments were performed on an X'Pert PRO MPD (PANalytical; Natick, MA) multi-purpose x-ray diffraction system equipped with a molybdenum x-ray source, diverging incident beam optics, and a solid state X'Celerator detector (PANalytical; Natick, MA). The instrument was equipped with HTK 2000 platinum strip furnace

(Anton-Paar; Graz, Austria) capable of reaching a maximum temperature of 1400 °C and operated under a helium gas atmosphere.

The HTXRD study used specimens with disk shape geometry (approximately 16 mm diameter and 3 mm thickness) sectioned from the same epoxy-cast rod used for the DTA study and high-strain rate impact experiments. The specimen was placed on a thin alumina sheet in direct contact with the furnace heating element, which prevented damaging the platinum strip during heating. The furnace chamber was first evacuated and then purged several times with helium gas to attain an oxygen-free atmosphere. Scans were performed for a $2\theta$ range of 10 – 40 °, while helium gas flowed throughout the experiment. The sample was heated from room temperature to 1300 °C with a heating rate of 25 °C/min. Approximately one-minute x-ray scans were performed at every 25 °C starting at 100 °C. The x-ray data for each scan was collected using X'Pert High Score (PANalytical; Natick, MA) and then exported to Jade 7.0 (Materials Data Inc.; Livermore, CA) XRD analytical software analysis package. Chemical species and phases were identified by comparing traces with XRD standards obtained through the International Center for Diffraction Data (ICDD) [149].

## 3.4 Mechanical Property Characterization

Mechanical properties were evaluated for epoxy-cast Al+$Fe_2O_3$ and pure epoxy specimens using several different mechanical test configurations. The mechanical characteristics of polymers and polymeric composites were generally very sensitive to the rate of deformation (strain rate). Experiments were conducted to ascertain material

properties such as elastic modulus, yield strength, modulus of rupture, *etc.* Details for each type of quasistatic and low strain rate experiment will be discussed followed by properties obtained from dynamic mechanical analysis (DMA). Mechanical property evaluation using ultrasonic nondestructive testing techniques were also used and will be discussed next.

### 3.4.1 Ultrasonic Material Analysis

Ultrasonic material analysis is based on a simple principle that the motion of any wave will be affected by the medium through which it travels. Thus, changes in the measurable transit time associated with the passage of a high frequency sound wave through a material is correlated with changes in physical properties such as elastic modulus, shear modulus, compressibility or bulk modulus, *etc.* Ultrasonic sound velocity measurements were conducted according to ASTM standard E 494-95 [150]. Sound pulses are generated and received by piezoelectric transducers that have been acoustically coupled to the test material. For dilatational (or longitudinal) sound velocity measurements, a single transducer with a frequency of 4.5 MHz was coupled to one side of the specimen using glycerin (Fisher Chemical; Fair Lawn, NJ) and served as both the transmitter and receiver (pulse/echo mode) of the signal. However, distortional (or transverse or shear) sound velocity measurements used separate transmitting and receiving transducers with a frequency of 1.9 MHz located on opposite sides of the specimen (pulse transmission mode). Pulse transmission measurements were necessary since these types of waves were more difficult to transmit through the specimen due to

attenuation or scattering of the signal. The sound waves travel through the test material, either reflecting off the far side to return to its point of origin (pulse/echo), or received by another transducer at that point (pulse transmission). The received signals were then amplified and analyzed using a NCA 1000 analyzer (SecondWave Systems: Boalsburg, PA).

Ultrasonically measured longitudinal, $C_L$ and transverse, $C_T$ wave speeds are related to bulk mechanical properties [16] according to:

$$C_T^2 = \frac{\mu}{\rho}, \tag{3.2}$$

$$C_L^2 = \frac{\lambda + 2\mu}{\rho}, \tag{3.3}$$

where $\lambda$ is Lamé's constant and $\rho$ is density. Both longitudinal, $C_L$ and transverse, $C_T$ sound velocities are combined to calculate the bulk sound velocity, $C_0$ for an isotropic solid through the relation:

$$C_0 = \sqrt{C_L^2 - \left(\frac{4}{3}C_T^2\right)}. \tag{3.4}$$

The shear modulus, $\mu$ was calculated directly from the transverse wave speed and density measurements according to equation (3.2). The elastic modulus, $E$, is then calculated from elastic theory according to:

$$E = \frac{\mu\left(3 + 2\frac{\mu}{\lambda}\right)}{1 + \frac{\mu}{\lambda}}. \qquad (3.5)$$

Similarly, other material properties such as bulk modulus, $K$, and Poisson's ratio, $\nu$, were calculated from identities listed in Table 3.4 (shown on the following page) inter-relating the foregoing material parameters. Lastly, the longitudinal wave impedance, $Z$ was obtained from the relation:

$$Z = C_L \rho. \qquad (3.6)$$

**Table 3.4** Relation among the elastic constants for isotropic materials.

| Elastic Constants | $E,\nu$ | $E,G$ | $K,\nu$ | $K,G$ | $\lambda,\mu$ |
|---|---|---|---|---|---|
| $E$ | $= E$ | $= E$ | $= 3K(1-2\nu)$ | $= \dfrac{9K}{1+\dfrac{3K}{G}}$ | $= \dfrac{\mu\left(3+\dfrac{2\mu}{\lambda}\right)}{1+\dfrac{\mu}{\lambda}}$ |
| $\nu$ | $= \nu$ | $= \dfrac{E}{2G}-1$ | $= \nu$ | $= \dfrac{1-\dfrac{2G}{3K}}{2+\dfrac{2G}{3K}}$ | $= \dfrac{1}{2\left(1+\dfrac{\mu}{\lambda}\right)}$ |
| $G$ | $= \dfrac{E}{2(1+\nu)}$ | $= G$ | $= \dfrac{3K(1-2\nu)}{2(1+\nu)}$ | $= G$ | $= \mu$ |
| $K$ | $= \dfrac{E}{3(1-2\nu)}$ | $= \dfrac{E}{9-\dfrac{3E}{G}}$ | $= K$ | $= K$ | $= \dfrac{2\mu}{3}+\lambda$ |
| $\lambda$ | $= \dfrac{E\nu}{(1+\nu)(1-2\nu)}$ | $= \dfrac{E\left(1-\dfrac{2G}{E}\right)}{3-\dfrac{E}{G}}$ | $= \dfrac{3K\nu}{1+\nu}$ | $= K-\dfrac{2G}{3}$ | $= \lambda$ |
| $\mu$ | $= \dfrac{E}{2(1+\nu)}$ | $= G$ | $= \dfrac{3K(1-2\nu)}{2(1+\nu)}$ | $= G$ | $= \mu$ |

### 3.4.2 Quasistatic Compression Tests

Quasistatic compression experiments were performed according to ASTM standard D 695-02a for determining compressive properties of rigid plastics [147]. Cylindrical shaped specimens with a length to diameter ratio of 2:1 were prepared from epoxy-cast rods. Epoxy-cast rods were first machined using a lathe to a diameter of 0.5 ± 0.01". The specimen length was cut slightly greater than 1" to allow for surface finishing steps that included lapping with 45 μm and then 15 μm diamond suspensions. Final specimen lengths were 1.0 ± 0.05" with a fine surface finish and parallel to within 0.0005". Ten compression specimens were prepared for each composition.

Compression tests were performed on an Instron 1332 hydraulic load-frame (Instron Corporation; Canton, MA) with a 55,000 lbf (245 kN) load cell capacity. The load cell was zeroed before each test and brought in close proximity to the face of the test specimen. Care was taken to make sure the specimen was perfectly aligned and centered on the platens. The specimen's contact surfaces with the anvil were lubricated to reduce friction and prevent severe barreling (complex stress state within the material) of the specimen during compression. Specimens were tested using a continuous displacement mode with a ramp rate of 0.585 in/min, which corresponded to a strain rate of approximately $1.0 \times 10^{-2}$ 1/s. The platen ramping program was started and diagnostic equipment triggered once loading began. Loading was stopped once the specimen fractured. Load and displacement data was collected at a 10 ms interval.

Universal testing instrument drive systems always exhibit a certain level of compliance as a function of load frame stiffness, drive system wind-up, load cell

compliance, and fixture compliance. To accurately measure the test material response, the compliance was measured and empirically subtracted from the test data. The compliance of the load frame was determined by bringing the platens together and applying the same loading program as used for the test specimens. The resulting compliance curve was plotted and fit with a polynomial curve. The experimental results were adjusted by subtracting the load frame compliance from overall measurements and the stress-strain history was calculated.

### 3.4.3 Continuous Spherical Ball Indentation Tests

Continuous ball indentation hardness measurements [143] were also used for quasistatic mechanical property evaluation of epoxy-cast specimens. The values generated by conventional fixed hardness test (*i.e.* Rockwell, Brinell, *etc.*) do not provide measurements of well-defined material properties, but only supply relative information about a material's resistance to indentation or penetration. Additionally, conventional hardness determination relies on microscopic examination to resolve the elastically recovered indent. Elastic material that surrounds the plastic zone of the indentation acts to hinder plastic flow. Exploring the combined elastic and plastic deformation behavior during hardness testing allows for the deduction of the elastic contribution to the final plastic indentation. Thus, useful information can be resolved from hardness testing if load and penetration depth are continuously monitored during indentation. Using this technique provided a means for making hardness measurements, which do not introduce any strain-hardening effects. Accordingly, this technique presents an absolute measure of

hardness and elastic modulus. The advantage of using a relatively large spherical indentation tip permits the measurement of bulk elastic modulus for a multiphase material including porosity as an additional phase.

Continuous indentation tests were performed using a modified tensile testing Instron 5500R screw driven load frame with a 100 N load cell capacity (Instron Corporation; Canton, MA) and operated in the compression mode. The applied load, $P$, versus the crosshead displacement or depth of indentation, $h$, was continuously recorded throughout the experiment. The machine crosshead was screw driven at a constant velocity of $1.0 \times 10^{-4}$ mm/s. A fixture was designed to couple a standard Rockwell spherical indenter (steel ball with a diameter of 1.5875 mm) directly to a load cell located in the crosshead of the load frame and is shown in Figure 3.4. A maximum load of 50 N was applied to each specimen. Each test was typically repeated five times at different

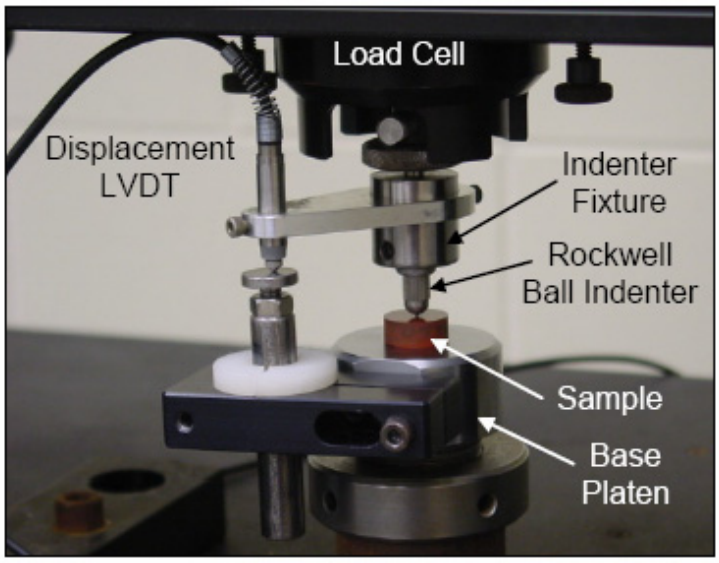


**Figure 3.4** Continuous indentation test apparatus used to measure load and displacement of the indenter tip throughout the experiment [143]. A standard Rockwell spherical indenter tip is coupled to a load cell using a custom mounting fixture.

locations on the surface of the specimen. The machine deflection or compliance for this configuration was measured by indenting a Rockwell hardness reference standard ($HR_C$ 31.7) through the entire load range that the epoxy-cast specimens were examined. Experimental load-displacement results were adjusted by subtracting the measured load frame compliance using a similar approach described previous for compression experiments.

### 3.4.4 Flexural (Three-Point Bend) Tests

Flexural (three-point bend) tests were performed according to ASTM standard D 790-03 for determining flexural properties of plastics and reinforced plastics [144]. A bar shaped specimen of rectangular geometry rests on two supports and was loaded with a constant load midway between the supports. The loading nose and supports for the flexural test fixture had a cylindrical surface with a radius of 5 mm. The span between the two loading supports was set to 50.8 mm. To ensure the alignment and proper positioning of the loading nose, a spacing jig was used to set the span and locate the loading nose in the center of the fixture. The load frame and fixture compliance was measured by placing a smooth steel bar across the support span. The steel bar had a significantly greater flexural stiffness than the test specimens. The compliance curve was plotted and experimental results were adjusted from the empirically established relationship.

Three-point bend tests were performed on the same Instron 5500R screw driven load frame described previously for continuous indentation experiments along with the

100 N capacity load cell. Before each test, the specimen width and thickness were measured in close proximity to the center of the specimen where the loading nose would be located. The load cell was zeroed before each test and positioned close to the center of the specimen with a minimal preload (less than 1 N). The rate of the crosshead motion for the load frame was set at a constant 0.05 in/min and corresponded to a strain rate of approximately 2.0 x $10^{-4}$ 1/s. Termination of the test occurred upon the specimen breaking. The flexural stress, $\sigma_f$ was calculated for any point on the load-deflection curve using the following equation [144]:

$$\sigma_f = \frac{3PL}{2bd^2}, \tag{3.7}$$

where $P$ is the load, $L$ is the support span distance, $b$ is the width of the beam, and $d$ is the depth of the beam. Similarly, flexural strain, $\varepsilon_f$ was calculated according to [144]:

$$\varepsilon_f = \frac{6Dd}{L^2}, \tag{3.8}$$

where $D$ is the maximum deflection of the center of the beam or displacement, $d$ and $L$ are the same as the previous equation.

Test specimens were prepared by casting material into a Nalgene mold forming a rectangular casting with nominal dimensions of $6-5/8$" by $3-3/4$" and approximately 1/2" thick. Ten flexural specimens were machined from a single casting in the shape of a

flat bar with a width, *b*, of 0.05 ± 0.01", thickness, *d*, of 0.125 ± 0.001", and a length of 5.0 ± 0.01".

### 3.4.5 Charpy Impact Toughness Experiments

Charpy impact toughness tests were also performed on specimens made in the rectangular shaped Nalgene mold and five specimens were machined from a single casting. The specimens were a simple beam with an angled notch having dimensions according to Figure 3.5. Charpy impact experiments were conducted following ASTM standard D 6110-02 for determining impact resistance of notched plastics [148]. These experiments were conducted on a model 92T plastic impact testing machine (Tinius Olsen Testing Machine Co., Inc.; Horsham, PA) at room temperature.

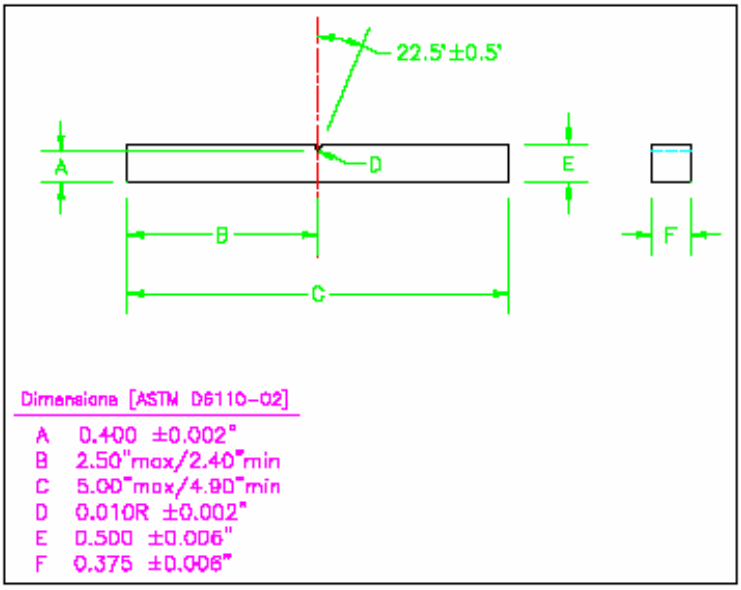


**Figure 3.5** Charpy impact specimen dimensions according to ASTM standard D 6110-02 [148].

Specimen width and notch depth were measured for each specimen prior to testing. The notch machined into the specimen creates a stress concentration zone which promotes brittle, rather than ductile, fracture. The notched specimen was supported on either end horizontally and broken with a single swing of the pendulum from the testing apparatus. The pendulum strikes the specimen midway between the supports and directly opposite of the notch. The net break energy, $E_S$ was directly determined from the testing machine. The test was good if the net breaking energy was less than 85 % the nominal pendulum energy. The impact resistance, $I_S$ was determined by dividing the net break energy by the measured individual width of each specimen.

### 3.4.6 Dynamic Mechanical Analysis (DMA)

Dynamic mechanical analysis (DMA) is a technique used to study and characterize materials, particularly for observing the viscoelastic nature of polymers. An oscillating stress is applied to a sample and the resultant strain is measured as functions of both oscillatory frequency and temperature. From this, a comprehensive knowledge of the relationships between the various viscoelastic parameters may be obtained, *e.g.* storage and loss moduli, mechanical damping parameter (tan $\delta$), and dynamic viscosity. The transitions of polymeric materials from the glassy state to the rubbery state reveal important material properties. The DMA identifies these transition regions and determines elastic modulus (or storage modulus, $E'$), viscous modulus (or loss modulus, $E''$), and damping coefficient (tan $\delta$) as a function of temperature, frequency or time. The storage modulus is related to stiffness, and the loss modulus to damping and

energy dissipation. Glassy, viscoelastic, elastic, and liquid polymers can be differentiated by DMA, and some details of polymer structure can be inferred from the results. DMA is particularly useful for evaluating viscoelastic polymers that have mechanical properties, which exhibit time, frequency, and/or temperature effects.

In the present work, DMA was used to measure the physical influence that solid particles dispersed in a polymer matrix have on overall bulk mechanical properties with the variation of epoxy content for Al+$Fe_2O_3$ epoxy-cast composites. The influence of particle size was also examined by using both micron- and nano-scale aluminum particles in Al+$Fe_2O_3$ powder mixtures disperse in epoxy. Experiments were conducted using a TA Instruments Q800 DMA (TA Instruments; New Castle, DE) apparatus operated in tension with a constant oscillation frequency of 1 Hz. The specimens were initially equilibrated at 25 °C and then heated at a rate of 5 °C/min to a maximum temperature of 170 °C. DMA experiments provide valuable data for characterizing the properties of materials, particularly polymers and polymer composites. The experimental results were used to estimate the crosslink density of the epoxy-cast materials and the influence epoxy volume fraction and powder particle size has on this measure.

### 3.5 Time-Resolved Instrumented Impact Experiments

Instrumented impact experiments were conducted using a single-stage light gas gun (Figure 3.6), which uses expanding helium gas to drive a projectile along the length of a barrel. The gas gun is comprised of an 80 mm diameter barrel that is approximately 9 m in length and can attain impact velocities in excess of 1000 m/s depending on the

projectile mass. The barrel is keyed along its entire length, which prevents projectile rotation or yaw during firing. The downrange end of the barrel has a 14.5" nominal diameter muzzle face with several attachment points for securing targets and instrumentation shown in Figure 3.6(*b,c*). The muzzle is precisely placed normal to the

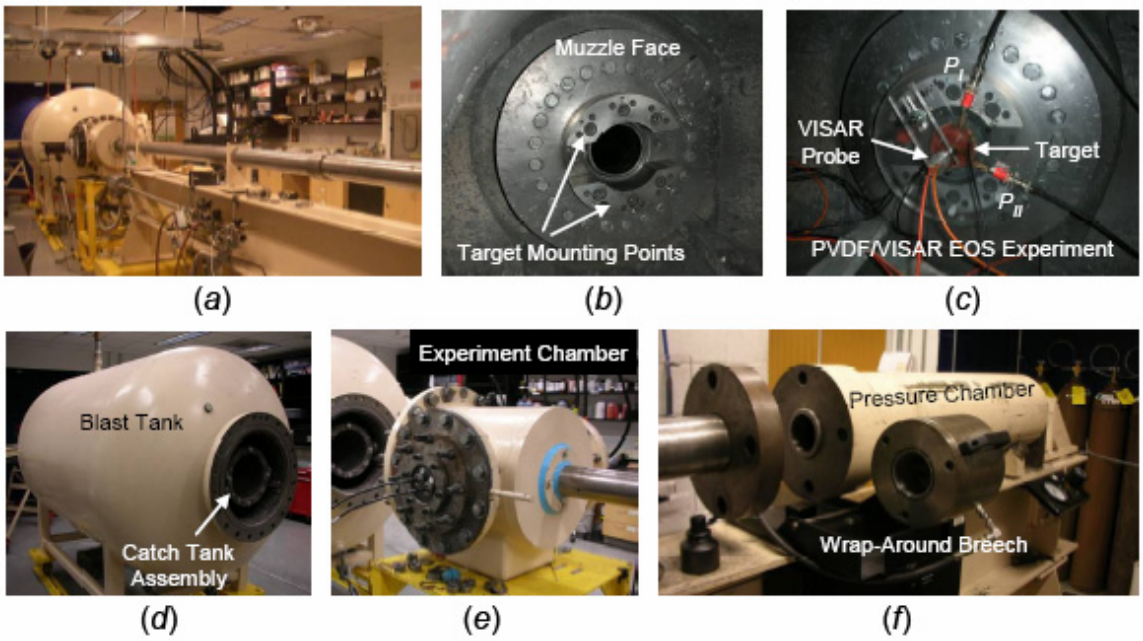


**Figure 3.6** High-strain rate facility showing *a*) the down range view of the 80 mm compressed-gas gun, *d*) the blast tank and catch tank assembly, *e*) experiment chamber, and *f*) high-pressure chamber and wrap-around breech sections. The experiment chamber contains the *b*) muzzle face used for attaching the target as shown in *c*) for a PVDF/VISAR equation of state (EOS) experiment.

barrel offering exceptional control of tilt or misalignment of the impact surfaces (typically 2.5 mrad or less). The range tankage consists of an *i*) experiment chamber (Figure 3.6(*e*)) for containing the blast and debris associated with near-muzzle projectile impact experiments, *ii*) the blast tank (Figure 3.6(*d*)) designed to provide open volume for the driver gas to expand and to contain the catch tank assembly, and *iii*) the catch tank

assembly (Figure 3.6(*d*)) used for "soft-recovery" of the projectile and target. The soft recovery containment vessel is stuffed with rags and provides sufficient length for the debris moving at high velocity to come to rest. A shock absorber is attached to the downrange end of the catch assembly, which also helps absorb the impulse of the impact experiment. Experiments are performed under vacuum with levels typically 50 to 80 mtorr.

Projectile impact velocity was measured using a series of five metallic pins, the spacing between which is precisely measured typically with an accuracy of ± 0.01 mm. The projectile touches each of the pins prior to target impact, causing a short circuit and the discharge of a capacitor bank. The voltage spike from each pin was measured using a series of electronic counters (Hewlett Packard HP 53131A; Palo Alto, CA) giving the time difference between each pin. A redundant measurement of pin discharge was also conducted using a digitizing oscilloscope (Tektronix TDS 784A; Richardson, TX) with gigahertz frequency response. Four separate velocity measurements were made prior to impact and were typically within 1 to 2 % of each other.

A highly repeatable method was devised for precisely measuring the distance between each of the velocity pins. A metallic jig was used to secure the velocity block and position the depth micrometer above the pins. One lead from a multi-meter was attached to the ground of the velocity pin and the other was attached to the metallic jig in contact with the depth micrometer. The depth micrometer measures down to the tip of each pin from a common height and completes the continuity of the circuit with a measurable resistance. This provides a precise way for determining when the micrometer

was in contact with the crush pin and gave excellent reproducibility in measuring velocity pin distances.

Obtaining a material's Hugoniot equation of state requires measurements of two parameters in shock wave experiments. Normally, these are the shock velocity and either the stress or particle velocity behind the shock front. Time-resolved instrumented impact experiments were conducted in which the loading conditions were measured using piezoelectric polyvinyl di-floride (PVDF) stress gauges (Ktech Corp; Albuquerque, NM) and velocity interferometry with a commercial VISAR (Velocity Interferometry System for Any Reflector) from Valyn International (Albuquerque, NM). PVDF gauges provide a direct measure of the arrival of the stress wave (shock velocity) and magnitude, and further permit the calculation of particle velocity. The velocity interferometry system was used to directly measure particle velocity at a window/specimen interface (used for EOS experiments discussed in section 4.5) or a free surface (used for reverse Taylor impact experiments discussed in section 4.4) depending on the type of experimental being conducted.

VISAR is a widely used diagnostic technique that makes use of coherent single-frequency light from a laser source to measure the motion of a diffuse, reflective surface [151,152]. The system measures the Doppler shift in the wavelength of light reflecting from a moving surface and hence, used to track object motion. The features of a conventional push-pull VISAR [153] system are shown schematically in Figure 3.7. A fiber optic probe is used to bring and collect the laser light at a focused spot (approximately 600 μm in diameter) on the reflective surface of the target. The optical signal is split into two distinct paths and later recombined. A small part of the reflected

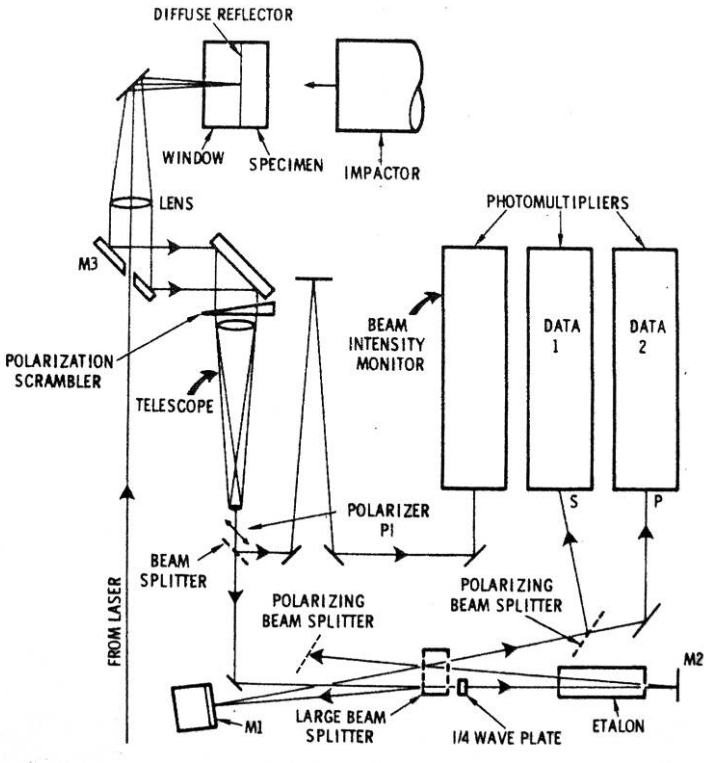


**Figure 3.7** Schematic diagram for a push-pull VISAR system [153].

light is separated to an intensity monitor (known as the beam intensity monitor or BIM), and the remainder is routed through the main beamsplitter of the interferometer. Half of this signal is sent through a reference path whose medium is air. The remaining half is sent through a path that delays the signal using fused silica optical lenses (etalons). The beam is delayed by a time, $\tau$ caused by the difference in the index of refraction for the fused silica and air. The beam is recombined at the main beamsplitter, where interference fringes are produced and are proportional to the velocity change. The target motion produces a Doppler shift of the scattered light that in turn causes the interference fringes to shift. The determination of the fringe shift yields a velocity history of the target

material. The basic equation relating the surface velocity $u(t)$, to the VISAR fringe count, $F(t)$ is given by [151]:

$$u\left(t-\frac{\tau}{2}\right)=\frac{\lambda F(t)}{2\tau\left(1+\frac{\Delta\nu}{\nu_0}\right)(1+\delta)}, \tag{3.9}$$

where $t$ is time, $\tau$ is the interferometer delay time, $\lambda$ is the wavelength of the laser light (514.5 nm), and $\delta$ is a function of the index of refraction for the etalon material and the laser wavelength. The factor $(1+\Delta\nu/\nu_0)$ corrects for the effect of changes in refractive index, which is equal to zero unless a window material is placed on the specimen's reflective surface. The velocity of the moving target surface at any time, $t$ is equal to the total number of fringes recorded, $F(t)$, times a velocity-per-fringe constant, VPF, given by [154]:

$$VPF=\frac{\lambda}{2\tau\left(1+\frac{\Delta\nu}{\nu_0}\right)(1+\delta)}. \tag{3.10}$$

The VPF constant is selected by the user according to the expected velocity range and the use of well characterized window materials such as PMMA, fused silica, sapphire, and LiF [154-156]. Light passing through a window material travels more slowly than it would in a vacuum, thus altering the optical transit time which leads to a substantial velocity correction. The VISAR system obtains surface (particle) velocity measurements with better than 1 % accuracy and a time resolution of approximately 2 ns [154].

The push-pull VISAR [153] produces four fringe signals in two pairs that are 180° out-of-phase. The two 180° out-of-phase signals from each pair are subtracted using differential amplifiers, thereby reducing the data from four to two fringe signals. These two signals have the same fringe information with a known phase difference of approximately 90°. The light signals are converted to an electrical voltage from quick response photomultipliers (PM) with 1 ns resolution. A third photomultiplier output monitors the intensity of the light beam or BIM entering the interferometer. The loss of fringe contrast has been observed when the reflecting surface has a nonuniform velocity and provides valuable information regarding the specimen's particle velocity distribution and equilibration rate [157]. The three PM signals are captured using a digitizing oscilloscope (Tektronix TDS 784A; Richardson, TX ) with GHz frequency response.

Piezoelectric polyvinyl di-floride (PVDF) stress gauges were used to measure the impact and propagated stress histories that the target material experiences during high velocity impact experiments. PVDF is a tough, flexible polymer readily available in the form of a thin film which can be made piezoelectric. The gauges are manufactured using biaxially stretch 25 μm (± 5 %) thick PVDF film material that has been characterized and poled using the Bauer process [158,159] to a remnant polarization of 9.2 $\mu C/cm^2$. Figure 3.8 shows the orientation of the square poled sensor area relative to the PVDF '1' and '2' stretching axes. Metal electrodes are prepared by sputtering gold over platinum onto the surfaces of the film. The polled region of the film is highly controlled within the active sensor area (shown in Figure 3.8) located between the crossed electrodes.

The gauges have highly reproducible shock response characteristics and sensitivity to loading. The dependence of charge output on stress has been determined

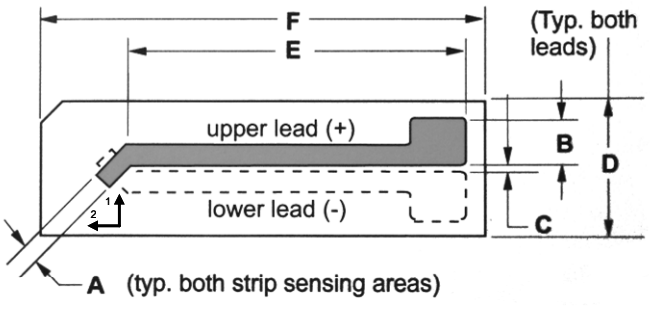


| | Dimension [mm] |
|---|---|
| A | 1x1 |
| B | 10 |
| C | 0.05 |
| D | 30 |
| E | 50 |
| F | 60 |

**Figure 3.8** Schematic diagram of a PVDF stress gauge dimensions.

from a series of uniaxial plate impact experiments and calibrated using a "negative-current orientation" from 0.01 to 10 GPa [10,160]. This orientation was observed to have significantly higher output currents as compared to the "positive-current" orientation at high pressures [160]. Operated in the current mode, a precision current viewing resister (CVR) is connected across the electrodes of the gauge and a measure of the current generated during an impact experiment is deduced from the recorded voltage drop. The recorded signal is proportional to the differential of the stress wave profile. The signal is integrated to obtain the stress wave profile.

### 3.5.1 Equation of State Hugoniot Experiments

Equation of state (EOS) experiments were conducted on two different epoxy-cast compositions consisting of 60 and 78 *vol.%* epoxy combined with stoichiometric quantities of $Al+Fe_2O_3$ powder mixture. Impact stresses ranged from 2.7 to 8.5 GPa for the 60 *vol.%* epoxy composition and 2.1 to 4.7 GPa for the 78 *vol.%* epoxy composition using the 80 mm compressed-gas gun. Details for the 60 and 78 *vol.%* epoxy

**Table 3.5** Data summary for Al+$Fe_2O_3$+60 *vol.%* epoxy EOS experiments.

| Shot Number | Specimen ID | Specimen Thickness [mm] | *Specimen Density [g/cm$^3$] | Flyer Material | Flyer Thickness [mm] | Driver Material | Driver Thickness [mm] | Impact Velocity [m/s] | ☺ $P_I$ [GPa] |
|---|---|---|---|---|---|---|---|---|---|
| 0627 | 121C-5 | 2.159 ± 0.013 | 2.4020 | Al+$Fe_2O_3$ + 60 *vol.%* epoxy | 3.868 ± 0.010 | none | n/a | 714.1 ± 2.5 | 2.71 ± 0.01 |
| 0505 | 121C-6 | 2.182 ± 0.008 | 2.4057 | Al+$Fe_2O_3$+ 60 *vol.%* epoxy | 3.871 ± 0.006 | none | n/a | 1035.9 ± 4.2 | 4.14 ± 0.02 |
| 0608 | 121C-3 | 2.763 ± 0.001 | 2.4050 | OFHC Cu | 6.221 ± 0.004 | OFHC Cu | 2.154 ± 0.005 | 997.0 ± 62.9 | 5.91 ± 0.14 |
| 0507 | 121C-7 | 2.172 ± 0.010 | 2.3990 | W | 4.994 ± 0.003 | OFHC Cu | 2.149 ± 0.008 | 972.1 ± 15.9 | 7.23 ± 0.15 |
| 0628 | 121C-8A | 1.525 ± 0.037 | 2.4013 | W | 2.558 ± 0.004 | OFHC Cu | 1.535 ± 0.001 | 1022.0 ± 4.2 | 7.66 ± 0.03 |
| 0609 | 121C-4 | 2.756 ± 0.005 | 2.4010 | W | 5.624 ± 0.003 | OFHC Cu | 2.171 ± 0.003 | 1166.5 ± 68.8 | 8.54 ± 0.24 |

*Measured densities were within 99.8 % TMD for target specimens and epoxy-cast flyer materials used for symmetric impact experiments.

☺Impact pressure, $P_I$ or stress measured from PVDF gauge located on the impact face of the target specimen.

**Table 3.6** Data summary for gas gun and plane wave lens (PWL) explosively driven equation of state experiments conducted for Al+$Fe_2O_3$+78 *vol.%* epoxy. Shot numbers with "JJH" prefix were performed by J. Jordan and R. Dick [161,162].

| Shot Number | Specimen Density [g/cm$^3$] | Test Method | Flyer Material | Driver Material | Impact Velocity [m/s] | $P_I$ [GPa] |
|---|---|---|---|---|---|---|
| 0303 | 1.7900 | Gas Gun | OFHC Cu | OFHC Cu | 523.3 ± 26.5 | 2.11 ± 0.02 |
| 0308 | 1.8645 | Gas Gun | OFHC Cu | OFHC Cu | 556.0 ± 21.7 | 2.28 ± 0.03 |
| 0311 | 1.8503 | Gas Gun | OFHC Cu | OFHC Cu | 716.0 ± 89.5 | 3.10 ± 0.05 |
| 0403 | 1.8581 | Gas Gun | OFHC Cu | OFHC Cu | 943.7 ± 3.8 | 4.66 ± 0.31 |
| JJH8 | 1.850 | PWL/TNT | n/a | Al | n/a | 16.40 |
| JJH9 | 1.850 | PWL/TNT/PMMA | n/a | 6061-T6 Al | n/a | 10.82 |
| JJH10 | 1.850 | PWL/TNT | n/a | PMMA | n/a | 14.45 |
| JJH11 | 1.850 | PWL/Octol | n/a | 6061-T6 Al | n/a | 17.29 |
| JJH12 | 1.850 | PWL/Octol/PMMA | n/a | 6061-T6 Al | n/a | 19.00 |
| JJH13 | 1.850 | PWL/Octol | n/a | PMMA | n/a | 23.09 |
| JJP22/23 | 1.850 | PWL/TNT | n/a | 6061-T6 Al | n/a | 19.21 |
| JJH24 | 1.850 | PWL/TNT | n/a | OFHC Cu | n/a | 7.22 |
| JJH25 | 1.850 | PWL/Baratol | n/a | OFHC Cu | n/a | 3.94 |
| JJH26 | 1.850 | PWL/Octol | n/a | OFHC Cu | n/a | 14.77 |

composition experiments are listed in Table 3.5 and Table 3.6, respectively. Several higher pressure experiments not attainable using the compressed-gas gun, but performed using explosive loading are also detailed in Table 3.6 for the 78 *vol.%* epoxy composition. These high-pressure experiments were conducted at the Air Force Research Laboratory (AFRL) by Jordan, *et al.*, [161,162]. In these high pressure Hugoniot measurement experiments, data for the 78 *vol.%* epoxy composition was obtained using explosive plane wave lenses (PWL) in conjunction with TNT, Octol, or Baratol booster pads. A donor material with known shock parameters and an optional PMMA attenuator plate was placed on the explosive pad. The sample was placed in contact with the donor material and the shock wave within the donor and the specimen was measured using piezoelectric pins located at different thicknesses. This permits the determination of shock velocity through the donor plate and specimen of interest. Using the measured shock velocities in the donor material and the specimen, the remaining Hugoniot properties for the specimen were determined using impedance matching.

Experiments conducted for the 60 *vol.%* epoxy composition were carried out using only parallel-plate impact experiments on Georgia Tech's compressed-gas gun. It was challenging to obtain a large range of impact pressures using this technique with a low impedance polymer composite. However, several impact pressures were obtained using different combinations of tungsten and copper flyer and driver materials. Two different experimental configurations were utilized; *i*) low pressure symmetric parallel plate impacts using similar epoxy-cast material for the flyer and target, and *ii*) higher pressure configurations utilizing high density flyer and driver material combinations to "drive up" the pressure experienced by the target specimen. Figure 3.9 shows a

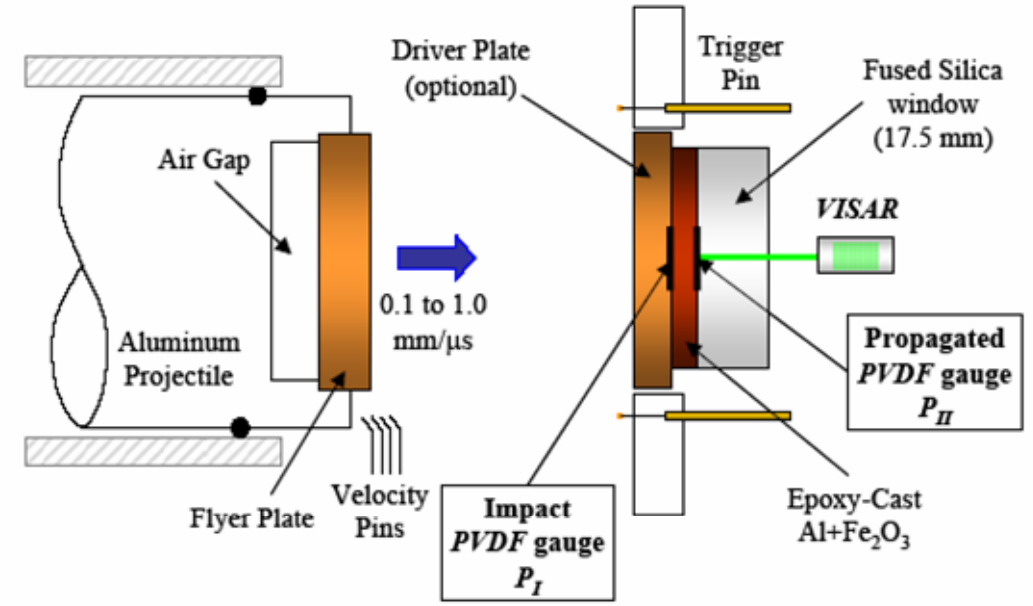


**Figure 3.9** Schematic diagram of EOS experiments using PVDF stress gauges and VISAR. Flyer plate materials used for this study consisted of tungsten, copper, and epoxy-cast Al+$Fe_2O_3$ for symmetric impacts. The figure illustrates a flyer-driver configuration. However, the driver material is not utilized when conducting a symmetric impact experiment where the flyer and target materials are the same composition.

schematic of the parallel-plate impact experiment configuration used with the gas gun to measure the composite material's EOS. All of the experiments were shock and release type impacts, where the target was loaded to a compressive high-pressure state and then unloaded when the release wave entered the target material. The target thickness was carefully selected to ensure the normal wave propagation through the material was measured before a complex stress state was introduced from radial waves reflecting from the specimen's edge. The projectile assembly consisted of a flyer mounted on an aluminum sabot, which was backed by an air gap with a small step for attaching the flyer. The sabot face was machined to remove material with a slightly smaller diameter than the flyer. A step was machined with a depth approximately half the thickness of the flyer

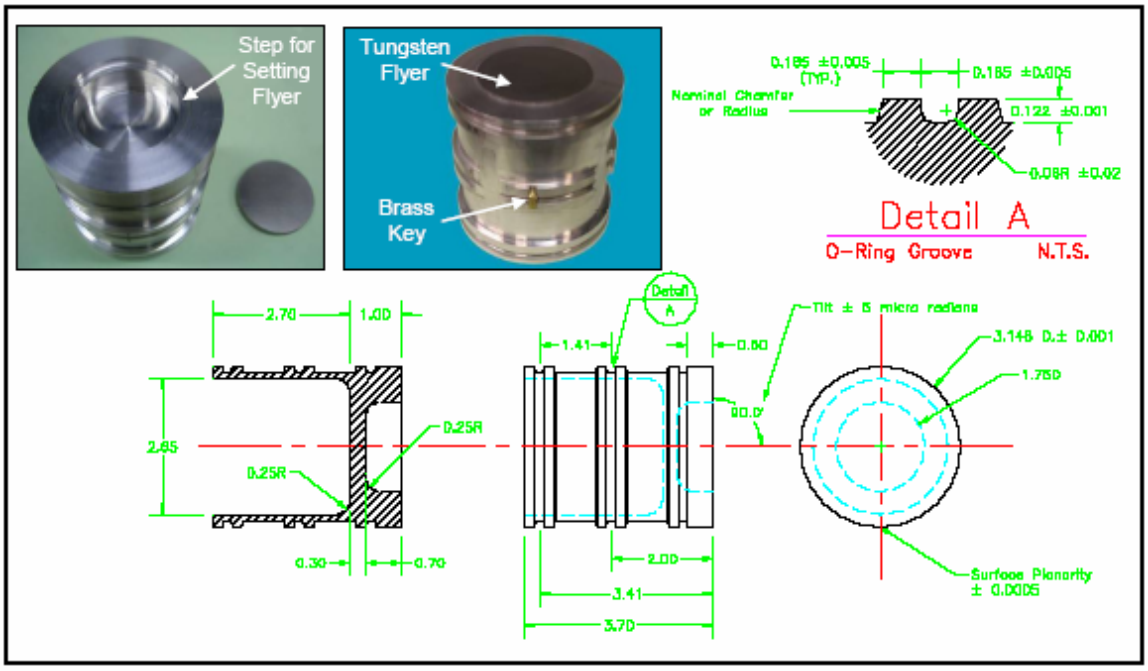


**Figure 3.10** Schematic diagram of a high-speed aluminum projectile and final assembly used for EOS experiments.

(see Figure 3.10). The flyer was attached to the sabot along its circumference using Hystal thin film epoxy. Typical dimensions used for the sabot and flyer assembly are shown in Figure 3.10, along with a photograph of a finished assembly.

Polyvinyl di-floride (PVDF) stress gauges were used to measure the arrival and magnitude of the shock wave at two locations; as it entered and exited the target specimen. Additionally, velocity interferometry (VISAR) was used to directly measure the particle velocity at the back surface of the specimen and window interface. High purity fused silica (Corning 7980 HPFS Standard Grade; Corning, NY) was used as the window material attached to the back surface of the target. VISAR measurements were corrected for the impedance difference between fused silica and the target material to give a redundant measure of specimen particle velocity. Figure 3.11(*a*,*c*) gives a detailed

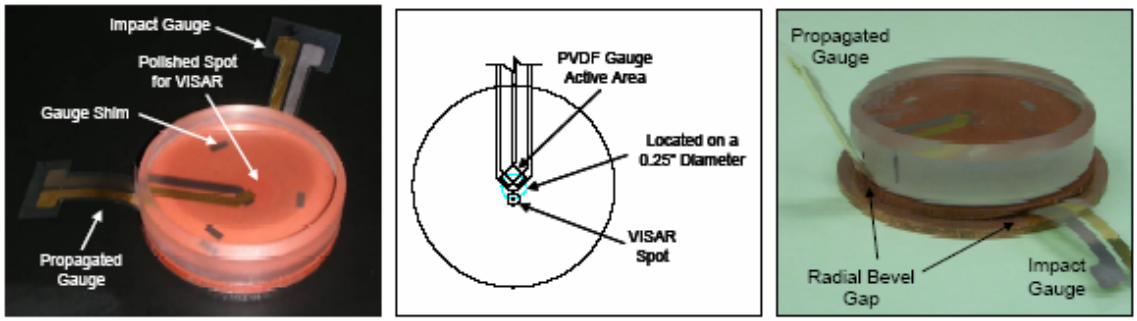


**Figure 3.11** Target assembly shown from *a*) above and *c*) the side, PVDF gauges located on either side of the Al+$Fe_2O_3$+epoxy composite and backed by a fused silica window. *b*) Schematic diagram showing the orientation of PVDF gauge and VISAR on back surface of target (propagated gauge location).

view of the target assembly which consists of the PVDF gauge package located on either side of the target material, backed with a fused silica window. In some cases there was also a metallic driver material attached to the front of the target specimen. The gauge package consists of alternating layers of PTFE insulation which were attached with thin film epoxy on both sides of the PVDF stress gauge and shown schematically in Figure 3.12.

Preparation of the target began with lapped, disk shaped specimens with a nominal diameter of 50.8 mm and typically 1.5 to 3 mm thick. Physical dimensions and density were measured prior to the assembly process. During the target assembly, PVDF gauges were placed on the impact and back face of the specimen to measure stress and arrival times of the shock wave. The sharp edges of the specimen circumference, where the gauge leads cross, were removed to extend the life of the gauge during the experiment [163]. A radial bevel, shown in Figure 3.13(*c*,*d*), was filed along the outer sharp edge in the proximity of the gauge lead location. The fused silica windows used on the back surface of the target already had a ⅛" radial bevel machined for this same

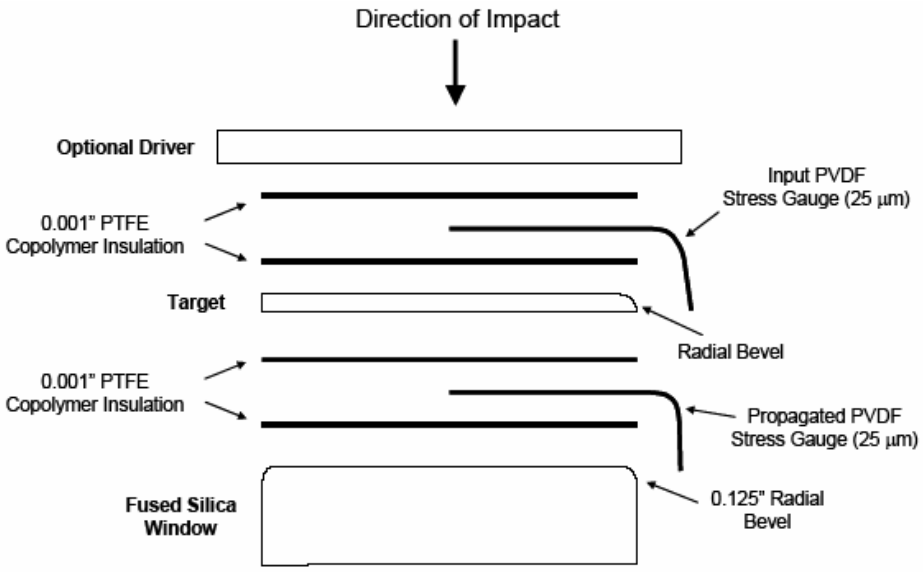


**Figure 3.12** Schematic diagram illustrating the different layers that comprise the target assembly with use of PVDF stress gauges.

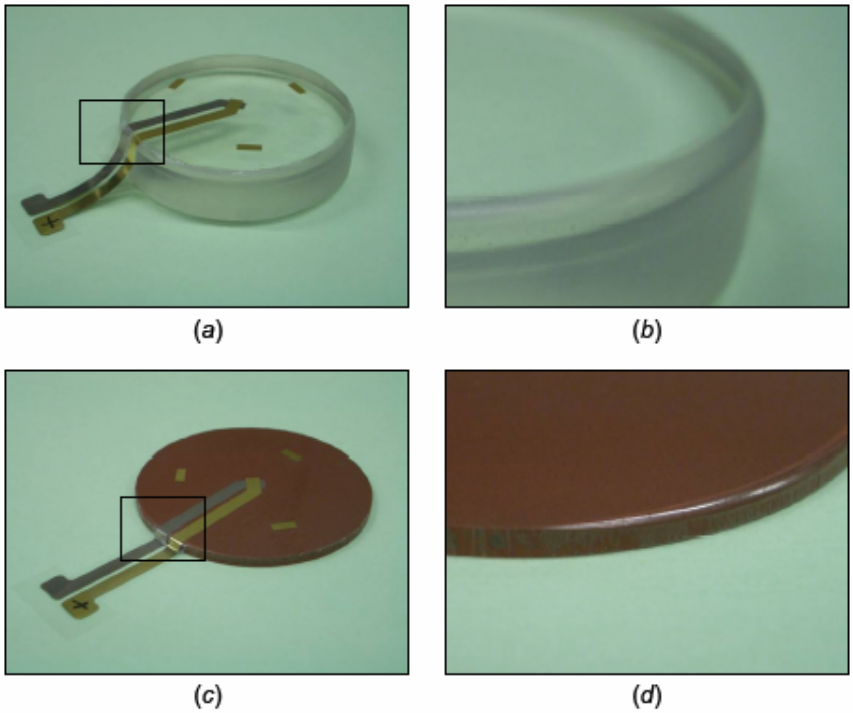


**Figure 3.13** Images showing the radial bevel on the *a*,*b*) fused silica window and *c*,*d*) Al+$Fe_2O_3$+epoxy target designed to extend PVDF gauge life. Images *b*) and *d*) show a close-up view of the bevel before PTFE insulation and the PVDF gauge are attached to the surface.

purpose also shown in Figure 3.13(*a*,*b*). Figure 3.11(*c*) shows the gap formed from the bevel in the location where the PVDF gauge leads extend from the target's surface, which helps extend the lifetime of the gauge during an experiment. In most EOS experiments, both PVDF gauges and VISAR diagnostics were used to capture a redundant measure of particle velocity. A location close to the center of the specimen's back surface was polished with 1 μm diamond paste to give a mirror-like finish and then purposely scratched using an abrasive pad to create an ideal diffused surface for the VISAR laser measurement. The gauge placement and the location of VISAR measurement are shown schematically in Figure 3.11(*b*). The delay time or velocity per fringe (VPF) constant (using a fused silica window) was selected for each experiment based on expected particle velocity.

The overall experimental design was adopted from an arrangement used originally at Sandia National Laboritories, in Albuquerque, NM [10,12,160,163] and subsequently implemented with the Georgia Tech. gas gun. The target assembly consists of several gluing steps using Hystol (RE 2038 and HD 3475) thin film epoxy (Henkel Corporation; Olean, NY). The assembly begins with attaching a 0.0254 mm (0.001") thick PTFE insulating film to the impact face of the target and the window surfaces. Once cured, piezoelectric stress gauges were placed separately at the approximate center of the target and fused silica window. Then supplied metallic shims (having identical thicknesses as the gauge) were placed on the impact face to maintain planarity over the face of the target and window materials. Several drops of thin film epoxy were placed under the gauge and shim locations. The PVDF stress gauges were less than 25 μm thick and had an active area of 9 $mm^2$ where the stress measurement was taken. Several drops of thin film epoxy

were placed evenly on the gauge surface and another 0.0254 mm (0.001") thick layer of PTFE film was placed over the gauges. A small metallic cylinder was used to roll out the thin film epoxy evenly across the gauge assembly surface and remove trapped air bubbles. Once all of the air bubbles were removed, the gauge assembly was weighted to remove remaining trapped air bubbles and compress the gauge package assembly. Glue layers between the insulation, gauge, and mating surfaces comprising the target assembly were typically 1 to 2 μm thick. Finally, the target with the gauge package on its impact face and the fused window with the propagated gauge package on its face were glued together. A small amount of thin film epoxy was added to the back face of the target and the front face of the gauge package on the fused silica window, and the two were placed together making sure the impact and propagated gauges were perpendicular to each other and shown in Figure 3.11(*a*,*c*).

PVDF stress gauges are high-impedance electrical sources and are inherently good pickup devices for electrical noise [163]. Locating the impact and propagated gauges 90° apart from each other helped to reduce the coupling of electrical noise that comes from the "cross-talking" of the two gauges [163]. Again, weight was placed on the target assembly to remove any excess trapped air. During each step of the assembly process, measurements were taken to obtain the thickness of each layer of the gauge package. Typical gauge package thicknesses were approximately 80 μm thick or less. Some experiments used a metallic driver and this was glued to the target assembly as the final step in assembling the target package. The target and window material have a beveled radius in the location where the gauge electrodes overlap the sharp circumference

edge. Removing the sharp edge on the specimen and window material significantly extends the life of the stress gauge by several microseconds [163].

With the target assembly completed, it was mounted in an acrylic ring that was attached to the muzzle face located at the downrange end of the compressed-gas gun barrel and an example of this is shown in Figure 3.6(*c*). The entire assembly was lapped prior to mounting on the gas gun muzzle face to ensure a planar impact. After lapping, two shorting crush pins (Dynasen Inc.; Goleta, CA) were placed on the target ring extending ahead of the impact plane by a few millimeters to trigger electronic diagnostics (PVDF and VISAR oscilloscopes) prior to impact.

The PVDF gauges were operated in a current viewing mode which had the advantage of low susceptibility to electrical noise [160,164]. In the current mode, the gauge was connected to a current-viewing resistor or CVR (T & M Research Products; Albuquerque, NM) across the electrodes of the gauge. The gauge leads were mechanically attached to the CVR using low-temperature indium-bismuth solder (Ktech Corporation; Albuquerque, NM). The gauge was operated in a "negative-current" orientation where the positive gauge lead (marked with a "+") was facing the impact direction. The negative lead of the gauge was attached to the center conductor of the CVR and the positive lead was attached to the sheathing. The CVR was connected in series with a 50 Ω high frequency, low-loss coaxial transmission cable, 12.8 meters in length (Andrew LDF4-50A; Westchester, IL). A disposable RG-233/U jumper cable 0.6 meters in length was used to connect the CVR inside the experiment chamber through a ground isolated BNC bulkhead connector and then to the Andrews cable which carried the signal to a digitizing oscilloscope located in the control room. The voltage signal

across the CVR was split using a 50 Ω power-T (Team Specialty Products Corporation (TSP); Albuquerque, NM), permitting the measurement at two complimentary sensitivities (typically 10:1 ratio). A primary channel captured the very high-stress rates (shock-jump conditions) and another channel monitored very low-stress rates. The waveforms were later combined providing high-resolution voltage-time profiles using PlotData software [165]. After combining, the voltage data was converted to current and integrated with respect to time. The current trace was divided by the gauge active area to give the charge as a function of time and the stress was obtained for the experimentally determined charge and stress relationship for PVDF gauges [160,164]. Experiment design factors for a given impact stress, such as selecting the proper CVR resistance, were determined using the empirical relationship [164]:

$$\sigma_I = \frac{\lambda_I - 4.97}{102}, \tag{3.11}$$

where $\sigma_I$ is the initial stress with units of GPa and $\lambda_I$ is the current density [A/cm$^2$]. Current densities were observed to have rise times less than the transit time of the shock wave through the gauge [12]. Therefore, the gauge was regarded as "thick" relative to the rise time of the loading pulse.

The cables were checked prior to each experiment using a pulse generator (Stanford Research, Inc. Digital Delay Pulse Generator Model DG535; Sunnyvale, CA) that sends a square wave with a 1 ns rise time and 10 ns wide pulse duration through a spare transmission cable to the target chamber and returns to an electronic digitizing oscilloscope (Tektronix TDS784A; Beaverton, OR) used during the experiment. This

method of "pulsing" the cables identified faulty or damaged cables and connectors, as well as verifying the proper cable connections from the target to the oscilloscope were used.

### 3.5.2 Taylor Anvil Impact Experiments

Taylor anvil impact experiments were used to characterize the constitutive response of epoxy-cast Al+$Fe_2O_3$ composites. Experiments were conducted using "direct" and "reverse" impact configurations. All of the experiments used high-speed photography to capture transient deformation profiles of the specimens. The next section gives details about the experimental configuration and the data captured during these experiments. Target assembly and alignment procedures are discussed as well as image analysis techniques used for these experiments.

#### 3.5.2.1 Reverse Taylor Anvil Impacts

Taylor anvil impact experiments were used to characterize the constitutive response of epoxy-cast Al+$Fe_2O_3$ composites. In the traditional Taylor test configuration, dynamic material data is normally obtained from post impact measurements of the deformed specimen. However, reverse Taylor anvil impact experiments were conducted for use in a compressed-gas gun, which provides a major advantage with the capability of measuring dynamic material data continuously throughout the experiment. For this configuration, the rod-shaped specimen was held stationary and its deformation was

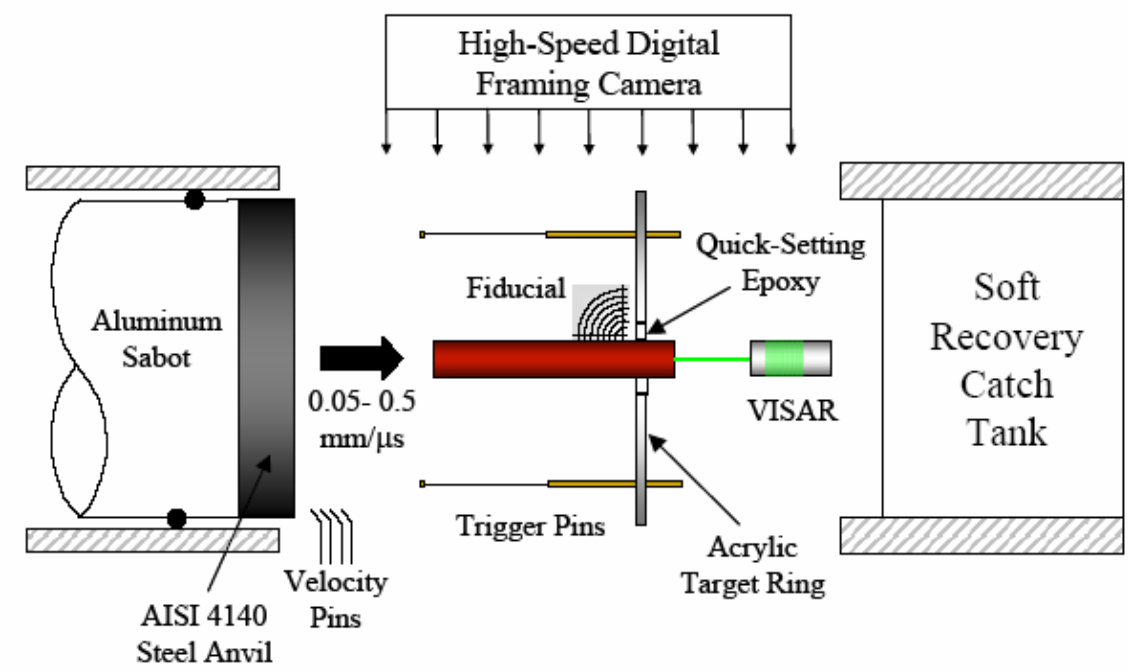


**Figure 3.14** Schematic diagram for reverse Taylor impact experiments.

caused by the impact of a rigid anvil mounted on the face of an aluminum sabot. Figure 3.14 shows a schematic diagram for reverse Taylor impact experiments. The anvil was made from AISI 4140 heat treated steel ($HR_C$ 52-56) and had disk geometry with a nominal diameter of 76.2 mm and 9.525 mm thick. There were three radial spaced countersunk holes for accepting screws used to secure the anvil to the aluminum sabot. All of the experiments rely on high-speed photography to capture transient specimen deformation profiles. Additionally, the experimental configuration permits the use of VISAR for measuring the specimen's free surface velocity as a function of time. High-speed photographs were time synchronized with free surface velocity measurement to give a complete description of the deformation process experienced by the specimen.

Experiment preparation began by carefully measuring density, and the specimen's length and diameter at several locations. Both ends of the specimen were polished using 15 and then 3 μm diamond pastes. For experiments using VISAR to measure free surface velocity, the back end of the specimen was polished using 1 μm diamond paste. A fiducial marker, shown in Figure 3.15, was made from concentric arcs placed 0.635 mm apart and was mounted on the center axis of the specimen for calibrating high-speed

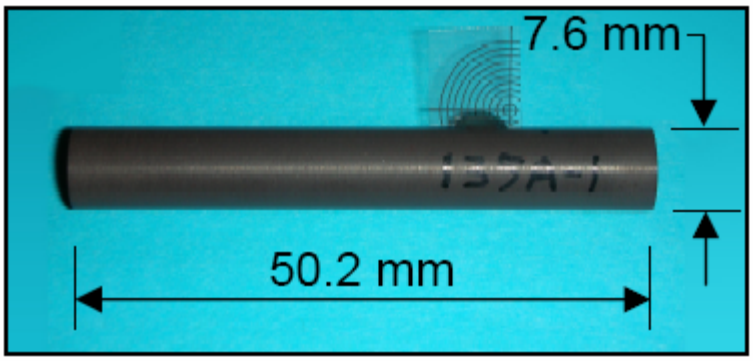


**Figure 3.15** Reverse Taylor impact specimen (nano-Al+$Fe_2O_3$+70 *vol.%* epoxy specimen shown) with nominal dimensions indicated. Image also shows the fiducial marker to calibrate high-speed images and align camera with specimen.

images acquired during the experiment. The fiducial marker was precisely placed on the center axis of the specimen using shims to position the marker exactly half the diameter of the specimen. The specimen and shims were placed on a granite measuring stone and the fiducial marker was attached to the specimen using epoxy. The marker was permanently secured to the specimen with a single drop of epoxy in a notch located at its base. The marker also has an additional benefit by providing a means for precisely

placing the camera perpendicular to the specimen (both in-plane and out-of-plane locations).

The specimen was mounted in an acrylic ring that was used to position the target in front of the gas gun barrel. A ⅛" thick acrylic target ring was machined with a ½" diameter hole in the center for locating the Taylor specimen and two adjacent locations for self-shorting crush pins used for triggering diagnostic equipment prior to impact. The specimen was mounted in the target ring using quick-setting epoxy (V.O. Baker Company; Mentor, Ohio) in such a way that its back surface extended approximately ¼" beyond the acrylic ring. The epoxy holding the specimen in the target ring was designed to break away once the specimen began to move, offering little resistance to this movement. The specimen was carefully positioned such that the fiducial marker and the two crush pin locations were perfectly aligned and coincided along the specimen's center axis. This ensured the crush pins did not interfere with camera images taken of the specimen deformation and also helped camera alignment with the specimen. With the specimen mounted in the target ring, two self-shorting crush pins were located on either side of the specimen. The procedure for mounting these pins involved placing the specimen's impact face down on a granite measuring stone, where a glass slide was located between the impact face of the specimen and the granite, to provide a small offset distance for the crush pins to extend beyond the impact face of the specimen. The crush pins were carefully positioned in the target ring making sure they were parallel (both in-plane and out-of-plane) to the target specimen and secured to the target ring using quick-setting epoxy. After the epoxy was completely cured, the offset distance was measured between each of the crush pins and target impact face using a similar "continuity circuit"

technique as described previously for measuring velocity pin distances. The completed target assembly consisting of the Taylor specimen and two triggering pins are shown in Figure 3.16(*a,b*).

The target assembly was now ready to be placed in the experiment chamber of the gas gun and aligned perpendicular to the barrel ensuring a perfectly parallel impact. A three-axis mounting fixture (Figure 3.17(*a*)) was placed on the muzzle face of the gas gun and the target ring assembly is secured. A laser was placed on another three-axis position fixture located at the uprange end of the barrel and shining its beam towards the downrange direction. The laser was first aligned parallel within the barrel ensuring that the beam coincides closely with the center axis of the barrel. This was accomplished by placing an aluminum plug with a precisely machined center hole in the barrel, in front of the laser beam and placing a piece of card stock at the downrange end. The beam was positioned until the two center points coincided and the beam projected a spot on the center of the card stock. The card stock has a small pin hole precisely placed in the

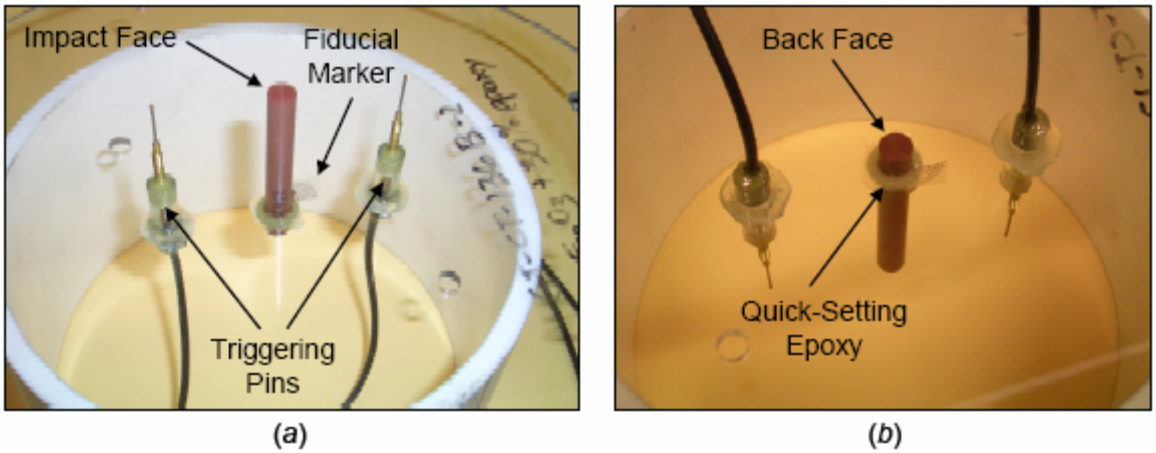


Figure 3.16 Completed target assembly for a reverse Taylor impact experiment showing *a*) impact face and *b*) back face views of specimen.

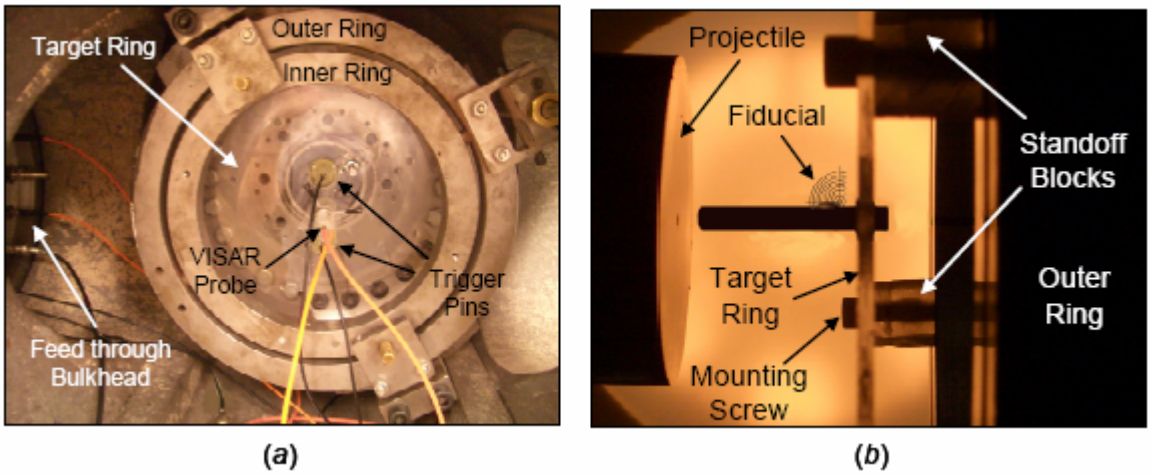


**Figure 3.17** Three-axis mounting fixture used for aligning the impact face of Taylor specimens with the projectile face showing images of *a*) front and *b*) side views.

center that coincides with the axial center of the barrel. A small general purpose, dielectric mirror (Newport Corporation; Irvine, CA) is placed at the end of the impact face of the specimen for reflecting the laser. The mirror had dimensions of 50.8 mm diameter and 0.236 mm thickness with a λ/10 surface flatness and a reflectance, $R > 99$ % for 0-45° angle of incidence. A small spot with the diameter of the pin hole was projected on the card stock and the sample was positioned so the spot overlaps the pin hole. The three-axis fixture was securely fastened at the outside ring axis points and the pin hole card stock was removed. The aluminum plug was removed from the uprange end of the barrel and replaced with another piece of card stock that has a ¼" diameter hole located in the center. This permits the laser from being unobstructed from the card stock reaching the mirror on the sample face and reflecting a spot back to the card stock. The center ring of the three-axis fixture was finely positioned using brass setscrews for

adjusting the tilt of the specimen impact face. Because the laser light travels a long distance from the uprange end of the barrel to the downrange end and back, the spot has a diameter of approximately $\frac{5}{8}$". The sample was aligned when the spot was located at the approximate center of the card stock and all point on the three-axis mounting fixture was secured. Using this technique, a maximum deviation from planarity at the most extreme case when the spot was located away from the center of the barrel was 2.6 mrad. However, the return spot was located at the center of the barrel for each experiment conducted in this study, resulting in the planarity of the impact estimated to be 1.4 mrad.

High-speed cameral images of the specimen's axial profile were taken using a back lighting condition. The compressed-gas gun experiment chamber uses two viewing ports with translucent lexan windows located on opposite sides of the target specimen. The camera was placed perpendicular to the specimen and opposite of a halogen light source (Power Light 2500DR, Photogenic; Boardman, OH). Camera alignment to the specimen was crucial for obtaining accurate measurements of specimen profiles during deformation. Alignment was accomplished by viewing the specimen in real time (camera's focus mode) while making minor adjustments to the camera's position. These included raising and lowering the camera, changing tilt and translating in the axial plane of the specimen. The fiducial marker was instrumental in making the alignment procedure simple and easily reproducible. Observing concentric arcs in the camera's field of view insured that it was perpendicular to the specimen. The fiducial marker was also important for focusing the camera's lens along the axial length of the specimen. Since the specimen has a cylindrical in shape, it was difficult to focus using the top a bottom rounded profile edges of the specimen. Once the camera was positioned

correctly, a series of images was taken to verify physical sample dimensions from camera images. The fiducial marker was used to calibrate the axial length and radial pixel dimensions. The difference between image and physically measured specimen dimensions was typically 0.1 to 0.2 %.

The camera's field of view was designed to give the best resolution of the specimen possible, while providing sufficient room behind the specimen to capture its final deformed length before moving out of the field of view. Typically, there was approximately 5 mm before the impact face and 20 mm behind the back surface of the specimen. Captured images had an average resolution of 18.65 ± 1.40 pixel/mm, which varied according to the sample length and hence field of view.

An Imacon-200 high-speed digital camera (DRS Technologies, Inc.; Parsippany, NJ) was used to capture images of the specimen deformation. The camera can record 16 still frames with 1200 x 980 pixel resolution with frame speeds from 100 fps to 200 million fps and 5 ns exposure times. To arrest the deformation motion in the photograph, the maximum exposure time, $T$ was calculated based on [166]:

$$T = \frac{L}{500v}, \tag{3.12}$$

where $L$ is the largest dimension of the subject to be captured and $v$ is the subject velocity in the same units as $L$ per second. Since the plastic deformation wave velocity was unknown and one of the desired parameters being experimentally measured, the wave velocity was estimated to be a fraction of the material's elastic wave speed ($C_P = 1/4\, C_0$). Typical exposure times used for reverse Taylor impact experiments ranged from 175 to

200 ns. Camera frame times were selected to capture the experiment at three different critical time intervals. One image was captured just prior to impact and three frames were captured towards the end of the experiment before the back surface of the specimen moved out of the cameras filed of view. The remaining 12 frames captured the time starting with impact and an interval divided evenly over ¼ the specimen's length given by:

$$t = \frac{L_0}{u(\#\,frames)}, \tag{3.13}$$

where $t$ is the time per frame in units of [μs], $L_0$ is the specimen length prior to impact, and $u$ is the velocity of the specimen approximated using the impact velocity. The camera used a 105 mm Nikon® lens (Nikon, Inc.; USA) with the aperture set at f/5.6. A typical transient image is shown in Figure 3.18(*b*).

Captured images were imported into Adobe® Photoshop® software (Adobe; San Jose, CA) for measuring incremental length and diameter changes during the experiment. Static images were first analyzed to accurately measure the specimen length and diameter prior to impact. A filtering routine was applied to each of the images using the "find edges" command in Photoshop®. The find edges filter identifies the areas of the image with significant contrast transitions and emphasizes the edges. This was ideally suited for the Taylor test images that show a significant contrast difference between the dark sample and white background. Specimen edges were located for each frame and the length and diameter were measured for several locations. The same routine was applied to images captured during the experiment showing the specimen deforming.

For some select experiments, a special containment fixture was designed to capture the specimen in an effort to preserve deformation caused purely from the impact and prevent any further deformation occurring during the recovery stage. Post-impact dimension measurements of recovered specimens showed good correlation with "final" specimen length and diameter measurements obtained from high-speed camera images taken at sufficient times after impact and are compared in Table 3.7. This provides verification that dimensional measurements using high-speed camera images are adequate and essential for experiments where the specimen was not recovered intact.

Laser interferometry was used to measure the free surface velocity of Taylor specimen. The VISAR system uses glass etalons to set the fringe spacing for measuring

**Table 3.7** Comparison of initial and final specimen lengths measured using digital and physical techniques from both reverse and direct Taylor impact experiments.

| Shot Number | Specimen ID | Epoxy *vol.%* (*wt.%*) | Initial Length, $L_0$ [mm] | | Final Length, $L$ [mm] | |
|---|---|---|---|---|---|---|
| | | | Physical | Image | Physical | Image |
| [D] RM-23 | 085D-1 | 46.94 (20) | 50.77 | 50.80 ± 0.04 | 49.61 ± 0.01 | n/a |
| [R] 0621 | 119A-1 | 60.27 (30) | 51.69 ± 0.01 | 51.54 ± 0.08 | 50.79 ± 0.01 | 50.61 ± 0.19 |
| [D] RM-22 | 079C-2 | 60.27 (30) | 50.76 | 50.79 ± 0.05 | 49.16 ± 0.01 | 48.99 ± 0.04 |
| [D] RM-21 | 101D-1 | 70.23 (40) | 50.80 | 50.85 ± 0.05 | 49.79 ± 0.01 | n/a |
| [R] 0601 | 091D-1 | 100 (100) | 49.79 ± 0.02 | 49.72 ± 0.08 | 49.76 ± 0.02 | 49.80 ± 0.06 |
| [R] 0637 | 138B-1 | 100 (100) | 53.15 ± 0.01 | 53.10 ± 0.04 | 53.17 ± 0.01 | 53.12 ± 0.03 |
| [R] 0638 | 139A-2 | 100 (100) | 50.41 ± 0.01 | 50.24 ± 0.08 | 50.43 ± 0.03 | 50.29 ± 0.03 |
| [R,n] 0648 | 135A-2 | 70.23 (40) | 52.30 ± 0.03 | 52.32 ± 0.03 | 52.11 ± 0.03 | 51.99 ± 0.11 |
| [R,n] 0649 | 134C-1 | 70.23 (40) | 52.37 ± 0.01 | 52.35 ± 0.06 | 51.41 ± 0.03 | 50.96 ± 0.16 |

[D] Direct Taylor impact experiment.
[R] Reverse Taylor impact experiment.
[n] Nano-Al+$Fe_2O_3$+70 *vol.%* epoxy composition.

the velocity of the reflecting surface that is moving. The fringe spacing was selected based on the estimated free surface velocity resulting for an impact with the anvil and epoxy-cast composite. The free surface velocity was calculated based on the equality of the particle velocities between the two materials with knowledge of their respective equation of state. Most of the reverse Taylor experiments conducted in this work had impact velocities that produced free surface velocities of 200 m/s or less. Correspondingly, the VPF constant was selected to be 99.4 m/s/Fr and typically gave two or three fringes used for calculating free surface velocity.

3.5.2.2 Direct Taylor Anvil Impacts

Direct Taylor impact experiments were conducted at the Air Force Research Laboratory test range. Specimens were launched from a 30 caliber powder gun into a massive steel anvil. The anvil was made from high-strength 4340 steel heat-treated to $HR_C$ 50 hardness. The anvil face had a mirror finish and located 76.2 mm from the end of the barrel. After each experiment, the anvil was rotated so the next experiment would impact a "new" region of the anvil surface. A Cordin 330A high-speed film framing camera was used to image transient deformation profiles, typically with a 3 μs framing interval and a total of 82 images. Backlighting was used to enhance the contrast and clearly trace specimen edges. Figure 3.18(*a*) shows a typical image captured during the experiment, with the anvil located on the left side of the image. A marker placed in the proximity above the impact location was used to spatially calibrate the images and

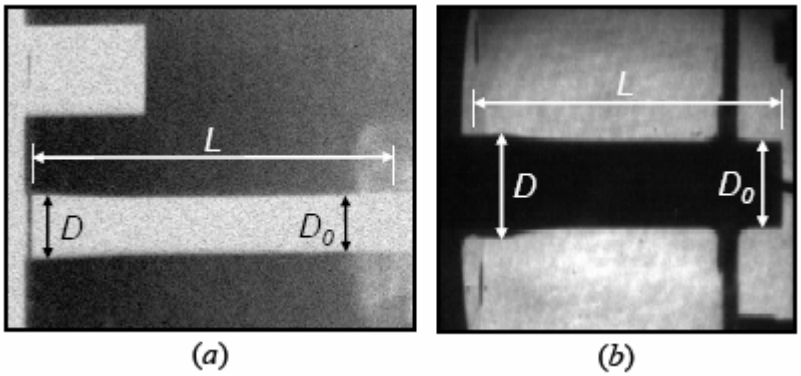


**Figure 3.18** Representative images captured from *a*) direct and *b*) reverse Taylor impact experiments.

precisely determine the anvil face in the image. The fiducial marker had a cylindrical shape with a thin gap machined on the face where it attached to the anvil magnetically.

Velocity was measured using a two-beam laser interrupt system located just prior to the anvil's impact face. A redundant system was also used by measuring the arrival of a pressure pulse at two pressure transducers located a fixed distance from each other at the end of the barrel. Typical impact velocities for these experiments ranged between 85 and 200 m/s.

# CHAPTER IV

# RESULTS AND DISCUSSION

The present investigation focuses on understanding the Hugoniot equation of state (EOS), high-strain rate mechanical properties, and mechanochemical reactivity for a structural energetic material system comprised of micron-scale and/or nano-scale reactants dispersed in an epoxy matrix. The reactive properties of energetic materials are strongly affected by their microscopic and mesoscopic morphologies whereby the alteration, for example, of the reactants' particle size or other microstructural features may enhance or inhibit specific energetic and structural characteristics. The mechanical response of the reactive constituents and the matrix also influences the reaction response. Hence, the challenge is to understand the synergistic behavior of structural and energetic properties and the effect their manipulation may have on overall material behavior.

The investigation addresses the general area of dynamic response of an epoxy-cast metal-oxide-type material system motivated by the need to understand their fundamental behavior when subjected to rapidly applied loads. Applied stress, strain, and strain rates likely to be experienced particularly during high-speed impacts and penetrations are systematically studied in conjunction with chemical reactivity attributed to a mechanical stimulus in the form of a transient deformation wave. The experimental approach involved conducting time-resolved instrumented shock-loading tests under a

range of loading conditions. The material system was also fully investigated and characterized using microstructural analysis both prior to impact and from post-mortem recovered material.

In this chapter, the processing and characterization of epoxy-cast thermite composites will first be presented. This is followed by experimental results obtained from mechanical characterization at several different strain rates. These include relatively low-strain rate experiments such as quasistatic compression, three-point bend tests, and Charpy impacts. Additionally, high-strain rate parallel-plate impact experiments for determining the composite material's EOS and Taylor impacts tests for obtaining the constitutive response will be discussed. Special attention was also given to characterizing the composite materials' energetic/reactive response through post-mortem differential thermal analysis (DTA), performed on the recovered impacted samples. DTA and *in situ* high-temperature x-ray diffraction (HTXRD) was also used to characterize the energetics of thermally initiated reactions.

## 4.1 Processing and Characterization of Aluminum-Hematite Composites

Structural energetic materials consisting of Al+$Fe_2O_3$ thermite powder mixtures dispersed in epoxy were processed using a cast-cure technique and formed into specific geometries useful for mechanochemical characterization experiments conducted in this study. Commercial nano- and micron-scale aluminum and submicron hematite powders were measured into stoichiometric quantities (25.26 *wt.%* Al and 74.74 *wt.%* $Fe_2O_3$) corresponding to the thermite reaction $2\,Al + Fe_2O_3 \rightarrow 2\,Fe + Al_2O_3$, and mixed in a

v-blender. The combined powders were dispersed in epoxy with 47 to 78 *vol.%* concentrations. Transmission electron microscopy (TEM) was used to image and characterize the starting constituent powders, while scanning electron microscopy (SEM) was used to image and characterize the combined powder mixtures, as well as processed epoxy-cast materials. Optical microscopy was also utilized for quantitative microstructural characterization of the epoxy-cast composites.

The particle morphologies for each of the constituents and their mixtures are shown in Figure 4.1(*a*-*c*) and Figure 4.2(*a*,*b*), respectively. Figure 4.1(*a*,*b*) shows TEM images of the precursor aluminum powders, with both nano-scale (55.3 nm average particle size according to manufacturer) and micron-scale (3.2 μm average particle size according to manufacturer) particles exhibiting spherical morphologies. The particle sizes observed through the TEM images revealed that the nano-scale aluminum particles had an average diameter range between 50 and 100 nm, and the micron-scale aluminum had particle diameters from approximately 0.5 to 3 μm. Figure 4.1(*c*) shows a TEM image of the as-received hematite powder, which was comprised of particles with a hexagonal platelet structure and a high aspect ratio (in the range 5:3 to 4:1). The long axis of the hematite particles were approximately 100 to 300 nm and have a thickness of 40 to 50 nm. Figure 4.2(*a*,*b*) show SEM images of the combined Al+$Fe_2O_3$ powders using *a*) nano-scale and *b*) micron-scale aluminum powders after mixing in a v-blender for 48 hours. Images of the powder mixture show the nano-scale aluminum particles are on the order of the hematite particle sizes and appear to combine uniformly within the higher concentration of hematite. Conversely, micron-scale aluminum was significantly larger (in most cases) than the hematite particles, which have been observed to coat the

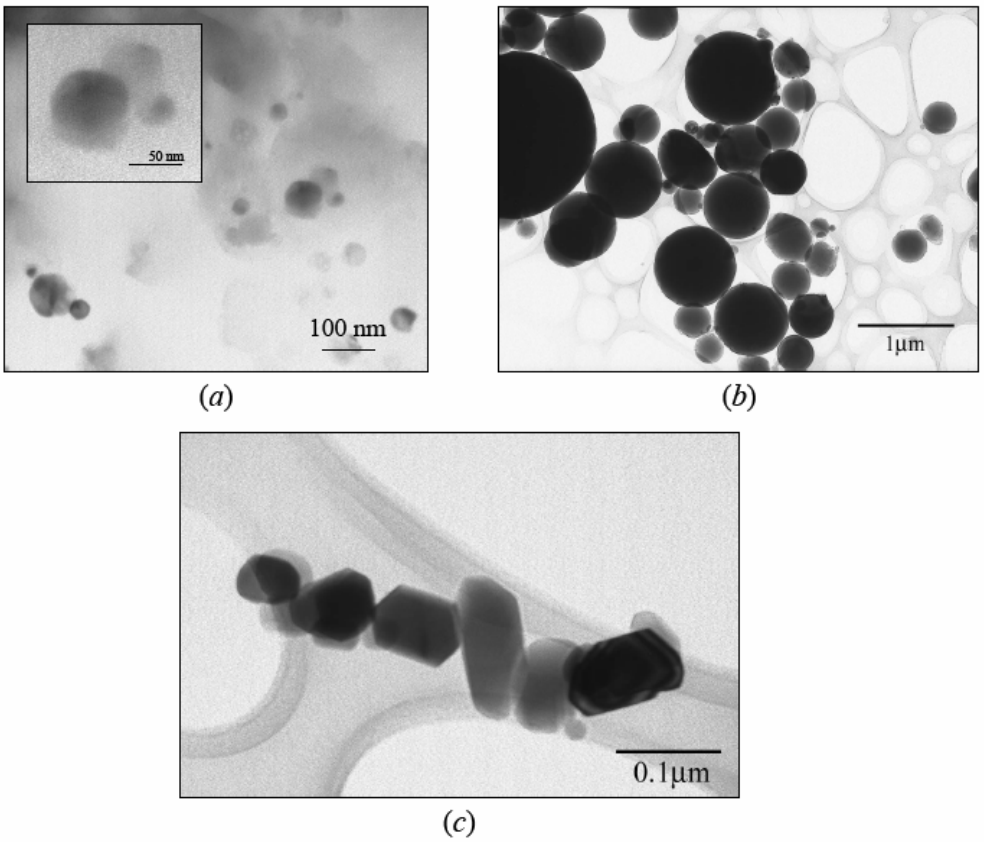


**Figure 4.1** TEM images of *a*) nano-scale and *b*) micron-scale aluminum particles showing spherical morphologies. Image *c*) is an image of hematite particles which have a hexagonal platelet structure with a high aspect ratio.

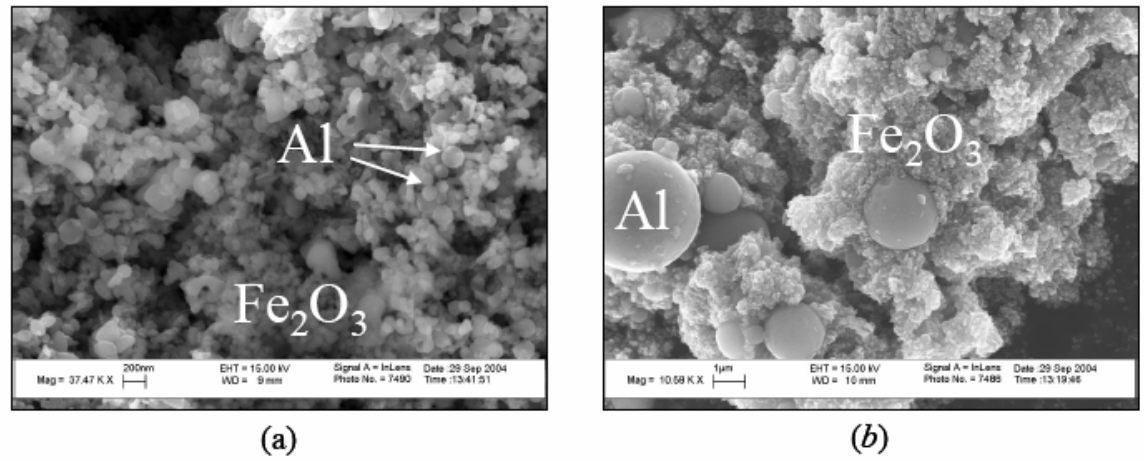


**Figure 4.2** SEM images of mixed Al+$Fe_2O_3$ powders in a v-blender with *a*) nano-scale and *b*) micron-scale aluminum particles sizes.

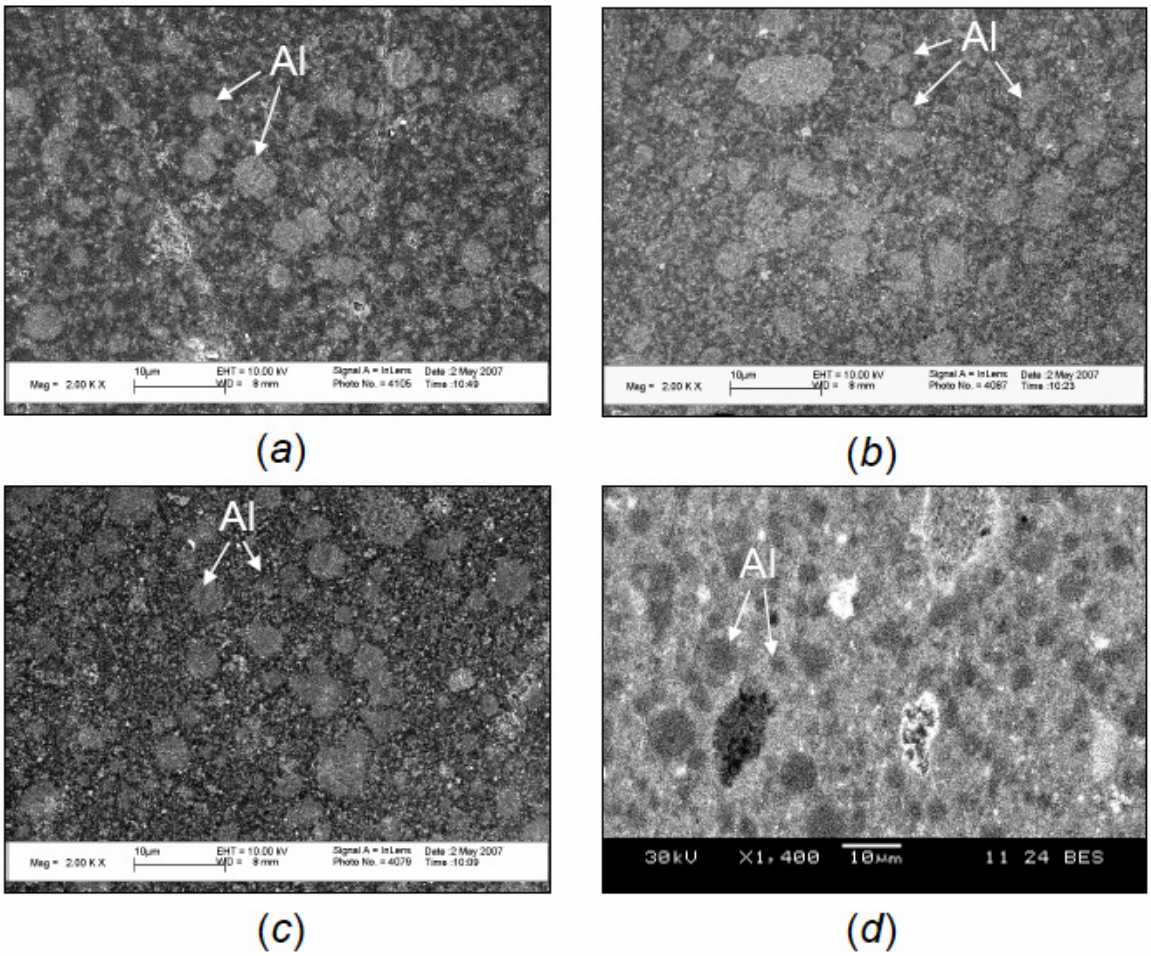


**Figure 4.3** Typical microstructures evolving for epoxy-cast Al+$Fe_2O_3$ composites. SEM images show representative microstructure features obtained for composites containing *a*) 78, *b*) 70, *c*) 60, and *d*) 47 *vol.%* epoxy. Light contrast circular areas are aluminum particle in *a*) through *c*). However, *d*) uses the backscatter detector for obtaining images of the microstructure and dark contrast circular areas are the aluminum particles.

large-scale aluminum particles. SEM images also show that hematite particles form agglomerates during the mixing process. This observation was more apparent when examining polished cross-sections of the epoxy-cast specimens from both optical microscope and SEM images, as shown in Figure 4.3(*a-d*).

### 4.1.1 Quantitative Microstructural Characterization

The mixing of precursor powders and their dispersion within an epoxy matrix influence the overall microstructural features and the composite's bulk mechanical and chemical properties. To investigate these effects, the evolving microstructures of each composition were examined using stereological techniques. Specimens were processed using a cast-cure method described in section 3.1 by adding premixed Al+$Fe_2O_3$ powders to various concentrations of epoxy. Typical SEM images obtained for each composition using micron-scale aluminum are shown in Figure 4.3(*a-d*) according to their nominal epoxy concentrations ranging from 78 to 47 *vol.%*, respectively. While the aluminum particles qualitatively appear to be uniformly dispersed throughout the composite, the hematite particles show a tendency to agglomerate over several size ranges. The degree of agglomeration appears to increase in size as the epoxy concentrations decrease for a given composition.

Quantitative microstructural characterization was performed to obtain size and distribution of aluminum particles, hematite agglomerates, and pores observed through digitally captured (1390 x 1040 pixels) optical microscope images. Several random locations from a polished plane were selected and individual features were measured.

Aluminum particle sizes were obtained using a 50x objective lens magnification and digital images were captured with a corresponding pixel resolution of 0.0925 μm/pix. The optical microscope at this magnification can resolve features to 0.5 μm or approximately 5 x 5 pixel array.

Likewise, hematite agglomerates were observed using a 2.5x magnification objective lens, since these features were much larger in size. Typically, hematite agglomerate section sizes (diameters measured from a two-dimensional plane) range between 10 and 50 μm depending on the amount of epoxy in the composite. However, small fractions of hematite agglomerate sections were found to be of larger size and closer to 70 to 90 μm, again depending on epoxy concentration. The optical microscope at this magnification has a pixel resolution of 1.8657 μm/pix and can resolve approximately 9 μm features (again using a 5 x 5 pixel array). This low magnification (2.5x) was also chosen to quantify the hematite agglomerates because they were defined by aluminum particles surrounding their boundary. This made their precise size measurement challenging and required sacrificing some resolution to minimize the distance between aluminum particles that defined the edge of the agglomerates. Furthermore, a threshold routine was utilized to "flatten" the image background (low contrast) and reveal the hematite agglomerate as dark contrast regions. Individual hematite particles (sizes between 100 and 300 nm) were not resolvable using an optical microscope, but were qualitatively evaluated using SEM images and appear to be uniformly dispersed within the epoxy matrix. Qualitative observations obtained for each composition will be discussed later in this section.

Inherent pores produced during the casting process were evaluated using the same images captured for the hematite agglomerates. Because of the complexity of these microstructures, it was challenging to resolve individual pores on a background of hematite particles dispersed in epoxy. The pores were typically observed in the hematite/epoxy matrix as a result of being trapped during processing despite a degassing step of the mixture. The epoxy was also translucent, which added to the difficulty of resolving pores along a polished plane. However, a threshold method was employed to resolve inherent porosity within a hematite/epoxy background.

Figure 4.4(*a*) shows a typical optical microstructure image captured for measuring hematite agglomerates and porosity. Two separate threshold routines were applied to this

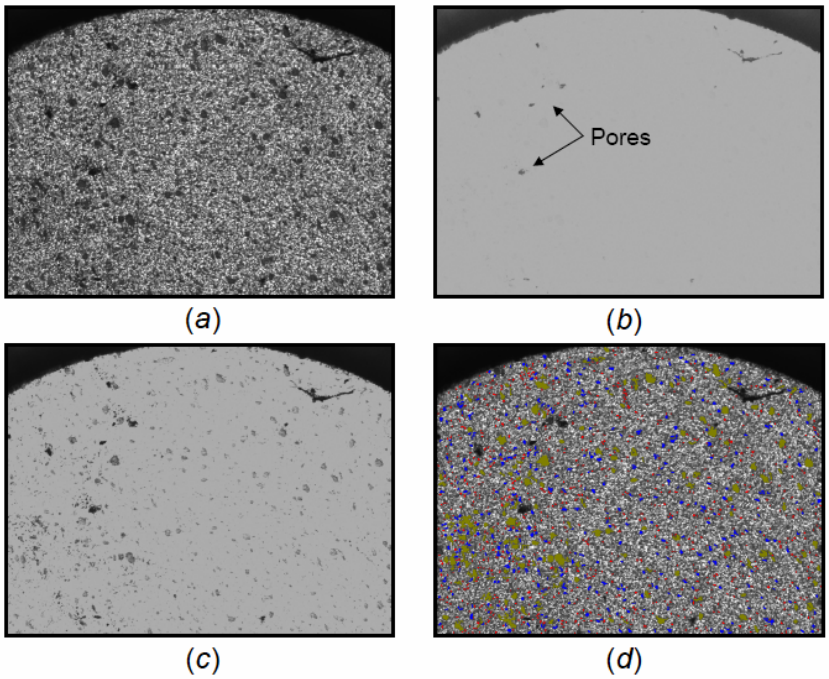


**Figure 4.4** *a*) Typical optical micrograph obtained for measuring feature sizes from an image threshold routine, resolving *b*) pores and *c*) hematite agglomerates. *d*) The pore features were subtracted and hematite agglomerates are shown superimposed over the original image shown in *a*).

image to resolve hematite agglomerates shown in Figure 4.4(*c*) and pores shown in Figure 4.4(*b*). Since the agglomerates and pores have the same dark contrast in the threshold images, it was necessary to track each feature, respectively, and subtract the pores from the hematite agglomerate threshold image. Figure 4.4(*d*) shows the combined original image with only the hematite agglomerates superimposed with each color representing a specific agglomerate size class.

Quantitative characterization of each microstructure was carried out by observing the internal structure of the composite from a two-dimensional image. This ultimately leads to a loss of information, which confuses the interpretation of three-dimensional spatial organization and content. However, by randomizing slice position and orientation (for an anisotropic microstructure), the three-dimensional properties of the microstructural features can be estimated. The distribution of spherical particles of various sizes intersected by a random plane can be deduced from the number and measured sizes of the feature sections on the plane. The Schwartz-Saltykov method [167] was used to relate particle section distributions to particle size distributions in a three-dimensional volume. The method essentially employs dividing the section diameters, $d_i$, into discrete size groups or class intervals. Ten class intervals were used in calculating each of the observed features for the epoxy-cast composites. The particles within each interval are considered to have the same diameter and the probability, $p$, of a plane intersecting a sphere of diameter, $D_j$, yielding a section diameter, $d_i$, and the number of section diameters per unit area, $N_A$. Under these conditions, the number of particles in a unit volume, $N_V$, is given by [167]:

$$N_V(j) = \frac{N_A(i,j)}{D_j\, p}, \tag{4.1}$$

where the index $j$ designates the group of particles which form the given section diameters from a polished plane ($j$ = 1 to $k$) and the index $i$ refers to the size group of those sections ($i$ = 1 to $k$). This leads to the general relation for calculating $N_V(j)$ as:

$$N_V(j) = \frac{\alpha(i)N_A(i) - \alpha(i+1)N_A(i+1) - \alpha(i+2)N_A(i+2) - \cdots - \alpha(k)N_A(k)}{d_{\max}/k}, \tag{4.2}$$

where $\alpha(i)$, $\alpha(i+1)$ are coefficients calculated by Saltykov [167] and $k$ is the total number of measured section diameter classes ($k$ = 10 for this analysis). Once $Nv$ is calculated, the three-dimensional diameter can be evaluated using [167]:

$$D_j = \frac{N_A(i)}{N_V(j)}. \tag{4.3}$$

Individual results obtained for the Al+$Fe_2O_3$+60 *vol.%* epoxy composition from quantitatively measured aluminum particle, hematite agglomerate, and pore sizes and their distributions are shown in Figure 4.5(*a-c*), respectively. These results indicate that a relatively broad size distribution is observed for each of the features that comprise the composite's microstructure. The results for each of the four evaluated compositions are summarized in Figure 4.6 and show that the average aluminum particle sizes (1.84 ± 0.07 μm) are relatively constant (with a fixed distribution) for each composition. However, the average pore sizes show a slight dependency on epoxy concentration,

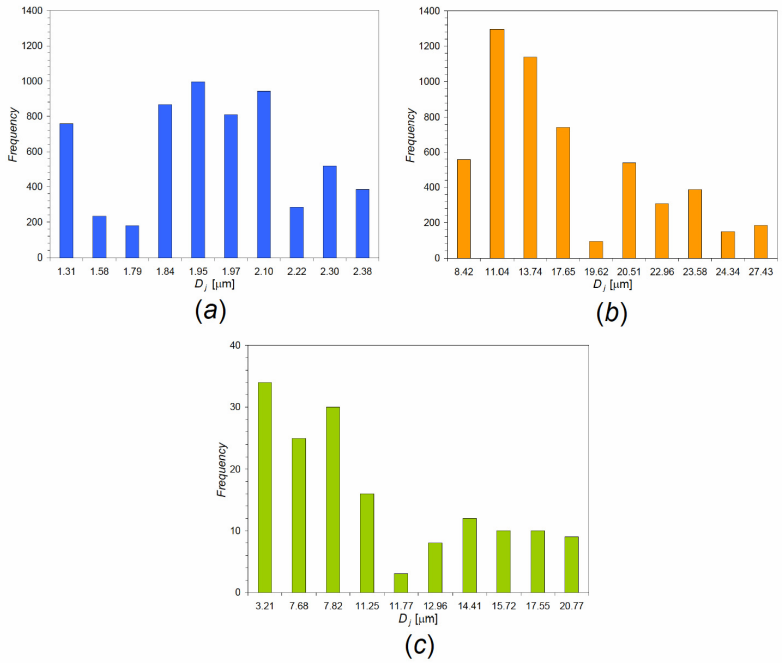


**Figure 4.5** Size distributions for *a*) aluminum particles, *b*) hematite agglomerates, and *c*) pores for Al+$Fe_2O_3$+60 *vol.%* epoxy composite.

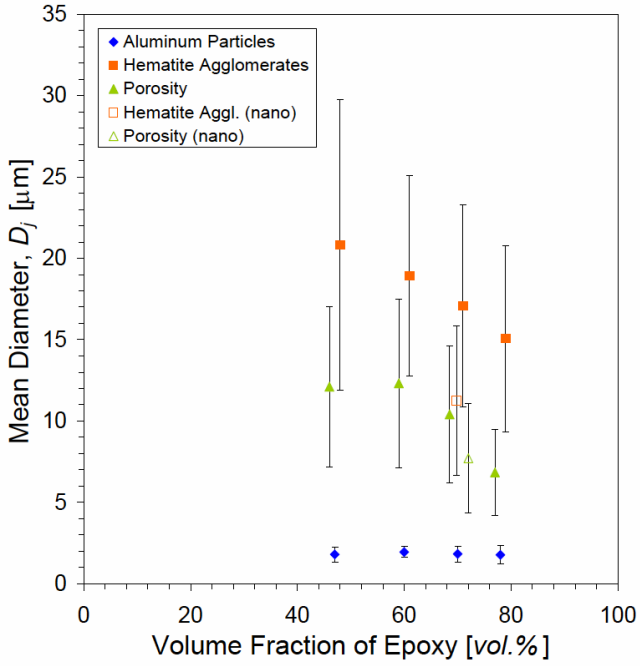


**Figure 4.6** Mean diameter measurements for each phase of epoxy-cast Al+$Fe_2O_3$ composites as a function of epoxy volume fraction.

increasing as epoxy concentration decreases, and reaching a steady value of 12.21 ± 0.15 μm for the 47 and 60 *vol.%* epoxy compositions. Furthermore, the average pore size distributions show a rather significant range, ± 4 to 5 μm. Hematite average agglomerate sizes similarly show a dependency on epoxy concentration and increase in size as the epoxy concentration decreases. Hematite agglomerates had an average particle size ranging from 15 to 20 μm with a significant size distribution range of ± 6 to 9 μm.

Examination of Figure 4.5(*a*-*c*) for the Al+$Fe_2O_3$+60 *vol.%* epoxy composition shows that it may be more appropriate to compare the distribution mode size for each of the features because of their significance in the overall microstructure description. This was a typical characteristic for all of the compositions examined, and Figure 4.7

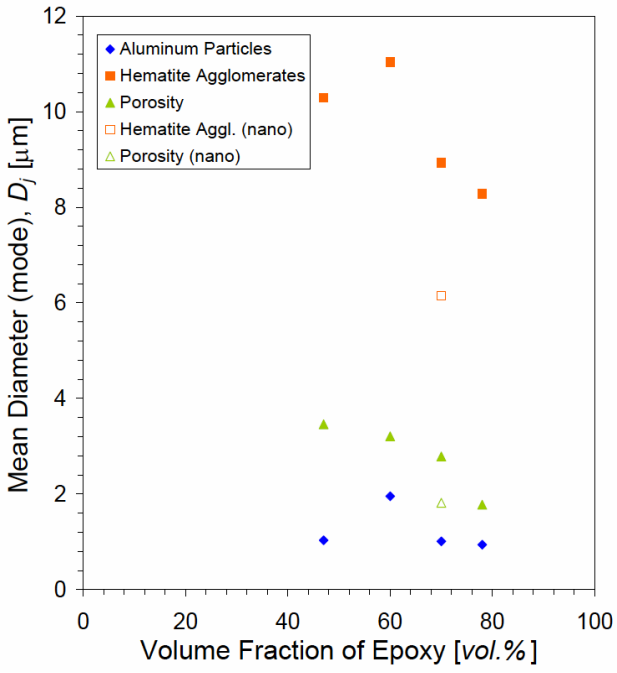


**Figure 4.7** Mean diameter measurements based on distribution mode values for each phase of epoxy-cast Al+$Fe_2O_3$ composites as a function of epoxy volume fraction.

compares the distribution mode values obtained for each. These results show that the void size dependency on epoxy concentration is similar to that shown in Figure 4.6, however exhibiting a significantly smaller size range (1.77 to 3.46 μm) as epoxy concentration increases, respectively. Aluminum particle sizes show a relatively stable and slightly smaller particle size for each of the compositions (approximately 1 μm) except for the 60 *vol.%* epoxy composite. The 60 *vol.%* composite has an almost identical average particle size (1.95 μm) as shown in Figure 4.6, but is slightly higher when compared to the distribution mode sizes obtained for the other compositions. The hematite agglomerate particle sizes show a similar dependence on epoxy concentration as stated previously, increasing in size as the volume fraction of epoxy decreases. However, as observed for the aluminum particle mode sizes, the Al+$Fe_2O_3$+60 *vol.%* epoxy composition deviates from this trend and shows a slightly higher hematite agglomerate size (11.04 μm).

With knowledge of the number of particles per unit volume, $N_V$ for a given phase, it is possible to calculate the average distance, $\overline{\lambda_V}$, between the nearest neighboring particle centers in a volume. This is given by Underwood [167] according to:

$$\overline{\lambda_V} = 0.544\left(N_V\right)^{-1/3}. \qquad (4.4)$$

These results are presented in Figure 4.8 according to the distribution mode values for each composition. The nearest neighbor particle distances indicate that the aluminum particles are fairly uniformly dispersed and in close proximity to each other in all the compositions (approximately 1.54 μm for each), however, a slight decrease in distance

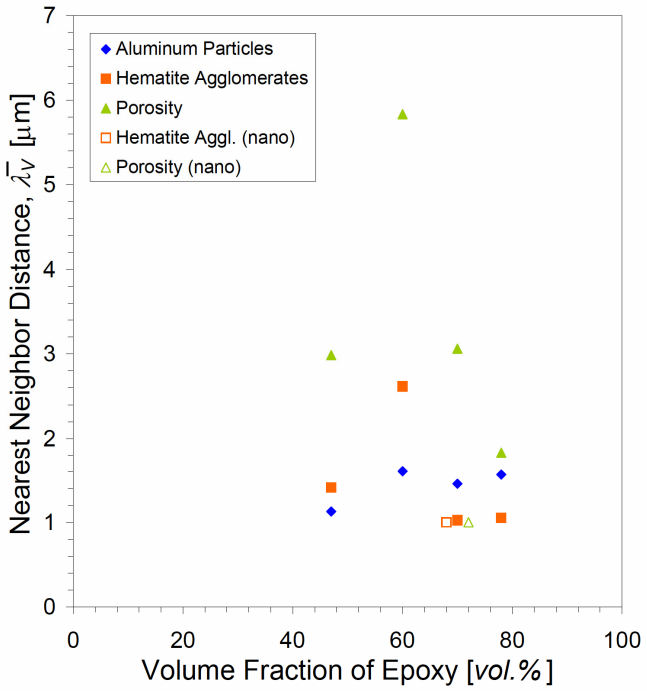


**Figure 4.8** Average distance between the nearest neighboring particle centers in a volume for each phase of epoxy-cast Al+$Fe_2O_3$ composites as a function of epoxy volume fraction.

was observed for the Al+$Fe_2O_3$+47 *vol.%* epoxy composition (1.13 µm). The distance between the hematite agglomerates also appears to show a uniform nearest neighbor distance for each composition (1.16 µm for each), except for the 60 *vol.%* epoxy composition, which shows a larger distance or separation between each agglomerate (2.62 µm). This effect was also apparent for pore distances, which show a significantly larger distance for the 60 *vol.%* epoxy composition (5.83 µm) as compared to a relatively closer distance for the 47 and 70 *vol.%* epoxy compositions (both approximately 3 µm). The Al+$Fe_2O_3$+78 *vol.%* epoxy composition has the closest distance between pores (1.83 µm), which is also very close to their overall particle size (1.77 µm).

The concentration of each feature can also be evaluated using $N_V$. This is depicted in Figure 4.9, which shows the number per unit volume of each feature as a function of epoxy concentration. Again, using the values calculated from the distribution mode, the number of features was significantly larger for each of the compositions when compared to the Al+$Fe_2O_3$+60 *vol.%* epoxy composite. Cracks and other stress concentrators play an important role in the overall strength of a composite material. Spherical inclusions, such as aluminum particles or hematite agglomerates, and voids act as stress concentrators. Effectively, the microstructural characterization results indicate that the 60 *vol.%* epoxy composition has a fairly uniform size distribution of aluminum particles, hematite agglomerates, and pores that are spread out from each other within the material volume. In contrast, the other compositions have average sized hematite

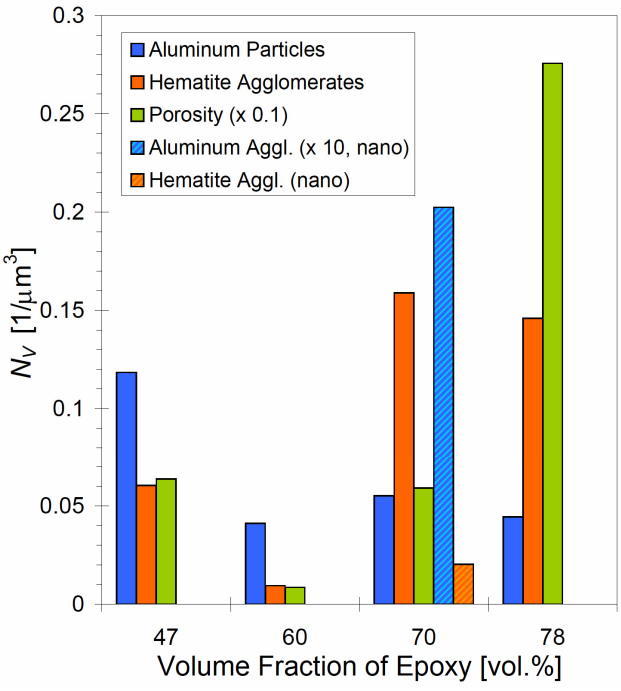


**Figure 4.9** Number per unit volume, $N_V$, of each feature (such as aluminum particles, hematite agglomerates, and pores) as a function of epoxy concentration.

agglomerates and pores that are in relatively close proximity to each other, thus all contributing to increased effective stress concentration regions throughout the material volume.

The microstructures for an epoxy-cast composite prepared with nano-scale aluminum were also characterized using the same technique as just described. The optical microscope was found to be the best way to observe these particular microstructure features. Typical images obtained for nano-Al+$Fe_2O_3$+70 *vol.%* epoxy composition are shown in Figure 4.10(*a-c*). The addition of nano-scale aluminum produced unique microstructures that exhibit regions containing high concentrations of nano-scale aluminum particles (or nano-agglomerates). Figure 4.10(*a*) shows a relatively low magnification image of the typical overall microstructure, while Figure 4.10(*b,c*) shows higher magnification images of the concentrated nano-agglomerate aluminum regions. Quantitative microstructural analysis was not performed on the individual nano-scale aluminum particles since they were significantly smaller than the smallest resolvable feature limit imposed by the optical microscope. However, the relative number of nano-aluminum particles within the concentrated nano-agglomerate regions was compared to regions with uniformly dispersed nano-aluminum. Figure 4.11(*a,b*) shows an image of a *a*) nano-agglomerate region and that same region *b*) after applying a threshold routine to flatten the background and enhance the nano-aluminum particles contrast. The number of nano-aluminum particles was counted from threshold images captured at several locations separately containing nano-agglomerate and uniformly dispersed nano-aluminum particle regions. The counts within both of these regions showed that over 70 % of the nano-aluminum particles were located within the nano-

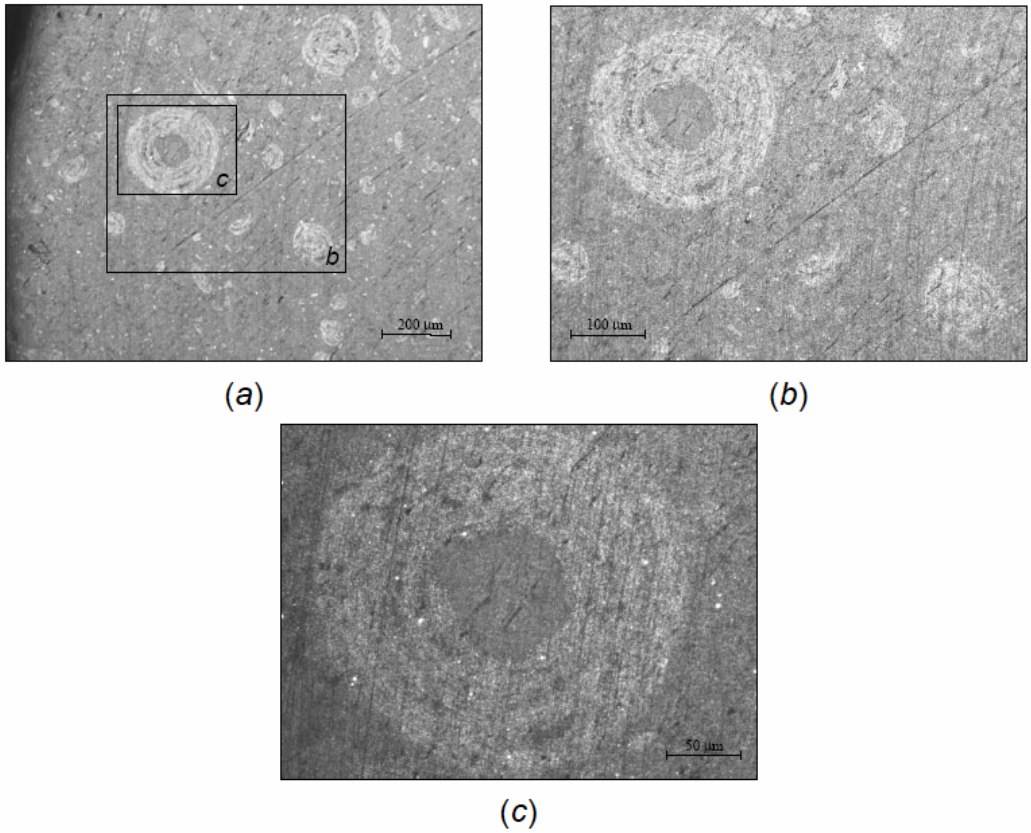


**Figure 4.10** Optical micrographs of nano-Al+$Fe_2O_3$+70 *vol.%* epoxy composite showing formation of highly concentrated nano-aluminum particle regions (light contrast). Higher magnification images of *a*) with their corresponding locations outlined are shown in *b*) and *c*).

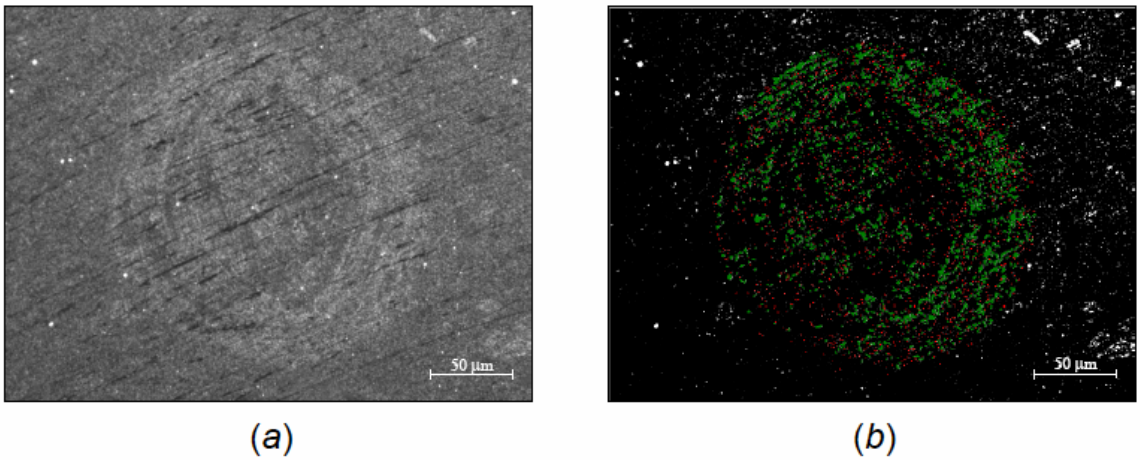


**Figure 4.11** Optical micrographs obtained from nano-Al+$Fe_2O_3$+70 *vol.%* epoxy composition showing highly concentrated nano-aluminum regions *a*) before and *b*) after image threshold.

agglomerate region. Qualitatively, these regions varied in size and ranged between 50 and over 200 μm in diameter.

The nano-scale composite microstructures also exhibited similar features that were observed for the micron-scale composites. They specifically showed the tendency for hematite particles to agglomerate, and their sizes were evaluated similarly using the Schwartz-Saltykov method [167] described previously. These results are shown in Figure 4.6 along side the micron-scale composite values. The average pore size appears to be smaller when compared to the micron-scale composite with the same 70 *vol.%* epoxy concentration. It has an average value of 7.71 μm, which compares more closely with the average pore size measured for the 78 *vol.%* epoxy composition (6.84 μm). Comparison between the two composite materials also shows the average hematite agglomerate size is significantly smaller and has a value of 11.24 μm as compared to 17.07 μm. As mentioned previously, based on the broad measured particle size distributions, it was more appropriate to compare particle sizes based on the distribution of mode values. Figure 4.7 shows that the hematite agglomerates (6.15 μm) are significantly smaller when compared to the micron-scale composite (8.93 μm) and the pore sizes follow similarly with 1.81 and 2.78 μm for the nano-scale and micron-scale composites, respectively. Shown in Figure 4.8 are the nearest neighbor distance values which also show deviation from the micron-scale composite measurements. The hematite agglomerates have a 2.03 μm distance between neighboring particle centers compared to 1.02 μm for the micron-scale composite. The distance between pores was 0.81 μm as compared to 3.06 μm for the micron-scale composite.

Qualitative observations obtained from SEM images show details of the hematite particle and agglomerate distributions. Figure 4.3(*a-d*) shows select SEM images obtained for each composition and reveal a typical trend for hematite particles and agglomeration sizes, showing three different size ranges. In general, each microstructure had uniformly dispersed hematite particles within the epoxy matrix regardless of the volume fraction of epoxy. There was also a tendency for relatively large hematite agglomerates to form in the range of 10 to 15 μm and 20 to 50 μm in size. Since this was an observable feature for each composition regardless of different epoxy concentrations, it suggests the agglomeration of hematite particles occurs during the dry mixing process of precursor powders before their addition to epoxy resin.

Some hematite agglomerates are typically broken up during the mixing process after their addition to the epoxy resin. The epoxy volume fraction influences the ease of mixing by essentially reducing the mixture's viscosity. This promotes the breakup of agglomerates as the volume fraction increases. However, there is an optimal volume fraction where agglomerate break occurs and high concentrations of epoxy resin possibly allow the agglomerates to move freely throughout the mixture without breaking up. Figure 4.12(*a,b*) shows SEM images of hematite agglomeration achieved purposely by under-mixing during processing for micron-Al+$Fe_2O_3$+60 *vol.%* epoxy composite. Notice that the agglomerate shown in Figure 4.12(*a,b*) was extremely large (approximately 150 μm), similar to that observed for composites fabricated with nano- aluminum powders shown in Figure 4.10(*a-c*) and Figure 4.11(*a,b*).

Closer observation of hematite agglomerates shows they actually consist of individual hematite particles encapsulated in the epoxy matrix and do not appear to have

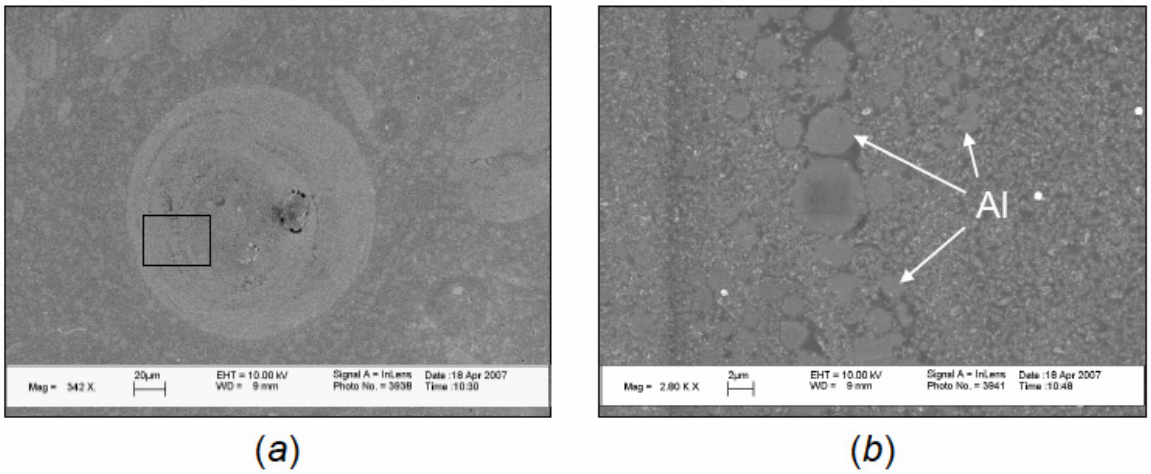


**Figure 4.12** Purposely under mixed micron-Al+$Fe_2O_3$+60 *vol.%* epoxy composite showing the *a*) formation of highly concentrated hematite regions (agglomerates). *b*) Higher magnification location outlined in *a*), shows individual hematite particles within the agglomerated region and micron-scale aluminum particles that tend to cluster together.

any open porosity. This was apparent in Figure 4.13(*a*) showing a close-up view of agglomerated hematite that has an overall size of approximately 30 μm. Figure 4.13(*b*) shows the boundary of the same agglomerate that clearly indicates a tighter arrangement of hematite particles within the agglomerated region (left side of image). Hematite particles also tend to "coat" micron-scale aluminum particles, possibly during the dry mixing of the constituent powders. This is evident in Figure 4.14(*a,b*) showing a cross-sectional view of an aluminum particle surrounded by hematite particles that remained during the casting process. Again, it appears that there is no obvious open porosity within this hematite region or in close proximity to the aluminum particle. These qualitative results indicate that both the aluminum and hematite features (individual particles and agglomerates) are infiltrated completely by the epoxy matrix.

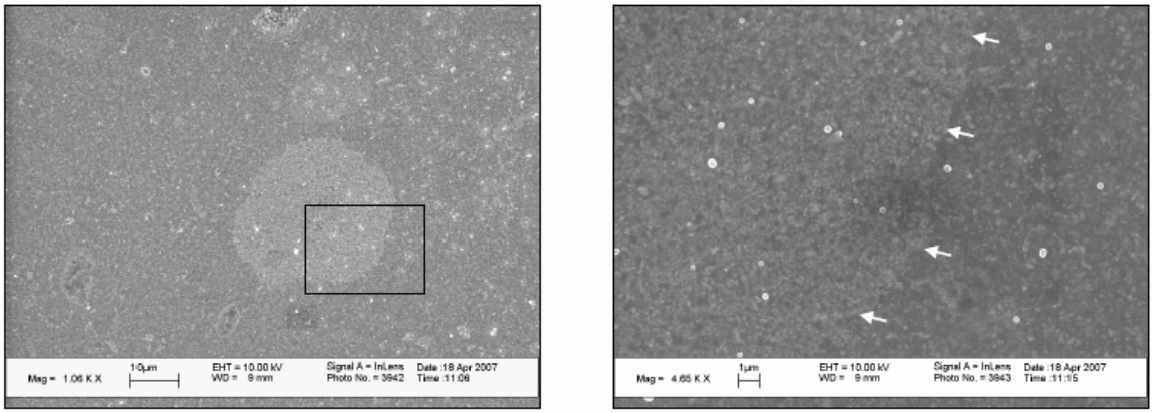


**Figure 4.13** *a*) SEM micrographs of Al+$Fe_2O_3$+60 *vol.%* epoxy composite showing a relatively large hematite agglomerate. *b*) Higher magnification of location outlined in *a*), shows agglomerated and dispersed hematite particles interface (indicated by arrows).

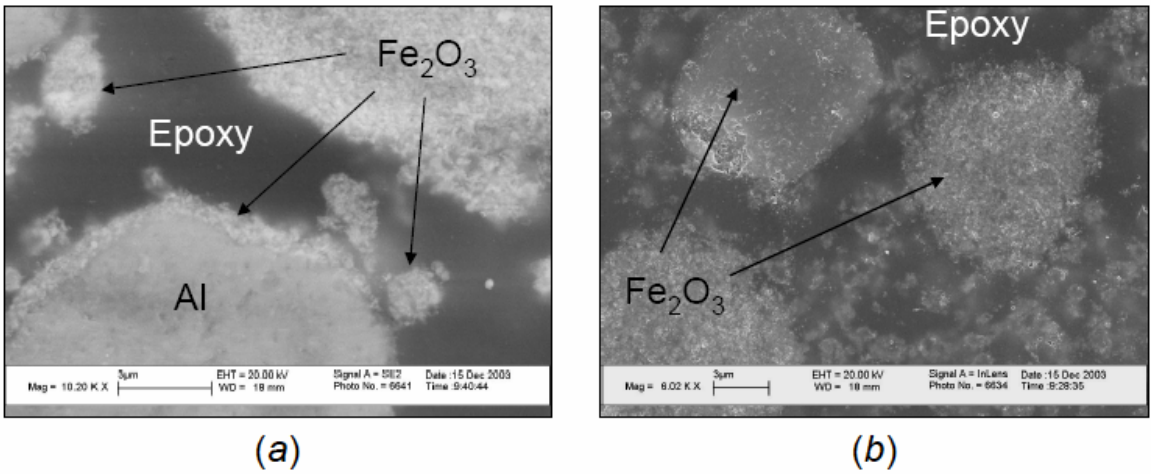


**Figure 4.14** Cross sectional view of an *a*) aluminum particle coated by hematite particles and *b*) hematite agglomerates for an Al+$Fe_2O_3$+78 *vol.%* epoxy composite.

### 4.1.2 Intrinsic Property Characterization

In addition to measuring intrinsic physical properties for each specimen used throughout this study, a detailed analysis of processing was conducted to optimize each cast-cured material composition. As the fraction of solid filler particles increases and/ or relative particle size decreases (therefore surface area increases for a given volume fraction of material), it becomes increasingly challenging to cast due to the increase of the overall mixture viscosity. Specific samples were prepared for obtaining details about the casting process, such as maximum castable solid particle fill fraction and resulting porosity. Cast rod shaped specimens were prepared and sectioned in multiple locations along the axial length. Qualitative microstructural observations were obtained for each of these polished sections (ten specimens in all). A representative specimen was selected for detailed quantitative optical microscopy measurements (discussed previously in section 4.1.1); however, there was no discernable difference between each sample for a given composition. Hence, the microstructures appeared to be uniform throughout the entire length of the cast rod specimens.

In addition to microstructural characterization, each section's density was measured using Archimedes' method (outlined in section 3.2). The measured densities of this multiphase composite material were compared to weight averaged (on the basis of volume fraction) properties of the individual constituents, and thus permitting the calculation of theoretical densities according to the Voigt rule of mixtures. Table 4.1 compares the measured values to the theoretically calculated densities obtained for each composition. Notice that the standard deviation for each was very low, suggesting there

**Table 4.1** Theoretically calculated densities using mixture theory for epoxy-cast compositions and pure epoxy. Measured and theoretical values are compared as a means of estimating retained porosity.

| Epoxy* [*vol.%*] | Aluminum☺ [*vol.%*] | Hematite☺ [*vol.%*] | Theoretical Density [g/cm$^3$] | Measured Density [g/cm$^3$] | TMD [%] | Estimated Porosity [%] |
|---|---|---|---|---|---|---|
| 46.94 | 20.98 | 32.07 | 2.809 | 2.682 ± 0.005 | 95.48 | 4.52 |
| 60.27 | 15.71 | 24.02 | 2.404 | 2.366 ± 0.002 | 98.32 | 1.58 |
| 70.23 | 11.77 | 17.99 | 2.101 | 2.047 ± 0.003 | 97.43 | 2.57 |
| 70.23 nano | 11.77 | 17.99 | 2.101 | 2.082 ± 0.003 | 99.10 | 0.90 |
| 77.97 | 8.71 | 13.32 | 1.866 | 1.836 ± 0.002 | 98.39 | 1.61 |
| 100 (batch *A*) | 0 | 0 | 1.197 | 1.195 ± 0.002 | 99.82 | 0.18 |
| 100 (batch *B*) | 0 | 0 | 1.197 | 1.200 ± 0.002 | 100 | 0 |

*Theoretical densitity for epoxy was calculated from 1.17 and 1.097 g/cm$^3$ obtained for EPON® 826 resin [140] and diethanolamine hardener [168], respectively.

☺Reference densities for aluminum and hematite are 2.705 and 5.237 g/cm$^3$, respectively [109].

was little or no density variation within the cast rod specimens. The amount of porosity (also listed in Table 4.1) was estimated using the theoretical density as a reference and was found that the specimens typically contained a few percent or less (2.57 % maximum) porosity. However, the 47 *vol.%* epoxy composition exhibited a higher concentration of porosity (4.52 %), which was attributed to reaching a maximum solid particle fill fraction that caused the mixture to have a relatively high viscosity and made the casting of a low porosity composite challenging.

Ultrasonic wave speed measurements, including elastic and transverse waves, were also measured for each of the sectioned samples. The bulk mechanical (elastic) properties were estimated from the ultrasonic wave speed data and density measurements using equations (3.2) through (3.4). These equations relate the ultrasonic wave speed

measurements to Lamé's elastic material constants ($\mu$ and $\lambda$), thus allowing the calculation of shear (transverse) and elastic moduli. With knowledge of Lamé's constants, the remaining bulk mechanical properties were evaluated from the elastic identities listed in Table 3.4 for isotropic materials. Table 4.2 lists a summary of the ultrasonic wave speed measurements and calculated bulk mechanical properties for each composition. Two different epoxy batches (labeled *A* and *B*) were listed separately since they had significantly different bulk mechanical properties despite being fabricated in an identical manner.

It is apparent from Table 4.2 that, in general, as epoxy concentration decreases, bulk mechanical properties such as elastic and shear moduli increase. However, it appears that the particle morphology may influence this relationship, showing the nano-scale 70 *vol.%* epoxy composition has calculated elastic properties that significantly deviate from that of the micron-scale 70 *vol.%* epoxy composition. Both compositions appear to have comparable longitudinal wave speeds with values of 2.619 ± 0.039 and 2.776 ± 0.032 mm/μs for the micron- and nano-scale composites, respectively. However, the measured ultrasonic shear wave shows an increase for the micron-scale composite and contributes to the deviation in the calculated bulk mechanical properties between the two compositions. Thus, comparison shows that the bulk modulus and Poisson's ratio decrease while the elastic modulus and shear modulus increase. This deviation may be attributed to the increased probability for elastic wave scattering due to the different particle morphologies and their distribution throughout the material volume. Wave attenuation is also due to absorption in the matrix [169]. When the wave impedance increases, signal scattering occurs and is caused by the traveling wave impinging on an

**Table 4.2** Summary of ultrasonic wave speed measurements (longitudinal, transverse, and bulk wave speeds, $C_L$, $C_T$, and $C_0$, respectively) for each composition. Material properties, such as the Lamé constant, Poisson's ration, elastic, plastic, shear, and bulk modui, $\lambda$, $\nu$, $E$, $\mu$, and $K$, respectively, are calculated from wave speed and density, $\rho$, measurements.

| Epoxy [*vol.%*] | $C_L$ [mm/μs] | $C_T$ [mm/μs] | $C_0$ [mm/μs] | $\lambda$ [GPa] | $E$ [GPa] | $\mu$ [GPa] | $K$ [GPa] | $\nu$ | $\rho$ [g/cm$^3$] |
|---|---|---|---|---|---|---|---|---|---|
| 46.94 | 2.711 ± 0.016 | 1.471 ± 0.016 | 2.113 ± 0.018 | 8.109 ± 0.242 | 14.985 ± 0.280 | 5.802 ± 0.129 | 11.977 ± 0.209 | 0.291 ± 0.006 | 2.682 ± 0.005 |
| 60.27 | 2.936 ± 0.013 | 1.335 ± 0.013 | 2.499 ± 0.017 | 11.962 ± 0.239 | 11.550 ± 0.203 | 4.217 ± 0.084 | 14.773 ± 0.206 | 0.370 ± 0.004 | 2.366 ± 0.002 |
| 70.23 | 2.619 ± 0.039 | 1.310 ± 0.018 | 2.138 ± 0.051 | 7.018 ± 0.468 | 9.364 ± 0.218 | 3.513 ± 0.097 | 9.360 ± 0.441 | 0.333 ± 0.009 | 2.047 ± 0.003 |
| 70.23 nano | 2.776 ± 0.032 | 1.067 ± 0.005 | 2.487 ± 0.033 | 11.299 ± 0.341 | 6.705 ± 0.076 | 2.372 ± 0.025 | 12.881 ± 0.356 | 0.413 ± 0.002 | 2.082 ± 0.003 |
| 77.97 | 2.630 ± 0.009 | 1.044 ± 0.007 | 2.337 ± 0.011 | 8.696 ± 0.112 | 5.630 ± 0.073 | 2.002 ± 0.028 | 10.030 ± 0.103 | 0.406 ± 0.002 | 1.836 ± 0.002 |
| $^A$100 | 3.222 ± 0.064 | 1.375 ± 0.009 | 2.803 ± 0.072 | 7.887 ± 0.482 | 6.275 ± 0.086 | 2.260 ± 0.029 | 9.393 ± 0.487 | 0.388 ± 0.005 | 1.195 ± 0.001 |
| $^B$100 | 2.587 ± 0.007 | 0.996 ± 0.006 | 2.318 ± 0.008 | 5.640 ± 0.044 | 3.354 ± 0.039 | 1.187 ± 0.015 | 6.431 ± 0.042 | 0.413 ± 0.001 | 1.197 ± 0.001 |

$^{A,B}$ Correspond to batch *A* and *B* epoxy, respectively.

impedance discontinuity that will partially reflect and transmit the wave at that interface. Using pure epoxy as an impedance baseline, it can be seen from Table 4.3 that the longitudinal wave impedance, $Z_L$, increases as the composition's solid particle fill concentration also increases. However, comparison between the micron- and nano-scale composites shows that scattering in the measured longitudinal wave speed has a significant jump in impedance for the nano-scale composite. Since the only difference between the two compositions is their particle morphologies, the impedance increase is attributed to the increased probability for elastic wave scattering. Now considering the shear (or transverse) wave impedance, $Z_T$, Table 4.3 indicates that the micron-scale composite has a significant increase when compared to the nano-scale composite. Using the same logic, the shear wave appears to have a higher probability for elastic (shear) wave scattering. Figure 4.15 shows measured ultrasonic longitudinal and shear wave impedances plotted as a function of epoxy concentration. Both the longitudinal and shear

**Table 4.3** Longitudinal and shear wave impedance values measured for each Al+$Fe_2O_3$ epoxy-cast composite and pure epoxy (batch *A* and *B*).

| Epoxy [*vol.%*] | $Z_L$ [kg/m$^2$s] x $10^6$ | $Z_T$ [kg/m$^2$s] x $10^6$ |
|---|---|---|
| 46.94 | 7.272 ± 0.048 | 3.945 ± 0.046 |
| 60.27 | 6.947 ± 0.031 | 3.159 ± 0.013 |
| 70.23 | 5.361 ± 0.078 | 2.681 ± 0.037 |
| *70.23 | 5.779 ± 0.072 | 2.222 ± 0.013 |
| 77.97 | 4.829 ± 0.019 | 1.917 ± 0.013 |
| $^A$100 | 3.849 ± 0.077 | 1.643 ± 0.011 |
| $^B$100 | 3.097 ± 0.009 | 1.192 ± 0.007 |

$^{A,B}$ Correspond to batch *A* and *B* epoxy, respectively.
* Epoxy-cast composite containing nano-aluminum.

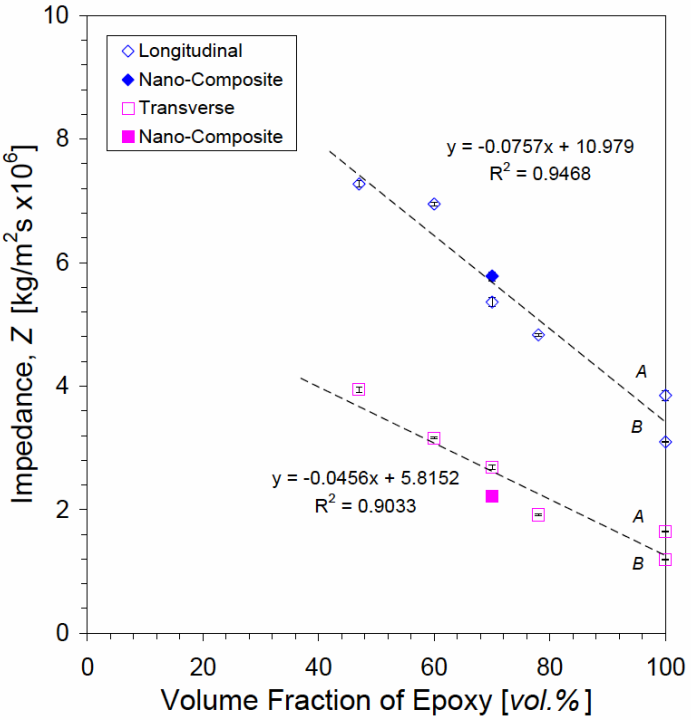


**Figure 4.15** Longitudinal and shear impedance values obtained for each epoxy-cast composite composition.

wave impedances increase linearly with decreasing epoxy concentration. However, there appears to be a slight jump in longitudinal impedance for the Al+$Fe_2O_3$+60 *vol.%* epoxy composition. As described previously, an impedance increase is associated with elastic wave scattering and may possibly be attributed to particle morphology effects.

## 4.2 Characterization of Thermochemical Reaction Energetics

Thermal analysis was conducted on the epoxy-cast Al+$Fe_2O_3$ structural energetic composites to characterize the energetics of thermally initiated reactions and transformations such as crystallization or melting. The examinations of these composites include differential thermal analysis (DTA) for identifying temperatures where

exothermic and endothermic events occur. High temperature *in situ* x-ray diffraction (HTXRD) experiments were also utilized for identifying chemical species evolving during thermal heating. These two techniques provide a detailed characterization of thermochemical events that effectively probe thermal histories for each specimen composition and identify the occurrence of structural changes as a function of epoxy volume fraction, and particle size or morphology effects. These analyses provide insight into observed chemical reactivity and a foundation for correlating thermochemical transformations that arise from effects of high-strain rate deformation.

### 4.2.1 Differential Thermal Analysis (DTA)

Differential thermal analysis (DTA) primarily measures thermal properties and allows the estimation of enthalpy ($\Delta H$) changes that occur when chemical reactions or phase transformations, such as melting, take place. When the sample passes through a transition state, its temperature ($T_s$) departs from that of its surroundings (the program furnace temperature) and the differential temperature ($\Delta T = T_s - T_r$), obtained from comparison of the inert reference sample temperature ($T_r$), is either positive (exothermic reaction) or negative (endothermic reaction). The magnitude of $\Delta T$ depends on the thermal properties of the equipment, particularly the thermal capacity, as well as the mass of the sample and thermal conductivity. For this reason, it is challenging to extract quantitative measurements of the thermal properties of the sample using DTA, though the temperatures at which transitions occur can be identified fairly accurately.

Thermal characterization was conducted on the precursor powders, pure cured epoxy, and fabricated epoxy-cast composite materials. The signature of thermally initiated events was determined by DTA measurements, which were conducted for a steady heating rate (10 °C/min) over a temperature range of 50 to 1200 °C for most experiments. Some experiments continued to a higher maximum temperature of 1500 °C and all runs were made in an inert argon atmosphere. The effect of changing aluminum particle size and epoxy volume fraction for each composite was examined, in addition to the behavior of individual constituents.

#### 4.2.1.1 DTA of Initial Powder Reactants

Figure 4.16 shows results of DTA measurements performed on the individual aluminum powders (nano- and micron-scale particle sizes) used in fabricating composite materials. The scans were repeated three times for each powder material using the same experimental conditions and identical sample preparation techniques. The powders were pressed to form relatively low density pellets (0.25 g of powder) that were randomly sectioned to obtain a sample size (≈ 10 mg) used in the DTA. The figure plots heat flow as a function of temperature, showing only a very narrow temperature range (600 to 700 °C) where the transformation takes place. Both particle sizes exhibit endothermic peaks close to the handbook melting temperature value for aluminum (658.55 °C) [109]. However, the nano aluminum (trace *a*) shows a slightly lower melting onset of 650.2 ± 1.9 °C compared to 654.1 ± 1.1 °C for micron-scale aluminum (trace *b*). The measured enthalpy calculated from the peak areas were -262.9 ± 19.4 J/g and

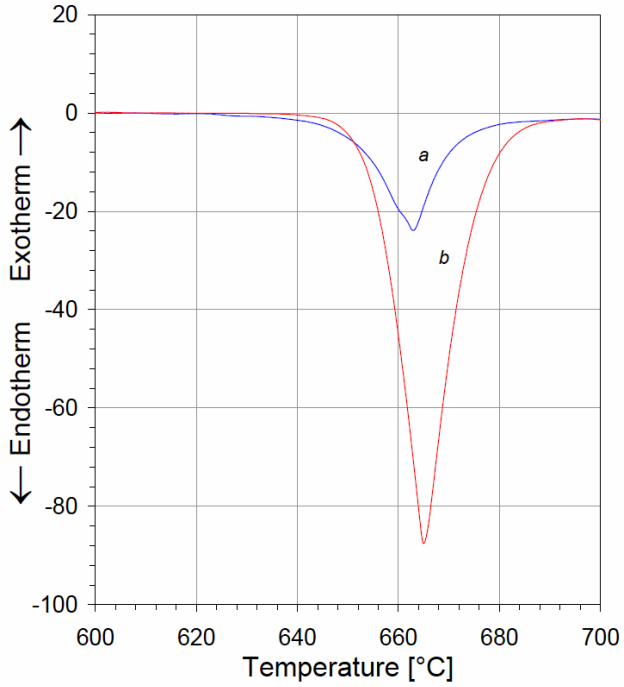


**Figure 4.16** DTA traces obtained for nano- and micron-scale aluminum pressed powder pellets. The nano-aluminum powder (trace *a*) shows a slightly lower melting onset temperature (650.2 ± 1.9 °C) as compared to micron-aluminum (trace *b*, 654.1 ± 1.1 °C).

-334.1 ± 51.1 J/g, respectively for nano- and micron-scale aluminum. The handbook value for aluminum is -398.8 J/g and is in good agreement with the measured value for micron-scale aluminum, however, it is slightly low for the nano-scale aluminum. This discrepancy may be attributed to the possible oxide coating present on the nano-scale aluminum particles.

The thermal response of submicron hematite powders examined by DTA is shown in Figure 4.17. Pressed powder pellets were also used for these experiments, however, only one scan was performed to characterize the reduction behavior of hematite with heating to a maximum temperature of 1500 °C. The DTA trace was compared to the known behavior of hematite from literature [117,170] and the Fe-O (Figure 2.28) binary phase diagram [119].

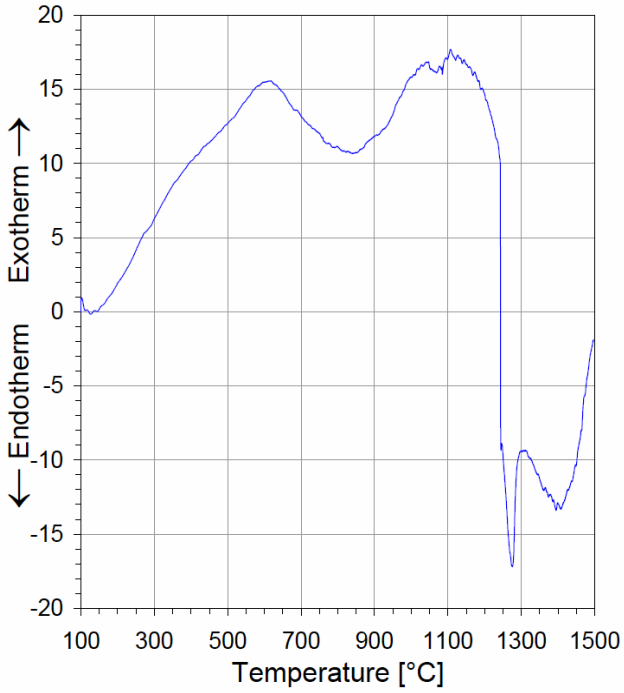


**Figure 4.17** DTA trace obtained for hematite pressed powder pellet showing the peaks associated with the characteristic reduction stages of hematite to iron.

The first exothermic peak occurred at approximately 600 °C and corresponded to the reduction of hematite ($Fe_2O_3$) to magnetite ($Fe_3O_4$). The onset of this reaction appears to begin immediately upon heating, however, even pure oxides such as hematite usually contain some structural –OH [170] contributing to the relatively low temperature reaction onset. Additionally, the associated loss of absorbed $H_2O$ [170] may also be present and contribution to the exothermic rise to approximately 300 °C. Considering these effects, the estimated onset for magnetite formation occurred at approximately 500 °C. This corresponds to a measured enthalpy of 604.5 J/g, which was in good agreement with the reference value of 632.9 J/g [109]. The next exothermic reaction had an onset temperature of 850 °C and a double peak in the vicinity of 1050 and 1100 °C. The first peak (1050 °C) may correspond to the formation of wüstite ($Fe_{1-x}O$, where 1-$x$

ranges between 0.83 to 0.95 [170]), while the second peak (1100 °C) was related to the formation of iron ($\gamma$-Fe). The formation of wüstite had a measured enthalpy of 798.3 J/g, which corresponds well with the handbook value of 751.7 J/g [109]. The measured enthalpy for $\gamma$-Fe was 51.1 J/g and greater than the handbook value (11.2 J/g) [109]. This is followed by a significant endothermic peak which was possibly associated with eutectic melting from trace impurities present in hematite and may also contribute to the relatively low enthalpy value measured for the $\gamma$-Fe formation. The next endothermic feature occured at approximately 1395°C (onset 1320 °C) and was in good agreement with the melting temperature of wüstite taking place at 1370 °C according to the Fe-O phase diagram [119]. The final exothermic peak, just beginning to appear at 1400 °C, was possibly associated with the formation of $\delta$-Fe and agreed well with the Fe-O phase diagram [119].

4.2.1.2 DTA of Mixed Reactant Powders

The processing of epoxy-cast thermite composites first entailed the stoichiometric dry mixing of aluminum and hematite powders prior to their combination with epoxy resin and hardener. Thermal analysis was also conducted for these powder mixtures to characterize the classic alumino-thermic reaction [1] of aluminum with hematite and to compare the behavior of nano- and micron-scale aluminum powders. The DTA traces obtained for both particle size mixtures and pure hematite for reference (discussed in section 4.2.1.1) are shown in Figure 4.18. Strikingly different responses are apparent between the Al+$Fe_2O_3$ powder mixtures containing nano- and micron-scale aluminum

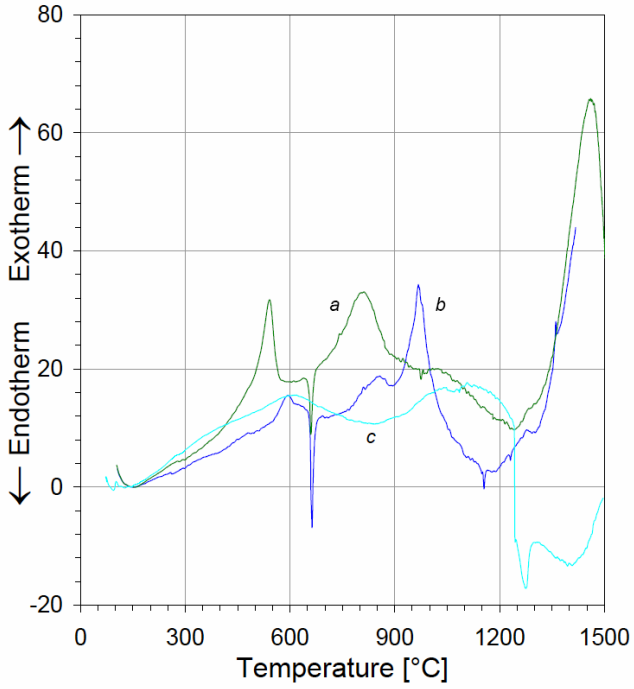


**Figure 4.18** DTA traces obtained for stoichiometric mixtures of aluminum and hematite pressed powder pellets using nano- (trace *a*) and micron-scale (trace *b*) aluminum. These traces are compared to pure hematite from Figure 4.17 (trace *c*).

(traces *a* and *b*, respectively). The transformation of hematite to magnetite occurs at a significantly lower temperature for the nano-aluminum mixture, evident from the exothermic peak with an onset temperature of 499.7 ± 14.2 °C. This is compared to the powder mixture containing micron-scale aluminum, resulting in a greater onset temperature of 570.2 ± 3.8 °C. These contrasting behaviors are attributed to greater packing density of the nano-scale particles which alter the overall bulk diffusion properties of the compact. The formation of magnetite obtained from the hematite powder (trace *c*) corresponds well with the micron-scale aluminum mixture. The DTA traces for Al+$Fe_2O_3$ powder mixtures both had similar aluminum melting temperatures compared to values obtained for the individual particle sizes (discussed in

section 4.2.1.1); resulting in 651.8 ± 2.3 and 654.7 ± 3.2 °C for nano- and micron-scale aluminum, respectively.

Following the melting endotherm for micron-scale aluminum, the formation of wüstite ($Fe_{1-x}O$) began at 805.1 ± 53.1 °C. It is possible that aluminum oxide ($Al_2O_3$) also forms close to this temperature. This is followed by another exotherm with an onset temperature of 944.4 ± 10.0 °C that corresponds to the formation of $\gamma$-Fe, $Al_2O_3$, and possibly $FeAl_2O_4$. This two stage reaction has also been observed by J. Mei, *et al.*, [116] for a slightly higher temperatures of 960 °C producing $Fe_3O_4$ and $Al_2O_3$, while the next reaction occurred at 1060 °C forming Fe, $FeAl_2O_4$, and $Al_2O_3$. However, this study had significantly larger aluminum and hematite particle sizes (20 and 5 μm, respectively) that possibly contribute to the observed higher temperature reactions. It is also possible that aluminum-iron compounds (AlFe and $AlFe_3$) form in this temperature range. The final exothermic peak, beginning at approximately 1200 °C, corresponds to the formation of $\delta$-Fe. Notice that there is a small endothermic peak at 1300 °C which corresponds to the melting of wüstite.

In contrast for nano-aluminum, the formation of wüstite ($Fe_{1-x}O$) began at 708.7 ± 30.6 °C, approximately 100 °C lower than micron-scale aluminum, immediately following the melting endotherm for nano-scale aluminum. This is followed by the formation of $\gamma$-Fe, $Al_2O_3$, and possibly $FeAl_2O_4$ at approximately 1025 °C (relatively small exotherm). There is an identical exotherm for the formation of $\delta$-Fe beginning at a slightly greater temperature of approximately 1250 °C.

The addition of aluminum (micron- and nano-scale particle sizes) to hematite powder causes the formation of aluminum-hematite compounds and enhances the

reduction process for hematite, resulting in initiating these reactions at lower temperatures. The addition of nano-scale aluminum also decreases the temperature where the reduction of hematite begins by approximately 50 to 100 °C. All of these effects are attributed to the nano-scale aluminum particles altering the bulk diffusion properties of the powder compacts.

#### 4.2.1.3 DTA of Epoxy and Epoxy-Cast Composites

Thermal analysis was also carried out for Al+$Fe_2O_3$ epoxy-cast composites with 47 to 78 *vol.%* epoxy and cured epoxy specimens. Figure 4.19 shows representative DTA traces for each particle-filled composite composition and pure epoxy.

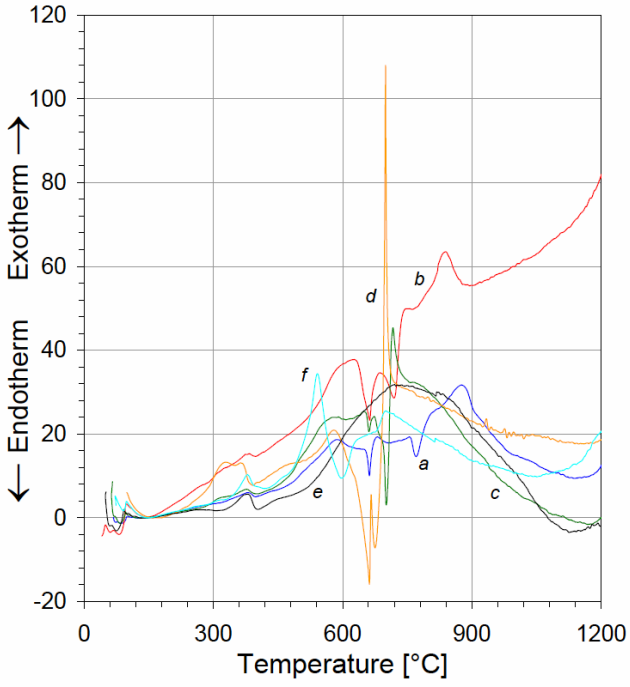


**Figure 4.19** DTA traces for epoxy-cast Al+$Fe_2O_3$ composites with *a*) 47, *b*) 60, *c*) 70, *d*) 78 *vol.%* epoxy, *e*) pure epoxy, and *f*) nano-Al+$Fe_2O_3$+70 *vol.%* epoxy compositions.

These experiments were repeated several times with excellent reproducibility and typically, included a total of 3 to 5 runs. The DTA results obtained for each composition appear to show similar exothermic and endothermic reaction peaks as expected for the $Al+Fe_2O_3$ thermite system. The addition of epoxy typically lowers the temperatures where the intermediate and main reactions take place and also contributes to the overall strength of the reaction.

Each composition shows an initial exothermic peak at 383.1 ± 6.1 °C due to crystallization. This is known as cold crystallization and occurs upon heating polymers that are amorphous or have very low crystallinity [171]. The 78 *vol.%* epoxy composition appears to experience a longer exothermic reaction, with an initial peak of 334.3 °C followed by a second peak at 371.1 °C, closer to the average crystallization temperature observed for all of the composites and pure epoxy.

The crystallization peaks were followed immediately by an endoderm that ranged between 397 and 410 °C, corresponding to the decomposition of epoxy. Pure epoxy has a decomposition temperature of 410.2 ± 0.7 °C, which is in fairly good agreement with many studies conducted for epoxy resin cured with numerous hardeners [172-174]. The thermal stability in cured-epoxy resin systems will depend, in part, on the chemical structure and bonds, as well as on the functionality and crosslinking density of the resin [171]. The volatile products evolving from the decomposition of epoxy typically include water, carbon dioxide, and carbon monoxide [172], however, the specific makeup is primarily dictated by the resin and hardener composition.

The addition of solid particles appears to slightly influence the decomposition temperature. The epoxy-cast composites using micron-scale aluminum (47 to

78 *vol.%* epoxy) had an average decomposition temperature of 403.5 ± 4.4 °C, while the nano-aluminum composites decomposed at 423.6 ± 2.1 °C.

The next exothermic peak corresponds to the reduction of hematite to magnetite and occurs at a similar temperature as observed for the thermite Al+$Fe_2O_3$ powder mixtures discussed in section 4.2.1.2. The dispersion of the thermite powder mixture within epoxy does not appear to alter this reaction. The nano-aluminum containing epoxy composite similarly experiences this reduction process at a lower temperature, following the result obtained for the thermite powder mixture reaction also discussed in section 4.4.1.2. This was followed by an immediate endotherm at approximately 600 °C and possibly corresponds to the melting of aluminum at a significantly low temperature. The melting of aluminum triggered other exothermic events, with a slight peak at approximately 630 °C followed by the main exhothermic reaction occurring at approximately 700 °C. These reactions occur at significantly lower temperatures as compared to the intermediate (708.7 °C) and main reactions (1025 °C) observed for the nano-Al+$Fe_2O_3$ thermite powder mixtures without an epoxy binder.

Following the formation of magnetite, the 78 *vol.%* epoxy composition shows an immediate endotherm (approximately 660 °C) corresponding to the melting of aluminum, followed by a small exothermic peak at approximately 670 °C. The second peak possibly corresponds to the formation of intermediate phases such as FeO and/or $FeAl_2O_4$. The possible intermediate phase formations were immediately followed by a significant exotherm corresponding to the main thermite reaction between aluminum and hematite, possibly forming Fe and $Al_2O_3$ if the reaction goes to completion. The other compositions also showed evidence of the characteristic aluminum melting endotherm

occurring at approximately 660 °C. In contrast to the 78 *vol%* epoxy composite behavior, the melting of aluminum was followed by a distinct delay before the main reaction between aluminum and hematite took place. The main exothermic reaction initiation temperatures for each composition follow in order with the decreasing volume fraction of epoxy. It also follows that the size of the associated endothermic peak decreases as the concentration of epoxy increases.

### 4.2.2 High-Temperature X-Ray Diffraction Characterization (HTXRD)

The high-temperature x-ray diffraction (HTXRD) characterization of select epoxy-cast composites describe the sequence of transformations and reactions occurring during the oxidation of hematite and the exothermic reaction of aluminum and hematite. The Al+$Fe_2O_3$ epoxy-cast composites were heated in the temperature range of 25 to 1300 °C in an inert helium atmosphere and investigated by *in situ*, real time x-ray diffraction. This analysis combined with the DTA experiments discussed in section 4.2.1 correlate exothermic and endothermic events with the products obtained from each reaction. The HTXRD experiments were conducted for Al+$Fe_2O_3$+60 *vol.%* epoxy, nano-Al+$Fe_2O_3$+70 *vol.%* epoxy, and an Al+87 *vol.%* epoxy composite.

Figure 4.20 shows a three-dimensional rendering overlaying x-ray diffraction patterns obtained for the Al+$Fe_2O_3$+60 *vol.%* epoxy composite, with measurements obtained at 25 °C temperature interval. The transformation sequence of hematite to magnetite begins at about 475 °C and is completed by 600 °C. Other complex phases form over the next 200 °C including alumina, before the presence of iron beginning at

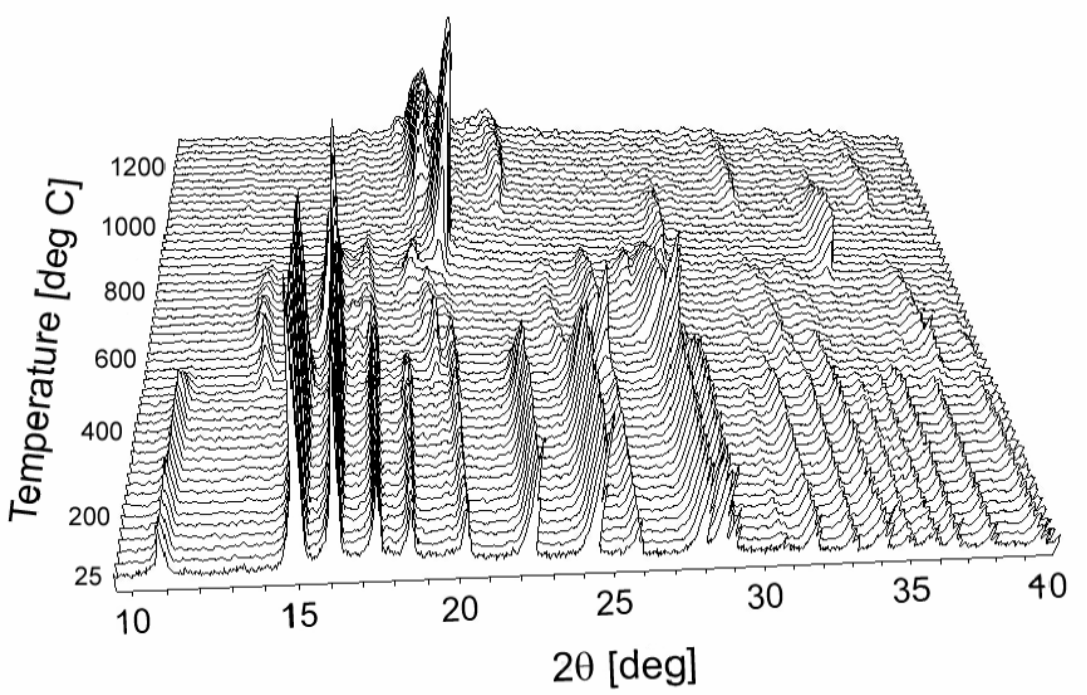


**Figure 4.20** High-temperature x-ray diffraction (HTXRD) patterns obtained for Al+$Fe_2O_3$+60 *vol.%* epoxy composition heated from 25 to 1300 °C at 25 °C/min. Image shows a three-dimensional rendering overlaying x-ray diffraction patterns measured at temperature intervals of 25 °C.

approximately 800 °C. The detailed analysis of the diffraction patterns obtained at each temperature increment identifies the phases present during the heating of the composites.

Figure 4.21 shows the x-ray diffraction patterns obtained for select temperatures used to identify particular phases present during the transformation and reactions of the epoxy-cast composite. The color coded reference phase lines are shown overlaying each diffraction pattern presented. The initial pattern is taken at room temperature (25 °C) prior to heating and shows an excellent agreement with reference (ICDD) values for hematite (01-089-0597) and aluminum (00-004-0787). Upon heating, the peaks begin to gradually shift left (a maximum of approximately 0.2° 2$\theta$) at 450 °C, possibly due to the decomposition of epoxy. Magnetite (00-019-0629) begins to form at 475 °C at the

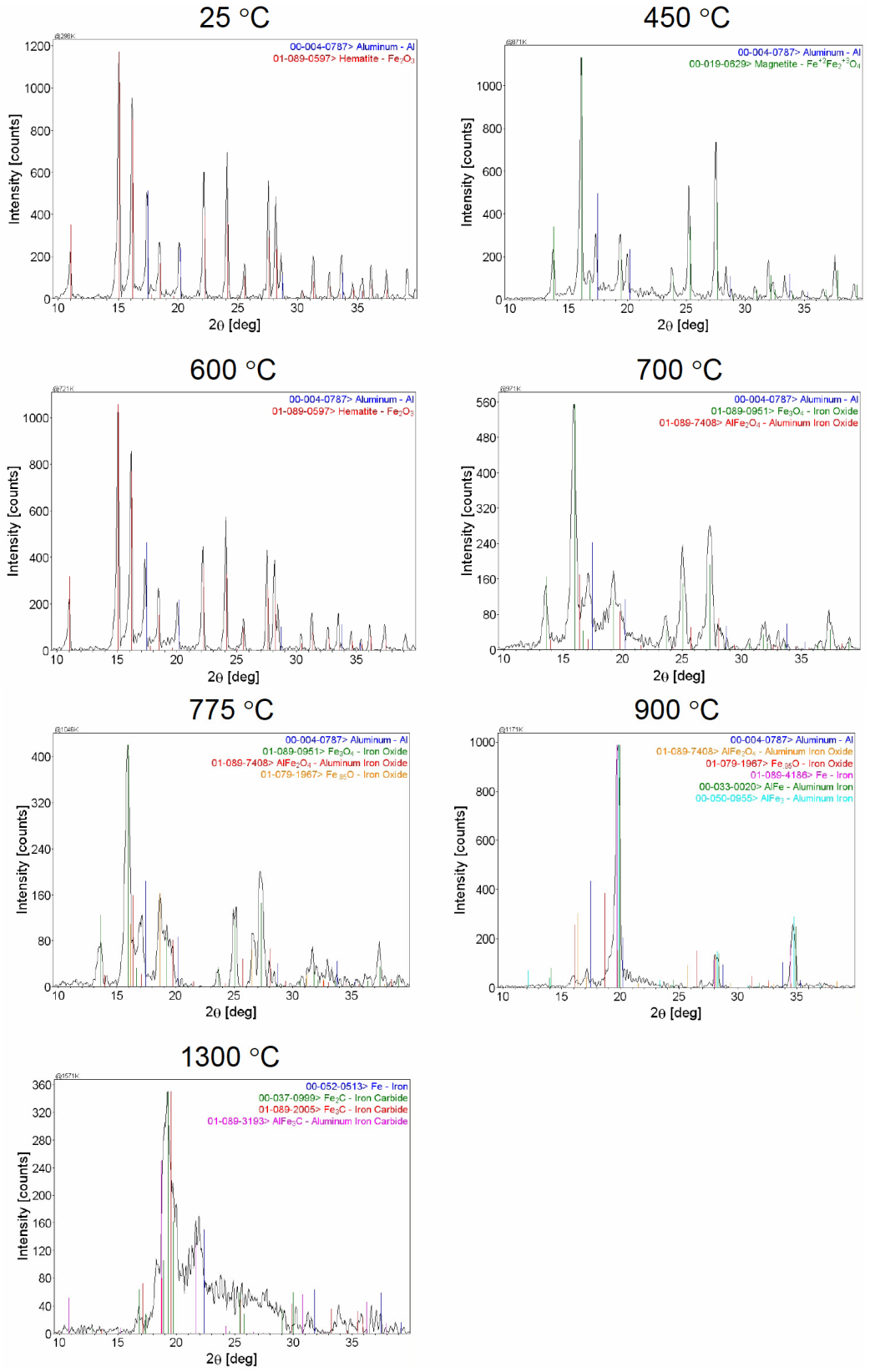


**Figure 4.21** X-ray diffraction patterns obtained at select temperatures for Al+$Fe_2O_3$+60 *vol.%* epoxy composite heated from room temperature to 1300 °C.

expense of hematite. The hematite to magnetite transformation appears to be direct, without the formation of any metastable intermediate phases. No more hematite phase is detected and the transformation is complete by 600 °C. This is followed by the reduction of magnetite to FeO (00-046-1312), initiating at approximately 650 °C and also the trace formation of non-stoichiometric alumina, $Al_{2.667}O_4$ (01-080-1385). These reactions initiate over the temperature range where aluminum begins to melt. Aluminum had an onset melting temperature of 654.1 °C and a peak melting endotherm at 665.1 °C determined from DTA measurements in section 4.2.1.1. The FeO begins its reduction process at approximately 725 °C, possibly forming $Fe_{0.98}O$ (00-039-1088) and/or $Fe_{0.95}O$ (00-039-1088). Stoichiometric FeO is very unstable and typically is observed as $Fe_{1-x}O$ (where $x$ ranges between 0.83 to 0.95) [170]. This temperature also shows evidence for the formation of an aluminum iron-oxide compound, $FeAl_2O_4$ (01-089-7408). These findings follow well with the observations of Korchagin and Podergin [117], proposing that the decomposition of $Fe_3O_4$ to FeO precedes the interaction of iron-oxide and aluminum and the formation of $FeAl_2O_4$. As the temperature rises to 800 °C, the formation of $\alpha$-Fe (01-089-4186) and aluminum-iron compounds, AlFe (00-033-0020) and/or $AlFe_3$ (00-050-0955), were first detected. These are followed by the consumption of magnetite at 900 °C and the disappearance of $Fe_{1-x}O$, Al, $Al_{2.667}O_4$, and $FeAl_2O_4$ at 950 °C. At approximately 975 °C, $\gamma$-Fe peaks begin to form at the expense of the $\alpha$-Fe phase, where the peak intensities begin to drop and are completely gone by 1275 °C. Other phases also form during the $\alpha$-Fe to $\gamma$-Fe transformation and possibly include the formation of iron carbides, namely $Fe_2C$ (00-037-0999) and/or $Fe_3C$ (01-089-2005), and

aluminum-iron carbide $AlFe_3C$ (01-089-3193) with the unlimited availability of carbon from the decomposition of epoxy.

The HTXRD analysis for the Al+$Fe_2O_3$+60 *vol.%* epoxy is correlated with the DTA study (discussed in section 4.2.1.3) conducted on the same composition. Figure 4.22 shows the corresponding phases identified by x-ray diffraction with exothermic and endothermic events observed by the DTA (trace *a*), in addition to the DTA traces obtained for pure hematite pressed powder pellets (trace *b*) and Al+$Fe_2O_3$ mixed powders (trace *c*). The green data points correspond to the temperature at which

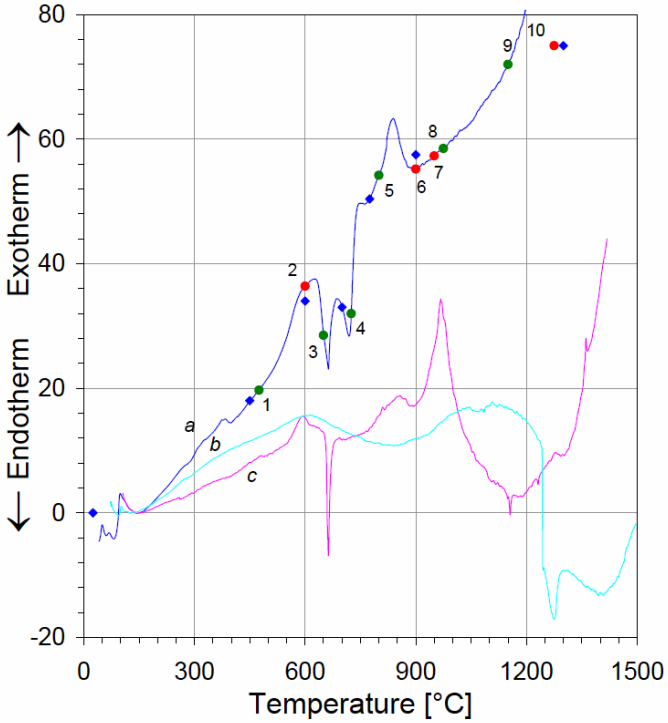


**Figure 4.22** DTA curve obtained for Al+$Fe_2O_3$+60 *vol.%* epoxy composite (trace *a*) correlating HTXRD phase identifications for specific temperatures. Green circles indicate phases forming, while red circles indicate phases consumed. The numbers listed next to each transformation correspond to events and specific phases listed in Table 4.4. The blue diamond points identify temperatures for the x-ray diffraction patterns shown in Figure 4.21. The DTA traces for hematite powder (trace *b*) and Al+$Fe_2O_3$ mixed powder (trace *c*) are also shown for reference.

**Table 4.4** Correlation of HTXRD and DTA measurements for Al+$Fe_2O_3$+60 *vol.%* epoxy composites. Event numbers correspond to phases forming or being consumed at specific temperatures, which are indicated on the DTA trace shown in Figure 4.22.

| Event Number | Temperature [°C] | Phase Forming | Phase Consumed |
|---|---|---|---|
| 1 | 475 | $Fe_3O_4$ (Magnetite) | |
| 2 | 600 | | $Fe_2O_3$ (Hematite) |
| 3 | 650 | $Al_{2.667}O_4$ and FeO | |
| 4 | 725 | $Fe_{0.98}O$, $Fe_{0.95}O$, and $FeAl_2O_4$ | |
| 5 | 800 | $\alpha$-Fe, AlFe, and $AlFe_3$ | |
| 6 | 900 | | $Fe_3O_4$ |
| 7 | 950 | | $Al_{2.667}O_4$, Al, FeO, $Fe_{0.98}O$, $Fe_{0.95}O$, and $FeAl_2O_4$ |
| 8 | 975 | $\gamma$-Fe | |
| 9 | 1150 | $Fe_2C$, $Fe_3C$, and $AlFe_3C$ | |
| 10[☺] | 1275 | | $\alpha$-Fe, AlFe, and $AlFe_3$ |

[☺] Point does not correspond to a specific location on the DTA curve since these measurements were only conducted up to 1200 °C.

phase(s) are beginning to form, while the red data points indicate the end temperature for the consumption of a particular phase(s) that is no longer observed. The corresponding number (1 through 10) associated with each event is correlated with the respective phases observed at that particular temperature from HTXRD scans and listed in Table 4.4. Figure 4.22 also graphically indicates (blue diamond data points) the corresponding temperature where the phases for select x-ray diffraction patterns are identified and shown in Figure 4.21. Examination of Figure 4.22 and Table 4.4 shows good correlation between the exothermic and endothermic events obtained from the DTA trace and the respective phases identified from HTXRD analysis.

An identical analysis, correlating DTA and HTXRD scans, was also conducted for the nano-Al+$Fe_2O_3$+70 *vol.%* epoxy composition. Figure 4.23 shows the DTA trace and corresponding reaction events that are listed in Table 4.5, and the respective phases related to those events. Figure 4.24 shows the corresponding HTXRD patterns obtained for the nano-aluminum epoxy-cast composite at select temperatures. Additional temperatures are shown for assisting the direct comparison of diffraction patterns obtained for the micron-scale aluminum composite (Figure 4.21) at identical temperatures. In general, similar phases were formed for the nano-aluminum composites

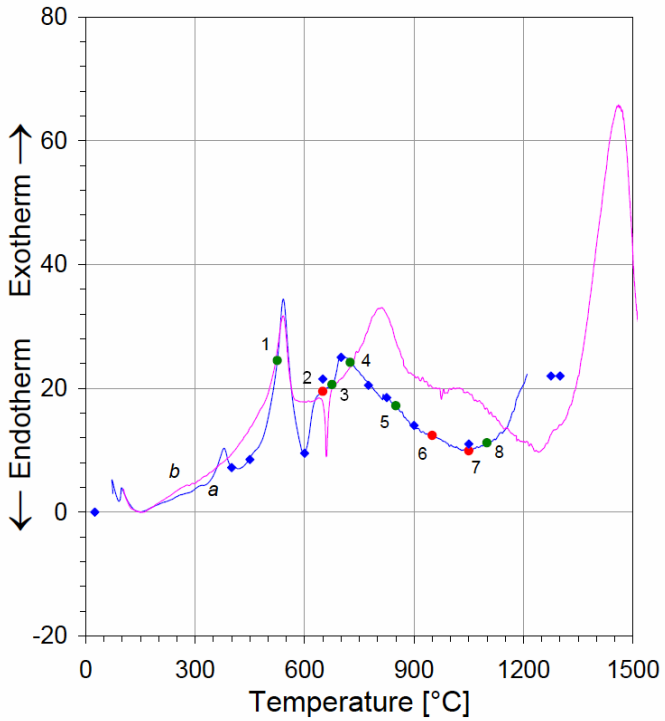


**Figure 4.23** DTA curve obtained for the nano-Al+$Fe_2O_3$+70 *vol.%* epoxy composite (trace *a*) correlating HTXRD phase identifications for specific temperatures. Green circles indicate phases forming, while red circles indicate phases consumed. The numbers listed next to each transformation correspond to events and specific phases listed in Table 4.5. The blue diamond points identify temperatures for the x-ray diffraction patterns shown in Figure 4.24. The DTA trace of nano-Al+$Fe_2O_3$ mixed powder (trace *b*) is also shown for reference.

**Table 4.5** Correlation of HTXRD and DTA measurements for nano-Al+$Fe_2O_3$+70 *vol.%* epoxy composites. Event numbers correspond to phases forming or being consumed at specific temperatures, which are indicated on the DTA trace shown in Figure 4.23

| Event Number | Temperature [°C] | Phase Forming | Phase Consumed |
|---|---|---|---|
| 1 | 525 | $Fe_3O_4$ (Magnetite) | |
| 2 | 650 | | $Fe_2O_3$ (Hematite) |
| 3 | 675 | FeO | |
| 4 | 725 | $Al_{2.667}O_4$, $FeAl_2O_4$, AlFe, and $AlFe_3$ | |
| 5 | 850 | $\alpha$-Fe | |
| 6 | 950 | | $Fe_3O_4$ |
| 7 | 1050 | | $Al_{2.667}O_4$, Al, FeO, and $FeAl_2O_4$ |
| 8 | 1100 | $\gamma$-Fe, $Fe_2C$, $Fe_3C$, and $AlFe_3C$ | |

as were identified for the micron-aluminum composite. However, there were some slight differences that will be highlighted next.

The reduction of hematite to magnetite initiated at a relatively higher temperature (approximately 525 °C) than was observed for the micron-scale Al+$Fe_2O_3$+60 *vol.%* epoxy composition through the HTXRD analysis. However, the transformation as observed by the onset of the exothermic DTA peak occurred at approximately 500 °C, essentially the same temperature observed for the micron-scale aluminum composite. This discrepancy may be associated with the actual reaction initiating just above 500 °C and not being detected until the following XRD scan carried out at 525 °C. Taking this into consideration, it appears that the two compositions have essentially the same onset

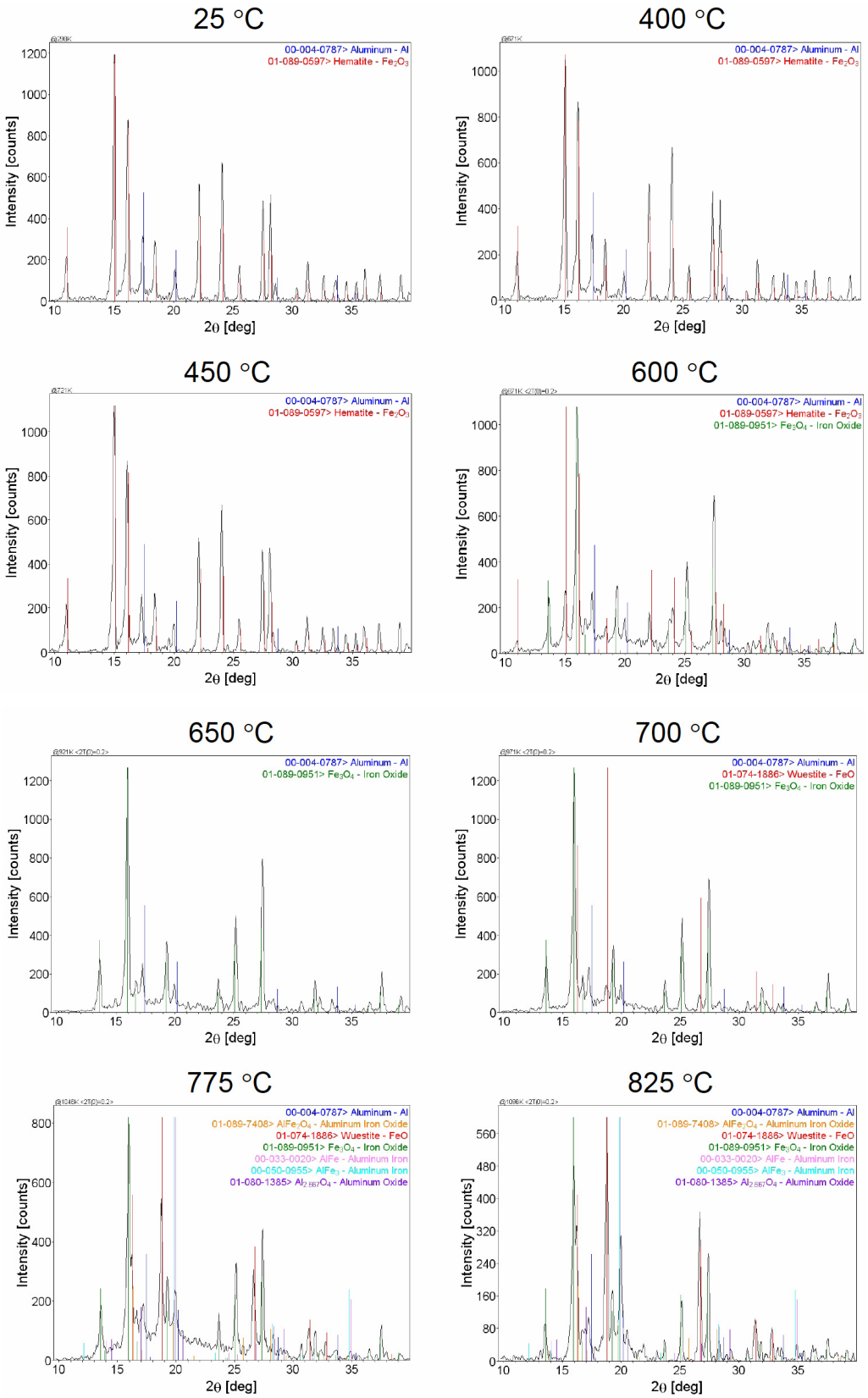


**Figure 4.24** (continued on next page)

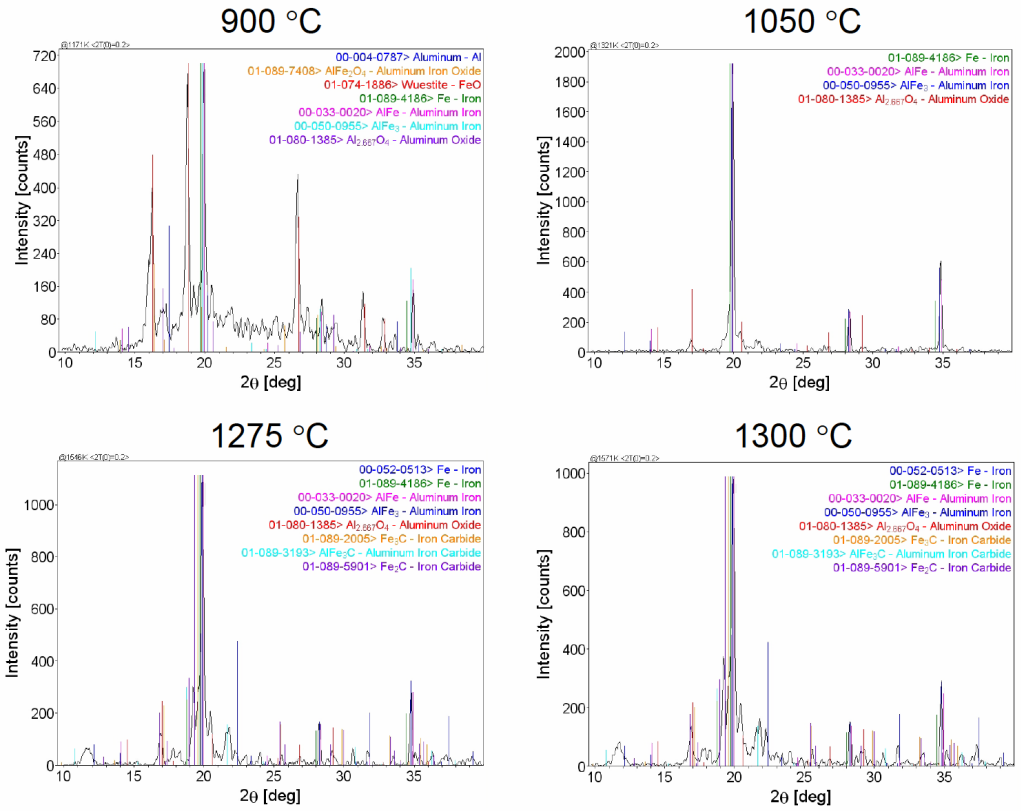


**Figure 4.24** X-ray diffraction patterns obtained at select temperatures for nano-Al+$Fe_2O_3$+70 *vol.%* epoxy composite heated from room temperature to 1300 °C.

temperature for this hematite reduction reaction, however, the nano-aluminum composite has a significantly narrower and relatively lower exothermic peak. Furthermore, the reduction of hematite is directly followed by the melting of aluminum at a significantly lower temperature (approximately 600 °C) which causes the reduction process to possibly be interrupted. This interruption may alter the remaining reactions and extend the transformation and reaction initiation temperatures. In most cases, the nano-aluminum composite reactions take place at temperatures 50 to 75 °C higher. However, there are exceptions to this, for example, the transformation of $\alpha$-Fe to $\gamma$-Fe occurred at 1100 °C, which is approximately 125 °C higher than that observed for the micron-aluminum

composite. Conversely, the lower melting temperature of aluminum for the nano-composite showed the possible formation of AlFe and/or $AlFe_3$ occuring approximately 75 °C lower at 725 °C.

The nano-Al+$Fe_2O_3$+70 *vol.%* epoxy composition also experiences peak shifting in the XRD pattern at approximately 425 °C, similar to that occurring for the micron-scale aluminum composite. The peaks shifted the same amount to the left with a maximum of approximately 0.2° 2$\theta$. However, in this case the peak shift was abrupt, possibly due to the higher epoxy concentration used for this composite. Peak shifting in these composites and the effect of epoxy concentration was evaluated by examining a

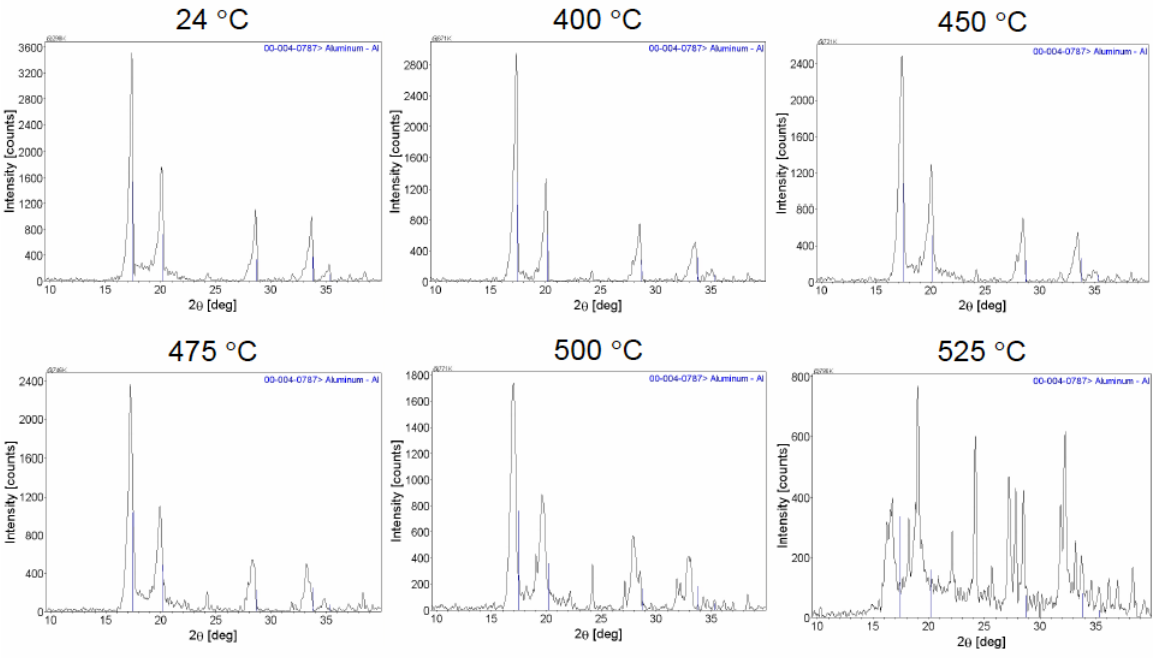


**Figure 4.25** X-ray diffraction patterns obtained for Al+87 *vol.%* epoxy composite heated from room temperature to 1300 °C. The decomposition of epoxy is evident by the severe shift in peaks corresponding to aluminum between 500 and 525 °C. The figure only shows select diffraction patterns obtained up to 525 °C due to the decomposition of epoxy and the significant peak shifting that occurred for higher temperatures.

micron-Al+87 *vol.%* epoxy composite composition under identical experimental conditions. The HTXRD pattern shown in Figure 4.25, indicates a rather abrupt shift in the aluminum peaks between 500 and 525 °C, corresponding to the decomposition of the epoxy. Although less apparent, the peaks actually begin to shift slightly at a lower temperature of 475 °C. The differences in the compositon may also affect the decomposition temperature as observed in the DTA results discussed in section 4.2.1.3 between nano- and micron-scale aluminum composites. Since there is no potential for other reactions to take place in this aluminum and epoxy mixture, the peak shifting is attributed to the decomposition of epoxy. In fact, the Al+$Fe_2O_3$ epoxy-cast composite samples were recovered after the HTXRD experiments. However, the epoxy completely decomposed and only aluminum remained for the aluminum-epoxy composite.

## 4.3 Static Mechanical Property Characterization

Mechanical properties of epoxy-cast Al+$Fe_2O_3$ structural energetic composites were characterized using several different experimental techniques. Each technique is utilized for obtaining specific material data to describe the composites' behavior attributed to mechanical loading at specific stresses, strain, and strain rates. Since the epoxy-cast composites have a large volume fraction of a crosslinked polymer that exhibits viscoelastic and viscoplastic behaviors, the measured mechanical values would therefore be expected to have strain rate dependence. The main mechanical measurements conducted for these composites are used to calculate material parameters such as elastic modulus, $E$, yield stress and strain, $\sigma_y$ and $\varepsilon_y$, failure stress and strain,

$\sigma_f$ and $\varepsilon_f$, together with the critical stress intensity factor, $K_{IC}$, and fracture energy, $G_{IC}$. The following section describes the experimental results obtained from mechanical tests conducted on each of the epoxy-cast Al+$Fe_2O_3$ composites. These results are compared to theoretical values calculated using various rule of mixture models derived for particle-filled polymer composites.

### 4.3.1 Dynamic Mechanical Analysis (DMA)

Polymers exhibit a range of elastic properties that depend on their structure, as well as the subjected test conditions. Dynamic mechanical analysis (DMA) was used to characterize the bulk mechanical behavior directly affecting material performance by essentially measuring the viscoelastic response to an applied oscillating force over a 25 to 175 °C temperature range. Fortunately, viscoelastic polymer behavior is especially sensitive to transitions, morphological changes, and structural changes. Thus, DMA readily conveys detailed structural characteristics or intrinsic properties of polymers and modified filled polymer composites. These include the strong dependence of properties on temperature and time as a result of the viscoelastic nature of polymers.

Experiments were conducted for particle-filled Al+$Fe_2O_3$ epoxy-cast composite compositions, as well as pure epoxy, to understand the influence of structural modifications (such as particle morphology and filler volume fraction) on altering the overall bulk mechanical response. The experimental results are first discussed in detail for the pure epoxy system since they provide a baseline for comparison with the particle-filled compositions. Figure 4.26 shows a typical DMA result obtained for pure

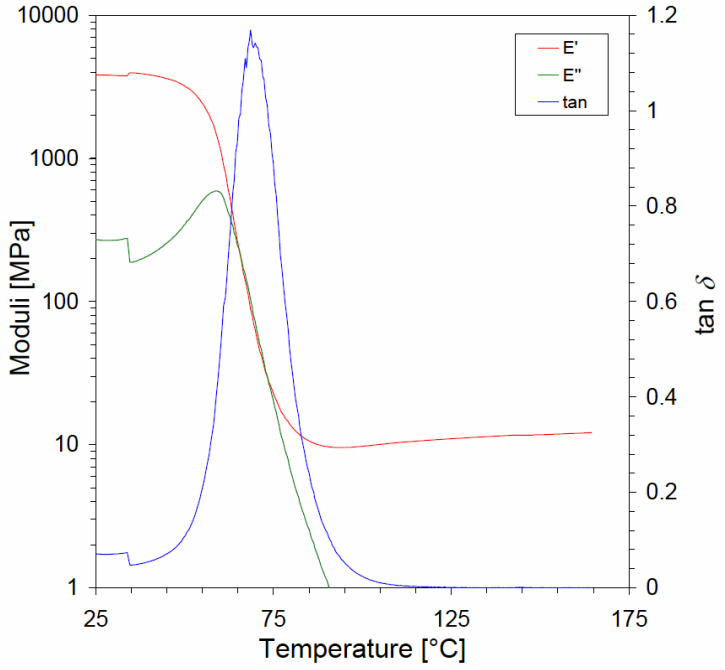


**Figure 4.26** Typical storage modulus, *E'*, loss modulus, *E''*, and tan $\delta$ DMA curves obtained for pure epoxy.

epoxy, where the complex response of the material is resolved into the elastic or storage modulus ($E'$) and the viscous or loss modulus ($E''$). Between approximately 55 and 75 °C, the storage modulus drops by over two orders of magnitude, indicating that the epoxy-cast composite has lost most of its usefulness as a structural material. This abrupt change is associated with the onset of short-range molecular motions initiating at the glass transition temperature, $T_g$. Notice that the loss modulus rises to a maximum as the storage modulus is in its most rapid rate of descent. A rise in the loss modulus indicates an increase in the structural mobility of the polymer. This is a relaxation process that permits motion along larger portions of individual polymer chains. The peak of the loss modulus is conventionally known as the glass transition temperature and identified as a softening point for amorphous polymers. Pure epoxy was observed to have an average

glass transition temperature (obtained from five experiments) of 57.92 ± 0.78 °C. Studies conducted by Adolf [175] measured a glass transition value of 68.96 °C for a very similar epoxy system fabricated with EPON 828 resin and the same DEA curing agent.

The storage modulus exhibits three distinct response regions over the increasing temperature interval examined. Initially, the response is that of a glassy polymer and compares well with room temperature elastic modulus values. As temperature increases, the response enters the glass transition region leading to a rubbery material response. The storage modulus within the rubbery region is related to the crosslink density according to the kinetic theory of rubber elasticity and permits the calculation of crosslink density from the equilibrium shear modulus, $G$, according to [176]:

$$G = \frac{\rho RT}{M_c} = \nu RT \,, \tag{4.5}$$

where $\rho$ is the density of the polymer, $M_c$ is molecular weight between crosslinks, $R$ is the gas constant (8.314 J/mol K ), and $T$ is temperature in Kelvin. The ratio of density and molecular weight between crosslinks, $\nu$, gives the number of moles of network chains per unit volume of polymer or the crosslink density. These experiments measured the storage modulus in pure tension and therefore need to be associated with the shear modulus for estimating the crosslink density according to equation (4.5). The shear modulus is related to $E'$ by assuming $3G = E'$ and upon substitution into equation (4.5), results in:

$$\nu = \frac{E'}{3RT}. \qquad (4.6)$$

For this assumption to be valid, the sample volume must not vary during the experiment and the value of the loss modulus must be negligible compared to the storage modulus, *E'* [177]. The resulting equation was evaluated in the rubbery plateau region (at 150 °C) of the storage modulus and had an average crosslink density of 1054 ± 132 mol/m$^3$ for pure epoxy. This value is in good agreement with 957 mol/m$^3$ reported for the identical cured epoxy system [66].

The applied stress and resulting strain obtained from DMA experiments are typically out of phase with each other, reflecting the time lag associated with a viscoelastic response or elastic recovery, by the phase angle or damping term (tan $\delta$). Part of the energy used in producing the deformation is recoverable, while the rest is dissipated as heat during viscous flow. The tan $\delta$ curve follows the loss modulus curve very closely and provides a successive count of the ratio of the elastic and viscous phases ($\tan\delta = E''/E'$) within the polymer. This quantity effectively gives a measure of viscoelasticity and provides a convenient means for comparing polymers where the storage and loss modulus values change because of alterations in composition, geometry, and/or processing conditions. At low temperatures leading up to the glass transition, tan $\delta$ is typically below 0.1. The rapid rise in the tan $\delta$ curve for pure epoxy above approximately 50 °C coincides with the equally rapid decline in the storage modulus. In general, a relatively small peak phase angle (< 1.0) indicates high elasticity while a relatively large phase angle (> 1.0) is associated with highly viscous response [178].

Above approximately 65 °C, the loss modulus (Figure 4.26) for pure epoxy is equal to or greater than that of the storage modulus, thus indicating a predominant viscous component contribution to the overall response. This signifies that the polymer has undergone irreversible deformation and has reached a soft and pliable material state.

Crosslinked epoxy systems have distinct temperature-dependent behaviors that make them easily distinguishable from other networked polymer systems. The patterns presented in Figure 4.26 for pure epoxy is typically observed for crosslinked amorphous polymers [178]. The DMA measurements provide several key indicators about structural properties. For example, tan $\delta$ values above the glass transition return to pre-glass transition levels for crosslinked systems. Additionally, relatively low tan $\delta$ values (below 1.0) are typically observed for crystalline materials and values above 1.0 are associated with an amorphous system [178]. However, the magnitude of the loss modulus and tan $\delta$ peaks also vary with the severity of the decline in the storage modulus. Therefore, care must be taken in interpreting the structural details obtained from DMA measurements.

As observed for the pure epoxy system in Figure 4.26, the tan $\delta$ values peak above 1.0 and lose 99 %+ of its storage modulus as it passes through the glass transition temperature. This indicates a greater tendency for viscous flow close to the glass transition temperature and therefore a possible increase in the overall bulk toughness during impact experiments with a minimal amount of bulk heating. There is also evidence for the onset of solid-state crystallization as the storage modulus begins to slowly increase above the glass transition temperature. This is indeed the case for the cured epoxy system used in this study, and crystallization has been observed at a

significantly higher temperature (approximately 400 °C) than the range examined for the DMA experiments. Solid-state crystallization has been verified by differential thermal analysis (DTA) measurements discussed in section 4.2.1.3.

It is well known that adding filler or a reinforcement phase to a polymer increases the overall room temperature modulus of the system. However, DMA scans of unfilled materials and their filled counterparts show that the increase in room temperature properties is only a small part of their overall improvements. Figure 4.27 shows the storage modulus plots for unfilled epoxy and four similar systems that contain different amounts of filler reinforcement (epoxy volume fractions of 47, 60, 70, and 78 %). Relatively steady improvements were observed with solid particle filler additions to the epoxy matrix. The storage modulus typically increased in both the glassy and rubbery

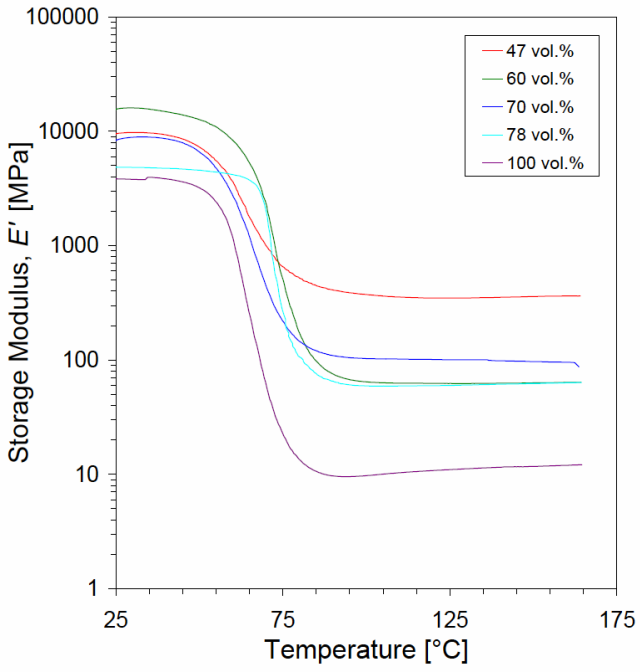


**Figure 4.27** Comparison of measured storage modulus curves for each composition over a 25 to 175 °C temperature range.

regions with the addition of solid particles. It follows since the filler materials are purely elastic systems with extremely high thermal resistances, while the polymer and filler/polymer interface have a viscoelastic response. However, the 60 *vol.%* epoxy composition appears to show some irregularity in this general trend, possessing a significantly high modulus in the glassy region and relatively low modulus in the rubbery region.

The elastic contribution to the overall system response is observed as a reduced effect that the glass transition has on decreasing the elastic modulus. Table 4.6 gives some key properties obtained from DMA experiments for the unfilled epoxy and filled epoxy composite materials. The $T_g$ does not change significantly with filler content except for the 60 *vol.%* and 78 *vol.%* epoxy compositions obtained from the loss modulus peaks in Figure 4.28. The 60 *vol.%* epoxy composition had an average glass transition value of 63.42 ± 4.80 °C, while the 78 *vol.%* epoxy composition had an even higher average value of 68.42 ± 3.96 °C. These were approximately 7 to 11 °C higher than the

**Table 4.6** Measured DMA properties obtained for epoxy-cast Al+$Fe_2O_3$ composite compositions and pure epoxy (batch *B*).

| Epoxy [*vol.%*] | $E'$ at 40 °C [MPa] | $E'$ at 150 °C [MPa] | Temperature at tan $\delta$ peak [°C] | $T_g$ [°C] | $\nu_e$ [mol/m$^3$] |
|---|---|---|---|---|---|
| 47 | 8222 ± 618 | 321 ± 32 | 69.81 ± 2.96 | 58.31 ± 5.64 | 30383 ± 2996 |
| 60 | 26620 ± 14557 | 77 ± 8 | 79.75 ± 5.02 | 63.42 ± 4.80 | 7317 ± 789 |
| 70 | 8235 ± 1708 | 97 ± 3 | 70.85 ± 2.14 | 56.09 ± 3.04 | 9220 ± 271 |
| nano-70 | 9707 ± 2984 | 123 ± 13 | 91.11 ± 3.45 | 81.50 ± 2.79 | 11675 ± 1253 |
| 78 | 4342 ± 430 | 61 ± 4 | 75.57 ± 1.87 | 68.42 ± 3.96 | 5757 ± 383 |
| 100 | 2628 ± 700 | 11 ± 1 | 68.39 ± 0.91 | 57.92 ± 0.78 | 1054 ± 132 |

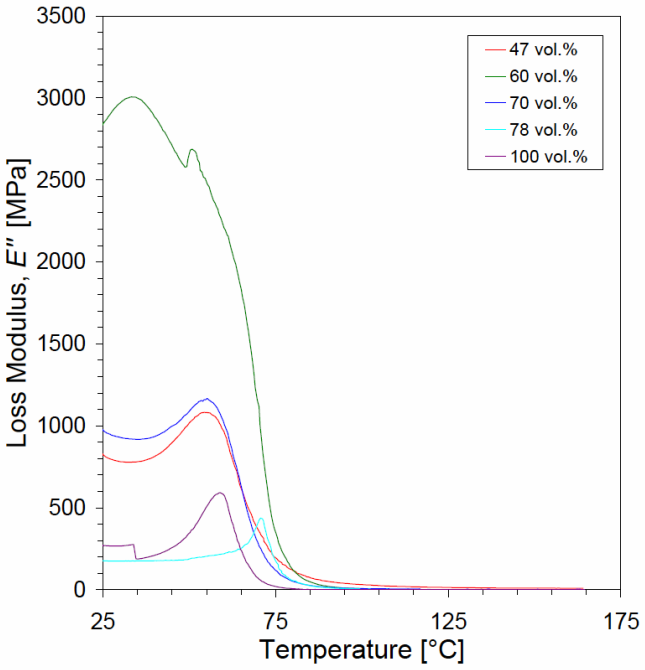


**Figure 4.28** Comparison of measured loss modulus curves obtained for each composition. Corresponding peak locations indicate the glass transition temperature, $T_g$.

remaining compositions including pure epoxy (average $T_g$ was 57.44 ± 1.19 °C). Crosslinking tends to reduce the specific volume of the polymer which means the free volume is reduced and the $T_g$ is raised because molecular motion is more difficult. The temperature observed for the tan $\delta$ peak is also very sensitive to crosslink density, in addition to filler content and molecular weight [178]. However, the tan $\delta$ curve mainly indicates the load-bearing capability of the composites and the elastic contribution of the filler, thus increasing as the peak height decreases and broadens. Figure 4.29 shows the tan $\delta$ relationship between each of the compositions. The shift of the tan $\delta$ peak or the loss modulus for the 60 *vol.%* and 78 *vol.%* epoxy compositions suggests an increase in crosslink density. However, the calculated crosslink density of 7317 ± 789 mol/m$^3$ for 60 *vol.%* epoxy composition was relatively low when compared to the other composites

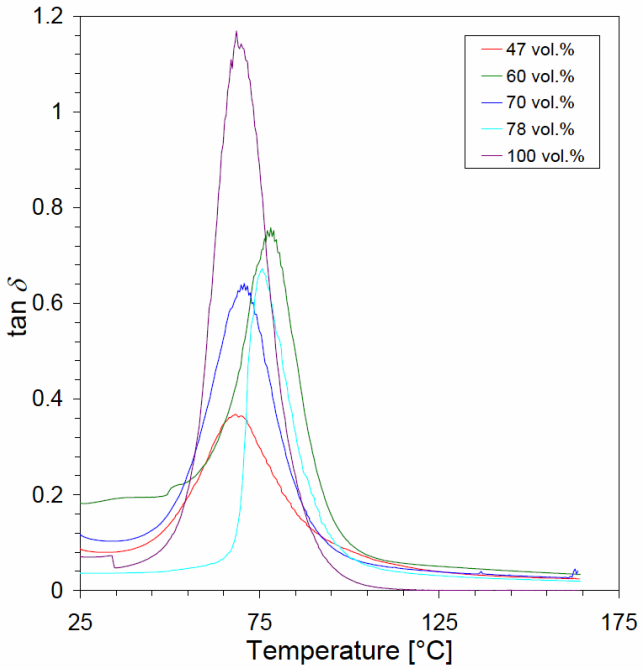


**Figure 4.29** Comparison of measured tan $\delta$ curves obtained for epoxy-cast Al+$Fe_2O_3$ compositions and pure epoxy.

(listed in Table 4.6), which suggests that the relatively higher glass transition temperature and shifting of the tan $\delta$ peak to a higher temperature may not be directly related to crosslink density. The 78 *vol.%* epoxy composition had a crosslink density of 5757 ± 383 mol/$m^3$, which appears to be a reasonable value that falls between the 70 *vol.%* epoxy composition and pure epoxy (Figure 4.30).

Effective crosslinking, which is due to trapped entanglements, and chemical crosslinking both contribute to improving the storage modulus. However, the observed plateau in the rubbery region (temperatures above the $T_g$) of the storage modulus reaches a level that reflects the immobility of only chemical crosslinks. Therefore, solid micron-scale aluminum particles possibly inhibit the epoxy crosslinking during polymerization for the 60 and 78 *vol.%* epoxy compositions. These relatively large

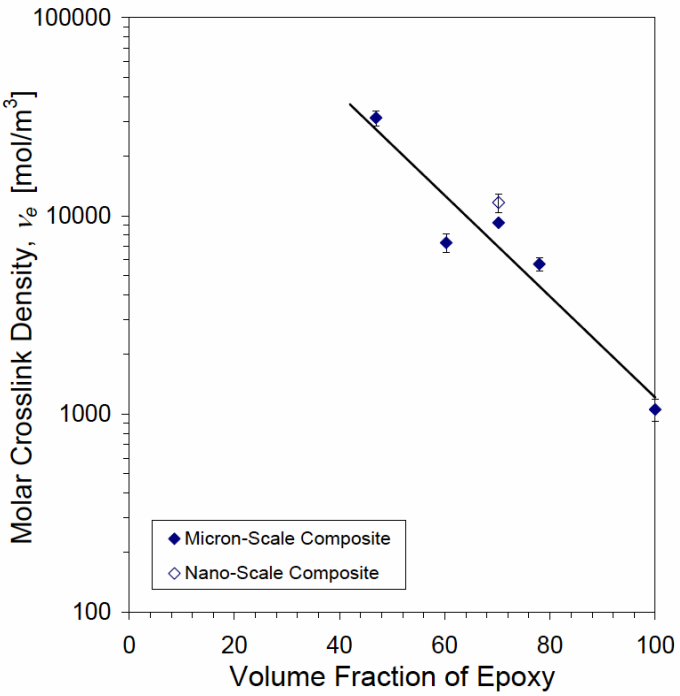


**Figure 4.30** Summary of measured molar crosslink density values, $\nu$, obtained for each epoxy-cast Al+$Fe_2O_3$ composition and pure epoxy.

inclusion features dominate the deformation response in the glassy region by transferring the load from the matrix to the inclusions. This would explain the significantly high modulus exhibited by the 60 *vol.%* epoxy composition in the glassy region below the glass transition temperature. However, as the temperature is increased above the $T_g$, the composite response is dominated by molecular chain motions that are not inhibited by the relatively large inclusion features. This results in a relatively low storage modulus in the rubbery region. Uniformly dispersed submicron hematite particles and hematite agglomerates possibly assist in retaining the load capability of the composite above the glass transition by inhibiting molecular chain motions since they are on the same geometrical size order and promote entanglements. However, the composite cannot overcome the significantly large inclusion features, which act as "open voids" and permit

the unaltered molecular chain motions, thus, reducing the storage modulus in the rubbery region.

The hematite agglomerates may be improving the local mechanical properties of the composite, since the individual hematite particles are still uniformly dispersed, only now in closer proximity to each other. However, the significantly large spherical aluminum particles are much greater than the polymer chains and serve to reduce the overall crosslink density, particulary if they cluster and form significantly large agglomerates. Quantitative microstructural analysis (discussed in section 4.1.1) shows that both the aluminum and hematite mean diameters are relatively larger for the 60 *vol.%* epoxy composition, as indicated in Figure 4.7. Additionaly, the number of hematite agglomerates within the volume was significantly low as compared to the other compositions, illustrated in Figure 4.9. This would be expected if the hematite agglomerates are truly contributing to the overall mechanical properties of the composite and their reduction in number consequently lowers the bulk mechanical behavior.

Filled polymer systems with the same volume fraction and type of filler are directly comparable and emphasize the effect filler particle size has on the overall composite response. It is suggested that the dispersion of nanoscale particles throughout a polymer matrix provide physical entanglements and lead to a loss in mobility of polymer chain segments [59]. Figure 4.31 shows the tan $\delta$ curves for two Al+$Fe_2O_3$+70 *vol.%* epoxy compositions reinforced with micron and nano-scale aluminum particles. Notice the composition with nano-scale aluminum particles has a significantly higher temperature for the tan $\delta$ peak and indicates a higher crosslink density when compared to the micron-scale aluminum composite. Equation (4.6) was

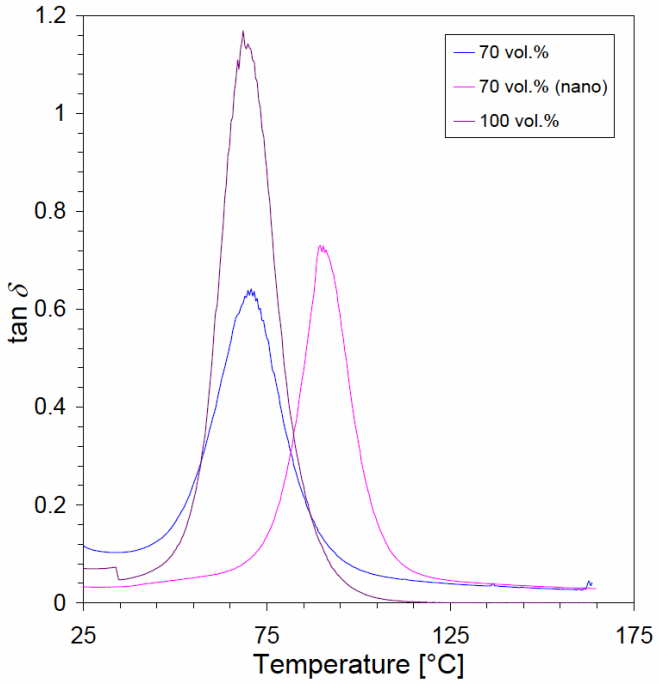


**Figure 4.31** Comparison of tan $\delta$ curves obtained for epoxy-cast Al+$Fe_2O_3$ composites with 70 *vol.%* epoxy containing nano- and micron-scale aluminum. The pure epoxy tan $\delta$ curve is also shown as a baseline reference.

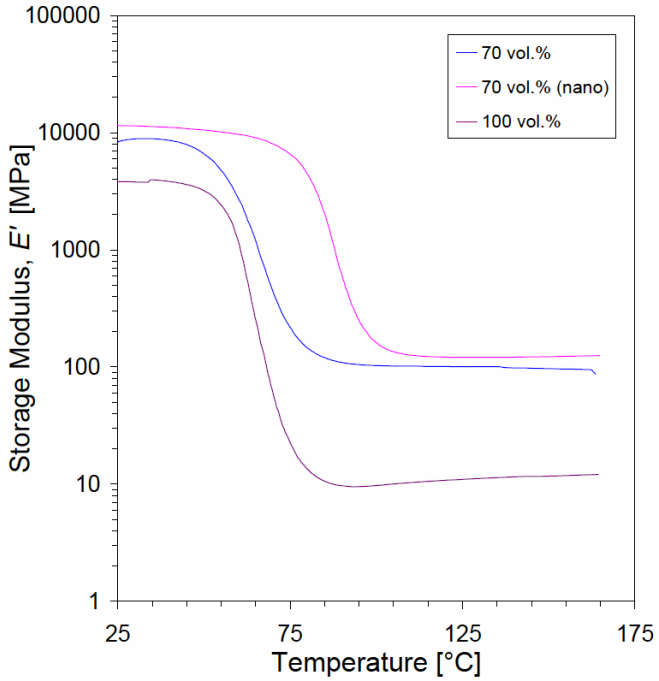


**Figure 4.32** Comparison of storage modulus curves obtained for epoxy-cast Al+$Fe_2O_3$ composites with 70 *vol.%* epoxy containing nano- and micron-scale aluminum. The pure epoxy storage modulus curve is shown as a baseline reference.

used to estimate the crosslinking density and represents approximately 80 % percent increase in the crosslink density for a composite containing nanoscale aluminum particles. Crosslink densities were 9220 ± 271 and 11675 ± 1253 mol/$m^3$ for the micron- and nano-scale Al+$Fe_2O_3$+70 *vol.%* epoxy composites, respectively. Table 4.6 lists complete details and composite properties obtained from DMA experiments. The use of nano-scale aluminum particles in the composite was also apparent in raising the glass transition temperature and improving the load capability in the rubbery modulus region, as shown in Figure 4.32.

### 4.3.2 Continuous Spherical Ball Indentation Tests

The local mechanical behavior of epoxy-cast Al+$Fe_2O_3$ composites was probed using instrumented continuous indentation experiments, where the penetration depth of a spherical tipped indenter was measured as a function of an applied load. Using this approach, the localized elastic and plastic behavior of a material may be investigated, as well as the onset of ductility or yielding. Upon indentation, the contact area is continuously computed from the known indenter geometry and the measured depth of the impression. However, the contact area of a particular indenter depends on both the shape of the indenter, as well as the elastic-plastic material response of the specimen.

A spherical tipped indenter was used for evaluating the epoxy-cast composites since it is more suitable than sharp tip shapes that are invariably rounded. At small applied loads leading to small stresses, the resulting strains in the sample and, hence, the

contact between indenter and sample are purely elastic. When the load is increased beyond a certain value, the stresses induced by the indenter will exceed the critical shear stress of the specimen and a part of the strain is relieved by plastic deformation. The material is in an elastic-plastic state where plastic flow is constrained, *i.e.* the plastically deformed zone is surrounded by elastic material. To further expand the plastic boundary into the elastically deformed material, the applied stress needs to be maintained and, thus, the load on the indenter must be increased. In doing so, the plastically deformed zone grows, as the indenter is completely in contact with plastically deformed material. The transition from a purely elastic to a fully plastic contact and, hence, the hardness obtained from the projected contact area at maximum load characterizes the local resistance of the investigated material against combined elastic and plastic deformation. However, the use of a spherical tipped indenter allows the separation of the elastic and plastic components of the deformation. This is particularly useful for characterizing the viscoelastic-viscoplastic behavior typically observed for polymeric materials.

The analysis of continuous indentation tests is based on the elastic contact solution for a spherical ball elastically deforming in a spherically shaped indent (Hertzian contact problem [179]). Oliver and Pharr [180] focused on an elastic analysis of the unloading behavior for a plastic indentation and derived the Hertzian-based relationship for the load dependence of penetration depth, *dP/dh*, and the contact area, *A*, given by:

$$\frac{dP}{dh} = \frac{2\sqrt{A}E_r}{\sqrt{\pi}}. \qquad (4.7)$$

The reduced modulus, $E_r$, accounts for deformation of both the indenter and the sample given by the relation [179]:

$$E_r = \left[ \frac{1-\nu_i^2}{E_i} + \frac{1-\nu_s^2}{E_s} \right]^{-1}, \tag{4.8}$$

where $E_i$ and $E_s$ are elastic moduli and $\nu_i$ and $\nu_s$ are Poisson's ratios for the indenter and the specimen, respectively. For many materials, the unloading curve can be fit by a power law expression of the form [180]:

$$P = \alpha h^m, \tag{4.9}$$

where $\alpha$ is a constant dependent on indenter geometry, elastic modulus and Poisson's ratio for both the sample and indenter, and $h$ is the contact depth or displacment. The power law exponent, $m$, is related to the indenter geometry and has a value of 1.5 for the Hertz description of a spherical geometry. The contact area is computed from $h$ according to the following expression for a rigid ball [180]:

$$A = \pi h(D - h), \tag{4.10}$$

where $D$ is the diameter of the spherical identer tip.

The important feature of spherical tipped indenters is that the initial response of a material during indentation is elastic and then, at a critical load, the initiation of plasticity occurs. Conversely, for ideally pointed indenters, plastic deformation starts immediately

after contact. Since the displacement during the initial loading is purely elastic for spherical tipped indenters, the relationship between the loading curve and the elastic modulus of the material are easily described by Hertzian elastic contact theory [179]. The stress field generated by a spherical tipped indenter is well known, which does not exhibit the stress singularities inherent in perfectly sharp pointed indenters. The stress field scales with the mean contact pressure and the contact diameter. Spherical tipped indenters provide the resolution necessary for measuring relatively small loads and displacements, as well as the capability of resolving the elastic-plastic transition during indentation. The measurement of the elastic contribution in the initial loading behavior of a material before complication of added plastic deformation seems to be an advantage. Accurately measuring the initial generally small loading region of elastic loading behavior is admittedly a challenging endeavor, particularly for relatively "hard" materials. However, the relatively "soft" response of particle-filled epoxy-cast composites and the precision of a micromechanical indentation probe enable the measurement of load-displacment behavior and the determination of stress-strain properties.

An example of a load-displacment curve obtained for Al+$Fe_2O_3$+60 *vol.%* epoxy composite is shown in Figure 4.33(*a*). The initial elastic deformation response is demonstrated here by fitting the loading curve with the Hertz relation [179]:

$$P = \frac{1}{3}\sqrt{8D}E_r h^{3/2}. \qquad (4.11)$$

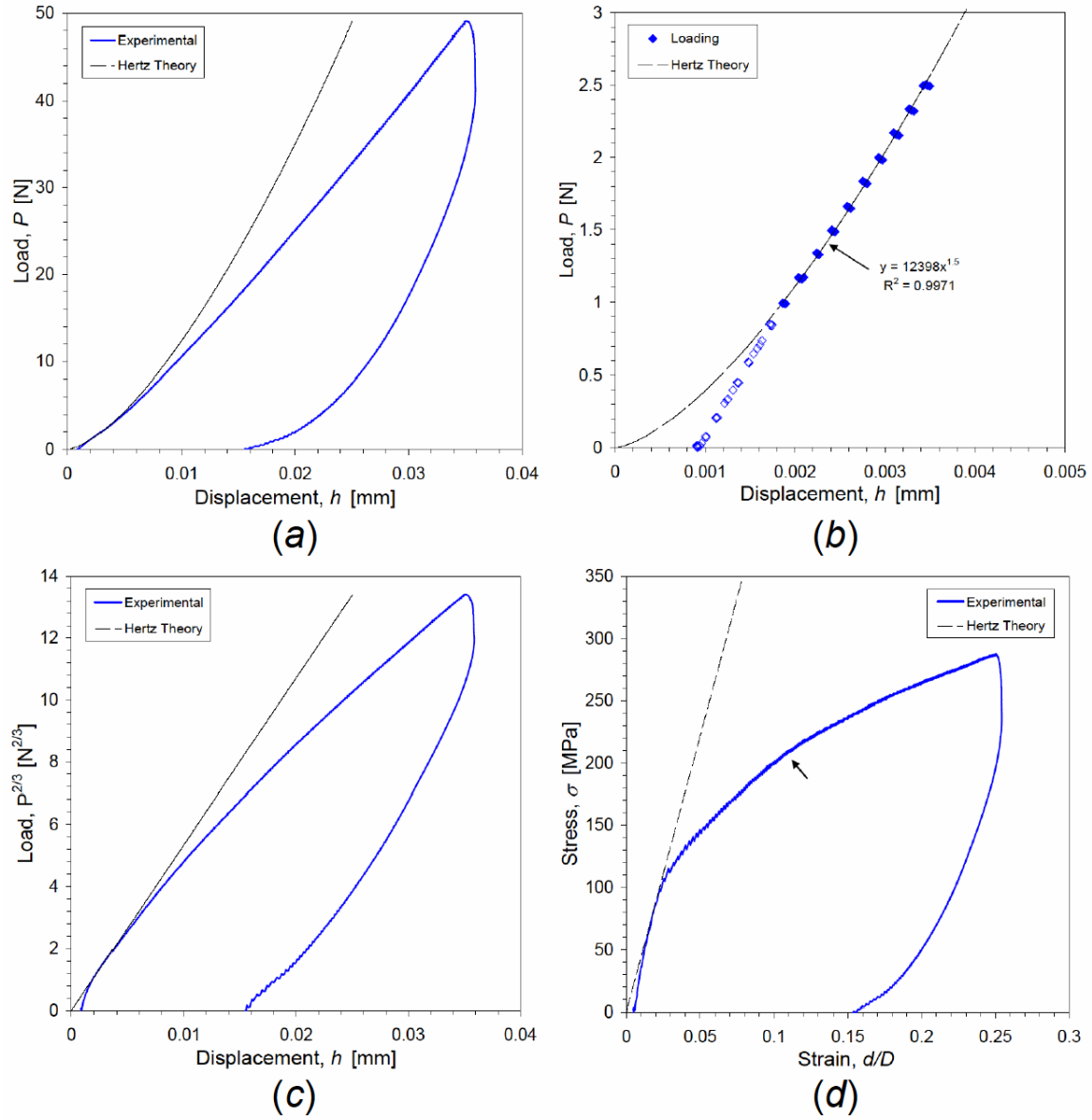


**Figure 4.33** Example of an undamaged response from continuous indentation test data obtained for Al+$Fe_2O_3$+60 *vol.%* epoxy composite showing *a*) load-displacement and *b*) a zoomed view of the purely elastic loading-displacement region, *c*) load to the 2/3 power displacement dependence, and *d*) the stress-strain response. The stress-strain response typically showed viscoelastic and viscoplastic (indicated by arrow) yield points. Each figure includes the theoretically calculated elastic response obtained from Hertzian contact theory [179].

Figure 4.33(*b*) shows the elastically loaded region in expanded form with the best fit power law expression having an exponential value equivalent to that derived for a spherical indenter ($m$ = 1.5). Notice that the data shows excellent correlation with the response predicted by the Hertz theory [179] up to the elastic-plastic transition point at a load of 2.5 N and the corresponding displacement of 3.5 μm. However, the initial contact behavior for displacements less than 1.75 μm are extremely sensitive and eventually approach the theoretical elastic response once "good" contact is made between the specimen and indenter tip.

The elastic contact model used for evaluating the load-displacement curves is based on the assumption of a single contact between the indenter tip and a homogeneous, perfectly elastic material having a smooth surface [179]. Although the surfaces of each specimen were lapped and polished to a 3 μm finish, multiple area contacts between the indenter tip and asperities of the surface are formed instead of a single contact, causing the stress in this area to become relatively large. The asperity deforms plastically at a very early stage of the indentation experiment and causes the load-displacement curve to exhibit larger displacements than in the case of a sample with a perfectly smooth surface. This effect becomes more prevalent for "hard" materials, which generally have a significantly larger elastic compliance. The dissimilar phases that make up the particle-filled composites may also contribute to this effect if the indent makes contact in aluminum or hematite rich areas of the microstructure.

According to equation (4.11), the elastic loading response is linear when plotted as a function of, $P^{2/3}$, as illustrated in Figure 4.33(*c*). This permits the identification of the initial contact point by extrapolating the linear curve to zero load and adjusting the

displacement for initial imperfect contact between the indenter tip and the specimen. The composite's elastic modulus is determined from combining equations (4.9) and (4.11), given by:

$$\alpha = \frac{1}{3}\sqrt{8D}E_r, \tag{4.12}$$

and solving for the reduced modulus, $E_r$, given by equation (4.8). With knowledge of the the elastic modulus and Poission's ratio for the steel indenter, and Poisson's ratio obtained from ultrasonic measurements for the composite (described in section 4.1.2), the elastic modulus for the specimen, $E_s$, is easily obtained.

An instrumented indentation hardness test provides the ability to measure the indenter penetration, $h$, under the applied load, $P$, throughout the testing cycle and is, therefore, capable of measuring both the elastic and plastic deformation of the material. Hardness has conventionally been defined as the resistance of a material to permanent penetration by another harder material, with the measurement being made after the applied force has been removed. The mean pressure between the surface of the indenter and the indentation is equal to the load divided by the projected area of the indentation, known as the Meyer hardness, $H_M$. Following Tabor [181], the hardness strain is defined as the ratio of contact and ball diameters, $d/D$, respectively. The hardness pressure or stress is computed for increasing strains, as the indenter is pressed into the test material, which provides a continuous measure of stress and strain. Figure 4.33(*d*) shows the measured stress-strain response, which initially follows the Hertzian elastic contact stress given by [179]:

$$\sigma_H = \frac{4}{3\pi} E_r \left( \frac{d}{D} \right). \tag{4.13}$$

The hardness stress is obtained from the experimental data according to:

$$\sigma = \frac{4P}{\pi d^2}, \tag{4.14}$$

where the contact diameter, $d$, is computed from the penetration depth, $h$, using the hard sphere relationship given by:

$$d = 2\sqrt{h(D-h)}. \tag{4.15}$$

The stress-strain response shown in Figure 4.33(*d*) identifies the elastic-plastic transition or viscoelastic yield point, where the response departs from the purely elastic Hertzian relationship [179]. The figure also identifies a second viscoplastic yield point exhibiting a much greater yield stress, indicated by an arrow. The viscoelastic-viscoplastic behavior is also apparent in the unloading curve, which makes the separation of the viscoelastic recovery of the indent much more challenging. Traditionally, using the method of Oliver and Pharr [180], the elastic modulus is determined by experimentally measuring the peak (plastic) load, the depth of the indentation tip at peak load, and the initial unloading dependence of $P$ and $h$. This study illustrates the importance of evaluating the initial loading behavior prior to the complication of added viscoplastic (time-dependent) deformation.

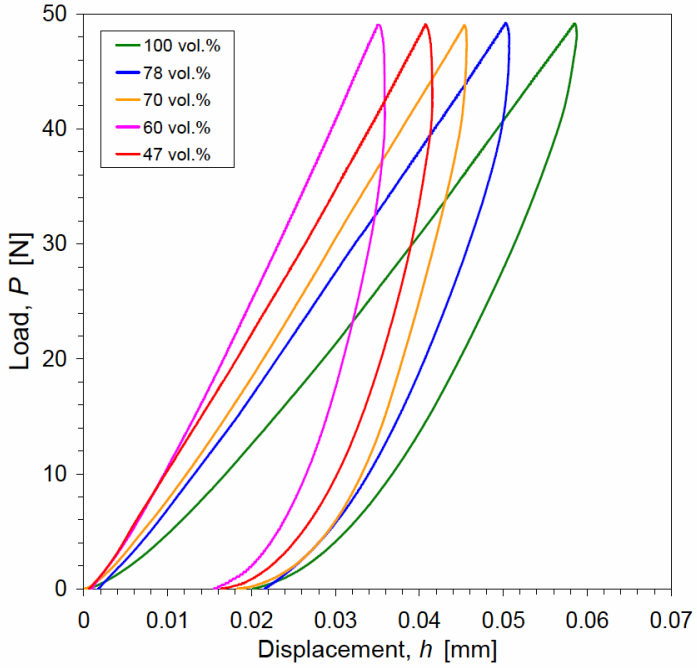


**Figure 4.34** Representative load-displacement curves obtained from continuous indentation experiments for each Al+$Fe_2O_3$ epoxy-cast composite composition.

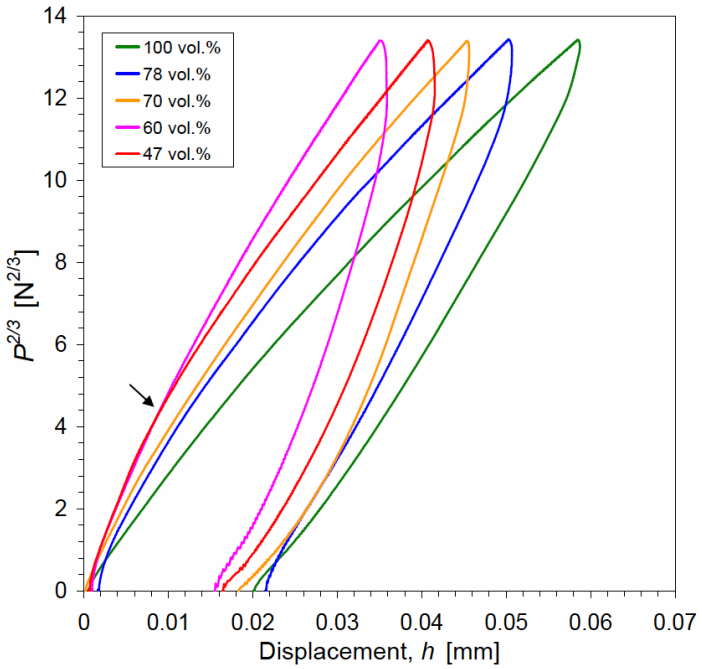


**Figure 4.35** Representative load to the 2/3 power displacement dependence curves obtained from continuous indentation experiments for each Al+$Fe_2O_3$ epoxy-cast composite composition. The arrow identifies the elastic-plastic transition point for the 47 and 60 *vol.%* epoxy composite.

The continuous indentation analysis, previously discussed in more detail for the Al+$Fe_2O_3$+60 *vol.%* epoxy composite, has been conducted for each epoxy-cast composite composition. Figure 4.34 shows the load-displacement data obtained from a representative sampling of each composition. The behavior illustrates the influence of epoxy concentration on the relative response, with the 60 *vol.%* epoxy composite being most resistant to penetration as indicated by the shallowest indentation depth at the peak loading point. The other compositions' resistance to penetration follow in decreasing order for 47, 70, and 78 *vol.%* epoxy, followed by pure epoxy. Figure 4.35 shows that the 60 and 47 *vol.%* epoxy composites have very similar elastic responses as observed from the load dependence to the 2/3 power with depth of the indent. However, the 47 *vol.%* epoxy composite has a significantly greater penetration depth beyond the elastic/plastic transition point, as identified by the arrow in Figure 4.35. Also notice that the slope of the initial linear response in the purely elastic loading region decreases as the epoxy concentration increases for the remaining composites. The stress-strain response for each composition is shown in Figure 4.36, with the 60 and 47 *vol.%* epoxy again illustrating very similar elastic responses, as well as similar viscoplastic yield points. However, the 47 *vol.%* epoxy has a more defined yielding response with less of an observable strain hardening effect as exhibited by the 60 *vol.%* epoxy composite. The experimental data obtained from continuous indentation experiments is available in Appendix A, which shows the load-displacement, load to the 2/3 power displacement dependence, and the stress-strain responses for each composition studied.

The relative comparison of each composition shows that the 60 *vol.%* epoxy composite has the greatest toughness and resistance to penetration or hardness. The other

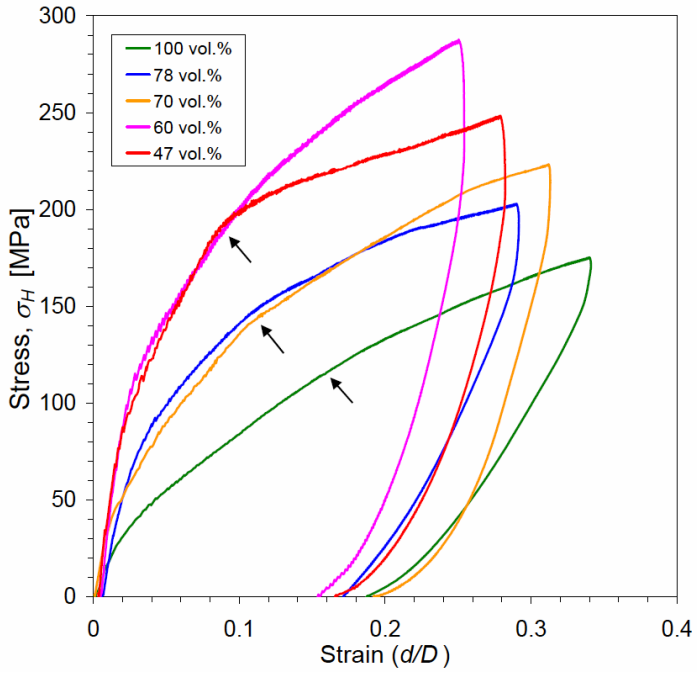


**Figure 4.36** Representative stress-strain curves obtained from continuous indentation experiments for each Al+$Fe_2O_3$ epoxy-cast composite composition. Arrows indicate the approximate viscoplastic yield point locations for each composition.

compositions and pure epoxy show relatively low viscoelastic and viscoplastic yield points as the epoxy concentration increases. Table 4.7 lists the experimentally measured parameters obtained for each composition. The elastic moduli of the specimen, $E_s$, are observed to increase in order as the epoxy concentration decreases. These values compare fairly well with those obtained from quasistatic compression experiments presented next in section 4.3.3. While the elastic moduli measured from the continuous indentation tests and compression tests compared fairly well, the measured yield stresses were typically significantly greater for the indentation experiments of all the compositions except for pure epoxy. This is associated with the significantly small volume sampled during the indentation experiment, which captures the response of the

**Table 4.7** Measured data obtained from continuous ball indentation experiments for Al+$Fe_2O_3$ epoxy-cast composites and pure epoxy (batch *B*). The elastic/plastic limit of each composite is identified by load and displacement values, *P* and *h*, respectively.

| Epoxy [*vol.%*] | $E_r$ [GPa] | $E_s$ [GPa] | $h$ [μm] | $P$ [N] | $\sigma_{y(ve)}$ [MPa] | $\sigma_{y(vp)}$ [MPa] | $H_M$ [MPa] |
|---|---|---|---|---|---|---|---|
| 47 | 11.22 ± 0.72 | 10.84 ± 0.73 | 3.91 ± 1.05 | 3.24 ± 1.20 | 76.90 ± 11.44 | 194.81 ± 10.04 | 250.15 ± 13.16 |
| 60 | 10.40 ± 0.69 | 9.43 ± 0.66 | 4.70 ± 1.09 | 3.95 ± 1.27 | 81.17 ± 34.41 | 196.64 ± 14.21 | 276.69 ± 12.89 |
| 70 | 8.59 ± 0.19 | 7.95 ± 0.18 | 3.38 ± 1.60 | 2.08 ± 1.46 | 40.36 ± 0.38 | 153.70 ± 13.27 | 230.32 ± 10.13 |
| 78 | 5.87 ± 0.45 | 5.04 ± 0.40 | 6.65 ± 2.92 | 3.83 ± 2.31 | 47.83 ± 20.40 | 143.93 ± 18.36 | 198.87 ± 6.73 |
| 100 | 4.22 ± 0.58 | 3.57 ± 0.50 | 10.02 ± 7.20 | 6.01 ± 6.49 | 29.35 ± 9.15 | 128.51 ± 13.63 | 183.63 ± 13.76 |

individual constituents (microscopic response) and their interaction, better than the bulk material response observed from compression experiments (macroscopic response). Continuous indentation tests give a local measure of the composites mechanical properties by probing individual features of the microstructure. However, the pure epoxy specimens are not significantly influenced by the testing technique since the mechanical behavior is relatively continuous throughout the sample space.

Table 4.7 also lists the measured viscoelastic and viscoplastic yield stress values, $\sigma_{y(ve)}$ and $\sigma_{y(vp)}$, respectively, the elastic/plastic transition points identified by the load, *P*, and displacement, *h*, and the calculated Meyer hardness values. The 60 *vol.%* epoxy composite exhibits the greatest Meyer hardness of 276.69 ± 12.89 MPa, followed by decreasing hardness values, in order, for the other compositions containing 47, 70, and

78 *vol.%* epoxy. Pure epoxy had the lowest hardness of 183.63 ± 13.76 MPa. Each of the hardness values were evaluated at the peak load and displacement points for the compositions.

Tabor [181] related the indentation hardness, $H$, to yield stress, $\sigma_y$, according to:

$$H = C\sigma_y \tag{4.16}$$

where $C$, the constraint factor, depends on the ratio of $E/\sigma_y$ of the material. For most metals, for which $E/\sigma_y \geq 100$, the constraint factor has a value of $C \approx 3$ [181]. For small $E/\sigma_y$, *e.g.* for polymers ($E/\sigma_y \geq 10$), the constraint imposed by the surrounding elastic material is relatively small and the indentation hardness is only slightly greater than the material's yield stress, therefore, $C \leq 1.5$ [181]. Table 4.8 compares the yield stress values obtained for each composition from equation (4.16) using a value of 1.5 for $C$ and the viscoplastic yield point identified from the stress-strain behaviors shown in Figure 4.36 and the data available for each indentation test shown in Appendix A.

**Table 4.8** Comparison of yield stress values measured from stress-strain curves and those calculated from equation (4.16) according to measured Meyer hardness values.

| Epoxy [*vol.%*] | *Measured from* $\sigma$-$\varepsilon$ *Curves* | *Tabor* [181] $\sigma_y = H_M / 1.5$ | *% diff.* |
|---|---|---|---|
| | $\sigma_y$ [MPa] | $\sigma_y$ [MPa] | |
| 47 | 194.81 ± 10.04 | 166.78 ± 8.78 | 7.75 |
| 60 | 196.64 ± 14.21 | 184.46 ± 8.60 | 3.20 |
| 70 | 153.70 ± 13.27 | 153.55 ± 6.75 | 0.05 |
| 78 | 143.93 ± 18.36 | 132.58 ± 4.48 | 4.10 |
| 100 | 128.51 ± 13.63 | 122.42 ± 9.17 | 2.43 |

The experimental values listed in Table 4.7 for the continuous indentation experiments were obtained from indents considered to be of "high quality". Each indent was later examined using an optical microscope to identify the uncharacteristic responses observed for some experiments that are not included in the tabulated values. Typically these indents were influenced by the microstructural features such as aluminum and hematite rich areas, which gave significantly large elastic modulus values or yield stresses. In contrast, some indents experienced damage that caused the modulus and yield stress to be significantly low. Figure 4.37(*a*-*d*) shows the measured response for an Al+$Fe_2O_3$+60 *vol.%* epoxy composite with evidence of voids in the contact area of the indent. Figure 4.37(*a*) shows the load-displacement curve, while Figure 4.37(*b*) shows a zoomed view of the elastic loading region. This figure illustrates the indent initally has extremely good contact with the specimen at relatively low applied load, in contrast to the behavior observed in Figure 4.33(*b*) for the same composition. This particular indent has a lower elastic modulus of 6.97 GPa as compared to 9.43 GPa measured from indents that were considered uninfluenced by microstructural features. Additionally, the viscoelastic and viscoplastic yield stresses were significantly lower, having values of 42.76 and 141.89 MPa, respectively. This is compared to the more typical values of 81.17 and 196.64 MPa, respectively. Figure 4.37(*d*) shows the stress-strain response observed for this particular indent exhibiting the significantly low viscoelastic yield point.

The optical micrographs obtained for the two indents discussed previously are shown in Figure 4.38(*a*-*d*). Figure 4.38(*a*) illustrates a view of the remaining indent on the specimen's surface for the case where damage is observed in the contact area.

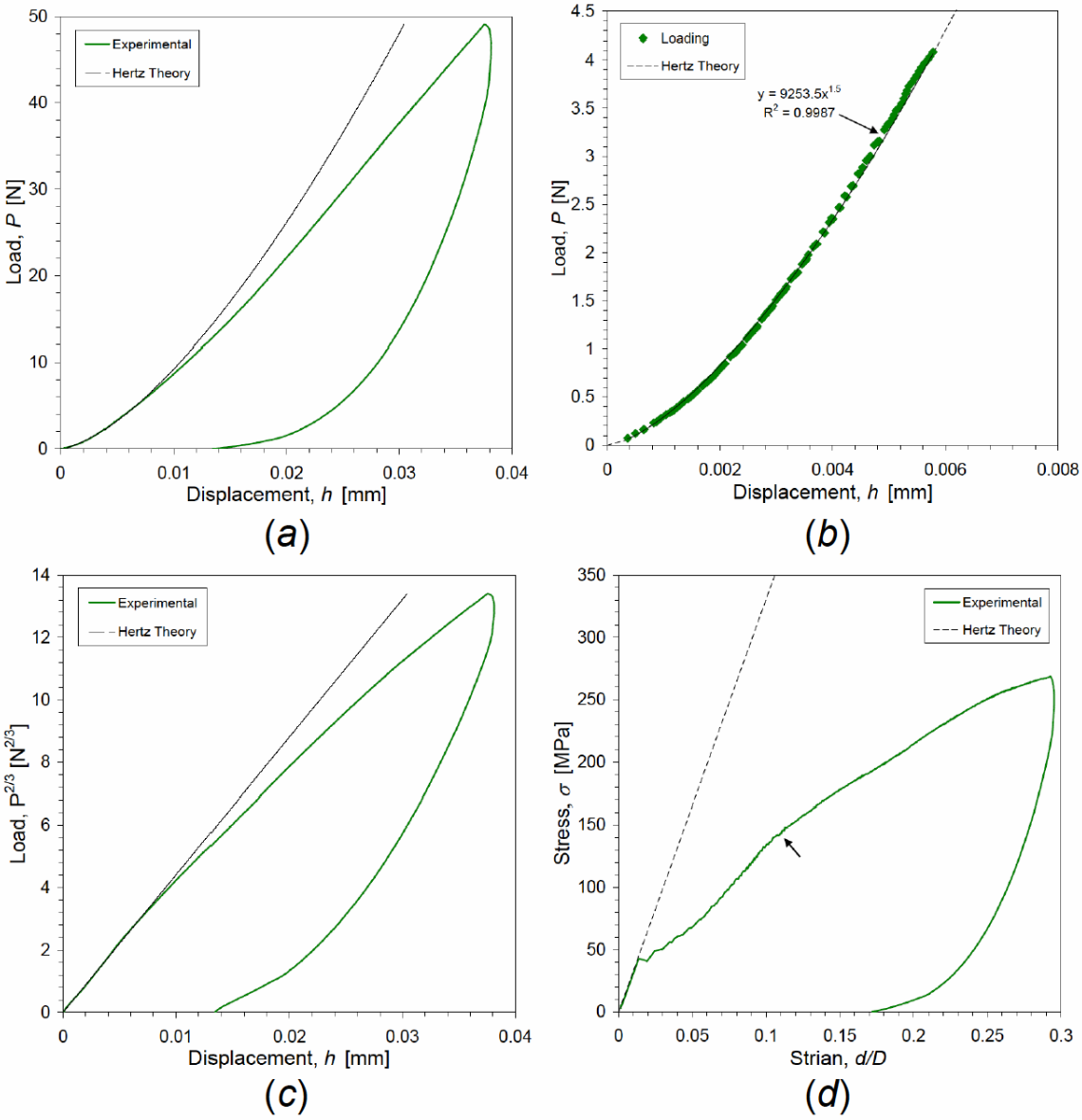


**Figure 4.37** Example of a damaged response observed for continuous indentation test data obtained for Al+$Fe_2O_3$+60 *vol.%* epoxy composite showing *a*) load-displacement and *b*) a zoomed view of the purely elastic loading-displacement region, *c*) load to the 2/3 power displacement dependence, and *d*) the stress-strain response. The stress-strain response typically showed viscoelastic and viscoplastic (indicated by arrow) yield points. Each figure includes the theoretically calculated elastic response obtained from Hertzian contact theory [179].

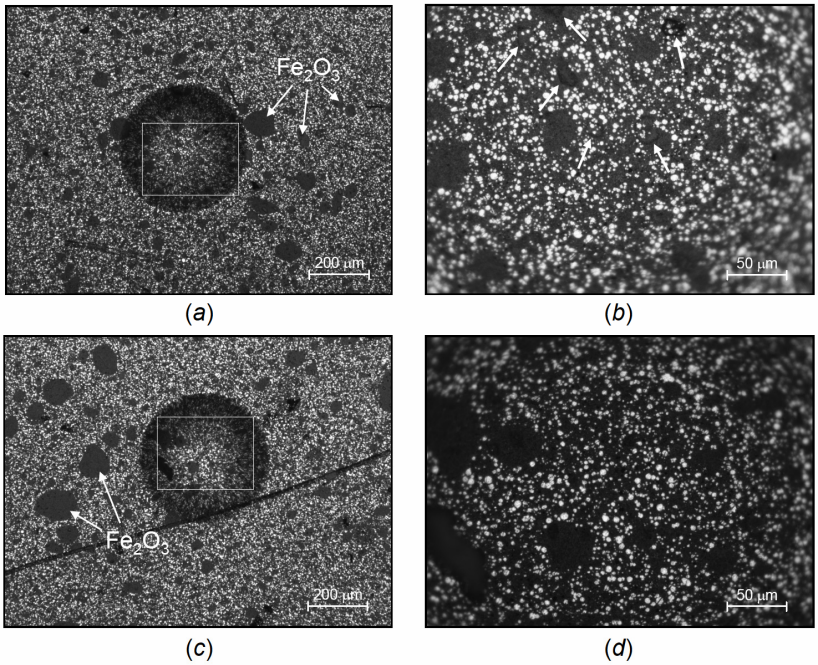


**Figure 4.38** Optical micrographs obtained from continuous indentation experiments for Al+$Fe_2O_3$+60 *vol.%* epoxy composites showing *a,b*) damage corresponding to data obtained from Figure 4.37 and *c,d*) undamaged behavior corresponding to data obtained from Figure 4.33. The indent contact region indicated in *a*) is enlarged in *b*) where the damage is shown by the arrows. Similarly, the indent contact region indicated in *c*) is enlarged in *d*) and observed to have no obvious damage.

Figure 4.38(*b*) shows a zoomed view of the contact area where damage or voids were observed, indicated by the arrows. Similar views obtained for the indent which does not exhibit damage or microstructural features that influence the indentation results, are shown in Figure 4.38(*c,d*). The quality of each indent was evaluated using optical microscopy, as well as precisely measuring the remaining contact diameter. Table 4.9 compares the optically measured diameters to those computed from equation (4.15) and the experimentally measured displacement, *h*. The spherical indentations typically had contact diameters of a few hundred microns and penetration depths resolvable at sub-micrometer dimensions. The optically measured indent diameters were 4.5 to 7.0 %

**Table 4.9** Comparison of indent diameters computed from the projected area measurment and those physically measured using an optical image of the indent.

| Epoxy [*vol.%*] | *Projected Area Measurement* | *Optical Measurement* | *% diff.* |
|---|---|---|---|
| | $d_{proj.}$ [μm] | $d_{opt..}$ [μm] | |
| 47 | 500.78 ± 12.88 | 457.78 ± 13.69 | 4.49 |
| 60 | 475.40 ± 11.23 | 434.22 ± 4.76 | 4.53 |
| 70 | 521.43 ± 10.59 | 458.48 ± 17.70 | 6.42 |
| 78 | 561.01 ± 9.67 | 486.76 ± 2.45 | 7.09 |
| 100 | 584.47 ± 20.77 | 525.51 ± 10.62 | 5.31 |

smaller than those computed. This illustrates the elastic recovery that occurs once the indenter tip is removed from the specimen. The benefit of this type of analysis provides insight into the response and interaction of each constituent that comprise the composite. Furthermore, the indentation tests probe areas large enough to obtain the local response and influence of the microstructural features.

### 4.3.3 Quasistatic Compression and Flexural (Three-Point Bend) Tests

In the present work, epoxy reinforced with energetic particle mixtures are used to toughen and improve the bulk mechanical properties of the composite in addition to providing enhanced energetic attributes. Quasistatic compression and flexural bend tests were performed on each epoxy-cast Al+$Fe_2O_3$ composition, as well as pure epoxy specimens. The true stress-true strain curves obtained from quasistatic compression tests, shown in Figure 4.39, illustrate the effect solid particle fillers have on bulk mechanical properties. These experiments were conducted on five separate specimens (for each

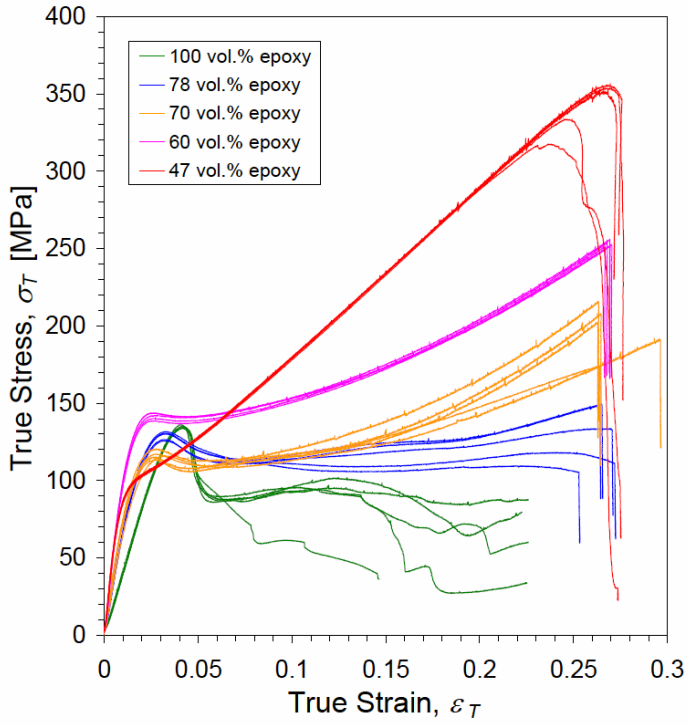


**Figure 4.39** Comparison of true stress-strain curves obtained from compression tests for epoxy-cast Al+$Fe_2O_3$ composites and pure epoxy (batch *B*).

composition) and the contact surfaces (both for the platens and specimen) were lubricated with grease according to ASTM Standard D 695-02a for compression tests of rigid plastics [147]. The specimens did experience some barreling and the tests were stopped at the onset of barreling (approximately 25-30 % strain). Additionally, pure epoxy was also tested and found to experience relatively more barreling than the other filled compositions before observed fracture.

The results indicate that the slope of the elastic region increases with decreasing epoxy concentration. However, the apparent yield points for each composition is less obvious and somewhat scattered, with the 60 *vol.%* epoxy composite showing the greatest, and the 47 *vol.%* epoxy composite having lowest strength, due mainly to a relatively high inherent porosity (4.52 %). Each of the compositions, except for the

47 *vol.%* epoxy composite, experienced an apparent yield point following linear elastic loading. The 47 *vol.%* epoxy composite did not show a defined apparent yield point and began to strain harden immediately upon the onset of yielding until failure occurred at approximately 25 % strain. The 60 and 70 *vol.%* epoxy composites experienced strain softening immediately following the apparent yield point before strain hardening began. In contrast, the 78 *vol.%* epoxy composite displayed strain softening following the apparent yield point with minimal strain hardening and the pure epoxy specimens failed immediately after the apparent yield point (approximately 5 % strain). The comparison of apparent yield points for each composition with pure epoxy did not show an appreciable enhancement from the addition of solid particles. However, the improved elastic modulus and strain hardening effect were the most apparent enhancements from the addition of the reinforcement particles. The addition of particles to the polymer matrix also appears to reduce the inherent brittleness experienced for pure epoxy.

Flexural (three-point bend) tests were conducted using three specimens for each composition and typical true flexural stress-strain curves are shown in Figure 4.40. These results show similar behaviors experienced for quasistatic compression tests in regard to the elastic moduli increasing as the volume fraction of solid particles increase. The elastic moduli determined from flexural experiments have a slightly greater value than those obtained from quasistatic compression tests. However, the measured yield strength from flexural experiments is lower than values obtained from quasistatic compression tests. In general, flexural specimens experience a maximum tensile stress that dictates its overall strength. This difference arises from the flexural specimen being subjected to both compressive (top region of specimen) and tensile (bottom region of

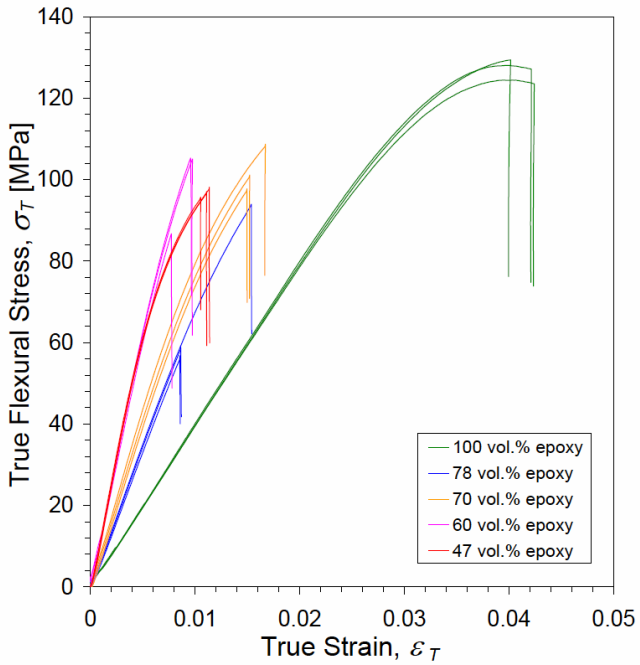


**Figure 4.40** Comparison of true stress-strain curves obtained from flexural (three-point bend) experiments for epoxy-cast Al+$Fe_2O_3$ composites and pure epoxy (batch *B*).

specimen) stresses from the geometry of the experiment, as well as the increased probability of an existing crack-producing flaw that consequently decreases the flexural strength. The modulus of rupture or failure strength is also measured for each composition. It is apparent that the pure epoxy specimen has a significantly higher failure point compared to the particle-reinforced composites. Each of the other compositions have comparable failure strengths with the exception of 78 *vol.%* epoxy composition which exhibits the lowest. This particular batch of material had a moderately high porosity concentration (close to 2 %) with unusually large pores that contributed to the extremely low failure strength. Table 4.10 summarizes the mechanical property measurements obtained from quasistatic compression and flexural (three-point

**Table 4.10** Data summary for compression and flexural (three-point bend) test values obtained for epoxy-cast Al+$Fe_2O_3$ composites and pure epoxy (batch *B*).

| Epoxy [*vol.%*] | *Compression Test* | | *Flexural Test* | |
|---|---|---|---|---|
| | $E$ [GPa] | $\sigma_{yd}$ [MPa] | $E$ [GPa] | $\sigma_{yd}$ [MPa] |
| 47 | 11.83 ± 0.13 | 97.40 ± 1.71 | 12.77 ± 0.18 | 95.93 ± 1.19 |
| 60 | 10.67 ± 0.18 | 141.44 ± 2.27 | 12.48 ± 0.42 | 98.14 ± 10.45 |
| 70 | 7.30 ± 0.29 | 115.88 ± 2.39 | 8.29 ± 0.57 | 100.93 ± 5.42 |
| 78 | 6.60 ± 0.13 | 128.69 ± 2.56 | 6.84 ± 0.29 | 69.19 ± 20.25 |
| 100 | 3.98 ± 0.02 | 133.96 ± 0.38 | 3.92 ± 0.03 | 122.33 ± 2.43 |

bend) tests. It is interesting to note that although the flexural test failure stress was significantly reduced for the 78 *vol.%* epoxy composition with a high concentration of porosity, the elastic modulus calculated from both testing techniques do not appear to show significant deviation.

Representative macroscopic images obtained from the flexural experiment fracture surfaces are shown in Figure 4.41 for each composition. The two halves of the specimen are oriented with the top (compressive stressed region) located at the outer edges and the bottom (tensile stressed region) located at the interior edges. Notice each specimen, except for pure epoxy, has ductile shear lips located near the compressive stress surface. Thorough examination of the fracture surfaces shows that the failure typically occurs in the bottom region where the specimen is loaded in tension and corresponds to the approximate center of the bending span, directly below the concentrated load point. This feature is observed using higher resolution SEM images in Figure 4.42(*a,b*), showing three distinct fracture surface morphology regions originating from the failure initiation site (right side of image). The failure site shows coalescence of

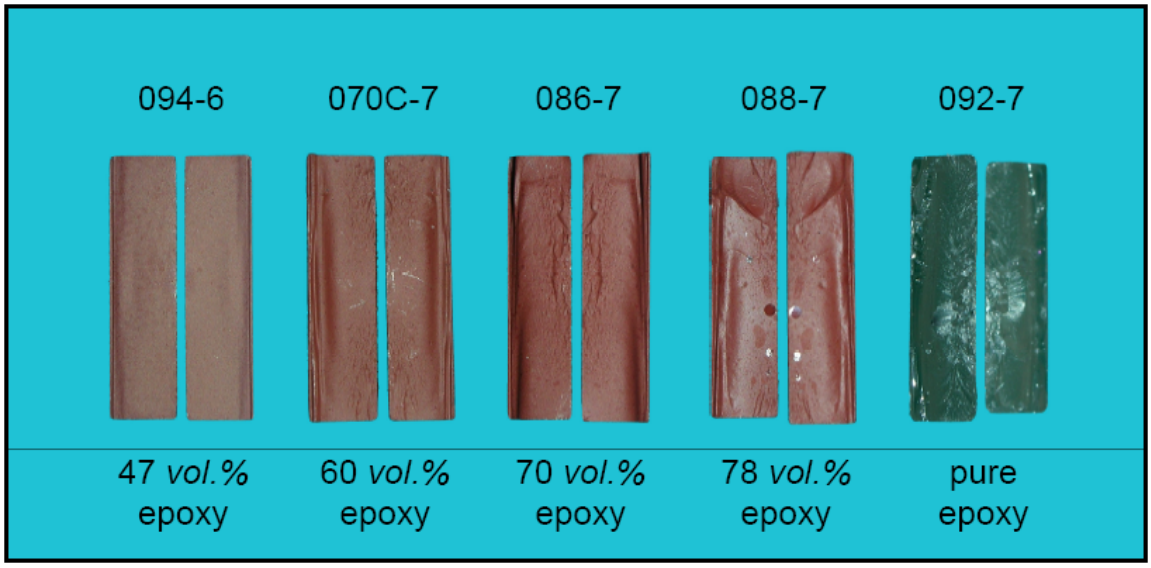


**Figure 4.41** Macroscopic images of fracture surfaces obtained from flexural test specimens. The two specimen halves are oriented side by side with the compressively loaded region on the outer edges and the tensile loaded region located at the interior edges.

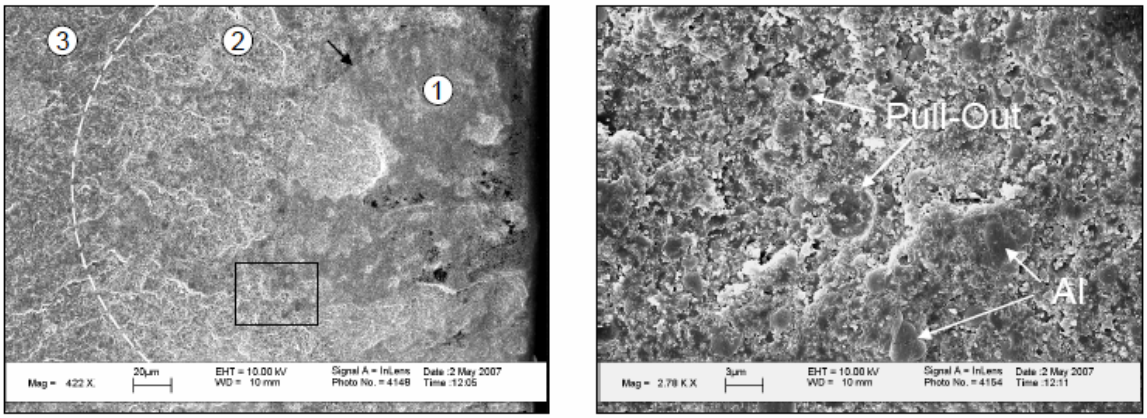


**Figure 4.42** Flexural specimen fracture surface showing *a*) three distinct fracture surface morphology regions originating from the failure initiation site (right side of image). Dark contrast areas within the mirror zone (region '1') are void formations close to the fracture initiation site. Region '2' consists of debonded and plastically deformed aluminum particles, while region '3' has a relatively rough fracture surface with no evidence of deformed aluminum particles. Deformed aluminum particles and pull-out sites are shown at a higher magnification in *b*) for a location just beyond the mirror zone indicated by the box in *a*).

porosity within an obvious mirror zone (region '1') defined by a radial marking emanating from the initiation site. Beyond the radial mark (region '2'), the fracture zone consists of debonded aluminum particles from the matrix and plastic deformation of other aluminum particles. A higher magnification image outside the mirror zone in Figure 4.42(*b*) shows both matrix decohesion and plastic deformation of aluminum particles. This region is followed by a fracture surface morphology generally attributed to fast crack propagation (region '3') and possesses no evidence of aluminum particle pull-out from the matrix.

Similarly, pure epoxy specimens show fracture initiation occurs in the tensile loaded region with evidence of initial relatively slow crack propagation in this region. However, these samples also show a crack transition region closer to the center of the specimen's rectangular cross section, approximately one-third away from the bottom surface. The pure epoxy specimens have fascinating fracture surfaces with highly defined feature morphologies indicating mostly brittle fracture. These features are illustrated in Figure 4.43(*a*-*d*), where a relatively low resolution image shows a significant *a*) mirror zone at the fracture transition zone surrounded by fast crack propagation regions with distinctive "fish-scale" features on one side and slower propagating crack region on the tensile loaded side of the specimen. It is believed that these fish scale features are associated with the precursor of secondary cracks formed ahead of the main crack or craze [182]. Additional crazing regions are also apparent near the compressively loaded area showing "stress-whitening" features also indicated in Figure 4.43(*a*). A higher resolution image of this region in *d*) shows a significant concentration of "crumbled" clusters of the polymer attributed to the initial plastically

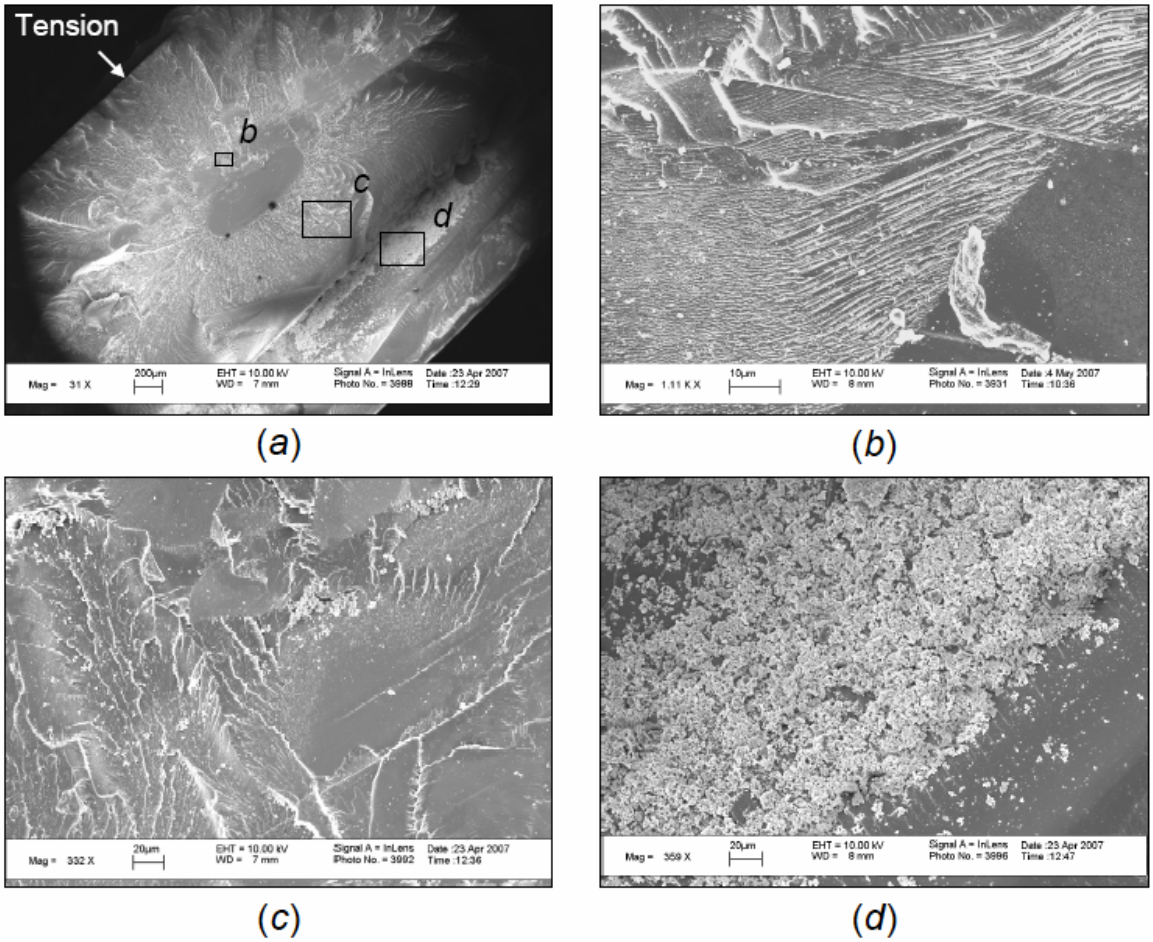


**Figure 4.43** Typical SEM images obtained from the fracture surface of pure epoxy, showing *a*) the complete thickness of the flexural (three-point bend) specimen. The crack initiates at the tensile loaded side of the specimen, indicated in *a*), and propagates relatively slowly until reaching the mirror zone (approximately one-third from the tensile loaded region). Location *b*) is within the slow crack propagation region showing evidence of flow lines that indicate shear yielding and cold drawing in close proximity to the failure origin. The specimen undergoes catastrophic failure and proceeds rapidly, where region *c*) exhibits highly defined hackles and river markings, associated with brittle fracture. Region *d*) shows "crumbled" clusters of the polymer attributed to the initial plastically formed crazes and localized heating.

formed crazing and localized heating. The pure epoxy specimen also has flow lines that indicate shear yielding and cold drawing in close proximity to the failure origin, illustrated in Figure 4.43(*b*). Pure epoxy fracture surface shown in Figure 4.43(*a*) also exhibits regions that contain highly defined hackles and river markings, shown up-close in Figure 4.43(*c*), in addition to arrest lines and striations. The striations are said to be formed by the break-up of the crack front as the crack grows through a plastic zone which is constrained by the elastically deformed material [183].

The fracture surfaces of the flexural specimens indicate several different strengthening mechanisms that contribute to the overall resistance to failure for the particle-filled composites. For particle-reinforced composites, these mechanisms include crack pinning, decohesion of particles from the matrix, which also introduces crack tip blunting [183]. Examination of the other composition's fracture surfaces shows similar features and fracture morphologies highlighted in Figure 4.42(*a*). However, decohesion of the hematite particles was not observed for any of the composite's fracture surfaces. A qualitative trend is observed for the different compositions, showing decohesion of the matrix from the solid aluminum filler particles becomes less apparent as the filler volume fraction increases. Figure 4.44(*a*) shows the high concentration of aluminum particle and matrix decohesion for the 78 *vol.%* epoxy composite, while, Figure 4.44(*b*) shows a higher magnification image of this region, indicating several sites where aluminum particles were once located and some aluminum particles that show clear decohesion form the matrix. Additionally, deformation of the aluminum particles was not apparent for this particular composition, but the unusually high amount of porosity for this specific batch of material is evident in the image. Figure 4.44(*c*) shows the fracture surface of the

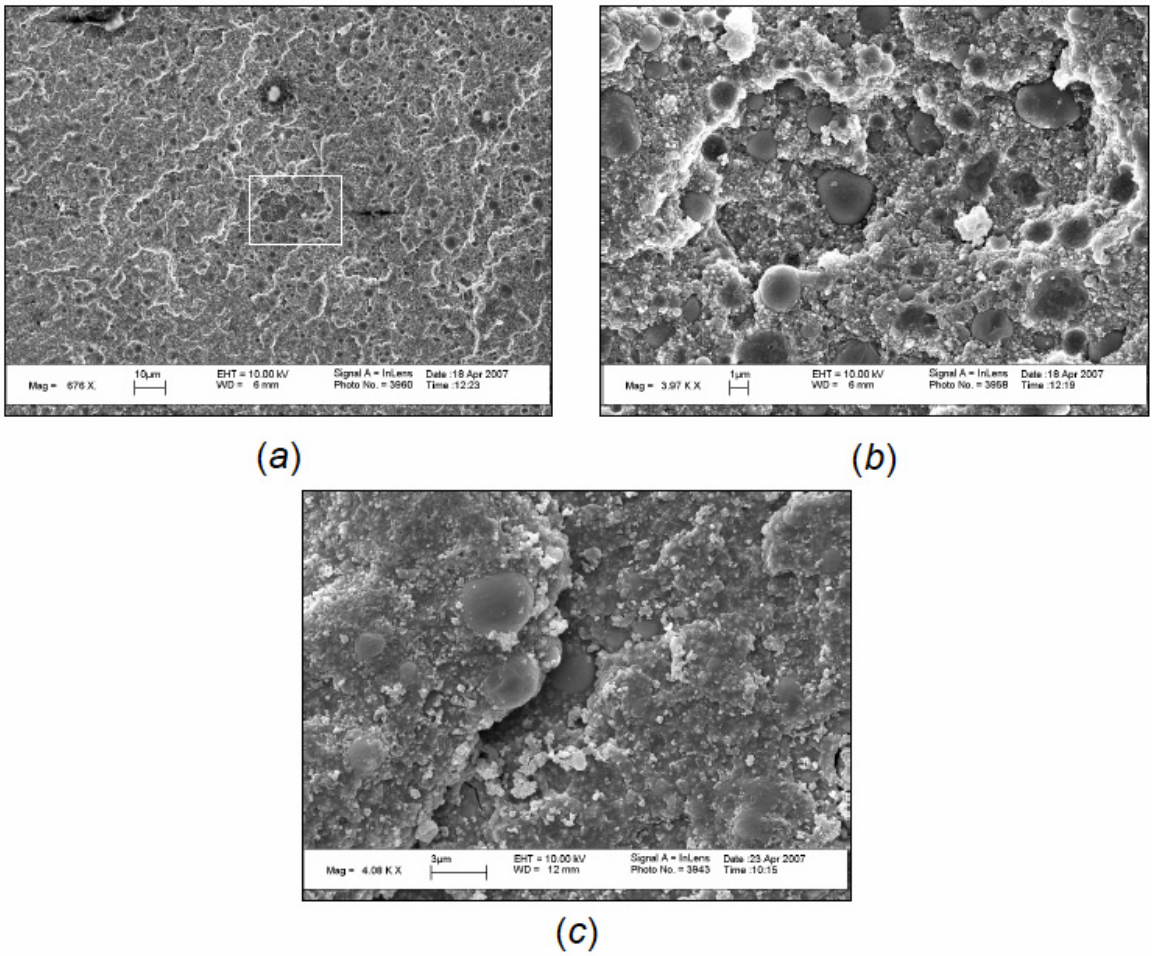


**Figure 4.44** Flexural specimen fracture surface for Al+$Fe_2O_3$+78 *vol.%* epoxy composite containing extensive *a*) pore regions and particle pull-out sites. Higher magnified regions show *b*) aluminum pull-out sites and porosity for the area identified in image *a*), while *c*) shows aluminum particles with good epoxy matrix adhesion for Al+$Fe_2O_3$+60 *vol.%* epoxy composite.

60 *vol.%* epoxy composite, representing a surface that illustrates the aluminum particles have better adhesion with the matrix and less tendency to pull-out.

Theoretically calculated values were also obtained from various rule of mixture models and compared to experimental results discussed previously. These models included simple mechanics of materials approach which assumes each phase of the composition experiences the same strain (Voigt model) or the same stress (Reuss model). This yields results that give a considerable overestimate of the composite's elastic modulus, for example, using the Voigt model or somewhat underestimated using the Reuss model. However, neither model provides an accurate enough prediction of the material response to quasistatic loading.

Other models, such as that proposed by McGee and McCullough [184], provide a more realistic approach that deals with the internal distribution of stress and strain. The model considers two extreme behaviors with upper and lower bounds. The lower bound of the calculated modulus considers a dispersion of solid filler particles as a continuous polymer matrix. The upper bound calculation considers inclusions of the polymer in a continuous phase using material properties of the filler material. From these extremes, the composite's bulk and shear moduli can be calculated from elastic material constants obtained for the polymer and filler. The elastic modulus is obtained from these values ($K$ and $\mu$) and the isotropic material identities listed in Table 3.4. The measured elastic moduli obtained from compression and three-point bend tests are compared to theoretically calculated values and shown in Figure 4.45. The Voigt model is not included in this plot since it is the simplest model and gives an extremely large overestimate of elastic modulus. However, the McGee and McCullough [184] approach

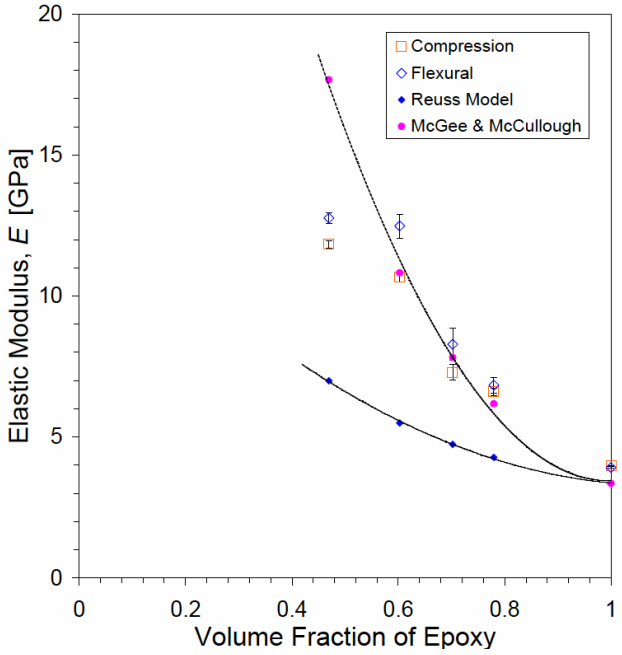


**Figure 4.45** Variation of elastic modulus values measured for composites containing different epoxy volume fractions, obtained from compression and flexural bend experiments, and compared to theoretical curves based on the Reuss model and a model proposed by McGee and McCullough [184].

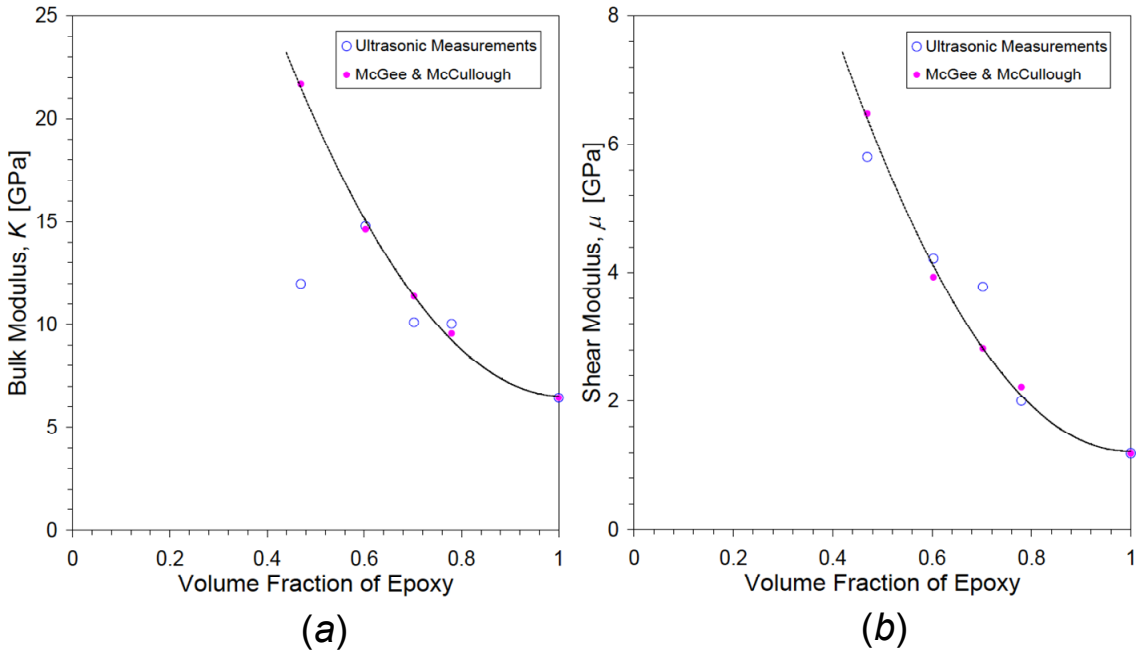


**Figure 4.46** Calculated *a*) bulk and *b*) shear moduli values ($K$ and $\mu$, respectively) obtained from ultrasonic measurements and compared to theoretical curves based on a model proposed by McGee and McCullough [184].

presents excellent agreement for both experimentally determined elastic moduli obtained from compression and flexural tests. Notice that the elastic modulus reaches a "saturation-point" and remains fairly constant above a specific solid particle filler concentration which corresponds to 60 *vol.%* epoxy. The inherently large concentration of porosity for the 47 *vol.%* epoxy composite also contributes significantly to this effect. The theoretical bulk and shear moduli are plotted and compared to ultrasonically measured values for each composition in Figure 4.46(*a*,*b*). There is extremely good agreement between these values and, interestingly the shear modulus shows no significant deviation for the 47 *vol.%* epoxy composition, which has the highest concentration of solid particle filler material. However, the bulk modulus shows a very significant effect at this concentration and reduces the compressibility of the material by approximately half the theoretically predicted value.

### 4.3.4 Charpy Impact Experiments

Charpy impact experiments were conducted to measure the fracture resistance of the epoxy-cast composites. The blunt notch cut in the specimen produces a stress concentration that promotes brittle fracture. The test apparatus measures the net energy absorbed by the specimen from the impact and subsequent breakage. This process includes the dissipation of energy from plastic deformation prior to fracture as well as the energy associated with crack nucleation and propagation. The specimen's resistance to impact, $I_S$, is reported as the energy per unit area [J/m$^2$], where the area is the cross-sectional area under the notch. The net breaking energy must be less than 85 % the

pendulum capacity for the test to be valid. For these experiments, the pendulum capacity was fixed at 0.223 J and all the tests resulted in the specimen completely breaking from a single impact.

The measured impact resistance obtained for each of the Al+$Fe_2O_3$+epoxy composites and pure epoxy specimens is shown in Figure 4.47. The impact resistance for each of the composites appear to show very little variation with solid particle fill and have an average value of 825.6 ± 64.8 J/m$^2$. Examination of fracture surfaces indicates these specimens exhibit mostly brittle fracture. Conversely, the pure epoxy specimens have a significantly higher average impact resistance of 1339.1 ± 97.2 J/m$^2$ that may be

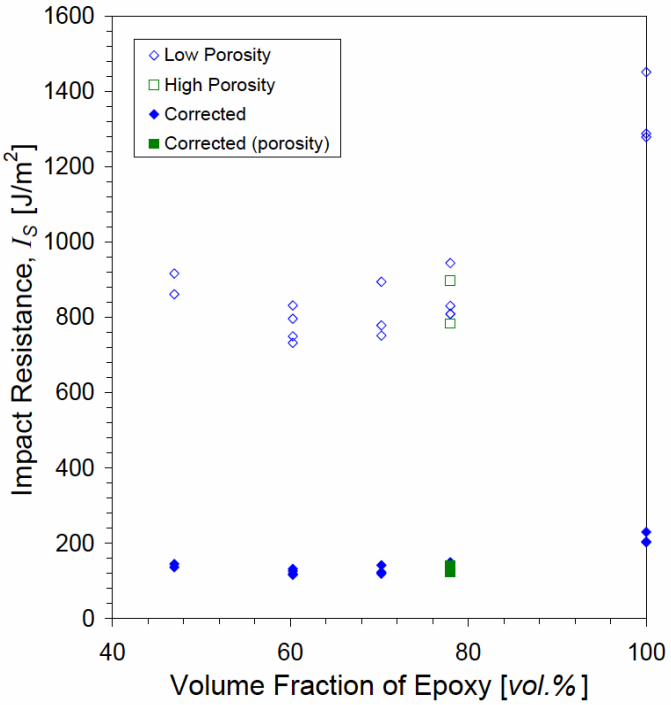


**Figure 4.47** Measured impact resistance, $I_s$, values obtained from Charpy tests for epoxy-cast Al+$Fe_2O_3$ composites and pure epoxy. Experimental values obtained for a relatively high porosity batch of Al+$Fe_2O_3$+78 *vol.%* epoxy composite are also identified. Blunt notch "corrected" impact resistance values are also shown, gradually increasing with increasing volume fraction of epoxy.

attributed to a considerable amount of ductile fracture that occurs towards the later stages of failure. Figure 4.47 also contains impact resistance values obtained for two different 78 *vol.%* epoxy composite batches that have significantly different concentrations of porosity. However, the introduction of porosity does not appear to have a significant effect on the measured impact resistance values.

Impact resistance values obtained from Charpy experiments are a measure of energy required to form new surfaces, and therefore should have a relationship with the critical energy release rate, $G_{IC}$. However, there are several significant differences between the Charpy test and fracture mechanics tests that preclude their direct correlation. For example, the Charpy specimen contains a blunt notch, while fracture mechanics specimens have sharp fatigue cracks. Plati and Williams [185] have derived a relationship between the impact resistance from a blunt-notched specimen and that containing a sharp crack. They showed that for many polymers, a linear relationship exists between the two specimen configurations resulting in a constant value of $G_{IC}$. This is given by [185]:

$$\frac{G_{IB}}{G_{IC}} = \frac{\left(1+\frac{\rho}{2r_p}\right)^3}{\left(1+\frac{\rho}{r_p}\right)^2}, \qquad (4.17)$$

where $G_{IB}$ and $G_{IC}$ are energy release rates for a blunt-notched specimen and a specimen containing a sharp crack, respectively; $\rho$ is the notch radius and $r_p$ is a critical distance ahead of the crack tip where fracture occurs (plastic zone size). If $\rho$ is significantly

greater than $r_p$, equation (4.17) reduces to [185]:

$$\frac{G_{IB}}{G_{IC}} = \frac{1}{2} + \frac{\rho}{8r_p}, \tag{4.18}$$

The notch radius, $\rho$, and the critical energy release rate for a blunt notch, $G_{IB}$, are directly measured for Charpy impact experiments performed on the epoxy-cast composites and pure epoxy. However, the plastic zone size, $r_p$, is not easily measurable and must therefore be approximated from known material parameters for pure epoxy. The plastic zone size at the tip of a crack is given by [185,186]:

$$r_p = \frac{\pi}{8}\frac{K_{IC}^2}{\sigma_y^2}, \tag{4.19}$$

where the critical stress intensity factor, $K_{IC}$, is equal to 0.5 $\text{MPa}\sqrt{\text{m}}$ [187,188]; and the yield stress, $\sigma_y$, is equal to 134 MPa measured from compression experiments discussed in section 4.3.3. These values correspond to a plastic zone size of 5.47 μm.

The calculation of "corrected" Charpy impact energies from blunt-notched specimens using equations (4.18) and (4.19) are also shown in Figure 4.47. These values represent a significant reduction in measured impact energies that now correspond more appropriately with values obtained from traditional linear elastic fracture mechanics (LEFM) testing techniques. The critical energy release rates, $G_{IC}$, for the particle-filled composites ranged between 123.3 ± 7.2 (60 *vol.%* epoxy) and 141.0 ± 6.1 $\text{J/m}^2$ (47 *vol.%* epoxy), while pure epoxy specimens were 212.4 ± 15.4 $\text{J/m}^2$. For reference,

the typical value of $G_{IC}$ obtained for PMMA is 500 J/m$^2$ [187,189], that of a highly brittle material such as glass is 7-10 J/m$^2$ [189], and very tough polymers such as polycarbonate have an average value of 4000 J/m$^2$ [189]. A reference value obtained for pure epoxy was 100 J/m$^2$ [187,190], although the exact resin and hardener chemistry was not listed. It is difficult to directly compare different epoxy materials because of a broad choice of resins and hardener chemistry, curing procedures, and even batch-to-batch variability. The difference between reference and measured energy release rates for pure epoxy may be attributed to physical differences in the epoxy makeup or ductile deformation behavior occurring near the tip of the advancing crack, which is not accounted for in the analysis presented by Plati and Williams [185]. The Charpy impact strengths are found to be quite sensitive to the polymer composition. A peak in impact strength, reported by Kim, *et al.* [191], corresponded to an excess of amine curing agent over the stoichiometric composition. The examination of fracture surfaces for pure epoxy also indicate that ductile yielding and possibly thermal softening may have occurred towards the latter stages of the fracture advancement, also contributing to an increase in measured energy release rates. Furthermore, the fracture surfaces for pure epoxy show evidence of crazing at the crack tip which can cause the specimen to also exhibit higher energy release rate values [192].

Figure 4.48 shows macroscopic images of each composition's fracture surface. The two halves of the specimen are oriented top to bottom with the notch located towards the center. The pure epoxy specimen exhibits so-called Wallner lines that emanate from the notch surface discontinuity and move almost completely across the specimen. While all the specimens appear to exhibit mostly brittle fracture, pure epoxy specimens have

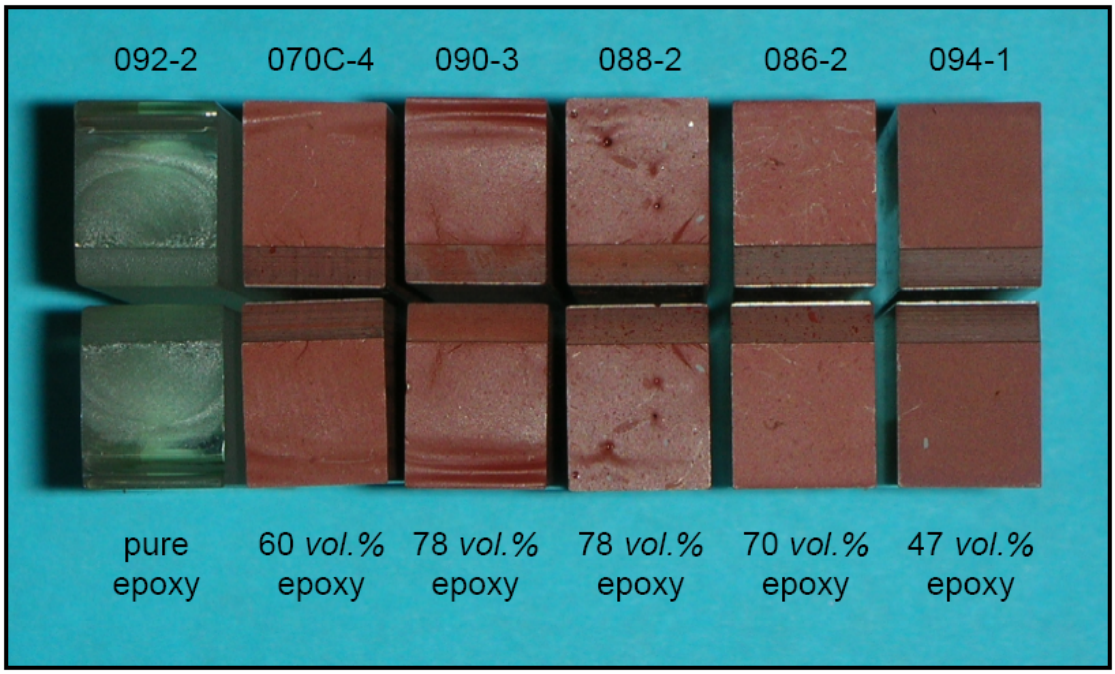


**Figure 4.48** Macroscopic fracture surface images obtained from Charpy impact experiments conducted on epoxy-cast Al+$Fe_2O_3$ composites and pure epoxy. Each half of the fractured sample is oriented top to bottom with the notch located at the interior edges.

significant ductile shear lips located near the impact location (opposite of the notch) on the specimen. The Wallner lines help define where the ductile deformation region begins. Although less evident, shear lips are also observed for 78 *vol.%* (low porosity batch) and 60 *vol.%* epoxy specimens. The macroscopic images also show details of the higher porosity 78 *vol.%* epoxy composite batch with a cross-sectional view of the inherent pores, in addition to relatively large aluminum and hematite agglomerate sites. Comparison of the two types of specimens indicates, qualitatively, that the higher porosity specimen exhibits relatively more brittle behavior.

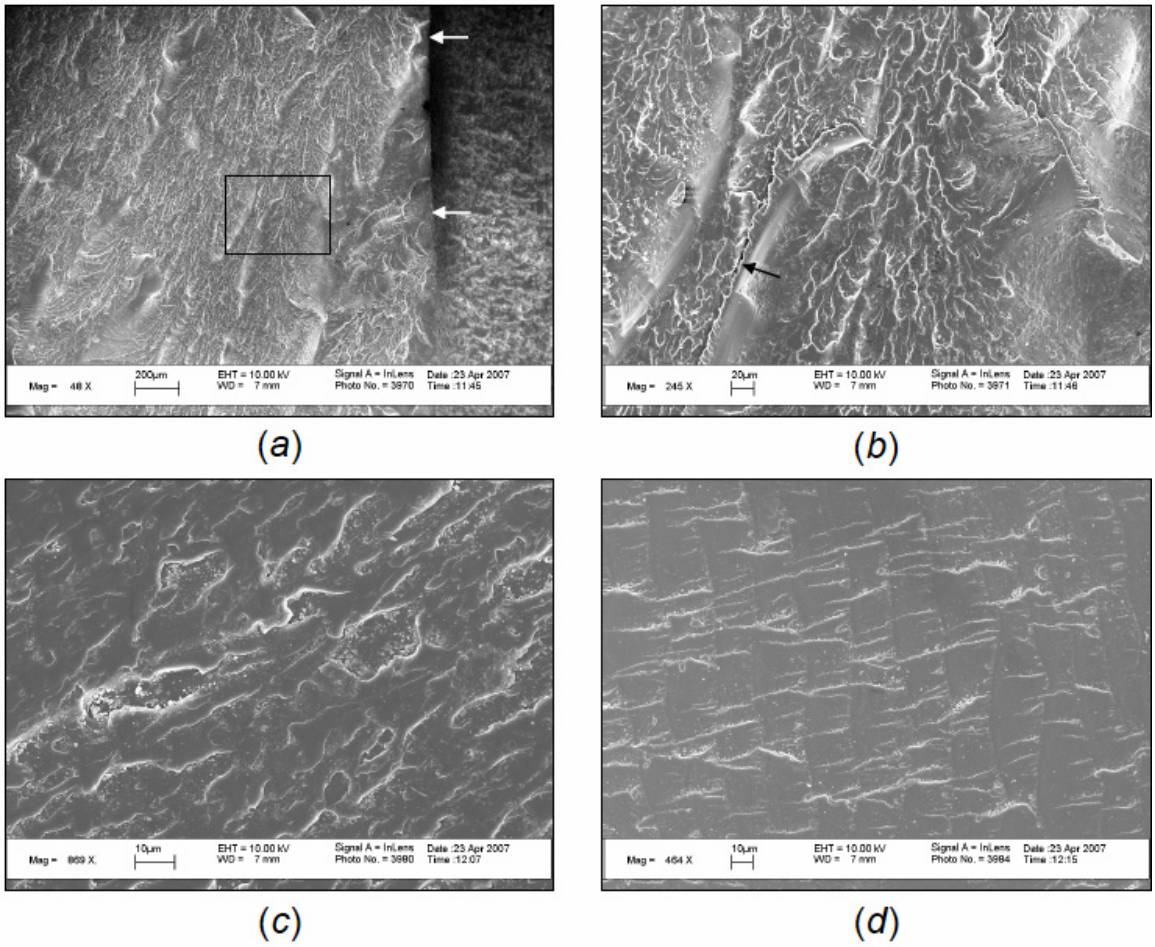


**Figure 4.49** Typical SEM images obtained from Charpy impacted fracture surfaces for a pure epoxy specimen showing characteristic "fish scale" crack advancement features. Images show the fracture signature at different locations through the thickness of the sample, starting with the *a*) fracture initiation site along the notch (indicated by arrows) and followed by a location close to the *c*) middle and *d*) end of the sample's thickness. A band of rapidly advancing fracture front is separated by a region where the craze has been stripped off (dark contrast region indicated by arrow) is shown in *b*) for the area indicated in *a*).

Typical SEM images obtained for pure epoxy fracture surfaces are shown in Figure 4.49(*a-d*) and indicate the features observed along the entire fracture surface. The direction of crack propagation is from right to left for all of the images. The fracture surface in Figure 4.49(*a*) shows a fast crack propagation region with the distinctive "fish scale" feature emanating from the initiation site (upper right corner of the image). The specimen's blunt notch edge is indicated by the arrows in the image. A close up region from Figure 4.49(*a*), shown in Figure 4.49(*b*), gives a more detailed view of the fracture surface features and indicates a band of crazes separated by a region where the craze has been stripped off (dark contrast region indicated by arrow). Images also show the fracture advancement at the approximate center of the specimen (through thickness) and towards the end in Figure 4.49(*c,d*), respectively. During the terminal stage of fast fracture, the crack front outpaces the craze tip, identified by hackle bands. The crack advances by propagating through one bundle of crazes, at which point a new bundle is formed and the process is repeated [193].

Examination of fracture surfaces for the epoxy-cast Al+$Fe_2O_3$ particle-filled composites typically showed craze features in a patch type pattern. These are illustrated in Figure 4.50(*a-c*) for 60 and 70 *vol.%* epoxy composite compositions. The other compositions examined also exhibited a similar patch pattern. Figure 4.51(*a-d*) shows a higher magnification of the typical fracture surfaces observed for the particle-filled composites. In some cases, the aluminum particles deformed and inhibited the advancement of the fracture front. This was observed for the 47 *vol.%* epoxy composition and shown in Figure 4.51(*a*). The arrows point to craze regions along the boundary of aluminum particles. A closer view of the craze region identified in

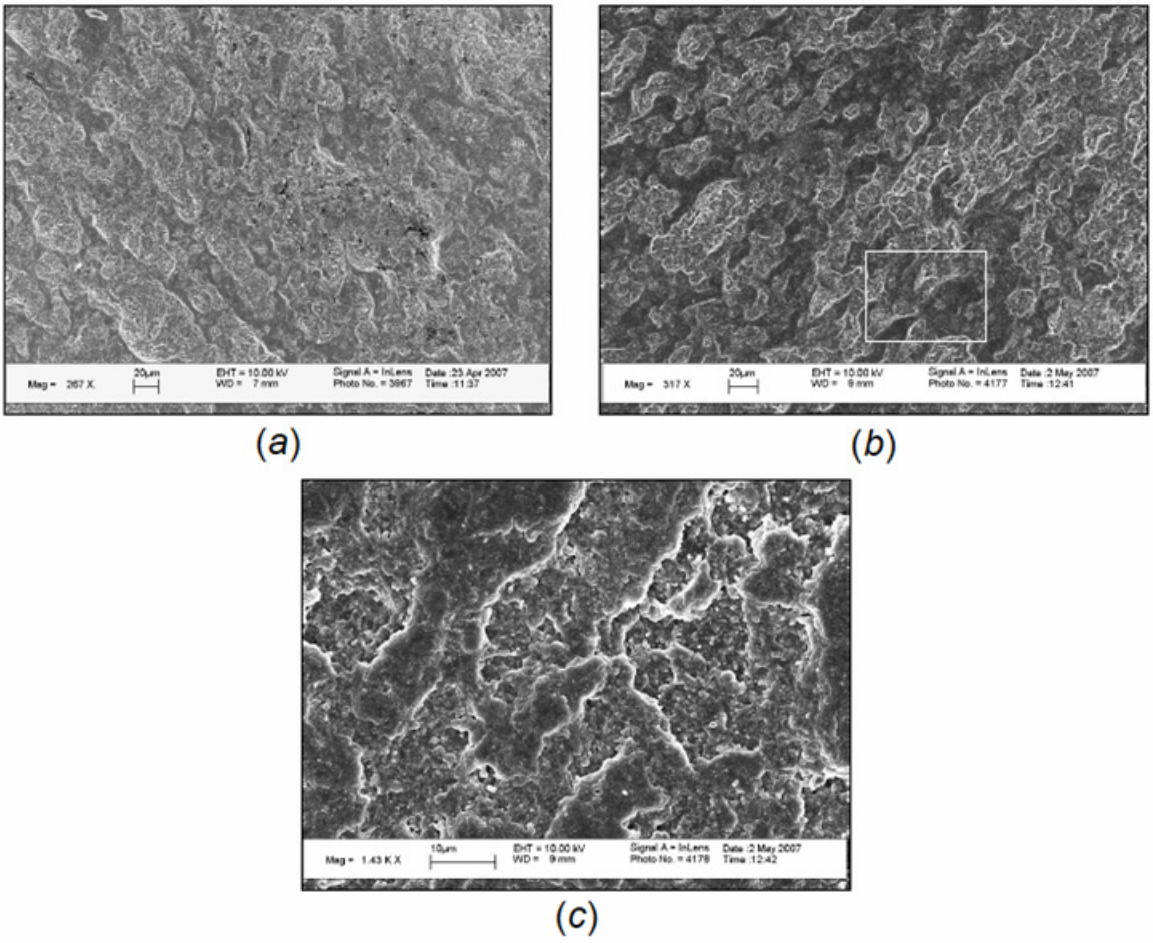


**Figure 4.50** Typical fracture surfaces for particle-filled Al+$Fe_2O_3$ composites with *a*) 60 *vol.%* and *b*) 70 *vol.%* epoxy, exhibiting a patch pattern from a rapidly advancing crack front. A higher magnified region identified in *b*) is shown in *c*).

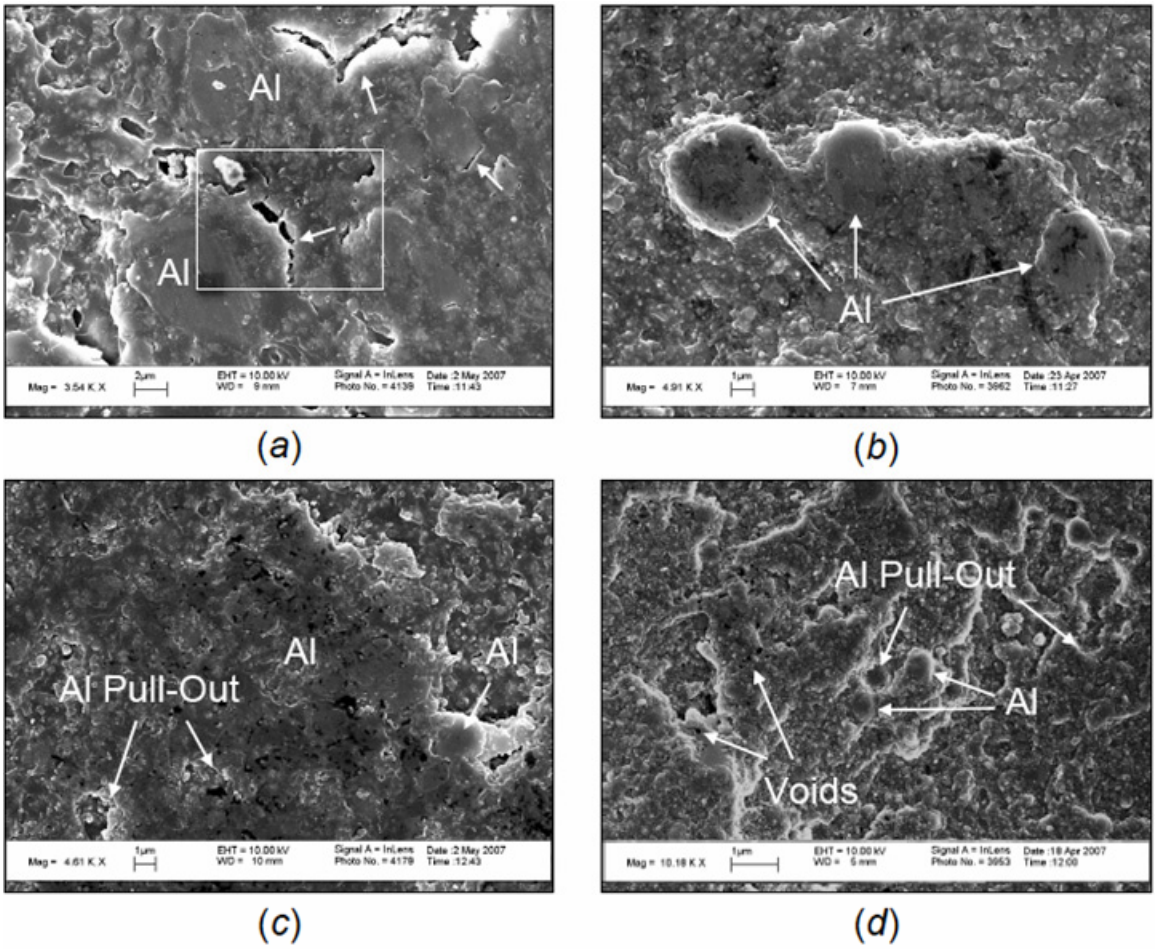


**Figure 4.51** Charpy impact fracture surfaces for epoxy-cast Al+$Fe_2O_3$ composites with *a*) 47, *b*) 60, *c*) 70, and *d*) 78 *vol.%* epoxy. Deformed aluminum particles and craze regions (indicated by arrows) were typically found for the 47 *vol.%* epoxy composition, while the 60 and 70 *vol.%* epoxy compositions showed a mixed behavior exhibiting both particle pull-out and deformation. Conversely, the 78 *vol.%* epoxy composition showed no evidence of deformed particles and only particle pull-out.

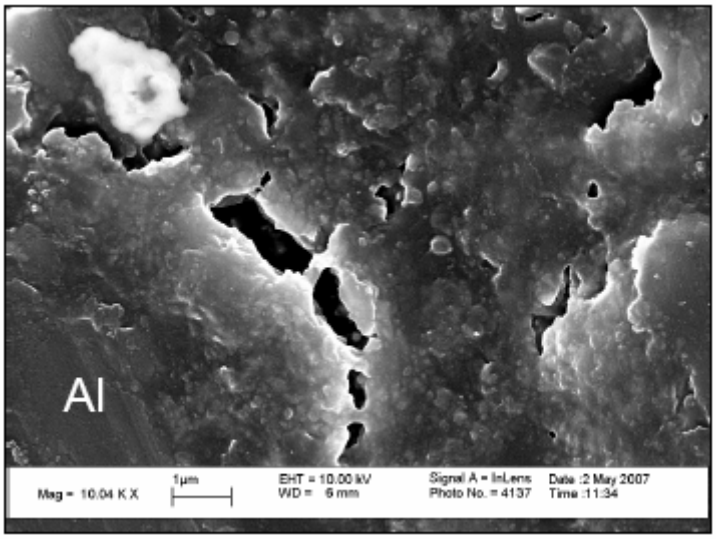


**Figure 4.52** Close-up view from a region in Figure 4.51(*a*) showing craze formations around a deformed aluminum particle.

Figure 4.51(*a*) is shown in Figure 4.52. Other compositions, such as 60 and 70 *vol.%* epoxy, had a mixed response, where evidence of aluminum particles deforming (to a lesser degree than the 47 *vol.%* epoxy composition) and aluminum particle pull-out was observed. These features are shown in Figure 4.51(*b,c*) for 60 and 70 *vol.%* epoxy, respectively. Figure 4.53 shows a region where aluminum particles have been removed and pulled-out for the 60 *vol.%* epoxy composition. In contrast, the 78 *vol.%* epoxy composite typically showed no evidence of deformed particles, and only particle pull-out was observed as illustrated in Figure 4.51(*d*).

The failure of a material is associated with the concentration of stresses in the vicinity of flaws. Therefore, it is desirable to relate material toughness in terms of resistance to crack propagation (in addition to $\sigma_y$ and $E$). There are two material parameters in fracture mechanics that define the material's ability to resist crack propagation; the energy release rate, $G$, and the stress intensity factor, $K$. At the moment

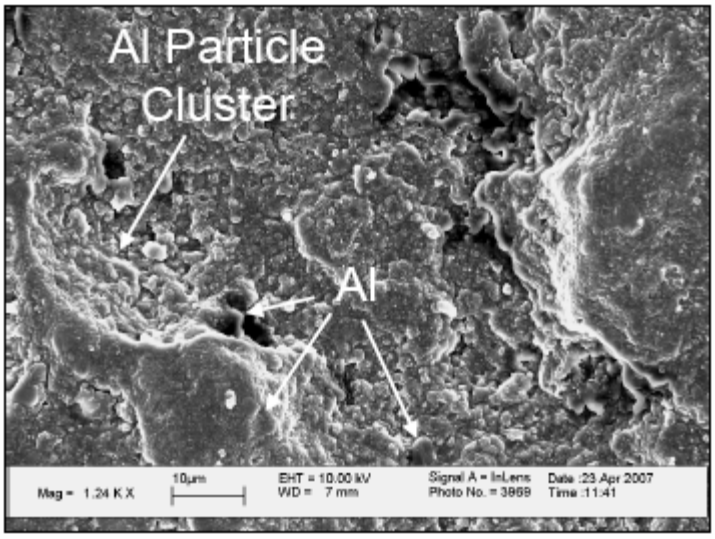


**Figure 4.53** Charpy impact fracture surface for Al+$Fe_2O_3$+60 *vol.%* epoxy showing clustered aluminum particles pull-out site and remaining individual aluminum particles in close proximity.

of fracture, the energy release rate is equal to the critical energy release rate ($G = G_C$). According to the Griffith energy criterion [194], fracture occurs when the energy available for crack growth is sufficient to overcome the resistance of the material. Conversely, the stress intensity approach assumes a material fails locally at a critical combination of stress and strain, and therefore fracture occurs at the critical stress intensity, $K_{IC}$. The energy and stress intensity approaches are essentially equivalent and can be related through [194]:

$$G_{IC} = \frac{K_{IC}^2}{E}, \tag{4.20}$$

where $E$ is the elastic modulus.

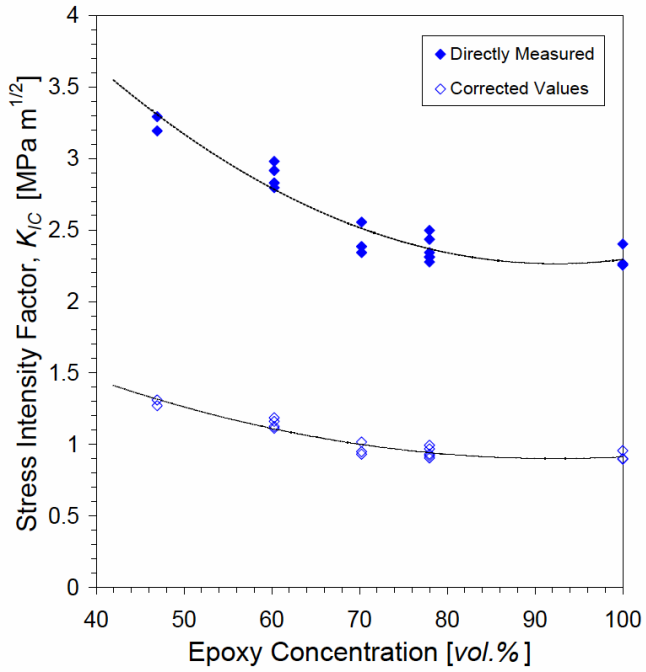


**Figure 4.54** Critical stress intensity values obtained from Charpy impact experiments for epoxy-cast Al+$Fe_2O_3$ composites and pure epoxy showing both directly measured and blunt notch "corrected" values.

The energy release rates calculated from equation (4.18) and shown in Figure 4.47 are used to estimate fracture toughness according to equation (4.20), and are plotted in Figure 4.54 as a function of epoxy concentration for each type of composite and reference pure epoxy. The addition of rigid particles to a relatively brittle polymeric matrix can significantly affect the $K_{IC}$ and $G_{IC}$ values. Figure 4.54 shows that the $K_{IC}$ increases for increasing filler volume fraction. The fracture toughness values range between 2.3 and 3.2 $\text{MPa}\sqrt{\text{m}}$ using directly measured impact resistance values, while the "corrected" fracture toughness values range between 0.9 and 1.3 $\text{MPa}\sqrt{\text{m}}$. As reference, the fracture toughness value listed for pure epoxy is 0.5 $\text{MPa}\sqrt{\text{m}}$ [187,188].

It is convenient to classify materials in terms of a toughness/strength ratio rather than merely toughness or strength alone. Table 4.11 lists calculated toughness/strength

**Table 4.11** The ratio of fracture toughness ($K_{IC}$ "corrected" values) to flexural strength (three-point bend test) is listed in descending order according to brittleness.

| Epoxy [*vol.%*] | $K_{IC}$ [MPa $\sqrt{\text{m}}$] | $\sigma_f$ [MPa] | $K_{IC}/\sigma_f$ [$\sqrt{\text{m}}$] |
|---|---|---|---|
| 100 | 0.918 ± 0.033 | 122.33 ± 2.43 | 0.008 ± 0.0003 |
| 70 | 0.966 ± 0.045 | 100.93 ± 5.42 | 0.010 ± 0.001 |
| 47 | 1.291 ± 0.028 | 95.93 ± 1.19 | 0.013 ± 0.0003 |
| 78 | 0.940 ± 0.034 | 69.19 ± 20.25 | 0.014 ± 0.004 |
| 60 | 1.147 ± 0.033 | 98.14 ± 10.45 | 0.017 ± 0.001 |

($K_{IC}/\sigma_f$) ratios for each composition in descending order from the most brittle to the most ductile using "corrected" $K_{IC}$ and flexural strength values obtained from three-point bend tests. These values are compared to materials traditionally thought of as being highly brittle and relatively ductile, such as glass (0.005 $\sqrt{\text{m}}$ [189]) and low-carbon steel (0.60 $\sqrt{\text{m}}$ [189]), respectively. The toughness/strength ratios listed in Table 4.11 provide a gradual ranking for the particle-filled epoxy-cast composites evaluated in this study. Pure epoxy is positioned at the top of the list with a relatively brittle behavior, close to that of glass. However, the addition of solid particles to the epoxy matrix lessens the brittleness and the Al+$Fe_2O_3$+60 *vol.%* epoxy composite ranks close to that of PMMA (0.02 $\sqrt{\text{m}}$ [189]). For additional reference, extremely tough polymers such as polycarbonate have a value of 0.05 $\sqrt{\text{m}}$ [189].

Failure in polymeric materials may occur in a brittle or a ductile manner. The composite materials were characterized in terms of stress and inherent flaw sizes using both the measured stress intensity factor obtained from Charpy impact experiments and

measured yield or failure strength values from compression and three-point bend experiments, respectively. For a specimen containing a through crack, the failure stress is related to $K_{IC}$ based on the Griffith criterion according to [194]:

$$\sigma_{uc} = \left( \frac{K_{IC}^2}{\pi a} \right)^{1/2}, \tag{4.21}$$

where $\sigma_{uc}$ is the ultimate failure stress for the composite, and $a$ is half the crack length. Using measured fracture toughness values for each composition and pure epoxy, Figure 4.55 shows the theoretical curves for the variation of failure stress as a function of half crack length, $a$. An indication of inherent critical flaw sizes is obtained by plotting measured compressive yield stress values (obtained for each composition) on the failure stress axis and noting the intersection points on the theoretical failure stress curves. These points correspond to inherent flaw sizes that influence the material's mechanical behavior to Charpy impacts. For example, the Al+$Fe_2O_3$+60 *vol.%* epoxy composite has a corresponding inherent flaw size of approximately 10.5 μm. For cracks above 10.5 μm, the sample breaks in a brittle manner because the overall stress in the specimen is too low to cause significant bulk yielding. However, if the flaws present in this sample are smaller than 10.5 μm, then a sufficient stress may be applied and cause bulk yielding resulting in plastic flow.

The introduction of solid particles to the polymer matrix effectively introduces flaws, and their sizes depend on the individual particle sizes and their distribution throughout the matrix phase. The tendency for solid particles to agglomerate may be sufficient to cause relatively large clusters of particles and significantly large flaw sites.

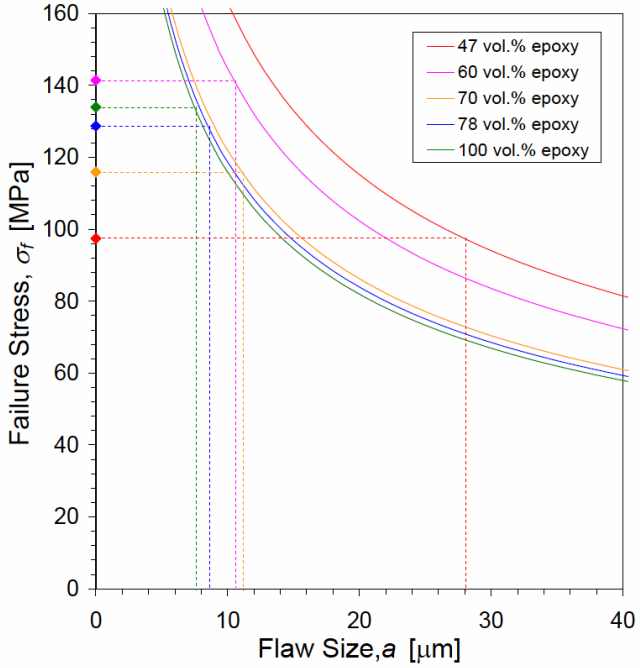


**Figure 4.55** Theoretical estimation of critical flaw sizes that result in either ductile or brittle fracture behaviors for Charpy impact experiments. Measured compressive yield stresses (points on the failure stress axis) are used to determine corresponding flaw sizes.

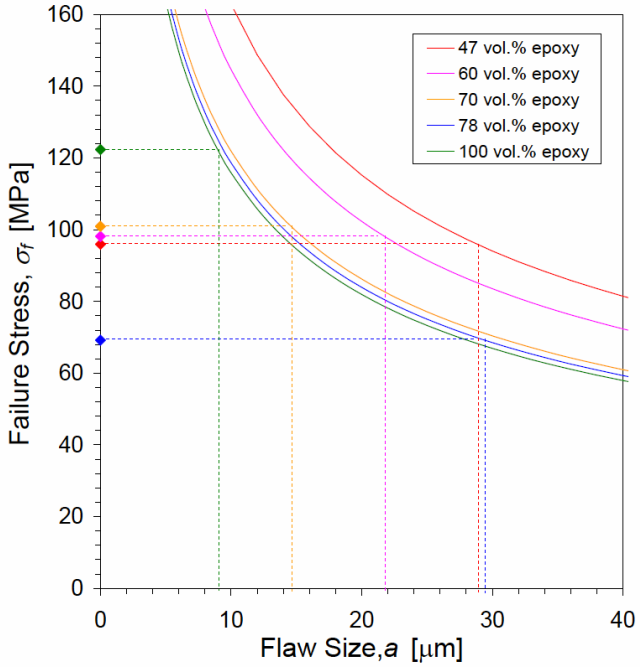


**Figure 4.56** Critical flaw sizes that influence material behavior during Charpy impact experiments were calculated from measured failure stress values obtained from flexural experiments for each composition. Flexural failure stress values are more sensitive to flaws than compressive yield stress values used to determine flaw sizes in Figure 4.55.

However, it is interesting that the increasing volume fraction of solid particles for the 60, 70, and 78 *vol.%* epoxy compositions do not significantly affect the critical flaw size until a sufficient amount is reached by the 47 *vol.%* epoxy composition. Figure 4.55 indicates that each of the compositions including pure epoxy have inherent critical flaw sizes ranging between 7.5 and 11.1 μm, except for the Al+$Fe_2O_3$+47 *vol.%* epoxy composition which had a significantly larger value of 28 μm.

Since compressive yield stress values are essentially flaw insensitive, the flexural failure stress measured for each composition was also used for determining a critical flaw size for initiating brittle or ductile failure, as shown in Figure 4.56. Additionally, the flexural strength test subjects the specimen to loading conditions that are closer to those experienced during a Charpy impact. The failure stress values range between approximately 70 to 120 MPa for the compositions and correspond to critical flaw sizes with a relatively broad range between 9 and 30 μm. The critical flaw size for pure epoxy was 9 μm, while the 78 and 47 *vol.%* epoxy compositions had critical flaw sizes of 29.3 and 28.8 μm, respectively. The 78 *vol.%* epoxy composition had almost 2 % porosity with uncharacteristically large pores for the particular batch used in flexural tests (discussed in section 4.3.3), which significantly influenced the critical flaw size as illustrated by the comparison of flaw sizes calculated from compressive yield strength values. Conversely, flaw sizes calculated for the 47 *vol.%* epoxy composition showed good agreement between the two methods and may be influence significantly by the high concentration of porosity exhibited by this composition. Table 4.12 summarizes the critical flaw sizes for each composition, obtained using both methods.

**Table 4.12** Theoretically determined critical flaw size, *a*, for epoxy-cast Al+$Fe_2O_3$ composites and pure epoxy obtained from Figure 4.55 (using compressive strength) and Figure 4.56 (using flexural strength).

| Epoxy [*vol.%*] | *Compressive Strength* | *Flexural Strength* |
|---|---|---|
| | *a* [μm] | *a* [μm] |
| 47 | 28.0 | 28.8 |
| 60 | 10.5 | 21.8 |
| 70 | 11.1 | 14.6 |
| 78 | 8.4 | 29.3 |
| 100 | 7.5 | 9.0 |

It is also important to consider that the particle sizes and their distribution throughout the matrix alone do not completely influence the brittle or ductile behavior for these compositions. The adhesion between the matrix and inclusion particles also has a significant effect on mechanical behavior. However, it is very challenging to quantitatively measure the adhesion of individual particles within a matrix.

There was no evidence of pores near the critical size ranges listed in Table 4.12 for the respective compositions and, therefore, one would expect ductile yielding to occur. The fracture surfaces showed some evidence of ductile yielding for pure epoxy, particulary early in the fracturing process. While the 47 and 78 *vol.%* epoxy compositions both had a critical flaw size of approximately 29 μm, the critical flaw sizes for the 60 and 70 *vol.%* epoxy were 21.8 and 14.6 μm, respectively. The critical flaw sizes follow in order according to epoxy concentration, with pure epoxy having the smallest, and the 47 *vol.%* epoxy composition having the largests flaw size. However, the 78 *vol.%* epoxy composition exhibited a slightly larger flaw size than the

47 *vol.%* epoxy composite because of the abnormally high inherent porosity observed for this particular batch of material.

## 4.4 Taylor Anvil Impact Experiments

The characterization of dynamic mechanical behavior of epoxy-cast stoichiometric mixtures of nano- and micron-scale aluminum and hematite powders is presented next. The experiments were conducted on rod-shaped samples using instrumented reverse-Taylor (anvil-on-rod) impact tests employing high-speed imaging and velocity interferometry. In some cases, direct Taylor impact experiments (rod-on-anvil) were also conducted for capturing the transient deformation of the sample at discrete times using high-speed imaging only.

Experimental results indicate that these composites exhibit both viscoelastic-viscoplastic deformation and brittle fracture behaviors. Upon impact, the samples displayed significant elastic and plastic deformation during both the loading and unloading stages, as determined from quantitative high-speed camera measurements of the transient deformation states. Approximately 50 % elastic recovery of total axial strain was observed to occur rapidly (within tens of microseconds) after impact. A one-dimensional elastic-plastic wave propagation analysis was used for estimating the composite's dynamic average yield stress and total plastic strain. The analysis additionally provided detailed information about elastic and plastic wave interactions within the rod specimen for discrete times up to the final state of the material.

The following section presents results obtained from estimating mechanical material properties during dynamic impact experiments. Calculations and observations through the coupling of high-speed camera images and velocity interferometry measurements are presented. These results will demonstrate that the instrumented Taylor test provides a detailed view of the general wave structure and its propagation within the material upon impact and at the same time enables a complete description of the dynamic stress-strain response. The results also indicate intrinsic property influences on the overall bulk dynamic mechanical response of these composites and their correlation with processing effects, specimen architecture, and particle size effects.

Reverse Taylor anvil-on-rod impact experiments were conducted for particle-filled Al+$Fe_2O_3$ epoxy-cast composites containing 47, 60, 70, and 78 *vol.%* epoxy. A majority of the experimental work was however, conducted on three of these epoxy-cast material systems. The first composite was comprised of stoichiometric micron-scale aluminum and hematite powder mixture dispersed in 60 *vol.%* epoxy, with experiments conducted at impact velocities ranging from 80 to 423 m/s. The next composite was comprised of nano-scale aluminum and hematite stoichiometric mixture cast in 70 *vol.%* epoxy. The higher concentration of epoxy (and thus a lower particle fill density) resulted from the nanometric scale particles having a large surface area, which made casting at lower epoxy concentrations impossible. Impact velocities for this material system ranged from 98 to 288 m/s. Pure epoxy was also examined with impact velocities ranging from 66 to 167 m/s. Table 4.13 lists starting densities and dimensions, and post-impact dimensions for specimens used for direct and reverse Taylor impact experiments conducted in this study.

**Table 4.13** Direct and reverse Taylor impact experiments conducted for epoxy-cast Al+$Fe_2O_3$ composite compositions and pure epoxy. Experiments are listed in order of increasing impact velocity for each composition.

| Shot Number | Specimen ID | Density $\rho$ [g/cm$^3$] | TMD [%] | Initial Diameter, $D_0$ [mm] | Initial Length, $L_0$ [mm] | Final Length, $L_f$ [mm] | Impact Velocity, $U$ [m/s] |
|---|---|---|---|---|---|---|---|
| *Al+$Fe_2O_3$+47 vol.% epoxy* | | | | | | | |
| 0618 | 085C-2 | 2.7131 | 96.59 | 7.50 ± 0.04 | 47.45 ± 0.13 | 46.29 ± 0.12 | 101.8 ± 3.7 |
| [D] RM-23 | 085D-1 | 2.6866 | 95.65 | [a] 7.43 ± 0.01 | [a] 50.77 | [b] 49.61 ± 0.01 | 105.2 ± 15.4 |
| [D] RM-26 | 085D-3 | 2.6888 | 95.72 | [a] 7.55 ± 0.02 | [a] 50.75 | fracture | 169.3 |
| [D] RM-27 | 085C-1 | 2.6923 | 95.85 | [a] 7.48 ± 0.01 | [a] 50.76 | fracture | 175.9 |
| [D] RM-25 | 085D-4 | 2.6861 | 95.63 | [a] 7.50 ± 0.10 | [a] 50.67 | fracture | 186.5 |
| [D] RM-24 | 085D-2 | 2.6872 | 95.67 | [a] 7.49 ± 0.00 | [a] 50.72 | fracture | 209.9 |
| *Al+$Fe_2O_3$+60 vol.% epoxy* | | | | | | | |
| [c] 0529 | 079D-1 | 2.3719 | 98.66 | 7.50 ± 0.04 | 46.39 ± 0.08 | 45.75 ± 0.15 | 80.1 ± 1.2 |
| 0621 | 119A-1 | 2.3875 | 99.31 | 7.60 ± 0.03 | 51.54 ± 0.08 | 50.61 ± 0.19 | 97.9 ± 0.9 |
| [c] 0530 | 079D-2 | 2.3734 | 98.73 | 7.51 ± 0.03 | 46.68 ± 0.07 | 45.50 ± 0.13 | 108.4 ± 1.5 |
| [D] RM-22 | 079C-2 | 2.3761 | 98.84 | [a] 7.44 ± 0.00 | [a] 50.76 | [b] 49.16 ± 0.01 | 109.8 ± 10.8 |
| [c] 0537 | 121A-2 | 2.3962 | 99.68 | 7.52 ± 0.05 | 49.90 ± 0.12 | 47.68 | 132.9 ± 2.4 |
| [c] 0541 | 121A-3 | 2.4039 | 100 | 7.58 ± 0.02 | 50.91 ± 0.04 | 48.02 ± 0.08 | 151.0 ± 1.7 |
| [c] 0535 | 079D-4 | 2.3702 | 98.59 | 7.43 ± 0.05 | 45.40 ± 0.10 | fracture | 158.2 ± 2.7 |
| [c] 0542 | 121B-3 | 2.3876 | 99.32 | 7.22 ± 0.04 | 50.40 ± 0.15 | 46.15 | 178.0 ± 5.6 |
| 0544 | 121B-2 | 2.3991 | 99.80 | 7.16 ± 0.06 | 51.46 ± 0.09 | fracture | 181.8 ± 2.6 |
| [c] 0531 | 079D-3 | 2.3743 | 98.76 | 7.44 ± 0.10 | 47.64 ± 0.13 | fracture | 207.0 ± 2.6 |
| [c] 0536 | 079C-3 | 2.3793 | 98.97 | 7.49 ± 0.04 | 31.31 ± 0.13 | fracture | 210.7 ± 7.1 |
| [c] 0603 | 121B-1 | 2.4027 | 99.95 | 7.15 ± 0.05 | 50.71 ± 0.12 | fracture | 236.6 ± 4.3 |
| [c] 0644 | 136C-2 | 2.3050 | 95.88 | 7.53 ± 0.03 | 53.02 ± 0.04 | fracture | 423.2 ± 0.1 |
| *Al+$Fe_2O_3$+70 vol.% epoxy* | | | | | | | |
| [c] 0617 | 101D-2 | 2.0252 | 96.38 | 7.45 ± 0.05 | 48.88 ± 0.13 | 47.82 ± 0.30 | 105.9 ± 0.6 |
| [D] RM-21 | 101D-1 | 2.0517 | 97.64 | [a] 7.57 ± 0.00 | [a] 50.80 | [b] 49.79 ± 0.01 | 110.6 ± 13.7 |

**Table 4.13** (continued)

| Shot Number | Specimen ID | Density $\rho$ [g/cm$^3$] | TMD [%] | Initial Diameter, $D_0$ [mm] | Initial Length, $L_0$ [mm] | Final Length, $L_f$ [mm] | Impact Velocity, $U$ [m/s] |
|---|---|---|---|---|---|---|---|
| *nano-Al+$Fe_2O_3$+70 vol.% epoxy* | | | | | | | |
| 0648 | 135A-2 | 2.1041 | 100 | 7.57 ± 0.03 | 52.32 ± 0.03 | 51.99 ± 0.11 | 97.8 ± 1.5 |
| [c]0649 | 134C-1 | 2.0905 | 99.49 | 7.54 ± 0.04 | 52.35 ± 0.06 | 51.25 ± 0.10 | 143.6 ± 0.4 |
| [c]0650 | 134C-2 | 2.0924 | 99.58 | 7.49 ± 0.05 | 52.35 ± 0.06 | 49.75 | 175.2 ± 0.3 |
| 0645 | 135B-2 | 2.0934 | 99.63 | 7.52 ± 0.04 | 52.99 ± 0.03 | 48.87 | 201.1 ± 1.2 |
| [c]0647 | 135A-1 | 2.0930 | 99.61 | 7.56 ± 0.03 | 52.34 ± 0.07 | fracture | 235.3 ± 1.1 |
| [c]0646 | 134A-1 | 2.0867 | 99.31 | 7.54 ± 0.03 | 52.44 ± 0.03 | fracture | 288.3 ± 0.9 |
| *Al+$Fe_2O_3$+78 vol.% epoxy* | | | | | | | |
| [D]RM-14 | 077C-3 | 1.8388 | 98.54 | [a]7.57 ± 0.00 | [a]50.75 | fracture | 87.0 |
| [c]0616 | 077C-1 | 1.8402 | 98.61 | 7.34 ± 0.03 | 48.51 ± 0.09 | 48.14 ± 0.10 | 94.0 ± 0.7 |
| *pure epoxy (batch A)* | | | | | | | |
| 0637 | 138B-1 | 1.1961 | 99.95 | 7.55 ± 0.04 | 53.10 ± 0.04 | 53.12 ± 0.03 | 66.4 ± 0.4 |
| 0638 | 139A-2 | 1.1943 | 99.80 | 7.54 ± 0.03 | 50.24 ± 0.08 | 50.29 ± 0.03 | 98.7 ± 0.6 |
| 0640 | 138B-2 | 1.1947 | 99.83 | 7.54 ± 0.03 | 51.91 ± 0.06 | 50.99 ± 0.04 | 127.9 ± 0.7 |
| 0639 | 139A-1 | 1.1938 | 99.76 | 7.53 ± 0.03 | 52.33 ± 0.05 | 50.94 | 143.2 ± 0.6 |
| 0641 | 139B-1 | 1.1947 | 99.83 | 7.56 ± 0.03 | 53.07 ± 0.04 | 51.40 | 150.3 ± 0.8 |
| 0643 | 139B-2 | 1.1950 | 99.86 | 7.53 ± 0.04 | 53.04 ± 0.05 | 50.76 | 166.7 ± 1.1 |
| *pure epoxy (batch B)* | | | | | | | |
| 0601 | 091D-1 | 1.2030 | 100 | 7.51 ± 0.04 | 49.72 ± 0.08 | 49.79 ± 0.06 | 65.6 ± 0.7 |
| 0642 | 091C-1 | 1.2003 | 100 | 7.35 ± 0.04 | 49.43 ± 0.07 | 49.17 ± 0.22 | 104.1 ± 0.7 |
| 0602 | 091D-2 | 1.1990 | 100 | 7.46 ± 0.02 | 49.63 ± 0.08 | 48.74 ± 0.09 | 121.0 ± 0.5 |
| 0614 | 091D-4 | 1.1991 | 100 | 7.46 ± 0.05 | 49.47 ± 0.11 | fracture | 152.4 ± 0.7 |
| 0613 | 091D-3 | 1.1980 | 100 | 7.50 ± 0.04 | 49.56 ± 0.11 | fracture | 179.7 ± 4.1 |

[a] Physically measured directly from specimen.

[b] Final length is measured from recovered specimen.

[c] Instrumented experiments using VISAR.

[D] Direct Taylor impact experiments.

The next section gives details about dynamic impact measurements conducted in this study, and highlights observed differences in the deformation behaviors of the material systems through high-speed camera images. This is followed by a detailed analysis for estimating dynamic yield stress and strain using a one dimensional linear-elastic perfectly-plastic material model [98]. The analysis permits the construction of a position-time plot depicting the complex wave interactions within the material. Additionally, high-speed camera images time synchronized with velocity interferometry measurements are employed to obtain details about the deformation process and to gain insight into the complex wave interactions occurring within the material during the experiment.

### 4.4.1 Transient Deformation State Observations

Upon impact, the epoxy-cast Al+$Fe_2O_3$ composite samples exhibit a highly deformed region confined to the impact end of the specimen. Detailed examination of camera images reveal two different deformation shapes emerging from high velocity impacts. High-speed camera images obtained for all reverse Taylor impact experiment conducted on each composition and pure epoxy are available in Appendix B. Representative images captured during the deformation of select experiments shown in Figure 4.57(*a,b*), reveal two types of deformation shapes described as "double-frustum" shown in Figure 4.57(*a*) and "extended-mushroom" shown in Figure 4.57(*b*). The double-frustum deformation shape has a highly non-uniform deformation zone concentrated at the impact face of the specimen. This shape has been identified in many studies examining metallic materials [195-197]. Balendra, *et al.* [197] reasoned that this

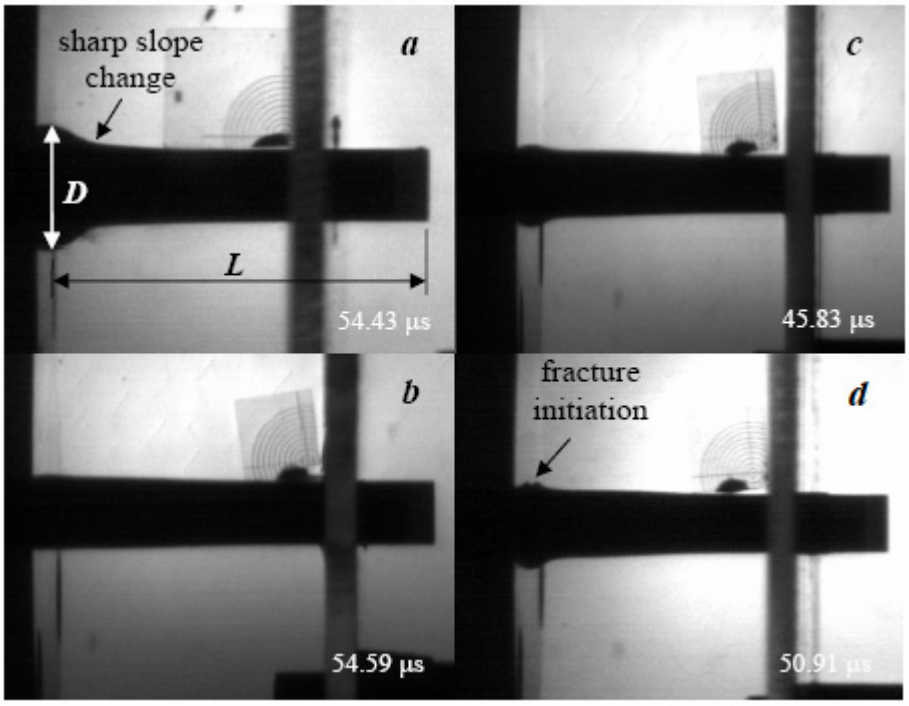


**Figure 4.57** High-speed camera images from reverse Taylor impact experiments illustrate distinctive deformation modes for two experiments with similar impact velocities of *a)* 158.2 and *b*) 151.0 m/s. Additionally, an image shown *c*) just prior and *d)* at fracture initiation (indicated by the arrow) correspond to an experiment with an impact velocity of 181.8 m/s. Images *a)*, *c),* and *d)* exhibit "double-frustum" type deformation while *b)* shows a uniform "mushroom" shape extending along the specimen's axial length. Fracture was typically observed for specimens that display "double-frustum" deformation.

shape is due to an extremely high radial velocity imparted to the impact face of the specimen initially, but was arrested as the deformation wave propagates into the specimen. In contrast, the extended-mushroom shape has a relatively small radial velocity but a larger deformation zone that extends further into the specimen.

Images shown in Figure 4.57(*a,b*) were obtained from two separate experiments performed on epoxy-cast Al+$Fe_2O_3$+60 *vol.%* epoxy composites at similar impact velocities of 158.2 (shot 0535) and 151.0 m/s (shot 0541), respectively. Both images were taken at approximately the same time, 54.43 and 54.59 μs after impact. Clearly

there are two significantly different deformation shapes emerging from these two similar experimental conditions. A highly deformed region localized near the impact face of the specimen shows the characteristic double-frustum deformation shape observed for shot 0535 with an impact velocity 158.2 m/s. Observations from several experiments conducted on epoxy-cast composite material system suggest that specimens displaying a double-frustum deformation shape fracture at the point where there was an appreciable slope change along the specimen's axial profile, as indicated in Figure 4.57(*a*). In contrast, shot 0541 with a slightly lower impact velocity of 151.0 m/s shows an extended-mushroom shape with minimal radial deformation and an extended axial plastic deformation zone. Specimens exhibiting an extended-mushroom type deformation shape show no evidence of fracture occurring within the time interval examined by high-speed camera images. Variation in the deformation response between the two specimens was attributed to porosity differences. Specimens that exhibit more than 1 % porosity tend to exhibit the characteristic double-frustum deformation shape, and tend to fracture close to the region where a sharp change in slope is observed from the axial profile edge.

One specimen showed mixed deformation modes that exhibited attributes from both double-frustum and extended-mushroom deformation shapes. For this particular experiment (shot 0544), the specimen fractured close to the impact face and not in the region where there was an abrupt slope change in the deformation zone, as observed for many other experiments. Figure 4.57(*c*) shows the deformation of the specimen 45.83 μs after impact, prior to the observation of fracture captured in the next image at 50.91 μs and as shown in Figure 4.57(*d*). Both images show evidence of mixed deformation modes by means of a double-frustum region located towards the impact face and a slight

barreling region (extended-mushroom) away from the impact face along the axial length of the specimen. It is believed that this particular specimen fractured prematurely due to a flaw located close to the impact region of the specimen.

Similar extended-mushroom deformation shapes were observed for nano-Al+$Fe_2O_3$+70 *vol.%* epoxy compositions which exhibited very low porosity (significantly less than 1 %). Of the six experiments conducted for this nano-composite composition, fracture was observed at impact velocities of 235.3 and 288.3 m/s. In both cases, the specimens exhibited a double-frustum deformation shape that developed very rapidly, however, it was restricted to a very small region away from the impact face unlike observations obtained on samples of Al+$Fe_2O_3$+60 *vol.%* epoxy and pure epoxy compositions. An extended-mushroom deformation shape was observed for all specimens that showed no evidence of fracture, regardless of composite composition.

Pure epoxy compositions, however, showed a noticeably different deformation response where double-frustum deformation shapes were observed for all experiments that had an impact velocity sufficient to cause plastic deformation. For these experiments, two different batches of pure epoxy were prepared, one which had a slightly greater average density of 1.1999 ± 0.0019 g/cm$^3$ (batch *B*) as compared to 1.1948 ± 0.0019 g/cm$^3$ (batch *A*). Although the controllable processing conditions were identical, it is possible that a slightly greater hardener concentration may have altered the density and dynamic mechanical properties. This theory is supported by the fact that the batch *B* densities are greater than the theoretical density (1.1967 g/cm$^3$) for this particular epoxy resin and hardener mixture. Furthermore, the color of batch *B* had a yellowish tint when compared to the clear (colorless) appearance of batch *A* material.

Dynamic impact testing of these epoxy specimens did not show evidence of fracture up to and including impact velocities of 166.7 m/s (shot 0643) for batch *A* material. However, epoxy specimens obtained from batch *B* material fractured at a lower impact velocity of 152.4 m/s (shot 0614). The measurable differences observed for these two epoxy batches will be discussed further, detailing the axial and areal strain response in section 4.4.2 and the dynamic yielding behavior in section 4.4.3.

### 4.4.2 Axial and Areal Strain Measurements

High-speed camera images were used to make quantitative measurements of transient axial and areal strains examined over a time interval of up to approximately 100 to 150 μs after impact. Axial strain was calculated for discrete times according to:

$$\varepsilon_L = ln\left(\frac{L_0}{L}\right), \tag{4.22}$$

where $L$ and $L_0$ are the incremental and initial lengths, respectively. Similarly, areal strain was calculated using:

$$\varepsilon_A = 1 - \left(\frac{A_0}{A}\right), \tag{4.23}$$

where $A$ and $A_0$ are the incremental and initial areas, respectively. Areal strain measurements were made at the impact face where the maximum deformation was

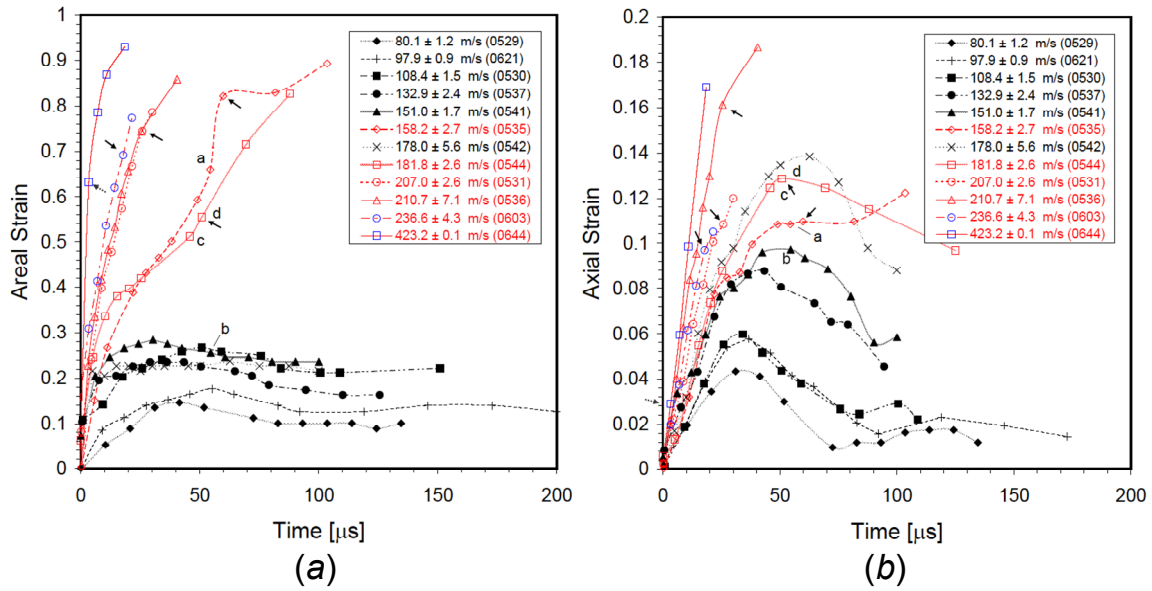


**Figure 4.58** *a*) Areal and *b*) axial strains measured from high-speed camera images show critical fracture strains (arrows indicate). Points *a* through *d* correspond to images shown in Figure 4.57 for Al+$Fe_2O_3$+60 *vol.%* epoxy composition.

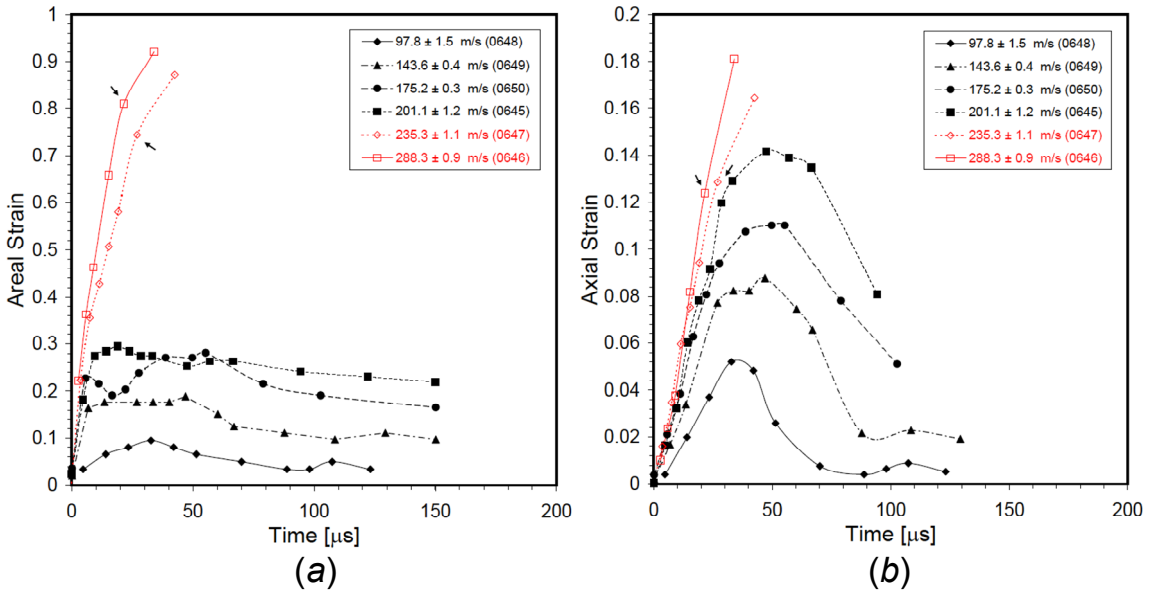


**Figure 4.59** *a*) Areal and *b*) axial strains measured from high-speed camera images show critical fracture strains (arrows indicate) for nano-Al+$Fe_2O_3$+70 *vol.%* epoxy composite.

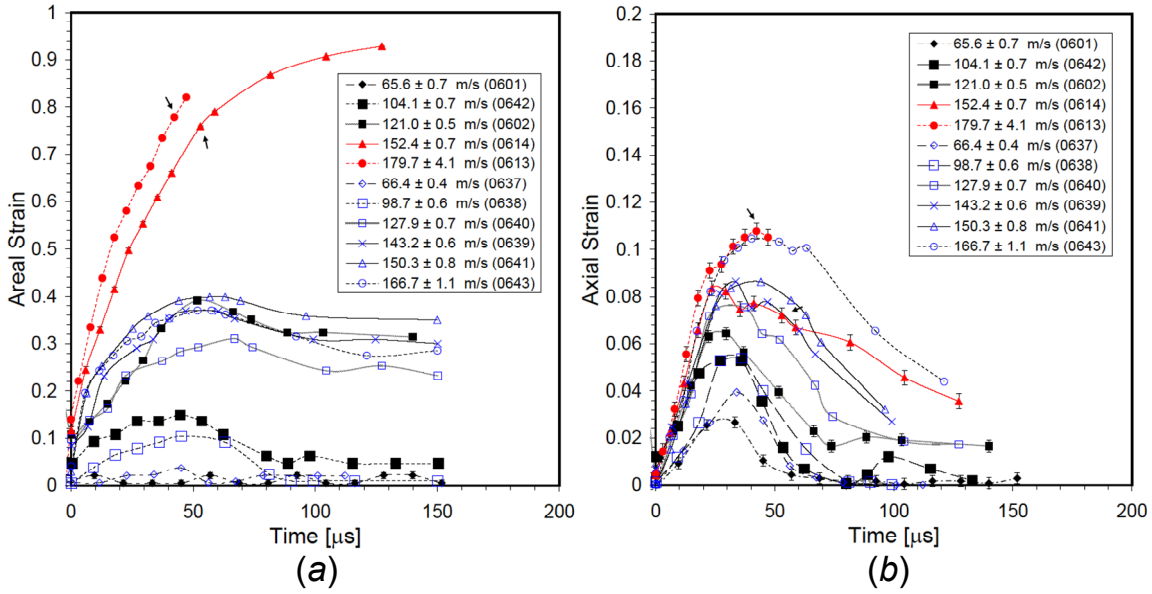


**Figure 4.60** *a*) Areal and *b*) axial strains measured from high-speed camera images show critical fracture strains (arrows indicate) for pure epoxy (batch *A* and *B*). Batch *A* material is shown with blue data points.

typically observed. Typical results of axial and areal strain measurements are presented in Figure 4.58(*a,b*), showing the deformation response over time for epoxy-cast Al+$Fe_2O_3$+60 *vol.%* epoxy composites for impact velocities ranging from 80 to over 400 m/s. Similar plots were also generated for experiments performed on nano-aluminum containing 70 *vol.%* epoxy composite (Figure 4.59(*a,b*)) and pure epoxy (Figure 4.60(*a,b*)) samples. Figure 4.60 includes the axial and areal response for epoxy prepared from batches *A* and *B*, which had slightly different densities and measurable differences in dynamic behavior.

In general, the areal and axial strain plots reveal that the specimens (for all compositions) undergo significant elastic and plastic deformation during both the loading and unloading stages of impact. Elastic recovery was more evident in axial strain measurements simply because of the limited peak strain scale as compared to relatively

large strains observed for areal strain measurements. However, elastic recovery was also observed in areal strain measurements, which typically correspond very well with axial strain recovery times. The elastic recovery was very rapid and began approximately 30 to 60 μs after impact depending on the impact velocity, with the longer recovery initiation occurring for higher impact velocities. All of the epoxy-cast compositions displayed similar behaviors; resulting in over 50 % elastic recovery from peak axial strain. This response was observed regardless of impact velocity or composition, with several experiments showing complete elastic recovery and no further change in specimen length after 70 to 100 μs following impact, again depending on impact velocity.

It was important for the estimation of dynamic yield stress and stress-strain calculations that the "final" specimen length was correctly captured before the sample moved out of the camera's field of view. The final length was determined from multiple measurements over a time period where the specimen was no longer experiencing length changes, and thus was completely recovered elastically. Axial strain measurements for higher velocity experiments only captured one or two data points during the elastic recovery stage before the specimen moved out of the field of view. However, it was observed from lower velocity experiments that elastic recovery times determined from areal strain measurements coincided very well with axial strain recovery times. From this observation, indication of full elastic recovery was obtained from areal strain measurements even when there were only one or two data points captured. This gave confidence in that the actual final axial strain imparted to the specimen, or the final length was measured accurately.

To further verify the final length determined from high-speed camera images,

several recovery experiments were conducted in which the impacted specimen was captured in a specially designed soft-recovery fixture. Comparison of the dimensions from high-speed camera images with physically measured initial and final specimen lengths showed close agreement (within 0.4 % difference) as shown by the values listed in Table 3.7 (discussed in section 3.5.2.1). This illustrates that the accuracy of transient deformation measurements obtained from high-speed camera images is quite good for obtaining estimates of the dynamic yield stress and stress-strain relationships.

Strain measurements also provided insight into the fracture behavior of these composite materials. The path to fracture initiation began with the areal strain exceeding a critical limit. Examination of areal strain measurements shown in Figure 4.58(*a*) for the Al+$Fe_2O_3$+60 *vol.%* epoxy composite, reveals that the specimens experience higher strain levels (open data points) upon exceeding a critical areal strain of approximately 30 %. This leads to observed fracture at strains of approximately 60 to 80 %. Direct comparison between two experiments performed at similar impact velocities of 207.0 and 210.7 m/s (shots 0531 and 0536, respectively) showed observed fracture occurring at identical strain levels (approximately 74 % indicated by an arrow in Figure 4.58(*a*)), at 25.50 and 25.81 μs after impact, respectively. A third experiment (shot 0603) with a slightly higher impact velocity of 236.6 m/s also showed a similar areal strain profile, with observed fracture occurring slightly earlier, as would be expected. Furthermore, the strain value at observed fracture decreases as impact velocity increases for specimens that fracture.

Points labeled *a* through *d* in Figure 4.58(*a,b*) correspond to captured images shown in Figure 4.57(*a-d*) and illustrate quantitatively different material response evident

from axial and areal strain measurements. The first example highlights the measured areal strain response differences observed for two specimens subjected to similar experimental conditions (shots 0535 at 158 m/s and 0541 at 151 m/s). For the 158 m/s experiment (shot 0535), point *a* corresponds to 54.43 μs in Figure 4.58(*a*), at the time corresponding to the image obtained in Figure 4.57(*a*). The specimen exceeds the critical areal strain and proceeds to fracture at approximately 82 % strain, marked by an arrow in Figure 4.58(*a*). In contrast, experiment 0541, with point *b* corresponding to the image in Figure 4.57(*b*), never exceeds the critical areal strain and, consequently, does not fracture. The different behaviors observed for these two experiments are attributed mainly to the detrimental effect of a small percentage of porosity (≈ 1.4 %) present in the sample for shot 0535 and its influence on mechanical properties. As a result of this porosity, observed differences in deformation shapes that manifest as either double-frustum or extended-mushroom types are distinctive for the two material behaviors. Another example revealing mixed deformation shapes was observed for shot 0544, as shown in Figure 4.57(*c,d*). In this case, the specimen had less than 1 % porosity, but still exceeded the critical areal strain of 30 %, and ultimately fractured. Figure 4.58(*a*) shows evidence of fracture occurring at a time corresponding to point *d* (approximately 51 % areal strain), although, examination of point *d* in Figure 4.58(*b*) shows a very similar axial strain history as shot 0542, subjected to a slightly lower impact velocity of 178.0 m/s. The fracture behavior observed in this case was possibly related to a flaw located in close proximity to the specimen's impact face as indicated by the fracture initiation point marked in Figure 4.57(*d*). All other specimens fractured close to the region where severe slope change was observed in the double-frustum deformation

shape, and not close to the impact face.

The nano-Al+$Fe_2O_3$+70 *vol.%* epoxy composition showed similar axial and areal strain behaviors as illustrated in Figure 4.59(*a,b*). The critical areal strain that lead to specimen fracture was approximately 30 %, similar to that observed for the micron-Al+$Fe_2O_3$+60 *vol.%* epoxy composition discussed previously. However, the nano-aluminum containing composite samples were observed to withstand higher impact velocities as compared to other compositions and did not fracture up to an impact velocity of 201.1 m/s. Strain measurements on the nano-aluminum composite materials showed similar peak axial strain magnitudes in comparison to pure epoxy specimens, but lower peak axial strain values in comparison to the Al+$Fe_2O_3$+60 *vol.%* epoxy composition for similar impact velocities.

Pure epoxy samples however showed a higher critical areal fracture strain of approximately 40 %. Furthermore, the epoxy specimens did not appear to easily fracture and withstood impact at velocities up to 166.7 m/s for batch *B* material. In contrast, batch *A* material fractured at a lower impact velocity of 152.4 m/s, thus suggesting an altered dynamic material response behavior. Direct comparison of two experiments (shot 0641 and 0614) with almost identical impact velocities (150.3 and 152.4 m/s, respectively) had similar axial strain behaviors, but completely different areal strain behaviors. Notice that the axial strain response for shots 0641 and 0614 in Figure 4.59(*b*) virtually overlap. However, the areal strain response for these two experiments shows shot 0614 exceeding a critical areal strain of 40 %, which leads to observed fracture at approximately 75 % strain. Similarly, comparing higher velocity shots 0643 (batch *A*) and 0614 (166.7 and 179.7 m/s, respectively) shows identical axial strain responses and

significantly different areal strain behaviors that result in observed fracture at approximately 78 % strain for shot 0614 (batch *B*).

Reverse Taylor impact experiments were also conducted for other epoxy-cast composite compositions (ranging from 47 to 78 *vol.%* epoxy). The behavior of each composition was evaluated by comparing the axial and areal strain response for a common impact velocity close to 100 m/s. Imposing a constrained impact velocity permits the evaluation of each composite under approximately identical loading conditions. The axial and areal strain results are presented in Figure 4.61(*a,b*) and include the responses of pure epoxy (batch *A*) and the nano-scale aluminum composite with 70 *vol.*% epoxy (shots 0638 and 0648, respectively). Each specimen shows an identical initial rise to peak strain, where the slope is the strain rate (approximately $2.0 \times 10^3$ 1/s for axial strain). Each specimen exhibits a slightly different peak strain approximately 35 μs after impact, although with no coherent order. Notice the 78 *vol.%* epoxy, pure epoxy, and the nano-scale 70 *vol.%* epoxy specimens had a rapid recovery response; resulting in complete elastic recovery approximately 100 μs after impact. There was virtually no significant difference in the axial strain response of these three compositions. In contrast, the remaining compositions show some dissimilarity between each other, with each experiencing a relatively slower recovery response with some retained permanent deformation in the 2 to 3 % range.

Comparing the axial strain response shown in Figure 4.61(*b*) for each of the compositions gives some details about the localization of strain at the impact face. Each composition has a significantly different areal strain response for similar impact conditions. The pure epoxy specimen exhibited the lowest peak areal strain and lowest

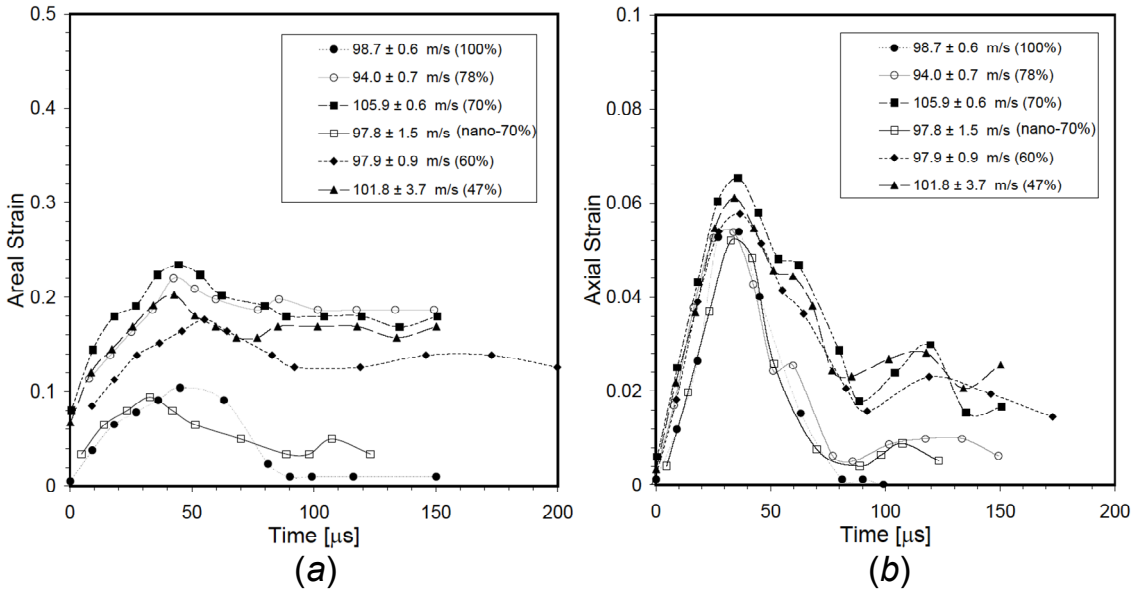


**Figure 4.61** Comparison of *a*) areal and *b*) axial strains measured from high-speed camera images for epoxy-cast Al+$Fe_2O_3$ composites (47 to 78 *vol.%* epoxy) and pure epoxy (batch *A*) at an impact velocity close to 100 m/s.

resulting permanent plastic deformation. The nano-scale aluminum composite showed a similar areal strain response resulting in slightly greater retained plastic deformation approximately 100 μs after impact. The other compositions show varying degrees of peak areal strain and retained plastic deformation.

While the volume fraction of epoxy and solid particle fill fractions for each composite appear to be important parameters, their effect did not directly emerge, and no obvious correlation of volume fraction with material response was observed. Other parameters such as particle size definitely show a significant effect on dynamic mechanical response. This was observed by contrasting the areal and axial strain response of composites with nano-scale and microns-scale aluminum containing 70 *vol.%* epoxy. The nano-aluminum composite appears to better withstand the impact; showing a measurable difference in the response characterized by a rapid axial recovery

and reaching a significantly lower peak areal strain for the impact velocity range examined.

### 4.4.3 Estimation of Dynamic Yield Stress

The dynamic yield stress for the various epoxy-cast composite materials was calculated using the analysis presented by Hutchings [98]. The original analysis estimated the dynamic yield stress for a polymeric material from post-impact measurements of the dimensions obtained from the recovered specimens. However, with the introduction of high-speed photography used to obtain transient deformation profiles, this same analysis can be applied to calculate material properties for all incremental changes in specimen geometry up to the materials' final state. The analysis was based on the assumption of a linear-elastic perfectly-plastic material model that accounts for polymers developing significant elastic strains before yielding.

Areal and axial strain measurements obtained for relatively low velocity impact experiments show that the specimens exhibit complete elastic recovery with no measurable permanent deformation following impact. The critical impact velocity identifies the minimum impact condition necessary for onset of plastic deformation within the material. It was determined by measuring the retained deformation within the specimen through length changes observed for several impact velocities. The fractional change in overall length was calculated and plotted as a function of impact velocity. The critical impact velocity was then obtained by extrapolating to zero length change from a linear fit trend line to these measurements. Epoxy-cast composites were subjected to

several different impact velocities for determining the critical impact velocity which was found to be unique for each composition. For these experiments, high-speed camera images were used to capture the final state of the material taken around 100 to 150 μs after impact. This typically provided sufficient time for the specimen to plastically deform and completely recover elastically. Final specimen lengths obtained in this manner are plotted in Figure 4.62 as a function of impact velocity for the two composites and the pure epoxy composition. The critical velocity for each composition gives an indication of relative material strength based on the stress limit or yield stress imparted to the specimen necessary to cause plastic deformation. With this in mind, the relative strengths of the three compositions can be quickly evaluated. As shown in Figure 4.62,

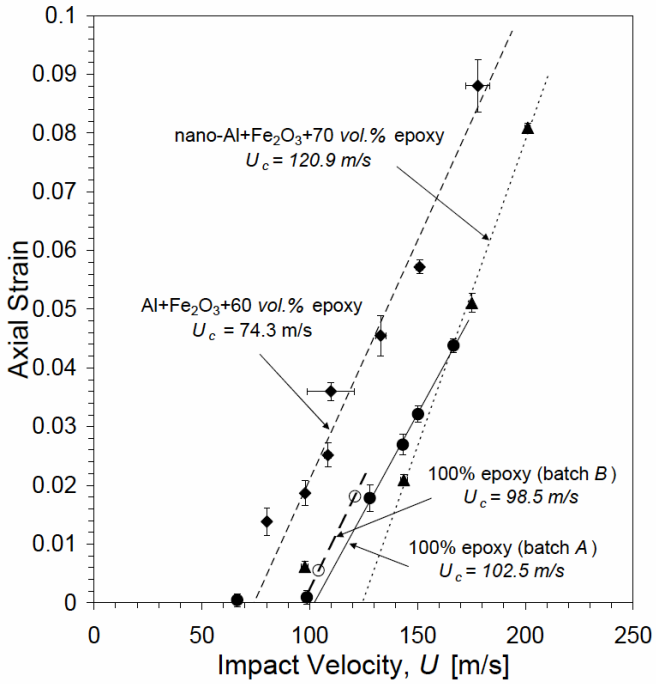


**Figure 4.62** Critical impact velocity determined from retained axial strain measurements for each composition. Notice the axial strains for experiments conducted below the critical impact velocity for pure epoxy (shots 0637 and 0638) and the nano-composite (0648) show complete elastic recovery and are not included in the linear fit.

the nano-Al+$Fe_2O_3$+70 *vol.%* epoxy composite has the highest critical velocity of 120.9 m/s. This is followed by the pure epoxy sample and the Al+$Fe_2O_3$+60 *vol.%* epoxy composite with critical velocities of 102.5 and 74.3 m/s, respectively. Experiments were also conducted below the critical velocity determined from Figure 4.62 for verification. These are listed in Table 4.13 (shown earlier), and include shot 0648 for the Al+$Fe_2O_3$+70 *vol.%* epoxy composite at an impact velocity of 97.8 ± 1.5 m/s, and experiments 0637 and 0638 for pure epoxy at velocities less than 100 m/s.

The critical velocity is a very sensitive measure of the dynamic material response and provides an indication of relative material strength, which is advantageous for comparing subtle differences between various polymers and polymeric composites. This was apparent when examining the dynamic material behavior and material strength for two different batches of pure epoxy with slightly different densities, previously highlighted in section 4.4.2. Batch *B* material had a slightly greater average density of 1.1999 ± 0.0019 g/cm$^3$ as compared to batch *A* material with a density of 1.1948 ± 0.0019 g/cm$^3$ although the controllable processing conditions were identical. Figure 4.62 also shows the critical impact velocity plots for both epoxy materials (batch *A* and *B*) and highlights the sensitivity of this parameter with dynamic yielding. Batch *B* material had a slightly lower critical impact velocity of 98.5 m/s as compared to 102.5 m/s for batch *A* material. Furthermore, batch *B* material yields at lower impact velocities than batch *A* material under identical loading conditions, thus suggesting that batch *A* material has a greater dynamic yield point and overall strength.

The response of material to dynamic loading was determined from equilibrium equations of motion and the material's constitutive relations using the technique

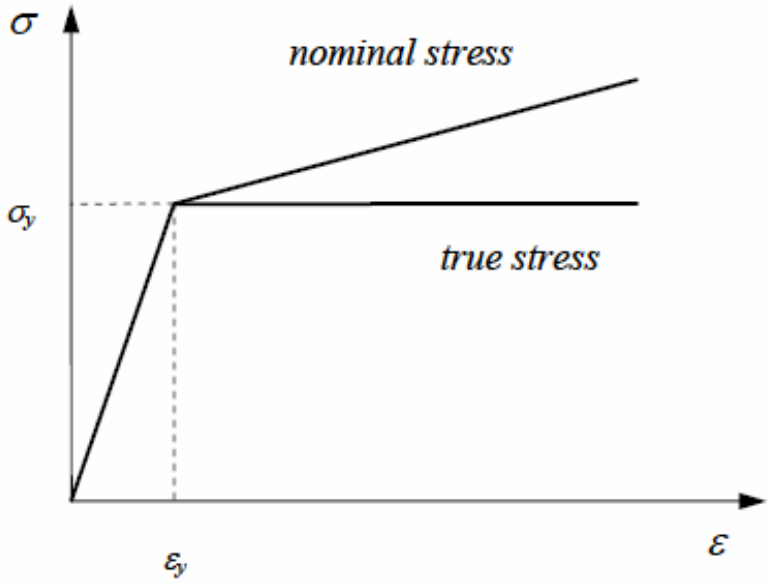


**Figure 4.63** Stress-strain diagram assumed for a linear-elastic perfectly-plastic material model proposed by Hutchings [98].

developed by Hutchings [98]. The propagation of a disturbance wave within a cylindrical bar takes on a two wave structure (elastic and plastic) when impact conditions are above the material's elastic limit. Hutchings [98] considered a polymeric material to be linear-elastic perfectly-plastic and with a (nominal and true) stress-strain relationship similar to that shown in Figure 4.63. Elastic strains propagate with a velocity $C_0$ given by [98]:

$$C_0 = \left( \frac{\sigma_y}{\rho_0 \varepsilon_y} \right)^{1/2} = \left( \frac{Y}{\rho_0 \varepsilon_y (1 - \varepsilon_y)} \right)^{1/2}, \qquad (4.24)$$

where $Y$ is true yield stress, $\sigma_y$ is nominal yield stress, $\varepsilon_y$ is yield strain, and $\rho_0$ is density. For the plastic wave, the nominal stress and strain is greater than the material's elastic limit; its propagation speed is expressed by [98]:

$$C_P = \left( \frac{\sigma - \sigma_y}{\rho_0 \left( \varepsilon - \varepsilon_y \right)} \right)^{1/2}. \tag{4.25}$$

The particle velocity behind the plastic wave is evaluated for an elastic and plastic component and is given by [98]:

$$U = \frac{\sigma_y}{\rho_0 C_0} + \frac{\sigma - \sigma_y}{\rho_0 C_P}. \tag{4.26}$$

The nominal stress behind the plastic wave front is then given by [98]:

$$\sigma = \rho_0 C_P U + \frac{Y}{1 - \varepsilon_y} \left( 1 - \frac{C_P}{C_0} \right). \tag{4.27}$$

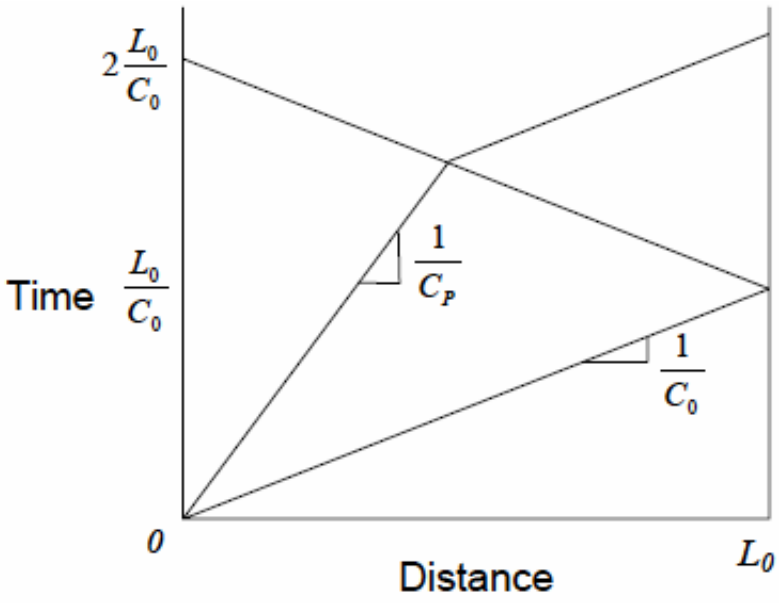


**Figure 4.64** Illustration showing ideal elastic and plastic wave propagation within the rod-shaped specimen (neglecting radial effects).

Hutchings [98] considered the deformation of a Taylor impact experiment sample by the propagation of elastic and plastic waves within the material, with the characteristic distance-time plot (*x*-*t* diagram) in Figure 4.64, showing the principle elastic and plastic wave interactions. Upon impact, an elastic and plastic wave forms at the impact face and propagates along the axial length of the specimen. The elastic compression wave, with a greater velocity, reaches the free surface and reflects back towards the impact face as a release wave. The advancing plastic compression wave, propagating at a much slower velocity, interacts with the reflected elastic release wave some distance away from the impact face. This distance is identified as the axially strained region. The plastic wave is dispersive in nature and attenuates as it propagates along the specimen length. The axially strained region is bounded by the impact face and the point where the elastic and plastic waves begin to interact with each other. This is also where the plastic wave ceases to advance and the elastic compression wave continues to traverse as an unloading wave, towards the impact face and in the undeformed region of the specimen.

Hutchings assumed that the plastic wave front stops advancing with the first elastic wave interaction. Thus, the final position of the plastic zone or axially strained region was measured by the fractional reduction in length, *k* given by:

$$k = 1 - \frac{L}{L_0}. \tag{4.28}$$

From the geometry shown in Figure 4.64,

$$k = \frac{2\overline{C}_P\left(\varepsilon - \varepsilon_y\right)}{1+\overline{C}_P}, \tag{4.29}$$

where, $\varepsilon - \varepsilon_y$ is the residual strain from the plastic wave moving across the material and

$$\overline{C}_P = \frac{C_P}{C_0} = \left(\frac{\varepsilon_y}{1-\varepsilon}\right)^{1/2}. \tag{4.30}$$

Solving for the strain, $\varepsilon$, results in [98]:

$$\varepsilon = \frac{1}{8\varepsilon_y}\left\{\left(8\varepsilon_y^2 + 4k\varepsilon_y - k^2\right) + \left[\left(k^2 - 8\varepsilon_y^2 - 4k\varepsilon_y\right)^2 - 16\varepsilon y\left(4\varepsilon_y^3 + 4k\varepsilon_y^2 + k^2\varepsilon_y - k^2\right)\right]^{1/2}\right\}. \tag{4.31}$$

Correspondingly, the dynamic yield strength according to Hutchings [98] is given by:

$$Y = \left(\frac{\overline{C}_P}{\left(\varepsilon_y - \varepsilon_y^2\right)^{1/2}}\left[\frac{1}{1-\varepsilon} - \frac{1-\overline{C}_P}{1-\varepsilon_y}\right]^{-1}\right)^2 \rho_0 U^2. \tag{4.32}$$

Equation (4.32) is represented only in terms of the two unknown quantities $Y$ and $\varepsilon_y$. A second relationship also exists between these two unknown parameters for the case when the impact velocity is equivalent to the critical velocity and deformation within the specimen is purely elastic. Accordingly, the dynamic yield stress and strain are related as [98]:

$$Y = \frac{U_C^2 \rho_0 \left(1 - \varepsilon_y\right)}{\varepsilon_y}. \qquad (4.33)$$

The dynamic yield stress and strain were estimated for epoxy-cast composites using the above equations and the measured changes in sample length, along with knowledge of the critical velocity for the onset of plastic deformation. Numerical methods were used to evaluate equations (4.32) and (4.33) simultaneously with an initial estimate of $\varepsilon_y$. Values of true yield stress, $Y$, nominal yield stress, $\sigma_y$, and nominal stress, $\sigma$, above the yield point were directly available upon convergence of the two equations. Additionally, yield strain, $\varepsilon_y$, and nominal strain, $\varepsilon$, above the yield point were also determined. The strain rate, $\dot{\varepsilon}$, was obtained from the change in nominal strain with camera imaging time. Strain rates varied over the duration of the impact, reaching rates as high as $10^5$ to $10^6$ 1/s at the first moment of impact down to $10^3$ to $10^4$ 1/s towards the end of deformation.

Results obtained based on the analysis of experiments for each composition are shown in Table 4.14. It should be noted that the calculated values are from experiments where the final length of the specimen was obtained from high-speed camera images and did not show evidence of fracture. The average final specimen length was determined from multiple measurements (in most cases) after elastic recovery was complete and specimen dimensions remained reasonably constant. The resulting values of yield stress and strain, thus obtained for each composition, have very little variation and are nearly independent of impact velocity. For example, the Al+$Fe_2O_3$+60 *vol.%* epoxy composite has average true yield stress $Y$ = 389.1 ± 8.6 MPa and yield strain $\varepsilon_y$ = 0.033 ± 0.001 for impact velocities ranging from 97.9 to 151.0 m/s. In a similar manner,

**Table 4.14** Calculated values obtained from reverse Taylor impact experiments using analysis developed by Hutchings [98].

| Shot Number | $U$ [m/s] | $Y$ [MPa] | $\sigma_y$ [MPa] | $\sigma$ [MPa] | $\varepsilon$ | $\varepsilon_y$ | $E$ [GPa] | $C_P$ [mm/μs] | $C_0$ [mm/μs] |
|---|---|---|---|---|---|---|---|---|---|
| *Al+$Fe_2O_3$+60 vol.% epoxy* | | | | | | | | | |
| 0621 | 97.9 | 390.3 | 403.5 | 427.6 | 0.089 | 0.034 | 11.89 | 0.429 | 2.274 |
| 0530 | 108.4 | 391.7 | 404.9 | 440.2 | 0.111 | 0.033 | 12.36 | 0.437 | 2.295 |
| 0537 | 132.9 | 377.0 | 390.2 | 452.2 | 0.166 | 0.034 | 11.50 | 0.442 | 2.191 |
| 0541 | 151.0 | 397.2 | 410.5 | 495.5 | 0.198 | 0.032 | 12.68 | 0.462 | 2.297 |
| *nano-Al+$Fe_2O_3$+70 vol.% epoxy* | | | | | | | | | |
| 0649 | 143.6 | 400.2 | 430.7 | 453.7 | 0.119 | 0.071 | 6.03 | 0.483 | 1.704 |
| 0650 | 175.2 | 395.3 | 425.9 | 482.5 | 0.181 | 0.072 | 5.93 | 0.498 | 1.683 |
| 0645 | 201.1 | 365.5 | 396.1 | 479.8 | 0.238 | 0.077 | 5.13 | 0.498 | 1.565 |
| *pure epoxy (batch A)* | | | | | | | | | |
| 0640 | 127.9 | 276.7 | 289.2 | 304.9 | 0.093 | 0.043 | 6.65 | 0.516 | 2.361 |
| 0639 | 143.2 | 296.0 | 308.6 | 334.8 | 0.116 | 0.041 | 7.59 | 0.541 | 2.521 |
| 0641 | 150.3 | 291.3 | 303.9 | 334.7 | 0.130 | 0.041 | 7.35 | 0.541 | 2.481 |
| 0643 | 166.7 | 287.5 | 300.0 | 341.9 | 0.159 | 0.042 | 7.17 | 0.546 | 2.449 |

$Y$ = 387.0 ± 18.8 MPa and $\varepsilon_y$ = 0.074 ± 0.003 for nano-Al+$Fe_2O_3$+70 *vol.%* epoxy composition with impact velocities ranging from 143.7 to 201.1 m/s. The yield stress deviation was slightly high for the experiments conducted for the nano-aluminum composite because the final length measurement obtained from one of the experiments (shot 0645) may have been prior to complete elastic recovery being achieved within the specimen before moving out of the high-speed image filed of view. The pure epoxy composition (batch *A*) had values of $Y$ = 287.9 ± 8.3 MPa and $\varepsilon_y$ = 0.042 ± 0.001 with impact velocities ranging from 127.9 to 166.7 m/s.

Calculated true stress-strain curves constructed for each of the compositions are shown in Figure 4.65 with a familiar linear-elastic perfectly-plastic form.

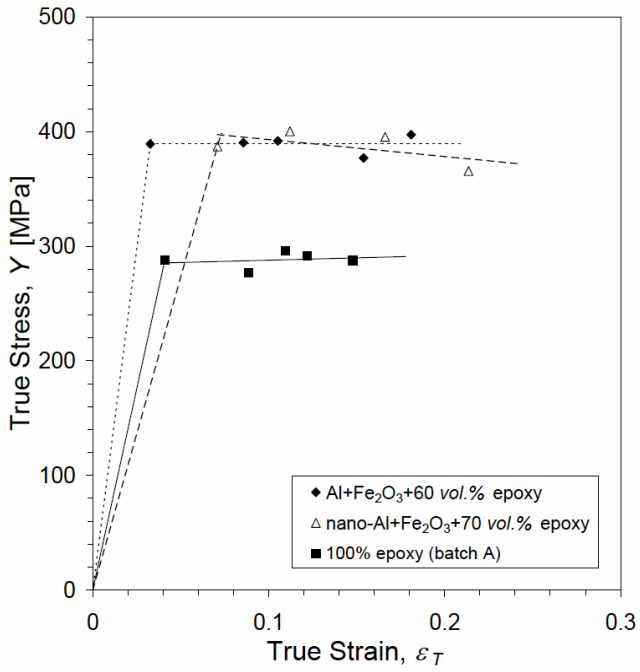


**Figure 4.65** True dynamic stress-strain diagram determined for Al+$Fe_2O_3$+60 *vol.%* epoxy, nano-Al+$Fe_2O_3$+70 *vol.%* epoxy, and pure epoxy (batch *A*).

The stress-strain curve for the nano-aluminum composition was comparable to the Al+$Fe_2O_3$+60 *vol.%* epoxy composition, in terms of the stress response, however, with a significantly different yield strain. The major difference in the overall dynamic response was observed in terms of elastic resilience of each of the three sample types. The resilience was obtained by calculating the area under the linear elastic region from the true stress-strain curves shown in Figure 4.65. The nano-Al+$Fe_2O_3$+70 *vol.%* epoxy composition showed the greatest resilience with a value of 15.45 ± 0.06 MPa. In contrast, the calculated resilience for Al+Fe2O3+60 *vol.%* epoxy and pure epoxy (batch *A*) compositions was 6.64 ± 0.04 and 6.31 ± 0.04 MPa, respectively. Thus, it appears that the addition of nano-scale aluminum particles has a profound influence on the elastic dynamic impact response in comparison to pure epoxy. However, the addition

of micron-scale particles shows a less evident influence as illustrated from only a slight increase in resilience as compared to pure epoxy. It is possible that the nano-scale aluminum particles influence the polymer composite's chain mobility and extends the elastic deformation response to a significantly greater elastic strain region for a comparable stress. Values of elastic moduli (also listed in Table 4.14) measured for each of the compositions in the linear-elastic portion of the stress-strain diagram show good agreement with those obtained from ultrasonic measurements, thus, providing confidence in the analysis and validity of the stress-strain curves obtained from dynamic impact experiments.

This analysis successfully permits the relative comparison of each composition's performance from several Taylor impact experiments which give quantitatively measurable differences in the mechanical behavior for each of the materials examined. The analysis also permits the estimation of elastic and plastic wave speeds propagating within the material. These are calculated directly from equations (4.24) and (4.25), respectively. Elastic wave speeds listed in Table 4.14 compare well with ultrasonic measurements for pure epoxy and Al+$Fe_2O_3$+60 *vol.%* epoxy composition. However, the elastic wave speed obtained for the nano-aluminum composite material deviates significantly from ultrasonic values.

### 4.4.4 Distance-Time Plots for Analysis of Elastic-Plastic Wave Interaction

Calculations thus far have been based on the final state of the impacted materials. It is also possible to characterize the incremental changes (due to deformation), observed

throughout the impact experiment, with the use of high-speed photography. As the elastic and plastic waves propagate within the specimen, incremental stress and strain values can be obtained to yield a detailed history of elastic and plastic wave propagation, thereby permitting the precise determination of all possible stress and strains that the material experiences throughout the impact. During the first moment of contact as the anvil impacts the target rod, an extremely large stress forms within the material. The peak stress dissipates as the plastic wave travels through the specimen, and upon its interaction with the elastic wave, reduces below the yield stress, where the wave ceases to propagate. The corresponding time can be identified experimentally using an *x-t*

**Table 4.15** High-speed camera transient deformation measurements are used to calculate the dynamic material property at discrete time intervals using analysis developed by Hutchings [98] for Al+$Fe_2O_3$+60 *vol.%* epoxy (shot 0530).

| Time [μs] | $L/L_0$ | $k$ | $Y$ [MPa] | $\sigma_y$ [MPa] | $\sigma$ [MPa] | $\varepsilon$ | $\varepsilon_y$ | $\dot{\varepsilon}$ [1/s] | $C_P$ [mm/μs] | $C_0$ [mm/μs] |
|---|---|---|---|---|---|---|---|---|---|---|
| 0.92 | 0.999 | 0.001 | 9855.2 | 9868.3 | 10035.8 | 0.018 | 0.001 | 19450 | 2.058 | 55.936 |
| 9.23 | 0.981 | 0.019 | 542.6 | 555.7 | 596.8 | 0.091 | 0.024 | 9835 | 0.508 | 3.150 |
| 17.54 | 0.963 | 0.037 | 247.0 | 260.2 | 289.1 | 0.146 | 0.050 | 8300 | 0.358 | 1.475 |
| 25.85 | 0.946 | 0.054 | 158.7 | 171.8 | 196.0 | 0.190 | 0.076 | 7364 | 0.299 | 0.974 |
| 34.16 | 0.942 | 0.058 | 143.7 | 156.8 | 180.1 | 0.202 | 0.084 | 5916 | 0.288 | 0.889 |
| 42.47 | 0.950 | 0.050 | 171.6 | 184.7 | 209.7 | 0.182 | 0.071 | 4274 | 0.308 | 1.047 |
| 50.78 | 0.957 | 0.043 | 209.8 | 222.9 | 250.0 | 0.161 | 0.059 | 3165 | 0.335 | 1.264 |
| 59.09 | 0.963 | 0.037 | 247.0 | 260.2 | 289.1 | 0.146 | 0.050 | 2464 | 0.358 | 1.475 |
| 75.71 | 0.974 | 0.026 | 369.3 | 382.4 | 416.9 | 0.114 | 0.034 | 1509 | 0.427 | 2.168 |
| 84.02 | 0.976 | 0.024 | 407.4 | 420.5 | 456.5 | 0.108 | 0.031 | 1282 | 0.446 | 2.383 |
| 100.64 | 0.972 | 0.029 | 337.1 | 350.3 | 383.4 | 0.121 | 0.037 | 1199 | 0.410 | 1.985 |
| 108.95 | 0.978 | 0.022 | 453.2 | 466.3 | 504.2 | 0.101 | 0.028 | 927 | 0.468 | 2.643 |

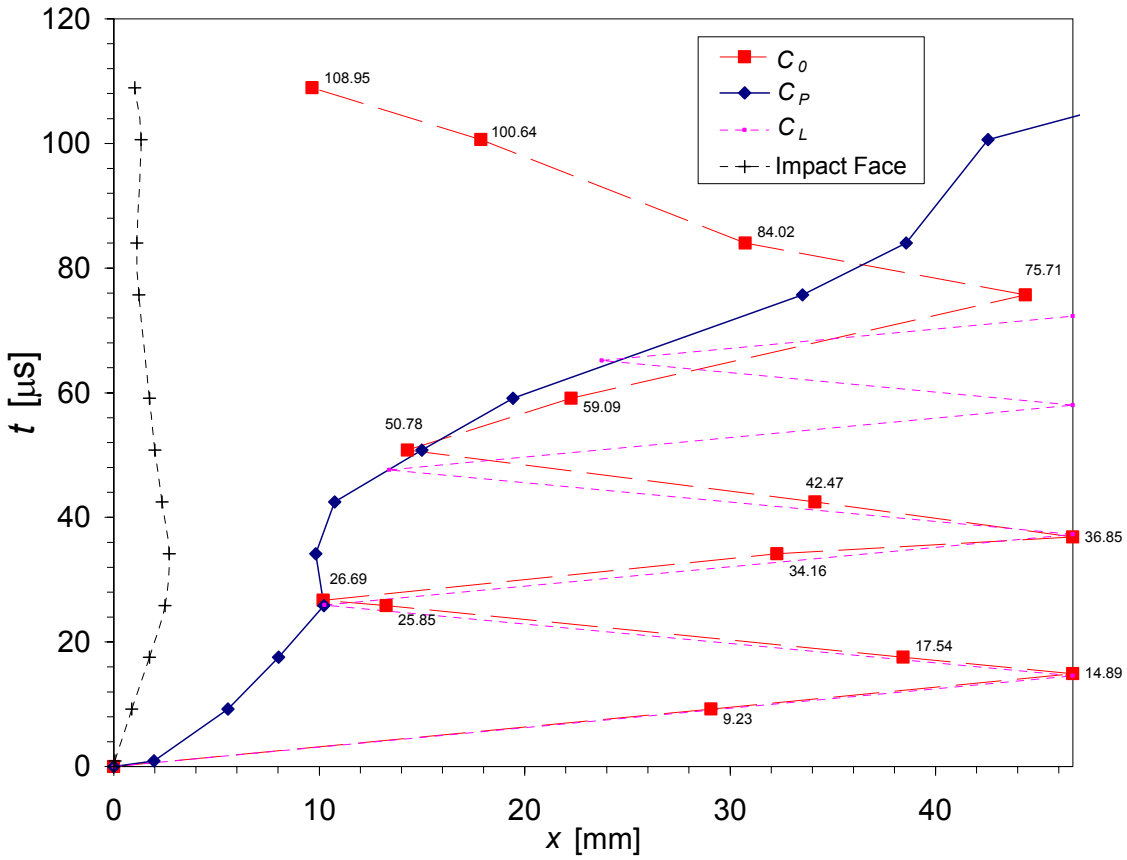


**Figure 4.66** Calculated *x-t* diagram showing the wave propagation within the specimen for shot 0530. Each position data point and corresponding time (after impact) is shown from measurements obtained from high-speed camera images and calculated using the relation $dx = Cdt$.

(distance-time) diagram constructed from incremental stress-strain calculations. The details of this analysis are discussed below for the Al+$Fe_2O_3$+60 *vol.%* epoxy material from shot 0530, and the calculated values for each time increment determined by high-speed camera image timing are listed in Table 4.15.

The *x-t* diagram in Figure 4.66 shows the propagation path of elastic and plastic waves determined from calculated $C_0$ and $C_P$ values at discrete times after impact. The relation $dx = Cdt$ was used to calculate the wave positions, where $C$ was either the elastic or plastic wave speed determined from equations (4.24) and (4.25), respectively. The

elastic wave, of speed consistent with the ultrasonically measured longitudinal wave, arrives at the back surface of the rod shaped sample 14.89 μs after impact. The elastic wave reflects from the free surface and arrives at the advancing plastic wave front after 26.69 μs and then returns to the free surface 36.85 μs after impact. The plastic wave front at the time of interaction with the elastic wave has propagated 10.25 mm into the specimen, and its calculated stress using equations (4.32) and (4.33) is reduced to approximately 159 MPa (listed in Table 4.15 at 25.85 μs after impact), which is significantly lower than the average dynamic yield stress of 389.1 ± 8.6 MPa obtained for this composition. As a consequence, the reduced yield stress suppresses further advancement of the plastic wave as indicated by calculated wave position values at later times. Figure 4.66 also incorporates the specimen's overall axial length change obtained from high-speed camera images including elastic recovery towards the end of the observed time interval. The onset of elastic recovery within the material shows good agreement with the interaction of the elastic and plastic waves. The elastic and plastic wave positions obtained from the analysis appear to overlap on their next encounter with each other approximately 50 μs after impact. This time coincides with the conclusion of elastic length recovery within the specimen. Velocity interferometry measurements verify the elastic wave arrival times and are discussed in more detail next (section 4.4.5).

Taylor's analysis [45] of such impact events assumes a rigid perfectly-plastic material model, and the elastic/plastic wave interaction theoretically causes the stress within the material to become zero, thus stopping the advancement of the plastic wave. However, for a viscoelastic-viscoplastic plastic material this may not be the case, and the plastic wave may continue to have some energy for continued propagation. This effect is

evident in the *x*-*t* diagram of Figure 4.66, which shows the elastic wave slowly taking over the plastic wave upon their second interaction. Eventually, the plastic wave dissipates completely and stops propagating. Experimental calculations show that this occurs during the time period where the elastic relaxation is taking place, which complicates the calculation of elastic and plastic wave positions. However, the calculated elastic and plastic wave positions show fairly good consistency, as illustrated in Figure 4.66. The impact velocity and, thus, the initial magnitude of the stress wave have a direct consequence in the behavior of the elastic/plastic wave interaction.

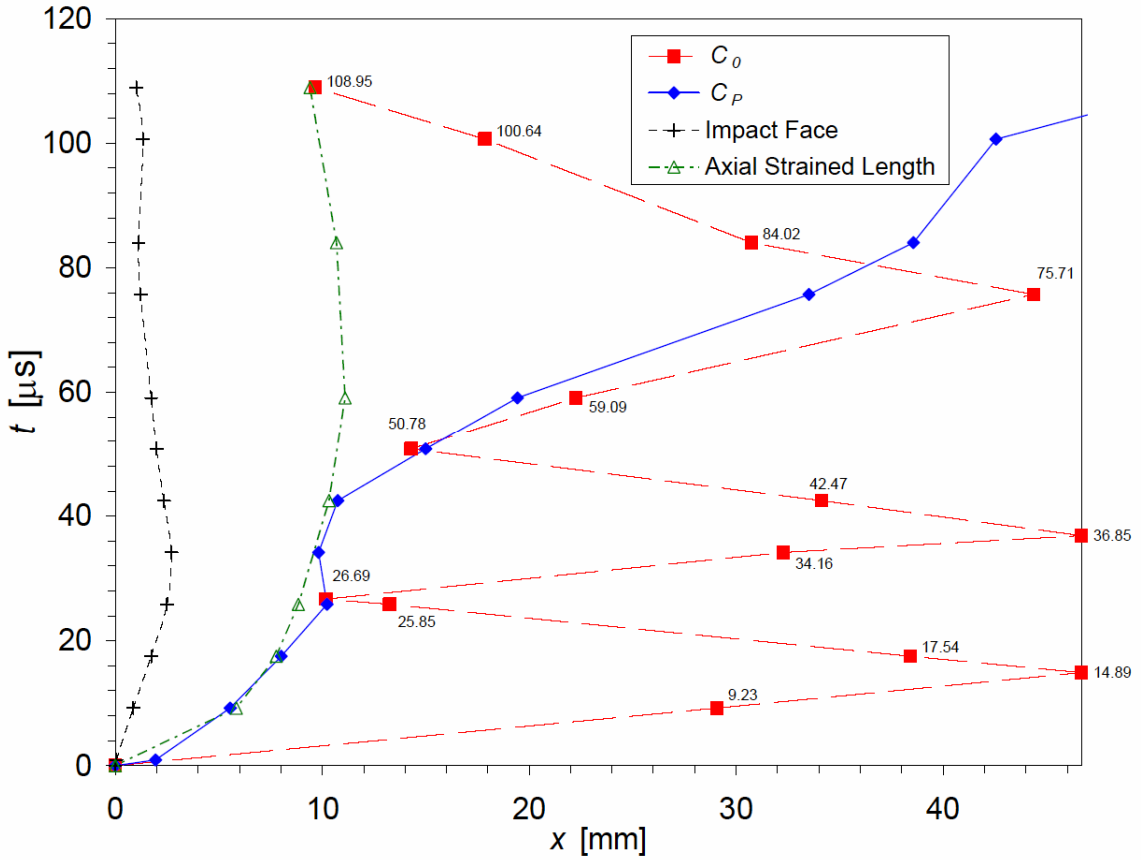


**Figure 4.67** Measured axial strained lengths from high-speed camera images are used to determine plastic wave position in the same *x*-*t* diagram as shown in Figure 4.66.

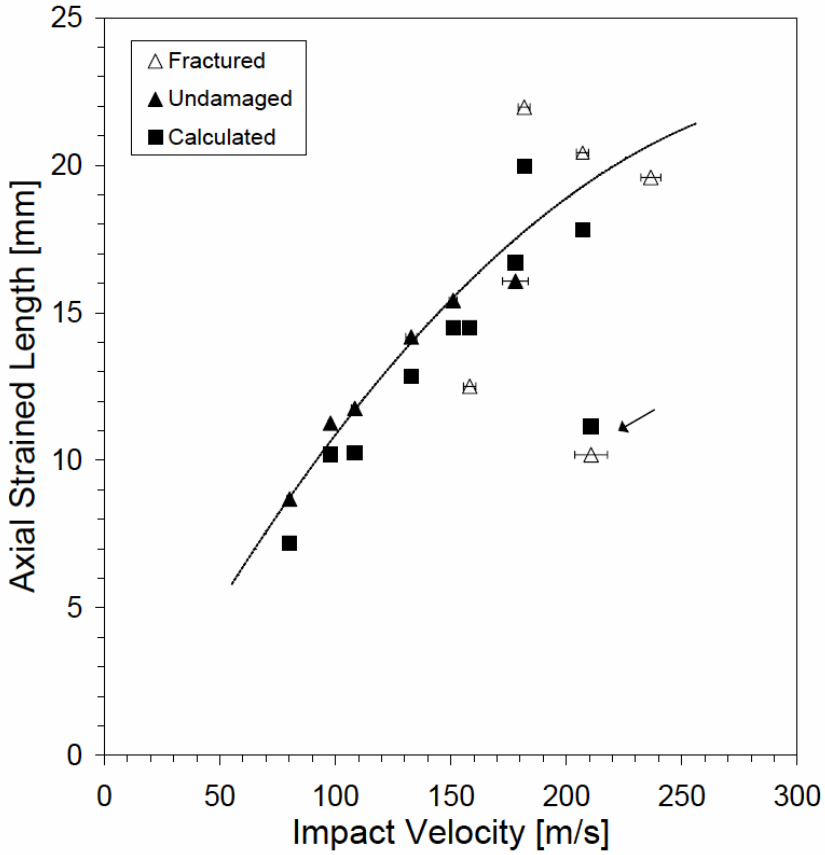


**Figure 4.68** Axial strained length measurements determined from high-speed camera images are compared to those determined from calculations using analysis developed by Hutchings [98]. Arrow indicates an experiment that uses an intentionally (approximately 30 %) shorter length specimen.

Plastic wave speed values obtained from Hutchings' analysis [98] for shot 0530 were verified by making measurements of the axially strained length over time for select high-speed camera images. Determination of the specimen's axially strained length can be challenging especially at early times during the impact where the plastic wave position movement is subtle. However, image analysis was performed by using a routine that measured the diameter of the deformed specimen at every pixel along the axial length. The axial strained length was determined by measuring along the axial length of the deformed specimen and recording the location where there was a 2 % increase in the

specimen's diameter. This method gave highly reproducible results for obtaining the plastic deformation distance from the impact face. The axial strained length was used to compare the calculated position of the plastic wave from Hutchings' analysis, as shown in the *x-t* diagram of Figure 4.67. The plastic wave position determinations show good correlation for the two methods and give excellent confidence in the calculated plastic wave values. Furthermore, the axial strained length for each of the experiments was measured using the latest possible image obtained from all the impact experiments conducted for the Al+$Fe_2O3$+60 *vol.%* epoxy composition. These results are plotted as a function of impact velocity and shown in Figure 4.68. This was compared to calculated values using Hutchings' analysis and, again shows good agreement even for specimens that fracture. The axially strained length was also measured for a specimen with an intentionally shorter initial length of 31.31 ± 0.13 mm (shot 0536), and was found to have a good correlation with a calculated value obtained from Hutchings' analysis. The specimen was approximately 30 % shorter than the other specimens used for reverse Taylor impact experiments, and thus, the elastic and plastic wave interaction took place at a significantly shorter region along the axial length of the specimen. This result is also shown in Figure 4.68 for an impact velocity of 211 m/s (indicated by the arrow).

### 4.4.5 Elastic-Plastic Wave Interaction Based on Time-Synchronized VISAR and Camera Measurements

Velocity interferometry measurements (VISAR) were perfored to obtain details about the material's wave propagation response during Taylor impact experiments by tracking the rod-shaped specimen's back (free) surface velocity. Figure 4.69 shows an

example of the corresponding VISAR signal and time synchronized axial and areal strain measurements obtained from high-speed camera images for Al+$Fe_2O_3$+60 *vol.%* epoxy composite (shot 0530). The time it takes for the elastic wave to travel the length of the specimen gives the characteristic longitudinal wave speed, which was unique for each material composition. With knowledge of specimen length, the longitudinal wave velocity was easily attainable by measuring the elastic wave arrival time at the back surface or free surface of the specimen. Longitudinal wave speed measurements were obtained for each epoxy-cast composition, with the exception of experiments conducted on pure epoxy specimens in which VISAR was not used. Longitudinal wave speeds determined from VISAR measurements generally showed very good agreement, typically 2 to 3 % greater than ultrasonic measurements. The average longitudinal wave speeds obtained from Taylor impact experiments compared with ultrasonic values are listed in Table 4.16.

Referring to Figure 4.69, it can be seen that the VISAR signal has an associated velocity rise with the arrival of the elastic wave at the free surface, at 14.6 μs compared to 14.89 μs, calculated from the elastic wave speed and sample length. The next change in slope is associated with the elastic and plastic wave interaction occurring at 26.3 μs.

**Table 4.16** Comparison of longitudinal wave speed values measured using ultrasonic and VISAR techniques.

| Composition | $C_L$ (*Ultrasonic*) [mm/μs] | $C_L$ (*VISAR*) [mm/μs] |
|---|---|---|
| Al+$Fe_2O_3$+60 *vol.%* epoxy | 2.936 ± 0.013 | 3.080 ± 0.185 |
| nano-Al+$Fe_2O_3$+70 *vol.%* epoxy | 2.778 ± 0.032 | 2.820 ± 0.022 |

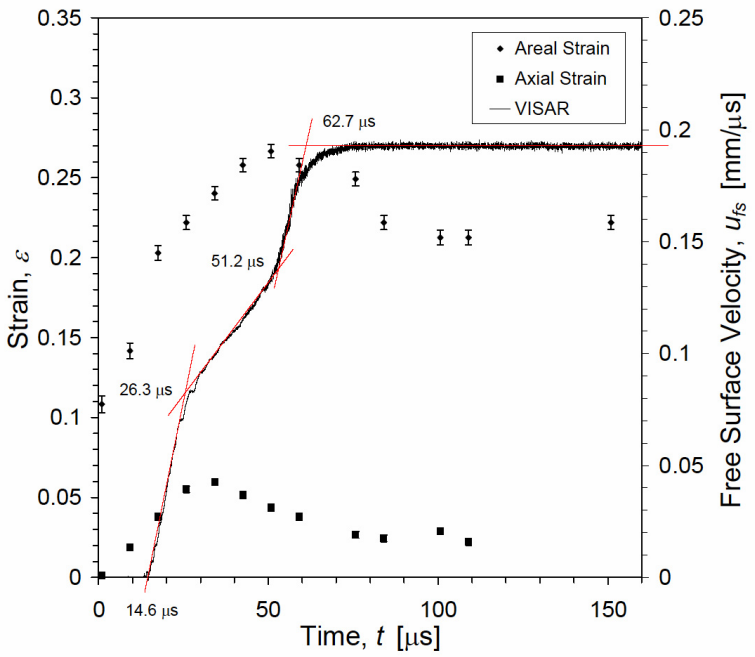


**Figure 4.69** Time-synchronized VISAR and camera measurements comparing axial and areal strain, and free surface velocity as a function of time for shot 0530. Corresponding wave interaction times are shown next to the free surface velocity trace at slope transition regions.

Again, this shows very good agreement with the calculated value of 26.69 μs. The final change in slope is associated with the elastic wave returning to the free surface at 51.2 μs (50.78 μs based on calculations). Notice that the onset of elastic recovery observed through strain measurements coincides precisely with the interaction of the elastic and plastic waves.

The elastic wave propagating within the material is not perfectly smooth or square-shaped and has an associated slope due to wave dispersion or an uneven front. Viscoelastic-viscoplastic material behavior also "smears" the response. However, the timing observed from x-t diagrams coincides perfectly with the arrival time of the elastic wave at the back surface and plastic wave boundary measured with VISAR. This was

typically observed for all of the experiments conducted in this study.

The VISAR signal can also be used to calculate the material's dynamic yield stress, strain at yield point, and the strain rate at yield, respectively, using the following relations [16]:

$$\sigma_Y = \frac{1}{2}\rho_0 C_0 \Delta u_{fs}, \tag{4.34}$$

$$\varepsilon = \frac{u_P}{C_0} = \frac{1}{2}\frac{u_{fs}}{C_0}, \tag{4.35}$$

$$\dot{\varepsilon} = \frac{d\varepsilon}{dt} = \frac{\varepsilon}{\Delta t}, \tag{4.36}$$

where $\Delta u_{fs}$ is the change in free surface velocity obtained from VISAR measurements, $C_0$ is the ultrasonically measured average elastic wave speed, $u_P$ is particle velocity, and $\Delta t$ is the time change associated with the change in free surface velocity. Figure 4.70 schematically illustrates the elastic and plastic wave interactions and the resulting VISAR response. The disturbance signal takes time to propagate within the specimen and corresponds to a response delay equivalent to the travel time through the length of the specimen. The VISAR measures a rise in free surface velocity when the elastic wave reaches the back surface. Meanwhile the impact area of the specimen is plastically deforming, and the signal associated with this disturbance takes time to propagate through the specimen before being detected by VISAR. In order to measure the response due to the deformation occurring at the impact face, the VISAR signal was time-shifted

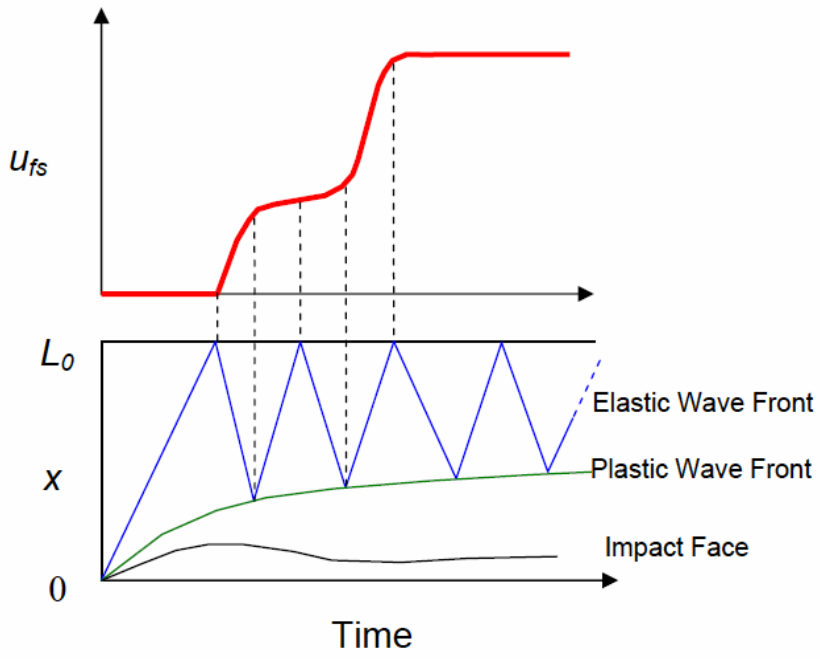


**Figure 4.70** Illustration depicting wave propagation within a specimen that coincides with free surface velocity measurements.

to coincide with these effects by compensating for the travel time required to traverse the specimen. Figure 4.71 shows the time-shifted VISAR response and strain measurements for shot 0530. Calculated values of yield stress obtained from equation (4.34), as well as strain and strain rate at the yield point from equations (4.35) and (4.36), respectively, are compared to values obtained from the convergence of equations (4.32) and (4.33) from Hutchings [98]. These values are listed in Table 4.17 for experiments that used VISAR diagnostics. Fairly good consistency between each experiment was observed for stress, strain, and strain rate values obtained from VISAR measurements. These values also compare well for select experiments with calculated values obtained from Hutchings' analysis (also listed in Table 4.17), for all experiments except for shot 0529; which yields at a significantly lower yield stress and strain as compared to that obtained from VISAR

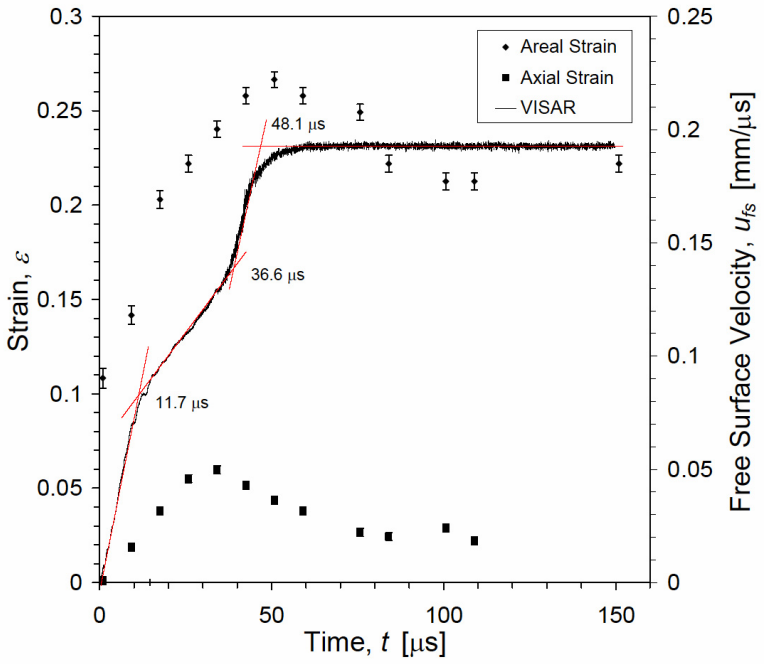


**Figure 4.71** Time-shifted VISAR and high-speed camera measurements to give instantaneous response measurements of elastic/plastic wave interaction for shot 0530.

analysis. Since shot 0529 was performed at an impact velocity of 80.1 ± 1.2 m/s, which is close to the measured critical velocity (74.3 m/s) for onset of permanent plastic deformation, the length measurements show only slight deformation (that are within experimental error) and therefore, Hutchings analysis may not be correctly applicable for this particular experiment.

Calculated values listed in Table 4.17 using Hutchings analysis that show evidence of fracture were evaluated for measurements obtained from camera images prior to fracture. Calculated strain rates show an order of magnitude increase as compared to specimens that did not fracture. These effects are not apparent in the values obtained from the VISAR signal since they are evaluated at the material's yield point before fracture occurs. Therefore, the analysis does not account for the change in density due to

**Table 4.17** Comparison of computed stress, strain, and strain rate values obtained from VISAR measurments and values obtained from the one-dimensional elastic-plastic wave analysis developed by Hutchings [98].

| Shot Number | $U$ [m/s] | $\Delta u_{fs}$ [m/s] | $\Delta t$ [μs] | $\sigma_y$ [MPa] | $\varepsilon_y$ | $\dot{\varepsilon}$ [1/s] | $Y$ [MPa] | $\varepsilon_y$ | $\dot{\varepsilon}$ [1/s] |
|---|---|---|---|---|---|---|---|---|---|
| | | *VISAR Measurements* | | | | | *Hutchings' Analysis* | | |
| *$Al+Fe_2O_3$+60 vol.% epoxy* | | | | | | | | | |
| 0529 | 80.14 | 110.44 | 30.32 | 327.3 | 0.022 | 729 | 101.8 | 0.122 | 1431 |
| 0530 | 108.4 | 110.77 | 25.87 | 328.5 | 0.022 | 857 | 391.7 | 0.033 | 1229 |
| 0537 | 132.9 | 117.08 | 26.51 | 350.5 | 0.023 | 884 | 377.0 | 0.034 | 1760 |
| 0541 | 151.0 | 112.25 | 26.64 | 337.2 | 0.023 | 843 | 397.2 | 0.032 | 2091 |
| *0535 | 158.20 | 123.67 | 27.76 | 366.3 | 0.025 | 891 | 309.6 | 0.041 | 10874 |
| +0542 | 177.95 | 121.20 | 26.63 | 361.6 | 0.024 | 911 | 343.2 | 0.037 | 2668 |
| *0531 | 207.03 | 110.95 | 27.08 | 329.2 | 0.022 | 820 | 389.2 | 0.033 | 14018 |
| *0536 | 210.74 | 111.07 | 16.38 | 330.2 | 0.022 | 1357 | 385.1 | 0.033 | 19891 |
| *nano-$Al+Fe_2O_3$+70 vol.% epoxy* | | | | | | | | | |
| 0649 | 143.6 | 186.32 | 36.18 | 486.7 | 0.037 | 1030 | 400.2 | 0.071 | 5701 |
| 0650 | 175.2 | 209.87 | 34.61 | 548.7 | 0.042 | 1213 | 395.3 | 0.072 | 7617 |
| *0646 | 235.29 | 161.74 | 32.16 | 423.0 | 0.032 | 1006 | 534.6 | 0.054 | 51170 |
| *0647 | 288.25 | 161.85 | 33.12 | 422.0 | 0.032 | 978 | 469.7 | 0.061 | 67381 |

*Indicate experiments where fracture was observed.
+Final state of specimen was not captured from high-speed images.

fracture and distension in the composite that alter the resulting elastic and plastic wave interaction behaviors. However, they do show good agreement for the ideal impact experiments where fracture was not observed.

An additional benefit of VISAR was the ability to detect evidence of fracture initiation within the specimen and its correlation with observations made from high-speed camera images. This combined with the calculated *x-t* diagrams, gives a complete description of the material's deformation behavior throughout the impact experiment. Time synchronized high-speed camera and VISAR data (time-shifted) for a specimen that

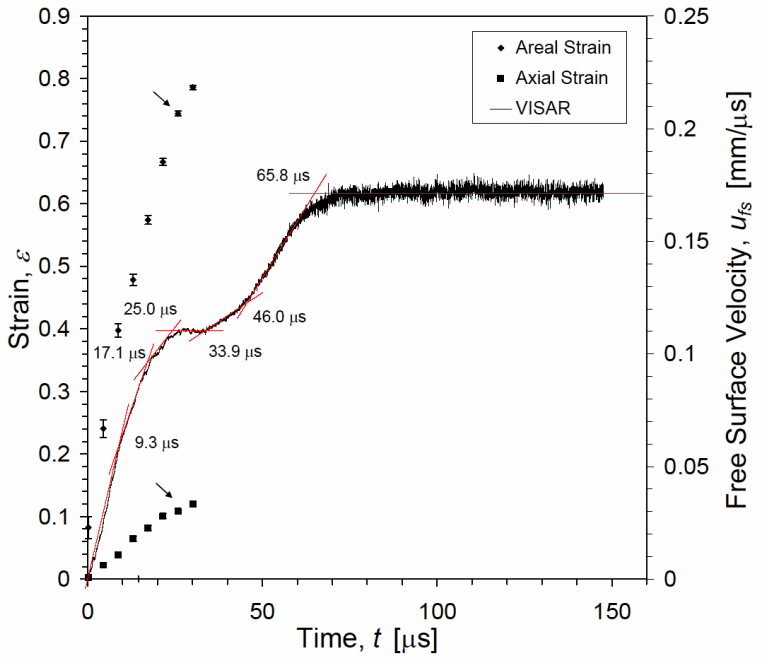


**Figure 4.72** Areal ♦ and axial ■ strains measured from high-speed camera images as a function of time after impact are time-shifted with the VISAR trace for impact velocity of 207.0 m/s (0531). While the specimen elastically recovers to a constant strain level approximately 75 μs after impact in the sample that does not fracture (as illustrated in Figure 4.69) for shot 0530, shot 0531 shows visual evidence of fracture at 25.81 μs after impact (indicated by the arrows). Notice the significantly greater strain scale for this experiment and that shown in Figure 4.71.

fractures is shown in Figure 4.72 for shot 0531. Upon impact, the elastic and plastic compression waves propagate along the axial length of the specimen, and a rise in free surface velocity is observed when the elastic wave arrived at the back surface. Upon reflection, the tensile elastic wave reaches the plastic wave approximately 9.3 μs after impact. The VISAR signal shown in Figure 4.72 has a slight change in acceleration following the elastic/plastic wave interaction at 17.1 μs, prior to reflecting from the rear surface of the specimen. The slope change indicates that the specimen has been damaged enough to modify the elastic wave propagation. As revealed from high-speed camera images, catastrophic fracture was not evident until 25.81 μs. The time of fracture

initiation is indicated by an arrow shown in the figure corresponding to the measured axial and areal strains. Additionally, the signature of catastrophic fracture is evident in the VISAR signal at approximately 25 μs, where the free surface velocity reaches a plateau of approximately 110 m/s, which corresponds (in time) very well with the observed fracture from high-speed images. Furthermore, the abrupt change of the VISAR signal in this region gives a clear indication that the material response to dynamic loading has been altered as compared to a specimen that does not fracture (as shown in Figure 4.71). Comparison of the VISAR signals in (Figure 4.71 for shot 0530 and Figure 4.72 for shot 0531), shows the initial acceleration associated with the elastic wave propagating through the material is identical, with slopes of approximately $5.8 \times 10^{-3}$ and $5.7 \times 10^{-3}$ mm/μs$^2$ for the undamaged and fractured specimen experiments, respectively. However, the final acceleration observed for the fractured specimen, after the elastic and plastic wave interaction, clearly has been altered.

### 4.4.6 Post-Mortem Characterization of Recovered Impacted Material and Fragments

Recovered specimens, including fully intact deformed rods, and fragments of fractured rods, were typically collected and analyzed following direct and reverse Taylor impact experiments. For reverse Taylor experiment, subsequent fragmentation typically occurred following the initial impact of the anvil and sabot assembly at significantly latter times, even for relatively low impact velocities. This was mainly due to the experimental configuration. Initially, the anvil and sabot assembly impact the specimen and the deformation is captured by a high-speed camera. A secondary impact occurs

within the "soft" recovery catch tank where the sample strikes the rags used to slow down the projectile and debris from the experiment. This is followed by the anvil and sabot assembly reaching the catch tank and impacting the sample once again. The additional deformation and fragmentation imparted to the specimen occurs at significantly later times and is not quantitatively characterized by any experimental parameters measured during the relatively short time duration (approximately 150 μm after impact) of the experiment. Some experiments were specifically designed to capture the relatively fragile specimen before entering the catch tank and recovering the sample without additional secondary damage. However, this type of experiment could not be performed in every instance since it interfered with the time-resolved VISAR diagnostics. Therefore, extensive characterization of recovered fragments has not been performed for the reverse Taylor impact configuration.

Conversely, most direct Taylor impact experiments avoid the problem of secondary impacts and subsequent damage to the test specimen. Typically the specimen impacts the anvil and drops to the bottom of the experiment chamber. Fragments were recovered for a series of direct Taylor impact experiments conducted on the Al+$Fe_2O_3$+47 *vol.%* epoxy composition at velocities ranging from 105.2 to 209.9 m/s. The lowest velocity experiment (105.2 ± 15.4 m/s) was recovered fully intact with no additional secondary impact damage observed. The remaining four experiments were at sufficient velocities to cause fracture upon impact and these fragments were collected for post-mortem analysis. Examples of recovered specimen materials are shown in Figure 4.73 for each impact experiment where fracture occurred. Typically, 90 to 95 % of the specimen's initial mass was recovered after the experiment. Approximately 75 to

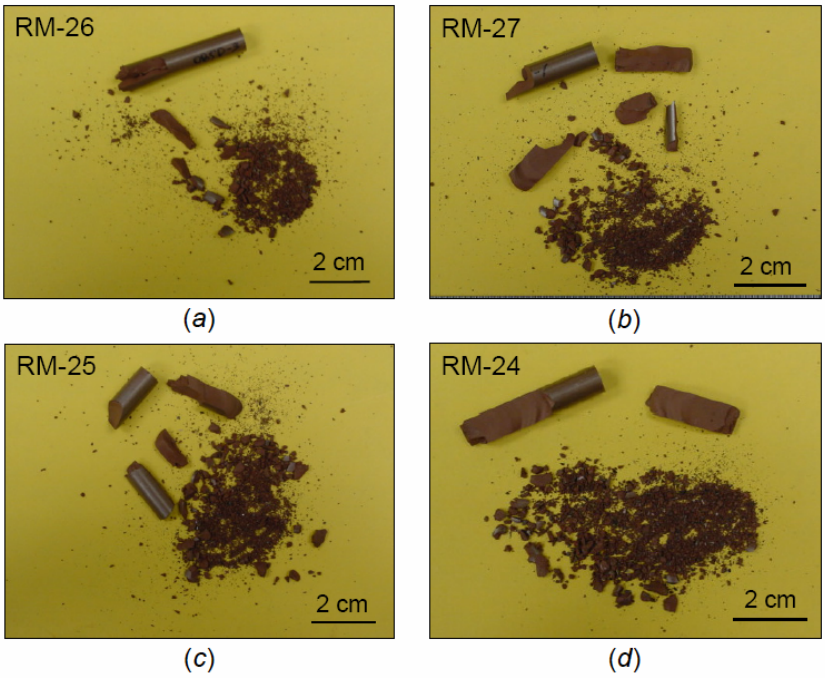


**Figure 4.73** Collected fragments recovered from direct Taylor impact experiments for Al+$Fe_2O_3$+47 *vol.%* epoxy composites with sufficient impact velocities to cause fracture. Impact velocities were *a*) 169.3, *b*) 175.9, *c*) 186.5, and *d*) 209.9 m/s.

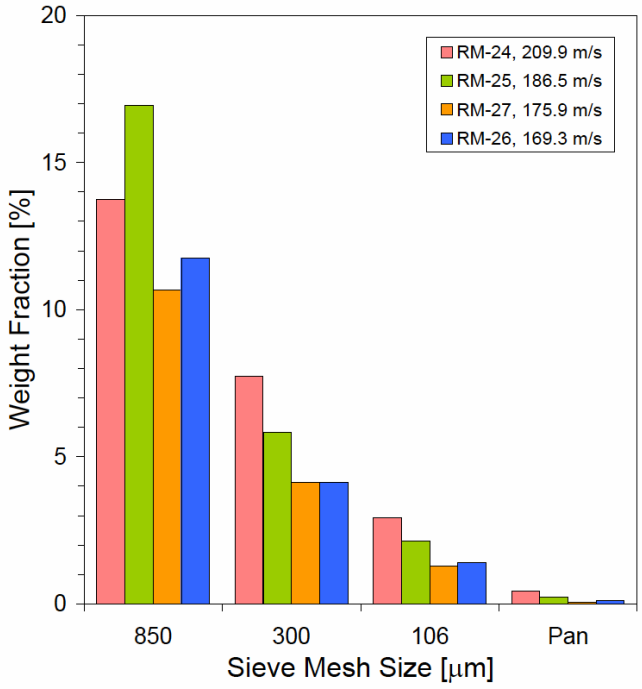


**Figure 4.74** Fragment size distributions based on weight fraction of collected material from direct Taylor impact experiments for Al+$Fe_2O_3$+47 *vol.%* epoxy composites.

85 % of this total mass consisted of relatively large pieces that were part of the back end of the specimen. The remaining 15 to 25 % of the fragments were located close to the impact face region of the specimen. The fragments from each experiment were sorted using 850, 300, and 106 μm sieves. Figure 4.74 shows the fragment size distribution based on the weight fraction of material collected from the specimen's impact face within the sieve size range. This figure does not include the relatively large pieces recovered from the back end of the specimen. In general, the fraction of particles within a particular size range increased as impact velocity increased. However, the fraction of particles collected for experiments RM-26 and RM-27 (169.3 and 175.9 m/s, respectively) had comparable size distributions within each size interval.

The fracture surfaces of fragments collected for each impact velocity were also examined and representative SEM images are shown in Figure 4.75(*a-d*) and Figure 4.76(*a,b*). The fracture surfaces typically showed a combination of features, such as aluminum particle pull-out regions as shown in Figure 4.75(*a,b*) or regions where epoxy is highly deformed and shows evidence of smearing while the hematite particles dispersed within the epoxy matrix show no evidence of deformation as illustrated in Figure 4.75(*c,d*). Other regions show the deformation of aluminum particles as demonstrated in Figure 4.76(*a,b*). For this particular case, a relatively large crack is inhibited from continued propagation by an aluminum particle that is possibly deformed from the interaction.

The examination of recovered fragment fracture surfaces provides some details about the behavior of the composite and its failure when subjected to high velocity impacts. It is desirable to correlate microstructural features with mechanical deformation

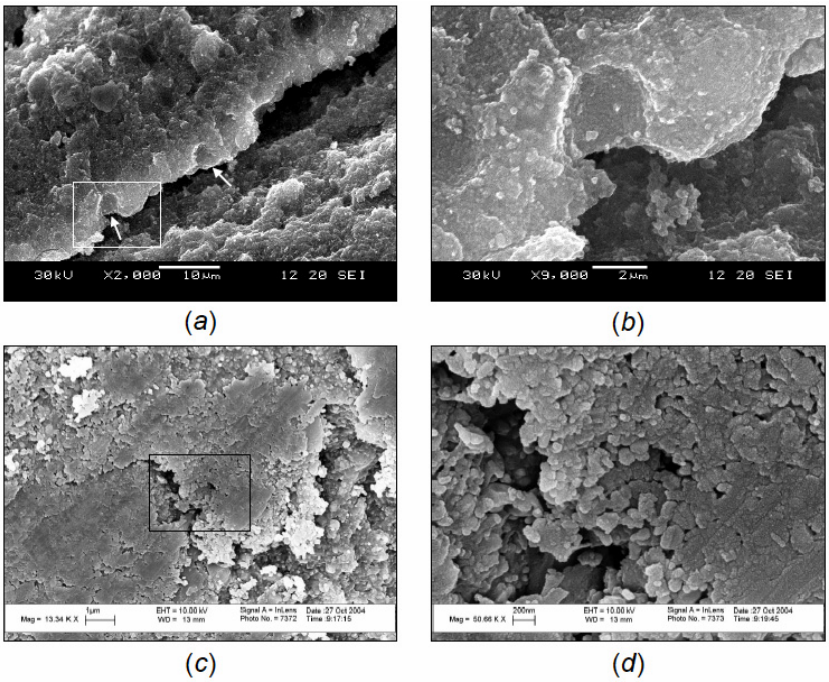


**Figure 4.75** Recovered fragment fracture surfaces from direct Taylor impact experiments *a,b*) RM-25 (186.5 m/s) and *c,d*) RM-27 (175.9 m/s). Specimens generally show *a,b*) aluminum particle pull-out features and *c,d*) highly deformed (smearing) epoxy phase regions. Higher magnification images illustrate an *b*) aluminum pull-out site, while *d*) shows a highly deformed hematite dispersed epoxy region with no apparent deformation of the individual hematite particles.

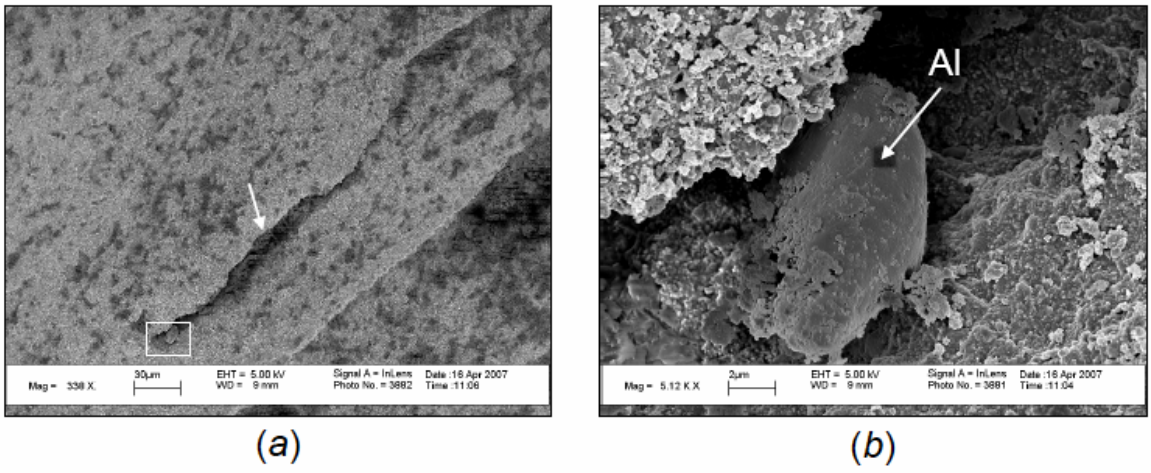


**Figure 4.76** SEM images of a recovered fragment fracture surface from the direct Taylor impact experiment RM-24 (209.9 m/s) showing *a)* relatively large crack inhibited by a *b*) deformed aluminum particle shown in a magnified view of the rectangular area identified in *a*).

and fracture behaviors. However, it is impossible to directly evaluate the composites bulk mechanical behavior as influenced by particle-scale microstructural effects, such as changing material architecture through particle morphology and size alterations. Recovered Taylor impact specimens were used to estimate the influence that microstructural features have on the composite's overall mechanical behavior. In some cases, post-impact specimens were recovered fully intact and examined, particularly looking at the imparted deformation localized to the impact region of the specimen. Figure 4.77(*a-d*) shows optical micrographs of the impact faces for recovered specimens with two different compositions and compares the influence of altering aluminum particle sizes on crack propagation in the extreme case for nano- and micron-scale particles. The images shown in Figure 4.77(*a,b*) were obtained from shot 0645 for nano-Al+$Fe_2O_3$+70 *vol.%* epoxy with an impact velocity of 201.1 m/s. The nano-composites have unique microstructural features which contain regions with high concentrations of nano-aluminum particles as shown in Figure 4.10(*a-c*) prior to impact (section 4.1.1). The concentrated nano-aluminum regions (indicated by arrows in Figure 4.77(*a,b*)) inhibit the crack propagation throughout the impact face of this sample. This was a common feature observed for all the nano-aluminum composite materials examined. Conversely, the micron-scale aluminum composite impact face shown in Figure 4.77(*c,d*), illustrates a completely different fracture behavior. The micrographs shown in this figure were obtained from a micron-Al+$Fe_2O_3$+60 *vol.%* epoxy specimen subjected to an impact velocity of 109.8 m/s (shot RM-22). The images illustrate significantly more damage and multiple fracture sites, many of which propagate across the impact face without being inhibited by the aluminum particles. There is also

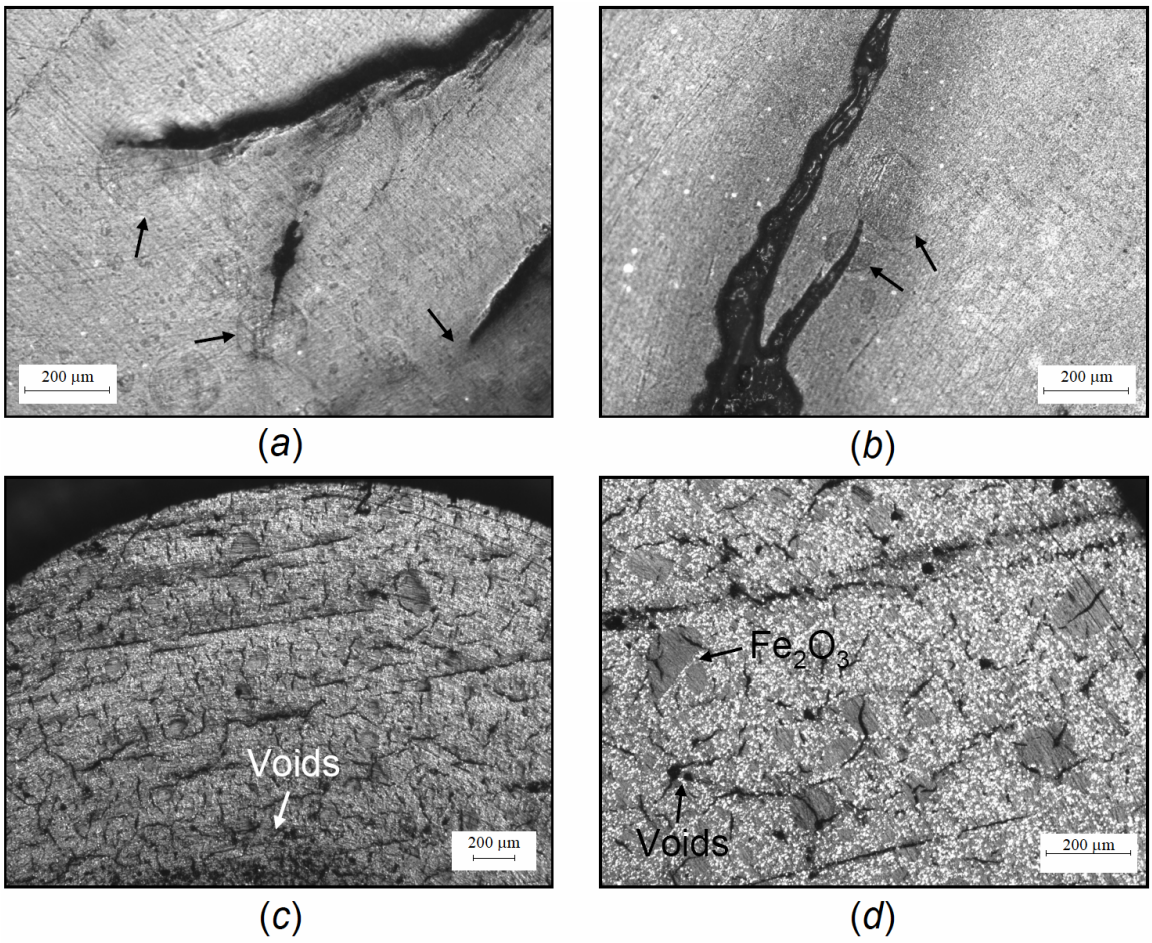


**Figure 4.77** Optical micrographs showing the impact faces of recovered (fully intact) Taylor specimens. Images compare the crack propagation behaviors for *a,b*) nano-Al+$Fe_2O_3$+70 *vol.%* epoxy with an impact velocity of 201.1 m/s (shot 0645) and *c,d*) micron-Al+$Fe_2O_3$+60 *vol.%* epoxy with an impact velocity of 109.8 m/s (shot RM-22). The highly concentrated nano-aluminum regions (indicated by arrows) inhibit the crack propagation in *a,b*), while the micron-scale aluminum composite exhibits intergranular crack propagation, typically between the aluminum particles. The micron-scale composite exhibits significantly more damage than its nano-scale counterpart.

significant concentration of voids, particularly in the central region of the specimen's impact face. Examinations of these two particular experiments illustrate the microstructural influence on the deformation behavior of these composites. The micron-scale aluminum composite had significantly more damage when compared to the nano-aluminum composite with approximately twice the impact velocity.

Reverse Taylor impact experiments, where the specimens fractured during the initial moments of impact, also reveal interesting features that permit the correlation of mechanical properties with microstructural features and chemical reactivity. Select reverse Taylor impact experiments with relatively high impact velocities (0644, 0646, and 0647) showed evidence of a dark footprint remaining on the anvil face. The recovered anvils are shown in Figure 4.78(*a-d*) after being removed from the recovered sabot. The entire anvil was placed in the SEM for further analysis, where closer examination of these footprints revealed evidence of localized chemical reactions and decomposition of the epoxy matrix. Chemical analysis using energy dispersive x-ray spectroscopy (EDS) indicated the presence of elemental aluminum, oxygen, and iron in concentrations that corresponded to the formation of $Al_2O_3$ and Fe (products of the $Al+Fe_2O_3$ thermite reaction) and other compounds in location '1' of Figure 4.78(*a-d*). Several other sites on the anvil face had identifiable debris, indicated in Figure 4.78(*a-d*) as locations '2' through '4', however, SEM analysis showed no evidence of chemical reaction in these other areas.

Post-mortem SEM analysis of the surfaces showed evidence of localized melting and re-solidification in addition to regions with no reaction, containing mostly hematite particles. Figure 4.79(*a-d*) shows SEM images acquired, from several locations within

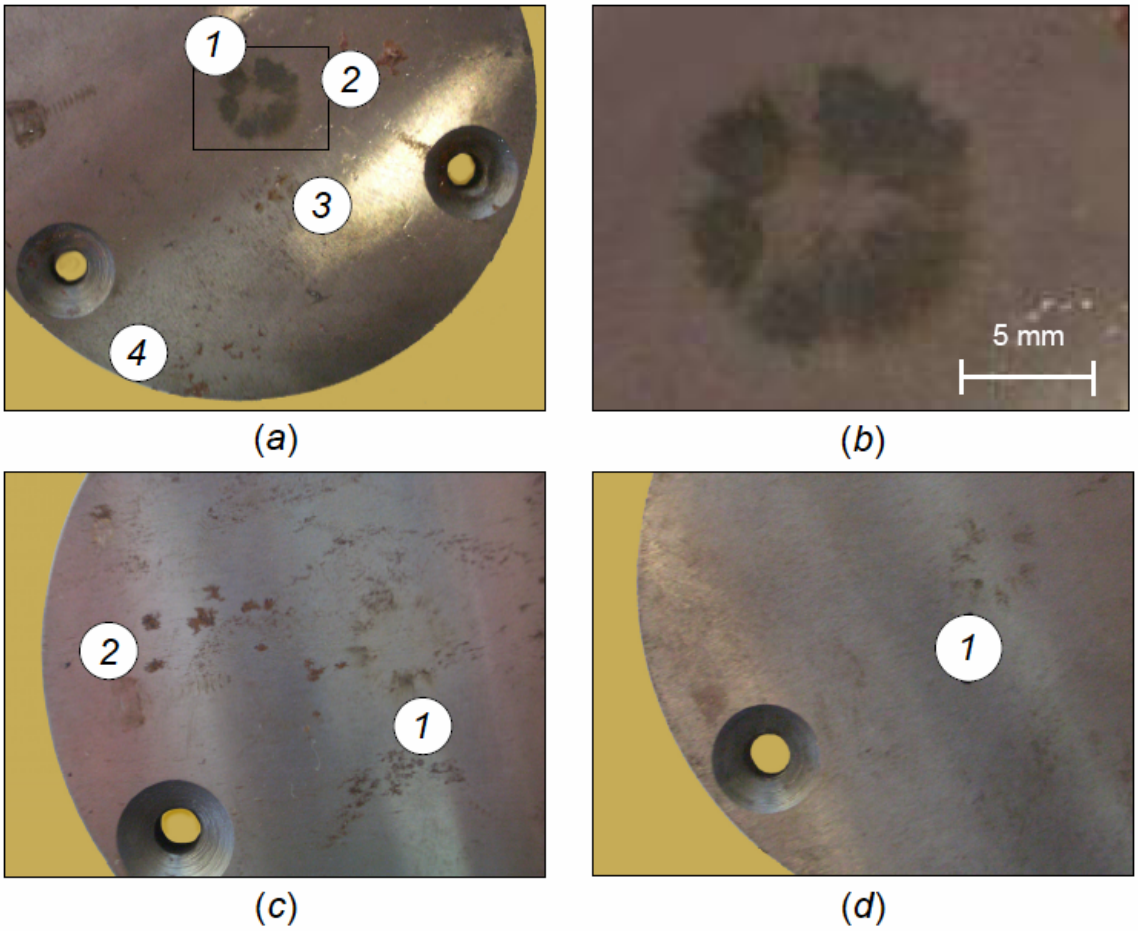


**Figure 4.78** Photos of recovered anvil plates from reverse Taylor impact experiments showing a dark footprint (location '1') and other specimen debris (locations '2' through '4') on the surface. The anvils were recovered from experiments with impact velocities of *a*) 423.2 m/s (shot 0644) for Al+$Fe_2O_3$+60 *vol.%* epoxy, and *c*) 288.3 m/s (shot 0646) and *d*) 235.3 m/s (shot 0647) for nano-Al+$Fe_2O_3$+70 *vol.%* epoxy. Image *b*) shows a close-up view of the footprint region identified in *a*).

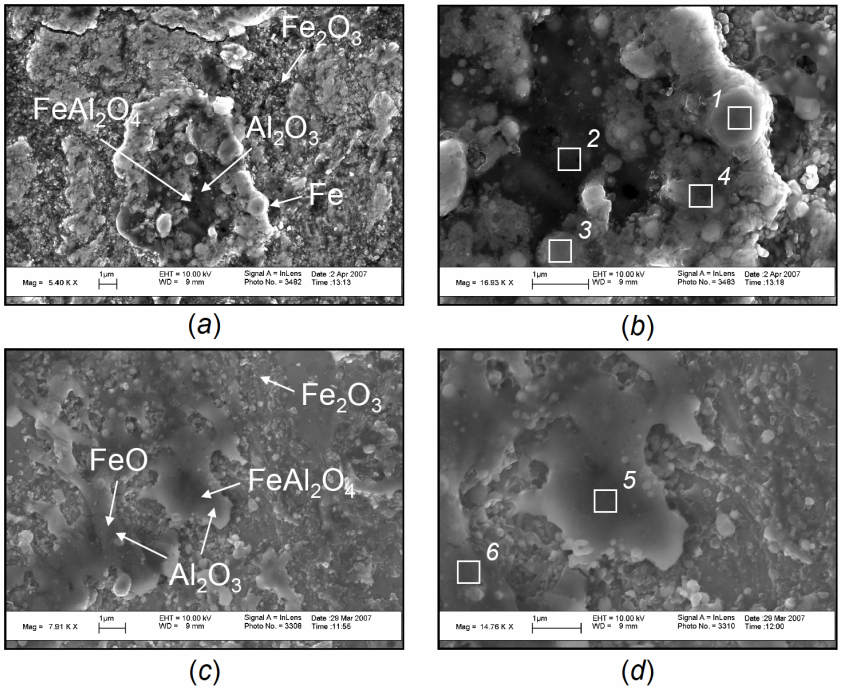


**Figure 4.79** Select SEM images obtained from the recovered anvil of shot 0644 within the footprint region, identified as location '1' in Figure 4.78(*a*). Images show melting and re-solidification with evidence of Al+$Fe_2O_3$ thermite reaction products determined from EDS scans. Images *b*) and *d*) show higher magnification views of *a*) and *c*), respectively, identifying EDS scan locations that are detailed in Table 4.18.

the footprint region for Al+$Fe_2O_3$+60 *vol.%* epoxy composite with an impact velocity of 423.2 ± 0.1 m/s (shot 0644). Figure 4.79(*a*) shows a localized reaction site with $Al_2O_3$ and Fe products in addition to an iron-alumina compound ($FeAl_2O_4$) at the bottom of a shell-like structure. The partially remaining structure possibly indicates that an aluminum particle was "coated" with a hematite shell before reaction. The background of this figure contains mostly hematite particles and possible epoxy decomposition products. Figure 4.79(*b*) shows a higher magnified view of Figure 4.79(*a*) indicating areas (labeled '1' through '4') where EDS scans were obtained to identify the chemical species present. The EDS results are listed in Table 4.18 along with the possible corresponding compounds for each location based on the identified elemental weight

**Table 4.18** Chemical analysis corresponding to locations identified in Figure 4.79(*b,d*) for Al+$Fe_2O_3$+60 *vol.%* epoxy composition. SEM and EDS was used to examine the recovered anvil from shot 0644 with an impact velocity of 423.2 m/s.

| Location | Fe [*wt.%]* | O [*wt.%]* | Al [*wt.%]* | Possible Phase(s) Present |
|---|---|---|---|---|
| 1 | 98.88 | 0 | 1.12 | Fe + Al |
| 2 | 24.49 | 33.00 | 42.51 | $FeAl_2O_4$ + $Al_2O_3$ |
| 3 | 87.64 | 4.91 | 7.45 | $AlFe_3$ + FeO + Fe |
| 4 | 52.90 | 27.52 | 19.58 | $Fe_2O_3$ + $Al_2O_3$ + Fe |
| 5 | 16.01 | 46.45 | 37.54 | $FeAl_2O_4$ + $Al_2O_3$ + AlO |
| 6 | 32.19 | 37.84 | 29.96 | FeO + $Al_2O_3$ |

percentages. This site also showed intermediate reaction products, such as $AlFe_3$ and FeO (location '3'). Figure 4.79(*c,d*) shows another location within the footprint area giving evidence of melting and re-solidification. The re-solidified reaction products appear to be on top of a layer of hematite particles. Figure 4.79(*d*) identifies areas (labeled '5' and '6') where EDS scans were also performed and the resulting probable reaction products are listed in Table 4.18. Other locations outside the dark footprint area showed identifiable debris remaining on the surface as shown in Figure 4.80, typically consisting of hematite with no evidence of reaction.

Post-mortem SEM analysis for epoxy-cast composites containing nano-aluminum were also conducted. Figure 4.81(*a-d*) and Figure 4.82(*a-d*) show images acquired from several locations on recovered anvils for shots 0647 (235.3 m/s) and 0646 (288.3 m/s), respectively. In general, the nano-aluminum composites showed more evidence of hematite reduction, however, there were some locations with Al+$Fe_2O_3$ thermite reaction products. Figure 4.81(*a-c*) shows evidence of melting and re-solidification of mostly

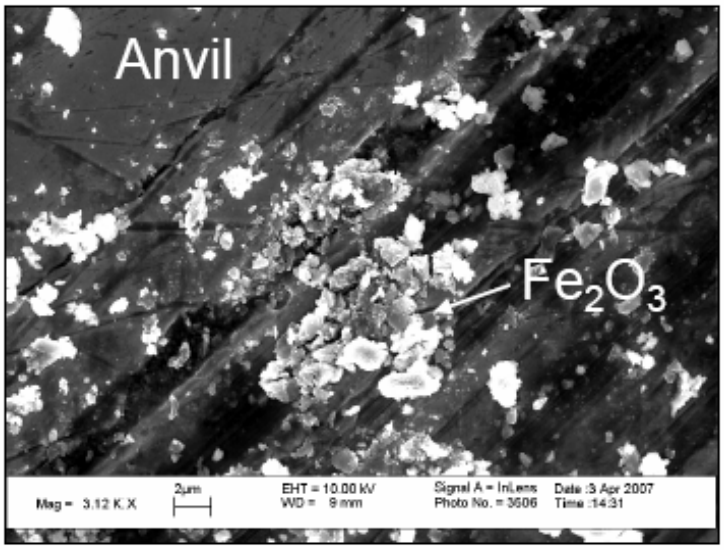


**Figure 4.80** Example of an SEM image obtained from external footprint areas (locations '2' through '4' in Figure 4.78), where hematite particles were found with no evidence of chemical reactivity.

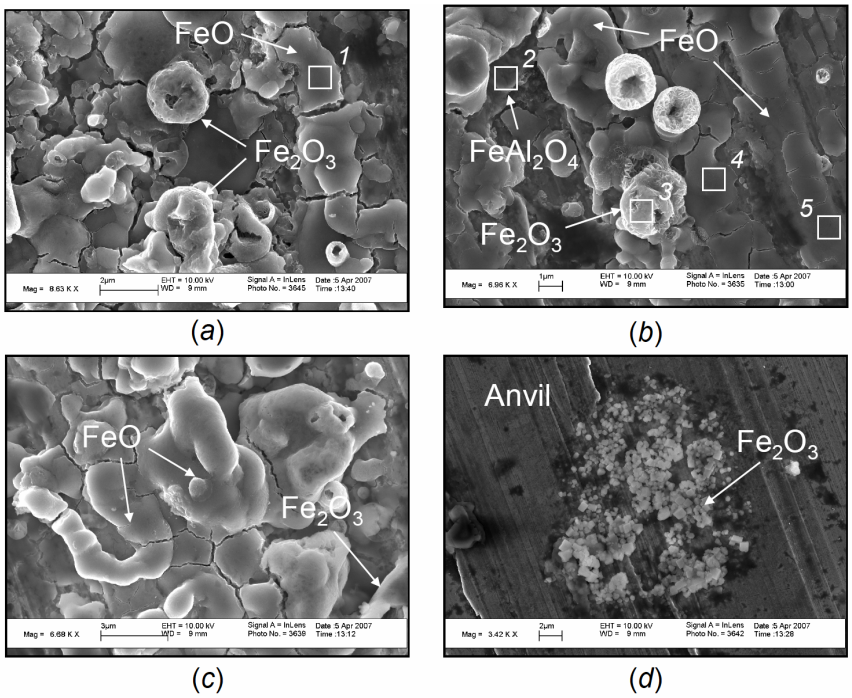


**Figure 4.81** Select SEM images obtained from the recovered anvil of shot 0647 within the footprint region, identified as location '1' in Figure 4.78(*d*). Images show evidence of melting and re-solidification. Images *a*) and *b*) show EDS scan locations that are detailed in Table 4.19, while *d*) shows a location outside the footprint region where hematite particles were found and no evidence of chemical reaction.

**Table 4.19** Elemental chemical analysis identifying possible phases located in the regions identified in Figure 4.79(*b,d*) for nano-Al+$Fe_2O_3$+70 *vol.%* epoxy composite. SEM and EDS was used to examine the recovered anvils from shots 0646 (288.4 m/s) and 0647 (235.4 m/s).

| Location | Fe [*wt.%]* | O [*wt.%]* | Al [*wt.%]* | Possible Phase(s) Present |
|---|---|---|---|---|
| 1 | 77.72 | 22.28 | 0 | FeO |
| 2 | 50.77 | 32.21 | 17.01 | $FeAl_2O_4 + Fe_2O_3$ |
| 3 | 69.93 | 30.07 | 0 | $Fe_2O_3$ |
| 4 | 72.11 | 27.89 | 0 | $Fe_3O_4$ |
| 5 | 84.65 | 15.35 | 0 | FeO + Fe |
| 6 | 30.84 | 69.16 | 0 | $Fe_2O_3$ |
| 7 | 71.40 | 28.60 | 0 | $Fe_3O_4$ |
| 8 | 72.31 | 27.69 | 0 | $Fe_3O_4$ |
| 9 | 76.71 | 23.29 | 0 | FeO |

hematite and unique hematite shell formations. The hematite shells possibly form by rapidly fusing initially clustered individual hematite ($Fe_2O_3$) particles (or agglomerates) before reducing to magnetite ($Fe_3O_4$). Table 4.19 lists chemical analysis results obtained from EDS scans for locations '1' through '5' identified in Figure 4.81(*a-c*). The nano-aluminum composites also had debris located on the anvil face in regions outside the footprint area, as indicated in Figure 4.81(*d*), which shows remaining hematite particles and no evidence of chemical reaction.

The higher velocity nano-aluminum composite impact experiment (shot 0646, 288.3 m/s) showed similar melting and re-solidification features (Figure 4.82(*a*)), as the previously discussed lower velocity experiment. However, some other locations within the impact footprint region showed rather interesting rapidly

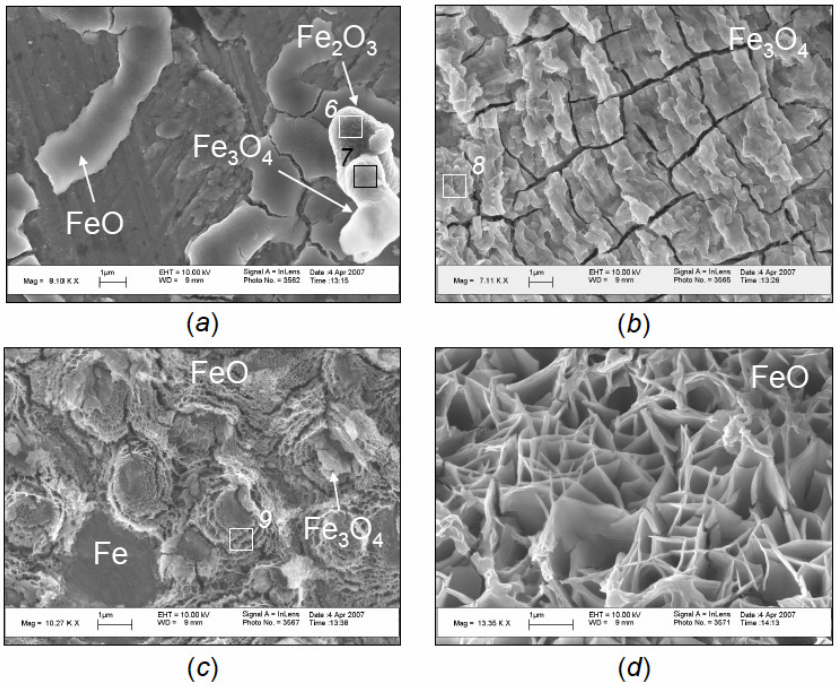


**Figure 4.82** Select SEM images obtained from the recovered anvil of shot 0646 within the footprint region, identified as location '1' in Figure 4.78(*c*). Image *a*) shows similar evidence of melting and re-solidification with EDS scan locations identified and detailed in Table 4.19. Images *b*) through *d*) show unique microstructures evolving due to rapid solidification and temperature gradients within the impact footprint region.

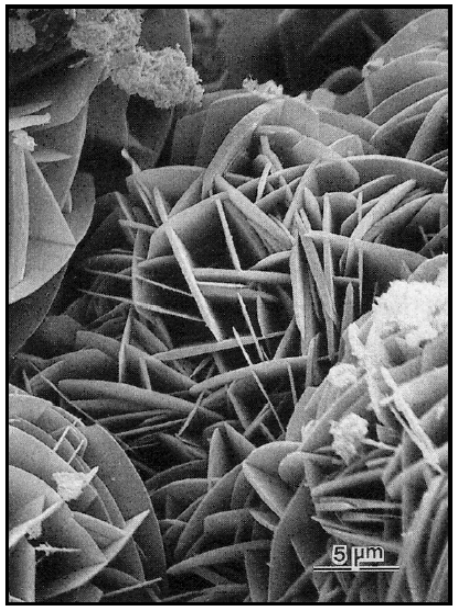


**Figure 4.83** Lepidocrocite ($\gamma$-FeOOH) formed by the slow oxidation of $Fe^{2+}$ solutions in the presence of solid $CaCO_3$ (calcite) [198-200].

solidified structures as shown in Figure 4.82(*b-d*). These unique structures appear to be forming from variations in solidification or oxidation rates. Figure 4.82(*b*) shows a layer of magnetite ($Fe_3O_4$) coating the surface while Figure 4.82(*c*) shows a field of solidified FeO structures with a remaining magnetite plate structure identified in the figure. These two sites were in adjacent locations radiating outward from the center of the footprint and indicate a possible temperature gradient that caused the differences in the structures formed. Figure 4.82(*d*) shows the structure that was located furthest from the central point of the impact footprint. This structure illustrates a rather unique formation that is associated with a relatively slow oxidation process. Very similar structures, shown in Figure 4.83, have been observed from the oxidized $Fe^{2+}$ solutions in the presence of solid $CaCO_3$ (calcite). The structures are formed by the oxidation in air, producing lepidocrocite ($\gamma$-FeOOH) and ferrihydrite ($Fe_5O_8H{\cdot}H_2O$) deposits on the calcite [198-200]. Lepidocrocite naturally occurs in rock, soils, and rust, often an oxidation product of $Fe^{2+}$ [170]. The lepidocrocite formed by the slow oxidation process has a very similar structure to that shown in Figure 4.82(*d*) for the nano-aluminum composite experiment.

### 4.4.7 Temperature Rise During Plastic Deformation

The mechanical work associated with plastic deformation partially transforms into heat with a resulting temperature rise of the specimen. The impact footprints remaining on the anvil face, for select reverse Taylor impact experiments, provides an instantaneous signature at the early moments of impact. The strain and corresponding stress were

estimated at the moment this footprint was created, in addition to estimating the bulk temperature rise associated with the mechanical work. The temperature rise has a significant effect on mechanical properties, particularly for polymers. For high-strain rates, it is reasonable to assume that the deformation process is essentially adiabatic [16]. The associated bulk adiabatic temperature rise from the plastic work associated with these strains was estimated using [16]:

$$\Delta T = \frac{\beta}{\rho C_p} \int_0^{\varepsilon_f} \sigma d\varepsilon \,, \tag{4.37}$$

where $\beta$ is the work rate to heat rate conversion factor, $C_p$ is heat capacity, and $\rho$ is density. The heat capacity of each composition was determined from mixture theory and the heat capacity for each constituent (0.90, 0.23, and 1.19 J/g K for aluminum [109], hematite [109], and epoxy [201], respectively). Although $C_p$ is readily available in tables (usually as a function of temperature), $\beta$ is not common and typically assumed to be constant in the range of 0.85 to 1.0 for metals [202]. However, Rittel [203] has found that $\beta$ is dependent on strain and strain rate (evaluated in the range of 5.0 to 8.0 x $10^3$ 1/s) during the plastic deformation of polycarbonate. The variation of $\beta$ with strain was very low for values up to a strain of about 20 %, however, it rapidly reaches a maximum value in the vicinity of 30 % strain and then decreases slowly with increasing strain. The maximum value of $\beta$ for polycarbonate increases from 0.4 ($\dot{\varepsilon}$ = 5.0 x $10^3$ 1/s) to 1.0 ($\dot{\varepsilon}$ = 6.5 x $10^3$ 1/s ) as strain rate increases. The same general behavior was reported by Trojanowski [204] for epoxy and also by Chou, *et al.* [205] for

polymethylmethacrylate, cellulose acetate butyrate, polypropylene, and nylon 6–6. Chou, *et al.* [205] also reported a low temperature rise at low strains followed by a noticeable rise with increasing plastic strain. Since there is a lack of available experimental data for $\beta$ as a function of strain and strain rate, particularly for filled epoxy composites, a constant value of 1.0 was used for the estimation of temperature rise. The use of this value was justified based on the experimental work of Rittel [203] showing the peak $\beta$ value rapidly reached 1.0 for polycarbonate at strain rates lower than those typically attained for Taylor impacts experiments ($10^4$ to $10^6$ 1/s initially upon impact). It is reasonable to assume this response is typical for most polymers, including the epoxy used for fabricating the structural energetic composites used in this current study.

The recovered anvils with the identifiable footprint markings discussed previous are shown in Figure 4.78(*a-d*) for each of the experiments. The diameter of the remaining footprints were precisely measured and the corresponding areal strain was calculated according to equation (4.23) in section 4.4.2; each resulting in a value close to 50 % strain. Table 4.20 lists the dimensions and corresponding areal strains calculated for each experiment.

The footprints were only observed for two different compositions at select impact velocities for each. The micron-Al+$Fe_2O_3$+60 *vol.%* epoxy composition showed evidence of a footprint at an impact velocity of 423.3 m/s. Unfortunately, the next lowest impact velocity for this particular composition was 236.6 m/s and showed no evidence of a footprint. The other composition, nano-Al+$Fe_2O_3$+70 *vol.%* epoxy, showed evidence of an impact footprint for two experiments at velocities of 235.3 and 288.3 m/s (shots 0646 and 0647, respectively). The next lowest impact velocity for this series of

**Table 4.20** Estimated temperature rise obtained from size measurements of footprint markings remaining on select anvils recovered from reverse Taylor impact experiments.

| Epoxy [*vol.%*] | Shot Number | Impact Velocity [m/s] | Initial Diameter [mm] | Footprint Diameter [mm] | Areal Strain [%] | ΔT [°C] |
|---|---|---|---|---|---|---|
| 60 | 0644 | 423.2 ± 0.1 | 7.53 ± 0.03 | 10.54 ± 0.01 | 48.88 ± 0.002 | 84.21 ± 0.37 |
| nano-70 | 0646 | 288.3 ± 0.9 | 7.54 ± 0.03 | 10.85 ± 0.01 | 51.72 ± 0.002 | 84.19 ± 0.35 |
| nano-70 | 0647 | 235.3 ± 1.1 | 7.56 ± 0.03 | 10.82 ± 0.01 | 51.23 ± 0.002 | 83.00 ± 0.35 |

experiments was 201.1 m/s and showed no remaining marks on the anvil face.

The remaining footprint observed from the micron-scale aluminum composite experiment was significantly darker and better defined than observed for the two nano-scale aluminum composite impact experiments. Close examination of each footprint (using both optical microscopy and SEM) indicated there was no damage to the anvil face, but rather, a residue that remained on the surface from the localized reaction or decomposition (detailed previously in section 4.4.6) of the epoxy-cast composites upon impact.

The corresponding work was obtained from the dynamic stress strain curves shown in Figure 4.65 (in section 4.4.3) for the respective compositions and the measured strain obtained from each footprint. The associated bulk temperature rise calculated according to equation (4.37) for the three experiments are listed in Table 4.20 and were all found to be above 80 °C. These temperatures are greater than the composite's measured glass transition, $T_g$ (63.4 and 81.5 °C for Al+$Fe_2O_3$+60 *vol.%* epoxy and nano-Al+$Fe_2O_3$+70 *vol.%* epoxy composites, respectively, and detailed in section 4.3.1). While the calculated bulk temperature is lower than the threshold temperature for

reaction between Al+$Fe_2O_3$ or epoxy decomposition (identified by DTA to be approximately 700 and 400 °C, respectively, and detailed in section 4.2.1.3), it is certainly greater than the $T_g$ measured for epoxy (57.9 °C). Since there is a significant volume fraction of epoxy in these composites, it is possible that local thermal softening takes place and triggers a series of subsequent events leading to extensive strains and consequent localized reaction.

The critical strain where thermal softening within the composite begins can also be estimated by using the measured glass transition temperatures obtained from DMA (section 4.3.1) and solving equation (4.37) for the corresponding strain associated with the plastic deformation. This was calculated for the 60 *vol.%* epoxy composite, the nano-70 *vol.%* epoxy composite, and pure epoxy. Using average densities for each type of composition, the corresponding strains were 39.10, 50.43, and 33.13 % for the 60 *vol.%*, nano-70 *vol.%*, and pure epoxy compositions, respectively. Comparing these values with the critical areal strains obtained from reverse Taylor impact experiments, where fracture was observed, indicate the influence of thermal softening for the observed areal deformation behaviors. While the critical areal fracture strain for the 60 *vol.%* and nano-70 *vol.%* epoxy composites were both approximately 30 %, the temperature rise associated with the plastic deformation up to this strain level does not appear to influence the continued areal deformation of the samples. However, once the specimen exceeds both the critical areal fracture strain and the critical thermal softening strain, the temperature rise appears to influence the composites' deformation behavior leading to significantly large areal strains (approximately 70 %) and eventual failure. This effect is further substantiated by the change in slope observed for the areal strain curves,

indicating the alteration in strain rate response associated with the critical thermal softening strain. Figure 4.58(*a*) from section 4.4.2 shows a significant slope change at an areal strain of approximately 35 to 40 %, in excellent agreement with the critical thermal softening strain of 39.10 %. This effect becomes less apparent, but is still observed for experiments with higher impact velocities. Similarly, the nano-70 *vol.%* epoxy composition also exhibits a change in slope at approximately 45 to 50 % strain as illustrated in Figure 4.59(*a*) from section 4.4.2 and compares well to the calculated critical thermal strain of 50.43 %. The thermal softening effect appears to be more significant for the 60 *vol.%* epoxy composite, since the critical strain for thermal softening occurs at lower levels of strain as compared to the nano-70 *vol.%* epoxy composite. This behavior could possibly contribute to the enhanced mechanochemical reactivity qualitatively observed for the 60 *vol.%* epoxy composition (discussed in section 4.4.8).

It is also interesting that the pure epoxy has a critical thermal softening strain below the critical areal fracture strain of approximately 40 %, observed from reverse Taylor impacts. In this case, the epoxy deformation behavior is influenced by the temperature rise associated with plastic deformation. For the particle-filled composites, observed fracture was always associated with the specimen having the characteristic double-frustum deformation shape, while specimens that recovered elastically exhibited an elongated-mushroom deformation shape (discussed in section 4.4.1). However, the pure epoxy always exhibits a double-frustum deformation shape for specimens that fractured and elastically recovered. Thermal softening causes the epoxy to have a rubbery behavior that possibly explains the deformation shape associated with this

particular composition and its higher critical areal fracture strain. The thermal softening effect is also evident in the measured areal strains shown in Figure 4.60(*a*) from section 4.4.2, indicating a change of slope at approximately 25 to 30 % strain, even for specimens that do not fracture.

### 4.4.8 DTA of Post-Mortem Recovered Composites

Epoxy-cast materials recovered from Taylor impact experiments were also studied using DTA to determine if chemical reactivity was altered due to the effects of dynamic deformation imparted to the specimens. Figure 4.84 shows the results obtained for pure epoxy, comparing a reference material prior to dynamic deformation (trace *a*) and recovered fragment following a Taylor impact experiment (trace *b*). The fragments were recovered from shot 0613, with the highest impact velocity for pure epoxy of 179.7 m/s, and show virtually identical responses.

In contrast, DTA experiments conducted for recovered fragments obtained from the Al+$Fe_2O_3$+60 *vol.%* epoxy composition show a slightly different response as compared to the reference non-impacted material. Figure 4.85 compares the DTA records obtained for the Al+$Fe_2O_3$+60 *vol.%* epoxy composite reference material (trace *a*) and three different Taylor tests at impact velocities of 158.2, 210.7, and 236.6 m/s (traces *b*, *c*, and *d*, respectively). Each of the traces shows the characteristic cold crystallization and decomposition peaks followed by the reduction of hematite to magnetite and the melting of aluminum. However, the next peaks associated with the formation of intermediate phases (possibly FeO and/or $FeAl_2O_4$) are shifted slightly to

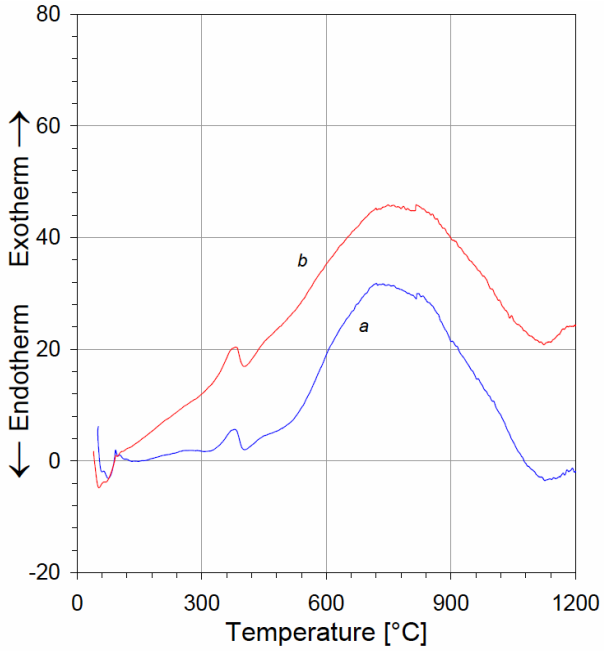


**Figure 4.84** DTA traces obtained for pure epoxy samples prior to dynamic deformation (trace *a*) and following a Taylor impact experiment from recovered fragments (trace *b*). Fragments were obtained from the highest velocity experiment (0613) with an impact velocity of 179.7 m/s.

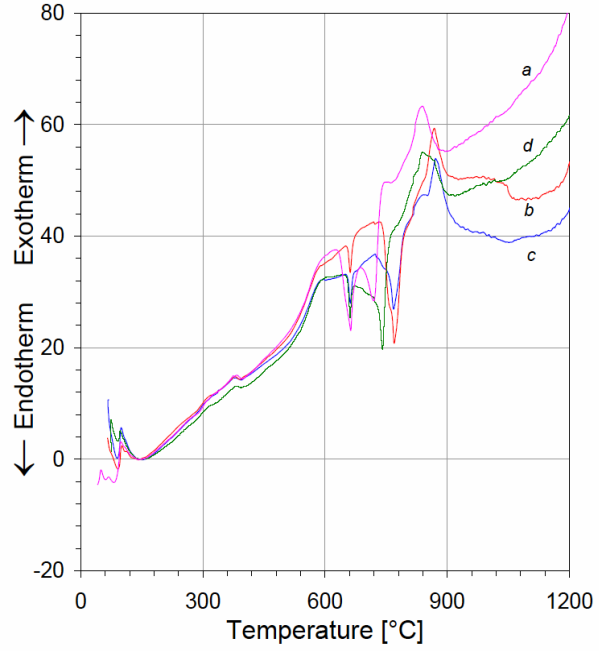


**Figure 4.85** DTA traces obtained for Al+$Fe_2O_3$+60 *vol.%* epoxy samples prior to dynamic deformation (trace *a*) and following Taylor impact experiments from recovered fragments (traces *b*-*d*). Fragments were obtained from experiments with impact velocities of *b*) 158.2 m/s (0535), *c*) 210.7 m/s (0536), and *d*) 236.6 m/s (0603).

higher temperatures. The main exothermic reaction peaks are also shifted to higher temperatures, possibly indicating a slight alteration of the composite's behavior post impact.

Similar DTA experiments were conducted for the nano-Al+$Fe_2O_3$+70 *vol.%* epoxy composition at the highest impact velocity tested, corresponding to 288.3 m/s (shot 0646). However, in this case there was no change in the exothermic or endothermic events that were observed for the reference sample. Figure 4.86 shows the DTA traces obtained for each of the specimens, which exhibit virtually identical responses.

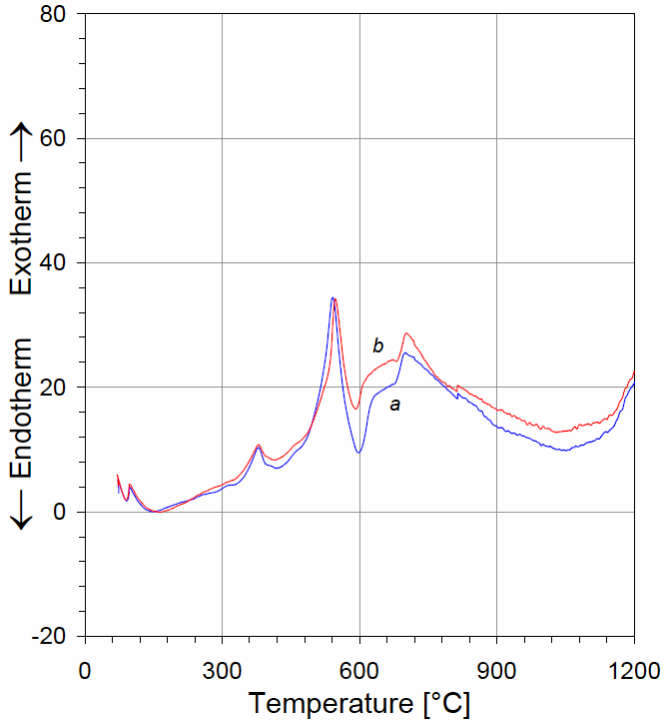


**Figure 4.86** DTA traces obtained for nano-Al+$Fe_2O_3$+70 *vol.%* epoxy samples prior to dynamic deformation (trace *a*) and following a Taylor impact experiment from recovered fragments (trace *b*). Fragments were obtained from the highest velocity experiment (0646) with an impact velocity of 288.3 m/s.

## 4.5 Time-Resolved Equation of State Experiments

Time-resolved high-strain rate impact experiments were performed on epoxy-cast $Al+Fe_2O_3$ composites for a range of loading conditions. Piezoelectric PVDF gauges placed on either side of the target were used to measure the stress magnitude and wave arrival times, while velocity interferometry directly measured the material's particle velocity. Data acquired from these measurements were used for obtaining the composite material's Hugoniot equation of state (EOS). The experimental configuration design specifies a state of uniaxial strain for the specimens, and each experiment yields a single data point on the Hugoniot. These experiments additionally provided characteristics about the shock wave and the material's response to dynamic loading over a finite time duration, limited by the survivability of the PVDF gauges.

Several compressed-gas gun impact experiments were performed in which the flyer plate impact velocity was varied or the flyer and driver materials were varied to achieve an array of loading stress levels. While a limited number of compressed-gas gun experiments were performed for the $Al+Fe_2O_3$+78 *vol.%* epoxy composite, additional explosively loaded experiments provided details within an extended pressure range up to approximately 25 GPa. The majority of the results presented in this section are for compressed-gas gun experiments conducted for the $Al+Fe_2O_3$+60 *vol.%* epoxy composition.

Experimental details for stress wave measurements and their analysis is presented in the following section. The stress waveforms obtained from PVDF gauge records and particle velocity histories measured by VISAR are presented and discussed first. This is

followed by the comparison of directly measured and calculated parameters obtained from these experiments. Calculations are performed to represent the experimentally determined data in Hugoniot $U_S$-$U_P$ and pressure-volume ($P$-$V$) space. The combined results for both compositions are next compared and the influence of particle reinforcement dispersed in an epoxy matrix is established. The Hugoniot curves indicate that the responses of the composites are altered with the addition of solid particles at a critical $U_S$ and $U_P$ value or pressure, possibly due to induced damage to the composite. The Birch-Murnaghan equation of state (BM-EOS) is used to characterize the composite's compressibility and account for the altered Hugoniot response by quantitatively characterizing the possible resulting damage. Additionally, experimentally determined material behavior was correlated with hydrodynamic calculations for evaluating the measured Hugoniot behavior.

### 4.5.1 Analysis of Stress Wave and Particle Velocity Profiles

Time-resolved impact experiments were performed on epoxy-cast Al+$Fe_2O_3$ composites containing 60 and 78 *vol.%* epoxy. A majority of the results presented and discussed in this section are for the compressed-gas gun impact experiments conducted for the Al+$Fe_2O_3$+60 *vol.%* epoxy composites. Three lower pressure compressed-gas gun experiments conducted for the 78 *vol.%* epoxy composite are combined with higher pressure explosively loaded data obtained in collaboration with Jordan, ***et al.*** [161,162]. The 78 *vol.%* epoxy composite materials in the low and high pressure studies were of identical composition, obtained from the same batch of material prepared for this work.

PVDF stress gauges were embedded on the impact and back surfaces of the target specimen as described in section 3.5.1, while velocity interferometry (VISAR) directly measured the particle velocity at the back surface of the target. The gauges measure the stress history experienced by the target specimen, typically including several microseconds after impact. In some cases, the gauges survived long enough to capture the unloading history of the impact. The gauge records provide a time signature of the stress wave arrival and the corresponding rise-to-peak stress at the impact plane and propagated back surface of the specimen. Additionally, the stress gauge records show details about the shock wave's interaction with boundaries that make up the gauge package, such as reflecting off the fused silica window attached to the back surface of the specimen. As described in the experimental procedure (section 3.5.1), the time-resolved gauge experiments consist of a loading configuration where the specimen is under a state of uniaxial strain. Upon impact, the shock-wave (or pressure pulse) has a distinct rise-to-peak stress followed by a constant stress of a defined duration that is dependent on the target geometry, and then an abrupt release to zero stress. The thickness and significantly large aspect ratio (diameter to thickness) of the flyer and driver plates directly affect the wave duration and shape the disturbance wave such that it provides a one-dimensional plane wave without edge attenuation effects over the time duration of interest (few microseconds). The rise time of the stress-pulse is also dependent on the planarity and angular alignment or tilt at impact. Every attempt was made to ensure impact planarity by lapping all surfaces that make up the target and projectile with additional attention directed towards the careful assembly of the target. The stress waveforms are obtained by measuring the voltage change of the PVDF gauge during the impact

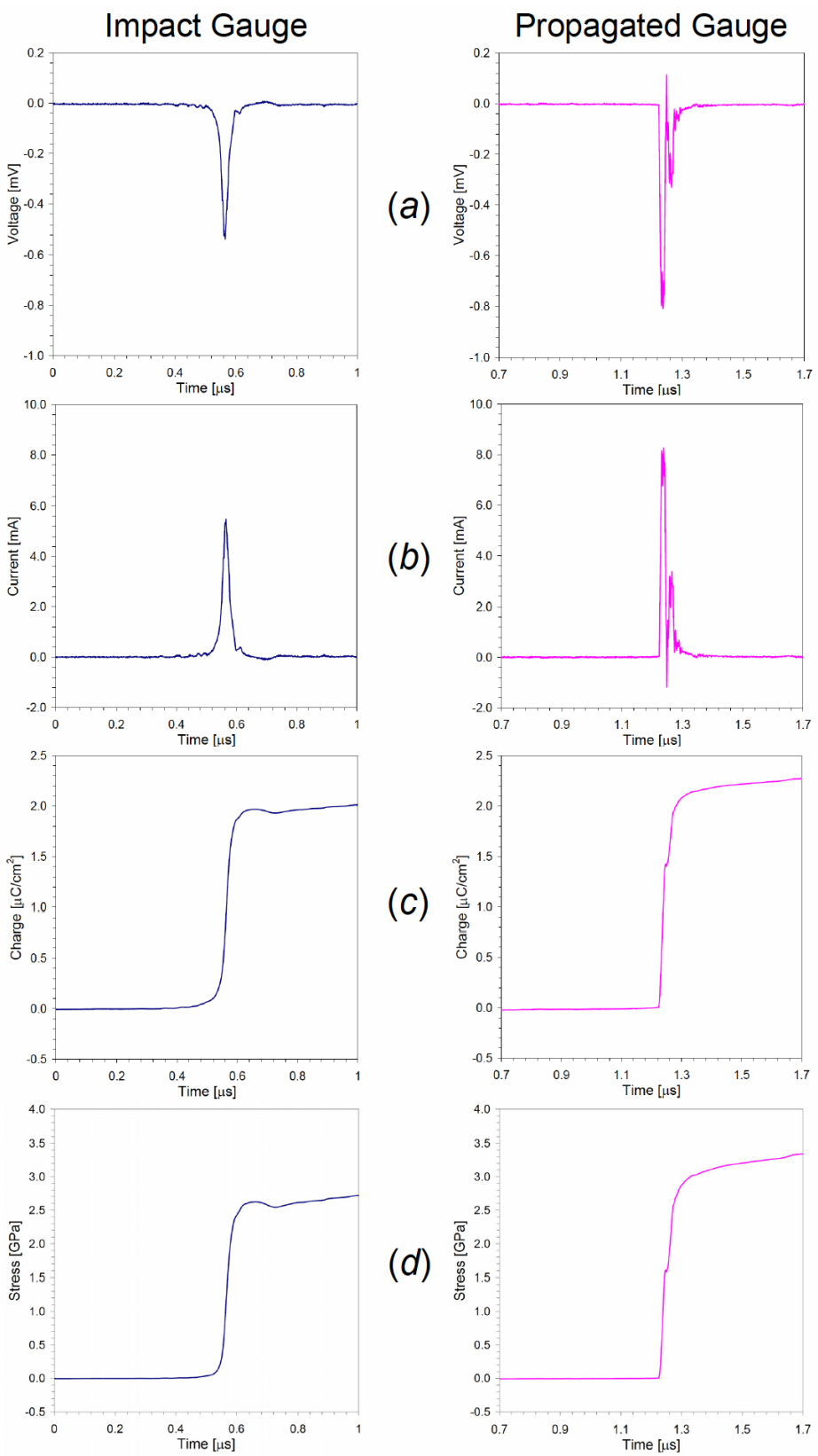


**Figure 4.87** The *a*) voltage, *b*) current, *c*) charge, and *d*) stress waveforms obtained from impact (*left*) and propagated (*right*) gauge records for shot 0627.

experiment and subsequent calculations to obtain current and charge histories. A typical example of the measured voltage waveforms obtained from the impact and propagated stress gauges of shot 0627 are shown in Figure 4.87(*a*), respectively. These voltage waveforms are converted to current by dividing the resistance of the current viewing resistor (CVR) used in the experiment and then integrated with respect to time to obtain the charge histories. The current waveforms for the impact and propagated gauge records are shown in Figure 4.87(*b*), respectively, while the resulting charge waveforms are shown in Figure 4.87(*c*), respectively. The PVDF gauges were developed under well-known conditions imposed by controlled shock-loading experiments and correlate the charge output with stress response [160,164]. PlotData [165] software package was used to convert current, charge, and resulting stress traces. The impact and propagated stress traces are shown in Figure 4.87(*d*), respectively. The voltage, current, charge, and stress waveforms obtained for all the Hugoniot experiments conducted in this study are included in Appendix C for reference.

A combined plot of the stress traces obtained for all of the experiments performed on Al+$Fe_2O_3$+60 *vol.%* epoxy composites is shown in Figure 4.88 and Figure 4.89 for the impact and propagated gauges, respectively. These plots only show early portions of the traces captured, however, the PVDF gauges typically gave reliable data up to 2 to 3 μs after impact. The longer data records typically show the shock wave interaction with the different materials that make up the target assembly. In some cases, the release wave was also captured and will be discussed in section 4.5.4. The detail data obtained for each of these experiments is also listed in Table 4.21.

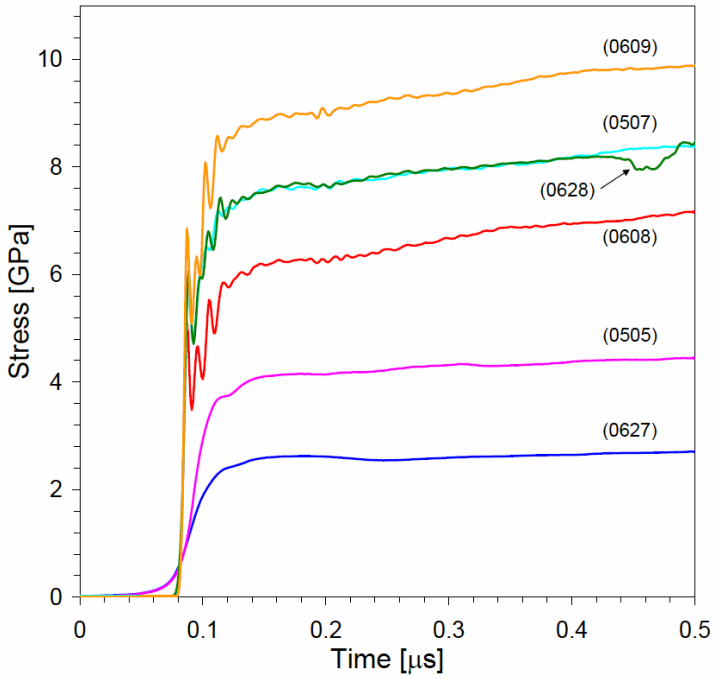


**Figure 4.88** A combined plot of the impact stress traces obtained for all parallel-plate impact experiments conducted for the Al+$Fe_2O_3$+60 *vol.%* epoxy composite.

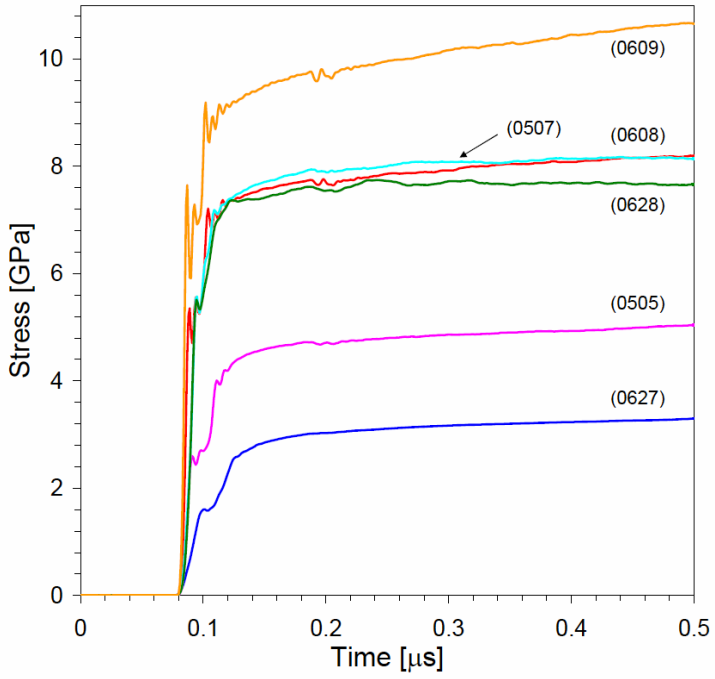


**Figure 4.89** A combined plot of the propagated stress traces obtained for all parallel-plate impact experiments conducted for the Al+$Fe_2O_3$+60 *vol.%* epoxy composite.

Interpretation of the stress profiles requires careful consideration of wave propagation through the different materials that comprise the gauge package and the target, because of shock impedance differences. The PVDF stress gauges are approximately 20 to 25 μm thick and placed between two 25.4 μm thick PTFE insulation layers. Typically, the total thickness of the gauge packages were approximately 70 to 80 μm after assembly, which include thin film epoxy layers (up to a micron thick) used for attachment. As the shock wave moves through the gauge package and into the target material, it will reflect off of high impedance interfaces and partially propagate back through the gauge package. However, the impedance mismatch between each of the components comprising the gauge package (PVDF, PTFE, and epoxy) and the target material are fairly similar. Therefore, the stress equilibrium is reached fairly rapidly with only minor reverberations observed for the traces, which travel back through the gauge package. The mechanical response time or stress equilibrium of the shock wave moving through the gauge package can be estimated by:

$$t = n\left(\frac{h}{U_S}\right), \tag{4.38}$$

where $h$ is the thickness of the gauge package, $U_S$ is the shock velocity of the disturbance wave through the gauge package, and $n$ is the number of reverberations necessary for the gauge to reach stress equilibrium. For many materials, $n$ = 3 if there is a shock impedance mismatch between the gauge package and the surrounding materials, and the response time of a 25 μm gauge is estimated to be between 10 and 50 ns [206].

Careful analysis of the impact and propagated stress profiles (Figure 4.88 and

**Table 4.21** Data summary for Hugoniot EOS experiments of Al+$Fe_2O_3$ epoxy-cast composites with 60 and 78 *vol.%* epoxy. Impact, $P_I$, and propagated, $P_{II}$, stresses (pressures) are measured directly from PVDF gauges located on opposite sides of the target specimen.

| Shot Number | Flyer Material | Driver Material | Impact Velocity [m/s] | Specimen Thickness [mm] | Specimen Density [g/cm$^3$] | $P_I$ [GPa] | $P_{II}$ [GPa] | $^*U_S$ [mm/μs] | $^{**}U_P$ [mm/μs] |
|---|---|---|---|---|---|---|---|---|---|
| **Al+$Fe_2O_3$+60 *vol.%* epoxy** | | | | | | | | | |
| 0627 | Al+$Fe_2O_3$+60 *vol.%* epoxy | none | 714.1 ± 2.5 | 2.159 ± 0.013 | 2.4020 | 2.71 ± 0.01 | 3.32 ± 0.02 | 3.26 ± 0.01 (3.28 ± 0.02) | 0.346 ± 0.002 (0.340 ± 0.006) |
| 0505 | Al+$Fe_2O_3$+60 *vol.%* epoxy | none | 1035.9 ± 4.2 | 2.182 ± 0.008 | 2.4057 | 4.14 ± 0.02 | 4.01 ± 0.17 | 3.61 ± 0.01 (3.58 ± 0.01) | 0.476 ± 0.003 ☺(0.518 ± 0.002) |
| 0608 | OFHC Cu | OFHC Cu | 997.0 ± 62.9 | 2.763 ± 0.001 | 2.4050 | 5.91 ± 0.14 | 7.36 ± 0.08 | 4.12 ± 0.00 (4.13 ± 0.00) | 0.596 ± 0.014 (0.567 ± 0.003) |
| 0507 | W | OFHC Cu | 972.1 ± 15.9 | 2.172 ± 0.010 | 2.3990 | 7.23 ± 0.15 | 7.30 ± 0.19 | 4.28 ± 0.02 (4.31 ± 0.02) | 0.705 ± 0.015 (0.727 ± 0.003) |
| 0628 | W | OFHC Cu | 1022.0 ± 4.2 | 1.525 ± 0.037 | 2.4013 | 7.66 ± 0.03 | 7.70 ± 0.06 | 4.55 ± 0.11 (4.60 ± 0.11) | 0.701 ± 0.017 (0.708 ± 0.011) |
| 0609 | W | OFHC Cu | 1166.5 ± 68.8 | 2.756 ± 0.005 | 2.4010 | 8.54 ± 0.24 | 8.99 ± 0.23 | 4.72 ± 0.01 (4.72 ± 0.01) | 0.753 ± 0.021 (0.758 ± 0.008) |
| **Al+$Fe_2O_3$+78 *vol.%* epoxy** | | | | | | | | | |
| 0303 | OFHC Cu | OFHC Cu | 523.3 ± 26.5 | 9.512 ± 0.003 | 1.7900 | †2.11 ± 0.02 | 1.76 ± 0.22 | (3.17 ± 0.01) | 0.372 ± 0.006 |
| 0308 | OFHC Cu | OFHC Cu | 556.0 ± 21.7 | 9.500 ± 0.003 | 1.8645 | 2.28 ± 0.03 | †2.62 ± 0.05 | (3.37 ± 0.01) | 0.363 ± 0.005 |
| 0311 | OFHC Cu | OFHC Cu | 716.0 ± 89.5 | 9.520 ± 0.003 | 1.8503 | 3.10 ± 0.05 | 3.12 ± 0.03 | (3.72 ± 0.01) | 0.452 ± 0.008 |
| 0403 | OFHC Cu | OFHC Cu | 943.7 ± 3.8 | 9.515 ± 0.003 | 1.8581 | 4.66 ± 0.31 | 3.56 ± 0.40 | (3.96 ± 0.02) | 0.607 ± 0.005 |

*Shock velocity, $U_S$, was measured using half-max and toe-to-toe values, where the latter are shown in brackets ($U_S$).

**Particle velocity, $U_P$, was calculated from conservation equations, while values in brackets ($U_P$) are measured directly by VISAR.

☺VISAR was not used for this symmetric impact experiment, however, the asymptotic particle velocity behind the shock is exactly half the flyer impact velocity.

†Indicates a calculated value.

Figure 4.89) resulted in measured reverberation times ranging between 5 and 10 ns. In most cases, there were four to five reverberations observed before reaching the peak equilibrium stress value, corresponding to approximately 40 to 50 ns after the arrival of the disturbance wave. These estimates give some confidence in the selection of equilibrated stress values obtained from the waveforms.

In general, the impact gauge equilibrated stress values increase steadily. Shots 0507 and 0628 performed under similar impact conditions on the same sample illustrate the repeatability of parallel-plate impact experiments conducted in this study. Both experiments used a tungsten flyer impacting a copper driver at comparable impact velocities in order to achieve the desired stress level. However, shot 0507 had a slightly lower velocity of 972.1 m/s, resulting in a correspondingly lower measured impact stress of 7.23 GPa as compared to 7.66 GPa for shot 0628 with an impact velocity of 1022.0 m/s. The propagated gauge records also follow this same trend, which result in equilibrated stresses of 7.30 and 7.70 GPa for shot 0507 and 0628, respectively. Figure 4.89 also indicates shot 0608 shows a similar propagated gauge response as shots 0507 and 0628, even though the impact stress for this experiment (shot 0608) was significantly lower (5.91 GPa). It is unclear why this particular experiment showed such an extremely high propagated gauge response. The expected equilibrated stress value was estimated from the measured VISAR particle velocity to be approximately 5.6 GPa.

The rise time to peak equilibrated stress was also estimated for impact and propagated gauge records obtained for each experiment. In general, the rise time for the impact gauge record decreased as the impact stress increased for the array of loading conditions encountered in these experiments. However, this general trend was not

observed for the propagated gauge records. Figure 4.90 compares the rise times associated with impact and propagated gauge records as a function of peak stress. Notice that the impact gauge shows a relatively smooth decrease in rise time as the impact stress increases. In contrast, there appears to be a rather abrupt transition and decrease of rise time following the lowest stress impact experiment, which had a rise time of 122.5 ns. The rise time associated with the remaining propagated gauge responses appear to be relatively constant, with an average value of approximately 40 ns. In fact, the rise-to-peak stress for the propagated gauge is typically more rapid than the impact gauge, as summarized in the measured rise times listed in Table 4.22 for both gauge locations. This is not a surprising result, since many studies have shown that particle-filled polymer composites have rather unique loading and unloading properties.

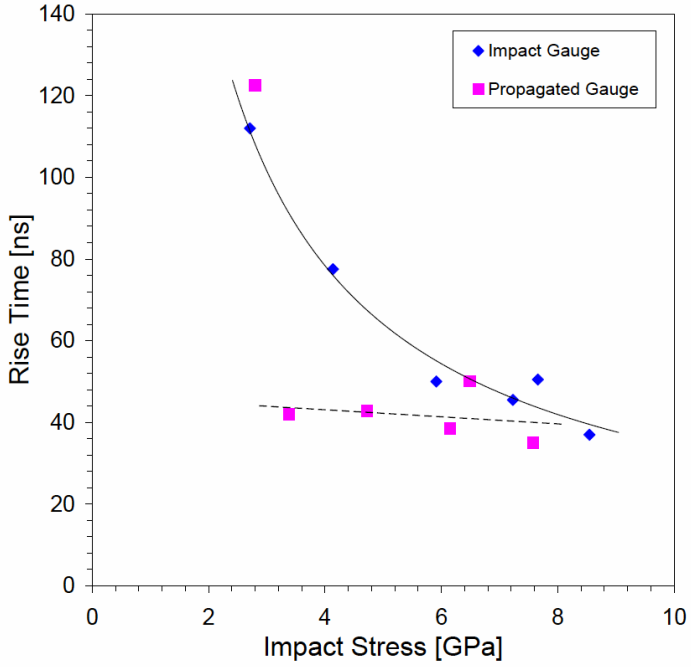


**Figure 4.90** Comparison of measured rise times to peak stress obtained for impact and propagated stress waveforms shown in Figure 4.88 and Figure 4.89, respectively.

**Table 4.22** Measured peak stress (pressure) rise times from impact and propagated gauge records obtained for Al+$Fe_2O_3$+60 *vol.%* epoxy composite.

| Shot Number | *Impact Gauge* | | *Propagated Gauge* | |
|---|---|---|---|---|
| | Pressure, $P_I$ [GPa] | Rise Time [ns] | Pressure, $P_{II}$ [GPa] | Rise Time [ns] |
| 0627 | 2.71 ± 0.01 | 112.0 | 3.32 ± 0.02 | 122.5 |
| 0505 | 4.14 ± 0.02 | 77.5 | 4.01 ± 0.17 | 42.0 |
| 0608 | 5.91 ± 0.14 | 50.0 | 7.36 ± 0.08 | 42.8 |
| 0507 | 7.23 ± 0.15 | 45.5 | 7.30 ± 0.19 | 38.5 |
| 0628 | 7.66 ± 0.03 | 50.5 | 7.70 ± 0.06 | 50.0 |
| 0609 | 8.54 ± 0.24 | 37.0 | 8.99 ± 0.23 | 35.0 |

For example, the extensively studied alumina-epoxy composite ALOX, exhibits extraordinarily large release-wave velocities [83,85,87,88]. It is clear that the relatively high wave speeds associated with aluminum and hematite particles are very influential on the bulk wave propagation behavior within the composite. Typically, wave dispersion is associated with a disturbance effect that attenuates the wave. However, for the case of higher shock impedance particles dispersed in a polymer matrix, the waves appears to actually intensify and increase the overall bulk wave velocity for the composite.

The time chosen for reaching stress equilibrium is based on observing the current traces. Due to the stress rate dependency of the output signal, very fast loading and unloading pulses cause large amplitude current spikes with durations of tens of nanoseconds [160]. These current spikes are separated by intervals of zero current corresponding to the gauge being stressed at a constant level and the stress rate is, therefore, zero [160]. The gauge current output is zero except during loading and unloading stages of the impact. The stress equilibrium determined for each experiment

was based on observing the time when the charge trace returned to zero and was in equilibrium. This is illustrated for the impact and propagated gauge records of shot 0609 in Figure 4.91(*a*), which identifies the arrival of the disturbance wave (red arrow), followed by a rise in current until the gauge equilibrates back to zero current again (green arrow). The identified times from the current traces in Figure 4.91(*a*) are used to obtain the corresponding equilibrated stresses shown in Figure 4.91(*b*) for the impact and propagated gauges, respectively.

The current traces also show a definite unloading during the rise-to-peak stress, indicated by the significant negative current peak before returning to positive values and equilibrating at zero current. The combined stress waveforms, shown in Figure 4.88 for

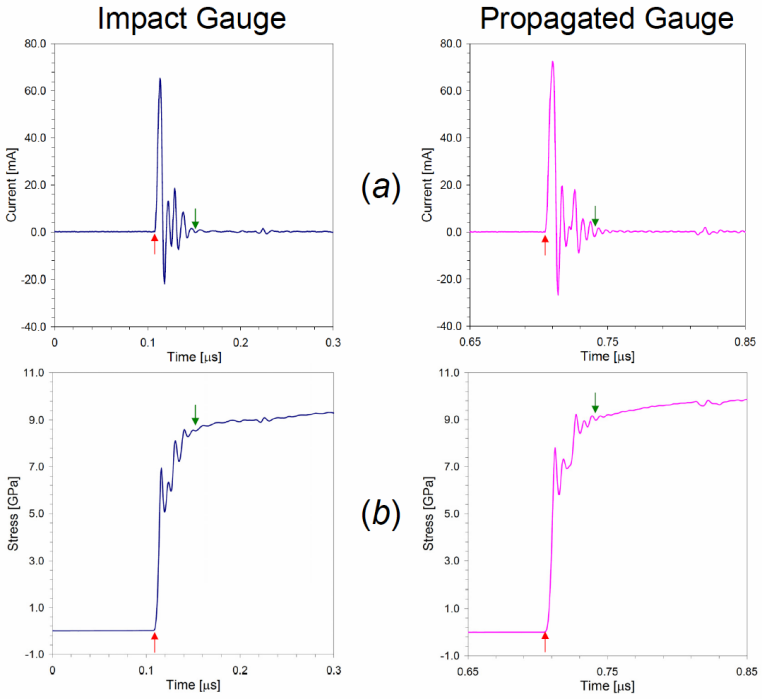


**Figure 4.91** Impact (*left*) and propagated (*right*) gauge records showing *a*) current and *b*) stress traces obtained for shot 0609. Red arrows indicate the arrival time of the disturbance wave, while green arrows indicate the equilibrium stress determined from the current trace returning to zero.

the impact gauge and Figure 4.89 for the propagated gauge, each indicate a "step" during the rise-to-peak stress. The impact gauge record for shot 0627 is the only trace that does not indicate a step, however, the propagated gauge record does. These steps or unloading correspond to a significant negative peak in the current trace, which typically have not been observed for other material systems [12,160,207,208]. Anderson and Wackerbarth [160] outline two possible general categories for PVDF gauge current outputs; *i*) mechanical ringing during stress reverberations in the gauge and *ii*) electrically inductive ringing, which shows a significant current peak during the rise-to-peak stress and significant noise in the record. The traces obtained from this study are extremely clean and do not appear to have electrically inductive ringing associated with the loading step. Lee, *et al.*, [207] have shown a similar stress response for Teflon, which clearly indicates a change in stress rate upon loading to the peak load. Therefore, the loading step may be linked with the viscoelastic-viscoplastic behavior typically associated with polymers.

While the impact gauge records showed a range of rise times (112 to 37 ns) for the equilibrated peak stress, decreasing as impact stress increased, and propagated gauge records had rise times close to 40 nanoseconds, the rise times associated with the impact and propagated step stresses had average values of 15.9 and 15.7 ns, respectively. This possibly gives evidence of a common viscoelastic-viscoplastic loading response associated with the relatively large volume fraction of epoxy used for these composites.

The material particle velocities were also obtained during these experiments, with exception to shot 0505, where VISAR was not used. Particle velocity was measured at the specimen and fused silica window interface in close proximity to the propagated

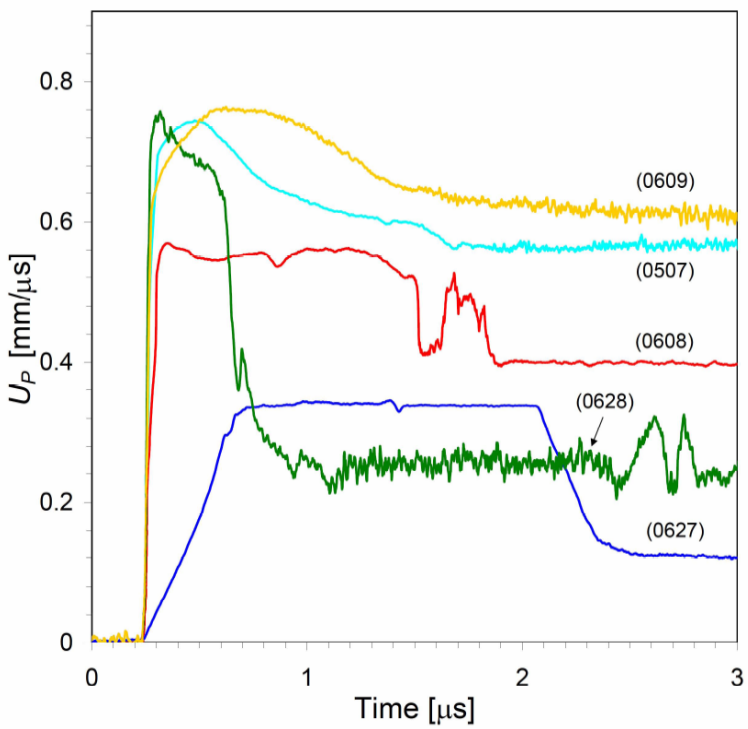


**Figure 4.92** VISAR traces obtained from the back surface of the target for parallel-plate impact experiments conducted for Al+$Fe_2O_3$+60 *vol.%* epoxy composites. Traces are shown for directly measured particle velocities after correction for impedance differences between the specimen and the fused silica window.

PVDF gauge location. Figure 4.92 shows the VISAR traces obtained for each impact experiment after correcting for the impendence differences between the sample and window material. These traces exhibit a much larger time window for the impact experiments than shown for the PVDF gauge records thus far.

The particle velocity traces typically show a rapid rise and slight rounding over as it approaches the peak velocity. In each experiment, a relatively constant particle velocity was observed for a reasonably long period of time after the peak velocity is reached. The release wave has a well defined arrival time in most cases, corresponding to specimen geometries that were thick enough for allowing ample time between the compressive wave reaching the back surface and completely releasing. Some select

experiments (shots 0628 and 0507) had specimen geometries such that the compressive and release waves interact to produce attenuation in the signal.

The VISAR traces show similar features that were observed for the PVDF gauge records, such as the arrival of the release wave and steps in the rise-to-peak particle velocity. The steps associated with the arrival of the shock wave are shown in a zoomed view of the VISAR traces in Figure 4.93, where the arrows indicate the step regions. These appear to occur at relatively similar times as those observed for the PVDF gauge records. However, since the VISAR and PVDF gauge signals are recorded on different oscilloscopes, the time synchronization of the respective signals is extremely challenging since these features occur a few nanoseconds after impact. The relative amplitude ratios

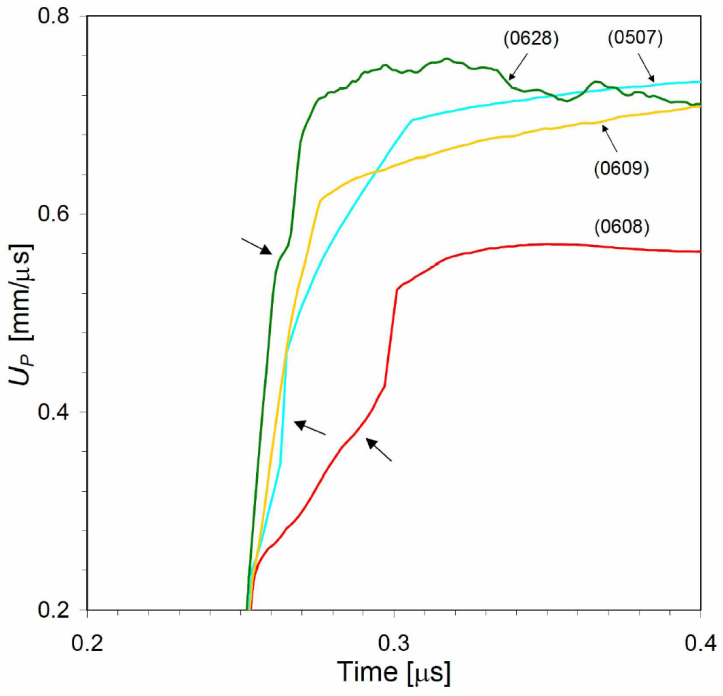


**Figure 4.93** Zoomed region of the VISAR traces shown in Figure 4.92 displaying steps (indicated by arrows) in the rise-to-peak particle velocity.

**Table 4.23** Steps were observed in the rise-to-peak stress and particle velocity traces for each parellel-plate impact experiment. The ratio of step stress (pressure) and peak stress (pressure) was calculated for the impact and propagated gauges. Similarly, the ratio of particle step velocity to peak velocity was also calculated and compares well with both the impact and propagated gauge step ratios.

| Shot Number | Impact Gauge | | Propagated Gauge | | VISAR Particle Velocity | |
|---|---|---|---|---|---|---|
| | Pressure Step, $P_{SI}$ [GPa] | Pressure Ratio $P_{SI}/P_I$ [%] | Pressure Step, $P_{SII}$ [GPa]] | Pressure Ratio $P_{SII}/P_I$ [%] | $U_{PS}$ Step [mm/μs] | $U_P$ Ratio $U_{PS}/U_P$ [%] |
| 0627 | 1.44 | 53.14 | 1.61 | 48.49 | 0.192 | 56.47 |
| 0505 | 2.91 | 70.29 | 2.60 | 64.84 | n/a | n/a |
| 0608 | 5.18 | 87.65 | 5.41 | 73.51 | 0.426 | 75.13 |
| 0507 | 5.68 | 78.56 | 5.61 | 76.85 | 0.463 | 63.68 |
| 0628 | 6.08 | 79.37 | 5.52 | 71.69 | 0.563 | 79.52 |
| 0609 | 6.95 | 81.38 | 7.79 | 86.65 | 0.613 | 80.87 |

were therefore calculated to compare the measured response from the impact gauge, propagated gauge, and VISAR records. The ratio of the step amplitude and the peak amplitude for the PVDF (impact and propagated) gauge records and the VISAR traces are calculated in Table 4.23. Comparison of the propagated gauge and particle velocity step amplitude ratios appears to be in relatively good agreement, both measuring similar responses at the specimen/window interface. As the peak stress increases for each experiment, the step occurs closer to the peak amplitude and indicates the influence of increasing loading rate or strain rate. The VISAR signal further verifies that the composite materials undergo some type of relaxation during the rise-to-peak stress, possibly associated with viscoelastic-viscoplastic deformation behavior.

### 4.5.2 Measured Parameters Obtained from Instrumented Impact Experiments

Directly measured parameters obtained from parallel-plate impact experiments include impact and propagated stress histories from PVDF gauges (discussed in section 4.5.1), shock velocity, $U_S$, from the transit time between the two gauges, and particle velocity, $U_P$, gained from VISAR measurements. These experiments were designed to give information necessary for developing the material's Hugoniot equation of state. In many cases, the directly measured parameters were also verified by redundancies built into the design of the experiments.

The wave speed through the composite specimen is obtained by measuring the transit time between the two gauges placed in direct contact with the opposite surfaces of the target specimen, less the travel time through the gauge insulation layers. The transit time was measured from the toe-to-toe and half-max locations of the stress waveform profiles and corrected for gauge package insulation thicknesses. This time was used to calculate the composite material's shock velocity, $U_S$, according to:

$$U_S = \frac{x}{t}, \tag{4.39}$$

where $x$ is the sample thickness and $t$ is the measured transit time through the two gauges. Shock velocities obtained for each experiment show excellent correlation, exhibiting less than 1 % difference between the toe-to-toe and half-max values listed in Table 4.21. This also gives an indication of the excellent planarity and tilt control maintained for these experiments. The directly measured peak impact pressures (stresses) and shock velocities

are plotted in Figure 4.94 for experiments conducted on the Al+$Fe_2O_3$+60 *vol.%* epoxy composite. Viewing the data in this way shows the relationship between the parameters without any assumptions about steady wave propagation through the specimen or hydrodynamic conditions necessary for calculating the material state using the well known Rankine-Hugoniot jump conditions [17]. The impact step pressures, $P_{SI}$, are also featured, along with corresponding propagated gauge, $P_{II}$, and propagated step pressure, $P_{SII}$, responses after impedance corrections. The impact and propagated step pressures correspond to the step observed in the waveform profile's rise-to-peak stress (discussed in section 4.5.1). The steps appear to be associated with the loading response of pure epoxy. The impact and propagated step pressures all shift and overlap the response observed from pure epoxy shock data obtained from Carter and Marsh [72], and Marsh [18]. Figure 4.94 also includes curves obtained for Kel-F [18,72] and the theoretically calculated response using mixture theory (inverse Hugoniot EOS discussed in section 4.5.4.2) obtained from aluminum and hematite shock data [18]. Kel-F is a fluro-polymer, also known as polychlorotrifluoroethylne (PCTFE), which has been studied to significantly high pressures and is frequently used for representing the behavior of the PVDF gauge package [10,207,209,210]. The step in gauge record responses does not appear to be associated with the gauge package response represented by the Kel-F curve. The measured impact and propagated gauge responses have a coupled pure epoxy component that influences the overall measured response of the composite. This trend continues until reaching a pressure over approximately 4 GPa, where there is a shift to even higher shock velocities possibly associated with a strengthening effect. A more detailed discussion about possible damage and

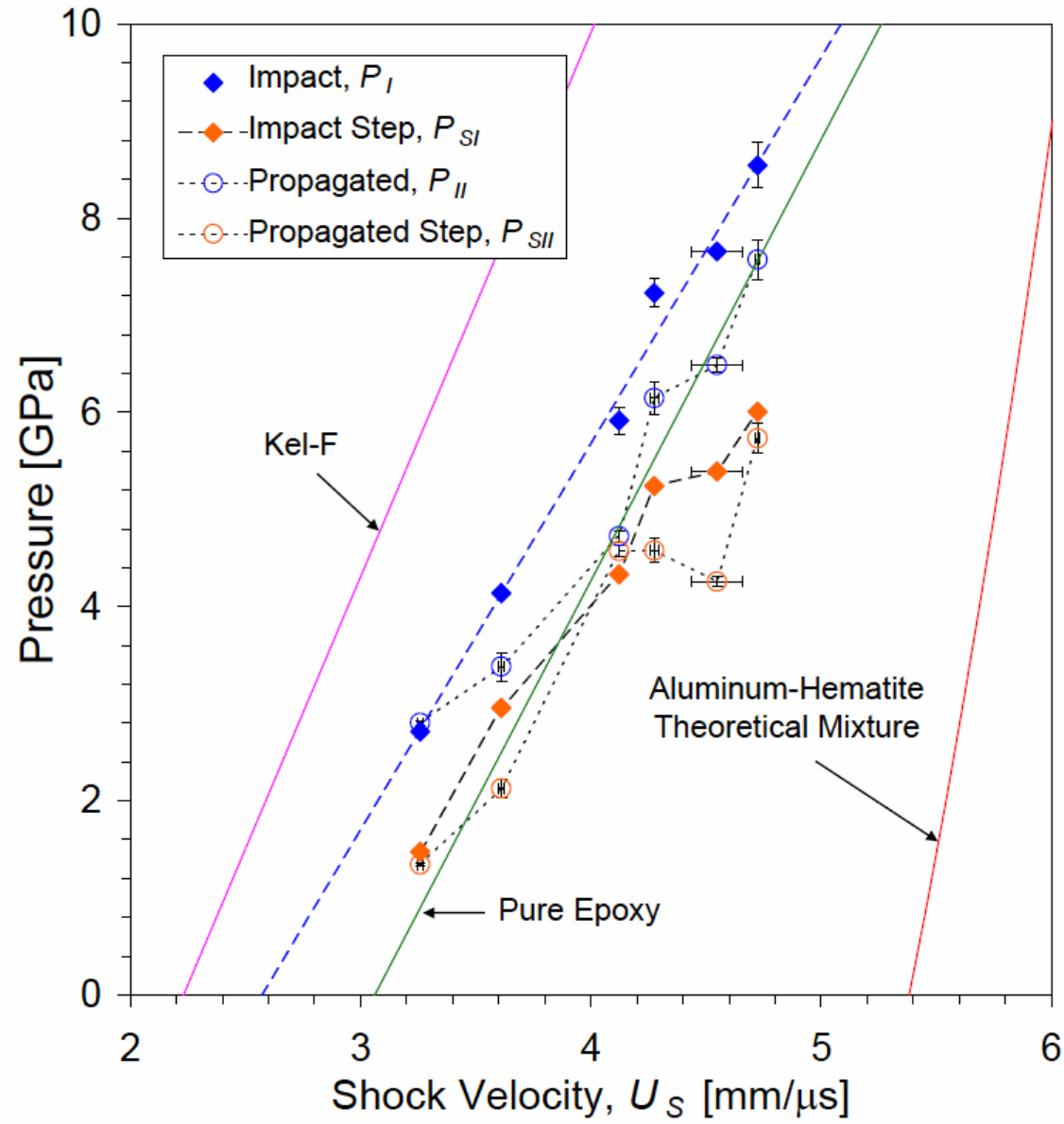


**Figure 4.94** Directly measured pressure and shock velocity parameters obtained for the Al+$Fe_2O_3$+60 *vol.%* epoxy composite are shown. The corresponding propagated gauge and propagated step pressures after impedance corrections are also featured. Pure epoxy and Kel-F data (representing the gauge package response) from Carter and Marsh [72] and Marsh [18] are included for reference, in addition to theoretically calculated response for Al+$Fe_2O_3$ using mixture theory.

strengthening mechanism follow in section 4.5.4.1.

At higher impact pressures, above 4 GPa, the impact and propagated step pressures and the propagated pressure converge, with values of 4.33, 4.57, and 4.72 GPa, respectively. From this point forward, the solid-particle reinforcement inclusions are participating in the loading response. Prior to this point, the epoxy matrix dominates the composite's response and the dispersed particles have little influence in the overall response. For higher impact pressure experiments above this 4 GPa critical limit, the propagated pressure response closely follows that observed for pure epoxy. The impact and impedance corrected propagated pressures should theoretically have identical responses if the shock wave response is not altered in any way by the composite material. However, the wave appears to become focused as it propagates through the specimen and thus shifts to higher shock velocities, as a result of relatively high impedance solid particles distributed throughout the epoxy matrix. If this is indeed the case, this trend would be expected to continue as the impact pressure for experiments increases, reaching a maximum value that would be close to the theoretical aluminum-hematite response curve shown in Figure 4.94. The measured shift to higher shock velocities above a critical pressure limit further verifies that the solid particles are influencing the overall response of the composite.

Steady wave propagation through the specimen and hydrodynamic conditions were assumed for calculating additional parameters using the Rankine-Hugoniot jump conditions [17]. The conservation of momentum equation was used for calculating the particle velocity, $U_P$, in terms of the initial density, $\rho_0$, the measured impact stress or pressure, $P_I$, and the shock velocity through the composite according to:

$$U_P = \frac{P_I}{\rho_0 U_S}. \qquad (4.40)$$

The particle velocity was also directly measured using VISAR for most of the experiments. Comparison of the two measures of particle velocity show good agreements, with an average of 1.2 % difference between the two techniques. However, the calculated particle velocity for shot 0608 was greater than the measured VISAR value, corresponding to 2.5 % difference. The particle velocity for shot 0505, where VISAR was not used, was obtained from a symmetric impact configuration where the flyer is the same material as the target so that the equilibrium particle velocity is known to the precision of the impact velocity measurement. For a symmetric impact, the particle velocity is equal to one-half the impact velocity. The calculated particle velocity using equation (4.40) for shot 0505 was less than the value calculated from the measured impact velocity, corresponding to a 4.2 % difference between the two measures.

Figure 4.95 shows impact pressure as a function of particle velocity, comparing the directly measured VISAR values and those calculated from equation (4.40) using shock velocity values obtained from the impact pressure waveform toe-to-toe and half-max measurements. The figure shows a polynomial fit to the pressure and particle velocity data for the half-max measured values, although, all the methods used for obtaining particle velocity show excellent correlation.

Similarly, Figure 4.96 shows the relationship between shock velocity, $U_S$, and particle velocity, $U_P$, again using several calculation methods with excellent correlation. The polynomial fit to the $U_S$-$U_P$ Hugoniot data is obtained from the half-max measured values. Many materials, particularly metals, typically have a linear $U_S$-$U_P$ relationship

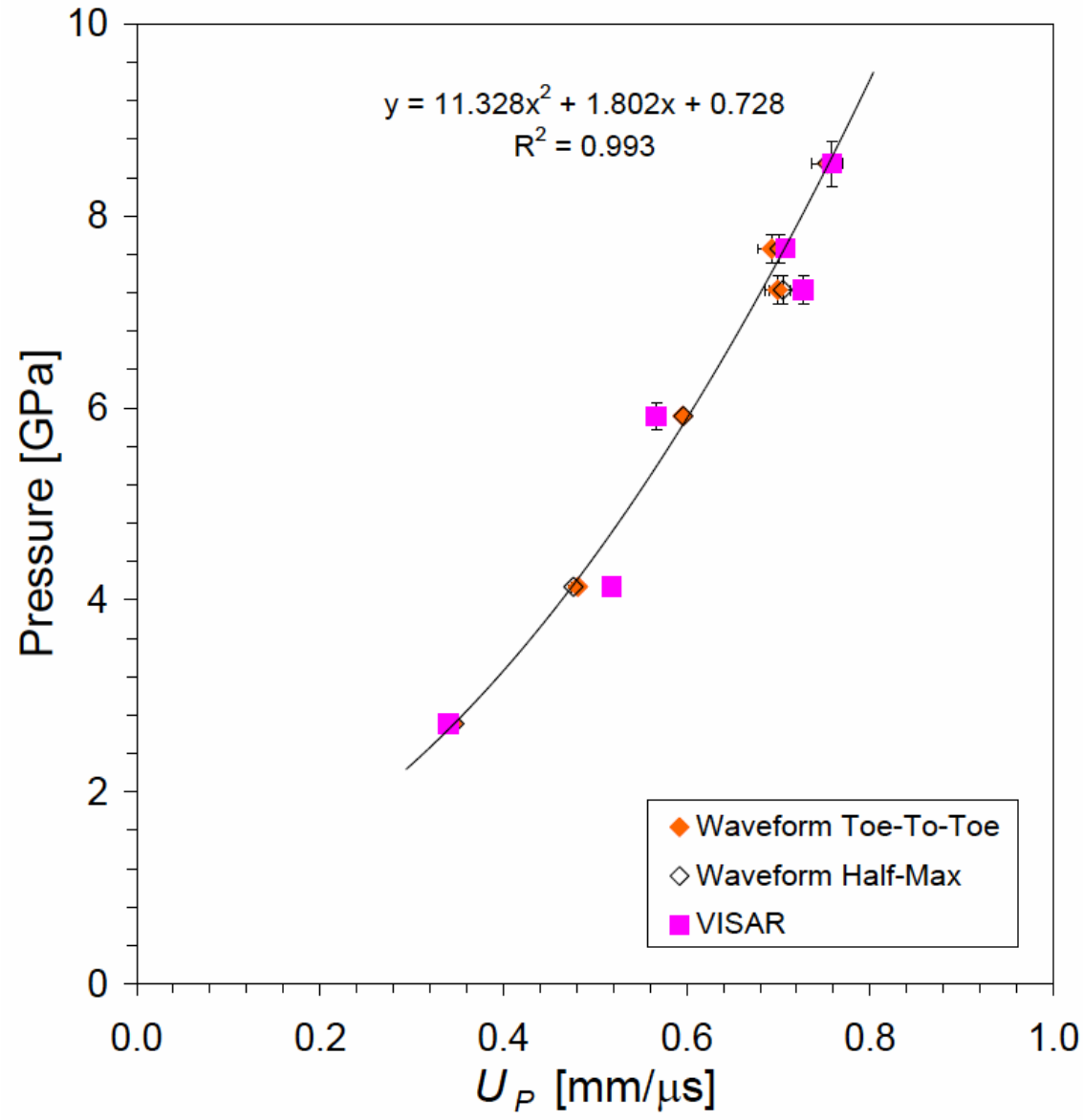


**Figure 4.95** Impact pressure and particle velocity measured directly by VISAR are compared with calculated values using equation (4.40). Shock velocity values are obtained from the impact pressure waveform toe-to-toe and half-max transient time measurements.

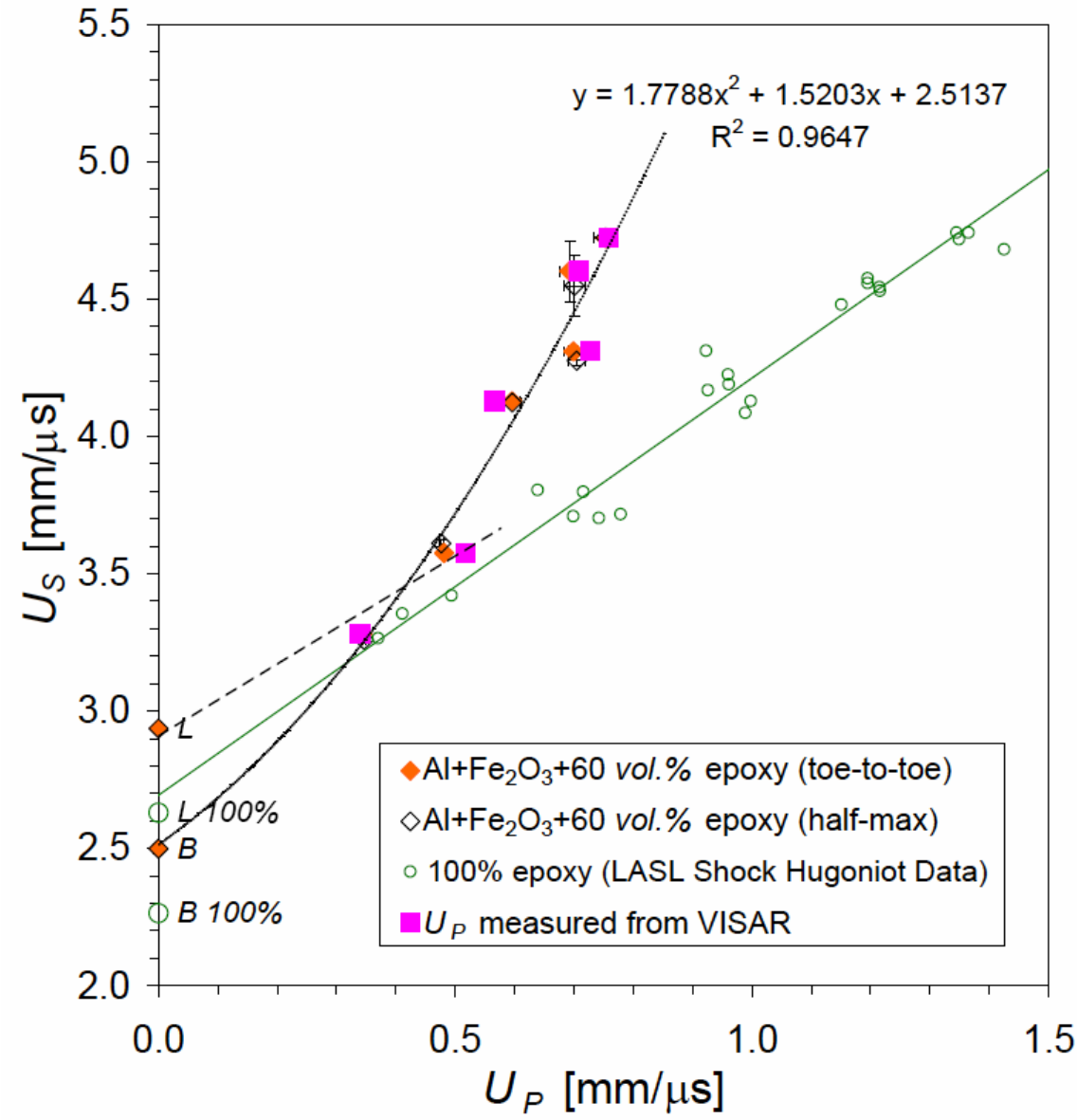


**Figure 4.96** Directly measured shock velocity and particle velocity (obtained by VISAR) are compared to calculated particle velocities using equation (4.40). Shock velocities from transient times calculated using toe-to-toe and half-max methods are used to calculate particle velocity. Pure epoxy data obtained from Carter and Marsh [72], and Marsh [18] is also shown for reference.

that describes the shock response fairly well for materials that do not experience a phase transformation. However, a particularly interesting feature common to most polymers shows a significant non-linear $U_S$-$U_P$ Hugoniot behavior within a relatively low pressure regime [72]. The non-linear behavior typically has a distinct concave curvature with an initially rapid shock velocity. The particle-filled Al+$Fe_2O_3$ epoxy-cast composite with 60 *vol.%* epoxy also shows non-linear $U_S$-$U_P$ Hugoniot behavior, however, the response is altered with the plot exhibiting a convex curvature with initially rapid particle velocity. The two lowest data points illustrate an initially similar behavior for the particle-filled composite and pure epoxy, which gradually deviate at a particle velocity above approximately 450 m/s. Further increase in particle velocity shows a significant deviation between pure epoxy and the 60 *vol.%* epoxy composite. This suggests that the composite's behavior is being altered at sufficiently high pressures or corresponding particle velocities that introduce a kink in the $U_S$-$U_P$ Hugoniot curve. It is possible that a sharply defined kink could occur at a particle velocity of approximately 500 m/s, however, there are only two data points within this region to support this idea.

Ultrasonically measured longitudinal and bulk sound velocities for the particle-filled composition and pure epoxy, indicated by *L* and *B*, respectively, in Figure 4.96, are specified along the shock velocity axis. The shock velocity intercept obtained by extrapolating $U_S$-$U_P$ data for pure epoxy coincides with its longitudinal wave speed value. This phenomenon is typically observed for polymeric materials, which display higher bulk sound velocities than obtained from ultrasonic measurements. In contrast, the 60 *vol.%* epoxy composition yields an intercept value significantly below the longitudinal sound velocity, but close to the bulk wave speed value. If the 60 *vol.%* epoxy composite

truly follows a similar response observed for pure epoxy both at ambient pressures and within the pressure regime for the two lowest data points, it is possible to construct a linear curve that would essentially identify the kink location on the $U_S$-$U_P$ Hugoniot curve. This is shown by the dashed line in Figure 4.96, which essentially offsets the response of pure epoxy to corresponding higher shock velocity values. This is an effect that would be expected when introducing higher shock impedance material to an epoxy matrix.

The compressibility of the composite material is also evaluated from the measured parameters obtained from parallel-plate impact experiments. The specific volume, $V/V_0$, is calculated using the conservation equations and result in the relation:

$$\frac{V}{V_0} = 1 - \frac{U_P}{U_S}. \qquad (4.41)$$

Figure 4.97 (shown on the next page) illustrates the compressibility behavior for the Al+$Fe_2O_3$+60 *vol.%* epoxy composite in comparison with pure epoxy data obtained from Carter and Marsh [72] and Marsh [18]. The introduction of solid particles improves the overall strength of the composite and significantly stiffens the compressibility response as compared to pure epoxy. This effect becomes increasingly more pronounced as impact pressure increases, over the pressure range studied.

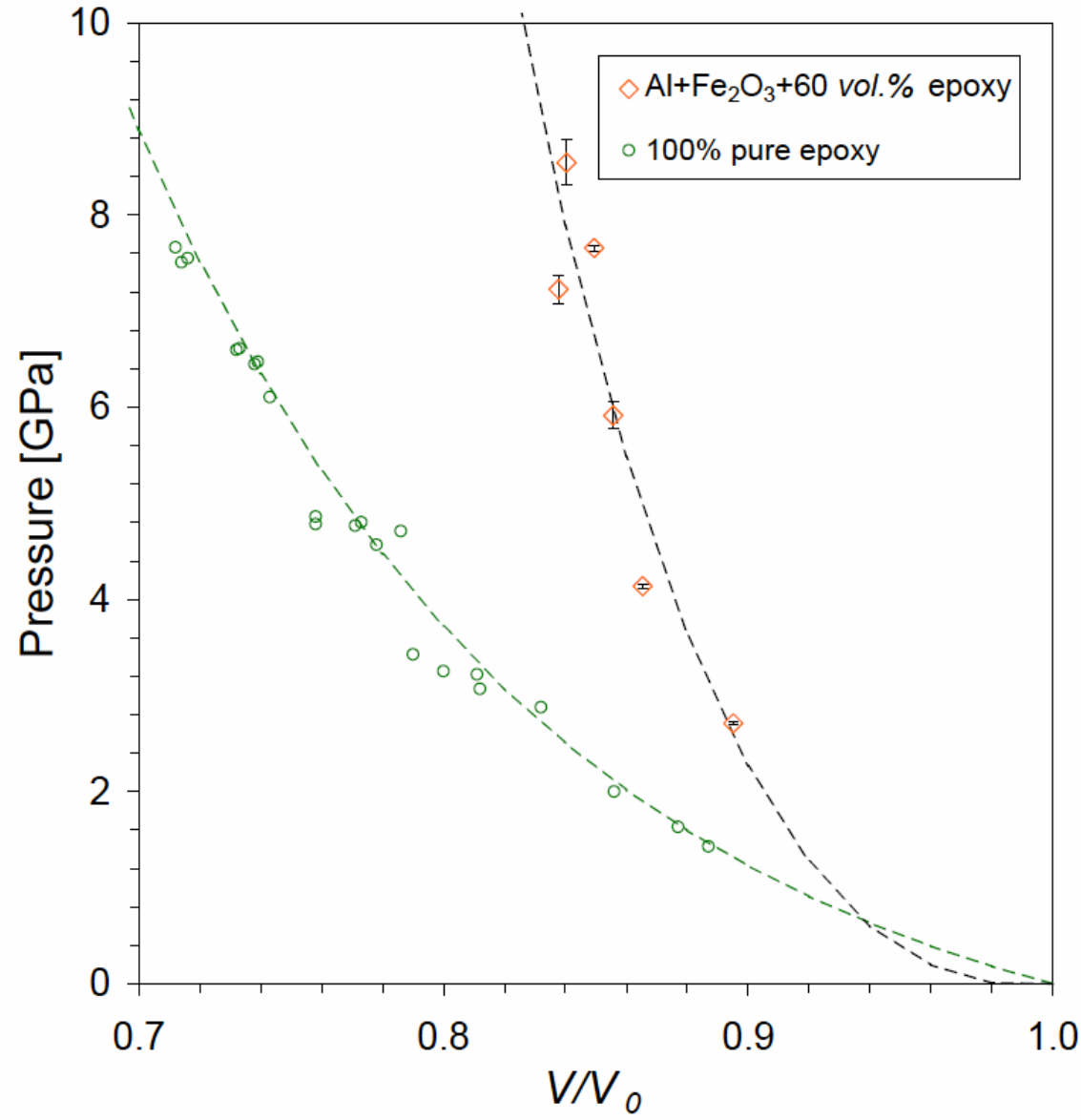


**Figure 4.97** Comparison of measured impact pressure and calculated relative volume values for Al+$Fe_2O_3$+60 *vol.%* epoxy and data obtained from Carter and Marsh [72], and Marsh [18] for pure epoxy.

### 4.5.3 Comparison of Shock Hugoniots Obtained for Epoxy-Cast Composites

Previously discussed results obtained for Al+$Fe_2O_3$+60 *vol.%* epoxy composite are compared with the higher epoxy containing composite, Al+$Fe_2O_3$+78 *vol.%* epoxy and pure epoxy data from Carter and Marsh [72], and Marsh [18]. Although there was a limited number of compressed-gas gun experiments performed for the 78 *vol.%* epoxy composite, higher-pressure explosively loaded experiments conducted by Jordan, *et al.* [161,162] are also included to give complete material behavior up to pressures of approximately 25 GPa. The 78 *vol.%* epoxy composite specimen used for one compressed-gas gun experiment (shot 0303) had a significantly lower density (1.7900 g/cm$^3$, 95.92 % TMD) as compared to other specimens (1.8576 ± 0.0071 g/cm$^3$, 99.54 % TMD) and the theoretical value of 1.8661 g/cm$^3$. Therefore, this particular experiment was not included in the characterizion of the 78 *vol.%* epoxy composite shock-compression behavior.

The direct comparison of both composites and pure epoxy allows the influence of particle-fill volume fraction or overall response of epoxy volume fraction to be evaluated with reference to the epoxy baseline. The $P$-$U_P$ response obtained for both epoxy-cast Al+$Fe_2O_3$ composites and the baseline response of pure epoxy are shown in Figure 4.98. The open data points in the figure correspond to compressed-gas gun experiments, while the filled triangles are for the explosively loaded higher pressure impact experiments. The curves show the influence of solid-particle additions to an epoxy matrix and the altered responses as the volume fraction of each component changes. The direct evaluation of each composition at the same pressure in Figure 4.98 corresponds to higher

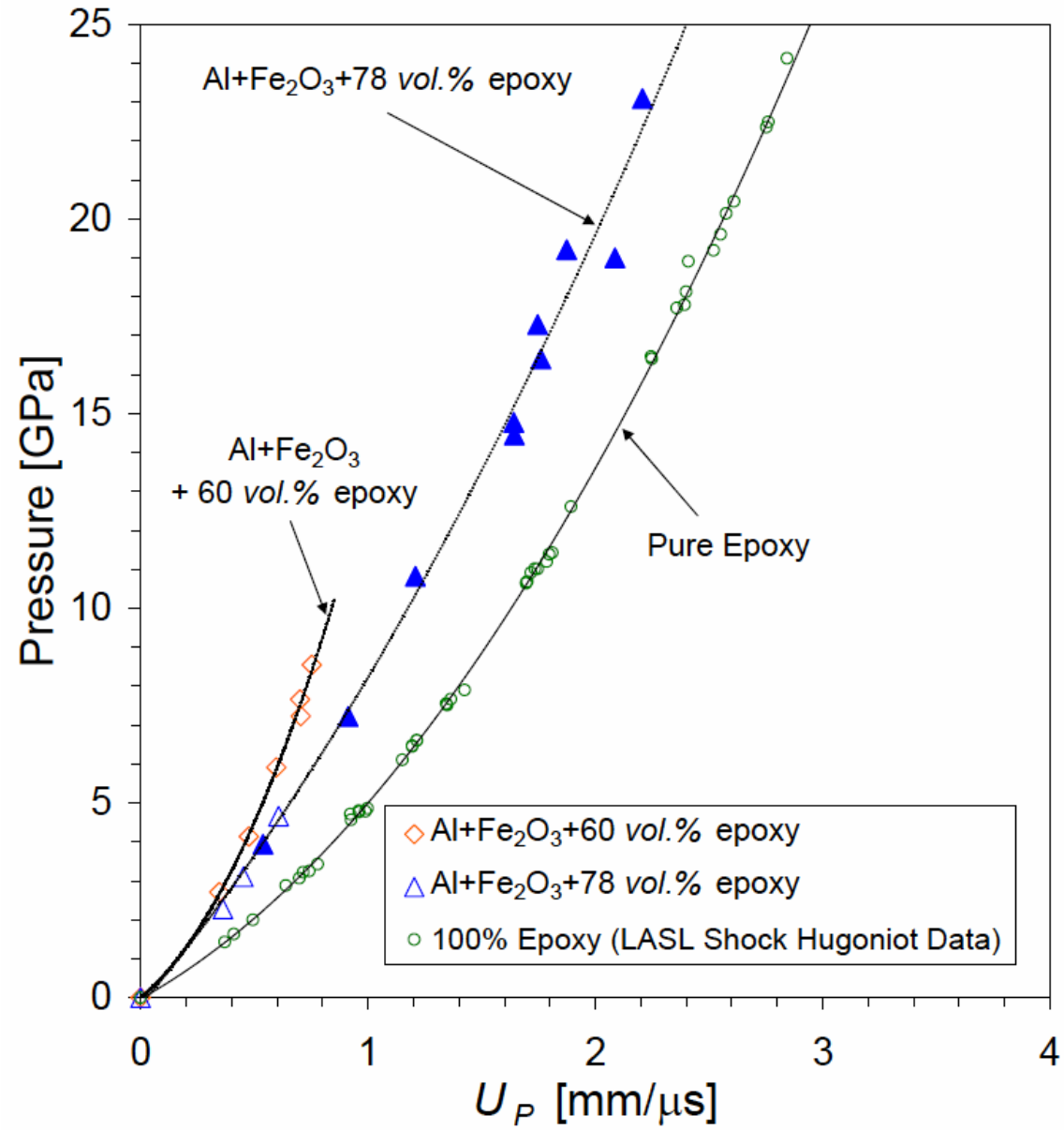


**Figure 4.98** Experimentally measured pressure data plotted as a function of calculated particle velocity, $U_P$, for 60 and 78 *vol.%* epoxy composite materials and pure epoxy data from Carter and Marsh [72], and Marsh [18].

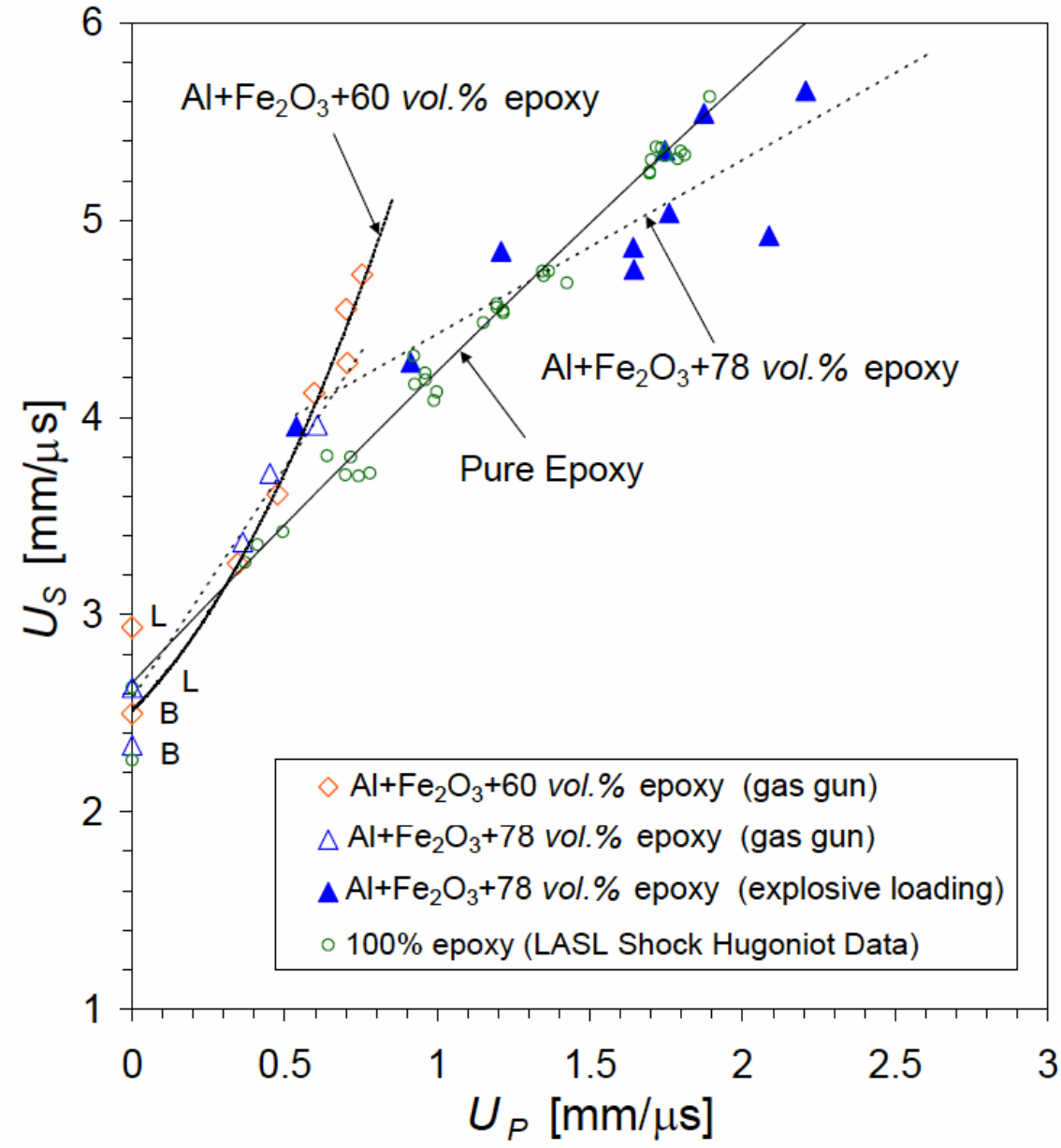


**Figure 4.99** Comparison of $U_S$-$U_P$ Hugoniot data obtained for epoxy-cast Al+$Fe_2O_3$ composites with 60 and 78 *vol.%* epoxy and pure epoxy data from Carter and Marsh [72], and Marsh [18].

particle velocities as the volume fraction of epoxy increases. For example, this physically represents the higher epoxy-containing material dissipates the shock energy ($= \frac{1}{2} m U_P^2$) imparted to the specimen more than the lower containing epoxy composites.

The $U_S$-$U_P$ Hugoniot shown in Figure 4.99 also indicates the altered response observed for the particle-filled epoxy composites. The filled polymers show a non-linear $U_S$-$U_P$ Hugoniot behavior exhibiting a convex curvature with initially rapid particle velocity. The comprehensive study conducted by Carter and Marsh [72] for many different polymers such as polyethylene, polymethylmethacrylate, and epoxy, which include both thermosetting and thermoplastic polymers, also exhibit similar behavior for relatively low pressure regime experiments. However, the non-linear behavior typically has a distinct concave curvature with an initially rapid shock velocity for the unfilled polymers. The contrasting curvatures observed for particle-filled (convex) and unfilled polymers (concave) illustrate the influence particles have on the overall dynamic response of particle-filled composites.

Ultrasonically measured longitudinal and bulk sound velocities for each epoxy-cast composite composition (discussed in section 4.1.2) are indicated by *L* and *B,* respectively in Figure 4.99 along the shock velocity axis. Shock velocity intercepts obtained by extrapolating $U_S$-$U_P$ data for pure epoxy and the 78 *vol.%* epoxy composition had similar responses. The two intercept values coincide with the ultrasonically measured longitudinal wave speed for the 78 *vol.%* epoxy composition. The pure epoxy and 78 *vol.%* epoxy composite have very similar ultrasonic properties resulting in longitudinal waves speeds of 2.63 [18,72] and 2.34 mm/μs, respectively. This illustrates the significant effect that epoxy has on the overall response of the composite due to the

relatively large volume fraction present in this composition. The 60 *vol.%* epoxy composition yields an intercept value significantly below its longitudinal wave speed, but close to the bulk wave speed of 2.50 mm/μs. Again, the response at ambient pressures appears to be influenced greatly by the relatively large volume fraction of epoxy present in these compositions.

The results illustrate an initially similar behavior for both the particle-filled composites and pure epoxy at close to ambient pressures, which gradually deviate at particle velocities above approximately 450 m/s or a pressure close to 4 GPa. Further increase in $U_P$ shows a significant deviation between the two composites at approximately 550 m/s, with the higher 78 *vol.%* epoxy containing composition exhibiting a sharp transition that approaches pure epoxy behavior. It is proposed that these contrasting behaviors are related to various degrees of damage nucleating at inclusion sites within the epoxy matrix. The damage initially provides a bulk toughening effect, which alters the composite's Hugoniot behavior until significant bulk failure occurs. This effect is illustrated by the 78 *vol.%* epoxy $U_S$-$U_P$ curve initially approaching and then falling below pure epoxy behavior at higher $U_P$ values.

### 4.5.4 Evolution and Characterization of Composite Material Damage

Theoretically determined bulk material response and hydrodynamic calculations are used to estimate and quantify the possible damage occurring in these composite materials. The critical stress is estimated by calculating the composite's compressive behavior using the Birch-Murnaghan equation of state (BM-EOS) [211] for damaged and

undamaged material responses. Additionally, the equilibrated Hugoniot pressure response for mixed phases with significantly varying shock impedances are calculated using the inverted Hugoniot EOS [212] from the individual constituent's Hugoniot data. Parallel-plate impact experiments are also modeled using a Eulerian shock physics code, CTH [213-215], with use of a viscous-elastic-plastic (VEP) constitutive model [216] and the Mie-Grüneisen nonlinear $U_S$-$U_P$ EOS. The simulations are used to reproduce the pressure waveforms obtained from the impact and propagated PVDF gauges using experimentally measured bulk material parameters.

#### 4.5.4.1 CTH Hydrodynamic Calculations

CTH [213-215] is a Eulerian code for numerical simulation of hydrodynamics and solid mechanics problems involving large stresses and deformations. It employs a standard two-step Eulerian scheme for solving the equations of hydrodynamic flow in finite difference form. There is a Lagrangian step, in which the computational mesh distorts with the material motion, followed by a remap step in which the flow variables are mapped back onto an Eulerian (stationary) mesh. In the code, the numerical solution proceeds by first moving the spatial mesh through displacements (Lagrangian step) determined by the material velocity field, and then remapping the mesh back to its original position. The mesh is fixed in space, and the material flows through the mesh in response to boundary and initial conditions. The volume, mass, momentum, and energy must be conserved across the Lagrangian step. The mass is conserved automatically because the mesh moves with the material during this step and no mass crosses the cell

boundaries. The remaining conservation equations are replaced with explicit finite volume representations of the original integral equations. After the Lagrangian step, the remap step is performed where the distorted cells are returned back to the initially fixed mesh.

Hydrocode simulations of dynamic problems also require models for the constitutive behavior of all the materials involved. The constitutive laws are applied at the cell centers following the remap step. The equation of state, which provides pressure and temperature as a function of mass density and internal energy density, is applied separately from the strength model, which provides the deviatoric stress rate tensor components as a function of the appropriate strain rate tensor variable. The composite materials examined in this work were described by a Mie-Grüneisen equation of state and the viscous-elastic-plastic (VEP) constitutive model [216] for a viscoelastic-viscoplastic deformation behavior.

The parallel-plate impact experiments conducted for the Al+$Fe_2O_3$+60 *vol.%* epoxy composites were modeled for yielding time-resolved material stress behaviors and compared to experimentally measured PVDF stress gauge waveforms. The highly viscoelastic and viscoplastic behaviors observed for the composite materials are incorporated in the code and tested with experimental data. The configuration utilized for these experiments is duplicated in the CTH DIATOM description. The calculations use a one-dimensional spatial mesh with a resolution of 12.5 μm. Several tracer points, which record the state variables, were located within the epoxy-cast composite target, fused silica window, and the impact and propagated gauge layers that make up the target

assembly. In general, the tracer points within the gauge layers and those close to the respective gauge/target or gauge/window interfaces exhibited almost identical responses.

The shock properties of the epoxy-cast composite were based on the Mie-Grüneisen equation of state using the experimentally determined quadratic relation between shock velocity and particle velocity. The shock properties of the copper flyer/driver, the tungsten flyer, and the fused silica window components were specified by the linear form of the Mie-Grüneisen equation of state, while the PVDF gauge packages, represented by Kel-F, were defined using the viscoelastic (VE) equation of state [217]. The material parameters were included in CTH for the VE equation of state, which uses a separate EOS for the instantaneous and equilibrated material states and relaxation rates controlled by the stress state of the material.

The constitutive behavior of the copper flyer/driver, the tungsten flyer, and the fused silica window components was governed by the Steinberg-Guinan model [218], while the viscous-elastic-plastic (VEP) constitutive model [216] was used for the PVDF gauge layers obtained from material parameters included in the CTH material database. The epoxy-cast composite behaviors were also governd by VEP constitutive model [216] using experimentally determined parameters. The dynamic behavior was captured through an elastic shear spring model that is in parallel with a series of five viscoelastic Maxwell elements. Each Maxwell element is comprised of an elastic spring and viscous damper that are correlated to capture the mechanical response at a given strain rate. In addition, a viscoplastic element is set in series with the composite Maxwell viscoelastic element arrangement. Many of the Maxwell element parameters, consisting of shear spring moduli and the damper viscosities, were first approximated for the

$Al+Fe_2O_3$+60 *vol.%* epoxy composite based on the significant work performed for solid rocket motor propellants (HTPB/AP/Al) [216,219-221] and PMMA [216]. The epoxy-cast composite shock loading behavior appeared to have a combination of features that were attributes of the generic HTPB/AP/Al propellant and PMMA. Some of the constituent parameters were obtained from measurements conducted in this study, while others were approximated by the response of propellant and PMMA. The parameters were adjusted until the model closely matched the experimentally measured composite's behavior.

Figure 4.100(*a-d*) shows a snapshot captured at four specific times, which follow the progression of the disturbance wave through the different materials that comprise the target assembly for the symmetric impact of shot 0627. Each snapshot shows the tracking of density, particle velocity, and stress values through the epoxy-cast flyer and target materials, and fused silica window material. Figure 4.100(*a*) corresponds to a time just after impact and the equilibrated particle velocity and pressure values in the flyer and driver materials. Notice that the particle velocity is cut in half as it enters the target material, and the density shows equal compressibility in the similar epoxy-cast flyer and target materials. The wave continues to propagate until it reaches the target/fused silica window interface, where there is a marked rise in stress and a significant decrease in particle velocity, as shown in Figure 4.100(*b*). Also notice the fused silica density is relatively unchanged and behaves as a nonlinear elastic solid up to its phase change, which occurs at approximately 9.8 GPa [155]. The elastic behavior is evident in Figure 4.100(*b*), which indicates the formation of the elastic step in the stress profile. Figure 4.100(*c*) shows the reflected wave from the target/fused silica window interface

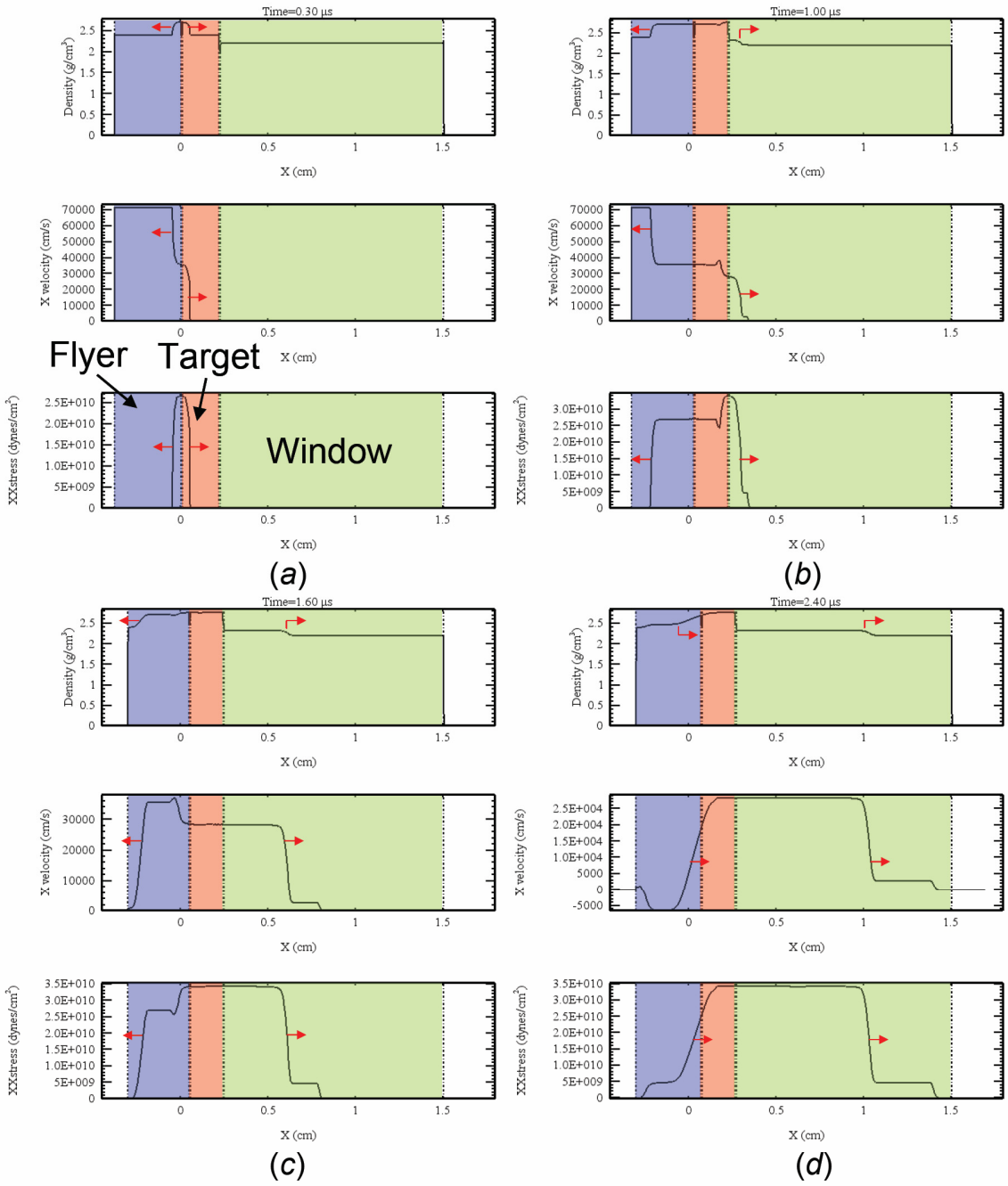


**Figure 4.100** Captured one-dimensional CTH simulation snapshots illustrating the waveform propagation (direction indicated by arrows) within the materials that make up the target assembly for shot 0627. The snapshots are captured at *a*) 0.3, *b*) 1.0 *c*) 1.6, and *d*) 2.4 µs after impact and show the variation of density, particle velocity, and stress waveform profiles (in order top-to-bottom) throughout the target assembly.

approaching the reflected wave from the back surface of the flyer. The epoxy-cast composite materials show the viscoelastic response as the densities return close to their original values, while the elastic wave is fully developed and propagating in the fused silica window. This is followed by Figure 4.100(*d*), which corresponds to a time after the reflected wave interactions of the flyer and target/fused silica interface. A reduction in stress due to the arrival of the release wave is observed at the impact gauge location. Similar snapshots for the other experiments conducted in this study are available in Appendix D.

The CTH simulations were also compared to experimentally measured stress waveforms. Figure 4.101(*a-f*) shows the results of each experiment conducted for the Al+$Fe_2O_3$+60 *vol.%* epoxy composite with a range of initial loading conditions. Comparison of embedded PVDF stress gauge measurements with one-dimensional CTH code at both the impact and propagated gauge locations shows excellent agreement for relatively low stress impacts as illustrated in Figure 4.101(*a,b*). However, the code overestimates once the input stress increases past a critical limit above which damage occurs. Each simulation predicts the correct shock velocity, however the particle velocity is typically overestimated as shown in Figure 4.102(*b-e*), which compares measured VISAR particle velocities with those simulated. This results in the overestimate of the stress response seen in Figure 4.101(*c-f*) for the higher impact stress experiments. Notice the comparison of particle velocities obtained from VISAR and CTH illustrated in Figure 4.102(*a*) show fairly good agreement for shot 0627, which has an impact stress below the critical damage stress.

Although the VEP model is capable of relaxing the total deviatoric strain rate as

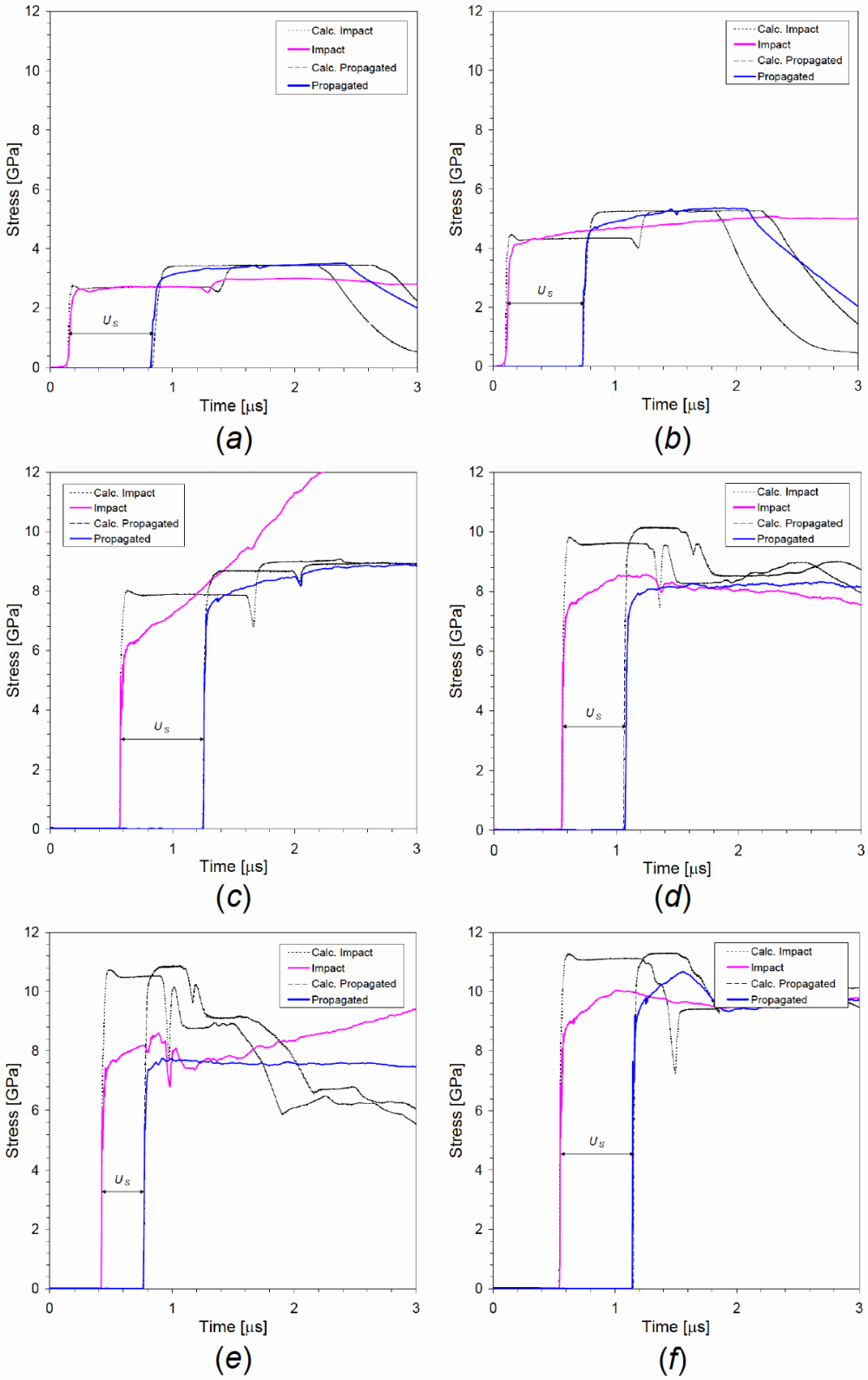


**Figure 4.101** Comparison of experimental and CTH calculated stress profiles obtained for Al+$Fe_2O_3$+60 *vol.%* epoxy composite. Results are shown for shots *a*) 0627, *b*) 0505, *c*) 0608, *d*) 0507, *e*) 0628, and *f*) 0609.

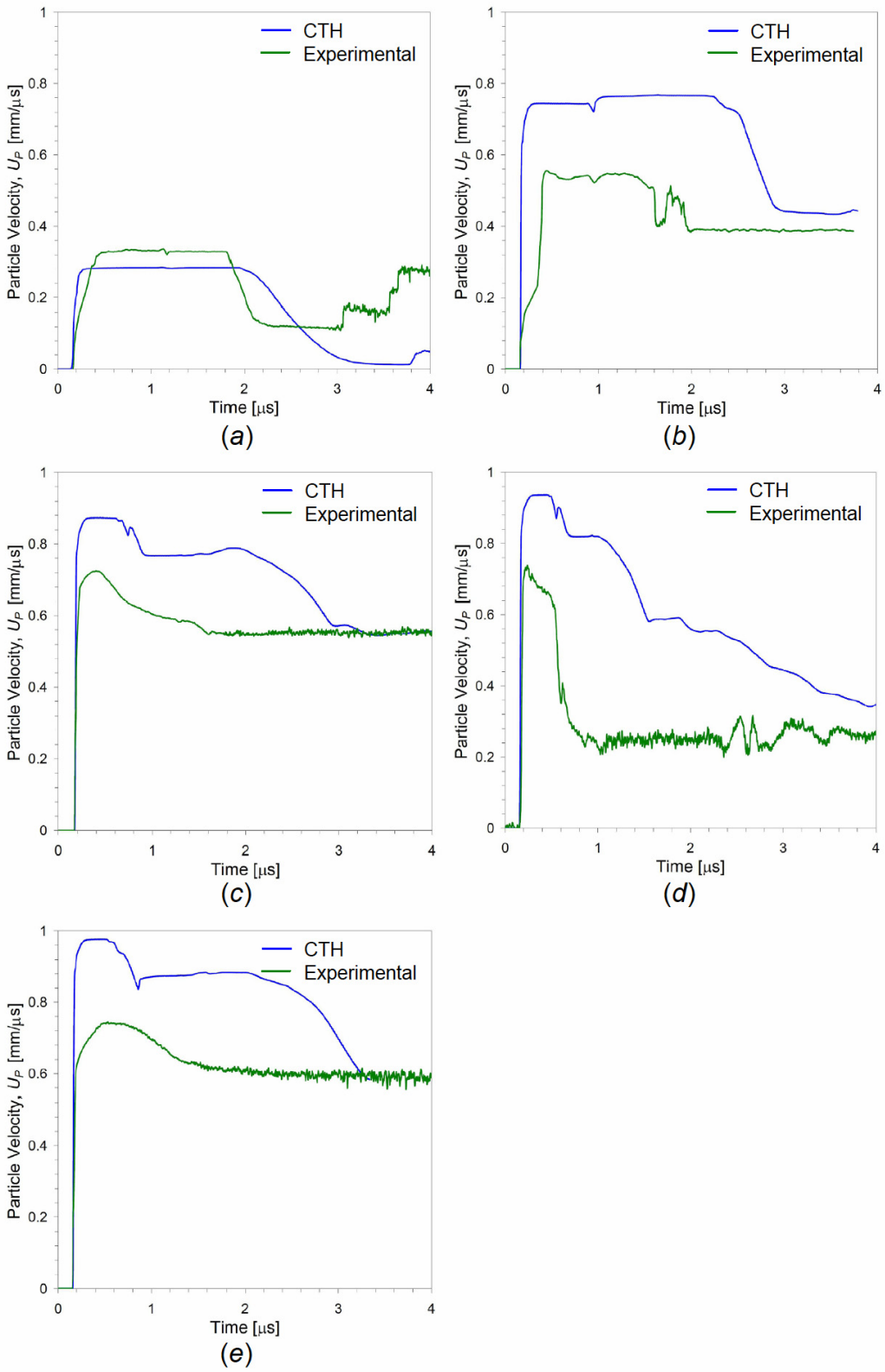


**Figure 4.102** Comparison of experimental (VISAR) and CTH calculated particle velocity profiles obtained for Al+$Fe_2O_3$+60 *vol.%* epoxy composite. Results are shown for shots *a*) 0627, *b*) 0608, *c*) 0507, *d*) 0628, and *e*) 0609.

induced damage in the material occurs, it does not compute the damage variable internally. Instead, the VEP model relies on the Tensile Damage and Distension (TDD) model [222] to acquire the damage level within the material. Unfortunately, this capability has not been fully developed in the CTH code (version 7.0), and the TDD model does not currently update the true damage variable, $D$, in the VEP constitutive model used to compute the effective damage, $D_{eff}$, which controls the material strength loss as well as void formation.

In the absence of a damage model that can be used with the CTH calculations, other methods were used to characterize the stress threshold level where damage occurs in the composite. These include predicting the undamaged material response using the inverted Hugoniot EOS [212] from individual constituent's Hugoniot data, and also by fitting both the damaged and undamaged material responses with the Birch-Murnaghan equation of state (BM-EOS) [211]. The results indicate the critical stress level for inducing damage within the composite materials and are discussed next (section 4.5.4.2).

#### 4.5.4.2 Theoretically Determined Hugoniot Behavior

The Birch-Murnaghan equation of state (BM-EOS) [211] was used to account for the altered Hugoniot response of particle-filled epoxy-cast composites and quantitatively characterize the resulting induced damage. The experimentally measured $U_S$-$U_P$ Hugoniot data was transformed into pressure-volume ($P$-$V$) space using the jump conditions and was fit using the BM-EOS in terms of normalized stress, $F$, and finite Eulerian strain, $f$. These are given by [211]:

$$F = \frac{P}{3f\left(1+2f\right)^{5/2}}, \tag{4.42}$$

where $P$ is the pressure and $f$ is given by [211]:

$$f = \frac{1}{2}\left[\left(\frac{V_0}{V}\right)^{2/3} - 1\right]. \tag{4.43}$$

The third-order BM-EOS is written as a polynomial with respect to strain according to [211]:

$$F = K_0 + \frac{3}{2}K_0\left(K_0^{'} - 4\right)f\ . \tag{4.44}$$

In this form, the BM-EOS gives a direct indication of the compressibility in terms of the bulk modulus, $K_0$, and the pressure derivative of the bulk modulus, $K_0^{'}$. The constants are evaluated from the *F-f* plot, which has a linear fit with a slope equal to $3/2\,K_0\left(K_0^{'} - 4\right)$ and an intercept of $K_0$. The utility of the BM-EOS and its parameters determined from the normalized stress and Eulerian finite strain curve is first demonstrated for the constituent materials used in the composites from Hugoniot data obtained for aluminum, hematite, and epoxy from Marsh [18].

The pressure-volume data for each constituent material is transformed to normalized stress-finite strain space as shown in Figure 4.103. The linear fit to the data allows the calculation of the bulk modulus and its derivative from the slope and intercept

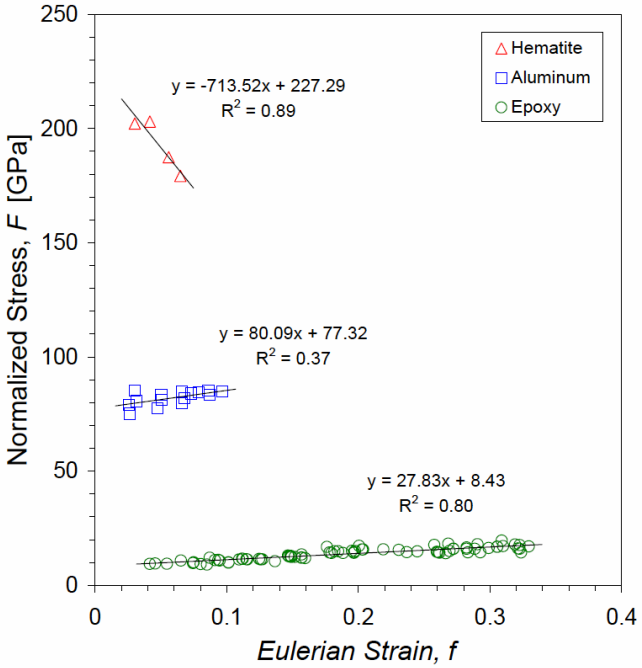


**Figure 4.103** Normalized stress and Eulerian strain curves obtained for hematite, aluminum, and epoxy data from Marsh [18] using the third-order Birch-Murnaghan equation of state (BM-EOS) [211].

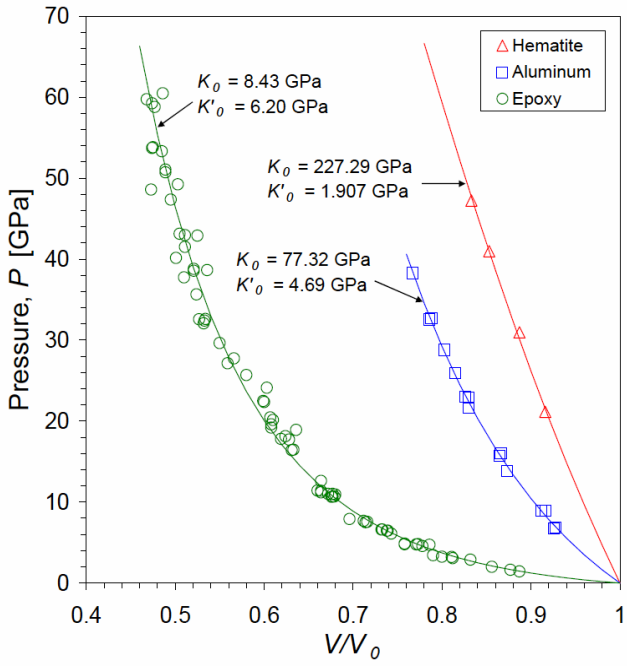


**Figure 4.104** Pressure-volume compressibility plot showing hematite, aluminum, and epoxy data points from Marsh [18] and the undamaged third-order Birch-Murnaghan equation of state (BM-EOS) [211] compressibility curves with parameters determined from the normalized stress and Eulerian strain curves in Figure 4.103.

values. While the Hugoniot for hematite was limited to a few data points prior to the phase transformation, the bulk modulus obtained from the *F-f* curves are slightly greater than those obtained ultrasonically, however, the parameters show an excellent fit (solid curves) to the measured compressibility behavior as illustrated in Figure 4.104.

The same technique was utilized for obtaining the parameters necessary to fit the compressibility behavior for the epoxy-cast composite materials examined in this study. The *P-V* data for the particle-filled composites and pure epoxy are transformed to normalized stress-finite strain space as shown in Figure 4.105 and Figure 4.106 for the Al+$Fe_2O_3$ composites with 60 and 78 *vol.%* epoxy, respectively. The Hugoniot curves comparing the $U_S$-$U_P$ behaviors for each composition, shown in Figure 4.99, indicate that the composite's response are altered at a critical $U_S$ and $U_P$ value. Therefore, the curves shown in Figure 4.105 and Figure 4.106 were divided in order to evaluate the two regions characterized as "damaged" and "undamaged" compressibility of each composition. Notice that the damaged and undamaged *F-f* response curves for the 78 *vol.%* epoxy composite show widely different behaviors; having positive and negative slopes, respectively. Although less apparent, the 60 *vol.%* epoxy composition behaviors are also divided. The justification becomes more evident when trying to calculate $K_0$ from a curve fit to all the data, which results in an unrealistic value (close to zero or negative). However, fitting the two lowest normalized stress data points with a linear curve, results in a more appropriate $K_0$ value that compares well with calculated bulk modulus values from ultrasonic measurements for this particular composition. The values obtained from the intercepts of these curves for both compositions are listed Table 4.24 along with $K_0$ values calculated from ultrasonic measurements. The pressure derivative of the bulk

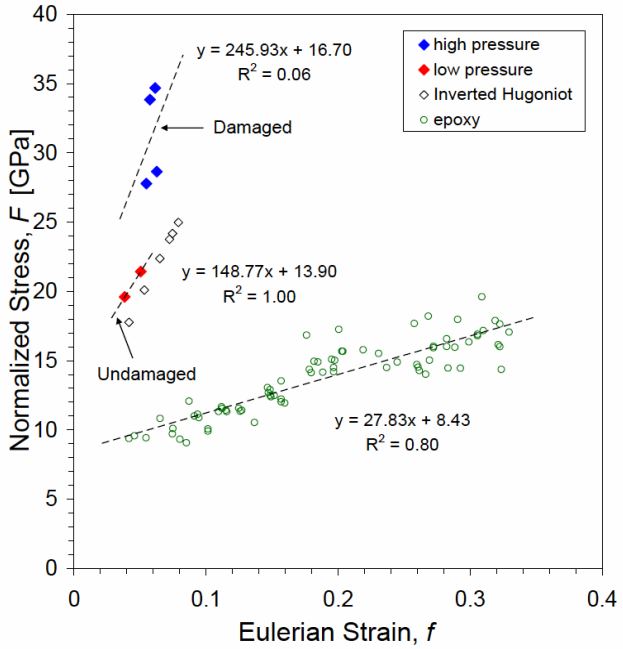


**Figure 4.105** Normalized stress and Eulerian strain curves obtained from experimental data for Al+$Fe_2O_3$+60 *vol.%* epoxy composite are shown. The theoretically calculated (undamaged) behavior using an inverted Hugoniot [212] and pure epoxy baseline data from Carter and Marsh [72], and Marsh [18] are included for reference.

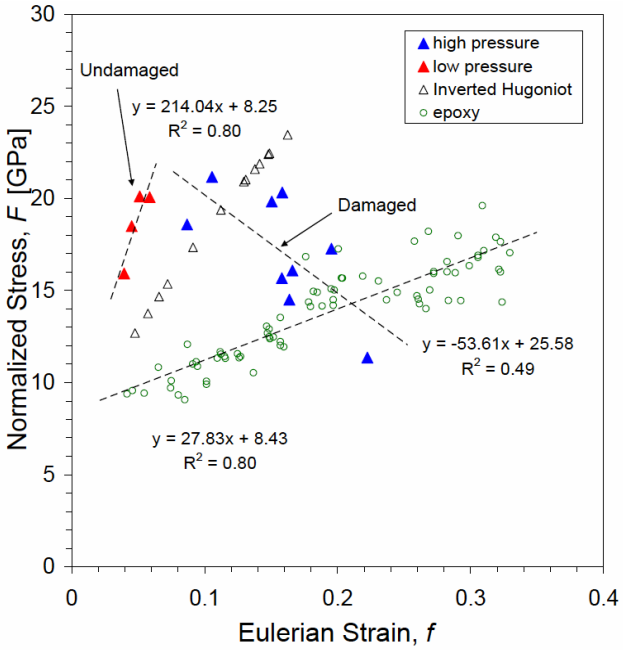


**Figure 4.106** Normalized stress and Eulerian strain curves obtained from experimental data for Al+$Fe_2O_3$+78 *vol.%* epoxy composite are shown. The theoretically calculated (undamaged) behavior using an inverted Hugoniot [212] and pure epoxy baseline data from Carter and Marsh [72], and Marsh [18] are included for reference.

**Table 4.24** Comparison of bulk modulus, $K_0$, values obtained from *F-f* curves and ultrasonic measurements.

| Material or Composition | Compressibility Response | *F-f Intercept* | *Ultrasonic* |
|---|---|---|---|
| | | $K_0$ [GPa] | $K_0$ [GPa] |
| Al+$Fe_2O_3$+ 60 *vol.%* epoxy | Undamaged | 13.90 | 14.77 |
| | Damaged | 16.70 | n/a |
| Al+$Fe_2O_3$+ 78 *vol.%* epoxy | Undamaged | 8.25 | 10.03 |
| | Damaged | 25.58 | n/a |
| Pure Epoxy [18,72] | Undamaged | 8.43 | 6.07 |
| Aluminum [18] | Undamaged | 77.32 | 74.28 |
| Hematite [223] | Undamaged | 227.29 | 206.60 |

modulus, $K_0'$, is computed from the slope of each curve in Figure 4.105 and Figure 4.106. The BM-EOS can now be applied to the experimental data by fitting the damaged and undamaged material responses using equation (4.44) to generate $P$-$V/V_0$ curves. These curves for both compositions are shown in Figure 4.107 along with the experimental data in pressure-volume space. The undamaged responses for both compositions overlap and show excellent agreement with the experimental data at pressures below approximately 4 GPa. As the pressure increases, the 60 *vol.%* epoxy composition shows a volume expansion that is not related to a phase change, but to the decohesion of inclusion particles from the epoxy matrix that causes the bulk compressibility to increase. These higher pressure values show good agreement with the damaged material curve. In contrast, the 78 *vol.%* epoxy composition approaches the pure epoxy response with no evidence of a volume expansion corresponding to particle decohesion. However, it is apparent that the loading is carried almost completely by the binder material, and the solid particle inclusions provide stress concentration sites that

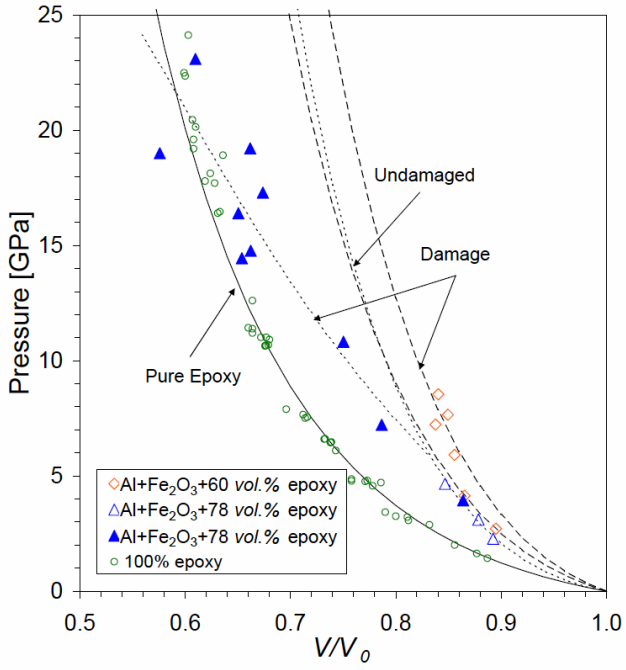


**Figure 4.107** Pressure-volume compressibility plot showing the experimentally measured data points with damaged and undamaged third-order Birch-Murnaghan equation of state (BM-EOS) [211] compressibility curves with parameters determined from the normalized stress and Eulerian strain curves in Figure 4.105 and Figure 4.106.

permit the nucleation of unobstructed crack growth and propagation. These curves show that both composite compositions experience damage at a critical stress of approximately 4 GPa. However, contrasting behaviors for each composition are observed at higher pressures, above this critical stress. While the 78 *vol.%* epoxy composition shows a transition from undamaged to damaged behavior that approaches pure epoxy response, the 60 *vol.%* epoxy composition exhibits a gradual toughening behavior that has not reached the maximum damage and consequent transition to lower compressibility response. It is possible that a similar damage transition observed for the 78 *vol.%* epoxy composition would be expected to occur for the 60 *vol.%* epoxy composition at higher impact stresses.

The theoretical Hugoniot behavior for Al+$Fe_2O_3$ epoxy-cast composites is evaluated using the inverse Hugoniot equation of state developed by Reaugh and Lee [212]. The model uses the constituent properties according to their relative volume fractions within the composite for describing the Hugoniot response. The pressure on the Hugoniot is expressed in terms of the volume using the empirical relation for the modulus of the Hugoniot, $K_h$, where [212]:

$$K_h = V\left(\frac{\partial P}{\partial V}\right)_h, \tag{4.45}$$

and $K_h$ is also a specific function of the Hugoniot pressure given by [212]:

$$K_h = K_0\left(1+\frac{\lambda P_h}{K_0}\right)^n. \tag{4.46}$$

In these expressions, $P$ is pressure, $V$ is volume, $K_0$ is the initial bulk modulus, $\lambda$ and $n$ are fitting parameters that are determined for each constituent material used in the composite. Equations (4.45) and (4.46) are combined and integrated to obtain a Hugoniot expression in terms of volume and is given by [212]:

$$V_h = V_0 \exp\left[\frac{1-\left(1+\frac{\lambda P_h}{K_0}\right)^{1-n}}{\lambda(1-n)}\right] \tag{4.47}$$

The values of $\lambda$ and $n$ are determined for each component of the composite by fitting equation (4.47) to experimentally measured $P$-$V$ Hugoniot data. Using regression analysis, the Hugoniot expression is solved by numerical iterations with initial guesses for $\lambda$ and $n$ until they converge. For example, the Hugoniot data for aluminum was fit using the bulk modulus, $K_0$ = 74.28 GPa, and the resulting parameters $\lambda$ and $n$ converge to 7.576 and 0.714, respectively. This compares well with the values obtained by Reaugh and Lee [212] for aluminum, taken to be 6 and 0.82 for $\lambda$ and $n$, respectively. The other components used in these composites had values of $\lambda$ = 2.403 and $n$ =1.465 for hematite and $\lambda$ = 12.941 and $n$ = 0.744 for epoxy.

Having determined the values for $\lambda$ and $n$ for each component, the Hugoniot of the composite is obtained by the weighted sum of the various component volumes given by [212]:

$$V_h = \sum_{i=1}^{N} \alpha_i V_{hi} \,, \tag{4.48}$$

where $\alpha_i$ is the initial volume fraction for the $i^{\text{th}}$ component. The shock velocity and particle velocity are then given by the usual expressions incorporating the composite's weighted volume response and expressed as:

$$U_S = \sqrt{\frac{P_h}{\left[\rho_0 \left(1 - V_h\right)\right]}}, \tag{4.49}$$

and

$$U_P = \frac{P_h}{\rho_0 U_S}. \tag{4.50}$$

The pressure-volume compressibility Hugoniot based on the weighted volumes are shown in Figure 4.108 for the 60 *vol.%* epoxy composite. The lowest two data points (shown as red diamonds) from the experimental Hugoniot represent the undamaged material response and show excellent agreement with the theoretically determined compressibility curve until approaching the critical pressure of approximately 4 GPa. The inverted Hugoniot calculations also show excellent agreement with the compressibility response determined by the BM-EOS. The theoretical values are

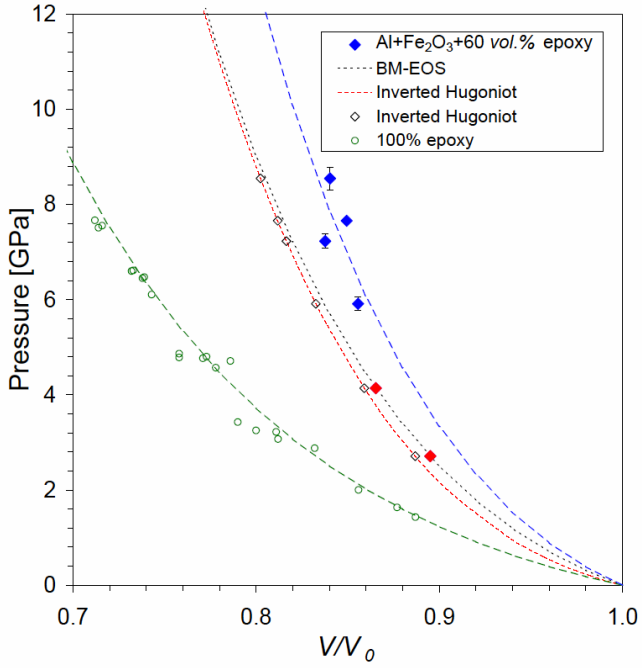


**Figure 4.108** Pressure-volume compressibility plot for the Al+$Fe_2O_3$+60 *vol.%* epoxy composite comparing the experimentally measured data points and the theoretical (undamaged) behavior predicted from the inverted Hugoniot [212]. The experimentally determined behavior for the undamaged response using the BM-EOS is extrapolated to higher pressures and shows good agreement with the inverted Hugoniot calculation.

additionally shown on the normalized stress–Eulerian strain plot (*F–f*) of Figure 4.105, substantiating the use of only two experimental data points for the undamaged response curve. The theoretical $U_S$-$U_P$ Hugoniot data points shown in Figure 4.109 compare well for the undamaged material response with experimental values and are calculated using equations (4.49) and (4.50) for the shock velocity and particle velocity, respectively.

While the theoretically determined compressibility for the 60 *vol.%* epoxy composite shows excellent agreement for the lower pressure (undamaged) material responses, the 78 *vol.%* epoxy composite shows rather significant deviation. Figure 4.110 shows the theoretically determined Hugoniot values compared to those experimentally measured. The response of the 78 *vol.%* epoxy composite appears to follow more closely with the behavior observed for the 60 *vol.%* epoxy composite at pressures below 4 GPa, as shown in Figure 4.107. The discreprency between the experimental and theoretical values for this composition could possibly be associated with the specimens exhibiting damage initially at very low pressures. This causes a bulk volume expansion due to the particle decohesion with the matrix and possibly introduces a strengthening mechanism that represents the experimental response shown in the figure. While the 60 *vol.%* epoxy composite shows strengthening at a critical pressure close to 4 GPa, the 78 *vol.%* epoxy composite possibly shows initial strengthening followed by significant damage at this critical pressure. The theoretical values are also included on the normalized stress-Eulerian strain plot (*F–f*) of Figure 4.106 and show the undamaged response of the composite experiencing relatively lower strains and corresponding lower normalized stresses as compared to the experimental values. The theoretical $U_S$-$U_P$ Hugoniot data points shown in Figure 4.111 indicate the calculated values are very close

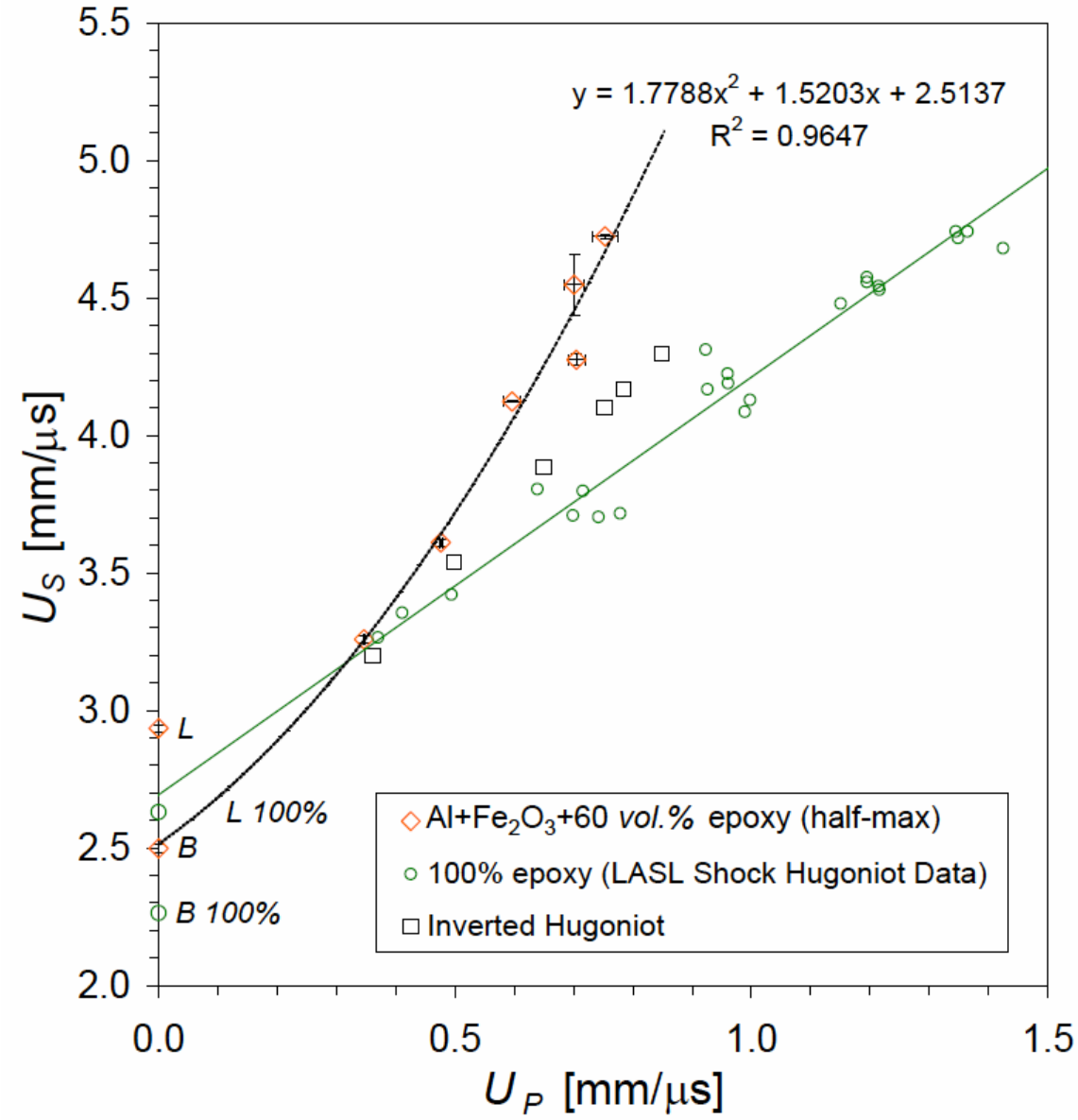


**Figure 4.109** Experimentally determined $U_S$-$U_P$ data points for Al+$Fe_2O_3$+60 *vol.%* epoxy composite are compared to theoretical inverted Hugoniot [212] values calculated for each experiment.

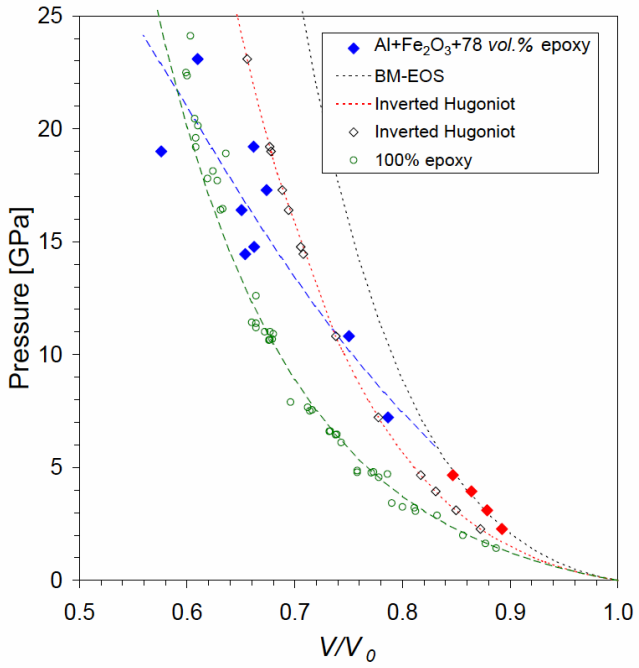


**Figure 4.110** Pressure-volume compressibility plot for the Al+$Fe_2O_3$+78 *vol.%* epoxy composite comparing the experimentally measured data points and the theoretical (undamaged) behavior predicted from the inverted Hugoniot [212]. The experimentally determined behavior for the undamaged response using the BM-EOS is extrapolated to higher pressures and shows good agreement with the inverted Hugoniot calculation.

to the response of pure epoxy.

From a damage standpoint, there are two major processes that introduce damage into the composite material. The first is caused by decohesion of solid particles from the polymer matrix due to stress-wave interactions. A typical stress-strain history shows that apparent yielding occurs at fairly low strain levels. Beyond this point, the specimen will undergo very large strains before failing. This is followed by the binder system carrying the load with an apparently lower shear modulus until failure occurs. From examining the compressibility (*P-V*) behavior obtained from parallel-plate impact experiments, the 60 *vol.%* epoxy composite shows a slight volume expansion at higher pressures. This volume expansion is attributed to decohesion of solid particles. One would expect that if

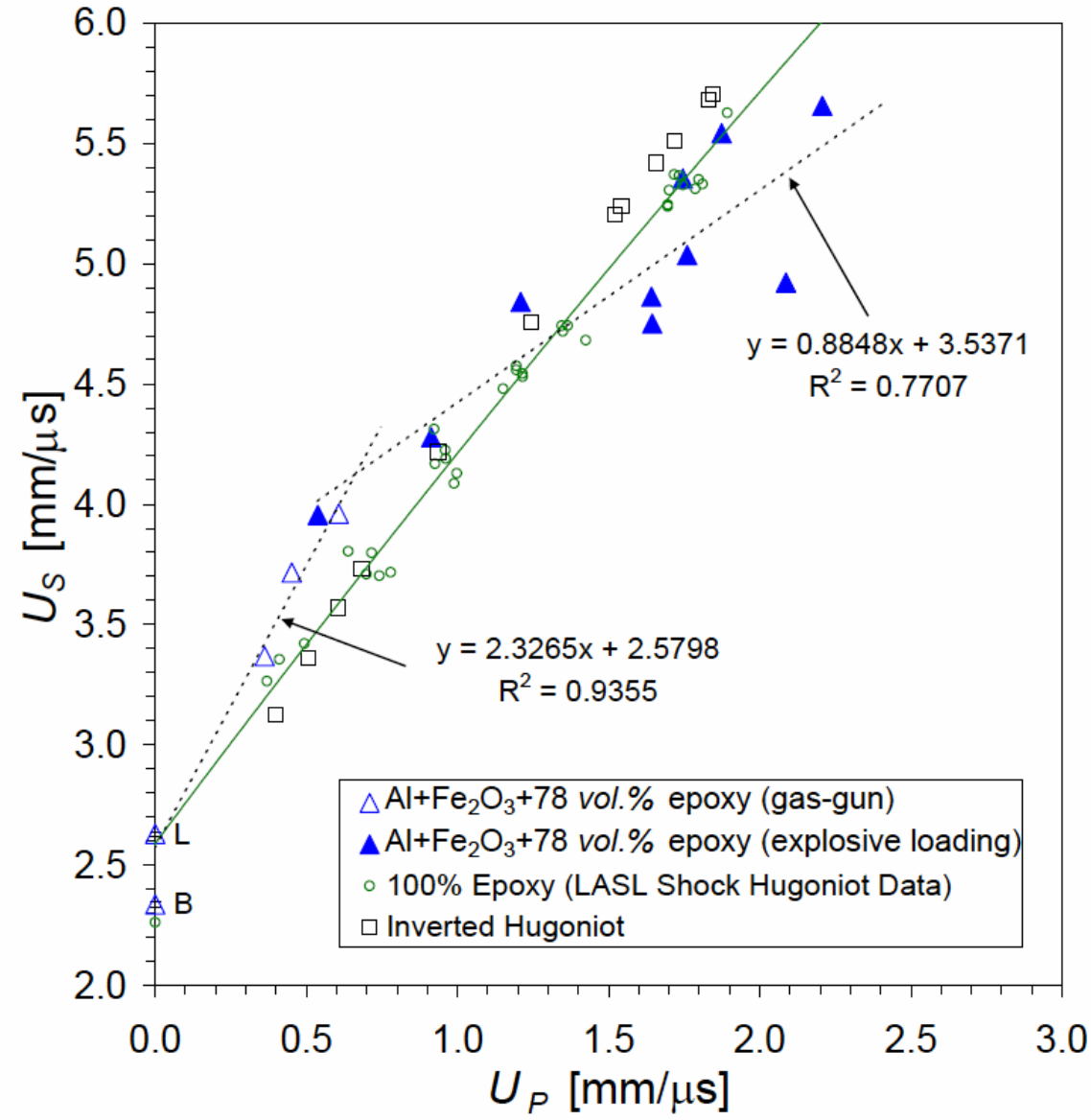


**Figure 4.111** Experimentally determined $U_S$-$U_P$ data points for Al+$Fe_2O_3$+78 *vol.%* epoxy composite are compared to theoretical inverted Hugoniot [212] values calculated for each experiment.

the material begins to yield, there should not be any volume change until fracture has occurred. However, decohesion of solid particles causes the volume to expand for the material system and is apparent above a critical impact stress of approximately 4 GPa.

In contrast, the 78 *vol.%* epoxy composite has less opportunity for solid particle decohesion from the binder matrix because of the composite's higher epoxy concentration and, therefore, less of an effect on the bulk material response. The damage within this composition does not offer much strengthening effect because of the relatively large distances between the solid particle inclusions. The damage can propagate through the composite without interaction with any of these particle inclusions. At higher stresses, the composite approaches pure epoxy behavior after reaching the same critical stress of 4 GPa observed for the 60 *vol.%* epoxy composite. It is expected that the 60 *vol.%* epoxy composite will approach the pure epoxy response in a similar manner at a significantly higher impact stresses.

# CHAPTER V

# ANALYSIS OF KEY ISSUES

Thermite mixtures undergoing oxidation-reduction reactions provide an opportunity of dual-functionality if these can also be processed as structural materials. The desire was to fabricate a material which possesses a highly reactive component that can be integrated within a binder to develop a material that has combined structural strength and enhanced chemical reactivity.

The intimate mixing of fuel and oxidizer is an essential condition for initiation and self-sustaining metal-oxide type reactive materials. Promoting the conditions necessary for reaction initiation by altering the microstructure and morphology of reactive constituents is essential. Specific microstructural features were examined for determining the degree of constituent fuel and oxide particle premixing within the epoxy matrix and additionally characterizing the effect epoxy and void concentrations have on mechanochemical reactions and strengthening. The degree of mixing had consequences on many scales, from nanometric mixing of individual particles to macroscopic mixing of fuel and oxidizer agglomerates.

The experimental and theoretical work conducted in this study provides a general design for the development and characterization of particle-filled energetic composite material systems. The work is intended to present insight into the fabrication, testing and

validation of structural energetic material behavior when subjected to high stress, strain, and strain rates and also to identify parameters that can be tuned for specific applications. This work provides a framework for conducting such a study and focuses on the most important parameters and variables influencing both structural/mechanical and chemical properties.

The following sections highlight the most useful and significant results presented in this study. These results are based on the characterization of intrinsic properties and their correlation with *i*) structural/mechanical material responses observed from static and dynamic loading conditions, *ii*) dynamic mechanochemical reactivity, and *iii*) shock-compression damage and strengthening effects.

## 5.1 Intrinsic Property Characterization of Epoxy-Cast Composites

The intrinsic properties of Al+$Fe_2O_3$ epoxy-cast composite materials were thoroughly examined for each fabricated composition. These include physical properties such as density and porosity, as well as, configurational features evolving from the cast-cure fabrication process, such as reactants' particle size distributions and microstructural morphologies. The composite's intrinsic properties are evaluated and later coupled with structural/mechanical and chemical material behaviors observed from dynamic impact loading experiments. These effects were mainly evaluated based on the volumetric mixture distribution of epoxy and the use of nano- versus micron-scale aluminum particles within the composites.

All of the fabricated compositions exhibited some degree of particle agglomeration, particularly observed for the fine hematite particles. Typically, each composition had hematite particle agglomerates with size classes characterized as fine (≤ 1 μm, typically individual particles), medium (5 to 10 μm), and large (20 to 50 μm). However, their distribution and frequency varied according to the volume fraction of epoxy. In general, quantitative optical microscopy revealed that the size of particle agglomerates increased as epoxy concentration decreased. This is directly attributed to the difficulty associated with mixing higher solid particle fraction composites that raise the mixture's viscosity. In contrast, the frequency or number of these features generally decreased as the volume fraction of epoxy also decreased. This effect was attributed to the increased interaction that particles have with each other during mixing, which causes the agglomerates to separate as the volume fraction of solid particles increases. However, the Al+$Fe_2O_3$+60 *vol.%* epoxy composition showed an exception to these trends, exhibiting slightly greater particle agglomerate sizes with significantly lower concentrations of these features as compared to the other fabricated composites. This particular composition appears to have particle and epoxy volume fractions that promote efficient mixing. While the other compositions showed a tendency for hematite particle agglomerates, micron-scale aluminum particles, and pores, to cluster in close proximity, the 60 *vol.%* epoxy composite tended to have less of these features which were relatively spread throughout the material volume, and thus, reduced the probability for introducing significantly large flaw sites within the bulk composite.

While the aluminum particles appeared to be uniformly dispersed throughout the epoxy matrix, the hematite particles displayed several degrees of particle agglomeration

ranging in size and frequency for each composition. The agglomeration of hematite particles were representative of tightly distributed individual hematite particles within the epoxy matrix, which possibly influence the bulk structural/mechanical properties of the composites. Most composites did not appear to exhibit significant open porosity, which was influenced by the mixture viscosity and, thus, the ability to thoroughly combine the solid particles within the resin, and the subsequent degassing step used to remove trapped air bubbles. However, the Al+$Fe_2O_3$+47 *vol.%* epoxy, containing the lowest volume fraction of epoxy, was particularly challenging to fabricate and exhibited relatively significant levels of open porosity of approximately 4.52 %. Average pore sizes showed a dependency on epoxy concentration, which increased as the volume fraction of epoxy decreased. The remaining compositions typically contained a few percent or less porosity, with a maximum value of 2.57 % for 70 *vol.%* epoxy composite.

As the particle sizes become significantly smaller, the bulk surface area significantly increases raising the viscosity for the mixture and making the mixing even more difficult. For compositions containing submicron-scale hematite and nano-scale aluminum powders, the lowest volume fraction of epoxy that could be fabricated was 70 *vol.%.* The addition of nano-scale aluminum particles produced unique microstructures that exhibited regions containing high concentrations of nano-scale aluminum particles or agglomerates. As similarly observed for the hematite agglomerates, the nano-aluminum agglomerates consist of individual tightly packed particles completely encapsulated in the epoxy matrix with no open porosity. The nano-aluminum agglomerates were significantly larger than the hematite agglomerates, and varied in size, ranging between 50 and over 200 μm in diameter. While the

formation of hematite agglomerates appear to occur during the dry mixing of the constituent powders, the nano-aluminum agglomerates appear to form during the wet mixing process after their addition to the epoxy resin. This was evident from microstructural observations illustrating a "turbulent" shape, which contained layered or swirling particle bands as illustrated earlier in Figure 4.10(*a-c*) and Figure 4.11(*a,b*). The microstructures also illustrate the formation of nano-aluminum agglomerates developed during premixing of constituent powders around hematite agglomerates.

## 5.2 Static Structural/Mechanical Behavior

The structural/mechanical behavior of epoxy-cast Al+$Fe_2O_3$ composites was examined using quasistatic or relatively low-strain rate loading experiments. These included dynamic mechanical analysis (DMA), continuous ball indentation, quasistatic compression, three-point flexural bend, and Charpy impact experiments. These tests were used to evaluate the relative behavior between each composition while altering the addition of epoxy volume fraction to the micron-scale aluminum and submicron-scale hematite powder mixtures.

It is well known that adding filler or reinforcement phases to a polymer increases the overall elastic modulus of the bulk composite. The addition of solid particles to the epoxy matrix typically improved the elastic loading region observed from the measured stress-strain behaviors for the epoxy-cast Al+$Fe_2O_3$ composites. The stress-strain curves were obtained from a number of testing techniques that included continuous ball indentation, quasistatic compression, and flexural three-point bend tests, each of which

showed fairly good agreement for each composition as illustrated in Table 5.1. The minor differences between these measurements are attributed to the significantly different loading conditions subjected to the specimen. While the continuous indentation test measures mechanical properties within extremely small material volumes at the microscopic and submicron scales, the compression tests give a bulk material response as does the flexural three-point bend tests. Therefore, the elastic moduli values listed in Table 5.1 for the continuous indentation tests include only indents that were within uniformly distributed phase regions of the composite. Indents that were in hematite rich regions, for example, gave significantly high elastic modulus values, which are not included. However, the 70 *vol.%* epoxy composite contained a significantly large number of hematite agglomerates, and avoiding hematite rich regions was impossible. This results in a slightly higher elastic modulus value for this composition as compared to the other testing techniques. In general, however, the flexural three-point bend tests had the greatest measured values of the different testing techniques, followed by compression

**Table 5.1** Comparison of elastic modulus measurements (GPa units) obtained from DMA, continuous ball indentation, quasistatic compression, and flexural (three-point bend) tests. These measurements are also compared to elastic values calculated from ultrasonic wave speed measurements.

| Epoxy [*vol.%*] | Ultrasonic (section 4.1.2) | DMA (section 4.3.1) | Indentation (section 4.3.2) | Compression (section 4.3.3) | Flexural (section 4.3.3) |
|---|---|---|---|---|---|
| 47 | 14.99 ± 0.28 | 8.22 ± 0.62 | 10.84 ± 0.73 | 11.83 ± 0.13 | 12.77 ± 0.18 |
| 60 | 11.55 ± 0.20 | 26.62 ± 14.56 | 9.43 ± 0.66 | 10.67 ± 0.18 | 12.48 ± 0.42 |
| 70 | 9.36 ± 0.22 | 8.24 ± 1.71 | 7.95 ± 0.18 | 7.30 ± 0.29 | 8.29 ± 0.57 |
| 78 | 5.63 ± 0.07 | 4.34 ± 0.43 | 5.04 ± 0.40 | 6.60 ± 0.13 | 6.84 ± 0.29 |
| 100 | 3.35 ± 0.04 | 2.63 ± 0.70 | 3.57 ± 0.50 | 3.98 ± 0.02 | 3.92 ± 0.03 |

tests and continuous indentation tests.

The measured elastic moduli for each composition also showed fairly good agreement with values calculated from ultrasonic elastic wave speed measurements that are listed in Table 5.1. However, the ultrasonic elastic moduli values tended to be 3.1, 8.8, and 11.9 % greater for average values (from continuous indentation, compression, and three-point bend tests) obtained for the 60, 70, and 47 *vol.%* epoxy composites, respectively, while the 78 *vol.%* epoxy composite and pure epoxy were 4.5 and 6.6 % less, respectively. Table 5.1 also lists elastic moduli values obtained from DMA experiments for each composition. These values show fairly good agreement with the other measurements and ultrasonic values obtained for the 70 and 78 *vol.%* epoxy composites and pure epoxy, however, the 47 and 60 *vol.%* epoxy composites show relatively poor agreement. While the relatively low elastic modulus of 8.2 GPa measured for the 47 *vol.%* epoxy is attributed to the high concentration of pores exhibited by this composition, the response for the 60 *vol.%* epoxy composite is more complicated. The 60 *vol.%* epoxy composite exhibits a significantly high elastic modulus of 26.6 GPa for the glassy response (temperatures below $T_g$) and a relatively low modulus of 77.0 MPa for the rubbery response (temperatures above $T_g$). These contrasting behaviors are attributed to solid micron-scale aluminum particles possibly inhibiting the epoxy crosslinking during polymerization. These relatively large inclusion features dominate the deformation response in the glass region by transferring the load from the matrix to the inclusions. However, as the temperature increases above the glass transition, $T_g$, the composite's response is dominated by molecular chain motions that are not inhibited by the relatively large aluminum inclusions. Furthermore, the quantitative microstructural

analysis for this composite shows a relatively low concentration of hematite agglomerates that are thought to significantly contribute to resisting molecular chain motions and thus raise the rubbery modulus of the composite.

While the elastic moduli increased with decreasing epoxy concentration fairly consistently, the apparent yield stresses for each composition were less obvious and somewhat scattered. However, the results generally indicate the importance of reducing the concentration of porosity for improving the bulk mechanical properties of the composite. The different testing techniques illustrate the relative sensitivity of the measured yield strength values with porosity concentration as shown in Table 5.2. While the 60 *vol.%* epoxy composite had the greatest yield stress from continuous indentation and compression tests, the pure epoxy showed the greatest yield stress from the flexural three-point bend tests. The continuous indentation tests are only slightly influenced by the porosity concentration because the indented material volume is relatively pore free, however, the flexural three-point bend tests are significantly influenced by pores and the relative pore size. While the 47 *vol.%* epoxy composite had the greatest porosity of

**Table 5.2** Comparison of yield stress measurements (MPa units) obtained from continuous ball indentation, quasistatic compression, and flexural (three-point bend) tests.

| Epoxy [*vol.%*] | Indentation (section 4.3.2) | Compression (section 4.3.3) | Flexural (section 4.3.3) | Porosity [%] |
|---|---|---|---|---|
| 47 | 194.81 ± 10.04 | 97.40 ± 1.71 | 95.93 ± 1.19 | 4.5 |
| 60 | 196.64 ± 14.21 | 141.44 ± 2.27 | 98.14 ± 10.45 | 1.6 |
| 70 | 153.70 ± 13.27 | 115.88 ± 2.39 | 100.93 ± 5.42 | 2.6 |
| 78 | 143.93 ± 18.36 | 128.69 ± 2.56 | *69.19 ± 20.25 | 1.6 |
| 100 | 128.51 ± 13.63 | 133.96 ± 0.38 | 122.33 ± 2.43 | 0.1 |

*Porosity for this particular batch of material was slightly higher, with a value of approximately 2 % and unusually large pores.

4.5 %, the particular batch of material used from the flexural three-point bend test for the 78 *vol.%* epoxy composition has a slightly higher porosity of approximately 2 %, compared to the material used for the other testing techniques for this composition, but had significantly large pores that were observable from fracture surface images. Because the load contact is concentrated to a single location of the test specimen, the size of the flaws or pores will significantly influence its strength and resistance to failure.

The failure of a material is associated with the concentration of stresses in the vicinity of flaws. The addition of rigid particles to a relatively brittle polymeric matrix significantly affects fracture toughness and shows an increasing value as the filler volume fraction increases. It is also convenient to classify materials in terms of a toughness/strength ratio ($K_{IC}$ /$\sigma_f$) rather than merely toughness or strength alone. This provides a gradual ranking for the particle-filled epoxy-cast composites evaluated in this study. The pure epoxy exhibited a relatively brittle behavior, while the addition of solid particles to the epoxy matrix lessens the brittleness. However, the 60 *vol.%* epoxy composite showed the highest ductility of the particle-filled composites, followed closely by the 78 *vol.%* epoxy composite.

The influence of flaw sizes on mechanical properties was evaluated using Charpy impact experiments. Charpy impact experiments measure the epoxy-cast composite's resistance to fracture. Although the measured impact resistances obtained for each of the Al+$Fe_2O_3$ epoxy-cast composites showed relatively little variation with the addition of solid particles, there was a slight improvement as the volume fraction of solid particles increased. Examination of the fracture surfaces indicates these specimens typically exhibited mostly brittle fracture. However, the pure epoxy specimens had a significantly

higher average impact resistance, which is attributed to a considerable amount of ductile fracture that occurs towards the later stages of failure. The examination of fracture surfaces for pure epoxy indicate that ductile yielding and possibly thermal softening may have occurred towards the latter stages of the fracture advancement, also contributing to a greater resistance to fracture.

The introduction of solid particles to the polymer matrix effectively introduces flaws, and their sizes depend on the individual particle sizes and their distribution throughout the epoxy matrix. The inherent critical flaw size was evaluated for each composition by calculating the failure stress, which is related to fracture toughness (obtained from Charpy impacts) according to the Griffith criterion [194]. The critical flaw sizes for each composition had a relatively broad range between 9 and 30 μm, and followed in order according to epoxy concentration, with pure epoxy having the smallest and the 47 *vol.%* epoxy composition having the largest. However, the 78 *vol.%* epoxy composite exhibited a slightly greater critical flaw size of 29.3 μm than the 47 *vol.%* epoxy composite, with a critical flaw size of 28.8 μm, because of the abnormally high inherent porosity observed for this particular batch of material.

## 5.3 High-Strain Rate Structural/Mechanical Behavior

High-strain rate reverse Taylor anvil impact experiments were conducted on epoxy-cast Al+$Fe_2O_3$ composites containing nano- and micron-scale aluminum as well as pure epoxy specimens. A limited number of experiments were conducted for each composition examined, however, based on the quasistatic mechanical property

evaluation, a majority of these experiments were conducted on the 60 *vol.%* epoxy composite and the pure epoxy specimens, in addition to the nano-aluminum containing composition with 70 *vol.%* epoxy.

High-speed camera images were used to make quantitative measurements of axial length and diameter changes observed for select times throughout the deformation process. From these measurements, incremental axial and areal strains (at the impact face) were calculated to give a quantitative measure of the deformation experienced during the impact. The detailed analysis of the images also captured two distinctive deformation behaviors. Specimens that have porosity levels above 1 % exhibited a characteristic "double-frustum" deformation shape. This type of deformation typically exceeded a critical axial strain that led to fracture at significantly higher strains. However, specimens which possess less than 1 % porosity have significantly less radial deformation and typically show an "extended-mushroom" deformation shape. This type of deformation promotes the absorption of impact energy along the axial length of the specimen and no fracture initiation was observed over the 100 to 150 μs time period examined for specimens exhibiting this type of deformation.

Quantitative measurements reveal that specimens undergo significant elastic and plastic deformation during both the loading and unloading stages of dynamic impact experiments. The elastic recovery is observed to occur very rapidly and begins within tens of microseconds after impact depending on impact velocity. Additionally, over 50% elastic recovery from peak axial strain is observed regardless of impact velocity or composition. Epoxy-cast composite compositions with dispersed $Al+Fe_2O_3$ powders typically fractured when exceeding a critical areal strain of 30 %. However, pure epoxy

showed a higher critical areal strain of 40 % before fracture initiation was observed. Pure epoxy undergoes thermal softening at strains below this critical fracture strain and, therefore, is in a rubbery state that has a more compliant deformation behavior. In contrast, the particle-filled composites undergo thermal softening at strains above 30 %, which leads to significantly large areal strains and ultimately fracture.

Dynamic yield stress and strain values were estimated using a one-dimensional linear-elastic perfectly-plastic wave propagation analysis developed by Hutchings [98]. Nominal and true stress-strain curves were constructed for each composition, and the analysis was successfully used to permit the relative comparison of each composition's performance. The nano-Al+$Fe_2O_3$+70 *vol.%* epoxy is the most resilient composition and capable of absorbing more energy during elastic deformation. Calculated values of the area under the linear-elastic region of true stress-strain curves show that the nano-aluminum containing composite has a resilience modulus over two times that of micron-aluminum composite and pure epoxy. Pure epoxy and micron-aluminum composite have comparable values of resilience, and the addition of micron-scale aluminum particles to epoxy does not appear to offer any significant benefit. This behavior is also evident in the critical impact velocity measurement, which shows that the nano-aluminum composite is able to absorb higher energy impacts through the greater resistance to plastic deformation and/or failure. The introduction of a higher volume fraction of epoxy should reduce the dynamic yield strength and strain. However, for the nano-aluminum composition, there is a significant increase in dynamic yield strength and strain compared to pure epoxy. These results illustrate that the addition of nano-scale

aluminum particles provide significant enhancement to the strength of the epoxy composite.

The analysis also allowed the calculation of the speeds of the elastic and plastic waves that propagate through the material. From this, detailed *x-t* diagrams can be constructed to show the elastic-plastic wave interactions occurring during these experiments. The position-time diagrams show that the plastic wave significantly slows upon interacting with the elastic wave, which, in some cases does not completely dissipate, and takes over the plastic wave upon their second interaction. Measurements of the axial strained length obtained from high-speed camera images were used to validate the position of the plastic wave, which showed good correlation with calculated results. Additionally, VISAR was used to substantiate the arrival times of the elastic wave at the free surface and the elastic/plastic interface, which was observed to have excellent correlation with the timing in *x-t* diagrams.

In addition, high-speed camera images time synchronized with VISAR measurements were used to capture the elastic and plastic wave interactions as well as show that the beginning of elastic recovery coincides with peak axial strain and the interaction of the reflected elastic tensile wave with the compressive plastic wave. In cases where the specimen fractures, there was a clear indication apparent in the VISAR signal which matches fracture initiation times observed from high-speed camera images.

The results illustrate that reverse Taylor impact experiments combining the use of high-speed camera images and velocity interferometry measurements provide a detailed view of the general wave structure within the material upon impact. The calculations obtained from the one-dimensional elastic-plastic wave analysis give a complete

description of the stress-strain behavior for particle-reinforced polymeric materials and pure epoxy.

### 5.4 Mechanochemical Reactivity

Exposing material systems to the combination of high pressure, shear, and assorted strain rates can lead to mechanochemical reactions. There are several key parameters that must collaborate to induce the mechanochemical reaction initiation in reactive metal-oxide powder mixtures. Material parameters such as particle size and morphology are important for the efficient mixing of reactants during deformation, while the viscoplastic deformation behavior observed for the epoxy matrix also contributes to the reactant mixing. Likewise, the complex stress states, strain rates, and their duration are furthermore important aspects that must be considered.

Post-mortem analysis of recovered anvil plates from reverse Taylor impact experiments showed evidence of strain-induced mechanochemical reactions. The recovered anvils had distinct dark colored footprints remaining on the impact surface. These markings were observed for the highest velocity experiment conducted for the 60 *vol.%* epoxy composition and two of the highest velocity experiments conducted for the nano-70 *vol.%* epoxy composite. In all cases, the markings consisted of a dark ring shape with evidence of radial fracture marks or petals. The petal shapes indicate the reaction initiation occurs some time before the radial fracture, and the reaction possibly continues after the specimen begins to fracture. High-speed camera images indicate the radial fracture occurs at strains close to approximately 70 %, while the strain associated

with the remaining footprint diameter was approximately 50 %. The time-synchronized areal strains measured from the high-speed camera images indicate that the possible reaction duration or the associated time between these two strain regimes was only a few microseconds for the 60 *vol.%* epoxy composite, while approximately 10 μs for the nano-70 *vol.%* epoxy composites. This effect may be related to the significantly higher impact velocity used for the 60 *vol.%* epoxy composition, and therefore higher associated strain rates. However, it illustrates that these reactions can proceed or initiate over relatively short or long time durations. This leads to the notion that the actual wave propagating within the material does not cause the reaction (shock-induced type of reaction), but rather, the high-shear and the complex strain state (strain-induced reaction initiation) is mostly attributed to the local chemical reactivity.

Post-mortem SEM analysis of the footprint regions showed evidence of localized melting and re-solidification in addition to regions with no reaction, which contained mostly hematite particles. The reaction products were identified using EDS and the most probable products from considering the concentration of elemental species present. Localized reaction sites had products that correspond to $Al_2O_3$ and pure Fe, in addition to an iron-alumina compound, $FeAl_2O_4$. Identified sites also showed regions where intermediate reaction products, such as $AlFe_3$ and $Fe_{1-x}O$, were observed.

The reaction products were correlated with thermal analysis experiments conducted using DTA and *in situ* high temperature x-ray diffraction (HTXRD) measurements. Chemical reactivity was validated by first studying the reaction products that form during heating at atmospheric pressures within an inert atmosphere. This was accomplished by conducting a series of DTA studies, where exothermic and endothermic

peaks were observed during constant heating rate experiments. These tests were then evaluated based on previous knowledge of the classic $Al+Fe_2O_3$ thermite reaction from phase diagrams and specific studies that focused on the reaction steps and mechanisms taking place. Exothermic and endothermic peaks obtained from the DTA studies were complimented by HTXRD scans used to identify each of the chemical species that formed during heating. This gave quantitative information for the epoxy-cast thermite composites regarding the phase formation and the resulting products.

The reaction products identified by HTXRD and indicated by DTA were similar to those identified from post-mortem investigation of the recovered anvils. The good correlation between the different experimental techniques gives confidence in the calculated reaction products obtained from the elemental species identified by EDS. The results showed the strong possibility of many of the same phases forming during high-velocity impacts as those identified from thermal analysis. However, this type of study does not indicate the kinetics involved in the reactions. The assumption is that the strain-induced reactions occur after the passage of the disturbance wave because they require time for thermal diffusion to occur.

The diameters of the footprint also allow the estimation of localized heating due to plastic work. The bulk temperature rise associated with the plastic deformation was typically above 80 °C for all three experiments, well above the thermal softening temperature identified from DMA experiments for the 60 *vol.%* epoxy composition. However, the temperature rise associated with plastic work for the nano-70 *vol.%* epoxy composites (84.19 °C and 83.00 °C) was only slightly above the measured glass transition temperature of 81.50 °C. It is possible that thermal softening triggered a series

of subsequent events leading to extensive strains and consequent reaction. While the calculated bulk temperature was lower than the threshold temperature for reaction between Al+$Fe_2O_3$ or epoxy decomposition, identified by DTA to be approximately 700 and 400 °C, respectively, it was certainly significantly higher than the $T_g$ measured for pure epoxy (57.92 °C). The bulk temperature rise may also be significantly lower than the temperature rise associated with the aluminum and hematite particle interactions achieving submicron-level mixing and, thus providing the driving mechanism for ultra fast chemical reactions during dynamic impact loading conditions. However, the thermal softening behavior of the epoxy binder enabled this particle-particle interaction and, therefore, is an important component of the strain-induced reaction initiation mechanism for structural energetic composites.

The footprint remaining for the 60 *vol.%* epoxy composite was much darker than observed for the nano-70 *vol.%* epoxy composite, qualitatively indicating different extent of reaction. This may be attributed to the significantly higher impact velocity used for the 60 *vol.%* epoxy composition. Further comparison of the nano-70 *vol.%* and 60 *vol.%* epoxy footprints shows that they all correspond to a strain of approximately 50%. It is difficult to conclude when the reaction took place with certainty. One possible scenario is that the reaction takes place at lower strain levels than identified by the footprint marking and proceeds to react as the footprint becomes larger. The footprint possibly identified the final moments of the reaction and the earliest moments of radial fracture. This led to catastrophic fracture, which caused the applied stress to drop significant and possibly conclude the reaction.

Many lower velocity experiments showed that upon impact, the specimens fracture and the fragments have secondary impacts with the anvil. However, these experiments did not show any evidence of mechanochemical initiated reactions for these secondary locations. The reactants need to be in intimate contact for the reaction to proceed. The post-mortem analysis of the recovered anvils shows that the dark colored footprints also had regions where material remained from secondary impacts. These locations also showed no evidence of mechanochemical reaction initiation. This further verifies that the significant viscoplastic deformation of the epoxy matrix is important for strain-induced reactions to take place.

The correlation of microstructural features and the compressibility behavior show that it is important to have a composite with relatively small inclusion particles that are uniformly dispersed throughout the matrix in order to optimize mechanical properties. However, it is also important for chemical reactively purposes, that there are a sufficient volume fraction of these reactant particles in close proximity to each other for causing chemical reactions upon impact and to sustain these reactions until the reactants are consumed.

## 5.5 Shock-Compression Damage and Strengthening Effects

The shock Hugoniot of polymers is known to exhibit a non-linear $U_S$-$U_P$ relationship at relatively low pressures and commonly displays a concave curvature with an initially rapid shock velocity. However, the experimentally measured shock Hugoniot obtained for Al+$Fe_2O_3$ particle-reinforced composites shows an opposite effect

displaying a convex curvature with an initially rapid particle velocity. Transformation to pressure-volume space shows an initial expansion that is not related to a low-pressure phase change or reaction. In contrast, the volume expansion is connected to damage associated with decohesion of solid particles from the polymer matrix. Equation of state experiments conducted for epoxy-cast Al+$Fe_2O_3$ composites show deviation from ideal Hugoniot behavior as a result of damage evolving at a critical impact stress. These experiments were conducted for the epoxy-cast Al+$Fe_2O_3$ composites with 60 and 78 *vol.%* epoxy. Two compositions prepared with significantly different volume fractions of the binder phase show damage occurring at approximately the same critical impact stress. The Birch-Murnaghan equation of state (BM-EOS) was used to characterize the composite's compressibility and identify the magnitude of the critical damage stress. Additionally, experimentally determined material behavior was correlated with hydrodynamic calculations for evaluating the measured Hugoniot behavior.

Comparison of embedded PVDF stress gauge measurements with one-dimensional CTH code simulations initially show excellent agreement with experimental stress waveform histories, but overestimate as the input stress increases past a critical limit above which damage occurs. The code currently does not account for damage in the epoxy-cast composite during shock loading. The stress overestimation for the hydrodynamic calculations also corresponds to overestimation by similar magnitudes for the particle velocity behind the shock front, which was compared to directly measured values using VISAR. The inverse Hugoniot, which is the theoretically determined pressure-volume compressibility response based on the weighted volumes for the constituent Hugoniots, along with fitting the compressibility behavior using the BM-EOS

for the damaged and undamaged material responses, both quantitatively identify the damage initiation stress threshold.

The experimental measured $U_S$-$U_P$ Hugoniot response illustrates an initially similar behavior for both the particle-filled composites and pure epoxy, which gradually deviate at particle velocities above approximately 450 m/s. Further increase in $U_P$ shows a significant deviation between the two composites at approximately 550 m/s, with the higher 78 *vol.%* epoxy containing composition exhibiting a sharp transition that approaches pure epoxy behavior. These contrasting behaviors are related to various degrees of damage nucleating at inclusion sites within the epoxy matrix as pressure increases. The damage initially provides a bulk toughening effect that alters the composite's Hugoniot behavior until significant bulk failure occurs. This effect is illustrated by the 78 *vol.%* epoxy $U_S$-$U_P$ curve initially approaching and then falling below pure epoxy behavior at higher $U_P$ values.

The BM-EOS was used to account for the altered Hugoniot response and quantitatively characterize the resulting damage. The experimentally measured $U_S$-$U_P$ Hugoniot data was transformed into pressure-volume space using the jump conditions and fit using the BM-EOS in terms of normalized stress and finite Eulerian strain. The $U_S$-$U_P$ Hugoniot curves indicate that the responses of the composites are altered at a critical $U_S$ and $U_P$ value. Therefore, the normalized stress-Eulerian strain curves were divided in order to evaluate the damaged and undamaged compressibility of each composition. The damaged and undamaged response curves for the 78 *vol.%* epoxy composite showed widely different behaviors; having positive and negative slopes, respectively. Although less apparent, the 60 *vol.%* epoxy composition behaviors are also

divided. The justification becomes more evident when trying to calculate $K_0$ from a curve fit to all the data, which results in an unrealistic value that is close to zero or negative. However, the values obtained from the intercepts of the undamaged response curves agree well with values calculated from ultrasonic measurements for both compositions. The BM-EOS was applied to the experimental data by fitting the damaged and undamaged material responses to generate $P$-$V/V_0$ compressibility curves. The undamaged responses for both compositions overlap and show excellent agreement with the experimental data at pressures below approximately 4 GPa. The experimental data and the BM-EOS fit for the undamaged response also correspond well with the theoretically obtained inverse Hugoniot for the 60 *vol.%* epoxy composition. However, the 78 *vol.%* epoxy composite shows a rather significant deviation and appears to follow the observed behavior for the 60 *vol.%* epoxy composite at pressures below 4 GPa. The discrepancy between the experimental and theoretical values for the 78 *vol.%* epoxy composite could possibly be associated with the specimens exhibiting damage initially, below pressures examined in this current work. This causes bulk volume expansions due to the particle decohesion with the matrix and possibly introduces a strengthening mechanism below 4 GPa. While the 60 *vol.%* epoxy composite shows strengthening at a critical pressure close to 4 GPa, the 78 *vol.%* epoxy composite possibly shows initial strengthening followed by significant damage at this same critical pressure.

As the pressure increases, the 60 *vol.%* epoxy composition shows a volume expansion that is related to decohesion of inclusion particles from the epoxy matrix and causes the bulk compressibility to increase. These higher pressure values show good agreement with the damaged material curve obtained from the BM-EOS. In contrast, the

78 *vol.%* epoxy composition approaches the pure epoxy response beginning at 4 GPa. It is apparent that the loading in this composition is carried almost completely by the binder material and the solid particle inclusions provide stress concentration sites that permit the nucleation of unobstructed crack growth and propagation due mainly to the compositional makeup.

### 5.6 Influence of Reactant Particle Size and Epoxy Volume Fraction

The addition of solid particles to an epoxy matrix significantly influences the structural/mechanical behavior and chemical reactivity of the bulk composite. In the present study, the composite's behavior has been altered by changing two main processing parameters; the reactants' particle size and the relative volume fraction of the epoxy matrix. These modifications ultimately alter the distribution and uniformity of reactant particle features throughout the material volume, which affects both the structural strength and chemical reactivity.

The mechanical behavior of epoxy-cast Al+$Fe_2O_3$ composites as a function of the influence of epoxy volume fraction has been evaluated for a variety of loading conditions and a broad range of strain rates, which include quasistatic loading experiments ($10^{-4}$ to $10^{-2}$ 1/s), medium-strain rate Charpy and Taylor impacts ($10^{3}$ to $10^{4}$ 1/s), and high-strain rate parallel-plate impact experiments ($10^{5}$ to $10^{6}$ 1/s). In general, structural strength and toughness were observed to improve as the volume fraction of epoxy decreases, regardless of the loading strain rate regime explored. However, the influence of microstructural aspects, such as particle distribution and porosity, has significant effect

on the bulk mechanical behavior. This is particularly observable for experiments that are very sensitive to porosity, such as flexural (three-point bend) tests and Charpy impacts. For these experiments, the largest flaw present in the composition, which may be a cluster of micron-scale aluminum particles or pores, significantly influences the bulk material behavior. High-strain rate Taylor impact experiments were even more sensitive to porosity, showing significantly different deformation behaviors for composites containing more than 1 % porosity that led to eventual failure.

For relatively low-strain rate experiments, the elastic modulus was observed to increase as the volume fraction of epoxy decreased. However, the influence of epoxy (or solid filler particle quantities) was less significant in altering the yield stress magnitudes, which were observed to be relatively similar for each composite. The primary toughening mechanism for low-strain rate loading of particle-filled composites has been associated with the debonding of the inclusion particles from the matrix [53]. The addition of solid particles to the epoxy matrix influences the composite's yielding behavior when debonding occurs prior to reaching the yield strain of the epoxy matrix, and thus, changes the stress state within the matrix material. This effect was apparent from quasistatic compression and flexural bend tests, illustrating an increasing yield strain as the epoxy concentration increases. The influence of the inclusion volume fraction was also apparent after yielding, which manifests as an increasing strain hardening effect associated with the decreasing volume fraction of epoxy. However, the yield stress was fairly similar for each composition, with exception of the lowest epoxy containing composite (47 *vol.%* epoxy) that was influenced by a relatively high concentration of pores. The similar yielding magnitudes suggest that the debonding of

inclusion particles from the matrix is unaltered by particle size and morphology differences and the variation of epoxy volume fraction observed for each composition. Furthermore, the relatively high concentration of submicron hematite particles present in each composite may initially control the yielding behavior, until significant debonding of the micron-scale aluminum particles occurs and creates fracture initiation sites.

The influence of particle size and morphology is also observed to be significant in altering the viscoelastic response of specimens subjected to Taylor impact experiments. While the addition of micron-scale aluminum particles to epoxy was observed to increase the dynamic yield stress, the dynamic yield strain was essentially the same for the particle-filled composite and pure epoxy. In contrast, the addition of nano-scale aluminum particles significantly increased the dynamic yield strain while providing only a slight improvement for the dynamic yield stress, when compared to the micron-scale aluminum composite. The influence of particle size and morphology was directly evaluated based on measurements of elastic resilience from the composite's dynamic stress-strain behaviors. The nano-aluminum containing composite exhibited over two times the resilience as observed for the micron-scale aluminum composite and pure epoxy. The significant elastic response is attributed to the introduction of nanoscale particles that provide physical entanglements which inhibit molecular polymer chain motions and improve the composite's impact resistance.

In addition to improved elastic properties, the use of nano-scale particles also contributes to inhibiting the propagation of cracks and the resistance to plastic deformation of the bulk composite. Microstructural observations of the impact faces from recovered specimens show that the nano-scale aluminum composite contains

significantly less damage as compared to the micron-scale composite. The damage is illustrated by multiple interparticle cracks propagating across the impact face, uninhibited by the micron-scale aluminum particles, and the formation of coalescing voids. In contrast, the nano-scale composite shows significantly less cracking on the impact face, which was inhibited by nano-scale aluminum agglomerate regions, with no evidence of void formation. Additionally, the critical impact velocity where plastic deformation was observed to initiate, illustrates the relative strength of these composites and the influence of nano- and micron-scale particle inclusions. Similarly, the nano-scale aluminum composite had the greatest resistance to plastic deformation and therefore the greatest strength of these composites. This is followed by pure epoxy and the 60 *vol.%* epoxy composite containing micron-scale aluminum particles. The influence of micron-scale particles becomes apparent through a lower resistance to plastic deformation by introducing large stress concentration sites that promote fracture initiation.

High-strain rate parallel-plate impact experiments were used to compare the response of 60 and 78 *vol.%* epoxy composites. Both composites experienced similar compressibility behaviors up to a critical impact stress of approximately 4 GPa. In the same regard, the distribution of aluminum and hematite particles and agglomerates significantly influences the composite's deformation and fracture behaviors. While the 60 *vol.%* epoxy composite shows initial strengthening, the 78 *vol.%* epoxy exhibits significantly low strengthening above the critical impact stress. The similar response of the two composites up to this point suggests that this critical stress is associated with the particle debonding behavior from the epoxy matrix. Similar to the lower strain rate experiments discussed previously, the influence of particle size and morphology does not

become apparent until the stress is significant enough to cause void formation near the particle and matrix interface. Additionally, the different compressibilities above the critical stress for the two composites may be associated with different crack diversion behaviors that partially absorb the impact energy. These differences manifest as crack deflections around closely packed particles which hamper the crack propagation. The 60 *vol.%* epoxy provides opportunities for crack deflection and additionally has a greater number of submicron hematite particles as compared to the 78 *vol.%* epoxy composite. Both of these factors contribute to the significant toughening effect observed above the critical impact stress for the 60 *vol.%* epoxy composite. The relatively spread out particle distribution for the 78 *vol.%* epoxy allows uninhibited crack propagation through the composite. Additionally, if the particles are contributing to crack propagation deflection, the relative size of the damage zone will be significantly larger due to the distance between the particles as compared to closer packed particle morphology observed for the 60 *vol.%* epoxy composite.

The distribution of particles and the epoxy matrix volume fraction also influences chemical reactivity. The recovery and post-mortem analysis for Taylor impact experiments have indicated evidence for strain-induced chemical reactions, which subject the composite to large shear conditions preceding the reaction. Chemical reactions were observed in composites that contain both micron and nano-scale aluminum particles for select high velocity impacts, which caused combined conditions of highly strained material that, are subsequently subjected to continued high stresses. The reactions were confined to specific locations that contained aluminum and hematite particles in close proximity to each other. Since the hematite particles were abundant, the distribution of

aluminum particles limited the locations where chemical reactions could take place. Although Taylor impact experiments showed evidence for chemical reaction initiation, these reactions were not sustained and are possibly rapidly quenched due to the relatively large distance between the reactants. Additionally, post-mortem analysis indicates that the epoxy matrix may hinder the sustainability of the reaction.

## 5.7 Significance and Impact of Research

Nano- and micro-scale aluminum and hematite powder mixtures combined with epoxy form a class of structural energetic materials that are capable of having both high-strength and enhanced chemical reactivity. Such reactive material systems are of significant interest because of their capability to release high heat content or energy with temperatures in excess of 3000°C, while remaining relatively insensitive to unintended initiation. The particular epoxy-cast metal-oxide mixture composite examined in this research was chosen as a model system for studying material strength at high-strain rates and the mechanochemical nature of strain-induced chemical reactions. Knowledge gained from this system can be applied to other thermite-based energetic material systems that are also highly reactive, such as Al+$MnO_2$, Al+$MoO_3$, or intermetallic-forming materials such as Ti+Si, Mo+Si, and Ni+Al, with and without the addition of polymeric binders. A key feature of reactive materials distributed within a polymer matrix, is their ability to release energy while additionally providing structural strength attributes.

### 5.7.1 Fabrication and Design of Structural Energetic Materials

The fabrication and design of structural energetic composites, which relies on the interaction of metal-oxide powder mixtures with the epoxy matrix and how their chemical and mechanical properties balance to provide structural integrity and energetics, require careful consideration. The ability to process these materials is of significant importance because processing dictates the composite's overall chemical and mechanical behavior and processing variables provide the ability to tune these behaviors. The challenge is to preserve the energetic characteristics of the metal-oxide powder mixture without sacrificing mechanical strength and vice versa. The results of the current study indicate an ideal composite should incorporate uniformly dispersed aluminum and hematite structural reinforcement particles that are within relatively close proximity for enhancing their intimate interaction and mixing for chemical reactivity. Furthermore, the composite's overall bulk behavior can be improved by considering the distribution, size, and shape of the reactant particles and avoiding the addition of particles that create significant stress concentration sites, which are detrimental to structural/mechanical strength.

The current study indicates that nano-scale reactant particles significantly improve mechanical behavior and can enhance chemical reactivity with their uniform distribution. The influence of particle size on structural strength has been demonstrated from Taylor impact experiments (discussed in section 4.4) by comparing the dynamic deformation behavior for epoxy-cast Al+$Fe_2O_3$ composites containing nano- and micron-scale aluminum particles. The results indicate that the nano-aluminum containing

composite exhibits significantly greater impact resistance and elastic resilience. The uniform dispersion of nano-scale particles is admittedly a challenging endeavor, however, the introduction of nano-scale particle agglomerates have been shown to improve the structural/mechanical behavior of the composites in the absence of significant porosity. These improvements are attributed to the nano-scale particles inhibiting molecular-scale polymer chain motions in the epoxy binder. Similarly, the submicron-scale hematite particles and agglomerates containing these closely-packed particles also possibly contribute to restricting polymer chain motions in a similar manner and, thus, improve overall bulk mechanical response. Similar strengthening effects for the nano-aluminum containing Al+$Fe_2O_3$+70 *vol.%* epoxy composite is observed in both the low-strain rate and high-strain rate regimes.

The introduction of nano-scale reactants additionally enhances the energy content by increasing the surface area, and effectively alters the reaction pathways. Post-mortem characterization of Taylor impact experiments indicate that these structural energetic composites undergo strain-induced mechanochemical reactions under specific impact conditions (discussed in section 4.4.6). The use of nano-scale reactants require an equal volumetric mixture of aluminum and hematite particles, to ensure the intimacy between the reactants and provide opportunities for intimate mixing throughout the material volume. Post-mortem characterization of specimens that have undergone strain-induced reactions show only localized chemical reactivity in regions that contain relatively larger scale micron aluminum particles in close contact with submicron hematite particles. The enhancement of chemical reactions for the composite mixtures require refinement of reactant particle distributions to introduce a significant number of local reaction initiation

sites that will additionally provide opportunities for sustained chemical reactivity throughout the composite.

While offering structural strength, the epoxy matrix effectively separates the individual reactant particles and provides a level of sensitivity that requires a specific mechanical stimulus to initiate chemical reactions. Unlike an explosive that contains the fuel and oxidizer components within a single molecule, thermite mixtures require the interaction of individual reactants for chemical reaction initiation. Mixing of these reactants is enhanced under specific loading conditions that cause significant mechanical work and introduce a temperature rise that causes thermal softening within the epoxy matrix. The associated adiabatic bulk temperature rise from the mechanical work of plastic deformation was significant enough to cause thermal softening (discussed in section 4.4.7), however, lower than the threshold temperature observed for the thermite reaction or decomposition of epoxy. The thermal softening triggers a series of subsequent events leading to extensive strains or deformation and consequent reaction. Thermal softening is an important component of the reaction mechanism in that it initiates a series of events culminating in the strain-induced chemical reaction initiation.

### 5.7.2 Damage Influence and Characterization

The introduction of solid micron-scale particles to the epoxy matrix effectively introduces flaws, and their sizes depend on the individual particle sizes and their distribution throughout the matrix phase. The tendency for solid particles to agglomerate may be sufficient to cause relatively large clusters of particles and significantly large flaw

sites. The failure of the epoxy-cast composites is associated with the concentration of stresses in the vicinity of these flaws or inclusion particles. The introduction of damage significantly alters the composite's response to dynamic loading and its bulk mechanical behavior. Additionally, damage may obstruct submicron-level reactant particle mixing that is thought to be the driving mechanism for mechanochemical reactions.

The influence of flaw sizes on mechanical properties was evaluated using Charpy impact experiments (discussed in section 4.3.4). The estimated critical flaw size that causes failure in the composite showed a dependence upon the volume fraction of solid particle additions. The critical flaw size increased and followed in order as the epoxy concentration decreased. It follows that as the epoxy concentration decreases, the number of solid particles increases and so does the tendency for particles to cluster.

High-strain rate impact experiments show a similar tendency towards structural/mechanical behavior with the introduction of solid inclusion particles. Taylor impact experiments were used to establish the influence of particle sizes by examining the extreme case of comparing the response of $Al+Fe_2O_3$ composites containing nano- and micron-scale aluminum particles (discussed in section 4.4.3). From a damage standpoint, the nano-aluminum containing composites showed significantly greater strengthening effects as compared to its micron-scale counterpart. The incorporation of nano-scale aluminum particles eliminates stress concentration sites and the formation of nano-scale particle agglomerates actually enhances their structural behavior and impact resistance for damage or failure. This result is contrary to the typical nanocomposites design goals for significantly enhancing structural strength of the bulk composite, which try to uniformly distribute nano-scale particles within the polymer matrix. Considerable

strengthening of nanocomposites can be realized for composites fabricated with nano-scale particle agglomerates, provided a relatively low porosity level is maintained.

Many energetic material systems including traditional explosives and new generation reactive thermite mixtures are dispersed within a polymeric binder. For the latter, the polymer binder holds the reinforcement phase (thermite powder mixture) in an arranged pattern that enhances transfer of the load among the individual particles. However, for relatively large volume fractions, the binder phase has a significant effect on the overall response of the composite.

In the present study, instrumented parallel-plate impact experiments were conducted on two types of epoxy-cast Al+$Fe_2O_3$ particle-filled composites prepared with 60 and 78 *vol.%* epoxy (discussed in section 4.5). These filled polymer composites show a non-linear $U_S$-$U_P$ Hugoniot behavior that has an altered response when compared to unfilled polymers. The altered Hugoniot behaviors emerge from the addition of local stresses applied to the rigid aluminum and hematite particles from compression of the compliant epoxy. It is proposed that these distinct behaviors are related to various degrees of damage nucleating at solid particle inclusion sites within the epoxy matrix. The damage initially provides a bulk toughening effect that alters the composite's Hugoniot behavior until significant bulk failure occurs. This effect is illustrated by the 78 *vol.%* epoxy $U_S$-$U_P$ curve initially approaching and then falling below pure epoxy behavior at higher $U_P$ values. It is also apparent that the loading is carried almost completely by the binder material and the solid particle inclusions provide stress concentration sites that permit the nucleation of unobstructed crack growth and propagation.

The observed bulk damage of the composites from time-resolved high-strain rate impact experiments have been characterized using the Birch-Murnaghan equation of state (BM-EOS) and hydrodynamic calculations. The BM-EOS was used to characterize this damage by fitting experimental data to curves that represent undamaged and damaged material behaviors. The experimentally measured $U_S$-$U_P$ Hugoniot data was transformed into pressure-volume ($P$-$V$) space using the jump conditions and fit using the BM-EOS in terms of normalized stress and finite eulerian strain. The comparison of both composites (60 and 78 *vol.%* epoxy) and pure epoxy allows the influence of particle-fill volume fraction on the altered Hugoniot response to be evaluated. The results illustrate an initially similar behavior for both particle-filled composites and pure epoxy within a relatively low impact stress range. However, as the impact stress increases past a critical limit, bulk damage alters the composites response.

The damage within the composite possibly manifests from decohesion of solid particles from the epoxy matrix. A similar response is observed from quasistatic compression tests (discussed in section 4.3.3), where changing the volume fraction of solid particles does not significantly influence the observed yield stress and possibly gives a measure of the cohesive strength between the solid particles and the epoxy matrix. The BM-EOS used to characterize the damaged material response indicates that the critical damage stress is approximately 4 GPa for both epoxy-cast composites. In a similar manner, the common critical stress observed from high-strain rate impact experiments is possibly related to decohesion of solid particles.

Comparison of embedded PVDF stress gauge measurements with one-dimensional CTH code simulations shows excellent agreement with experimental

stress histories up to a stress level below the damage threshold. However, the simulations overestimate the input stress past a critical limit above which damage occurs. The CTH strength model does not currently account for the evolution of damage, because of which, the associated overestimation of stress is observed. These results further illustrate that the composite's response is altered from the addition of solid particles to the polymer matrix and their influence on damage.

The high-strain rate impact experiments conducted in this study mainly characterize the overall bulk composite response to dynamic loading. Therefore, it is unclear how the damage is evolving at the particle-interface level. However, it is suggested that the damage occurs typically from decohesion of solid particles. The introduction of relatively rigid particles to a compliant epoxy matrix will have some type of damage associated with its response to dynamic loading at a specific stress level simply because of the significant contrasting bulk compressibility afforded by the different phases that comprise the composite. Similar behavior was also observed for quasistatic mechanical tests (compression and Charpy impact) and medium-strain rate (Taylor impact) experiments.

The use of micron-scale solid reactants introduce significant stress concentration sites that influence the overall bulk strength/mechanical behavior. In contrast, the agglomeration of submicron-scale hematite and nano-scale aluminum particles show improved strengthening effects by inhibiting polymer chain motions. The use of nano-scale constituent particles will alter the Hugoniot response even further and possibly offer significantly greater compressibility, while alleviating the introduction of

stress concentration sites. This in turn should be expected to improve the structural strength and the mixing of reactant particles for enhanced chemical reactivity.

# CHAPTER VI

# CONCLUDING REMARKS

The present investigation focuses on describing the principles underlying the deformation and fracture behavior, mechanochemical sensitivity and reaction response, and processing characteristics of epoxy-cast Al+$Fe_2O_3$ thermite composites. The mechanical response and reaction behavior are closely interlinked through the deformation characteristics of these composite materials. As such, it was important to identify and fully characterize the deformation mechanism of the epoxy-cast composites to further establish the influence that the various structural characteristics of the reactants have on the overall mechanical properties, as well as their connection to the nature of chemical reaction initiation. It was also desirable to establish the required stress and strain state or combination essential for initiating a chemical reaction in this material system.

The design and testing of energetic structural materials were performed by systematically altering the microstructure, morphology, and composition while observing the material response to dynamic loading denoted by chemical reactivity and mechanical strength. The following sections highlight the main conclusions and contributions obtained from this study, as well as suggestions for continued work that will serve

to improve upon the selection, design, and characterization of structural energetic material systems.

## 6.1 Conclusions

The research performed in the present investigation included the *i*) characterization of Al+$Fe_2O_3$ epoxy-cast composite's intrinsic properties and their correlation with structural/mechanical material responses observed from *ii*) static and *iii*) dynamic loading conditions, *iv*) dynamic mechanochemical reaction behavior, and *v*) shock-compression damage and strengthening effects. The main conclusions include:

*i)* The mixing of Al+$Fe_2O_3$ reactant powders and their dispersion within an epoxy matrix influences the composite's overall microstructural features and the bulk structural/mechanical and chemical behavior. These behaviors are closely interlinked through characteristics of deformation and intermixing of reactants. Quantitative characterization of the features of the evolving microstructures for each composition containing various volume fraction of epoxy, and the assessment of the influence of nano- and micron-scale aluminum particles reveal the following main features:

a. Relatively broad size distributions were observed for hematite agglomerates that comprise the composite's microstructure. Average hematite agglomerate and pore sizes show a dependence on epoxy

concentration, which increased as the volume fraction of epoxy decreased. However, an Al+$Fe_2O_3$ composition containing 60 *vol.%* epoxy showed relatively larger aluminum and hematite agglomerate feature sizes, and a significantly lower concentration of the features, which were distributed fairly uniformly throughout the material volume. Other compositions had hematite agglomerates and pores that were in relatively close proximity to each other, thus introducing the probability of significantly more stress concentration features that affect the overall structural/mechanical behavior of these composites.

b. The addition of nano-scale aluminum produced unique microstructures that exhibited regions containing high concentrations of nano-scale aluminum particles or agglomerates. These regions varied in size and ranged between 50 and over 200 μm in diameter. This composite also exhibited similar features such as hematite agglomerates and minor concentration of porosity, which were significantly smaller than the micron-scale composite counterpart. The agglomeration of submicron hematite and nano-scale aluminum particles appears to improve the structural/mechanical properties of these composites, when containing no appreciable porosity throughout the material volume.

c. Typically, each composition had hematite particle agglomerates with size classes characterized as fine (≤ 1 μm, typically individual particles),

medium (5 to 10 μm), and large (20 to 50 μm). However, their distribution and frequency varied according to the volume fraction of epoxy. This is directly attributed to the increased difficulty associated with mixing higher solid particle fraction composites and suggests the agglomeration of hematite particles occurs during the dry mixing process of precursor powders before their addition to the epoxy resin. In contrast, the agglomeration of nano-aluminum particles appears to occur during mixing, after their addition to the resin, signified by their turbulent spiral shape consisting of "layers" or "bands" of particles within the agglomerates.

d. Hematite and nano-aluminum agglomerates consist of individual tightly packed particles that are encapsulated in the epoxy matrix and do not appear to have any open porosity. This also suggests that some agglomeration may be beneficial for enhancing structural/mechanical properties of these composites, evident from continuous indentation tests that show significantly higher elastic moduli and yield stresses for these features. However, the agglomeration of micron-scale aluminum is not desirable, as evident from DMA experiments that show these features do not contribute to bulk strengthening by inhibiting polymer chain motions for the epoxy matrix.

*ii)* The influence of microstructure on mechanical behavior was examined using quasistatic or relatively low-strain rate loading experiments that include dynamic mechanical analysis (DMA), continuous ball indentation, quasistatic compression, three-point flexural bend, and Charpy impact experiments. These tests were used to evaluate the relative behavior between each composition while altering the addition of epoxy volume fraction to the micron-scale aluminum and submicron-scale hematite powder mixtures. The results from these experiments are as follows:

a. The addition of solid particles to the epoxy matrix typically improved the elastic modulus, observed from the measured stress-strain behaviors obtained from continuous ball indentation, quasistatic compression, and flexural three-point bend tests. DMA scans show relatively steady improvements, with the storage modulus typically increasing in both the glassy and rubbery states with the addition of solid particles. However, the 60 *vol.%* epoxy composition exhibited a significantly high modulus in the glassy region and a relatively low modulus in the rubbery region. These contrasting behaviors were attributed to solid micron-scale aluminum particles which possibly inhibit the epoxy crosslinking during polymerization. These relatively large inclusion features dominate the deformation response in the glassy region by transferring the load from the matrix to the inclusions. However, as temperature increases above the glass transition, the composite's response is dominated by molecular chain

motions that are not inhibited by the relatively large inclusion features, thus, resulting in a significantly low storage modulus in the rubbery region.

b. The glass transition temperature obtained from DMA experiments does not significantly change with solid particle filler content except for the 60 and 78 *vol.%* epoxy compositions. Higher glass transition temperatures are typically related to higher crosslink densities, which tends to increase as molecular motion becomes more difficult. However, the calculated crosslink density for the 60 *vol.%* epoxy composite was relatively low, while the 78 *vol.%* epoxy composite was relatively normal when compared to the other compositions. This suggests that the relatively high glass transition temperatures for these composites are not directly related to crosslink density, but possibly influenced more by microstructural features such as hematite agglomeration and the uniformity of aluminum particle distribution. The hematite agglomerates may be improving the local mechanical properties of the composite, since the individual particles are uniformly dispersed, however, in closer proximity to each other. Furthermore, as evidence for this effect, the significantly low number of hematite agglomerates present in the 60 *vol.%* epoxy composite are not sufficient to improve the overall mechanical behavior of this composite.

c. The dispersion of nanoscale particles provides physical entanglements that lead to a loss of polymer chain mobility, which in turn raises the glass transition temperature and increases the average crosslink density. The use of nano-scale aluminum particles was also apparent in improving the load capacity in the rubber modulus region above the glass transition temperature.

d. The apparent yield points for each composition are somewhat scattered and have less obvious responses, with the 60 *vol.%* epoxy composite having the greatest value. Inherent porosity significantly affects the composites response as illustrated by the significantly low yield stress observed for the 78 *vol.%* epoxy composite, which had moderately high porosity concentration (close to 2 %) with unusually large pores. However, the addition of solid particles to the epoxy matrix did not show significant improvements towards yielding. The most significant effect was improved elastic modulus and strain hardening from the addition of reinforcement particles. The addition of solid particles also reduced inherent brittleness of pure epoxy. The ratio of toughness and strength ($K_{IC}/\sigma_f$) provides a gradual ranking for the epoxy-cast composites, with pure epoxy showing the most brittle behavior, followed by 70, 47, 78, and 60 *vol.%* epoxy composites.

e. The introduction of solid particles to the polymer matrix effectively introduces flaws, and their sizes depend on the individual particle sizes and their distribution throughout the epoxy matrix. The inherent critical flaw sizes for each composition had relatively broad range between 9 and 30 μm and follow in order according to epoxy concentration, with pure epoxy having the smallest and the 47 *vol.%* epoxy composition having the largest. However, the 78 *vol.%* epoxy composite exhibited a slightly greater critical flaw size than the 47 *vol.%* epoxy composite because of the abnormally high inherent porosity observed for this particular batch of material.

*iii)* The influence of epoxy-cast composites containing nano- and micron-scale aluminum and hematite powders on the dynamic structural/mechanical behavior was evaluated using Taylor anvil impact experiments. These behaviors were compared to the dynamic response of pure epoxy. The results from these experiments are as follows:

a. The measurement of transient deformation dimensions obtained from high-speed camera images indicate the epoxy-cast Al+$Fe_2O_3$ composites exhibit both viscoelastic deformation and brittle fracture behaviors. Upon impact, the specimens display significant elastic and plastic deformation both during the loading and unloading stages of the deformation response.

Approximately 50 % elastic recovery of total axial strain was observed to occur rapidly (within tens of microseconds) after impact.

b. Strain measurements provide insight into the fracture behavior of these composite materials. The path to fracture initiation begins with the areal strain exceeding a critical limit. The epoxy-cast Al+$Fe_2O_3$ composites, including nano-aluminum containing composites, have critical areal strains of 30 %, above which the samples continue to strain to approximately 60 to 80 % prior to fracture. Pure epoxy specimens however showed a higher critical areal fracture strain of approximately 40 %, which is attributed to thermal softening permitting the rubbery response to accommodate greater radial deformation or higher areal strains. In contrast, the particle-filled composites exhibit thermal softening above the critical areal fracture strain.

c. Upon impact, the specimens reveal two types of deformation shapes that were observed from high-speed camera images. Specimens typically exhibited a "double-frustum" shape when the deformation was concentrated at the impact region of the specimen, causing the axial strain to exceed a critical value leading to radial failure at significantly high strains of 60 to 80 %. In contrast, the "elongated-mushroom" deformation shape promotes the absorption of the impact energy along the axial length of the specimen and no fracture initiation is typically observed. The

introduction of a small fraction of porosity, typically more than 1 %, significantly influences the deformation character, which manifests as the "double-frustum" deformation shape that leads to specimen failure.

d. The critical impact velocity identifies the minimum impact condition necessary for the onset of plastic deformation and is a sensitive measure that provides an indication of relative material strength. The highest strength was observed for the nano-70 *vol.%* epoxy composite, followed by pure epoxy and the 60 *vol.%* epoxy composite, respectively. Additionally, two different batches of pure epoxy that were processed using identical techniques showed slightly different behaviors. The lower density material (batch *A*), which was the closest to the theoretical density, had a slightly higher critical impact velocity. In contrast, the higher density material (batch *B*) possibly contained a slightly higher concentration of hardener, which in turn caused the density to be greater than the theoretically calculated value. This batch of material had a brittle behavior that caused a lower viscoplastic response, thus resulting in a lower critical impact velocity.

e. The stress-strain behavior for the nano-70 *vol.%* epoxy composition was comparable to the 60 *vol.%* epoxy composition in terms of stress response, however, exhibiting significantly different yield strains. The major difference in the overall dynamic response was observed in terms of

elastic resilience, with the nano-70 *vol.%* epoxy composition showing the greatest value, over twice that observed for 60 *vol.%* epoxy and pure epoxy. The calculated resilience for the 60 *vol.%* epoxy and pure epoxy compositions was very similar and the addition of micron-scale particles showed only a slight improvement.

f. The elastic/plastic wave interaction directly influences the composites response to dynamic loading. Position-time diagrams of the elastic and plastic waves coincide with elastic recovery if the stress magnitude is below the fracture strength of the composite. Specimens are observed to fracture following the elastic and plastic wave interaction if the stress magnitude is sufficiently high. The one-dimensional elastic-plastic wave analysis combined with time synchronized velocity interferometry measurements and high speed camera images identify the stress and strain magnitude in the vicinity of these interactions.

*iv)* Select reverse Taylor impact experiments with relatively high impact velocities showed evidence of a dark footprint remaining on the anvil surface. Post-mortem analysis identified localized chemical reactions and decomposition of the epoxy matrix. The characterization of thermochemical reaction energetics was used to identify the most probable reaction products observed from the strain-induced chemical reactions. The results obtained from Taylor impact experiments, which reveal evidence for mechanochemical reactions, are as follows:

a. Post-mortem SEM analysis of the footprints showed evidence of localized melting and re-solidification of melted reaction products. These sites display evidence of $Al_2O_3$ and Fe reaction products remaining on the anvil surface, in addition to an iron-alumina compound ($FeAl_2O_4$). Identified sites also showed regions where intermediate reaction products, such as $AlFe_3$ and $Fe_{1-x}O$, were observed. In some cases, the reaction products were in close proximity to hematite particles that were not involved in the reaction. The reactions appear to be localized to sites that contain aluminum within the vicinity of hematite particles. There was no evidence of aluminum particles remaining on the anvil surface, which thus, appears to be the limiting component for the thermite reaction.

b. Other locations outside the dark footprint area showed identifiable debris remaining on the surface from secondary impacts of the rod specimen fragments. The locations typically consisted of hematite particles with no evidence of chemical reaction. Additionally, no aluminum particles were found, indicating that the micron-scale particles are possibly ejected for the epoxy matrix upon impact. This indicates that fracture may inhibit the sustainability of the reaction and constrain it to a limited radial-strained region.

c. The reaction products identified from *in situ* high-temperature x-ray diffraction (HTXRD) and indicated by DTA were similar to those

identified from the post-mortem investigation of the recovered anvils. The good correlation of the reaction products identified from the different experimental conditions give confidence in the calculated reaction products obtained from the elemental species identified by EDS.

d. Both types of composites, containing micron- and nano-aluminum, showed evidence of reaction initiation. The initiation, indicated from the contact footprint remaining on the anvil surface, occurred at approximately 50 % areal strain, regardless of significantly different impact velocities.

e. The remaining impact footprints on the anvil face provide an instantaneous signature of the strain-induced reaction initiations. The strain and corresponding stress were estimated from the footprint, in addition to estimating the bulk temperature rise associated with the mechanical work from plastic deformation. While the associated temperature rise was sufficient to cause thermal softening, it was significantly lower than that needed for directly initiating the thermite reactants. However, thermal softening is an important component of the reaction mechanism and provides additional viscoplastic deformation that allows the intimate interaction of the reactant particles and submicron-level mixing, which is thought to be crucial for reaction initiation.

*v)* The shock Hugoniot of epoxy-cast Al+$Fe_2O_3$ composites containing 60 and 78 *vol.%* epoxy was compared. The study of particle-filled composites showed a deviation from ideal Hugoniot behavior that was initiated from the addition of solid particles and possible damage evolving at a critical impact stress. The results obtained from these experiments are as follows:

a. The addition of solid particles to the epoxy matrix altered the typically non-linear $U_S$-$U_P$ response observed for pure polymers. The particle-filled Al+$Fe_2O_3$ composites showed an opposite effect, displaying a non-linear $U_S$-$U_P$ response with an initially rapid particle velocity, resulting in a convex curvature. This effect is attributed to the addition of higher shock impedance particles that intensify and increase the overall bulk wave velocity for the composite. In contrast, the addition of lower shock impedance features, such as pores, show evidence of wave dispersion effects that attenuate the wave as it propagates through the specimen.

b. The $U_S$-$U_P$ Hugoniot behavior for each composition initially shows similar behaviors for the particle-filled composites and pure epoxy. However, this response gradually deviates at a critical value that corresponds to induced damage. While the 60 *vol.%* epoxy composite exhibits a gradually increasing particle velocity for higher impact stress, the 78 *vol.%* epoxy shows a sharp transition towards the response of pure epoxy. These

contrasting behaviors are related to various degrees of damage possibly nucleating at the particle inclusion sites.

c. The transformation of $U_S$-$U_P$ Hugoniot data to the pressure-volume space allows the determination of the critical impact stress that initiates damage in the composite materials. Comparing the experimentally determined compressibility to those calculated from fitting damaged and undamaged material responses with the Birch-Murnaghan equation of state (BM-EOS), indicates possible damage occurs at approximately 4 GPa for both compositions. The damage is connected to decohesion of solid particles from the epoxy matrix. While the 60 *vol.%* epoxy composite exhibits a toughening response above the critical damage stress, the 78 *vol.%* epoxy composite exhibits significantly more damage as the impact stress increases, introducing significantly more damage that can not support the greater loading.

d. Comparison of embedded PVDF stress gauge measurements with hydrodynamic simulations initially show excellent agreement with experimental stress waveforms, but overestimate as the input stress increases past a critical limit of approximately 4 GPa, above which damage occurs. The stress overestimation corresponds to induced damage, which is currently not accounted for in the models used for the numerical simulations.

## 6.2 Summary of Contributions

The experimental and theoretical work conducted in this study provides a general design for the development and characterization of particle-filled structural energetic composite material systems. The main contributions from this investigation are as follows:

*i)* Devised a method for obtaining dynamic material behavior of epoxy-cast composites using instrumented reverse Taylor anvil impact experiments by extending the one-dimensional elastic-plastic wave propagation analysis presented by Hutchings [98]. Experiments coupled high-speed camera images for capturing the transient deformation of the specimen and velocity interferometry (VISAR) to measure the surface velocity of the rear of the specimen. Time synchronizing the camera images with VISAR and calculations using the elastic-plastic wave propagation analysis provides a detailed account of the deformation behavior and identifies complex wave interaction phenomena throughout the entire deformation interval up to the final state of the specimen, including details about fracture initiation. This type of analysis specifically enables:

   a. High-speed camera images to quantitatively measure axial and areal strains at each time instance and calculate the stress-strain history from one-dimensional elastic-plastic wave propagation analysis. High-speed

camera images provided accurate specimen dimensions that compared well with physically measured post impact dimensions, within 0.4 % of each other.

b. Identification of the characteristic "double-frustum" deformation shape associated with specimen failure and the "elongated-mushroom" shape, which was observed for all specimens that showed no evidence of fracture, regardless of the particle-filled composites' composition.

c. Strain measurements used to identify compositions dispersed with Al+$Fe_2O_3$ powders typically showed evidence of fracture when exceeding a critical areal strain of 30 %, while pure epoxy endured higher critical areal strains of 40 % before fracture initiation was observed.

d. The detection of subtle differences between various epoxy-cast Al+$Fe_2O_3$ composites and pure epoxy batches through the measure of critical impact velocity, where the onset of plastic deformation occurs. The critical impact velocity is a very sensitive measure of dynamic material response and provides an indication of relative material strength.

e. Quantitative measurements revealing significant elastic and plastic deformation during both the loading and unloading stages, where over

50 % elastic recovery of total axial strain occurred rapidly (within tens of microseconds) after impact.

f. The detection of subtle plastic wave motion and the total axial strained length of the deformed body from captured high-speed camera images. An image analysis routine was employed for measuring the diameter of the deformed specimen at every pixel along the axial length, which was used to identify the axial position where the diameter was 2 % greater than the specimen's initial diameter.

g. Construction of *x-t* (*distance-time*) diagrams depicting the propagation of elastic and plastic waves from incremental stress-strain calculations using the one-dimensional elastic-plastic wave propagation analysis. The impact velocity, and thus, the initial magnitude of the stress wave have a direct consequence in the behavior of the elastic/plastic wave interaction. The analysis calculates the stress and strain magnitudes for discrete time increments from high-speed camera images of the transient deformation.

h. Coupling of high-speed camera images with VISAR data for characterizing the complex elastic-plastic wave interactions, which is used for validating predictions obtained from the one-dimensional elastic-plastic wave propagation analysis and identifying the moment of specimen failure.

*ii)* Post-mortem material analysis of relatively high velocity reverse Taylor anvil impact experiments indicates strain-induced mechanochemical reaction initiation. Select experiments showed evidence of a dark impact footprint remaining on the anvil surface containing reaction products consistent with those formed for the $Al+Fe_2O_3$ thermite system. The footprints also provide a signature identifying the stress, strain, and strain rates associated with the reaction initiation. The recovered anvils were used for:

a. Post-mortem SEM analysis of the footprint regions showing evidence of localized melting and re-solidification. The most probable reaction products were established from identified EDS chemical species compared with those identified from *in situ* high temperature x-ray diffraction (HTXRD) measurements and DTA exothermic and endothermic peak signatures.

b. Calculating the specific strains associated with the measured footprint contact diameters remaining on the anvil surface. The calculated strains were used to obtain the corresponding stress from the dynamic stress-strain behavior, while the strain rate was estimated from time-synchronized strain measurements obtained from high-speed camera images.

c. Calculating the associated bulk adiabatic temperature rise from the plastic work, corresponding to the measured footprint contact strain, and identifying the thermal softening effect that triggers a series of events culminating in strain-induced chemical reaction initiation.

*iii)* Conducted time-resolved impact experiments, using PVDF stress gauges and velocity interferometry (VISAR), for obtaining the composite material's Hugoniot equation of state (EOS). Several compressed-gas gun impacts were performed for the epoxy-cast Al+$Fe_2O_3$ composites containing 60 and 78 *vol.%* at relatively low impact pressures (2.7 to 8.5 GPa and 2.1 to 4.7 GPa, respectively). Additional explosively loaded experiments were performed to an extended pressure range up to approximately 25 GPa for the 78 *vol.%* epoxy composite in collaboration with Jordan, *et al.* [161,162]. The detailed analysis of the impact and propagated stress waveforms, and the particle velocity waveform provide shock loading behavior used to:

a. Identify a non-linear $U_S$-$U_P$ Hugoniot relationship for particle-filled composites, which exhibits a convex curvature with initially rapid particle velocity from the addition of solid particles with relatively high shock impedances. This response was contrary to the behavior typically observed for unfilled polymers, which have a non-linear concave curvature with an initially rapid shock velocity.

b. Identify a significantly rapid rise time-to-peak equilibrated stress for the propagated PVDF stress gauge waveform as compared to the impact stress gauge response. For composites that contain higher shock impedance particles dispersed in a low shock impedance polymer matrix, the wave intensifies as it propagates through the specimen and increases the overall bulk wave velocity.

c. Identify a "step" in the rise-to-peak stress (pressure) for both impact and propagated PVDF gauge waveforms linked to the viscoelastic-viscoplastic epoxy response behavior. A similar "step" was also detected in the VISAR rise-to-peak particle velocity waveforms.

d. Compare embedded PVDF stress gauge measurements with one-dimensional CTH code simulations that initially show excellent agreement with experimental stress waveforms, but overestimate as impact stress increases past a critical limit above which damage occurs. The hydrodynamic calculations also overestimate the particle velocity behind the shock front, by similar magnitudes, for directly measured values using VISAR.

e. Identify the critical impact stress where damage occurs by comparing transformed $U_S$-$U_P$ Hugoniot data to pressure-volume space with the calculated undamaged responses obtained from the Birch-Murnaghan

equation of state (BM-EOS) [211] and the theoretically determined equilibrated Hugoniot pressure response for mixed phases using the inverted Hugoniot EOS [212].

f. Directly compare the influence of particle-fill volume fraction for the epoxy-cast Al+$Fe_2O_3$ composites with 60 and 78 *vol.%* epoxy, with pure epoxy response. The particle-filled composites illustrate initially similar behaviors with pure epoxy, but gradually deviate at higher pressures or particle velocities. However, contrasting behaviors for each composition are observed at higher pressures, above the critical damage stress. While the 78 *vol.%* epoxy composition shows a transition from undamaged to damaged behavior that approaches pure epoxy response, the 60 *vol.%* epoxy composition exhibits a gradual toughening behavior.

*iv)* Correlation of the structural/mechanical response and chemical reaction behavior with quantitative microstructural analysis is conducted for the various compositions examined in this study. The bulk material response is closely interlinked through the characteristics of deformation and intermixing of reactants. Although the bulk material response for the different compositions is homogenized from the main response attributed to the relatively large volume fraction of epoxy used in these composites, some select cases directly illustrate the influence of the microstructure on mechanical behavior. Therefore, the influence of microstructural characteristics is obtained mainly as a function of

epoxy volume fraction (from 47 to 78 *vol.%*) and solid particle size effects observed for Al+$Fe_2O_3$ composites containing nano- and micron-scale aluminum. The microstructural analysis indicates:

a. The dynamic response obtained from Taylor impacts shows a minor influence in mechanical behavior when varying the epoxy concentration from 47 to 78 *vol.%* for the Al+$Fe_2O_3$ composites. The bulk material response is typically dominated by the viscoelastic-viscoplastic behavior observed for the epoxy matrix.

b. The dynamic stress-strain behavior obtained from the Taylor impact analysis shows that the use of nano-scale aluminum particles significantly increases the composites' elastic resilience and the ability to absorb the impact energy as compared to using micron-scale aluminum and pure epoxy response. The port-mortem analysis illustrates the strengthening mechanism of nano-aluminum agglomerates, which also improve the composite's elastic resilience and the ability to absorb high velocity impacts by inhibiting crack propagation. In contrast, composites containing micron-scale aluminum particles experienced uninhibited crack propagation between particles.

c. The strain-induced mechanochemical reactivity response for the epoxy-cast Al+$Fe_2O_3$ composites using micron- and nano-scale aluminum

particles appear to initiate at similar areal strain of approximately 50 %, regardless of impact velocity.

d. Hugoniot experiments conducted for the epoxy-cast Al+$Fe_2O_3$ composites with 60 and 78 *vol.%* epoxy indicate that the addition of solid particle inclusions alters the $U_S$-$U_P$ response as compared to pure epoxy behavior. The contrasting behaviors for each composition were observed at higher pressures, above a critical damage stress, where the 78 *vol.%* epoxy composition transitions rapidly from undamaged to damaged behavior and approaches the pure epoxy response. In contrast, the 60 *vol.%* epoxy composition exhibits a gradual toughening behavior as impact pressure increases.

e. Quasistatic or relatively low-strain rate mechanical testing, which include dynamic mechanical analysis (DMA), continuous ball indentation, compression, three-point flexural bend, and Charpy impacts, each typically showed that the specific measured parameter, for example, the elastic moduli, yield stress, or toughness increase as epoxy concentration decreases.

## 6.3 Future Research Recommendations

The current study has examined several aspects that are important for the development and enhancement of structural energetic materials. The established methods and techniques provide opportunities for extension into the future development of similar materials with enhanced dual-functionality between the reactants and matrix. As in most studies on relatively new and untested materials, unexpected results were encountered which could not be adequately pursued in more detail within the scope of the immediate work. The recommendations for future experimental and theoretical work are as follows:

*i)* It would be advantageous to identify the mechanical and chemical influence of micron- and nano-scale aluminum particles used within Al+$Fe_2O_3$ epoxy-cast composites. Additional reverse Taylor impact experiments for the Al+$Fe_2O_3$+70 *vol.%* epoxy composites would provide the opportunity to directly compare the behavior with the nano-Al+$Fe_2O_3$+70 *vol.%* epoxy composite already examined. Extending the characterization of this particular composition will assist in identifying the mechanochemical reaction threshold with more clarity, the relative degree of reactivity, and the direct influence of reactants' particle morphologies.

*ii)* The current study has examined the bulk material response to dynamic loading and explained the observed structural/mechanical behavior and mechanochemical reactivity. However, it would be beneficial to scale down the specimen size and

fabricate composites that contain highly controlled morphologies and distributions of the reactants. This would be beneficial for identifying the interaction of reactant particles and the associated mechanism(s) for mechanochemical reaction initiation, particularly for composites containing nanoscale reactants.

*iii)* What is the influence on the many possible epoxy systems and other polymeric binders that are typically used as a matrix material for particle-filled composites? There have been limited high-strain rate studies which correlate mechanical behaviors with well characterized polymers. It would be of interest to extend the Taylor impact study to include pure polymer structures that are characterized in terms of degree of crystallinity, crosslinking density, and other intrinsic polymer properties. Many of these intrinsic properties can be modified and tailored to meet specific needs of the composite system. It would also be benifical to conduct these studies at different temperatures for developing the constitutive relationship and the influence of temperature on structural/mechanical properties.

*iv)* Structural energetic materials subjected to significantly high velocity impacts have revealed a delayed reaction response from secondary impacts of highly strained and damaged materials with a rigid surface [8,46]. The geometry of the traditional right-circular cylindrical Taylor specimen can be modified to enhance strain-induced chemical reactivity by introducing a conical frustum tip (created by slicing the top of a cone). This geometry would enhance conditions for strain-induced chemical reactions by duplicating the loading conditions observed

for delayed reaction initiation experiments. The deformation behavior for the conical Taylor impact test would cause highly strained material from the tip to "jet" across the anvil face while undamaged material along the axial length of the specimen tip produces a "secondary" impact. This effectively introduces the undamaged material to impact in a cascading manner with damaged material. High-speed camera images can be used to quantitatively capture the transient deformation and calculate the stress, strain, and strain rates necessary for reaction initiation.

*v)* Metal honeycomb structures, termed linear cellular alloys (LCA's), are fabricated from an oxide paste extrusion process and subsequent reduction from thermal heat treatment [224]. These structures can be fabricated in a variety of geometries, while maintaining mechanical properties typically observed for traditionally processed metal alloys. The suitability of LCA's as energetic capsules were examined from a limited dynamic impact study, where the open structure of the LCA was filled with epoxy acting as an inert simulant [225]. The study found that the filled specimens experience increased overall strength and energy absorption capabilities upon impact. It would be interesting to continue this study and replace the inert epoxy with the well-characterized epoxy-cast Al+$Fe_2O_3$ filler material. Additionally, the fragmentation of the LCA introduces a significant shearing component and confinement that can help initiate and sustain chemical reactions.

*vi)* In the current study, the shock Hugoniot experiments for Al+$Fe_2O_3$+78 *vol.%* epoxy composite were conducted over a significantly greater pressure range than the Al+$Fe_2O_3$+60 *vol.%* epoxy composite. While the 78 *vol.%* epoxy composition shows a transition from undamaged to damaged behavior that approaches pure epoxy response, the 60 *vol.%* epoxy composition exhibited a gradual toughening behavior that never approached pure epoxy or a significantly damaged response. It is possible that a similar damage transition observed for the 78 *vol.%* epoxy composite is expected to occur for the 60 *vol.%* epoxy composition at significantly higher impact stresses. Extending the loading range for shock Hugoniot experiments conducted for the Al+$Fe_2O_3$+60 *vol.%* epoxy composite would permit the complete evaluation of damage at higher impact pressures. It would also be valuable to conduct additional experiment for evaluating the influence of nano-scale particles on the shock Hugoniot response of particle-filled epoxy-cast composites.

*vii)* The introduction of a damage model that couples the viscous-elastic-plastic (VEP) constitutive model [216], already in use, with the CTH hydrodynamic calculations would be beneficial for the complete description of the complex viscoelastic-viscoplastic behavior observed for the epoxy-cast composites. Currently, the hydrodynamic calculations show excellent agreement with experimentally determined stress waveforms, but overestimate as the input stress increases past a critical limit above which damage occurs. The introduction of a damage model will allow the calculation of distention and the degree of damage

induced from the high velocity impacts. This will account for the formation of pores during the debonding process and the subsequent microcracking and scission that take place in the binder material, thus reducing the predicted stress waveform magnitudes. It would also be beneficial to introduce a reactive flow model that accounts for the polymer disassociation and intermetallic reaction of the thermite constituents.

# APPENDIX A: Continuous Spherical Ball Indentation Tests

Instrumented continuous indentation experiments were conducted for evaluating the local mechanical behavior of epoxy-cast Al+$Fe_2O_3$ composites. The penetration depth or displacement, $h$, of the spherical tipped indenter is measured as a function of an applied load. The measured load-displacement curves are shown in Figure A.1(*a*-*e*) for *a*) pure epoxy, and the Al+$Fe_2O_3$ epoxy-cast composites with *b*) 78, *c*) 70, *d*) 60, and *e*) 47 *vol.%* epoxy, respectively. Similarly, load to the 2/3 power displacement dependence curves and stress-strain curves for each composition are shown in Figure A.2(*a*-*e*) and Figure A.3(*a*-*e*), respectively. Table A.1 lists the measured parameters obtained for each experiment. These include the calculated reduced and specimen elastic moduli ($E_r$ and $E_s$, respectively), the viscoelastic and viscoplastic yield stresses ($\sigma_{y(ve)}$ and $\sigma_{y(vp)}$, respectively), and Meyer hardness, $H_M$. The elastic/plastic limit for each composite is identified by load and displacement values, $P$ and $h$, respectively.

**Table A.1** Measured data obtained from continuous ball indentation experiments for Al+$Fe_2O_3$ epoxy-cast composites and pure epoxy (batch *B*). The quality of each indent was evaluated using optical microscopy to observe microstructural features that influence the indentation results.

| Specimen ID | $E_r$ [GPa] | $E_s$ [GPa] | *elastic/plastic* $h$ [μm] | *elastic/plastic* $P$ [N] | $\sigma_{y(ve)}$ [MPa] | $\sigma_{y(vp)}$ [MPa] | $H_M$ [MPa] | Indent Features* |
|---|---|---|---|---|---|---|---|---|
| **Al+$Fe_2O_3$+47 *vol.%* epoxy** | | | | | | | | |
| 085E-1,1 | 8.83 | 8.43 | 7.37 | 6.53 | 120.79 | 200.74 | 252.44 | P |
| 085E-1,2 | 9.75 | 9.34 | 6.82 | 6.41 | 132.68 | 232.93 | 271.16 | P |
| 085E-1,3 | 15.19 | 14.95 | 9.86 | 17.52 | 225.83 | 391.90 | 356.85 | Ag |
| 085E-1,4 | 11.76 | 11.38 | 3.69 | 3.04 | 66.50 | 183.14 | 262.03 | P, Ag |
| 085E-1,5 | 7.53 | 7.14 | 4.87 | 2.95 | 44.21 | 124.18 | 222.24 | P |
| 085E-5,1 | 8.33 | 7.93 | 4.29 | 2.75 | 86.40 | 185.60 | 234.87 | P |
| 085E-5,2 | 10.51 | 10.11 | 5.36 | 4.82 | 87.40 | 201.48 | 241.98 | P, Ag |
| 085E-5,3 | 6.92 | 6.54 | 2.58 | 1.06 | 41.62 | 133.13 | 220.99 | P |
| 085E-10,1 | 10.70 | 10.30 | 2.84 | 1.92 | 86.17 | 189.93 | 240.48 | P, Ag |
| 085E-10,2 | 11.92 | 11.55 | 3.74 | 3.20 | 67.51 | 204.69 | 230.62 | P, Ag |
| **Al+$Fe_2O_3$+60 *vol.%* epoxy** | | | | | | | | |
| 079E-1,1 | 19.15 | 18.13 | 3.54 | 4.73 | 174.66 | 278.85 | 296.33 | Ag |
| 079E-1,2 | 10.44 | 9.46 | 3.50 | 2.49 | 97.85 | 208.75 | 279.56 | G |
| 079E-5,1 | 7.79 | 6.97 | 5.78 | 4.08 | 42.76 | 141.89 | 261.98 | P |
| 079E-5,2 | 11.07 | 10.07 | 5.01 | 4.56 | 104.05 | 200.18 | 275.89 | G |
| 079E-5,3 | 7.84 | 7.02 | 8.09 | 6.78 | 44.23 | 173.91 | 249.05 | P |
| 079E-10,1 | 9.69 | 8.75 | 5.61 | 4.80 | 41.60 | 181.00 | 255.61 | G |

**P* and *Ag* represent pores and $Fe_2O_3$ agglomerates, respectively, located within the indent's contact area observed from optical micrographs. *G* corresponds to a good indent with relatively homogeneous phase distribution.

**Table A.1** (continued).

| Specimen ID | $E_r$ [GPa] | $E_s$ [GPa] | *elastic/plastic* $h$ [μm] | *elastic/plastic* $P$ [N] | $\sigma_{y(ve)}$ [MPa] | $\sigma_{y(vp)}$ [MPa] | $H_M$ [MPa] | Indent Features* |
|---|---|---|---|---|---|---|---|---|
| **Al+$Fe_2O_3$+70 *vol.%*** | | | | | | | | |
| 087E-1,1 | 8.72 | 8.08 | 4.51 | 3.11 | 40.09 | 163.08 | 231.09 | Ag |
| 087E-5,1 | 5.82 | 5.31 | 5.85 | 3.06 | 16.06 | 140.87 | 210.59 | P |
| 087E-10,1 | 8.45 | 7.82 | 2.25 | 1.05 | 40.62 | 144.32 | 216.79 | Ag |
| **Al+$Fe_2O_3$+78 *vol.%* epoxy** | | | | | | | | |
| 077E-1,1 | 5.94 | 5.10 | 9.77 | 6.67 | 75.49 | 146.15 | 196.48 | G |
| 077E-1,2 | 6.43 | 5.53 | 3.15 | 1.32 | 50.91 | 160.11 | 193.62 | G |
| 077E-1,3 | 5.33 | 4.57 | 8.15 | 4.55 | 31.61 | 117.76 | 182.62 | G |
| 077E-5,2 | 10.28 | 9.01 | 5.54 | 4.98 | 93.61 | 193.39 | 274.35 | Ag |
| 077E-5,1 | 3.20 | 2.71 | 2.53 | 0.50 | 12.56 | 147.41 | 186.99 | P |
| 077E-10,1 | 5.76 | 4.95 | 5.52 | 2.77 | 33.3 | 151.68 | 197.12 | G |
| **100 *vol.%* epoxy (batch *B*)** | | | | | | | | |
| 091E-1,1 | 4.48 | 3.79 | 12.41 | 7.26 | 46.88 | 155.88 | 179.80 | P |
| 091E-1,2 | 4.68 | 3.97 | 4.67 | 1.76 | 30.42 | 120.98 | 173.34 | P |
| 091E-1,3 | 4.49 | 3.81 | 9.25 | 4.69 | 25.8 | 121.45 | 173.73 | P |
| 091E-5,1 | 4.12 | 3.49 | 7.93 | 3.42 | 26.11 | 125.11 | 168.70 | G |
| 091E-5,3 | 3.10 | 2.61 | 2.87 | 0.57 | 20.48 | 126.83 | 164.39 | G |
| 091E-10,1 | 4.46 | 3.77 | 23.02 | 18.37 | 26.42 | 120.8 | 203.25 | G |

*$P$ and $Ag$ represent pores and $Fe_2O_3$ agglomerates, respectively, located within the indent's contact area observed from optical micrographs. $G$ corresponds to a good indent with relatively homogeneous phase distribution.

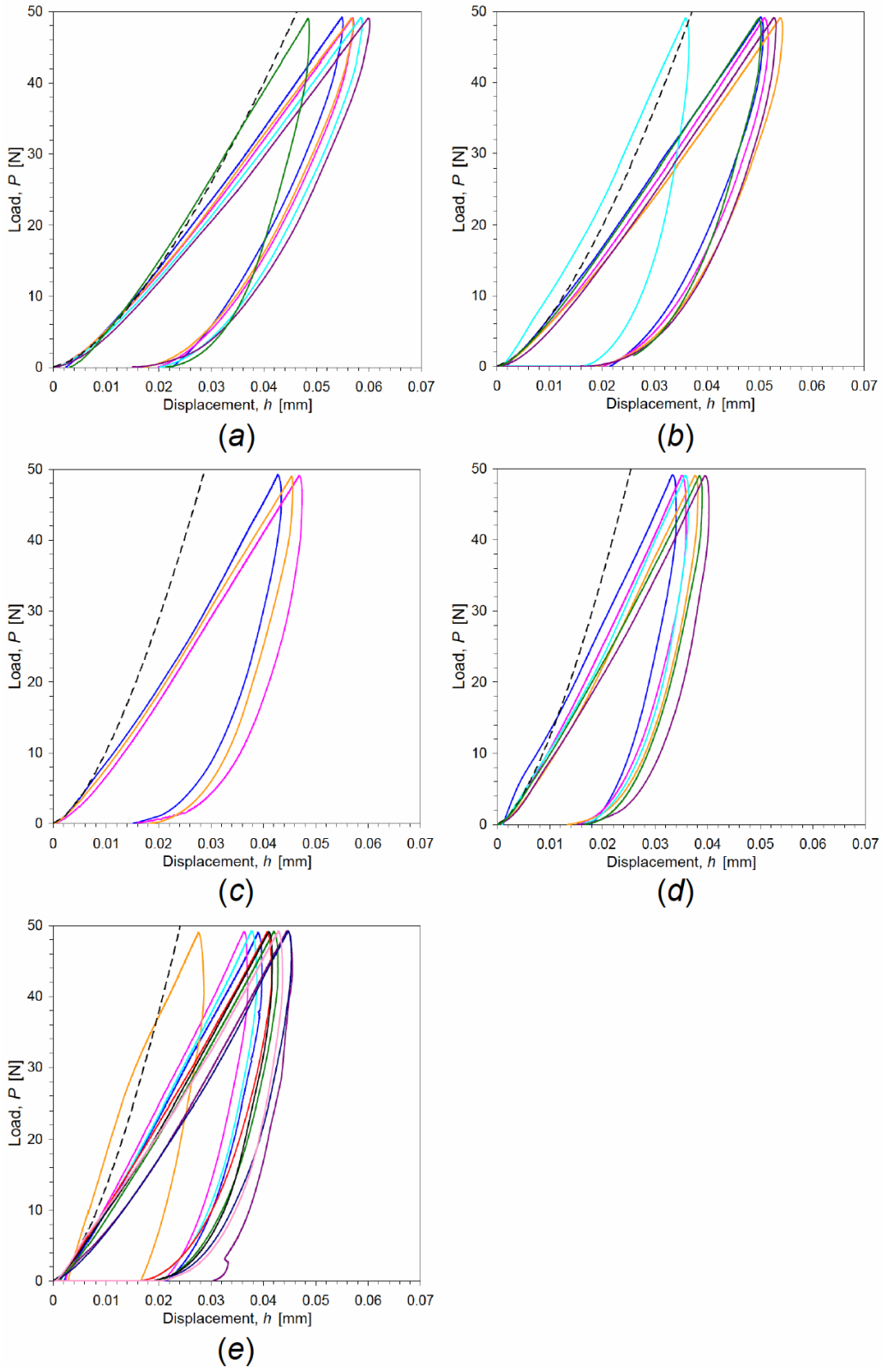


**Figure A.1** Load-displacement curves obtained from each continuous indentation experiment conducted for *a*) pure epoxy, and epoxy-cast Al+$Fe_2O_3$ composite with *b*) 78, *c*) 70, *d*) 60, and *e*) 47 *vol.%* epoxy.

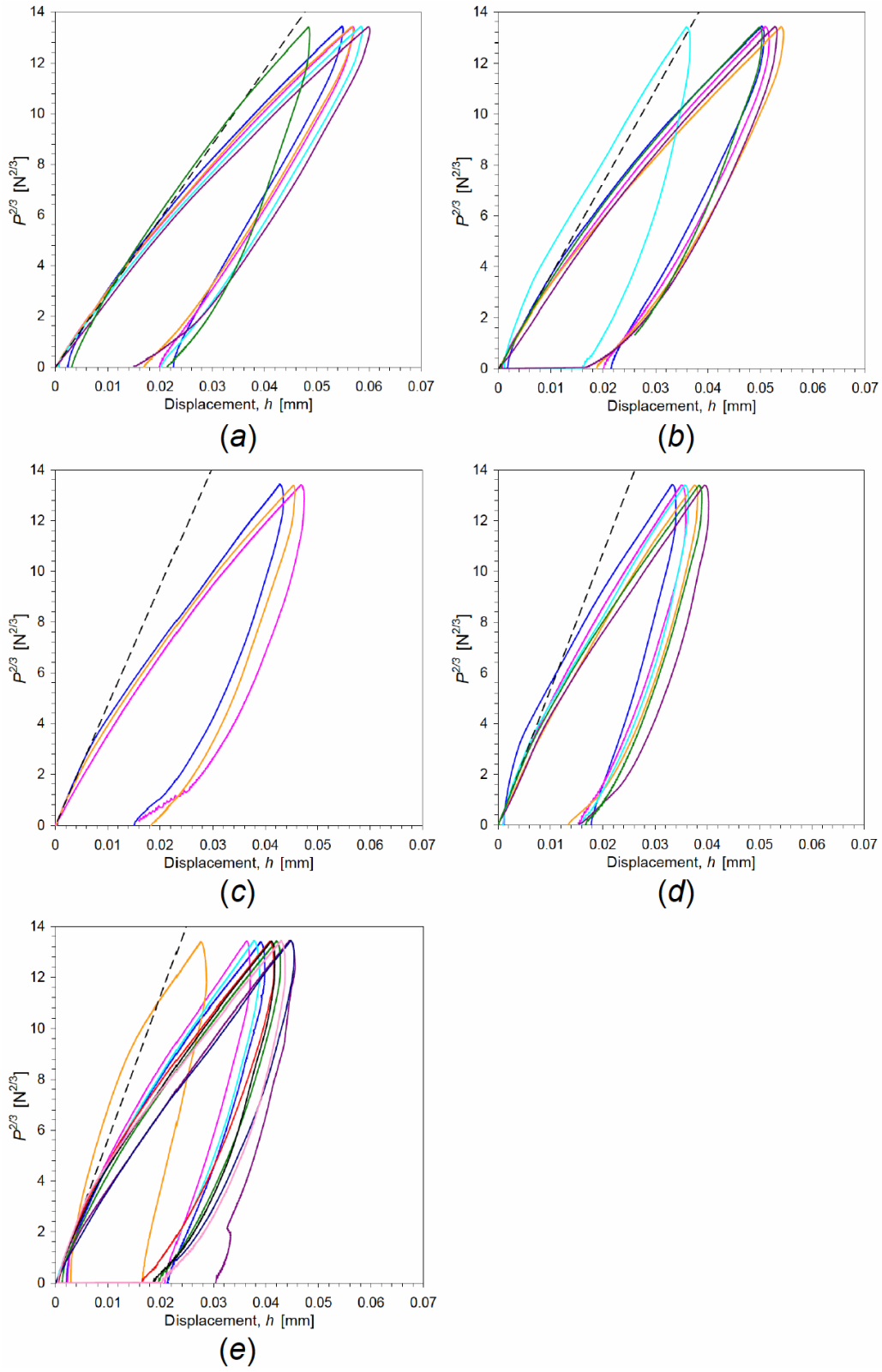


**Figure A.2** Load to the 2/3 power displacement dependence curves obtained from each continuous indentation experiment conducted for *a*) pure epoxy, and epoxy-cast Al+$Fe_2O_3$ composite with *b*) 78, *c*) 70, *d*) 60, and *e*) 47 *vol.%* epoxy.

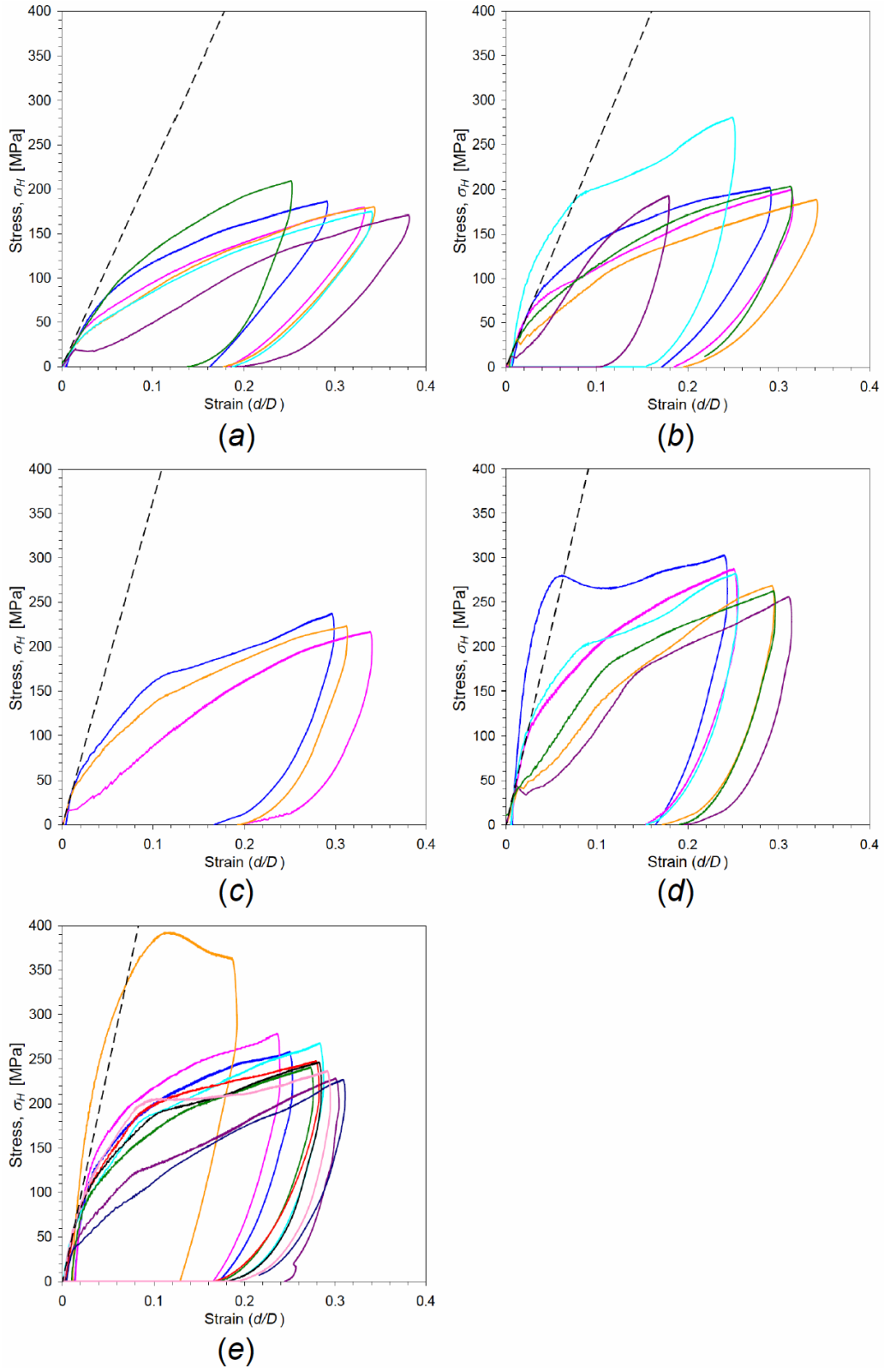


**Figure A.3** Stress-strain curves obtained from each continuous indentation experiment conducted for *a*) pure epoxy, and epoxy-cast Al+$Fe_2O_3$ composite with *b*) 78, *c*) 70, *d*) 60, and *e*) 47 *vol.%* epoxy.

# APPENDIX B: High-Speed Camera Images for Reverse Taylor Impacts

The measurements and calculations described in section 4.4 for reverse Taylor impact experiments relied on high-speed camera images capturing the transient deformation of the specimen. Images obtained for each reverse Taylor impact experiment, which was conducted for each composition and pure epoxy, are shown in Figure B.1 to B.32. The images consist of sixteen individual frames taken at specific times, which depend on impact velocity, to capture the specimen's deformation. For each experiment, the images are arranged in a rectangular (4x4) array, with the first image located in the upper left corner and the final image located at the lower right corner. The images generally increase in time from left to right for each row.

Each individual image shows the steel anvil coming from the left side of the frame. The specimen is held stationary by an acrylic ring and a cross-sectional view is shown towards the right end of the specimen, located approximately 1/4" from its back surface. Every image shows a fiducial marker consisting of concentric arcs, located to the left of the acrylic ring, that are fastened along the center axis of the specimen. In some cases, difficulties were encountered with the camera, where images misfired and show a completely black frame or a frame oversaturated by light.

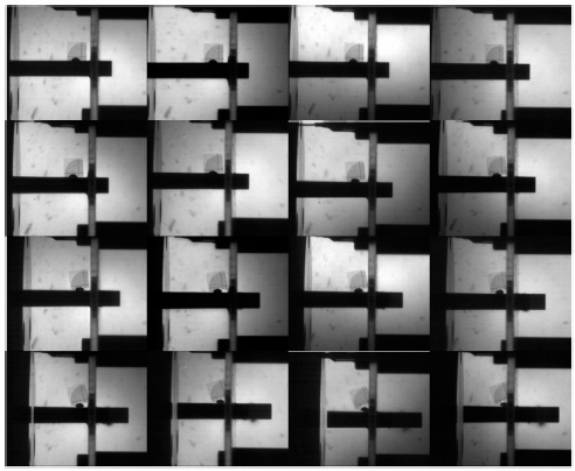

Shot 0618
Al+$Fe_2O_3$+47 *vol.%* epoxy
*U* = 101.8 ± 3.7 m/s

**Figure B.1** High-speed camera images obtained from reverse Taylor impact experiment for Al+$Fe_2O_3$+47 *vol.%* epoxy composite (shot 0618).

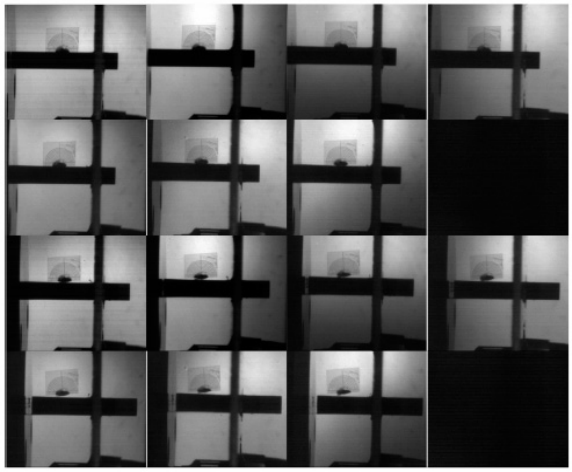

Shot 0529
Al+$Fe_2O_3$+60 *vol.%* epoxy
*U* = 80.1 ± 1.2 m/s

**Figure B.2** High-speed camera images obtained from reverse Taylor impact experiment for Al+$Fe_2O_3$+60 *vol.%* epoxy composite (shot 0529).

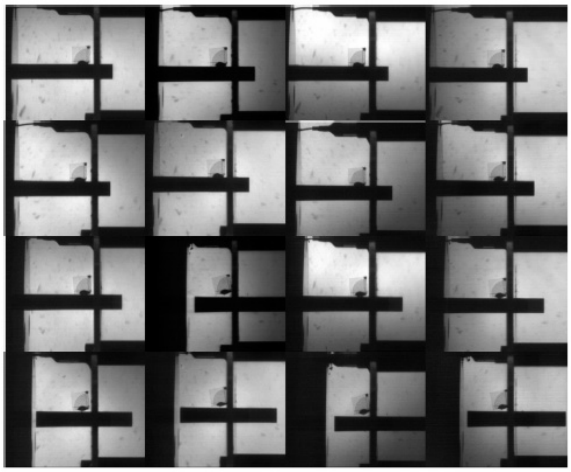

Shot 0621
Al+$Fe_2O_3$+60 *vol.%* epoxy
*U* = 97.9 ± 0.9 m/s

**Figure B.3** High-speed camera images obtained from reverse Taylor impact experiment for Al+$Fe_2O_3$+60 *vol.%* epoxy composite (shot 0621).

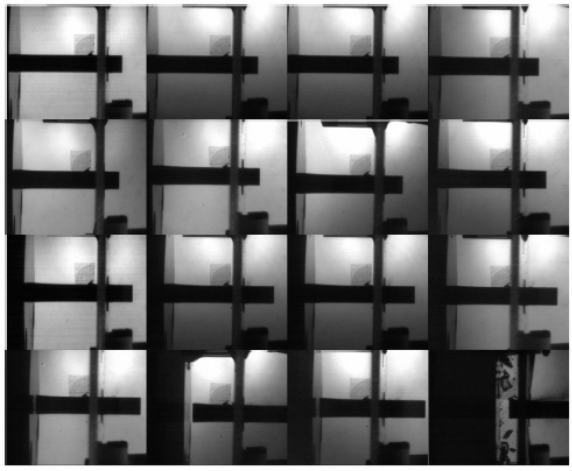

Shot 0530
Al+$Fe_2O_3$+60 *vol.%* epoxy
$U$ = 108.4 ± 1.5 m/s

**Figure B.4** High-speed camera images obtained from reverse Taylor impact experiment for Al+$Fe_2O_3$+60 *vol.%* epoxy composite (shot 0530).

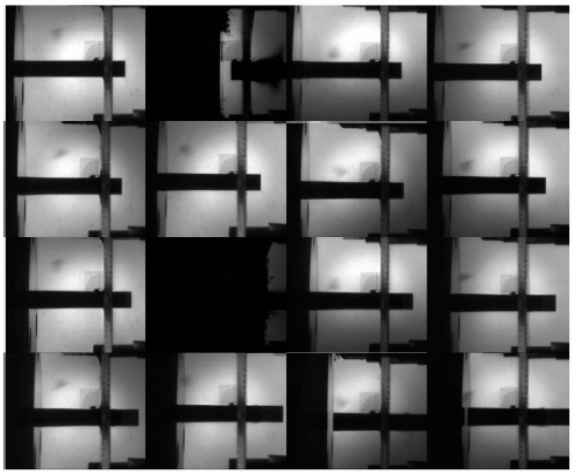

Shot 0537
Al+$Fe_2O_3$+60 *vol.%* epoxy
$U$ = 132.9 ± 2.4 m/s

**Figure B.5** High-speed camera images obtained from reverse Taylor impact experiment for Al+$Fe_2O_3$+60 *vol.%* epoxy composite (shot 0537).

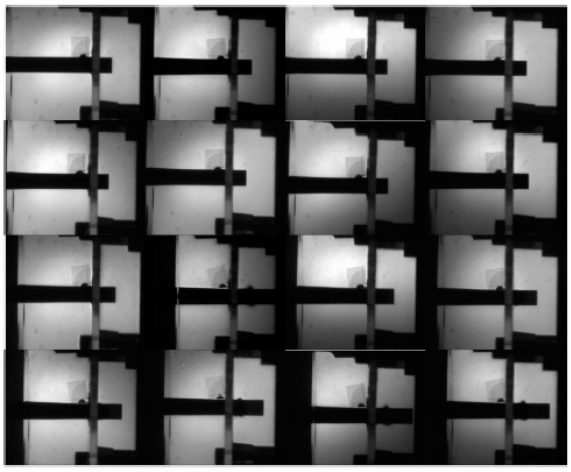

Shot 0541
Al+$Fe_2O_3$+60 *vol.%* epoxy
$U$ = 151.0 ± 1.7 m/s

**Figure B.6** High-speed camera images obtained from reverse Taylor impact experiment for Al+$Fe_2O_3$+60 *vol.%* epoxy composite (shot 0541).

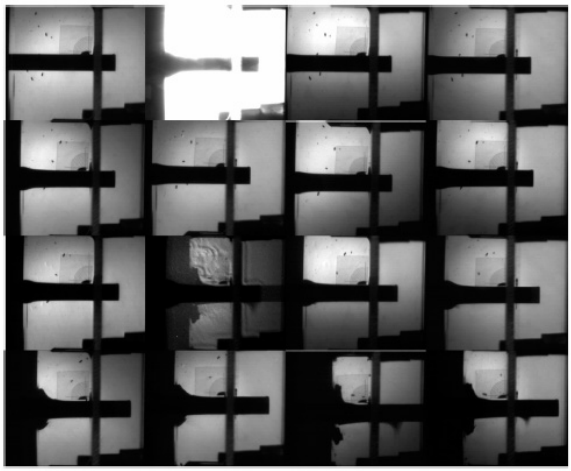

Shot 0535
Al+$Fe_2O_3$+60 *vol.%* epoxy
$U$ = 158.2 ± 2.7 m/s

**Figure B.7** High-speed camera images obtained from reverse Taylor impact experiment for Al+$Fe_2O_3$+60 *vol.%* epoxy composite (shot 0535).

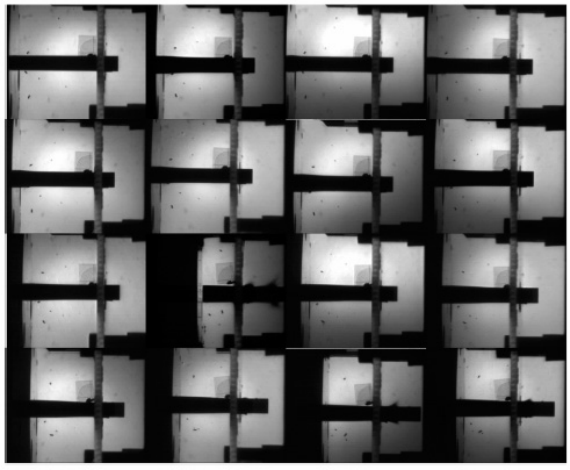

Shot 0542
Al+$Fe_2O_3$+60 *vol.%* epoxy
$U$ = 178.0 ± 5.6 m/s

**Figure B.8** High-speed camera images obtained from reverse Taylor impact experiment for Al+$Fe_2O_3$+60 *vol.%* epoxy composite (shot 0542).

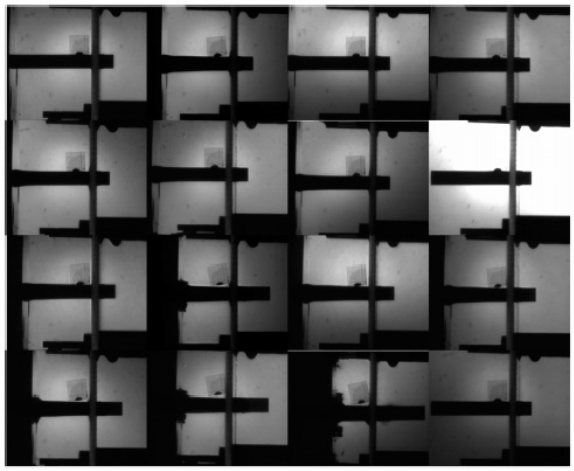

Shot 0544
Al+$Fe_2O_3$+60 *vol.%* epoxy
$U$ = 181.8 ± 2.6 m/s

**Figure B.9** High-speed camera images obtained from reverse Taylor impact experiment for Al+$Fe_2O_3$+60 *vol.%* epoxy composite (shot 0544).

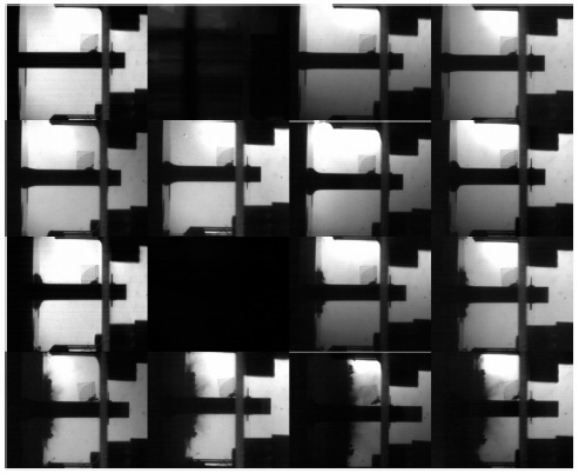

Shot 0531
Al+$Fe_2O_3$+60 *vol.%* epoxy
$U$ = 207.0 ± 2.6 m/s

**Figure B.10** High-speed camera images obtained from reverse Taylor impact experiment for Al+$Fe_2O_3$+60 *vol.%* epoxy composite (shot 0531).

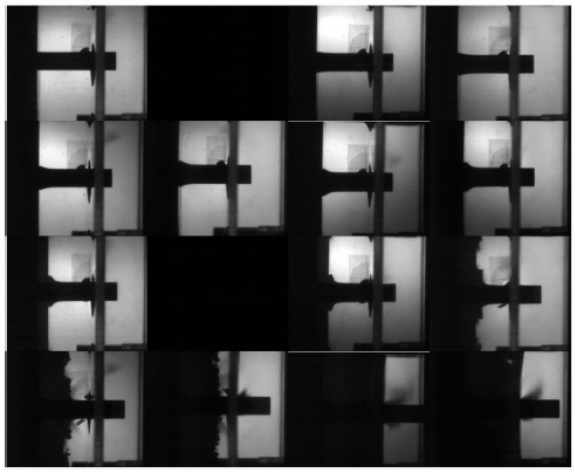

Shot 0536
Al+$Fe_2O_3$+60 *vol.%* epoxy
$U$ = 210.7 ± 7.1 m/s

**Figure B.11** High-speed camera images obtained from reverse Taylor impact experiment for Al+$Fe_2O_3$+60 *vol.%* epoxy composite (shot 0536).

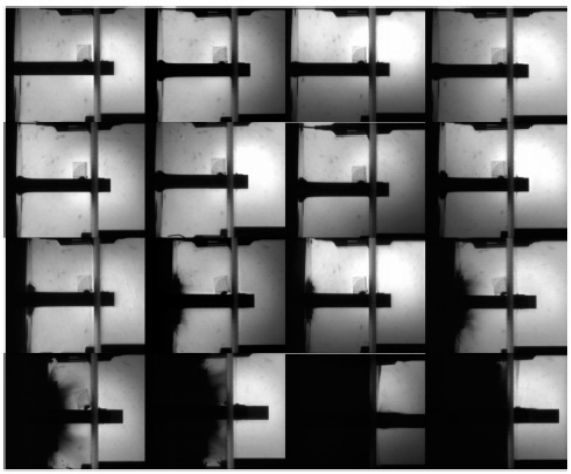

Shot 0603
Al+$Fe_2O_3$+60 *vol.%* epoxy
$U$ = 236.6 ± 4.3 m/s

**Figure B.12** High-speed camera images obtained from reverse Taylor impact experiment for Al+$Fe_2O_3$+60 *vol.%* epoxy composite (shot 0603).

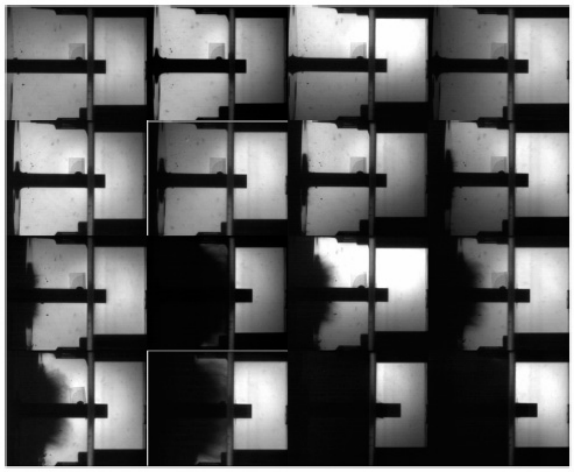

Shot 0644
Al+$Fe_2O_3$+60 *vol.%* epoxy
$U$ = 423.2 ± 0.1 m/s

**Figure B.13** High-speed camera images obtained from reverse Taylor impact experiment for Al+$Fe_2O_3$+60 *vol.%* epoxy composite (shot 0644).

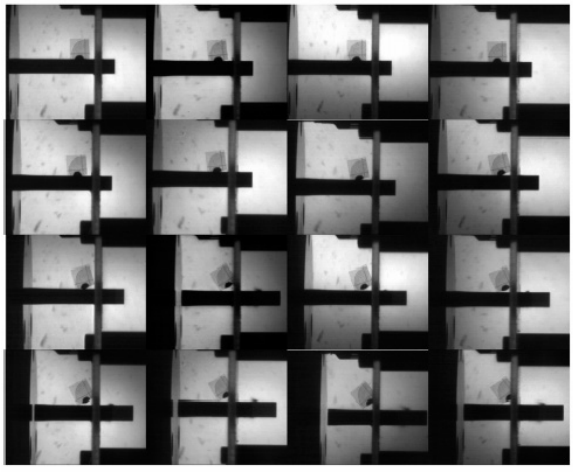

Shot 0617
Al+$Fe_2O_3$+70 *vol.%* epoxy
$U$ = 105.9 ± 0.6 m/s

**Figure B.14** High-speed camera images obtained from reverse Taylor impact experiment for Al+$Fe_2O_3$+70 *vol.%* epoxy composite (shot 0617).

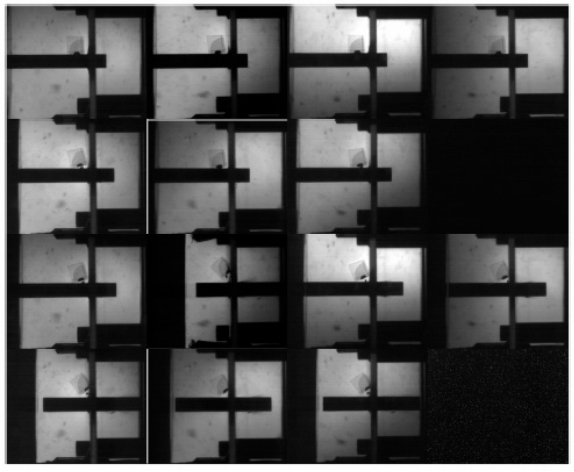

Shot 0648
nano-Al+$Fe_2O_3$+70 *vol.%* epoxy
$U$ = 97.8 ± 1.5 m/s

**Figure B.15** High-speed camera images obtained from reverse Taylor impact experiment for nano-Al+$Fe_2O_3$+70 *vol.%* epoxy composite (shot 0648).

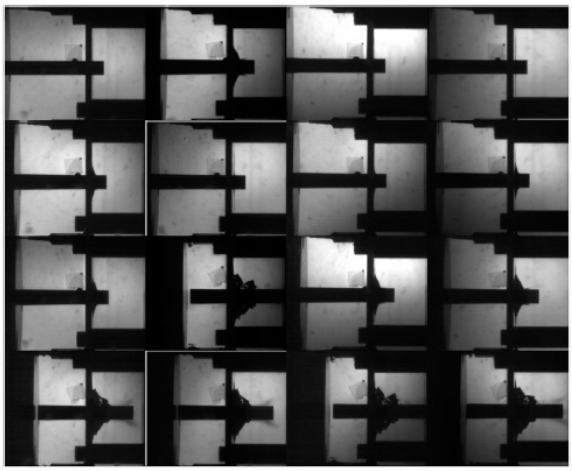

Shot 0649
nano-Al+$Fe_2O_3$+70 *vol.%* epoxy
$U$ = 143.6 ± 0.4 m/s

**Figure B.16** High-speed camera images obtained from reverse Taylor impact experiment for nano-Al+$Fe_2O_3$+70 *vol.%* epoxy composite (shot 0649).

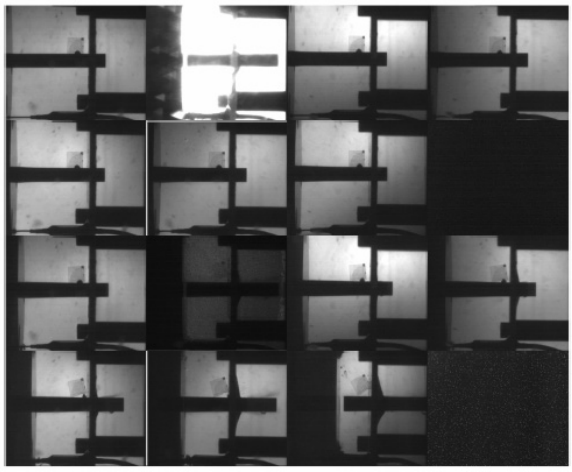

Shot 0650
nano-Al+$Fe_2O_3$+70 *vol.%* epoxy
$U$ = 175.2 ± 0.3 m/s

**Figure B.17** High-speed camera images obtained from reverse Taylor impact experiment for nano-Al+$Fe_2O_3$+70 *vol.%* epoxy composite (shot 0650).

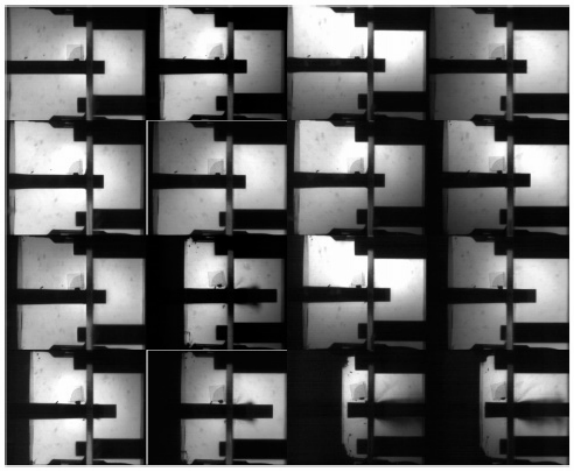

Shot 0645
nano-Al+$Fe_2O_3$+70 *vol.%* epoxy
$U$ = 201.1 ± 1.2 m/s

**Figure B.18** High-speed camera images obtained from reverse Taylor impact experiment for nano-Al+$Fe_2O_3$+70 *vol.%* epoxy composite (shot 0645).

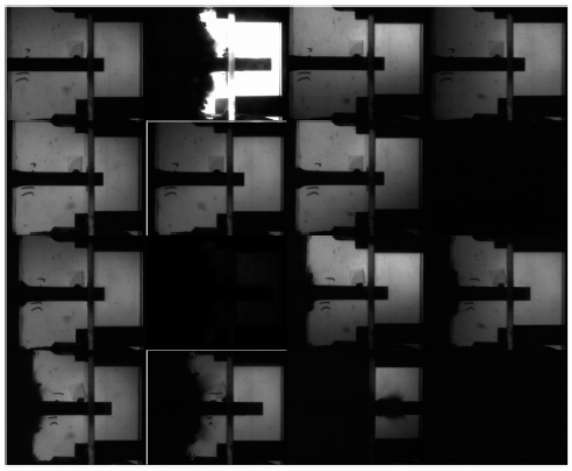

Shot 0647
nano-Al+$Fe_2O_3$+70 *vol.%* epoxy
$U$ = 235.3 ± 1.1 m/s

**Figure B.19** High-speed camera images obtained from reverse Taylor impact experiment for nano-Al+$Fe_2O_3$+70 *vol.%* epoxy composite (shot 0647).

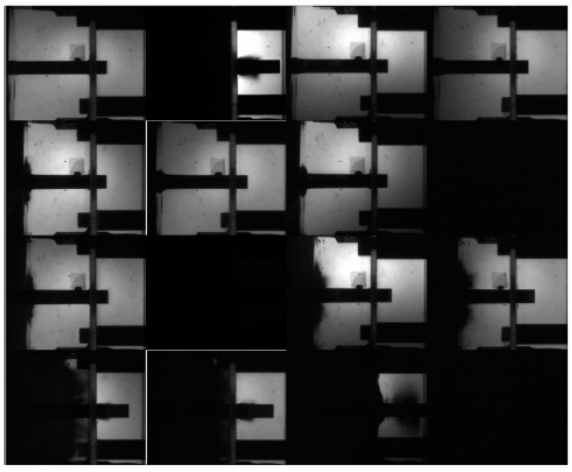

Shot 0646
nano-Al+$Fe_2O_3$+70 *vol.%* epoxy
$U$ = 288.3 ± 0.9 m/s

**Figure B.20** High-speed camera images obtained from reverse Taylor impact experiment for nano-Al+$Fe_2O_3$+70 *vol.%* epoxy composite (shot 0646).

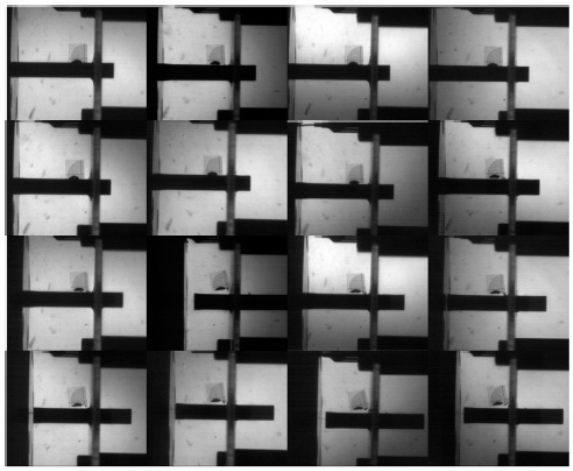

Shot 0616
Al+$Fe_2O_3$+78 *vol.%* epoxy
$U$ = 94.0 ± 0.7 m/s

**Figure B.21** High-speed camera images obtained from reverse Taylor impact experiment for Al+$Fe_2O_3$+78 *vol.%* epoxy composite (shot 0616).

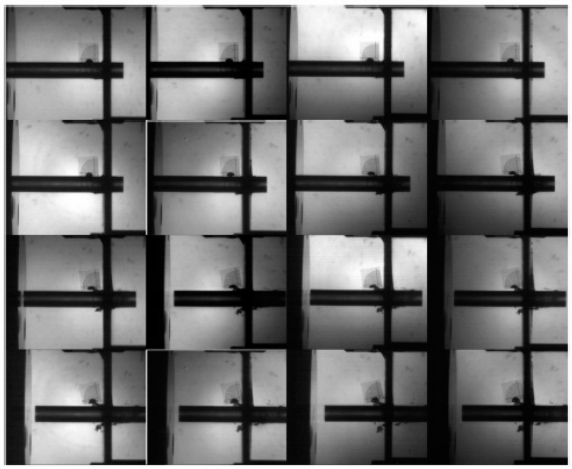

Shot 0637
100 *vol.%* epoxy (Batch A)
$U = 66.4 \pm 0.4$ m/s

**Figure B.22** High-speed camera images obtained from reverse Taylor impact experiment for 100 *vol.%* epoxy composite (shot 0637).

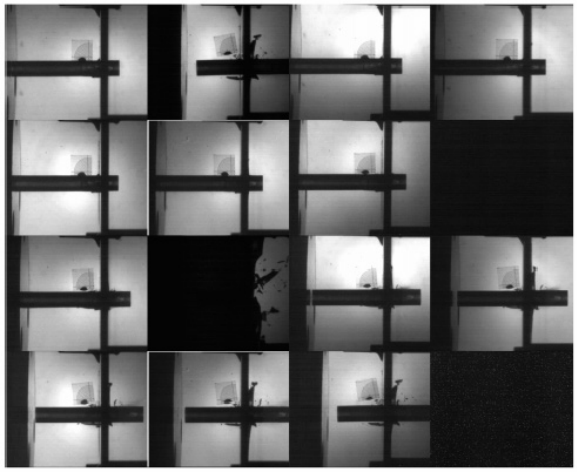

Shot 0638
100 *vol.%* epoxy (Batch A)
$U = 98.7 \pm 0.6$ m/s

**Figure B.23** High-speed camera images obtained from reverse Taylor impact experiment for 100 *vol.%* epoxy composite (shot 0638).

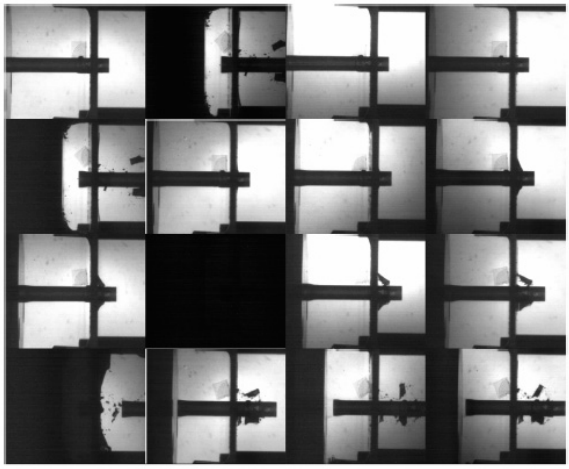

Shot 0640
100 *vol.%* epoxy (Batch A)
$U = 127.9 \pm 0.7$ m/s

**Figure B.24** High-speed camera images obtained from reverse Taylor impact experiment for 100 *vol.%* epoxy composite (shot 0640).

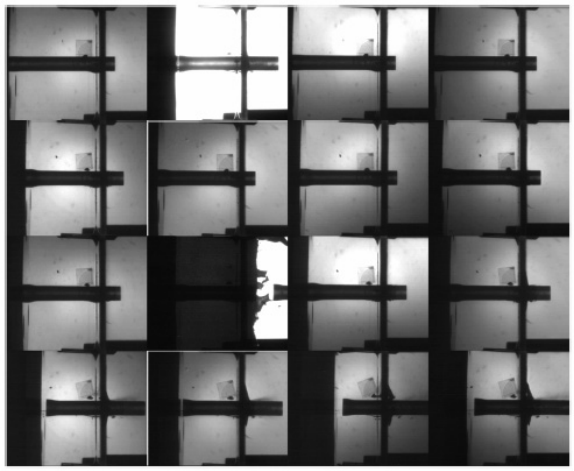

Shot 0639
100 *vol.%* epoxy (Batch A)
$U = 143.2 \pm 0.6$ m/s

**Figure B.25** High-speed camera images obtained from reverse Taylor impact experiment for 100 *vol.%* epoxy composite (shot 0639).

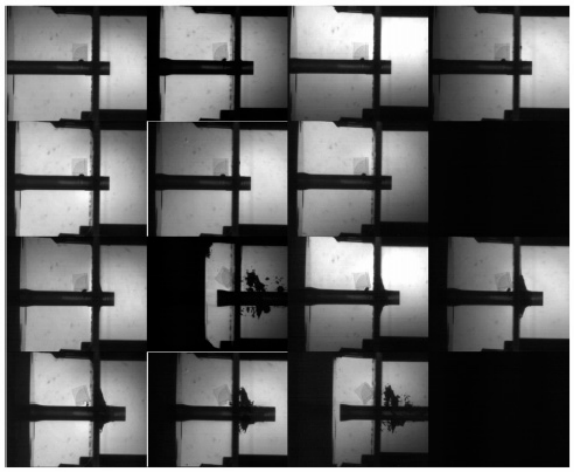

Shot 0641
100 *vol.%* epoxy (Batch A)
$U = 150.3 \pm 0.8$ m/s

**Figure B.26** High-speed camera images obtained from reverse Taylor impact experiment for 100 *vol.%* epoxy composite (shot 0641).

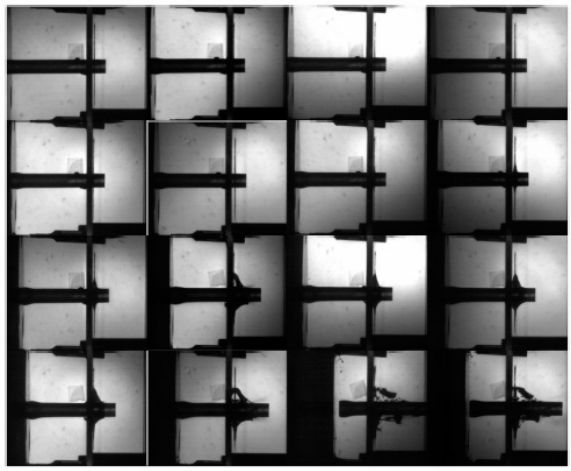

Shot 0643
100 *vol.%* epoxy (Batch A)
$U = 166.7 \pm 1.1$ m/s

**Figure B.27** High-speed camera images obtained from reverse Taylor impact experiment for 100 *vol.%* epoxy composite (shot 0643).

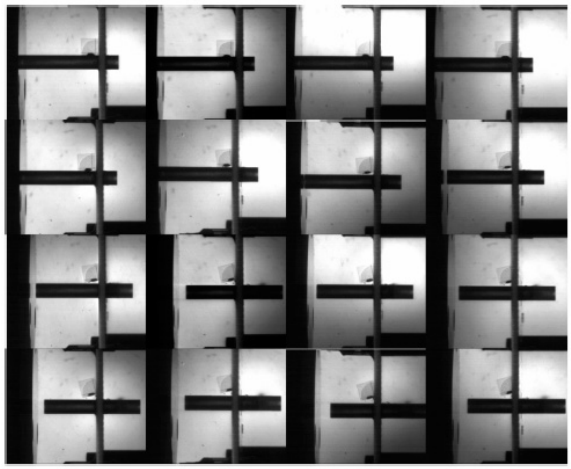

Shot 0601
100 *vol.%* epoxy (Batch B)
$U = 65.6 \pm 0.7$ m/s

**Figure B.28** High-speed camera images obtained from reverse Taylor impact experiment for 100 *vol.%* epoxy composite (shot 0601).

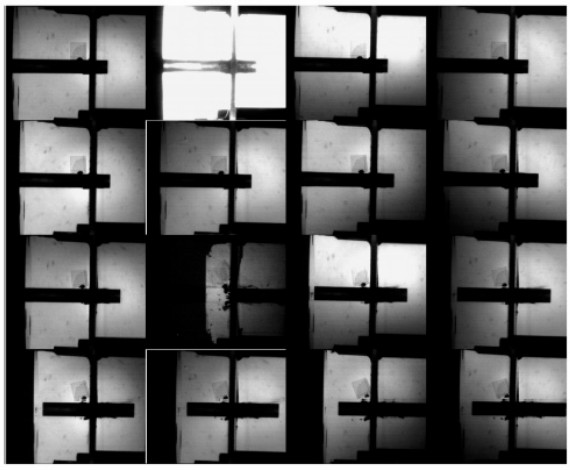

Shot 0642
100 *vol.%* epoxy (Batch B)
$U = 104.1 \pm 0.7$ m/s

**Figure B.29** High-speed camera images obtained from reverse Taylor impact experiment for 100 *vol.%* epoxy composite (shot 0642).

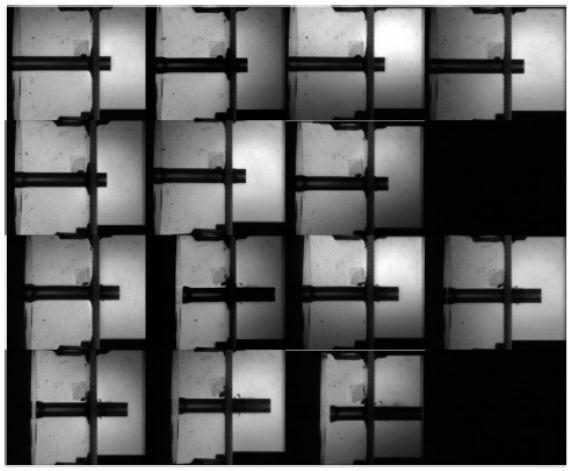

Shot 0602
100 *vol.%* epoxy (Batch B)
$U = 121.0 \pm 0.5$ m/s

**Figure B.30** High-speed camera images obtained from reverse Taylor impact experiment for 100 *vol.%* epoxy composite (shot 0602).

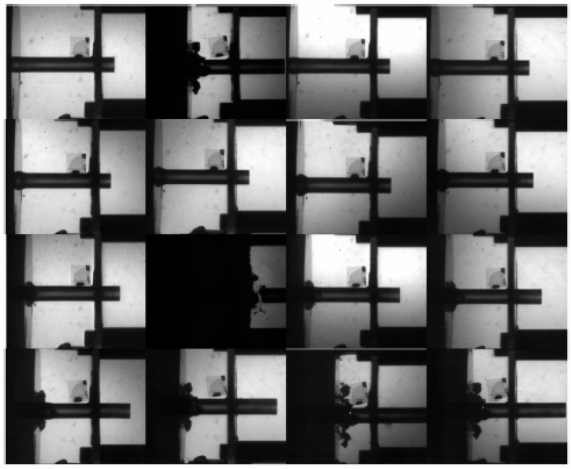


**Figure B.31** High-speed camera images obtained from reverse Taylor impact experiment for 100 *vol.%* epoxy composite (shot 0614).


**Figure B.32** High-speed camera images obtained from reverse Taylor impact experiment for 100 *vol.%* epoxy composite (shot 0613).

# APPENDIX C: Hugoniot Equation of State Data

Several equation of state experiments (EOS) using the Georgia Tech. compressed-gas gun were conducted for Al+$Fe_2O_3$ epoxy-cast composites with 60 and 78 *vol.%* epoxy. Shown below are the *a*) voltage waveforms and converted *b*) current, *c*) charge, and *d*) stress traces, using PlotData software [165], obtained from the PVDF gauges located on the impact and back surfaces of the epoxy-cast target materials. The waveforms obtained for each experiment are shown in Figure C.1 to C.10.

The complete voltage signal was not obtained for shots 0303 (Figure C.7) and 0308 (Figure C.8), where the peak voltages for the impact and propagated gauges were cut-off, respectively. These experiments were conducted for the Al+$Fe_2O_3$+78 *vol.%* epoxy composite and show only a portion of the voltage signal captured, thus, not allowing the calculation of stress. However, this did not impact the composite's Hugoniot, since shock velocity was still experimentally determined from the arrival signal in the propagated gauge (shot 0308). Shot 0303 was conducted on a lower density specimen with a significant amount of porosity and not included on the overall material's Hugoniot behavior.

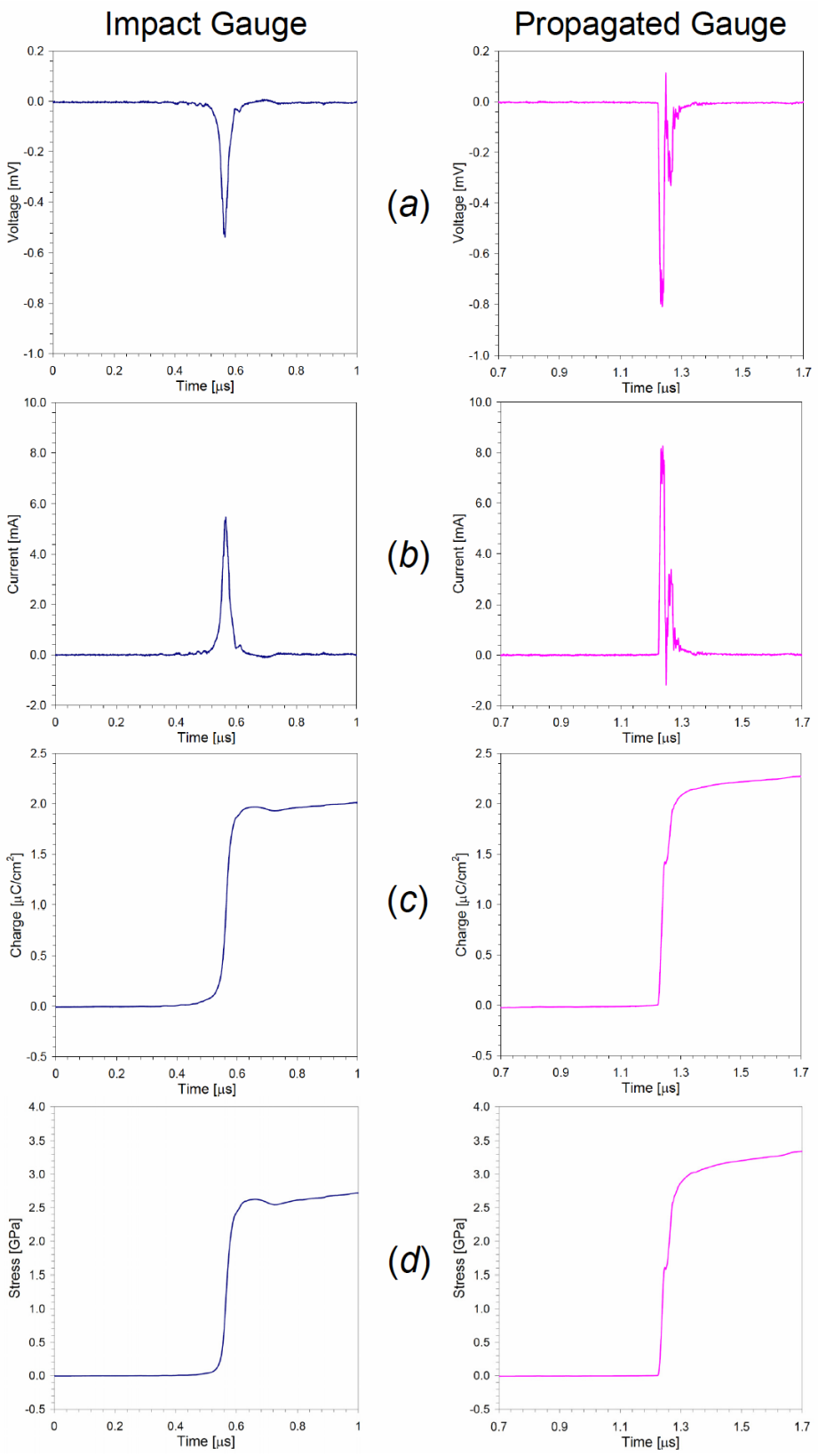


**Figure C.1** The *a*) voltage, *b*) current, *c*) charge, and *d*) stress waveforms obtained from impact (*left*) and propagated (*right*) gauge records for shot 0627.

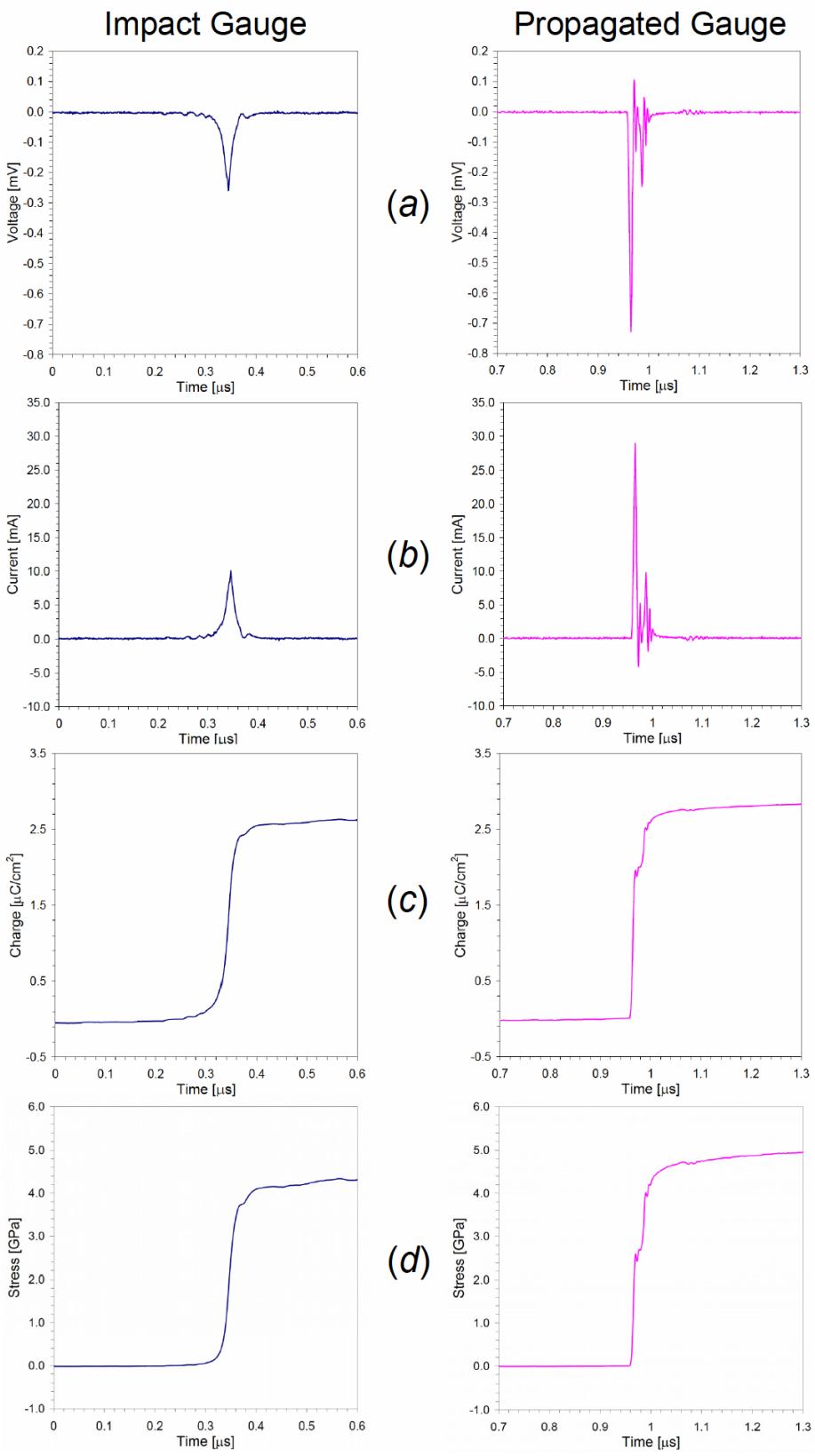


**Figure C.2** The *a*) voltage, *b*) current, *c*) charge, and *d*) stress waveforms obtained from impact (*left*) and propagated (*right*) gauge records for shot 0505.

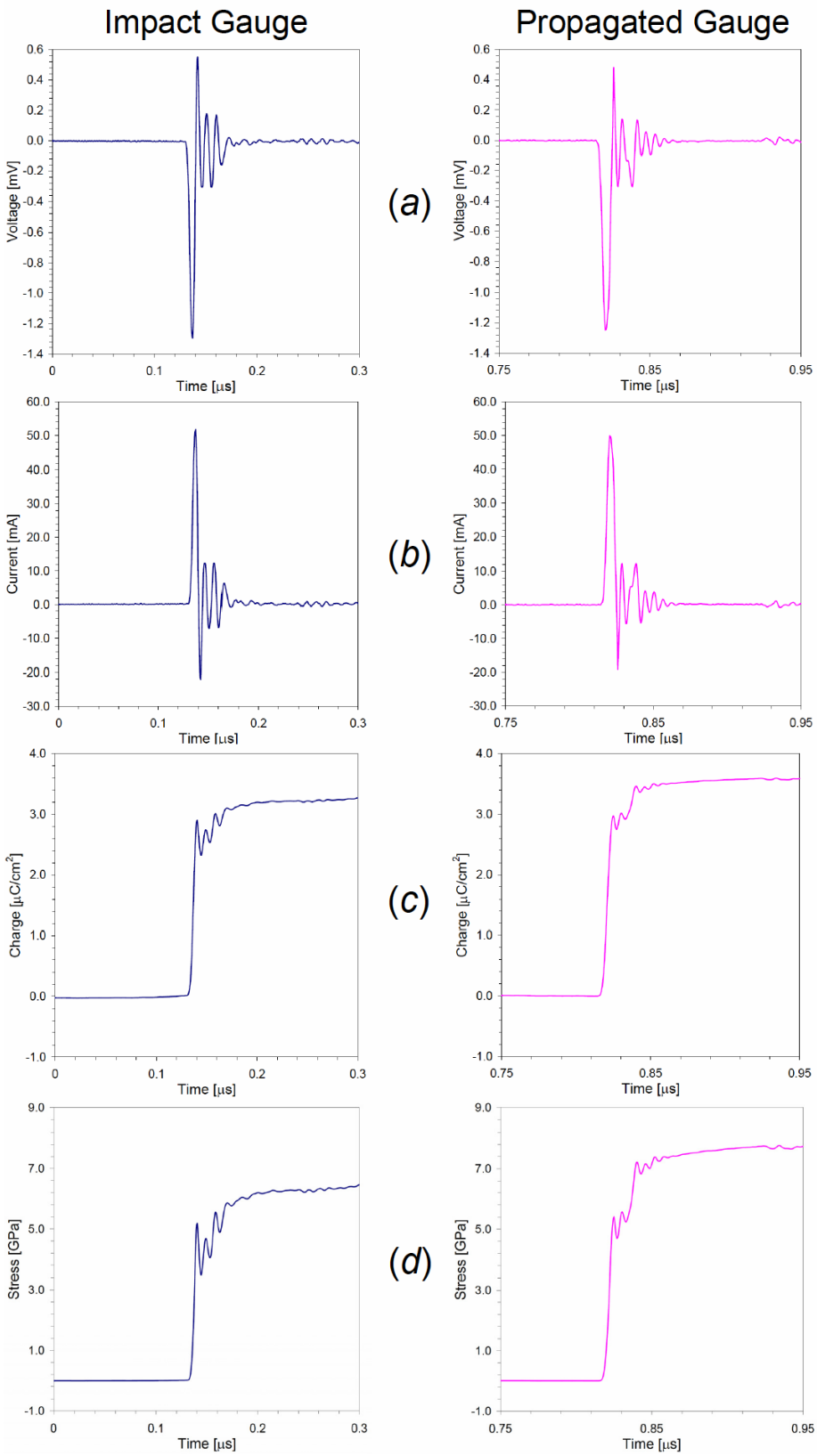


**Figure C.3** The *a*) voltage, *b*) current, *c*) charge, and *d*) stress waveforms obtained from impact (*left*) and propagated (*right*) gauge records for shot 0608.

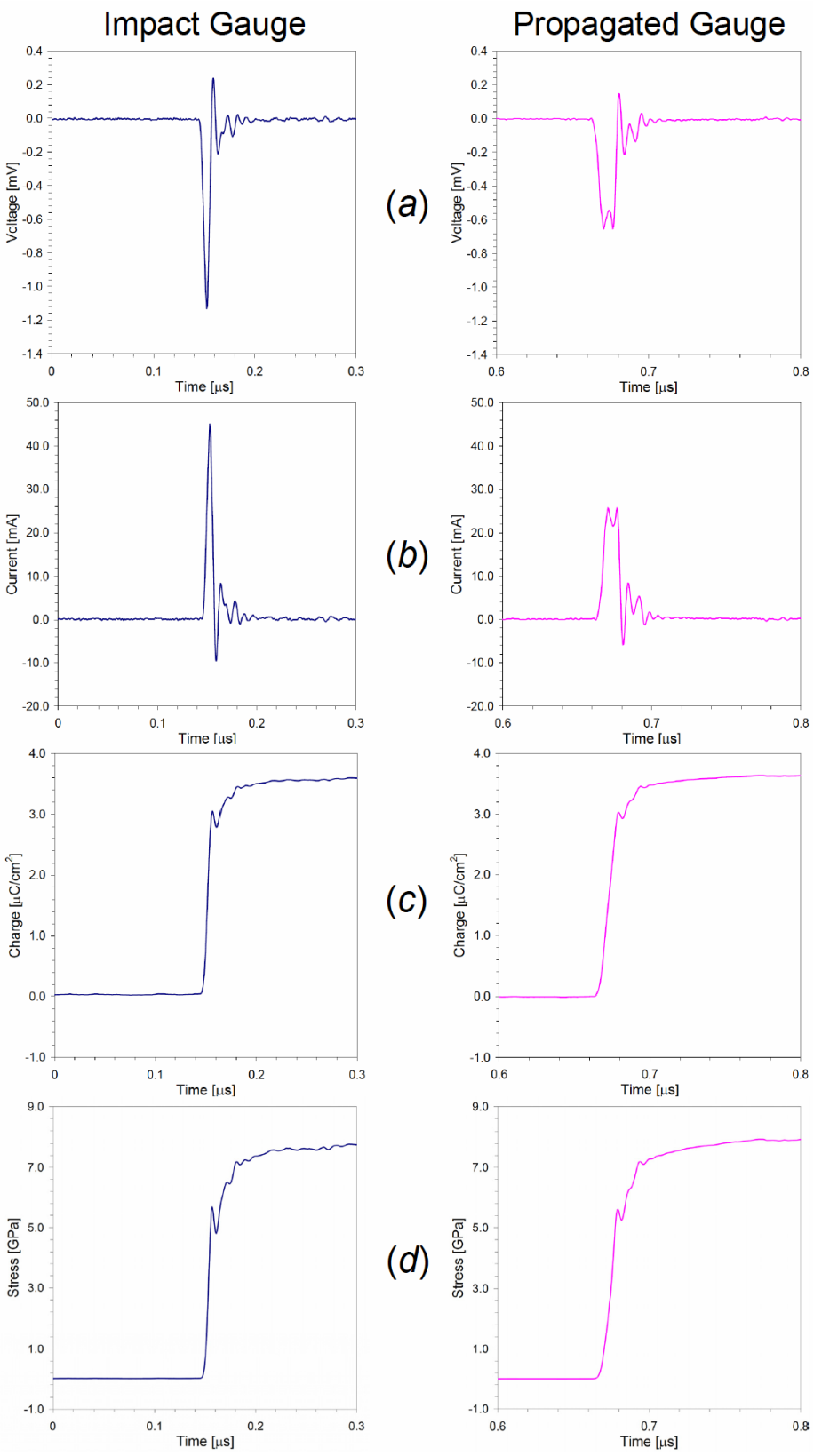


**Figure C.4** The *a*) voltage, *b*) current, *c*) charge, and *d*) stress waveforms obtained from impact (*left*) and propagated (*right*) gauge records for shot 0507.

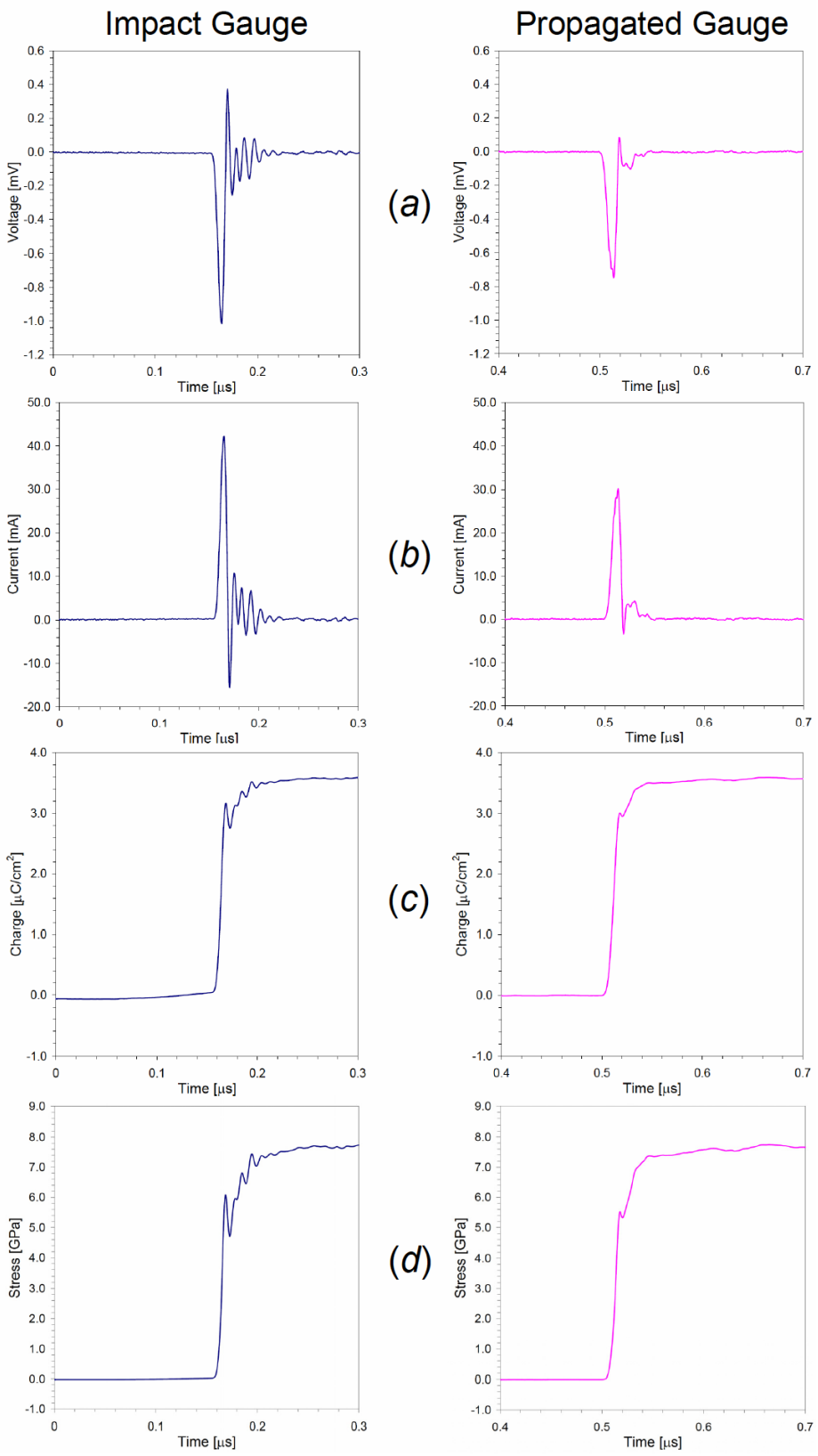


**Figure C.5** The *a*) voltage, *b*) current, *c*) charge, and *d*) stress waveforms obtained from impact (*left*) and propagated (*right*) gauge records for shot 0628.

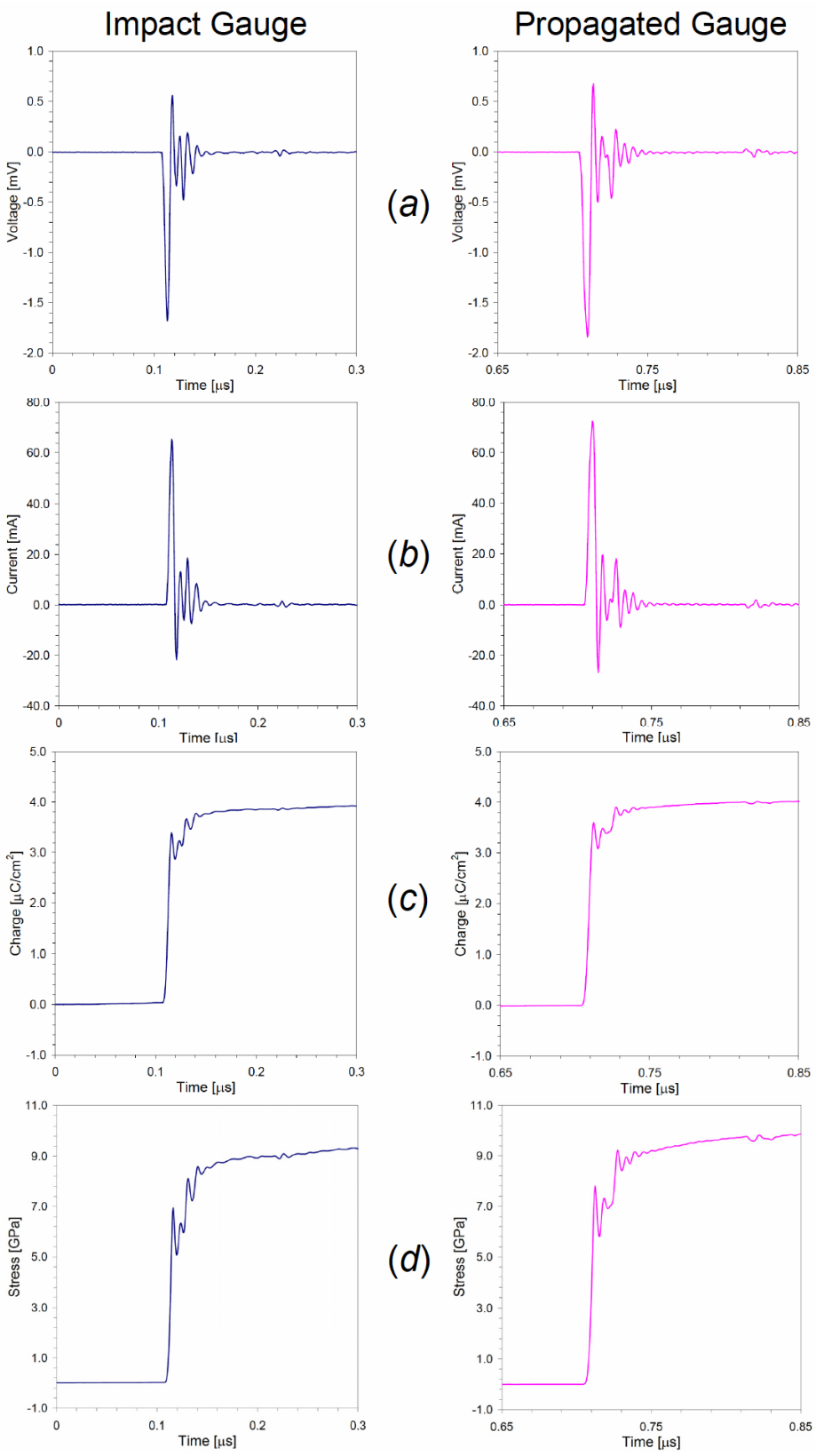


**Figure C.6** The *a*) voltage, *b*) current, *c*) charge, and *d*) stress waveforms obtained from impact (*left*) and propagated (*right*) gauge records for shot 0609.

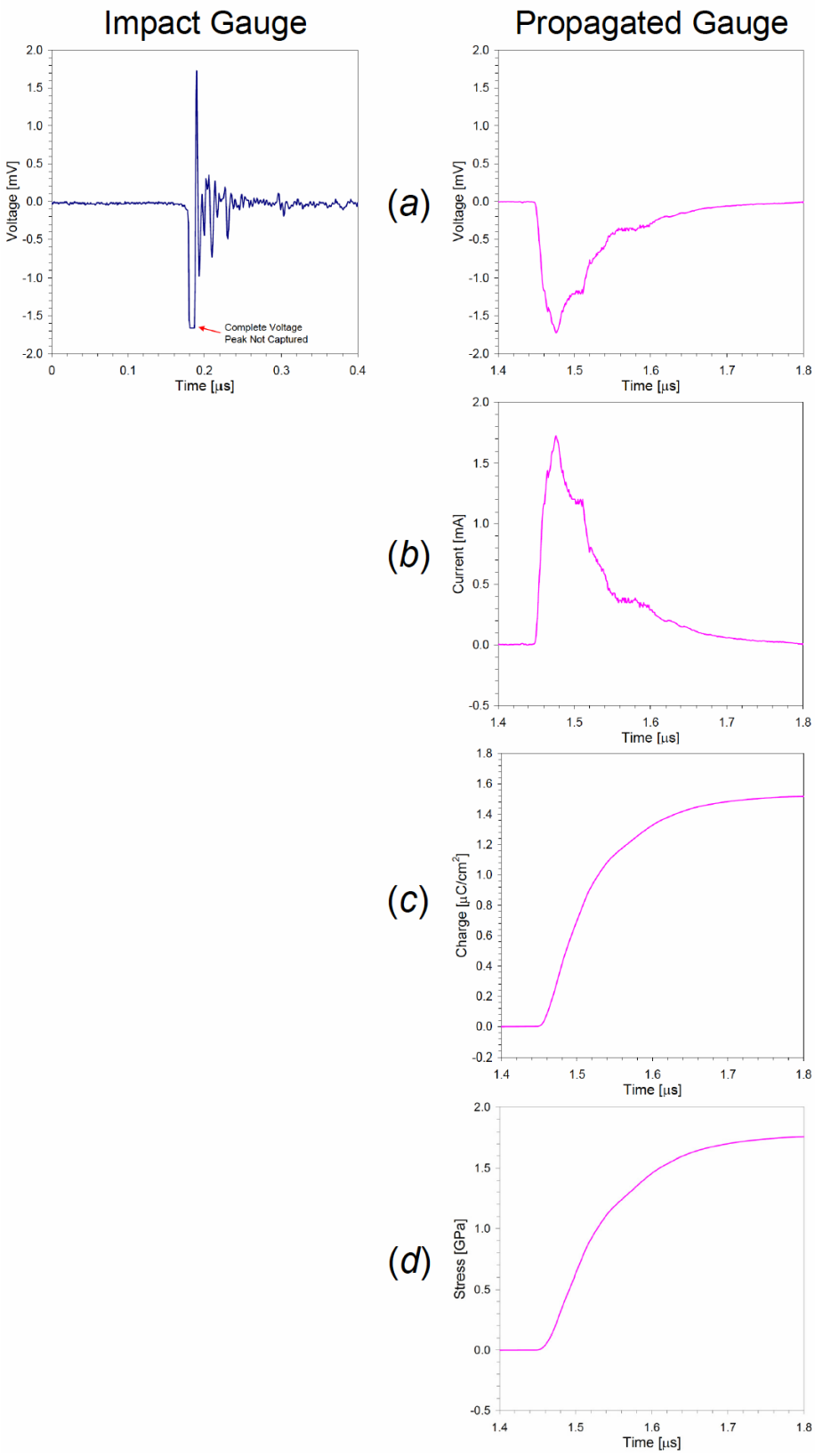


**Figure C.7** The *a*) voltage, *b*) current, *c*) charge, and *d*) stress waveforms obtained from impact (*left*) and propagated (*right*) gauge records for shot 0303.

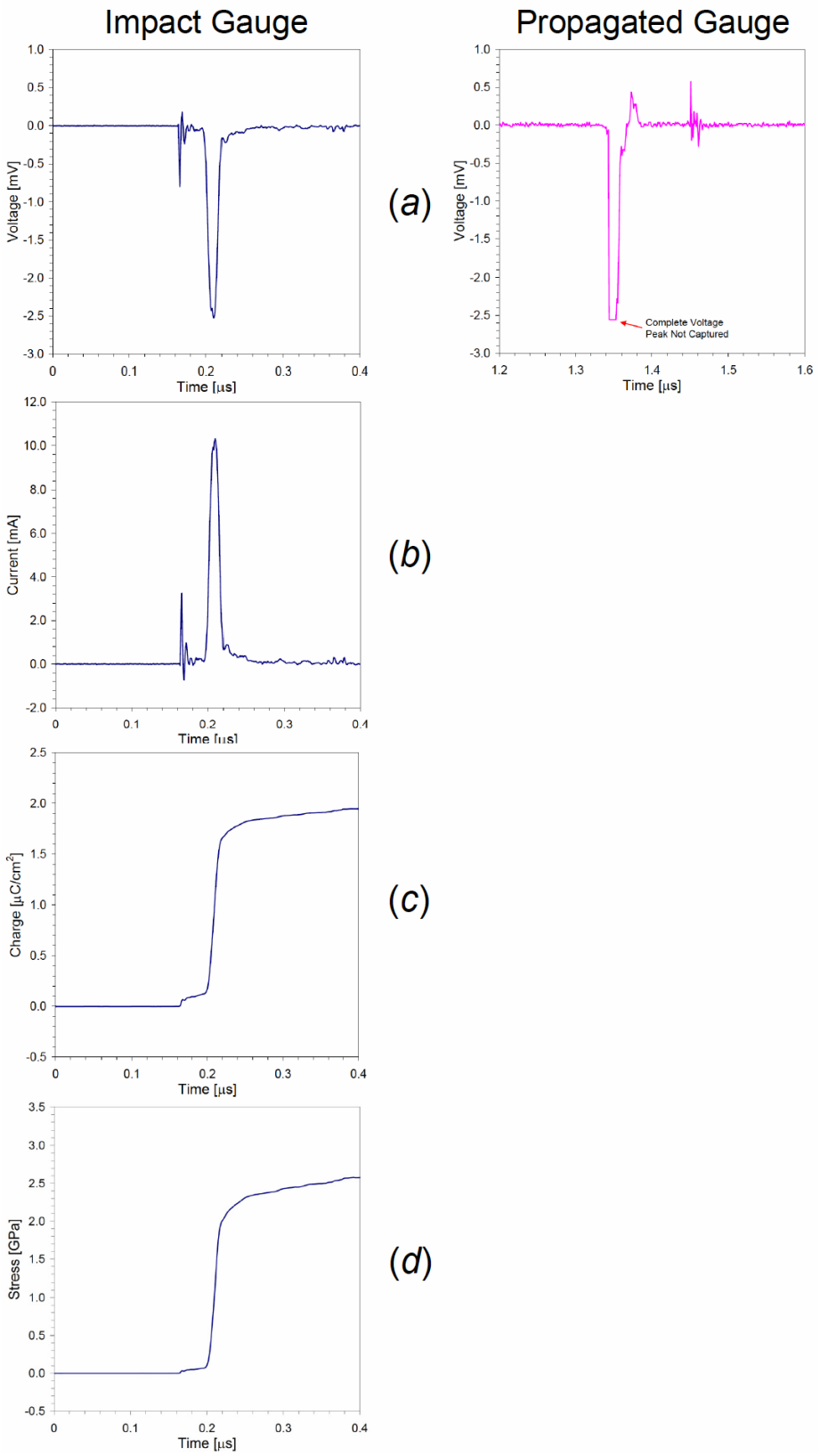


**Figure C.8** The *a*) voltage, *b*) current, *c*) charge, and *d*) stress waveforms obtained from impact (*left*) and propagated (*right*) gauge records for shot 0308.

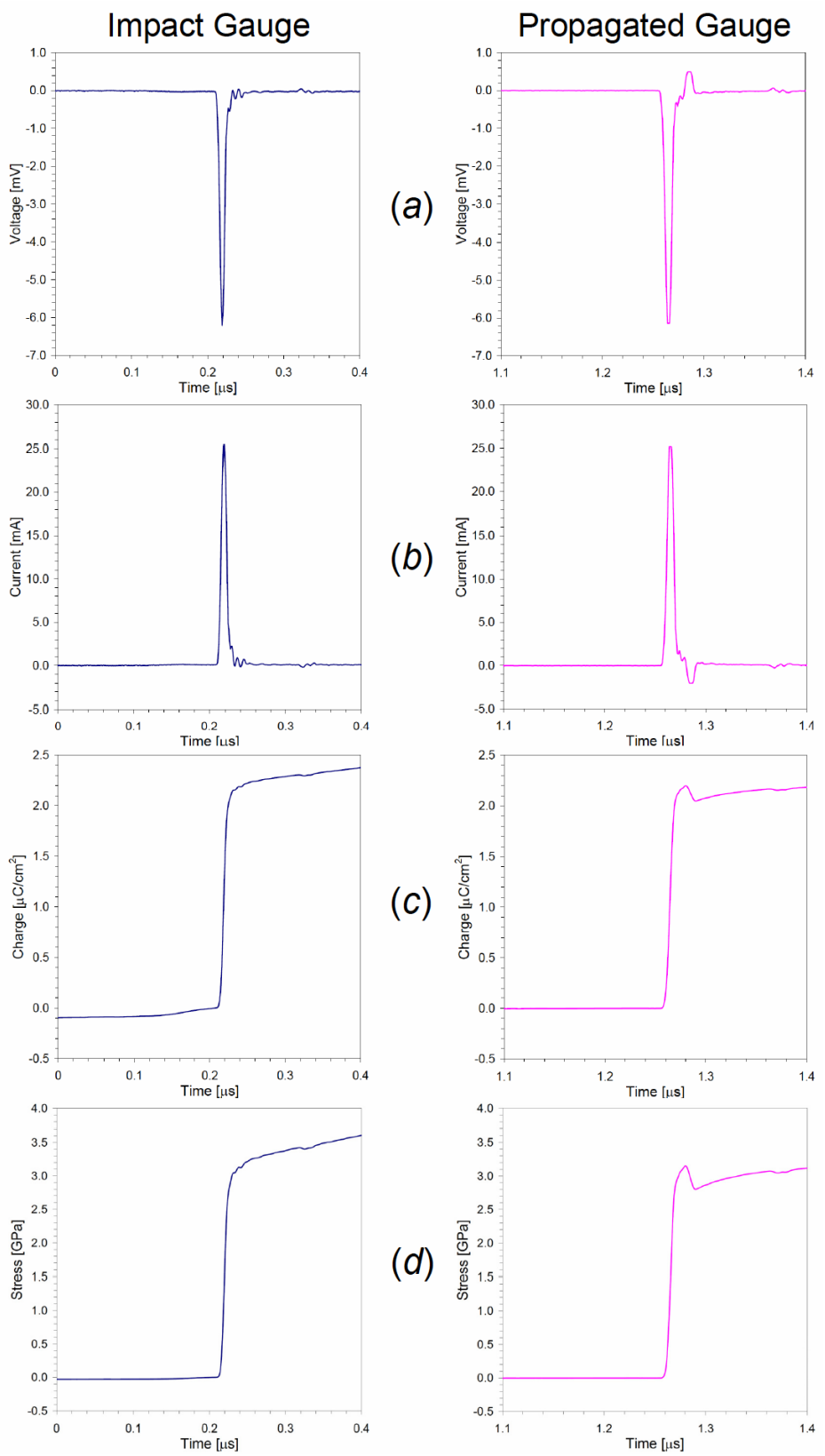


**Figure C.9** The *a*) voltage, *b*) current, *c*) charge, and *d*) stress waveforms obtained from impact (*left*) and propagated (*right*) gauge records for shot 0311.

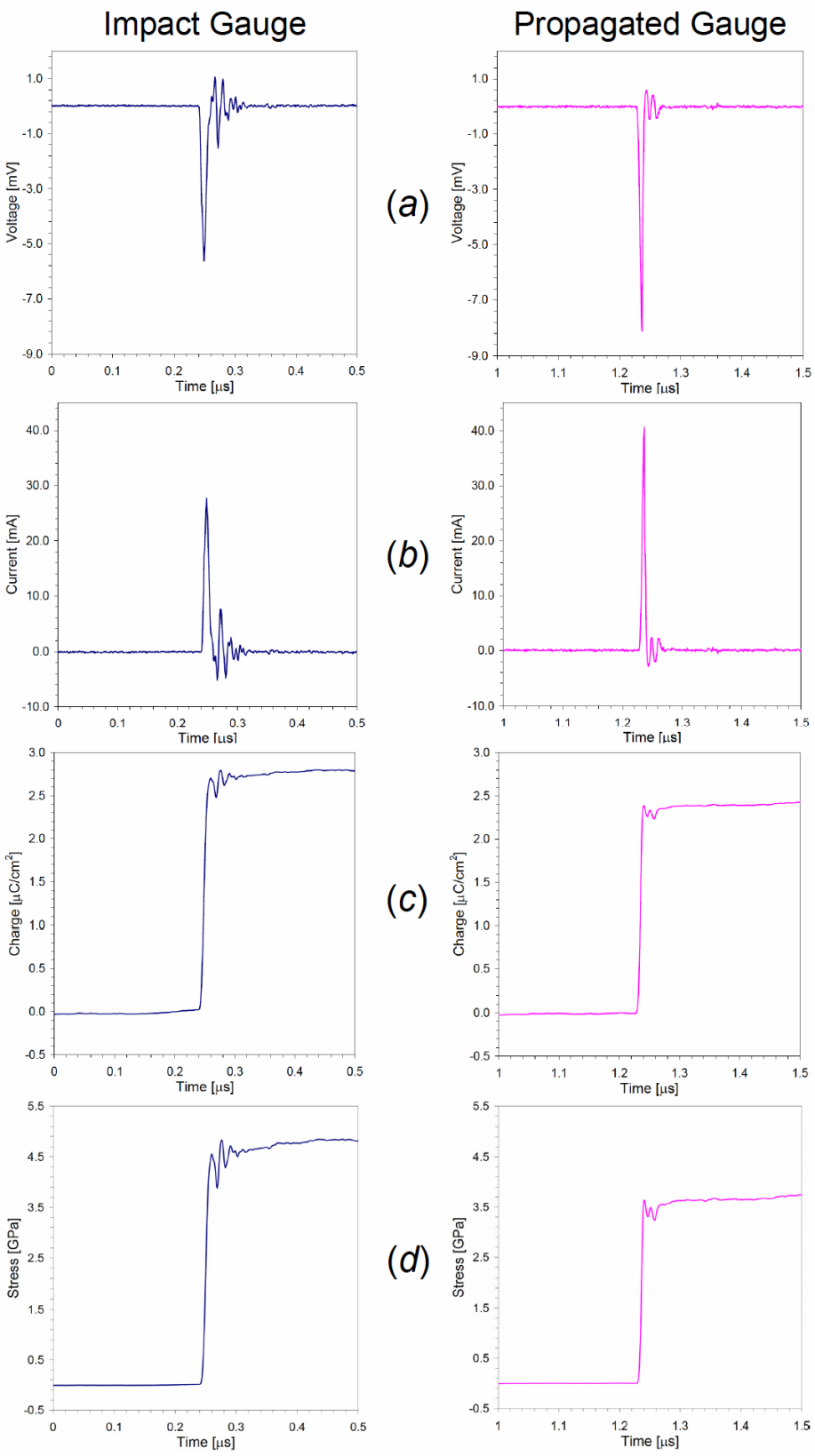


**Figure C.10** The *a*) voltage, *b*) current, *c*) charge, and *d*) stress waveforms obtained from impact (*left*) and propagated (*right*) gauge records for shot 0403.

# APPENDIX D: One-Dimensional CTH Simulation Snapshots

One-dimensional simulations using the Eulerian hydrodynamic code CTH [213-215] were conducted for each parallel-plate impact experiment performed for the Al+$Fe_2O_3$+60 *vol.%* epoxy composite. The exact configuration utilized for these experiments is duplicated in the CTH DIATOM description. The calculations use a one-dimensional spatial mesh with a resolution of 12.5 μm. Tracer points, which record the state variables, were positioned within the center of the impact and propagated gauge layers located on either side of the epoxy-cast target material.

The snapshots show the stress and particle velocity waveforms propagating within each material that comprise the target assembly for select time instances, in addition to the compressibility in terms of density changes. Typically, the first frame corresponds to the arrival of the stress wave within the target material. This is followed by the propagation of the disturbance wave through the target and reaching the target/fused silica window interface or propagated gauge location. The next snapshot shows the reflected waves from the back of the flyer and target/window interface approaching each other. The final snapshot shows the arrival of the release wave at the impact gauge location. Snapshots obtained for each experiment conducted for the Al+$Fe_2O_3$+60 *vol.%* epoxy composite are shown in Figure D.1 to D.6.

Shot 0627 and 0505 were symmetric type impacts, where the flyer and target are identical materials and therefore, the snapshots only show the flyer, target, and window materials comprising the target assembly. The remaining experiments use either a copper or tungsten flyer impacting a copper driver. Refer to Table 4.21 for a complete summary of these experiments.

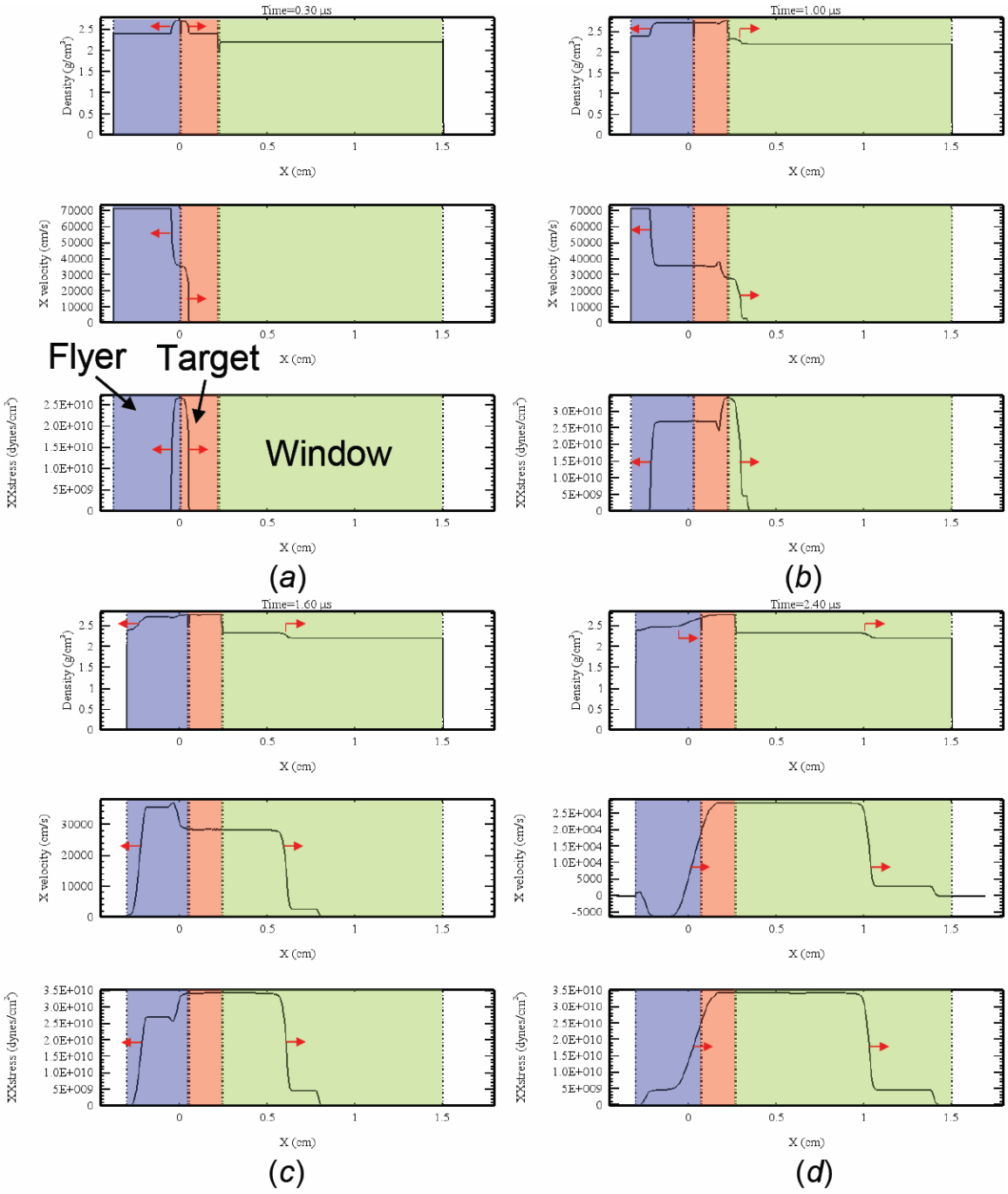


**Figure D.1** Captured CTH simulation snapshots illustrating the waveform propagation (direction indicated by arrows) within the materials that make up the target assembly for shot 0627. The snapshots are captured at *a*) 0.3, *b*) 1.0 *c*) 1.6, and *d*) 2.4 µs after impact and show the variation of density, particle velocity, and stress waveform profiles (in order top-to-bottom) throughout the target assembly.

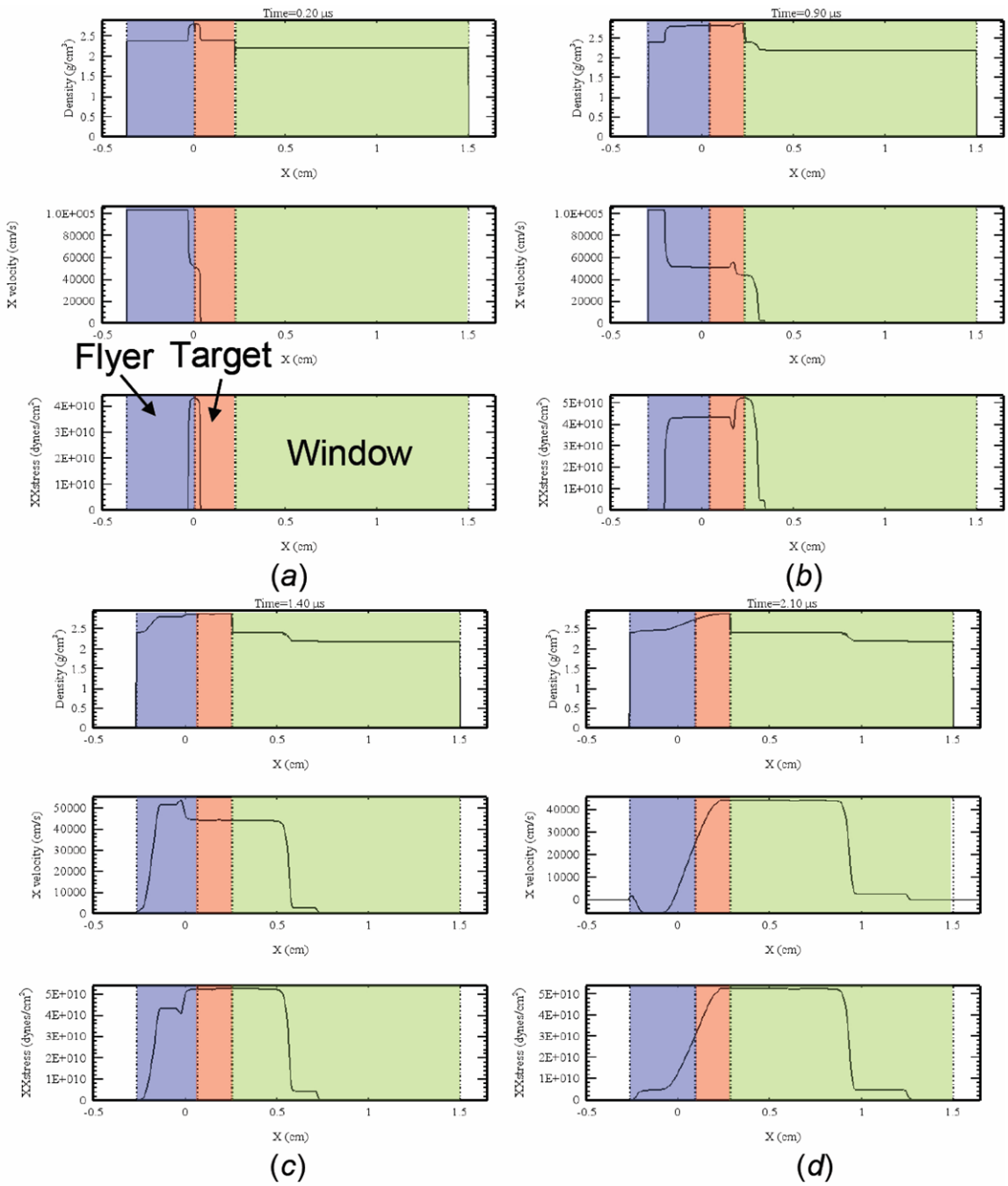


**Figure D.2** Captured CTH simulation snapshots illustrating the waveform propagation within the materials that make up the target assembly for shot 0505. The snapshots are captured at *a*) 0.2, *b*) 0.9 *c*) 1.4, and *d*) 2.1 µs after impact and show the variation of density, particle velocity, and stress waveform profiles (in order top-to-bottom) throughout the target assembly.

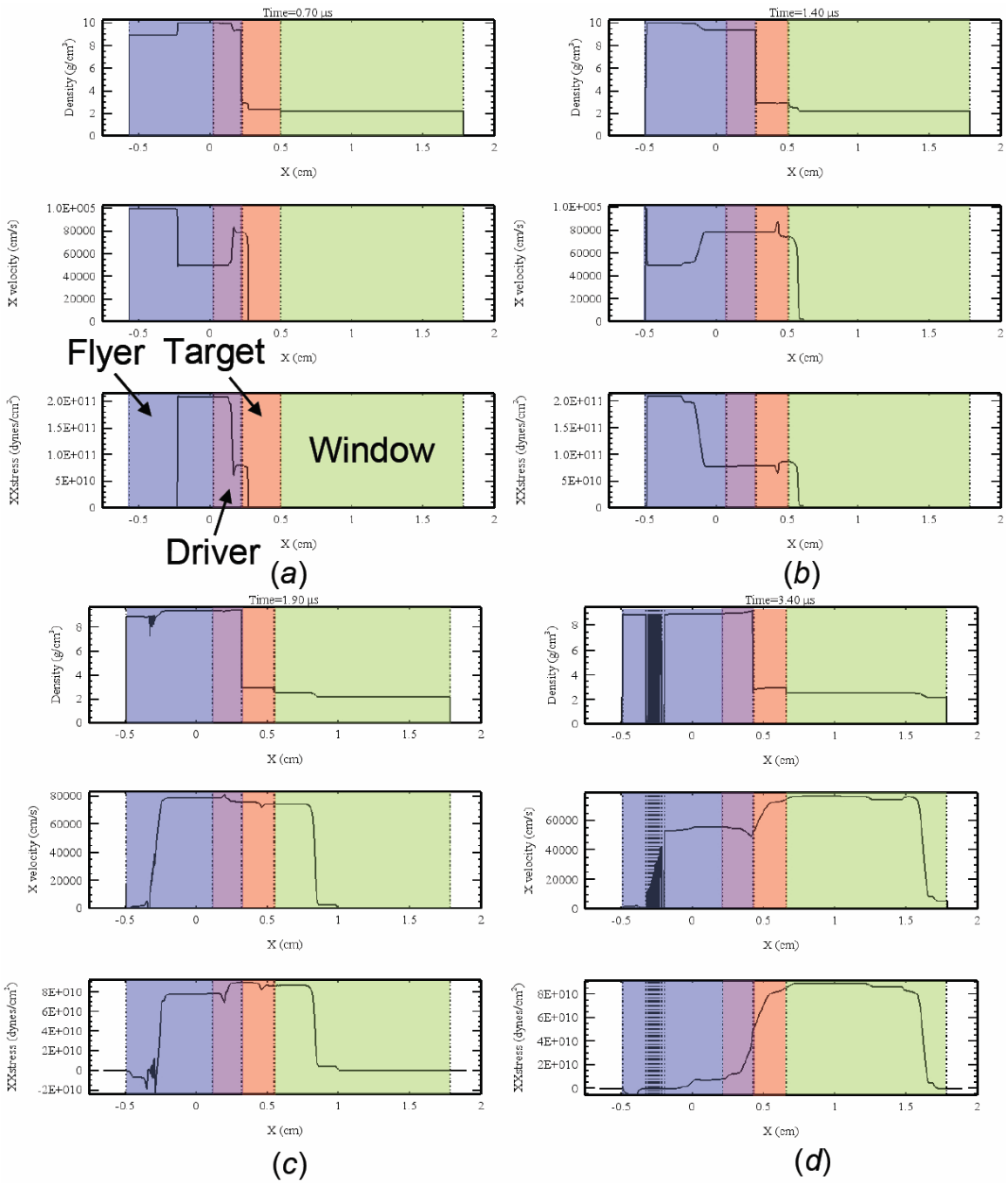


**Figure D.3** Captured CTH simulation snapshots illustrating the waveform propagation within the materials that make up the target assembly for shot 0608. The snapshots are captured at *a*) 0.7, *b*) 1.4 *c*) 1.9, and *d*) 3.4 µs after impact and show the variation of density, particle velocity, and stress waveform profiles (in order top-to-bottom) throughout the target assembly.

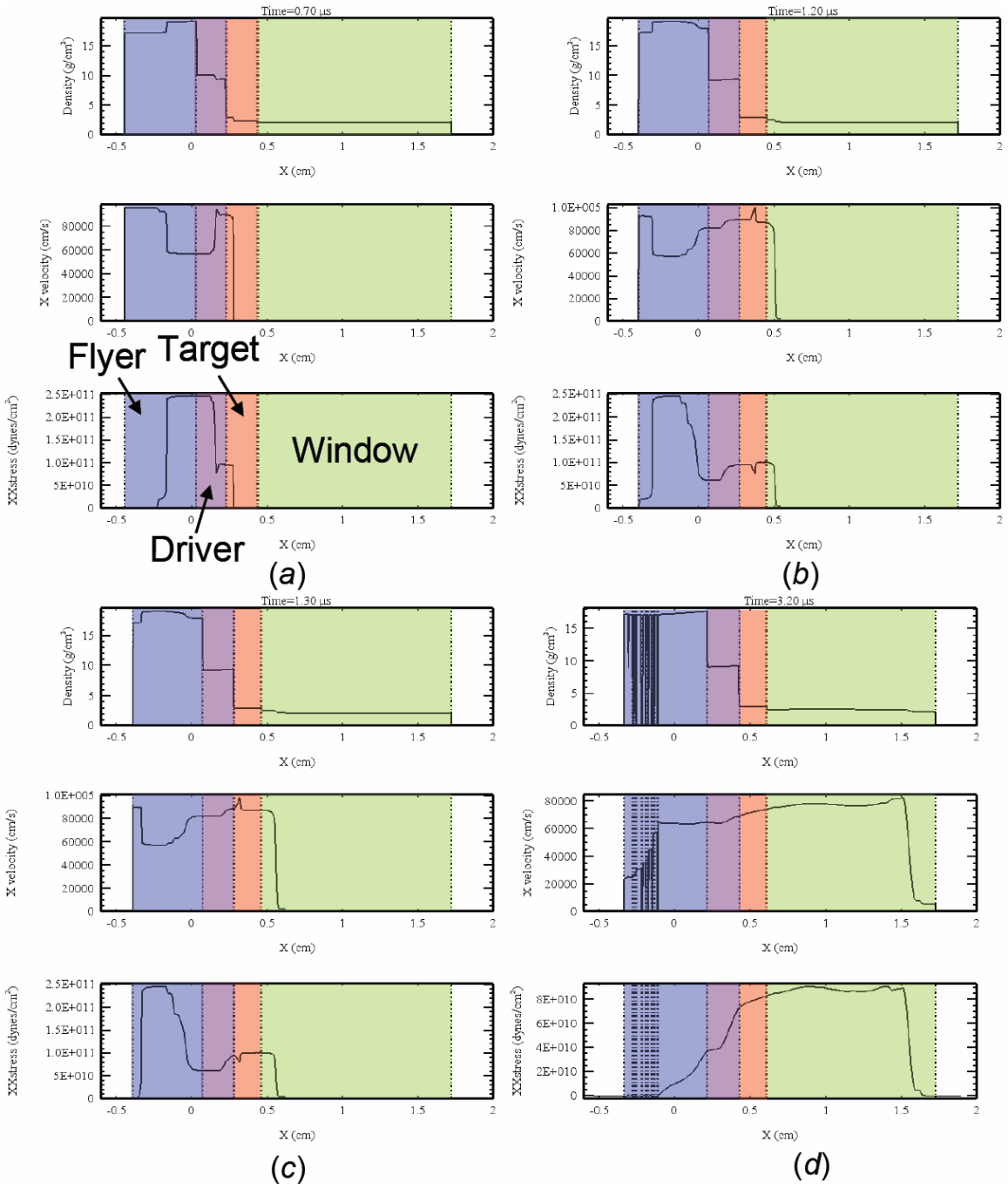


**Figure D.4** Captured CTH simulation snapshots illustrating the waveform propagation within the materials that make up the target assembly for shot 0507. The snapshots are captured at *a*) 0.7, *b*) 1.2 *c*) 1.3, and *d*) 3.2 µs after impact and show the variation of density, particle velocity, and stress waveform profiles (in order top-to-bottom) throughout the target assembly.

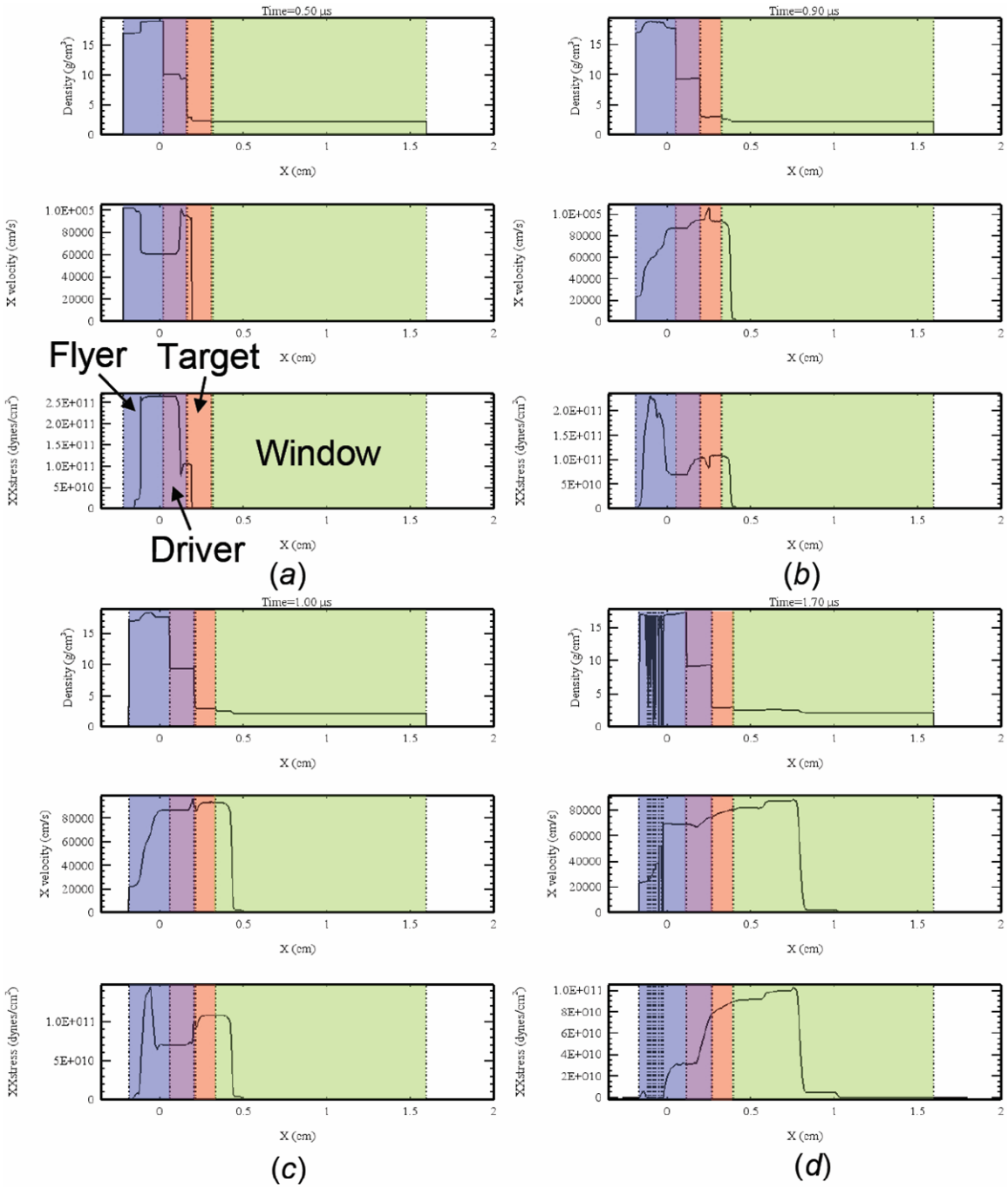


**Figure D.5** Captured CTH simulation snapshots illustrating the waveform propagation within the materials that make up the target assembly for shot 0628. The snapshots are captured at *a*) 0.5, *b*) 0.9 *c*) 1.0, and *d*) 1.7 µs after impact and show the variation of density, particle velocity, and stress waveform profiles (in order top-to-bottom) throughout the target assembly.

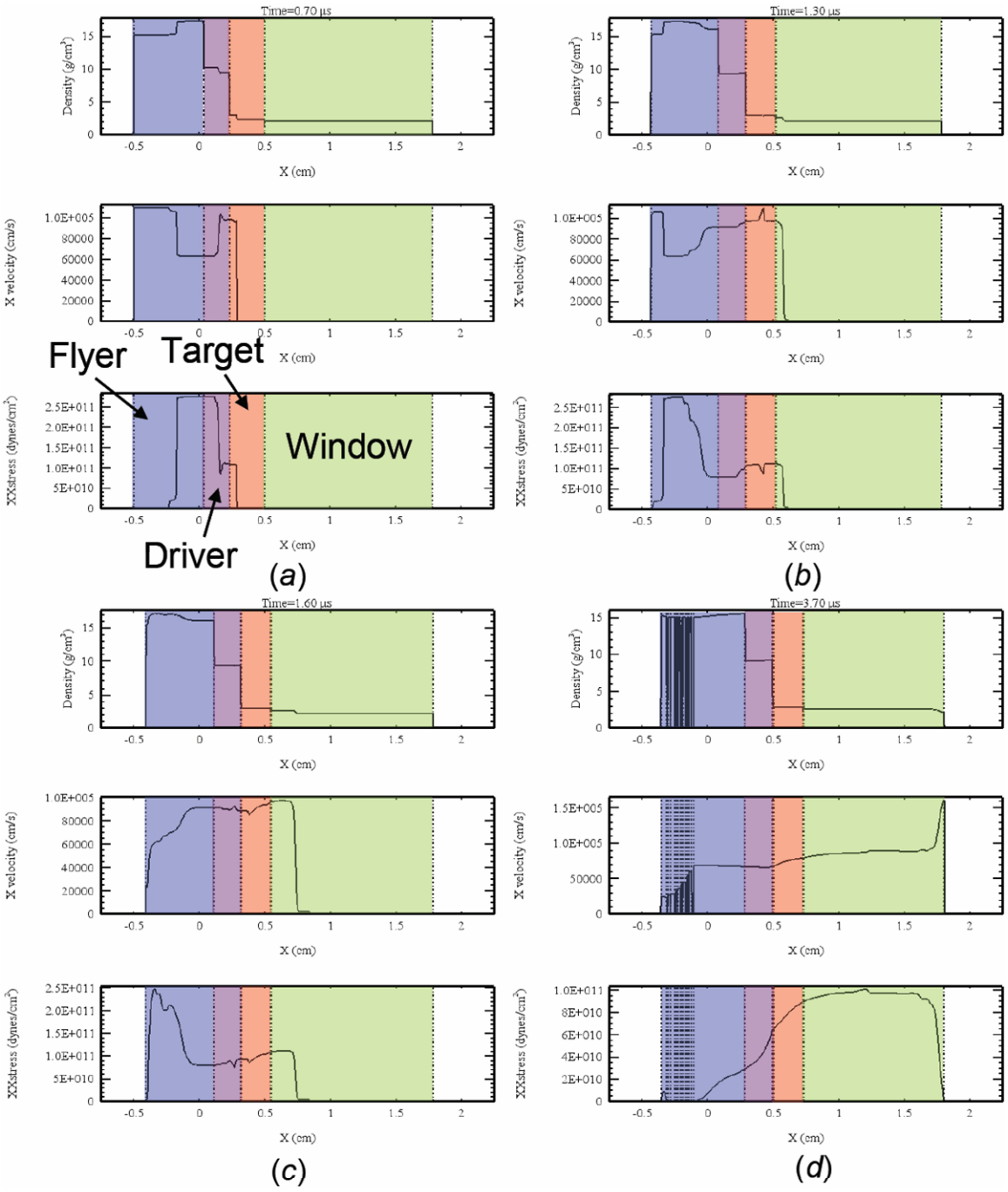


**Figure D.6** Captured CTH simulation snapshots illustrating the waveform propagation within the materials that make up the target assembly for shot 0609. The snapshots are captured at *a*) 0.7, *b*) 1.3 *c*) 1.6, and *d*) 3.7 µs after impact and show the variation of density, particle velocity, and stress waveform profiles (in order top-to-bottom) throughout the target assembly.

# REFERENCES


[1] The classic thermite is an alumino-thermic process involving reactions of oxides of certain metals with aluminum to yield aluminum oxide and a free metal. Thermite was invented in 1893 and patented in 1895 by German chemist Hans Goldschmidt.

[2] United States Naval Academy Weapons and Systems Engineering Department, "Fundamentals of Naval Weapons Systems," http://www.fas.org/man/dod-101/navy/docs/fun/index.html, September 2007.

[3] P.W. Bridgman, "Effects of High Shearing Stress Combined with High Hydrostatic Pressure," *Phys. Rev.* **48**, 825-847 (1935).

[4] P.W. Bridgman, "Polymorphic Transitions up to 50,000 kg/cm$^2$ of Several Organic Compounds," *Proc. Am. Acad. Arts. Sci.* **72**, 227-268 (1937a).

[5] P.W. Bridgman, "Shearing Phenomena at High Pressures, Particularly in Inorganic Compounds," *Proc. Am. Acad. Arts. Sci.* **71**, 387-460 (1937b).

[6] P.W. Bridgman, "The Effect of High Mechanical Stress on Certain Solid Explosives," *J. Chem. Phys.* **15**, 311-313 (1947).

[7] R.A. Graham, Solids Under High Pressure Shock Compression: Mechanics, Physics and Chemistry, (Springer-Verlag, New York, 1993)

[8] Air Force Research Laboratory - Munitions Directorate Energetic Materials Branch (AFRL/MNME), Eglin AFB, unpublished results (2001).

[9] N.N Thadhani, "Shock-Induced Chemical Reactions and Synthesis of Materials," *Progress in Materials Science* **37**, 117-226 (1993).

[10] R.A. Graham, M.U. Anderson, F. Bauer and R.E. Setchell, "Piezoelectric Polarization of the Ferroelectric Polymer PVDF from 10 MPa to 10 GPa: Studies of Loading-Path Dependence," in *Shock Compression of Condensed Matter*, Williamsburg, VA, 17-20 June 1991, edited by S.C. Schmidt, R.D. Dick, J.W. Forbes and D.G. Tasker, pp. 883-886 (1992).

[11] M.U. Anderson and R.A. Graham, "The New Simultaneous PVDF\VISAR Measurement Technique: Applications to Highly Porous HMX," in *Shock Compression of Condensed Matter*, Seattle, Washington, 13-18 August 1995, edited by S.C. Schmidt and W.C. Tao (American Institute of Physics), Vol. **370**, pp. 1101-1104 (1996).

[12] M.U. Anderson and R.A. Graham, "Prediction and Data Analysis of Current Pulses from Impact-Loaded Piezoelectric Polymers (PVDF)," in *Shock Compression of Condensed Matter*, Albuquerque, NM, 14-17 August 1989, edited by S.C. Schmidt, J.N. Johnson and L.W. Davison (American Institute of Physics), pp. 805-808 (1990).

[13] L.M. Barker and R.E. Hollenbach, "Interferometer Technique for Measuring the Dynamic Mechanical Properties of Materials," *Rev. Sci. Instrum.* **36**, [11] 1617-1620 (1965).

[14] K.J. Blobaum, M.E. Reiss, J.M. Plitzko and T.P. Weihs, "Deposition and Characterization of a Self-Propagating $CuO_x$/Al Thermite Reaction in a Multilayer Foil Geometry," *Journal of Applied Physics* **94**, [5] 2915-2922 (2003).

[15] K.K. Kuo, G.A. Risha, B.J. Evans and E. Boyer, "Potential Usage of Energetic Nano-sized Powders for Combustion and Rocket Propulsion," in *Synthesis, Characterization and Properties of Energetic/Reactive Nanomaterials*, Boston, Massachusetts, 1-4 December 2003, edited by R. Armstrong, N. Thadhani, W. Wilson, J. Gilman and R. Simpson, Vol. **800**, pp. 3-14 (2004).

[16] M.A. Meyers, Dynamic Behavior of Materials, (John Wiley & Sons, Inc., New York, 1994)

[17] M.H. Rice, R.G. McQueen and J.M. Walsh, Compression of Solids by Strong Shock Waves, in *Solid State Physics*, edited by F. Seitz and D. Turnbull (Academic Press, New York, 1958), Vol. **VI**, pp. 1-63.

[18] S.P. Marsh, LASL Shock Hugoniot Data, in *Los Alamos Series on Dynamic Material Properties*, edited by S.P. Marsh (University of California Press, Berkeley and Los Angeles, California, 1980).

[19] P.S. DeCarli and J.C. Jamieson, "Formation of Diamond by Explosive Shock," *Science* **133**, [3467] 1821-1822 (1961).

[20] G.E. Duvall and R.A. Graham, "Phase Transitions Under Shock Wave Loading," *Rev. Mod. Phys.* **49**, [3] 523-579 (1977).

[21] L.V. Al'tshuler, "Phase Transitions in Shock Waves (Review)," *Transulated from Zhurnal Prikladnoi Mekhaniki i Teknicheskoi Fiziki* **19**, [4] 93-103 (1978).

[22] P.S. DeCarli, "Method for Making Diamonds," U.S. Patent No. 3,238,019 (1 March 1996).

[23] D.J. Erskine and W.J. Nellis, "Shock-Induced Martensitic Transformation of Highly Oriented Graphite Diamond," *J. Appl. Phys.* **71**, [10] 4882-4886 (1992).

[24] S.S. Batsanov, G.S. Doronin, S.V. Kolchkov and A.I. Teut, "Synthesis Reactions Behind Shock Fronts," *Combustion, Explosion, and Shock Waves* **22**, [6] 765-768 (1986).

[25] S.S. Batsanov, I.I. Maximov, G.V. Simakov and A.V. Fedozov, "Shock Compressibility of CuI and TiCl," *Comb. Expl. Shock Waves* **30**, [1] 122-125 (1994).

[26] G.V. Simakov, I.I Maximov and S.S. Batsanov, "Shock Compressibility of CuCl and TiI," *Comb. Expl. Shock Waves* **31**, [4] 471-472 (1995).

[27] S.S. Batsanov and D.L. Gur'ev, "Interaction of Sulfur with Tin in Shock Waves," *Combustion, Explosion, and Shock Waves* **23**, [2] 236-238 (1987).

[28] S.S. Batsanov, M.F. Gogulya, M.A. Brazhnikov, E.V. Lazareva, G.A. Doronin, S.V. Klochkov, M.B. Banshcikova, A.V. Fedozov and G.V. Simakov, "Shock Compression of Reactants in the Tin–Chalcogen System," *Sov. J. Chem. Phys.* **10**, [12] 2635-2638 (1991).

[29] N.N. Thadhani, R.A. Graham, T. Royal, E. Dumbar, M.U. Anderson and G.T. Holman, "Shock-Induced Chemical Reactions in Titanium-Silicon Powder Mixtures of Different Morphologies: Time-Resolved Pressure Measurments and Materials Analysis," *J. Appl. Phys.* **82**, [3] 1113-1128 (1997).

[30] Y. Horie, R.A. Graham and I.K. Simonsen, "Synthesis of Nickel Aluminides Under High-Pressure Shock Loading," *Mater. Lett.* **3**, [9-10] 354-359 (1985).

[31] Y. Horie, R.A. Graham and I.K. Simonsen, Observations on the Shock Synthesis of Intermetallic Compounds, in *Metallurgical Applications of Shock-Waves and High Strain-Rate Phenomena*, edited by L.E. Murr, K.P. Staudhammer and M.A. Meyers (Marcel Dekker, New York, 1986), pp. 1023-1035.

[32] L.H. Yu, M.A. Meyers and N.N. Thadhani, "Reaction-Assisted Shock Consolidation of RSR Ti-Al Alloys," *J. Matl. Res.* **5**, [2] 302-312 (1990).

[33] S. Stavrev, V. Gospondinov, A. Doichev and R. Radev, "Synthesis of Intermetallic Compounds by Dynamic Compaction of Metal Powders," in *Proceedings of X International Conference on High Energy Rate Fabrication*, Ljubljana, Yugoslavia, 18-22 September, pp. 123-130 (1989).

[34] R.W. Armstrong, C.S. Coffey, V.F. DeVost and W.L. Elban, "Crystal Size Dependence for Impact Initiation of Cyclotrimethylenetrinitramine Explosives," *J. Appl. Phys.* **68**, [3] 979-984 (1990).

[35] R.A. Rugunanan and M.E. Brown, "Combustion of Binary and Ternary Silicon/Oxidant Pyrotechnic Systems; Part I: $Fe_2O_3$ and $SnO_2$," *Combust. Sci. Technol.* **95**, [61] (1994).

[36] R.A. Rugunanan and M.E. Brown, "Combustion of Binary and Ternary Silicon/Oxidant Pyrotechnic Systems; Part IV Kinetic Aspects," *Combust. Sci. Technol.* **95**, [85] 117-138 (1994).

[37] V. Subramanian and N.N. Thadhani, "Reaction Behavior of Shock Compressed Aluminum and Iron-Oxide Powder Mixtures," in *Shock Compression of Condensed Matter*, Seattle, Washington, 13-18 August 1995, edited by S.C. Schmidt and W.C. Tao (American Institute of Physics), Vol. **370**, pp. 681-684 (1996).

[38] G.T. Holman, R.A. Graham and M.U. Anderson, "Shock Response of Porous $2Al+Fe_2O_3$ Powder Mixtures," in *Shock Compression of Condensed Matter*, Colorado Springs, Colorado, 28 June - 2 July 1993, edited by S.C. Schmidt, J.W. Shaner, G.A. Samara and M. Ross (American Institute of Physics), Vol. **309**, pp. 1119-1122 (1994).

[39] N.N. Thadhani, K.S. Vandersall, R.T. Russell, R.A. Graham, G.T. Holman and M.U. Anderson, "Shock Compression of $Al+Fe_2O_3$ Powder Mixtures of Different Volumetric Distributions," in *Shock Compression of Condensed Matter*, Amherst, Massachusetts, 27 July - 1 August 1997, edited by S.C. Schmidt, D.P. Dandekar and J.W. Forbes (American Institute of Physics), Vol. **429**, pp. 553-556 (1998).

[40] N.S. Enikolopyan, A.A. Khzardzhyan, E.E. Gasparyan and V.B. Vol'eva, "Kinetics of Explosive Chemical Reactions in Solids," *Dokl. Phys. Chem. (Engl. Transl.)* **294**, [5] 1151-1154 (1987).

[41] M.B. Boslough, "A Thermochemical Model for the Shock-Induced Reaction (Heat Detonations) in Solids," *J. Chem. Phys.* **92**, [3] 1839-1848 (1990).

[42] S.M. Walley, J.E. Balzer, W.G. Proud and J.E. Field, "Response of Thermites to Dynamic High Pressure and Shear," *Proc. R. Soc. Lond. A* **456**, 1483-1503 (2000).

[43] J. Mei, R.D. Halldearn and P. Xiao, "Mechanisms of the Aluminum-Iron Oxide Thermite Reaction," *Scripta Materialia* **41**, [541-548] (1999).

[44] R.G. Ames, "Energy Release Characteristics of Impact-Initiated Energetic Materials," in *Multifunctional Energetic Materials*, Boston, Massachusetts, 28-30

November 2005, edited by N.N. Thadhani, R.W. Armstrong, A.E. Gash and W.H. Wilson (Materials Research Society), Vol. **896**, pp. 123-132 (2005).

[45] G.I. Taylor, "The Use of Flat-Ended Projectiles for Determining Dynamic Yield Stress: I Theoretical Considerations," *Proc. R. Soc. Lond. A* **194**, 289-299 (1948).

[46] R.J. Lee, Jr. W. Mock, J.R. Carney, W.H. Holt, G.I. Pangilinan, R.M. Gamache, J.M. Boteler, D.G. Bohl, J. Drotar and G.W. Lawrence, "Reactive Materials Studies," in *Shock Compression of Condensed Matter*, Baltimore, Maryland, 31 July - 5 August 2005, edited by M.D. Furnish, M. Elert, T.P. Russell and C.T. White (American Institute of Physics), Vol. **845**, pp. 169-174 (2006).

[47] J.J. Davis, A.J. Lindfors, P.J. Miller, S. Finnegan and D.L. Woody, "Detonation Like Phenomena in Metal-Polymer and Metal/Metal Oxide-Polymer Mixtures," in *Proceedings of the 11th International Detonation Symposium*, Snowmass, Colorado, 31 August - 4 September 1998, edited by J.M. Short and J.E. Kennedy, pp. 1007-1013 (1998).

[48] L. Yang, Y. Horie, A.J. Linfors and P.J. Miller, "An Analysis of Shock-Induced Reactions in a $Fe_2O_3$+Al+Teflon Powder Mixture," North Carolina State University Report N000 14094-1-0240-02, (1996).

[49] I. Lee, R.R. Reed, V.L. Brady and S.A. Finnegan, "Energy Release in the Reaction of Metal Powders with Fluorine Containing Polymers," *J. Therm. Anal. Calorim.* **49**, [3] 1699-1705 (1997).

[50] G.M. Swallowe and J.E. Field, "Effect of Polymers on the Drop-Weight Sensitiveness of Explosives," in *7th International Detonation Symposium*, Annapolis, Maryland, 16-19 June 1981, (Naval Surface Weapons Center), pp. 24-35 (1981).

[51] E.C. Koch, "Metal-Fluorocarbon Pyrolants: III. Development and Application of Magnesium/Teflon/Viton," *Propellants Explosives Pyrotechnics* **27**, [5] 262-266 (2002).

[52] T. Kawaguchi and R.A. Pearson, "The Effect of Particle-Matrix Adhesion on the Mechanical Behavior of Glass Filled Epoxies: Part 1. A Study on Yield Behavior and Cohesive Strength," *Polymer* **44**, 4229-4238 (2003).

[53] W.C.J. Zuiderduin, C. Westzaan, J. Hue'tink and R.J. Gaymans, "Toughening of Polypropylene with Calcium Carbonate Particles," *Polymer* **44**, 261-275 (2003).

[54] Z.H. Liu, K.W. Kwok, R.K.Y. Li and C.L. Choy, "Effects of Coupling Agent and Morphology on the Impact Strength of High Density Polyethylene/$CaCO_3$ Composites," *Polymer* **43**, [8] 2501-2506 (2002).

[55] Z. Bartczak, A.S. Argon, R.E. Cohen and M. Weinberg, "Toughness Mechanism in Semi-Crystalline Polymer Blends: II. High-Density Polyethylene Toughened with Calcium Carbonate Filler Particles," *Polymer* **40**, 2347-2365 (1999).

[56] B.M. Badran, A. Galeski and M. Kryszewski, "High-Density Polyethylene Filled with Modified Chalk," *J. Appl. Polym. Sci.* **27**, 3669-3681 (1982).

[57] S. Wu, "A Generalized Criterion for Rubber Toughening: The Critical Matrix Ligament Thickness," *J. Appl. Polym. Sci.* **35**, [2] 549-561 (1988).

[58] Z.H. Liu, X.D. Zhang, X.G. Zhu, R.K.Y. Li, Z.N. Qi, F.S. Wang and C.L. Choy, "Effect of Morphology on the Brittle Ductile Transition of Polymer Blends: 4. Influence of the Rubber Particle Spatial Distribution in poly(vinylchloride)/nitrile Rubber Blends," *Polymer* **39**, [21] 5035-5045 (1998).

[59] B. Wetzel, F. Haupert and M.Q. Zhang, "Epoxy Nanocomposites with High Mechanical and Tribological Performance," *Composite Science and Technology* **63**, 2055-2067 (2003).

[60] S. Goyanes, G. Rubiolo, A. Marzocca, W. Salgueiro, A. Somoza, G. Consolati and I. Mondragon, "Yield and Internal Stresses in Aluminum Filled Epoxy Resin. A Compression Test and Positron Annihilation Analysis," *Polymer* **44**, 3193-3199 (2003).

[61] S.A. Paipetis, G. Papanicolaou and P.S. Theocaris, "Dynamic Properties of Metal-Filled Epoxy Polymers," *Fibre Science and Technology* **8**, [3] 221-242 (1975).

[62] I.M. Ward and J. Sweeney, An Introduction to the Mechancial Properties of Solid Polymers, 2nd ed. (John Wiley & Sons, Ltd., England, 2004)

[63] S.M. Aharoni, "Increased Glass Transition Temperature in Motionally Constrained Semicrystalline Polymers," *Polymers for Advanced Technologies* **9**, 169-201 (1998).

[64] H.G.H. Van Melick, L.E. Govaert and H.E.H. Meijer, "On the Orgin of Strain Hardening in Glassy Polymers," *Polymer* **44**, 2493-2502 (2003).

[65] M. Martin, "Processing and Characterization of Energetic and Structural Behavior of Nickel Aluminum with Polymer Binders," Master's Thesis, Georgia Institute of Technology, 2005.

[66] M. Martin, S. Hanagud and N.N. Thadhani, "Dynamic Mechanical Behavior of Nickel+Aluminum Powder-Reinforced Epoxy Composites," *Materials Science and Engineering A* **443**, 209-218 (2007).

[67] S.C. Misra, J.A. Manson and L.H. Sperling, "Effect of Cross-Link Density Distribution on the Engineering Behavior of Epoxies," in *Epoxy Resin Chemistry, ACS Symposium*, Washington, D.C. (American Chemcial Society), Vol. **114**, p. 137 (1979).

[68] N.R. Patel, "Intermediate Strain Rate Behavior of Two Structural Energetic Materials," Master's Thesis, Georgia Institute of Technology, 2004.

[69] O.A. Hasan and M.C. Boyce, "Constitutive Model for the Nonlinear Viscoelastic Viscoplastic Behavior of Glassy Polymers," *Polym. Eng. Sci.* **35**, [4] 331-344 (1995).

[70] J.C.F. Millet and N.K. Bourne, "The Shock Induced Equation of State of Three Simple Polymers," *J. Phys. D: Appl. Phys.* **37**, 2901-2907 (2004).

[71] J.C.F. Millet and N.K. Bourne, "The Deviatoric Response of Polymethylmethacrylate to One-Dimensional Shock Loading," *J. Appl. Phys.* **88**, [12] 7037-7040 (2000).

[72] W.J. Carter and S.P. Marsh, "Hugoniot Equation of State of Polymers," Los Alamos National Laboratory Report LA-13006-MS, (1995).

[73] D.N. Schmidt and M.W. Evans, "Shock Wave Compression of 'Plexiglas' in the 2.5 to 20 Kilobar Region," *Nature* **206**, 1348-1349 (1965).

[74] D.J. Pastine, "*P*, *v*, *T* Equation of State for Polyethlene," *J. Chem. Phys.* **49**, [7] 3012-3022 (1968).

[75] D.J. Pastine, Les Proprietes des Solides Sous Pression, edited by D. Block (1970).

[76] R.W. Warfield, "Compressibility of Bulk Polymers," *Poly. Eng. and Science* **6**, [2] 176-180 (1966).

[77] P.W. Bridgman, "The Compression of 39 Substances to 100,000 kg/cm$^2$," *Proc. Am. Acad. Arts. Sci.* **76**, 55-70 (1948).

[78] D.E. Munson and R.P May, "Dynamically Determined High-Pressure Compressibility of Three Epoxy Resin Systems," *J. Appl. Phys.* **43**, [3] 962-971 (1972).

[79] J.C.F. Millet, N.K. Bourne and N.R. Barnes, "The Behavior of an Epoxy Resin Under One-Dimensional Shock Loading," *J. Appl. Phys.* **92**, [11] 6590-6594 (2002).

[80] R.G. McQueen, S.P. Marsh, J.W. Taylor, J.N. Fritz and W.J. Carter, The Equation of State of Solids from Shock Wave Studies, in *High-Velocity Impact*

*Phenomena*, edited by R. Kinslow (Academic Press, San Diego, California, 1970), pp. 293-417.

[81] Y.V. Bat'kov, S.A. Novikov and N.D. Fishman, "Shear Stress in Polymers Under Shock Compression," in *Shock Compression of Condensed Matter*, Seattle, Washington, 13-18 August 1995, edited by S.C. Schmidt and W.C. Tao (American Institute of Physics), Vol. **370**, pp. 577-580 (1996).

[82] D.E. Munson and K.W. Schuler, "Steady Wave Analysis of Wave Propagation in Laminates and Mechanical Mixtures," *J. Compos. Mater* **5**, 286-304 (1971).

[83] D.E. Munson, R.R. Boade and K.W. Schuler, "Stress-Wave Propagation in $Al_2O_3$-Epoxy Mixtures," *J. Appl. Phys.* **49**, [9] 4797-4807 (1978).

[84] M.U. Anderson, R.E. Setchell and D.E. Cox, "Shock and Release Behavior of Filled and Unfilled Epoxies," in *Shock Compression of Condensed Matter*, Snowbird, Utah, 27 June - 2 July 1999, edited by M.D. Furnish, L.C. Chhabildas and R.S. Hixson (American Institute of Physics), Vol. **505**, pp. 551-554 (2000).

[85] M.U. Anderson, R.E. Setchell and D.E. Cox, "Effects of Initial Temperature on the Shock and Release Behavior of Filled and Unfilled Epoxies," in *Shock Compression of Condensed Matter*, Atlanta, Georgia, 24-29 June 2001, edited by M.D. Furnish, N.N. Thadhani and Y. Horie, Vol. **620**, pp. 669-672 (2002).

[86] M.U. Anderson, R.E. Setchell and D.E. Cox, "Shock Compression and Release Properties of Alumina-Filled Epoxy," in *Shock Compression of Condensed Matter*, Portland, Oregon, 20-25 July 2003, edited by M.D. Furnish, Y.M. Gupta and J.W. Forbes (American Institute of Physics), Vol. **706**, pp. 685-688 (2004).

[87] M.U. Anderson, D.E. Cox, S.T. Montgomery and R.E. Setchell, "Compositional Effects on the Shock Compression and Release Properties of Alumina-Filled Epoxy," in *Shock Compression of Condensed Matter*, Baltimore, Maryland, 31 July - 5 August 2005, edited by M.D. Furnish, M. Elert, T.P. Russell and C.T. White (American Institute of Physics), Vol. **845**, pp. 789-792 (2006).

[88] R.E. Setchell and M.U. Anderson, "Shock-Compression Response of an Alumina-Filled Epoxy," *Journal of Applied Physics* **97**, 083518 (2005).

[89] Jr. W. Mock and W. H. Holt, "Shock-Wave Compression in an Alumina-Filled Epoxy in the Low Gigapascal Stress Range," *J. Appl. Phys.* **49**, [3] 1156-1158 (1978).

[90] J.C.F. Millet, N.K. Bourne and D. Deas, "The Equation of State of Two Alumina-Filled Epoxy Resins," *J. Phys. D: Appl. Phys.* **38**, 930-934 (2005).

[91] T. Nicholas, Elastic-Plastic Stress Waves, in *Impact Dynamics*, edited by J.A. Zukas, T. Nicholas, H.F. Swift, L.B. Greszczuk and D.R. Curran (John Wiley & Sons, New York, 1982), pp. 95-153.

[92] T. von Karman and P. Duwez, "The Propagation of Plastic Deformation in Solids," *Journal of Applied Physics* **21**, [10] 987-994 (1950).

[93] J.E. Field, S.M. Walley, W.G. Proud, H.T. Goldrein and C.R. Siviour, "Review of Experimental Techniques for High Rate Deformation and Shock Studies," *International Journal of Impact Engineering* **30**, 725-775 (2004).

[94] M.L. Wilkins and M.W. Guinan, "Impact of Cylinders on a Rigid Boundary," *J. Appl. Phys.* **44**, [3] 1200-1206 (1973).

[95] I. Rohr, H. Nahme and K. Thoma, "A Modified Taylor-Test in Combination with Numerical Simulations - A New Approach for the Determination of Model Parameters Under Dynamic Loads," *J. Phys. IV France* **110**, 513-518 (2003).

[96] J.W. House, B. Aref, J.C. Foster and P.P. Gillis, "Film Data Reduction From Taylor Impact Tests," *Journal of Strain Analysis* **34**, [5] 337-345 (1999).

[97] B.J. Briscoe and I.M. Hutchings, "Impact Yielding of High Density Polyethylene," *Polymer* **17**, [12] 1099-1102 (1976).

[98] I.M. Hutchings, "Estimation of Yield Stress in Polymers at High Strain-Rates Using G.I. Taylor's Impact Technique," *J. Mech. Phys. Solids* **26**, 289-301 (1979).

[99] J.C.F. Millett, N.K. Bourne and G.S. Stevens, "Taylor Impact of Polyether Ether Ketone," *International Journal of Impact Engineering* **32**, 1086-1094 (2006).

[100] P.J. Rae and E.N. Brown, "The Taylor Impact and Large Strain Response of Poly(Ether-Etherketone) (PEEK)," in *Shock Compression of Condensed Matter*, Baltimore, Maryland, 31 July - 5 August 2005, edited by M.D. Furnish, M. Elert, T.P. Russell and C.T. White (American Institute of Physics), Vol. **845**, pp. 1399-1402 (2005).

[101] R.I. Beecroft and C.A. Swenson, "Behavior of Polytetrafluoroethylene (Teflon) Under High Pressures," *Journal of Applied Physics* **30**, [11] 1793-1798 (1959).

[102] P.J. Rae, E.N. Brown, B.E. Clements and D.M. Dattelbaum, "Pressure-Induced Phase Change in Poly(Tetrafluoroethylene) at Modest Impact Velocities," *Journal of Applied Physics* **98**, 063521 (2005).

[103] P.J. Rae, G.T. Gray, D.M. Dattelbaum and N.K. Bourne, "The Taylor Impact Response of PTFE (Teflon)," in *Shock Compression of Condensed Matter*,

Portland, Oregon, 20-25 July 2003, edited by M.D. Furnish, Y.M. Gupta and J.W. Forbes (American Institute of Physics), Vol. **706**, pp. 671-674 (2004).

[104] F.J. Zerilli and R.W. Armstrong, "Application of Eyring's Thermal Activation Theory to Constitutive Equations for Polymers," in *Shock Compression of Condensed Matter*, Snowbird, Utah, 27 June - 2 July 1999, edited by M.D. Furnish, L.C. Chhabildas and R.S. Hixson (American Institute of Physics), Vol. **505**, pp. 531-534 (2000).

[105] F.J. Zerilli and R.W. Armstrong, "Thermal Activation Constitutive Model for Polymers Applied to Polytetrafluoroethylene," in *Shock Compression of Condensed Matter*, Atlanta, Georgia, 24-29 June 2001, edited by M.D. Furnish, N.N. Thadhani and Y. Horie (American Institiute of Physics), Vol. **620**, pp. 657-660 (2002).

[106] S.M. Walley and J.E. Field, "Strain Rate Sensitivity of Polymer in Compression from Low to High Rates," *Dymat Journal* **1**, [3] 211-227 (1994).

[107] W. Chen and B. Zhou, "Constitutive Behavior of Epon/T-403 at Various Strian Rates," *Mechanics of Time-Dependent Materials* **2**, 103-111 (1998).

[108] H. Lu, G. Tan and W. Chen, "Modeling the Constitutive Behavior for Epon 828/T-403 at High Strian Rates," *Mechanics of Time-Dependent Materials* **5**, 119-130 (2001).

[109] R.C. Weast, CRC Handbook of Chemistry and Physics, 67th ed. (CRC Press, Inc., Boca Raton, Florida, 1987)

[110] T.R. Gibbs and A. Popolato, LASL Explosive Property Data, in *Los Alamos Series on Dynamic Material Properties* (University of California Press, Berkeley California, 1980).

[111] L.L. Wang, Z.A. Munir and Y.M. Maximov, "Review Thermite Reactions: Their Utilization in the Synthesis and Processing of Materials," *J. Mater. Sci.* **28**, 3693-3708 (1993).

[112] A.G. Merzhanov, Self-Propagating High-Temperature Synthesis: Twenty Years of Search and Findings, in *Combustion and Plasma Synthesis of High-Temperatue Materials*, edited by Z.A. Munir and J.B. Holt (New York: VCH Publishers, Inc., 1990), pp. 1-47.

[113] A. Varma, "Form from Fire," *Scientific America*, 58-61 (2000).

[114] S.H. Fischer and M.C. Grubelich, "A Survey of Combustible Metals, Thermites, and Intermetallics for Pyrotechnic Applications," in *32nd AIAA, ASME, SAE, and ASEE, Joint Propulsion Conference and Exhibit*, Lake Buena Vista, FL, 1-3 July

1996, (American Institute of Aeronautics and Astronautics, Inc.), **AIAA Paper 96-3018** (1997).

[115] A. Varma, A.S. Rogachev, A.S. Mukasyan and S. Hwang, "Complex Behavior of Self-Propagating Reaction Waves in Heterogeneous Media," *Proc. Natl. Acad. Sci.* **95**, 11053-11058 (1998).

[116] J. Mei, R.D. Halldearn and P. Xiao, "Mechanisms of the Aluminum-Iron Oxide Thermite Reaction," *Scr. Mater.* **41**, [5] 541-548 (1999).

[117] M.A. Korchagin and V.A. Podergin, "Investigation of Chemical Transformations in the Combustion of Condensed Systems," *Combustion, Explosion, and Shock Waves* **15**, [3] 325-329 (1979).

[118] H.A. Wriedt, "The Al-O (Aluminum-Oxygen) system," *Bull. Alloy Phase Diagrams* **6**, [6] 548-553 (1985).

[119] O. Kubaschewski, Iron-Binary Phase Diagrams, (Springer Verlag, Berlin, 1982) pp. 5-9, 79-82.

[120] K. Rosenbach and J.A. Schmitz, "Investigations in the Ternary System Iron(II)-Oxide-Chromium(III) Oxide-Alumina," *Arch. Eisenhuttenwes* **45**, [2] 843-847 (1974).

[121] K.J. Blobaum, A.J. Wagner, J.M. Plitzko, D. Van Heerden, D.H. Fairbrother and T.P. Weihs, "Investigating the Reaction Path and Growth Kinetics in $CuO_x$/Al Multilayer Folis," *Journal of Applied Physics* **94**, [5] 2923-2929 (2003).

[122] S. Valliappan, J. Swiatkiewicz and J.A. Puszynski, "Reactivity of Aluminum Nanopowders with Metal Oxides," *Powder Technol.* **156**, 164-169 (2005).

[123] E.M. Hunt and M.L. Pantoya, "Ignition Dynamics and Activation Energies of Metallic Thermites: From Nano- to Micron-Scale Particulate Composites," *Journal of Applied Physics* **98**, 034909 (2005).

[124] M.L. Pantoya and J.J. Granier, "Combustion Behavior of Highly Energetic Thermites: Nano Versus Micron Composites," *Propellants, Explosives, Pyrotechnics* **30**, [1] 53-62 (2005).

[125] A.E. Gash, T.M. Tillotson, J.F. Poco, Jr. J.H. Satcher, L.W. Hrubesh and R.L. Simpson, "New Sol-Gel Synthetic Route to Transitional and Main-Group Metal Oxide Aerogels Using Inorganic Salt Precursors," *J. Non-Cryst. Solids* **285**, 22-28 (2001).

[126] A.E. Gash, J.H. Satcher and R.L. Simpson, "Strong Akaganeite Aerogel Monoliths Using Epoxides: Synthesis and Characterizations," *Chem. Mater.* **15**, 3268-3275 (2003).

[127] A.E. Gash, T.M. Tillotson, Jr. J.H. Satcher, L.W. Hrubesh and R.L. Simpson, "Use of Epoxides in the Sol-Gel Synthesis of Porous Iron(III) Oxide Monoliths from Fe(III) Salts," *Chem. Mater.* **12**, 999-1007 (2001).

[128] K.B. Plantier, M.L. Pantoya and A.E. Gash, "Combustion Wave Speeds of Nanocomposite Al/$Fe_2O_3$: The Effects of $Fe_2O_3$ Particle Synthesis Technique," *Combust. Flame* **140**, 299-309 (2005).

[129] A.W. Miziolek, "Nanoenergetics: An Emerging Technology Area of National Importance," *The AMPTIAC Newsletter* **6**, [1] 43-48 (2002).

[130] T. Lowe, "The Revolution in Nanometals," *Advanced Materials & Processes* **160**, [1] 63-65 (2002).

[131] T.M. Tillotson, A.E. Gash, R.L. Simpson, L.W. Hrubesh, Jr. J.H. Satcher and J.F. Poco, "Nanostructured Energetic Materials Using Sol-Gel Methods," *J. Non-Cryst. Solids* **285**, 338-345 (2001).

[132] C.E. Aumann, G.L. Skofronick and J.A. Martin, "Oxidation Behavior of Aluminum Nanopowders," *J. Vac. Sci. Technol. B* **13**, [3] 1178-1183 (1995).

[133] S.H. Kim and M.R. Zachariah, "Enhancing the Rate of Energy Release for NanoEnergetic Materials by Electrostatically Enhanced Assembly," *Adv. Mater.* **16**, [20] 1821-1826 (2004).

[134] R.W. Armstrong, B. Baschung, D.W. Booth and M. Samirant, "Enhanced Propellant Combustion with Nanoparticles," *Nano Lett.* **3**, [2] 253-255 (2003).

[135] R.A. Austin, "Numerical Simulation of the Shock Compression of Microscale Reactive Particle Systems," Master's Thesis, Georgia Institute of Technology, 2005.

[136] R.A. Austin, D.L. McDowell and D.J. Benson, "Numerical Simulation of Shock Wave Propagation in Spatially-Resolved Particle Systems," *Modelling and Simulation in Materials Science and Engineering* **14**, 537-561 (2006).

[137] D.J. Benson, "A Multi-Material Eulerian Formulation for the Efficient Solution of Impact and Penetration Problems," *Comput. Mech.* **15**, 558-571 (1995).

[138] V. Tomar, "Atomistic Modeling of the Al and $Fe_2O_3$ Mateiral System Using Classical Molecular Dynamics," Doctoral Thesis, Georgia Institute of Technology, 2005.

[139] V. Tomar and M. Zhou, "Classical Molecular-Dynamics Potentials for the Mechanical Strength of Nanocrystalline Composite *fcc* Al+ $\alpha$-$Fe_2O_3$," *Physical Review B* **73**, p. 174116 (2006).

[140] Resolution Performance Products LLC, "EPON® Resin Structural Reference Manual," (2001).

[141] D. Adolf, R. Strommen and H. Johnson, "Viscosities of Epoxy Encapsulants," Sandia National Laboratories Report SAND97-2631, (1997).

[142] C.V. Lundberg, "Diethanolamine as a Hardener for Epoxy Resins," *Ind. Eng. Chem. Prod. Res. Dev.* **19**, 319-326 (1980).

[143] L. Ferranti Jr., R.W. Armstrong and N.N. Thadhani, "Elastic/Plastic Deformation Behavior in a Continuous Ball Indentation Test," *Materials Science and Engineering A* **371**, 251-255 (2004).

[144] "ASTM Standard D 790-03: Standard Test Method for Flexural Properties of Unreinforced and Reinforced Plastics and Electrical Insulating Materials," (2003).

[145] "ASTM Standard D 5026-06: Standard Test Method for Plastics: Dynamic Mechanical Properties: In Tension," (2001).

[146] "ASTM Standard D 4092-01: Standard Terminology: Plastics: Dynamic Mechanical Properties," (2001).

[147] "ASTM Standard D 695-02a: Standard Test Method for Compressive Properties of Rigid Plastics," (2002).

[148] "ASTM Standard D 6110-02: Standard Test Method for Determining the Charpy Impact Resistance of Notched Specimens of Plastics," (2002).

[149] "PDF-4+ Database" (International Centre for Diffraction Data, Newtown Square, PA, 2006).

[150] "ASTM Standard E 494-95: Standard Practice for Measuring Ultrasonic Velocity in Materials," (2001).

[151] L.M. Barker and R.E. Hollenbach, "Laser Interferometer for Measuring High Velocities of Any Reflecting Surface," *Journal of Applied Physics* **43**, 4669-4675 (1972).

[152] L.M. Barker and K.W. Schuler, "Correction to the Velocity-Per-Fringe Relationship for the VISAR Interferometer," *Journal of Applied Physics* **45**, [8] 3692-3693 (1974).

[153] W.F. Hemsing, "Velocity Sensing Interferometer (VISAR) Modification," *Rev. Sci. Instrum.* **50**, [1] 73-78 (1979).

[154] L.M. Barker, V.J. Barker and Z.B. Barker, "VALYN VISARs User's Handbook," (1999).

[155] L.M. Barker and R.E. Hollenbach, "Shock-Wave Studies of PMMA, Fused Silica, and Sapphire," *Journal of Applied Physics* **41**, [10] 4208-4226 (1970).

[156] J.L. Wise and L.C. Chhabildas, "Laser Interferometer Measurements of Refractive Index in Shock-Compressed Materials," in *Shock Compression of Condensed Matter*, Spokane, WA, 22-26 July 1985, edited by Y.M. Gupta, pp. 441-444 (1986).

[157] J.R. Asay and L.M. Barker, "Interferometric Measurement of Shock-Induced Internal Particle Velocity and Spatial Variations of Particle Velocity," *Journal of Applied Physics* **45**, [6] 2540-2546 (1974).

[158] F. Bauer, "Method and Device for Polarizing Ferroelectric Materials," USA Patent No. 4,611,260 (9 September 1986).

[159] F. Bauer, "Device for Polarizing Ferroelectric Materials," USA Patent No. 4,684,337 (4 August 1987).

[160] M.U. Anderson and D.E. Wackerbarth, "Technique and Data Analysis for Impact-Loaded Piezoelectric Polymers (PVDF)," Sandia National Laboratories Report No. SAND88-2327, (1988).

[161] J.L. Jordan, R.D. Dick, L. Ferranti and N.N. Thadhani, "Equation of State of Aluminum - Iron Oxide - Epoxy Composite," *Journal of Applied Physics* **101**, 093520 (2007).

[162] J.L. Jordan, R.D. Dick, L. Ferranti, N.N. Thadhani, R.A. Austin, D.L. McDowell and D.J. Benson, "Equation of State of Aluminum - Iron Oxide ($Fe_2O_3$) - Epoxy Composite: Modeling and Experiment," in *Shock Compression of Condensed Matter*, Baltimore, Maryland, 31 July - 5 August 2005, edited by M.D. Furnish, M. Elert, T.P. Russell and C.T. White (American Institute of Physics), Vol. **845**, pp. 157-160 (2006).

[163] M.U. Anderson, Sandia National Laboratories, Albuquerue, NM, personal communication (2003).

[164] D.E. Wackerbarth, M.U. Anderson and R.A. Graham, "PVDF STRESS: A PC-Based Computer Program to Reduce Bauer PVDF Stress-Rate Gauge Data," Sandia National Laboratories Report No. SAND92-0046, (1992).

[165] D. E. Wackerbarth, Windows 95/98/2000/NT 4.0/XP "PlotData" (Sandia National Laboratories, Albuquerque, New Mexico, 2004).

[166] T. Rumbaugh, DRS Data & Imaging Systems, Inc., San Jose, CA, personal communication (2002).

[167] E.E Underwood, Quantitative Stereology, (Addison-Wesley Publishing Company, Reading. Massachusetts, 1970)

[168] C.A. May and Y. Tanakan, Epoxy Resins Chemistry and Technology, (Marcel Dekker, Inc., New York, 1973).

[169] S. Biwa, S. Idekoba and N. Ohno, "Wave Attenuation in Particulate Polymer Composites: Independent Scattering/Absorption Analysis and Comparison to Measurements," *Mechanics of Materials* **34**, 671-682 (2002).

[170] R.M. Cornell and U. Schwertmann, The Iron Oxides: Structure, Properties, Reactions, Occurences and Uses, 2nd ed. (WILEY-VCH Verlag GmbH & Co., KGaA, Weinheim, 2003)

[171] E.A. Turi, Thermal Characterization of Polymeric Materials, (Academic Press, New York, New York, 1997), Vol. **2**.

[172] L.H. Lee, "Mechanisms of Thermal Degradation of Phenolic Condensation Polymers II: Thermal Stability and Degradation Schemes of Epoxy Resins," *Journal of Polymer Science: Part A* **3**, 859-882 (1965).

[173] L. Barral, J. Cano, J. Lopez, I. Lopez-Bueno, P. Nogueira, M.J. Abad and C. Ramirez, "Decomposition Behavior of Epoxy-Resin Systems Cured by Diamines," *European Polymer Journal* **36**, 1231-1240 (2000).

[174] K.S. Chen, R.Z. Yeh and C.H. Wu, "Kinetics of Thermal Decomposition of Epoxy Resin in Nitrogen-Oxygen Atmosphere," *Journal of Environmental Engineering* **123**, [10] 1041-1046 (1997).

[175] D. Adolf, "Measurement Techniques for Evaluating Encapsulant Thermophysical Properties During Cure," Sandia National Labortories Report SAND96-1458, (1996).

[176] P.J. Flory, Principles of Polymer Chemistry, (Cornell University Press, Ithaca, New York, 1953)

[177] J.J. Aklonis and W.J. MacKnight, Introduction to Polymer Viscoelasticty, 2nd ed. (John Wiley & Sons, New York, New York, 1983)

[178] L.E. Nielsen and R.F. Landel, Mechanical Properties of Polymers and Composites, 2nd ed. (Marcel Dekker, Inc., New York, New York, 1994)

[179] K. L. Johnson, Contact Mechanics, (Cambridge University Press, Cambridge, UK, 1987)

[180] W.C. Oliver and G.M. Pharr, "An Improved Technique for Determining Hardness and Elastic Modulus Using Load and Displacement Sensing Indentation Experiments," *Journal of Materials Research* **7**, 1564-1583 (1992).

[181] D. Tabor, The Hardness of Metals, in *Oxford Classical Series* (Oxford University Press, Oxford, 2000).

[182] P.C. Yang, H. Sue and M. T. Bishop, Crazing in Intrinsically Tough-High-Performance Thermoset Resins, in *Polymer Toughening*, edited by C.B. Arends (Marcel Dekker, Inc., New York, 1996), pp. 113-130.

[183] W.J. Cantwell and A.C. Roulin-Moloney, Fractography and Failure Mechanisms of Unfilled and Particulate Filled Epoxy Resins, in *Fractography and Failure Mechanisms of Polymers and Composites*, edited by A.C. Roulin-Moloney (Elsevier Applied Science, New York, NY, 1989), pp. 233-290.

[184] S. McGee and R.L. McGullough, "Combining Rules for Predicting the Thermoelastic Properties of Particulate Filled Polymers, Polymers, Polyblends, and Foams," *Polymer Composites* **2**, [4] 149-161 (1981).

[185] E. Plati and J.G. Williams, "The Determination of the Fracture Parameters for Polymers in Impact," *Polym. Eng. Sci.* **15**, [6] 470-477 (1975).

[186] M.W. Birch and J.G. Williams, "The Effect of Rate on the Impact Fracture Toughness of Polymers," *International Journal of Fracture* **14**, 69-84 (1978).

[187] R.J. Young and P.A. Lovell, Introduction to Polymers, 2nd ed. (Chapman and Hall, New York, New York, 1991)

[188] W.D. Callister, Materials Science and Engineering: An Introduction, 5th ed. (John Wiley & Sons, Inc., New York, New York, 2000)

[189] D.K. Felbeck and A.G. Atkins, Strength and Fracture of Engineering Solids, (Prentice-Hall, Inc., Englewood Cliffs, NJ, 1983)

[190] A.J. Kinloch and R.J. Young, Fracture Behavior of Polymers, (Elsevier Applied Science Publishers Ltd., New York, New York, 1985)

[191] S.L. Kim, M.D. Skibo, J.A. Manson, R.W. Hertzberg and J. Janiszewski, "Tensile, Impact and Fatigue Behavior of an Amine-Cured Epoxy Resin," *Polym. Eng. Sci.* **18**, [14] 1093-1100 (1978).

[192] L.J Broutman and F.J. McGarry, "Fracture Surface Work Measurements on Glassy Polymers by a Cleavage Technique II: Effects of Crosslinking and Preorientation," *J. Appl. Polym. Sci.* **9**, 609-626 (1965).

[193] R.W. Hertzberg, Deformation and Fracture Mechanics of Engineering Materials, 4th ed. (John Wiley & Sons, Inc., New York, New York, 1996)

[194] T.L. Anderson, Fracture Mechanics: Fundamentals and Applications, 2nd ed. (CRC Press, New York, 1994)

[195] J.B. Hawkyard, "A Theory for the Mushrooming of Flat-Ended Projectiles Impinging on a Flat Rigid Anvil, Using Energy Considerations," *Int. J. Mech. Sci.* **11**, 313-333 (1969).

[196] J.B. Hawkyard, D. Eaton and W. Johnson, "The Mean Dynamic Yield Strength of Copper and Low Carbon Steel at Elevated Temperatures from Measurements of the "Mushrooming" of Flat-Ended Projectiles," *Int. J. Mech. Sci.* **10**, 929-948 (1968).

[197] R. Balendra and F.W. Travis, "An Examination of the Double-Frustum Phenomenon in the Mushrooming of Cylinderical Projectiles Upon High-Speed Impact with Rigid Anvil," *Int. J. Mech. Sci.* **13**, 495-505 (1971).

[198] R.H. Loeppert and E.T. Clarke, "Reactions of $Fe^{2+}$ and $Fe^{3+}$ in Calcareous Soils," *Journal of Plant Nutrition and Soil Science* **7**, 149-163 (1984).

[199] R.H. Loeppert and L.R. Hossner, "Reactions of Fe2+ and Fe3+ with Calcite," *Clays and Clay Minerals* **32**, 213-222 (1984).

[200] R.H. Loeppert, L.R. Hossner and P.K. Amin, "Formation of Ferric Oxyhydroxides From Ferrous and Ferric Perchlorate in Stirred Calcareous Systems," *Journal of Soil Science Society of America* **48**, 677-683 (1984).

[201] J.G. Noyes, J. Asher, O.C. Jones and G.F. Phillips, Kaye and Laby Table of Physical and Chemical Constants, (National Physical Laboratory, Essex, England, 1995).

[202] J.J. Manson, A.J. Rosakis and G. Ravichandran, "On the Strain and Strain Rate Dependence of the Fraction of Plastic Work Converted to Heat: An Experimental Study Using High Speed Infrared Detector and the Kolsky Bar," *Mechanics of Materials* **17**, [135-145] (1994).

[203] D. Rittel, "On the Conversion of Plastic Work to Heat During High Strain Rate Deformation of Glassy Polymers," *Mechanics of Materials* **31**, 131-139 (1999).

[204] A. Trojanowski, C. Ruiz and J. Harding, "Thermomechanical Properties of Polymers at High Rates of Strain," *Journal de physique IV* **7**, [C3] 447-452 (1997).

[205] S.C Chou, K.D. Robertson and J.H. Rainey, "The Effect of Strain Rate and Heat Developed During Deformation on the Stress-Strain Curve of Plastics," *Experimental Mechanics* **13**, [10] 422-432 (1973).

[206] J.A. Charest and C.S. Lynch, "The Response of $PVF_2$ Stress Gauges to Shock Wave Loading," in *Shock Compression of Condensed Matter*, Albuquerque, NM, 14-17 August 1989, edited by S.C. Schmidt, J.N. Johnson and L.W. Davison (American Institute of Physics), pp. 797-800 (1990).

[207] L.M. Lee, D.A. Hyndman, R.P. Reed and F. Bauer, "PVDF Applications in Shock Measurements," in *Shock Compression of Condensed Matter*, Albuquerque, NM, 14-17 August 1989, edited by S.C. Schmidt, J.N. Johnson and L.W. Davison (American Institute of Physics), pp. 821-824 (1990).

[208] L.M. Moore and R.A. Graham, "Response of Standardized PVDF Piezoelectric Polymers Gauges to Direct Shock Pressures Between 8 and 32 GPa," in *Shock Compression of Condensed Matter*, Albuquerque, NM, 14-17 August 1989, edited by S.C. Schmidt, J.N. Johnson and L.W. Davison (American Institute of Physics), pp. 813-816 (1990).

[209] L. Soulard and F. Bauer, "Applications of Standardized PVDF Shock Gauges for Shock Pressure Measurements in Explosives," in *Shock Compression of Condensed Matter*, Albuquerque, NM, 14-17 August 1989, edited by S.C. Schmidt, J.N. Johnson and L.W. Davison (American Institute of Physics), pp. 817-820 (1990).

[210] R.V. Hodges and L.E. McCoy, "Comparison of Polyvinylidene Fluoride (PVDF) Gauge Shock Pressure Measurements with Numerical Shock Code Calculations," *Propellants, Explosives, Pyrotechnics* **24**, 353-359 (1999).

[211] F. Birch, "Finite Strain Isotherm and Velocities for Single-Crystal and Polycrystalline NaCl at High Pressures and 300 K," *Journal of Geophysical Research* **83**, [B3] 1257-1268 (1978).

[212] J.E. Reaugh and E.L. Lee, "Shock Hugoniot Behavior of Mixed Phases with Widely Varying Shock Impedances," in *Shock Compression of Condensed Matter*, Amherst, Massachusetts, 27 July - 1 August 1997, edited by S.C. Schmidt, D.P. Dandekar and J.W. Forbes (American Institute of Physics), Vol. **429** (1998).

[213] D.A. Crawford, R.G. Schmitt and R.J. Butler, "Spymaster User's Guide" (Sandia National Laboratories, Albuquerque, New Mexico, 2005).

[214] D.A. Crawford, P.A. Taylor and R.G. Schmitt, "CTH Course Notes" (Sandia National Laboratories, Albuquerque, New Mexico, 2006).

[215] R.L. Bell, M.R. Baer, R.M. Brannon, D.A. Crawford, M.G. Elrick, E.S. Hertel Jr., R.G. Schmitt, S.A. Silling and P.A. Taylor, "CTH User's Manual and Input Instructions" (Sandia National Laboratories, Albuquerque, New Mexico, 2005).

[216] E. R. Matheson and P.A. Taylor, "CTH Reference Manual: The Viscous-Elastic-Plastic (VEP) Model," Sandia National Laboratories Report SAND2001-1985, (2001).

[217] E.S. Hertel Jr. and G.I. Kerley, "Recent Improvements to the CTH EOS Package," Sandia National Laboratories Report SAND99-2340, (1999).

[218] D. J. Steinberg, S. G. Cochran and M. W. Guinan, "A Constitutive Model for Metals Applicable at High-Strain Rate," *Journal of Applied Physics* **51**, [3] 1498-1504 (1980).

[219] E.M. Olsen, J.T. Rosenberg, J.D. Kawamoto, C.F. Lin and L. Seaman, "XDT Investigations by Computational Simulations of Mechanical Response Using a New Viscous Internal Damage Model," in *11th International Detonation Symposium*, Snowmass, Colorado, 30 August - 4 September 1998, (The Office of Naval Research, U.S. Navy), Vol. **11**, pp. 170-178 (1998).

[220] E.R. Matheson and J.T. Rosenberg, "A Mechanistic Study of Delayed Detonation in Impact Damaged Solid Rocket Propellant," in *Shock Compression of Condensed Matter*, Atlanta, Georgia, 24-29 June 2001, edited by M.D. Furnish, N.N. Thadhani and Y. Horie, Vol. **620**, pp. 464-467 (2002).

[221] L. Seaman, J.W. Simons, D.C. Erlich, E. Olsen, J.T. Rosenberg and E. Matheson, "Development of a Viscous Internal Damage Model for Energetic Materials Based on the BFRACT Microfracture Model," in *11th International Detonation Symposium*, Snowmass, Colorado, 30 August - 4 September 1998, (The Office of Naval Research, U.S. Navy), Vol. **11**, pp. 632-639 (1998).

[222] E.R. Matheson, "CTH Reference Manual: The Tensile Damage & Distension (TDD) Model," Sandia National Laboratories Report SAND01-XXX, (2001).

[223] R.J. Smyth and D.L. Bish, Crystal Structures and Cation Sites of Rock-Forming Minerals, (Allen & Unwin, London, England, 1988)

[224] J. Cochran, K. Hurysz, K.J. Lee and T. Sanders, "Extrusion and Thermo-chemical Processing of Layered Linear Cellular Alloys," *Materials Science Forum* **426-432**, 4295-4300 (2003).

[225] J.L. Clark, "Dynamic and Quasi-Static Mechanical Properties of Fe-Ni Alloy Honeycomb," Doctoral Thesis, Georgia Institute of Technology, 2004.

# VITA

Louis Ferranti, Jr. was born August 26, 1973 in Passaic, New Jersey. After graduating from Lyndhurst High School in New Jersey, he attended Bergen Community College where he pursued an Associate of Science degree in Engineering Science and graduated in the spring of 1996. Louis then attended New Jersey Institute of Technology (NJIT) and graduated Magma Cum Laude with a Bachelor of Science in Mechanical Engineering, spring of 1998. After working in the engineering department of a concrete form design company, he began attending Georgia Institute of Technology in Atlanta, Georgia in August of 1999. Louis graduated with a Master of Science degree in Materials Science and Engineering in the fall of 2001 with a thesis entitled "Processing and Characterization of Microstructurally Biased Two-Phase Titanium Diboride/Alumina Ceramic ($TiB_2$+$Al_2O_3$)." With his Masters degree, he began working at the Air Force Research Laboratory (AFRL) in the Energetic Materials branch of the Munitions Directorate (MNME) located at Eglin AFB, Florida for approximately one year. He then returned to Georgia Institute of Technology in pursuit of a Doctor of Philosophy degree in Materials Science and Engineering and participated in a graduate research internship, sponsored by the AFRL, throughout his studies. Louis earned his Doctor of Philosophy degree in October of 2007, and the results of this work have been published in three journal articles and five conference proceedings. He has authored seven and co-authored nine publications about his research, as well as presented his findings at five conferences.